FULL-SCALE CYCLIC EXPERIMENTS OF COMPOSITE MOMENT-RESISTING FRAME CONNECTIONS

Jerome F. Hajjar
Department of Civil Engineering
University of Minnesota
Minneapolis, Minnesota

Roberto T. Leon
School of Civil and Environmental Engineering
Georgia Institute of Technology
Atlanta, Georgia

Michael A. Gustafson
Ellerbe Becket
Minneapolis, Minnesota

Carol K. Shield
Department of Civil Engineering
University of Minnesota
Minneapolis, Minnesota

A Report from the National Earthquake Hazards Reduction Program
Northridge Earthquake Research Investigation

National Science Foundation Grant No. CMS-9416363

Report No. ST 98-02
Department of Civil Engineering
University of Minnesota
Minneapolis, Minnesota 55455

Report No. SEM 98-02
School of Civil and Environmental Engineering
Georgia Institute of Technology
Atlanta, Georgia 30332

March 1998

Abstract

The main objective of this research is to determine if the failures of steel moment-resisting frame connections during the Northridge, California earthquake of January 17, 1994, were due primarily to various structural characteristics of the connection rather than to problems related strictly to material properties. Structural phenomena which may have contributed to the failures include the presence of composite floor slabs, the location of the shear tab along the girder cross section, the placement of a backup bar at the outside surface of the bottom girder flange, local bending and shearing of the bottom girder flange near the access hole, and the potential triaxial tensile strain or stress state caused by restraint in the connection region.

To accomplish the objectives of the research, both an experimental and a corroborating computational research program were undertaken. The experimental research entailed the testing of three full-scale specimens representing interior steel moment-resisting frame subassemblies subjected to cyclic, quasi-static loading as well as to column axial tension loading. Two of the specimens had composite floor slabs (having 35% and 55% composite action, i.e., partially composite), while the other specimen had bare steel girders. The computational research included three-dimensional geometrically and materially nonlinear continuum finite element analyses of the test specimens. Two computational models were employed, including a model of the bare steel girder specimen and of the composite girder specimen.

All six connections tested in this research failed in the region of the bottom girder flange by fracture, three by a brittle failure at the weld-column interface and three by a low cycle fatigue fracture of the base metal of the girder flange emanating from the root of the access hole. In addition, the bottom region of the connections in the composite specimens generally sustained significantly more damage compared to the top region (as evidenced

by local flange buckling and extensive plastification at the bottom flange, and by the relative strain levels of the top and bottom flange regions).

The connections which failed by brittle fracture did so at an interstory drift of 1.5%, with plastic rotations in the range of 6 to 8 milliradians, and with moment strengths well below predicted moment strengths [M_p for the bare steel specimen and a nominal moment strength for composite beams as computed as per (AISC, 1993) for the composite specimens, both based on actual measured material properties]. The connections which failed by a low cycle fatigue fracture achieved 3.0% drift prior to fracture, but they sustained at most 3 cycles at this drift level, and they achieved plastic connection rotations of at most 25 milliradians.

Both the experimental and computational results clearly demonstrate a significant increase in straining in the bottom flange region of the connections, due to the effect of composite floor slabs. As indicated in the experimental results, the strains near the bottom access hole connection regions in the girders of the composite specimens reached levels that were up to six times higher than those near the top access hole connection regions. The neutral axis also shifted by approximately six to eight inches along the girder cross section of the composite girders during positive bending, located at a distance of 13.5" from the column face.

It is clearly shown in this research that steel moment-resisting connections are not symmetric connections, and that their inherent asymmetry may result in the focusing of large strains, and therefore ultimate failure, at the bottom flange region of these types of connections. Although composite floor slabs are understandably not included in current design methodologies of frame members in steel lateral-resisting systems, it is prudent to establish a connection design methodology which, at a minimum, takes into account the asymmetries in the connection region due to the presence of a concrete floor slab.

Acknowledgments

Funding for this research was provided by the National Science Foundation (Grant No. CMS-9416363) under Drs. Shih-Chi Liu and M. P. Singh; the American Institute of Steel Construction; the Federal Emergency Management Agency through the SAC Joint Venture; the University of Minnesota; and the Georgia Institute of Technology. SAC is a partnership of the Structural Engineers Association of California, the Applied Technology Council, and California Universities for Research in Earthquake Engineering. In-kind funding and materials were provided by LeJeune Steel Company, Minneapolis, Minnesota; L. H. Sowles Company, Minneapolis, Minnesota; Braun Intertec, Minneapolis, Minnesota; Lincoln Electric Company, Cleveland, Ohio; Nucor-Yamato Steel Company, Blytheville, Arkansas; and Northwestern Steel Company, Sterling, Illinois. Supercomputing resources were provided by the Minnesota Supercomputing Institute. The authors gratefully acknowledge this support. The forensic investigation of the Borax corporate headquarters was conducted by EQE International Inc., under the guidance of David P. O'Sullivan. The authors would also like to thank the following for their assistance in conducting the experiments and analyses on this project: Dr. Theodore V. Galambos, Dr. Gabriel P. Forcier, Lawrence A. Kloiber, Paul M. Bergson, Patrick C. Carlson, Brett C. Gourley, and Thomas J. Oberhofer. Any opinions, findings, and conclusions or recommendations expressed in this material are those of the authors and do not necessarily reflect the views of the sponsors.

Table of Contents

Abstract i

Acknowledgments iii

Table of Contents v

List of Figures xi

List of Tables xxiii

1 Introduction 1

1.1 Pre-Northridge Special Moment-Resisting Frame Connections 3

1.2 Damage to the Borax Corporate Headquarters Building 5

1.3 Previous Research on Pre-Northridge Composite MRF Connections 11

1.3.1 Performance of Composite MRF Subassemblages 11

1.3.2 SMRF Connection Failures Due to Structural and Metallurgical Phenomena 12

1.4 Research Objectives 16

1.5 Research Approach 17

1.6 Organization of Report 18

2 Experimental Procedure 19

2.1 Design and Description of Specimens 19

2.1.1 Girder and Column Design 22

2.1.2 Connection Design 24

2.1.3 Composite Girder Design 30
2.2 Material Properties 33
2.2.1 Steel Properties 33
2.2.2 Steel Material Hardness Properties 36
2.2.3 Concrete Properties 40
2.3 Monotonic and Cyclic Loading Systems 41
2.3.1 Structural Laboratory 41
2.3.2 Load Frame Assembly 43
2.3.3 Load Pin Assemblies 43
2.4 Instrumentation 46
2.4.1 Inclinometer 46
2.4.2 Linear Variable Differential Transformers 48
2.4.3 Strain Gages 50
2.4.4 Acoustic Emission Transducers 62

3 Specimen Load Histories and General Behavior 65
3.1 Load Histories of Specimens 68
3.2 Summary of Performance of the Specimens 71

4 Validation of Experimental Results 81
4.1 Effects of Load Pin Friction 81
4.2 Girder Tip Deflection Components 82
4.3 Actual, Calculated, and Equilibrium Girder Moments and Strains 92

5 Interpretation of Results 104
5.1 The Effect of Composite Floor Slabs 105
5.1.1 Strain Distribution Along the Girder Cross Section 106
5.1.2 Comparison of Straining at Top and Bottom Connection Regions 124
5.1.3 Force Transfer Behavior at the Column-Concrete Slab Interface..135

5.1.4 Comparison of Plastification at the Top and Bottom Connection Regions 142
5.2 The Effect of Backup Bars 146
5.2.1 Connection Performance and Failure Mechanisms 146
5.2.2 Acoustic Emission Activity Near Brittle Failure Zones 151
5.2.3 The Effects of Localized Girder Flange Bending and Shearing 153
5.2.4 Effects of Other Structural and Metallurgical Phenomena 157
5.3 The Effect of a Triaxial State of Stress Near the Bottom CJP Weld 158
5.4 Effects of Strain Concentrations at the Root of the Access Hole 161
5.4.1 Connection Performance and Failure Mechanisms 163
5.4.2 Strain Concentrations Near the Root of the Bottom Access Hole. 167
5.4.3 Acoustic Emission Activity Near Low-Cycle Fatigue Connection Failures 169

6 Conclusions 172
6.1 Classification of Various Structural Phenomena Contributing to Connection Failure 174
6.2 The Effect of Various Structural Phenomena on the Performance of the Specimens 175
6.2.1 The Presence of Composite Floor Slabs 175
6.2.2 The Location of the Shear Tab Along the Girder Cross Section 177
6.2.3 The Existence of Bottom Backup Bars 177
6.2.4 The Restraint of Critical Connection Elements 178
6.2.5 Construction Limitations and Metallurgical Phenomena 180
6.3 Closing Remarks 181

Appendix 182
A Effective Moment of Inertia 180
B Girder-to-Column Plastic Moment and Rotation 187

B.1 Computed Girder Moment Strength.....187
B.2 Experimental Girder Moment Strength.....192
B.3 Experimental Girder-to-Column Moment-Rotation..... 193
B.3.1 Uncorrected Girder-to-Column Moment-Rotation..... 193
B.3.2 Girder-to-Column Moment-Plastic Rotation..... 198
B.3.3 Back-Calculated Girder-to-Column Moment-Plastic Rotation.....202
C Panel Zone Shear Distortion 211
C.1 Calculation of Panel Zone Shear Distortion.....212
C.2 Moment-Panel Zone Shear Distortion Curves..... 213
D Structural Idealization of Specimens..... 217
D.1 Modeling of Reaction Components and External Loads..... 217
D.2 Modeling of Geometric and Material Properties..... 219
E Effects of Load Pin Resistance..... 221
E.1 Calculation of Load and Strain Moments.....221
E.2 Comparison of Results..... 225
F Girder Tip Deflection Components..... 237
F.1 Panel Zone Shear Distortion Component..... 237
F.2 Girder Flexure Deformation Component.....240
F.3 Column Flexure Deformation Components..... 241
F.3.1 Pinned Column Supports.....242
F.3.2 Fixed Column Supports.....245
F.4 Girder-to-Column Rotation Component.....248
F.5 Girder Shear Deformation Component.....249
F.6 Load Frame Deformation Component.....253
F.7 Measured Joint Rotation.....255
F.8 Verification of Calculated Girder Tip Deflection Components..... 256
F.8.1 Verification of Girder and Column Flexural Deformation Equations..... 257
F.8.2 Verification of Load Frame Deformation Equations.....259

F.8.3 Second-Order Effects of Column Axial Tension on Column Flexure Behavior....262
F.9 Discussion of Results....263
G Calculation of Girder Moments and Strains....288
G.1 Procedure for Calculating Girder Moments and Strains....288
G.2 Comparison of Results....300
G.2.1 Effects of a Nonlinear Strain Distribution....302
G.2.2 Measured Concrete Strains....312
G.2.3 Effects of Composite Slip....313
G.2.4 Effects of Concrete Modulus Variability....319
G.2.5 Effects of Concrete Resistance to Tensile Loading....320
H Specimen Event Histories: Strain and Acoustic Emission Activity Near the Bottom Connection Regions....326
H.1 Connection Strain Behavior and AE Activity Prior to Failure (Specimen 1)....328
H.2 Connection Strain Behavior and AE Activity At Failure (Specimen 1)....342
H.3 Connection Strain Behavior and AE Activity Prior to Failure (Specimen 2)....346
H.4 Connection Strain Behavior and AE Activity At Failure (Specimen 2)....357
H.5 Connection Strain Behavior and AE Activity Prior to Failure (Specimen 3)....362
H.6 Connection Strain Behavior and AE Activity At Failure (Specimen 3)....378
I Effects of a Triaxial State of Stress....382
I.1 Calculation of the Normal Stresses of Elements A and B....382
I.2 Approximation of Uniaxial and Triaxial States of Stress of Elements A and B....390

I.3 Existence of a Triaxial State of Stress..... 392

I.5 Non-Ductile Connection Failure Due to a Triaxial State of Stress .. 393

J List of Symbols..... 410

K List of Parameters..... 416

References..... 421

List of Figures

1.1 Typical Girder-to-Column Connection [after (Hajjar et al., 1995)] 2
1.2 Damage Type C2* (Girder Flange Pull-Out From Column Flange) 6
1.3 Damage Type C2 (Girder Flange Pull-Out From Column Flange) 6
1.4 Damage Type C4* (U-Shaped Column Flange Fracture) 7
1.5 Damage Type C4 (Column Flange Fracture) 8
1.6 Damage Types P4 & P6 (Column Panel Zone Fracture) 8
1.7 Damage Type W2 (CJP Weld Metal Fracture) 8

2.1 Borax Corporate Headquarters (Typical Floor Plan) [after (Hajjar et al., 1995)]. 20
2.2 West N-S Moment Frame Elevation [after (Hajjar et al., 1995)] 21
2.3 Specimen 1 23
2.4 Specimens 2 and 3 23
2.5 Elevation I: Connection Dimensions 25
2.6 Elevation I: Connection Elements 26
2.7 Elevation I: Connection Welds 26
2.8(a) Elevation I: View Locations of South Connection 27
2.8(b) Elevation I: View Locations of South Connection 27
2.9 Section A-A: Top of Column 28
2.10 Elevation III: Top Access Hole Region 29
2.11 Elevation IV: Bottom Access Hole Region 29
2.12 Section B-B: Composite Girder Cross Section 31
2.13 Elevation III: Shear Stud Locations 31
2.14 Rockwell Hardness Test Locations (East Girder Cross Section of Specimen 3) . 38
2.15 Hardness Distribution (East Girder Cross Section of Specimen 3) 39
2.16 Load Frame Assembly With Specimen 42
2.17 Section X-X: Top View of Load Frame and Top Load Pin Assemblies 44
2.18 Lateral-Torsional Buckling Braces 45
2.19 Bottom Load Pin Assembly 45
2.20 LVDT Locations of North Connection Region 47
2.21 LVDT Locations of South Connection Region 47
2.22 Elevation III: LVDT Locations of South Connection Region 49
2.23 Elevation IV: LVDT Locations of South Connection Region 49
2.24 Strain Gages of North Connection Region 52
2.25 Strain Gages of South Connection Region 52
2.26 Section B-B: Strain Gages of West Girder Cross Section 53
2.27 Section C-C: Strain Gages of East Girder Cross Section 53
2.28 Section D-D: Strain Gages of West Girder Cross Section 54
2.29 Section E-E: Strain Gages of East Girder Cross Section 54
2.30 Section F-F: Strain Gages of Panel Zone Cross Section 55
2.31 Section G-G: Strain Gages of Bottom of Bottom Girder Flanges 55
2.32 Section H-H: Strain Gages of Top of Bottom Girder Flanges 55

2.33 Section I-I: Strain Gages of Bottom of Top Girder Flanges 55
2.34 Strain Gages of Concrete Slab (Plan View) 56
2.35 AE Transducer Locations (East Connection of Specimen 1) 63
2.36 AE Transducer Locations (West Connection of Specimen 1) 63
2.37 AE Transducer Locations (East Connection of Specimens 2 and 3) 64
2.38 AE Transducer Locations (West Connection of Specimen 3) 64

3.1 Typical Interior Moment Frame (Reverse Curvature Bending) 66
3.2 Elevation III: Test Specimen (Reverse Curvature Bending) 66
3.3 Load History of Specimen 1 68
3.4 Load History of Specimen 2 69
3.5 Load History of Specimen 3 70
3.6 Girder-to-Column Moment-Rotation Curve (West Girder of Specimen 1) 73
3.7 Fracture of Bottom CJP Weld (West Girder of Specimen 1) 73
3.8 Girder-to-Column Moment-Rotation Curve (East Girder of Specimen 2) 74
3.9 Fracture of Bottom CJP Weld (East Girder of Specimen 2) 74
3.10 Girder-to-Column Moment-Rotation Curve (West Girder of Specimen 2) 75
3.11 Pull Out-Type Failure of Column Flange (West Girder of Specimen 2) 75
3.12 Girder-to-Column Moment-Rotation Curve (East Girder of Specimen 1) 76
3.13 Rupture of Bottom Girder Flange (East Girder of Specimen 1) 76
3.14 Girder-to-Column Moment-Rotation Curve (East Girder of Specimen 3) 77
3.15 Rupture of Bottom Girder Flange (East Girder of Specimen 3) 77
3.16 Girder-to-Column Moment-Rotation Curve (West Girder of Specimen 3) 78
3.17 Rupture of Bottom Girder Flange (East Girder of Specimen 3) 78

4.1 Strain Moment vs. Load Moment (Top Column Section of Specimen 3) 83
4.2 Strain Moment vs. Load Moment (Bottom Column Section of Specimen 3) 83
4.3 Strain Moment vs. Load Moment (Top Column Section of Specimen 1) 84
4.4 Strain Moment vs. Load Moment (Bottom Column Section of Specimen 1) 84
4.5 Strain Moment vs. Load Moment (Top Column Section of Specimen 2) 85
4.6 Strain Moment vs. Load Moment (Bottom Column Section of Specimen 2) 85
4.7 Strain Moment vs. Load Moment (Top Column Section of Specimen 3) 86
4.8 Strain Moment vs. Load Moment (Bottom Column Section of Specimen 3) 86
4.9 Actual vs. Calculated Girder Tip Deflection (West Girder of Specimen 1) 89
4.10 Actual vs. Calculated Girder Tip Deflection (West Girder of Specimen 1) 89
4.11 Actual vs. Calculated Girder Tip Deflection (West Girder of Specimen 2) 90
4.12 Actual vs. Calculated Girder Tip Deflection (West Girder of Specimen 2) 90
4.13 Actual vs. Calculated Girder Tip Deflection (West Girder of Specimen 3) 91
4.14 Actual vs. Calculated Girder Tip Deflection (West Girder of Specimen 3) 91
4.15 Girder and Panel Zone Girder Tip Deflection Components (West Girder of Specimen 3) 93
4.16 Girder and Panel Zone Girder Tip Deflection Components (West Girder of Specimen 3) 93

4.17 Column, Load Frame, and Connection Girder Tip Deflection Components (West Girder of Specimen 3) 94
4.18 Column, Load Frame, and Connection Girder Tip Deflection Components (West Girder of Specimen 3) 94
4.19 Force Components of the Girder Cross Section 96
4.20 Actual vs. Calculated Girder Moment (West Girder of Specimen 1) 98
4.21 Actual vs. Calculated Girder Moment (West Girder of Specimen 1) 98
4.22 Actual vs. Calculated Girder Moment (West Girder of Specimen 3) 99
4.23 Actual vs. Calculated Girder Moment (West Girder of Specimen 3) 99
4.24 Steel Girder Strain Distribution (West Girder of Specimen 1) 100
4.25 Steel Girder Strain Distribution (West Girder of Specimen 3) 100
4.26 Actual vs. Computed Concrete Strains (East Girder of Specimen 3) 101
4.27 Actual vs. Computed Concrete Strains (East Girder of Specimen 3) 101
4.28 Actual vs. Computed Concrete Strains (West Girder of Specimen 3) 103
4.29 Actual vs. Computed Concrete Strains (West Girder of Specimen 3) 103

5.1 Strain Gages Along the Steel Girder Cross Section 107
5.2 Section B-B: Strain Gages Along the Steel Girder Cross Section 107
5.3 Steel Girder Strain Distribution (East Girder of Specimen 1) 108
5.4 Steel Girder Strain Distribution (West Girder of Specimen 1) 108
5.5 Steel Girder Strain Distribution (East Girder of Specimen 1) 109
5.6 Steel Girder Strain Distribution (West Girder of Specimen 1) 109
5.7 Steel Girder Strain Distribution (East Girder of Specimen 2) 110
5.8 Steel Girder Strain Distribution (West Girder of Specimen 2) 110
5.9 Steel Girder Strain Distribution (East Girder of Specimen 2) 111
5.10 Steel Girder Strain Distribution (West Girder of Specimen 2) 111
5.11 Steel Girder Strain Distribution (East Girder of Specimen 3) 112
5.12 Steel Girder Strain Distribution (West Girder of Specimen 3) 112
5.13 Steel Girder Strain Distribution (East Girder of Specimen 3) 113
5.14 Steel Girder Strain Distribution (West Girder of Specimen 3) 113
5.15 Bare Steel Model Discretization 117
5.16 Composite Girder Specimen Model Discretization 117
5.17 Steel Girder Strain Distribution/ 0.50% Drift (Bare Steel Model vs. East and West Girders of Specimen 1) 119
5.18 Steel Girder Strain Distribution/ 1.00% Drift (Bare Steel Model vs. East and West Girders of Specimen 1) 119
5.19 Steel Girder Strain Distribution/ 0.50% Drift (Composite Model vs. East and West Girders of Specimen 2 and 3) 120
5.20 Steel Girder Strain Distribution/ 1.00% Drift (Composite Model vs. East and West Girders of Specimen 2 and 3) 120
5.21 Connection Region of Composite Specimen Model/ 3.0% Drift (Negative Girder Bending on Left; Positive Girder Bending on Right) 122
5.22 Connection Region of Composite Specimen Model/ 3.0% Drift (Negative Girder Bending on Left; Positive Girder Bending on Right) 123

5.23 Steel Girder Strain Distribution (East Girder of Specimen 3) 125
5.24 Steel Girder Strain Distribution (West Girder of Specimen 3) 125
5.25 Strain Gages of Connection Region (South View) 126
5.26 Section D-D: Strain Gages of East Connection Region 127
5.27 Section E-E: Strain Gages of West Connection Region 127
5.28 Top and Bottom Access Hole Strains (East Girder of Specimen 1) 128
5.29 Top and Bottom Access Hole Strains (West Girder of Specimen 1) 128
5.30 Top and Bottom Access Hole Strains (East Girder of Specimen 2) 129
5.31 Top and Bottom Access Hole Strains (West Girder of Specimen 2) 129
5.32 Top and Bottom Access Hole Strains (East Girder of Specimen 3) 130
5.33 Top and Bottom Access Hole Strains (West Girder of Specimen 3) 130
5.34 Girder Bottom Flange Strains (East Girder of Specimen 1) 131
5.35 Girder Bottom Flange Strains (West Girder of Specimen 1) 131
5.36 Girder Bottom Flange Strains (East Girder of Specimen 2) 132
5.37 Girder Bottom Flange Strains (West Girder of Specimen 2) 132
5.38 Girder Bottom Flange Strains (East Girder of Specimen 3) 133
5.39 Girder Bottom Flange Strains (West Girder of Specimen 3) 133
5.40 Strain Gages of Concrete Slab (Plan View of Specimens 2 and 3) 136
5.41 NW Concrete Slab Reinforcing Bars Strains (West Slab of Specimen 2) 137
5.42 NW Concrete Slab Reinforcing Bars Strains (West Slab of Specimen 2) 137
5.43 SW Concrete Slab Reinforcing Bars Strains (West Slab of Specimen 2) 138
5.44 NE Concrete Slab Reinforcing Bars Strains (East Slab of Specimen 2) 138
5.45 NE Concrete Slab Reinforcing Bars Strains (East Slab of Specimen 2) 139
5.46 SE Concrete Slab Reinforcing Bars Strains (East Slab of Specimen 2) 139
5.47 Top View of Concrete Slab-Column Interface (East Girder of Specimen 2) 140
5.48 Top View of Concrete Slab-Column Interface (West Girder of Specimen 2) 140
5.49 Top View of Concrete Slab-Column Interface (East Girder of Specimen 3) 141
5.50 Top View of Concrete Slab-Column Interface (West Girder of Specimen 3) 141
5.51 SE Connection Region (East Girder of Specimen 1) 143
5.52 NW Connection Region (West Girder of Specimen 1) 143
5.53 SE Connection Region (East Girder of Specimen 2) 144
5.54 SW Connection Region (West Girder of Specimen 2) 144
5.55 SE Connection Region (East Girder of Specimen 3) 145
5.56 SW Connection Region (West Girder of Specimen 3) 145
5.57 Girder-to-Column Moment-Rotation Curve (West Girder of Specimen 1) 148
5.58 Girder-to-Column Moment-Rotation Curve (West Girder of Specimen 1) 148
5.59 Girder-to-Column Moment-Rotation Curve (East Girder of Specimen 2) 149
5.60 Girder-to-Column Moment-Rotation Curve (East Girder of Specimen 2) 149
5.61 Girder-to-Column Moment-Rotation Curve (West Girder of Specimen 2) 150
5.62 Girder-to-Column Moment-Rotation Curve (West Girder of Specimen 2) 150
5.63 AE Event Source Location vs. Time (West Connection of Specimen 1) 152
5.64 AE Event Source Location vs. Time (East Connection of Specimen 2) 152
5.65 Elevation IV: Girder Flange Localized Bending Condition (Positive Girder Bending) 154

5.66 Elevation IV: Girder Flange Localized Shear Condition (Positive Girder Bending) 154
5.67 Strain Distribution Along Girder Axis at Top of Bottom Girder Flange-to-Column Connection (Composite Girder Specimen Model/ 3.0% Drift) 156
5.68 Elements A and B (Typical View of Bottom CJP Weld Region) 159
5.69 Normal Stresses at Elements A and B (SE Connection of Specimen 2) 161
5.70 Normal Stresses at Elements A and B (SE Connection of Specimen 3) 161
5.71 Normal Stresses at Elements A and B (SW Connection of Specimen 1) 162
5.72 Uniaxial Tensile and Triaxial 3-D Stress States Using Mohr's Circle [after (Cook and Young, 1985)] 162
5.73 Girder-to-Column Moment-Rotation Curve (East Girder of Specimen 1) 164
5.74 Girder-to-Column Moment-Rotation Curve (East Girder of Specimen 1) 164
5.75 Girder-to-Column Moment-Rotation Curve (East Girder of Specimen 3) 165
5.76 Girder-to-Column Moment-Rotation Curve (East Girder of Specimen 3) 165
5.77 Girder-to-Column Moment-Rotation Curve (West Girder of Specimen 3) 166
5.78 Girder-to-Column Moment-Rotation Curve (West Girder of Specimen 3) 166
5.79 Girder Bottom Flange Strains (East Girder of Specimen 1) 166
5.80 Girder Bottom Flange Strains (East Girder of Specimen 3) 166
5.81 Girder Bottom Flange Strains (West Girder of Specimen 3) 169
5.82 AE Event Source Location vs. Time (East Girder of Specimen 3) 170
5.83 AE Event Source Location vs. Time (West Girder of Specimen 3) 170

B.1 Composite Girder Plastic Stress Distribution (Positive Bending) [after (AISC, 1993)] 189
B.2 Composite Girder Plastic Stress Distribution (Negative Bending) [after (AISC, 1993)] 189
B.3 Load vs. Displacement (East Girder of Specimen 1) 194
B.4 Load vs. Displacement (West Girder of Specimen 1) 194
B.5 Load vs. Displacement (East Girder of Specimen 2) 195
B.6 Load vs. Displacement (West Girder of Specimen 2) 195
B.7 Load vs. Displacement (East Girder of Specimen 3) 196
B.8 Load vs. Displacement (West Girder of Specimen 3) 196
B.9 Girder Relative Rotation LVDT Configuration (North Connection Region) 197
B.10 View VII: Measured Girder-to-Column Rotation 197
B.11 Uncorrected Girder-to-Column Moment-Rotation (East Girder of Specimen 1) 199
B.12 Uncorrected Girder-to-Column Moment-Rotation (West Girder of Specimen 1) 199
B.13 Uncorrected Girder-to-Column Moment-Rotation (East Girder of Specimen 2) 200
B.14 Uncorrected Girder-to-Column Moment-Rotation (West Girder of Specimen 2) 200
B.15 Uncorrected Girder-to-Column Moment-Rotation (East Girder of Specimen 3) 201

B.16 Uncorrected Girder-to-Column Moment-Rotation (West Girder of Specimen 3) 201
B.17 Girder-to-Column Moment-Plastic Rotation (East Girder of Specimen 1) 203
B.18 Girder-to-Column Moment-Plastic Rotation (West Girder of Specimen 1) 203
B.19 Girder-to-Column Moment-Plastic Rotation (East Girder of Specimen 2) 204
B.20 Girder-to-Column Moment-Plastic Rotation (West Girder of Specimen 2) 204
B.21 Girder-to-Column Moment-Plastic Rotation (East Girder of Specimen 3) 205
B.22 Girder-to-Column Moment-Plastic Rotation (West Girder of Specimen 3) 205
B.23 Back Calculated Girder-to-Column Moment-Plastic Rotation (East Girder of Specimen 1) 207
B.24 Back Calculated Girder-to-Column Moment-Plastic Rotation (West Girder of Specimen 1) 207
B.25 Back Calculated Girder-to-Column Moment-Plastic Rotation (East Girder of Specimen 2) 208
B.26 Back Calculated Girder-to-Column Moment-Plastic Rotation (West Girder of Specimen 2) 208
B.27 Back Calculated Girder-to-Column Moment-Plastic Rotation (East Girder of Specimen 3) 209
B.28 Back Calculated Girder-to-Column Moment-Plastic Rotation (West Girder of Specimen 3) 209

C.1 Measurement of Panel Zone Shear Distortion [after (Krawlinker et al., 1971)]..211
C.2 View A: East Bottom LVDT on Panel Zone [after (Krawlinker et al., 1971)]....212
C.3 Panel Zone Shear Rotation (East Girder of Specimen 1) 214
C.4 Panel Zone Shear Rotation (East Girder of Specimen 1) 214
C.5 Panel Zone Shear Rotation (East Girder of Specimen 2) 215
C.6 Panel Zone Shear Rotation (East Girder of Specimen 2) 215
C.7 Panel Zone Shear Rotation (East Girder of Specimen 3) 216
C.8 Panel Zone Shear Rotation (East Girder of Specimen 3) 216

D.1 Actual Specimen Load Scheme 218
D.2 Structural Idealization of Specimen Loading Scheme 218

E.1 Free Body Diagram of Test Specimen 223
E.2 Elevation IV: View of Top Load Pin Assembly and Connection Region 223
E.3 Strain Moment vs. Load Moment (Top Column Section of Specimen 1) 228
E.4 Strain Moment vs. Load Moment (Bottom Column Section of Specimen 1)..... 228
E.5 Strain Moment vs. Load Moment (Top Column Section of Specimen 1) 229
E.6 Strain Moment vs. Load Moment (Bottom Column Section of Specimen 1)..... 229
E.7 Strain Moment vs. Load Moment (Top Column Section of Specimen 1) 230
E.8 Strain Moment vs. Load Moment (Bottom Column Section of Specimen 1)..... 230
E.9 Strain Moment vs. Load Moment (Top Column Section of Specimen 2) 231
E.10 Strain Moment vs. Load Moment (Bottom Column Section of Specimen 2)..... 231
E.11 Strain Moment vs. Load Moment (Top Column Section of Specimen 2) 232

E.12 Strain Moment vs. Load Moment (Bottom Column Section of Specimen 2)..... 232
E.13 Strain Moment vs. Load Moment (Top Column Section of Specimen 2) 233
E.14 Strain Moment vs. Load Moment (Bottom Column Section of Specimen 2)..... 233
E.15 Strain Moment vs. Load Moment (Top Column Section of Specimen 3) 234
E.16 Strain Moment vs. Load Moment (Bottom Column Section of Specimen 3)..... 234
E.17 Strain Moment vs. Load Moment (Top Column Section of Specimen 3) 235
E.18 Strain Moment vs. Load Moment (Bottom Column Section of Specimen 3)..... 235
E.19 Strain Moment vs. Load Moment (Top Column Section of Specimen 3) 236
E.20 Strain Moment vs. Load Moment (Bottom Column Section of Specimen 3)..... 236

F.1 Girder Tip Deflection Component Due to Panel Zone Distortion [after (Leon, 1983)] 238
F.2 Specimen Structural Idealization (Pinned Column Supports) 242
F.3 Elevation IV: Column and Panel Zone Sections B-A, C-B, and D-C 243
F.4 Specimen Structural Idealization (Fixed Column Supports) 246
F.5 Elevation IV: Column and Panel Zone Sections B-A, C-B, and D-C 246
F.6 Specimen and MTS Testing Machine 254
F.7 Structural Idealization of Load Frame Deformation 254
F.8 Computational Model of Specimen 3/ 0.25% Drift Level (Pinned Bottom Column Support/ Laterally Supported Top Column Support) 258
F.9 Computational Model of Specimen 3/ 0.25% Drift Level (Fixed Top and Bottom Column Supports)..... 258
F.10 Computational Model of Specimen 3/ 0.25% Drift Level (Fixed Bottom Column Support/ Top Support Laterally Supported With a Translational Spring)..... 260
F.11 Loaded Computational Model of Specimen 3/ 0.25% Drift Level (Pinned Bottom Column Support/ Laterally Supported Top Column Support) 260
F.12 Actual vs. Calculated Girder Tip Deflection (East Girder of Specimen 1) 267
F.13 Actual vs. Calculated Girder Tip Deflection (East Girder of Specimen 1) 267
F.14 Girder and Panel Zone Girder Tip Deflection Components (East Girder of Specimen 1) 268
F.15 Girder and Panel Zone Girder Tip Deflection Components (East Girder of Specimen 1) 268
F.16 Column, Load Frame, and Connection Girder Tip Deflection Components (East Girder of Specimen 1) 269
F.17 Column, Load Frame, and Connection Girder Tip Deflection Components (East Girder of Specimen 1) 269
F.18 Actual vs. Calculated Girder Tip Deflection (West Girder of Specimen 1) 270
F.19 Actual vs. Calculated Girder Tip Deflection (West Girder of Specimen 1) 270
F.20 Girder and Panel Zone Girder Tip Deflection Components (West Girder of Specimen 1) 271
F.21 Girder and Panel Zone Girder Tip Deflection Components (West Girder of Specimen 1) 271

F.22 Column, Load Frame, and Connection Girder Tip Deflection Components (West Girder of Specimen 1) 272
F.23 Column, Load Frame, and Connection Girder Tip Deflection Components (West Girder of Specimen 1) 272
F.24 Actual vs. Calculated Girder Tip Deflection (East Girder of Specimen 2) 273
F.25 Actual vs. Calculated Girder Tip Deflection (East Girder of Specimen 2) 273
F.26 Girder and Panel Zone Girder Tip Deflection Components (East Girder of Specimen 2) 274
F.27 Girder and Panel Zone Girder Tip Deflection Components (East Girder of Specimen 2) 274
F.28 Column, Load Frame, and Connection Girder Tip Deflection Components (East Girder of Specimen 2) 275
F.29 Column, Load Frame, and Connection Girder Tip Deflection Components (East Girder of Specimen 2) 275
F.30 Actual vs. Calculated Girder Tip Deflection (West Girder of Specimen 2) 276
F.31 Actual vs. Calculated Girder Tip Deflection (West Girder of Specimen 2) 276
F.32 Girder and Panel Zone Girder Tip Deflection Components (West Girder of Specimen 2) 277
F.33 Girder and Panel Zone Girder Tip Deflection Components (West Girder of Specimen 2) 277
F.34 Column, Load Frame, and Connection Girder Tip Deflection Components (West Girder of Specimen 2) 278
F.35 Column, Load Frame, and Connection Girder Tip Deflection Components (West Girder of Specimen 2) 278
F.36 Actual vs. Calculated Girder Tip Deflection (East Girder of Specimen 3) 279
F.37 Actual vs. Calculated Girder Tip Deflection (East Girder of Specimen 3) 279
F.38 Girder and Panel Zone Girder Tip Deflection Components (East Girder of Specimen 3) 280
F.39 Girder and Panel Zone Girder Tip Deflection Components (East Girder of Specimen 3) 280
F.40 Column, Load Frame, and Connection Girder Tip Deflection Components (East Girder of Specimen 3) 281
F.41 Column, Load Frame, and Connection Girder Tip Deflection Components (East Girder of Specimen 3) 281
F.42 Actual vs. Calculated Girder Tip Deflection (West Girder of Specimen 3) 282
F.43 Actual vs. Calculated Girder Tip Deflection (West Girder of Specimen 3) 282
F.44 Girder and Panel Zone Girder Tip Deflection Components (West Girder of Specimen 3) 283
F.45 Girder and Panel Zone Girder Tip Deflection Components (West Girder of Specimen 3) 283
F.46 Column, Load Frame, and Connection Girder Tip Deflection Components (West Girder of Specimen 3) 284
F.47 Column, Load Frame, and Connection Girder Tip Deflection Components (West Girder of Specimen 3) 284

G.1 Strain Gage Locations Along the Girder Cross Section 289
G.2 Calculated Strains Along the Girder Cross Section 292
G.3 Dimensions of Girder Cross Section 292
G.4 Force Components Along the Girder Cross Section 294
G.5 Centroids of Force Components Along the Girder Cross Section 298
G.6 Actual vs. Calculated Girder Moment (East Girder of Specimen 1) 303
G.7 Actual vs. Calculated Girder Moment (East Girder of Specimen 1) 303
G.8 Actual vs. Calculated Girder Moment (West Girder of Specimen 1) 304
G.9 Actual vs. Calculated Girder Moment (West Girder of Specimen 1) 304
G.10 Actual vs. Calculated Girder Moment (East Girder of Specimen 2) 305
G.11 Actual vs. Calculated Girder Moment (East Girder of Specimen 2) 305
G.12 Actual vs. Calculated Girder Moment (West Girder of Specimen 2) 306
G.13 Actual vs. Calculated Girder Moment (West Girder of Specimen 2) 306
G.14 Actual vs. Calculated Girder Moment (East Girder of Specimen 3) 307
G.15 Actual vs. Calculated Girder Moment (East Girder of Specimen 3) 307
G.16 Actual vs. Calculated Girder Moment (West Girder of Specimen 3) 308
G.17 Actual vs. Calculated Girder Moment (West Girder of Specimen 3) 308
G.18 Steel Girder Strain Distribution (East Girder of Specimen 1) 309
G.19 Steel Girder Strain Distribution (West Girder of Specimen 1) 309
G.20 Steel Girder Strain Distribution (East Girder of Specimen 2) 310
G.21 Steel Girder Strain Distribution (West Girder of Specimen 2) 310
G.22 Steel Girder Strain Distribution (East Girder of Specimen 2) 311
G.23 Steel Girder Strain Distribution (West Girder of Specimen 2) 311
G.24 Actual vs. Computed Concrete Strains (East Girder of Specimen 2) 314
G.25 Actual vs. Computed Concrete Strains (East Girder of Specimen 2) 314
G.26 Actual vs. Computed Concrete Strains (West Girder of Specimen 2) 315
G.27 Actual vs. Computed Concrete Strains (West Girder of Specimen 2) 315
G.28 Actual vs. Computed Concrete Strains (East Girder of Specimen 3) 316
G.29 Actual vs. Computed Concrete Strains (East Girder of Specimen 3) 316
G.30 Actual vs. Computed Concrete Strains (West Girder of Specimen 3) 317
G.31 Actual vs. Computed Concrete Strains (West Girder of Specimen 3) 317
G.32 Neutral Axis Position Along the Girder Cross Section (East Girder of Specimen 1) 323
G.33 Neutral Axis Position Along the Girder Cross Section (West Girder of Specimen 1) 323
G.34 Neutral Axis Position Along the Girder Cross Section (East Girder of Specimen 2) 324
G.35 Neutral Axis Position Along the Girder Cross Section (West Girder of Specimen 2) 324
G.36 Neutral Axis Position Along the Girder Cross Section (East Girder of Specimen 3) 325
G.37 Neutral Axis Position Along the Girder Cross Section (West Girder of Specimen 3) 325

H.1 Locations of High Elongation Strain Gages 326
H.2 Girder Bottom Flange Strains (East Girder of Specimen 1) 329
H.3 Top and Bottom Access Hole Strains (East Girder of Specimen 1) 329
H.4 Girder Bottom Flange Strains (West Girder of Specimen 1) 330
H.5 Top and Bottom Access Hole Strains (West Girder of Specimen 1) 330
H.6 Girder Bottom Flange Strains (East Girder of Specimen 1) 331
H.7 Top and Bottom Access Hole Strains (East Girder of Specimen 1) 331
H.8 Girder Bottom Flange Strains (West Girder of Specimen 1) 332
H.9 Top and Bottom Access Hole Strains (West Girder of Specimen 1) 332
H.10 Girder Bottom Flange Strains (East Girder of Specimen 1) 333
H.11 Top and Bottom Access Hole Strains (East Girder of Specimen 1) 333
H.12 AE Activity Load History (East Connection of Specimen 1) 336
H.13 AE Activity Load History (East Connection of Specimen 1) 336
H.14 AE Event Source Location vs. AE Test Time (East Connection of Specimen 1) 337
H.15 AE Event Source Location vs. AE Test Time (West Connection of Specimen 1) 337
H.16 Cumulative Events vs. Loading Increment (Specimen 1) 338
H.17 Cumulative Events vs. AE Test Time (First to fifth quarter cycles at 1.5% drift) 338
H.18 AE Source Location vs. Load and Displacement (First quarter cycle of the second cycle at 1.5% drift/ West Connection of Specimen 1) 339
H.19 AE Source Location vs. Load and Displacement (First quarter cycle of the first cycle at 1.5% drift/ East Connection of Specimen 1) 339
H.20 AE Source Location vs. Load and Displacement (First quarter cycle of the second cycle at 1.5% drift/ East Connection of Specimen 1) 340
H.21 Cumulative Events vs. AE Test Time (Third cycle at 2.0% drift and first cycle at 3.0% drift) 340
H.22 AE Source Location vs. Load and Displacement (First quarter cycle of the first cycle at 3.0% drift/ East Connection of Specimen 1) 341
H.23 AE Source Location vs. Load and Displacement (First quarter cycle of the third cycle at 3.0% drift/ East Connection of Specimen 1) 341
H.24 Girder Bottom Flange Strains (East Girder of Specimen 2) 347
H.25 Top and Bottom Access Hole Strains (East Girder of Specimen 2) 347
H.26 Girder Bottom Flange Strains (West Girder of Specimen 2) 348
H.27 Top and Bottom Access Hole Strains (West Girder of Specimen 2) 348
H.28 Girder Bottom Flange Strains (East Girder of Specimen 2) 349
H.29 Top and Bottom Access Hole Strains (East Girder of Specimen 2) 349
H.30 Girder Bottom Flange Strains (West Girder of Specimen 2) 350
H.31 Top and Bottom Access Hole Strains (West Girder of Specimen 2) 350
H.32 AE Activity Load History (East Connection of Specimen 2) 353
H.33 AE Event Source Location vs. AE Test Time (East Connection of Specimen 2) 353

H.34 Cumulative Events vs. Loading Increment (Specimen 2) 354
H.35 AE Source Location Error (Specimen 2) 354
H.36 AE Source Location vs. Load and Displacement (First quarter cycle of the first cycle at 1.5% drift/ East Connection of Specimen 2) 355
H.37 AE Source Location vs. Load and Displacement (Third quarter cycle of the first cycle at 1.5% drift/ East Connection of Specimen 2) 355
H.38 AE Source Location vs. Load and Displacement (First quarter cycle of the second cycle at 1.5% drift/ East Connection of Specimen 2) 356
H.39 AE Source Location vs. Load and Displacement (Third quarter cycle of the second cycle at 1.5% drift/ East Connection of Specimen 2) 356
H.40 Girder Bottom Flange Strains (East Girder of Specimen 3) 363
H.41 Top and Bottom Access Hole Strains (East Girder of Specimen 3) 363
H.42 Girder Bottom Flange Strains (West Girder of Specimen 3) 364
H.43 Top and Bottom Access Hole Strains (West Girder of Specimen 3) 364
H.44 Girder Bottom Flange Strains (East Girder of Specimen 3) 365
H.45 Top and Bottom Access Hole Strains (East Girder of Specimen 3) 365
H.46 Girder Bottom Flange Strains (West Girder of Specimen 3) 366
H.47 Top and Bottom Access Hole Strains (West Girder of Specimen 3) 366
H.48 Girder Bottom Flange Strains (East Girder of Specimen 3) 367
H.49 Top and Bottom Access Hole Strains (East Girder of Specimen 3) 367
H.50 Girder Bottom Flange Strains (West Girder of Specimen 3) 368
H.51 Top and Bottom Access Hole Strains (West Girder of Specimen 3) 368
H.52 AE Activity Load History (East Connection of Specimen 3) 371
H.53 AE Activity Load History (West Connection of Specimen 3) 371
H.54 AE Event Source Location vs. AE Test Time (East Connection of Specimen 3) 372
H.55 AE Event Source Location vs. AE Test Time (West Connection of Specimen 3) 372
H.56 Cumulative Events vs. Loading Increment (Specimen 3) 373
H.57 AE Source Location vs. Load and Displacement (Third quarter cycle of the first cycle at 2.0% drift/ East Connection of Specimen 3) 373
H.58 AE Source Location vs. Load and Displacement (Third quarter cycle of the second cycle at 2.0% drift/ East Connection of Specimen 3) 374
H.59 AE Source Location vs. Load and Displacement (Third quarter cycle of the third cycle at 2.0% drift/ East Connection of Specimen 3) 374
H.60 AE Source Location vs. Load and Displacement (Third quarter cycle of the first cycle at 3.0% drift/ East Connection of Specimen 3) 375
H.61 AE Source Location vs. Load and Displacement (First quarter cycle of the second cycle at 3.0% drift/ West Connection of Specimen 3) 375
H.62 AE Source Location vs. Load and Displacement (Third quarter cycle of the second cycle at 3.0% drift/ East Connection of Specimen 3) 376
H.63 AE Source Location vs. Load and Displacement (First quarter cycle of the third cycle at 3.0% drift/ West Connection of Specimen 3) 376

I.1 Elements A and B (Typical View of Bottom CJP Weld Region) 383
I.2 Element A (Specimens 1 and 2/SE Girder-to-Column Weld Region) 384
I.3 Element A (Specimen 3/SE Girder-to-Column Weld Region) 384
I.4 Mohr's Circle Diagram (Strain Gage Location) 386
I.5 Element A Strain Transformation (*x'-y'* plane) 387
I.6 Element A (Specimens 1 and 2/SE Girder-to-Column Weld Region) 388
I.7 Element A (Specimen 3/SE Girder-to-Column Weld Region) 388
I.8 Typical View of Bottom CJP Weld Region (Element B) 390
I.9 Uniaxial Tensile and Triaxial 3-D Stress States Using Mohr's Circle [after(Cook and Young, 1985)] 391
I.10 Normal Stresses at Elements A and B (SE Connection of Specimen 1) 394
I.11 Normal Stresses at Elements A and B (SE Connection of Specimen 1) 394
I.12 Normal Stresses at Elements A and B (SW Connection of Specimen 1) 395
I.13 Normal Stresses at Elements A and B (SW Connection of Specimen 1) 395
I.14 Normal Stresses at Elements A and B (SE Connection of Specimen 2) 396
I.15 Normal Stresses at Elements A and B (SE Connection of Specimen 2) 396
I.16 Normal Stresses at Elements A and B (SE Connection of Specimen 3) 397
I.17 Normal Stresses at Elements A and B (SE Connection of Specimen 3) 397
I.18 Normal Stresses at Elements A and B (SW Connection of Specimen 3) 398
I.19 Normal Stresses at Elements A and B (SW Connection of Specimen 3) 398
I.20 Normal Strains at Element A (SE Connection of Specimen 1) 399
I.21 Normal Strains at Element A (SE Connection of Specimen 1) 399
I.22 Normal Strains at Element A (SW Connection of Specimen 1) 400
I.23 Normal Strains at Element A (SW Connection of Specimen 1) 400
I.24 Normal Strains at Element A (SE Connection of Specimen 2) 401
I.25 Normal Strains at Element A (SE Connection of Specimen 2) 401
I.26 Normal Strains at Element A (SE Connection of Specimen 3) 402
I.27 Normal Strains at Element A (SE Connection of Specimen 3) 402
I.28 Normal Strains at Element A (SW Connection of Specimen 3) 403
I.29 Normal Strains at Element A (SW Connection of Specimen 3) 403
I.30 Shear Stresses at Elements A and B (SE Connection of Specimen 1) 405
I.31 Shear Stresses at Elements A and B (SE Connection of Specimen 1) 405
I.32 Shear Stresses at Elements A and B (SW Connection of Specimen 1) 406
I.33 Shear Stresses at Elements A and B (SW Connection of Specimen 1) 406
I.34 Shear Stresses at Elements A and B (SE Connection of Specimen 2) 407
I.35 Shear Stresses at Elements A and B (SE Connection of Specimen 2) 407
I.36 Shear Stresses at Elements A and B (SE Connection of Specimen 3) 408
I.37 Shear Stresses at Elements A and B (SE Connection of Specimen 3) 408
I.38 Shear Stresses at Elements A and B (SW Connection of Specimen 3) 409
I.39 Shear Stresses at Elements A and B (SW Connection of Specimen 3) 409

List of Tables

1.1 SAC Interim Guidelines Damage Identification 9
2.1 Existence of Backup Bars on Final Specimen Connections 30
2.2 A36 Structural Steel Lower Yielding Stress, Ultimate Tensile Stress, and Modulus of Elasticity 34
2.3 Experimental A36 and A572/50 Structural Steel Properties 35
2.4 Concrete Compressive Strength and Concrete Modulus 40
2.5 Strain Gage Locations (Northeast Region of Specimens) 57
2.6 Strain Gage Locations (Northwest Region of Specimens) 58
2.7 Strain Gage Locations (Southeast Region of Specimens) 59
2.8 Strain Gage Locations (Southwest Region of Specimens) 60

3.1 Specimen Load Histories: Level and Quantity of Drift Cycles 67
3.2 Specimen Load Histories: Specimen Load Stages vs. Drift Cycles 67
3.3 Specimen Performance Summary (Girder Strength and Ductility Behavior) 72
3.4 Specimen Performance Summary (Failure Characteristics) 72

4.1 Conditions Included in the Measurement and Calculation of the Girder Moments and Strains 95

5.1 Position of the Neutral Axis Along the Girder Cross Section 114
5.2 Existence of Backup Bars on Final Specimen Connections 147

6.1 Structural Characteristics Affecting the Performance of the Test Specimens 174

A.1 Composite Girder Strength and Stiffness Parameters 186

E.1 Percent Error of Strain Moment vs. Load Moment (Specimen 1) 226
E.2 Percent Error of Strain Moment vs. Load Moment (Specimen 2) 226
E.3 Percent Error of Strain Moment vs. Load Moment (Specimen 3) 227

F.1 Verification of Girder and Column Flexural Components (Specimen 3) 259
F.2 Verification of Load Frame Deformation Component (Specimen 3) 262
F.3 Percent Error of Calculated Girder Tip Deflection vs. Actual Girder Tip Deflection (Specimen 1) 264
F.4 Percent Error of Calculated Girder Tip Deflection vs. Actual Girder Tip Deflection (Specimen 2) 265
F.5 Percent Error of Calculated Girder Tip Deflection vs. Actual Girder Tip Deflection (Specimen 3) 266

G.1 Position of Steel Cross Section Strain Gages 289

G.2 Conditions Included in the Measurement and Calculation of the Girder Moments and Strains 301

H.1 AE Loading Increment Data (Specimen 1) 334
H.1 AE Loading Increment Data (Specimen 1) (Cont.) 335
H.2 AE Loading Increment Data (Specimen 2) 351
H.2 AE Loading Increment Data (Specimen 2) (Cont.) 352
H.3 AE Loading Increment Data (Specimen 3) 369
H.3 AE Loading Increment Data (Specimen 3) (Cont.) 370

I.1 Positions of Strain Gages Relative to Element A (inches) 385

Chapter 1

Introduction

On January 17, 1994 at approximately 4:31 A.M. PST, the San Fernando Valley in California was subjected to a 6.7 magnitude earthquake (EERI, 1996). The epicenter of the earthquake was located beneath the city of Northridge, approximately 20 miles northwest of Los Angeles. With damage estimates exceeding 30 billion dollars, this earthquake was rated the most expensive natural disaster in history. Even though the earthquake released only a moderate amount of energy, unusually high ground accelerations were recorded. The earthquake was unique in that it possessed excessively large horizontal, as well as vertical, accelerations and exhibited several, large pulses (Blackman and Popov, 1995).

After the earthquake, extensive damage and collapse of several reinforced concrete, masonry, and wood structures was initially observed, while most occupied steel-framed buildings indicated very little non-structural damage. As a result, it was concluded that most steel structures survived the earthquake with minimal or no structural damage. However, after observing connection damage to several steel-framed buildings under construction, fireproofing and architectural finishes were removed from many of the steel-framed structures in the region. Brittle fractures of moment-resisting frame (MRF) connections were then discovered in over a hundred steel-framed structures

throughout the San Fernando Valley and adjacent areas (Youssef et al, 1995). Successive investigations have led to the discovery of similar damage in more than 200 additional buildings.

The majority of the moment connection non-ductile failures occurred at or near the complete penetration groove welds connecting the bottom girder flange to the column (Yousef et al., 1995) (Figure 1.1).

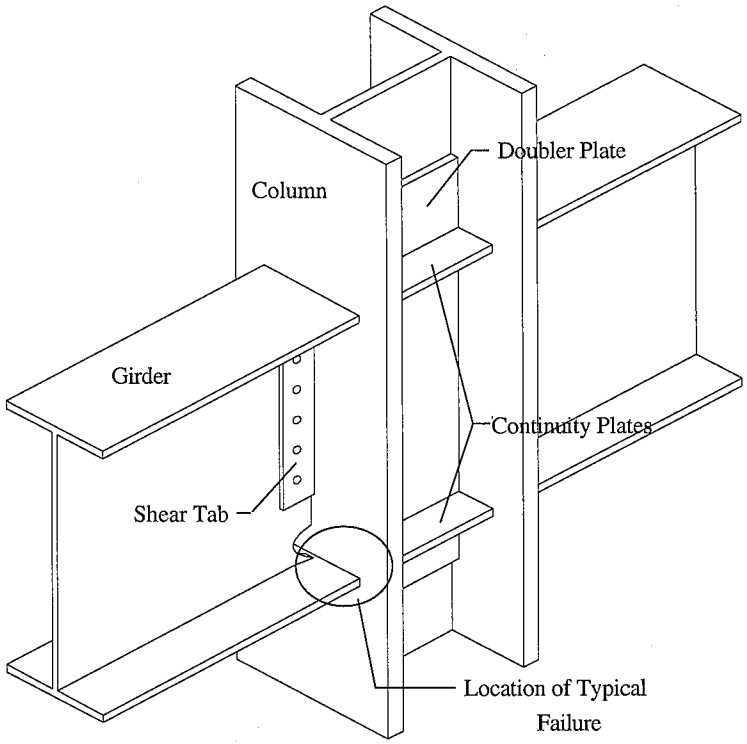

Figure 1.1 Typical Girder-to-Column Connection [after (Hajjar et al., 1995)]

It has been speculated that these steel structures may have sustained large permanent offsets and collapse if one or more large pulses occurred later on in the load history (Leon et al., 1997a). Many of the structures that were investigated demonstrated fracture mechanisms that had not been found in MRF structures after previous earthquakes occurring in the United States (Youssef et al., 1995). However, this type of failure had been observed in a few research studies (Uang and Bertero, 1986; Tsai and Popov, 1988; Engelhardt and Husain, 1993). Since 1994, however, a variety of steel-moment frame

connection fractures have been discovered in the San Francisco area, probably as a result of the 1989 Loma Prieta earthquake (SAC, 1996a).

The motivation for the research reported herein is to investigate possible structural phenomena which may explain the non-ductile performance of the pre-Northridge moment connections. Specifically, the effects of composite floor slabs on the performance of pre-Northridge connections are reported. When composite girders are subjected to bending, the presence of composite floor slabs may affect the strength, stiffness, and ductility behavior of moment connections. Furthermore, unsymmetric force transfer mechanisms may occur at the connection region, along with larger straining of the bottom girder flange region. However, in general, for seismic design it is assumed that the floor slab forms a rigid diaphragm and transfers only the in-plane loads to the moment-resisting frames. It is not customary to account for the presence of the slab in the structural calculations for in steel moment-frame connection design for a number of reasons:

- Many of the moment-resisting frames are on the perimeter of the building, and thus have a slab on only one side. There is little experimental data available to indicate what the degree of slab participation is in this case, and thus it would seem prudent to ignore its contribution to the strength and stiffness of the system.
- The number of shear connectors required to transfer diaphragm forces into the girders is small. Thus, the degree of composite action in these members due only to the shear studs is generally between 10% and 30%. However, in members with a low degree of composite action due to shear connectors, adhesion and friction often increase the degree of composite action under monotonic loads even at levels exceeding the service loads. Nevertheless, it is customary to ignore these force transfer mechanisms because their efficiency is assumed to decrease rapidly under large load reversals. Hence, composite interaction is commonly neglected in girder and connection design for both positive and negative bending.
- Most of the girders used in these systems are deep (e.g., W33 to W36) (Roeder and Foutch, 1996), and thus the influence of the slab on the strength and stiffness of the

girder is assumed to be relatively small when compared to more typical floor beams (e.g., W18 to W24).

- In many construction systems the slab is isolated from the columns during concrete casting, and thus a load transfer path between the slab and the column is not present.

However, based upon a capacity design philosophy, it may be unconservative to ignore the contribution of the concrete slab to the strength and stiffness of the structural system. It is possible to shift from a strong column-weak girder failure mechanism to a strong beam/weak column failure mechanism since existing design equations for SMRFs only require that the nominal capacities of the steel sections be used in these calculations (Leon and Hajjar, 1997). Because the stiffness of the girders also increases substantially due to the presence of a slab, the level of forces attracted to the connections increases, even if one assumes that the slab is isolated from the column. In fact, this isolation may be harmful because a larger proportion of the forces then needs to be transferred by the welds.

Other structural conditions are addressed, which are related to the restraint of key elements of steel moment connections, and may be correlated to the non-ductile performance of pre-Northridge moment connections. The brittle failures of the moment connections may also be attributed to a combination of metallurgical and construction issues. These issues, though discussed, are not specifically addressed in this research.

This chapter briefly discusses the details of the pre-Northridge moment connections. Damage sustained by a particular steel-framed structure is highlighted, based on a forensic study of its connection failures. Also, recent research on the behavior of steel moment connections is reviewed, primarily those including a full-scale composite slab subjected to cyclic loading. Finally, the goals of this research as well as its format of presentation are outlined.

1.1 Pre-Northridge Special Moment-Resisting Frame Connections

The connections utilized by steel-framed structures located in the San Fernando Valley prior to the 1994 Northridge Earthquake are special moment-resisting frame

(SMRF) connections (Blackman and Popov, 1995). These frame systems are designed to allow moderate energy dissipation (providing ample ductility) while preventing failures at critical locations within the framing system. Specifically, a strong column-weak girder concept is employed which forces the development of plastic hinges within the girders. There are two primary reasons why this approach is taken. First, global instability of the structure may occur if the columns develop substantial plastic hinging mechanisms, thus losing much of their stiffness, before the girders. Second, the development of plastic hinges in the girders potentially provides economical, ductile, cyclically stable mechanisms for energy dissipation in the structure.

The pre-Northridge connections normally incorporate deep I-girders (W27 to W36) framing into the flanges of heavy wide-flange columns (e.g., W14X145 or larger) (Leon et al., 1997a). The girder and column sections are typically rolled from A36 structural steel and A572/50 structural steel, respectively. Prior to the Northridge earthquake, it was typical for steel structures to be designed using a limited number of moment-resisting frames to resist lateral loads. The resulting heavy spandrels are required to control drift, while heavy column sections are needed so that the summation of their moment capacities at the joints exceeds that of the framing girders.

Complete joint penetration (CJP) welds are utilized to connect the girder flanges to the column flanges, supposedly providing excellent ductility and toughness (AISC, 1992). Single plate shear tabs are typically bolted to the girder web and welded to the column flange. Furthermore, if the girder flanges cannot transfer more than 70% of the plastic moment capacity of the cross section, welding of the shear tab to the girder web is required. Backup bars are typically tack-welded to the base of the top and bottom girder flanges in order to reduce the amount of slag runoff during the placement of the complete joint penetration welds.

The panel zone region of pre-Northridge connections is often designed to permit yielding of the panel zone in order to dissipate energy during an earthquake (Tsai, 1988). This form of yielding demonstrates strain-hardening and stable behavior which is desirable

for seismic design. If needed, doubler plates are also welded to the column web and extend above and below the top and bottom continuity plates, respectively.

During the 1970's and 1980's, several tests of SMRF connection assemblies were performed (Popov and Stephen, 1970; Krawlinker et al., 1971; Bertero et al., 1973; Popov, 1983; Tsai, 1988). After exhibiting acceptable standards of girder plastic hinging and panel zone shear yielding, this connection became prequalified in the AISC ASD and LRFD specifications as well as the UBC (Blackman and Popov, 1995). However, since several of the connections demonstrated poor levels of ductility during the 1994 Northridge Earthquake, the performance of these connections is being reexamined.

1.2 Damage to the Borax Corporate Headquarters Building

The four-story Borax Corporate Headquarters Building, which is located in Valencia, California, suffered substantial damage to nearly seventy-five percent of its steel moment-resisting frame connections during the 1994 Northridge Earthquake (Hajjar et al., 1995). The structure was less than one year old at the time of the earthquake. For the purpose of simulating moment connections similar to those found in steel structures prior to the earthquake, the details of this facility were utilized to design the test specimens for this research. Therefore, the damage sustained to this building is outlined here briefly to provide a summary of the basic types of failures seen in steel connections due to the Northridge earthquake. The typical location and description of the moment connection failures are identified and described using notation established in the SAC Interim Guidelines (SAC, 1995) and are summarized in Figures 1.2 through 1.7 and Table 1.1.

The steel moment frames under investigation were four special moment resisting frames located at the perimeter of the building. These frames resisted all lateral loads on the building. Two SMRF frames, four stories high and four bays wide, were located in the North-South direction, while two SMRF frames, four stories high and three bays wide, were oriented in the East-West direction.

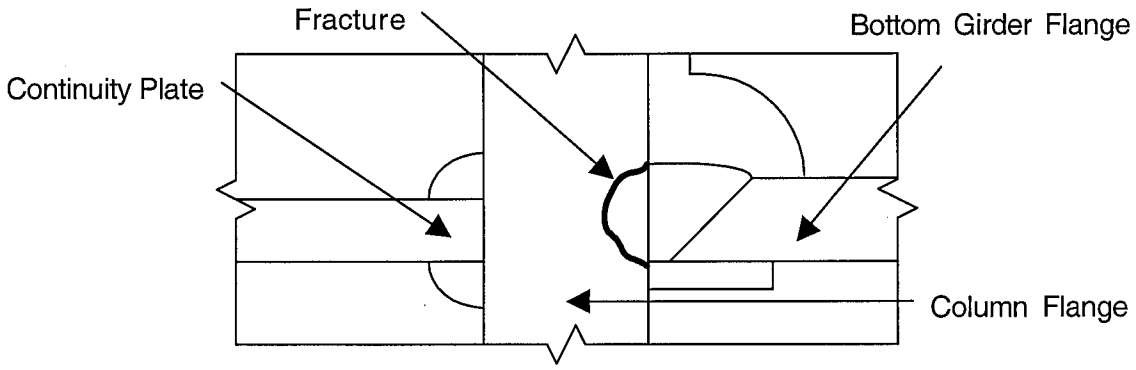

Figure 1.2: Damage Type C2* (Girder Flange Pull-Out From Column Flange)

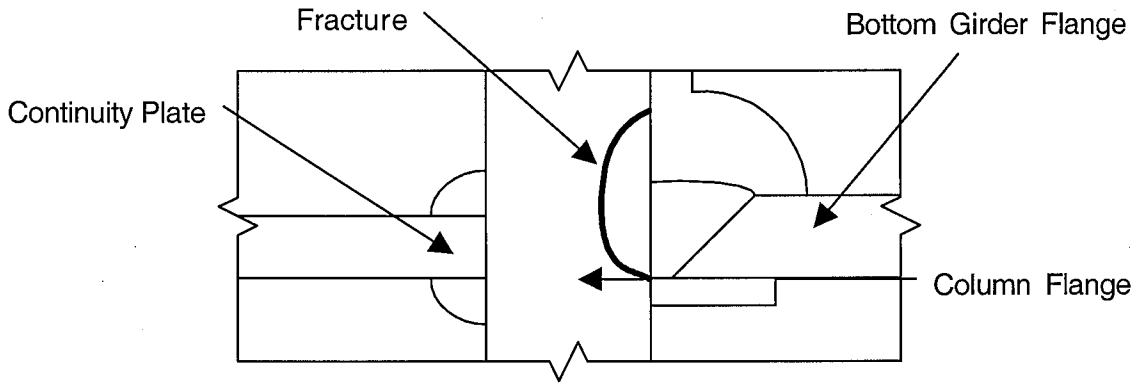

Figure 1.3: Damage Type C2 (Girder Flange Pull-Out From Column Flange)

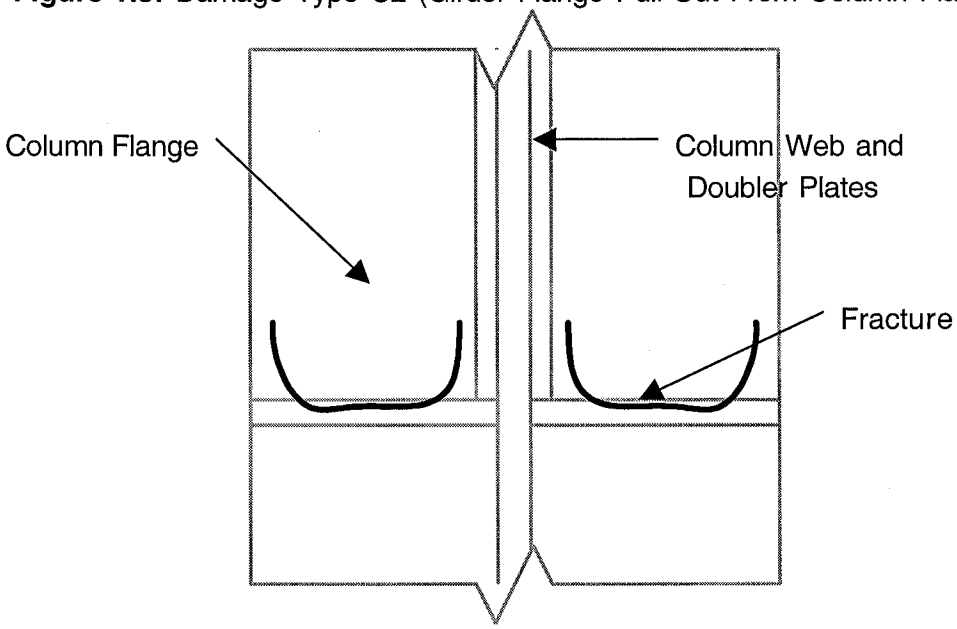

Figure 1.4: Damage Type C4* (U-Shaped Column Flange Fracture)

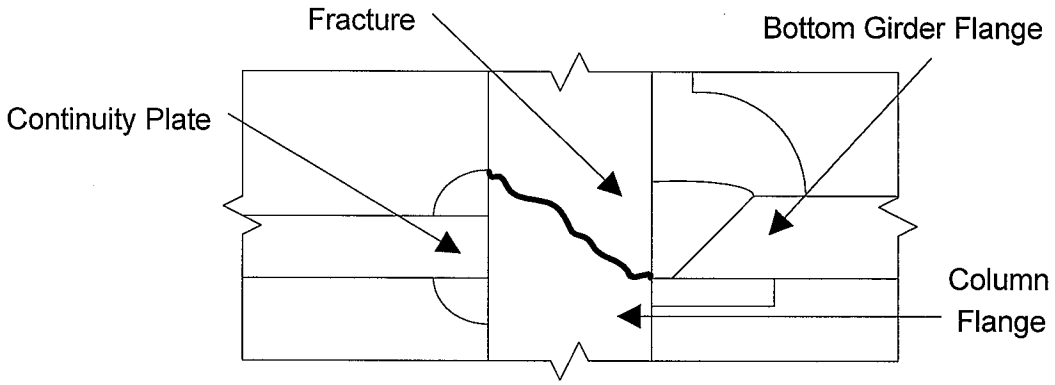

Figure 1.5: Damage Type C4 (Column Flange Fracture)

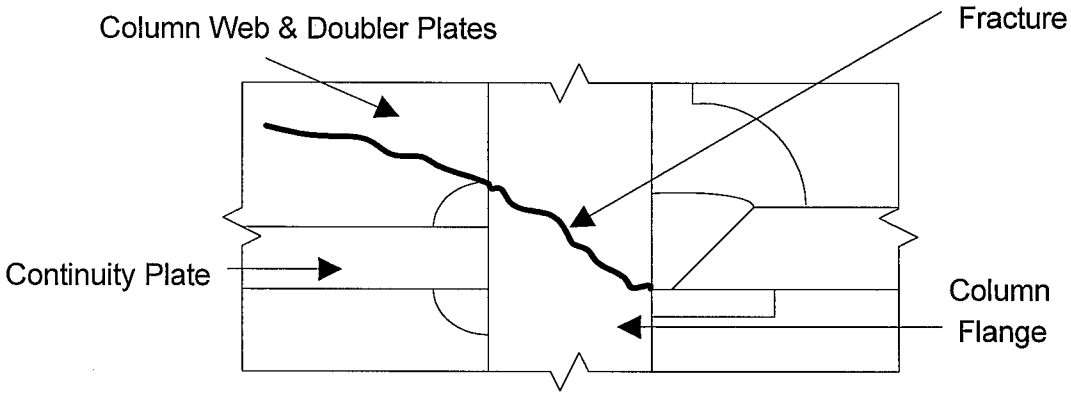

Figure 1.6: Damage Types P4 & P6 (Column Panel Zone Fracture)

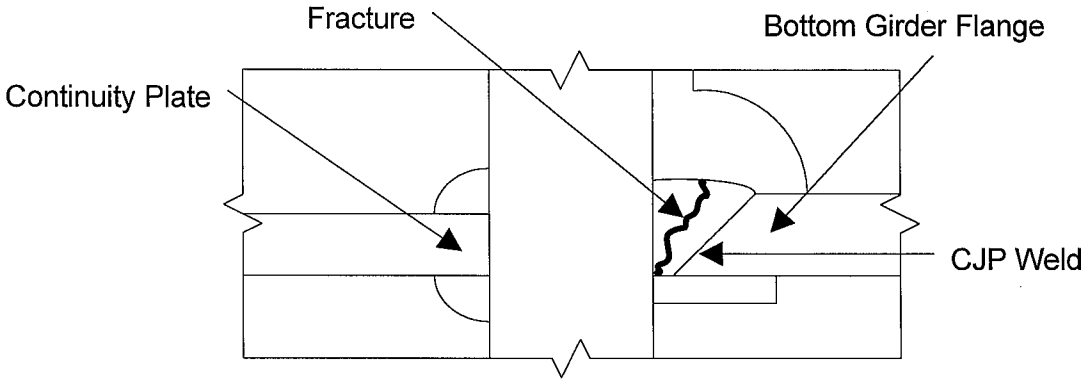

Figure 1.7: Damage Type W2 (CJP Weld Metal Fracture)

Table 1.1: SAC Interim Guidelines Damage Identification

Damage Type	*Description of Moment Connection Damage*
C2	Column flange divot or tear-out
C2*	Column flange divot or tear-out where fracture returns to the column flange outside surface at the top of the girder flange
C4	Full or partial column flange crack in the heat-affected zone (HAZ)
C4*	Partial U-shaped column flange crack in the HAZ
P5	Partial depth fracture in the doubler plate
P6	Partial depth fracture in the column web
W2	Crack through the thickness of the complete joint penetration weld

It was concluded that nearly all the observed fractures in the Borax facility occurred in a brittle fashion and may have fractured during only one or two strong pulses (Hajjar et al., 1995). The two primary failure mechanisms of moment connections were a pull-out of the girder flange from the column and column flange fracture. The girder flange pull-out was the most predominant mode of failure. This type of failure, which was observed at 56 locations in the four moment frames of the structure, exhibited a complete or partial pull-out of the girder flange from the column. A portion of these failures initiated at the root of the girder flange weld and propagated to the column flange surface at the top of the bottom girder flange (Type C2*, Figure 1.2). The path of failure passes through the heat affected zone (HAZ) of the complete joint penetration weld.

The other types of girder flange pull-out failures initiated at the root of the girder flange weld, where they extended well above the top of the girder flange or propagated back to the column flange surface (Type C2, Figure 1.3). Again, the failure path propagated with a curved path through the column flange base metal near the boundary of the HAZ. For several cases where the fracture was not visible at the column flange

surface, it was determined that the fracture depth exceeded 2 or more inches (Hajjar et al., 1995).

The second major type of connection failure, a column flange fracture, was observed in 30 locations in the building. These fractures typically initiated at the root of the girder flange weld and extended to the top of the bottom continuity plate fillet weld. While some of these fractures exhibited a U-shaped punching type failure through the column flange (Type C4*, Figure 1.4), the majority of the column fractures extended across the entire thickness of the column flange (Type C4, Figure 1.5). Over 75% of the column flange fractures entered the panel zone region, extending into the column web and doubler plates (Type P5 and P6, Figure 1.6).

Another type of connection failure entailed the fracturing through the weld metal in the girder flange connection, initiating at the edge of the girder flange (Type W2, Figure 1.7). This type of failure typically resulted in a pull-out type failure, since the crack eventually extended into column flange (Type C2 or C2*). Damage that was sustained by the shear tabs, consisting of cracking of the shear tab fillet welds, usually coincided with the girder or column flange fractures.

To investigate the initiation of the crack which led to column flange fracture within the HAZ of the bottom weld, several metallurgical investigations were carried out (Hajjar et al., 1995). Of the connections tested, one of the fractures initiated at the root of the girder flange weld, while another initiated at the toe of the top fillet weld at the continuity plate and column flange interface. A change in hardness was measured within the column flange near the girder flange and continuity plate welds which may have related to the failures. Other metallurgical studies concluded that 95% of the top flange welds exhibited rejectable defects due to either cracks in the girder flange welds or indications at the ends of the welds.

1.3 Previous Research on Pre-Northridge Composite MRF Connections

Extensive experimental and computational research, as well as forensic studies, have been conducted to study the performance of pre-Northridge moment-resisting frame connections. Many studies since the Northridge earthquake have focused on determining what conditions may have prompted premature and/or brittle modes of failure of the welded girder-to-column connections. A significant amount of post-Northridge research has investigated various aspects of fracture mechanics and connection configuration, while a limited amount of study has focused on the effects of composite floor slabs.

This section focuses primarily on various experimental and forensic investigations of SMRF connections with composite floor slabs that have been conducted mainly within the US and Japan before and after the 1994 Northridge Earthquake. Specifically, the effects of composite floor slabs on the stiffness and moment capacities of the connection elements and whether or not these parameters can be accurately modeled by the standard code specifications are discussed.

1.3.1 Performance of Composite MRF Subassemblages

Research has shown that the placement of composite floor slabs on the girders of moment-resisting frame assemblies complicates the behavior of the frame system, especially within the moment connection region. Such complexity may lead to behavior which is significantly different than that of a bare steel moment-resisting frame assembly. Despite the possible effects on various connection responses, such as strength, stiffness, and ductility, the effects of composite floor slabs are currently not included in the design of lateral-load resistant steel frame systems in the U.S.

Experimental research has shown that strength and stiffness of composite girder sections in joint subassemblages increase due to composite action, assuming that the girder-to-column connection provides adequate strength to resist the accompanying shear force during positive bending (Lee and Lu, 1989). Also, Mukudai and Matsuo (1983)

and Igarashi et al. (1984) demonstrated, using different elastic-plastic analysis methods, that increases in girder strength and stiffness due to composite action generally decrease the maximum lateral displacement and maximum rotation of the composite girder frames. However, in some cases, they observed that column failure occurred before composite girder failure, even when the bare steel girders were designed to plastify before the columns.

Lee and Lu (1989) also determined that the panel zone region of composite moment frame connections is larger than that of steel moment frame connections, resulting in an increase in the shear strength and stiffness of the panel zone even at large distortions. Their research has shown that experimental elastic stiffness and shear yield strength values of the panel zone correspond to an effective panel zone depth measured from the center of the bottom flange to the center of the concrete slab. Therefore, lateral-load resisting frames, which typically neglect the effect of composite floor slabs during design, may exhibit less energy dissipation capacity due to yielding of the panel zone than expected.

The effect of composite floor slabs on connection behavior are partly dependent upon the level of composite action. As a result, experimental research has been conducted in order to verify theoretical calculations of composite strength and stiffness parameters. Tagawa et al. (1989) has shown that the compressive forces in the concrete slab are affected by the bearing stress of concrete at the column face. In turn, once the concrete crushes and a void is created at the column-concrete slab interface, composite action is reduced until the void is closed during girder positive bending. Therefore, the level of composite action may not only be dependent upon the shear stud capacity (as specified in the design), but also upon the bearing stress at the column. In contrast, Tremblay et al. (1997) showed that if the slab is isolated from the column, and the girder purposely lacks shear connectors within several feet of the column face, the column is subjected to moments closer to the bare steel strength of the girder. Ongoing research continues to investigate the effect of composite floor slabs on the behavior of steel moment-resisting connections (Gross, 1997).

1.3.2 SMRF Connection Failures Due to Structural and Metallurgical Phenomena

Since the 1994 Northridge Earthquake, a substantial amount of research has focused on explaining the types and locations of damage sustained by the SMRF connections based on either structural or metallurgical phenomena or a combination of both. One area of metallurgical study has been on the fracture toughness of the weld metal used in constructing pre-Northridge moment connections. Kaufmann et al. (1996) determined that the use of E70T-4 electrodes, which were commonly used prior to the earthquake, resulted in the placement of welds possessing low fracture toughness properties. In fact, the weld material of some of the pre-Northridge connections demonstrated Charpy V-notch fracture resistance values of less than 10 ft-lbs at 70°F.

Another area of study has been on the HAZ of complete joint penetration welds of welded girder-to-column connections. Forensic studies have shown that the fracture toughness within the HAZ may be substantially lower than the weld and base metal surrounding it (Fisher et al., 1995). This material condition may occur due to the combination of different welding metals through the placing of the full penetration weld and the tack welding of the backup bar (AISC, 1993). Fisher et al. (1995) have also concluded that a decrease in fracture toughness exists near the web-flange junction of jumbo-sized W-sections. This is believed to be partly due to a decrease in the cooling rate across the steel cross section, resulting in the formation of large-coarse grained particles which, in turn, possess a lower toughness property. Also, straightening methods employed during the milling process may affect the fracture toughness.

Another metallurgical condition, material hardness, has been studied by Tide (1997). It has been shown that a variation in material hardness exists within the web-flange junction region of hot-rolled steel girders. Specifically, the region near the center of the web-flange junction may demonstrate a decrease in hardness, while the fillet region of the web-flange junction may exhibit an increases in hardness. Since material hardness is directly related to the ultimate tensile strength, web-flange junction regions exhibiting

deficient material hardness properties may reach the ultimate tensile stress before other regions along the girder flange.

After the 1994 Earthquake, the quality and workmanship of the welding procedures were under investigation. Kaufmann et al. (1996) experimentally tested several small-scale and full-scale pre-Northridge connections which demonstrated failure mechanisms similar to those observed during the earthquake. These connections utilized backup bars and E70T-4 weld metal at the girder-to-column CJP welds. Only when the backup bars were removed and high toughness E7018 weld metal was employed did the connections perform with adequate strength and ductility. It was also observed that a welded rather than bolted girder web-column flange connection optimized the behavior of SMRF connections.

After extensive forensic studies, Kaufmann et al. (1996) observed that the origin of fracture in 20 damaged pre-Northridge connections primarily occurred near the areas of substandard root penetration of the connection weld, predominantly due to the entrapment of slag or porosity at the backup bar-weld root interface. These deficiencies in welding workmanship occur predominantly near the bottom access hole, where it is the most difficult to effectively place the weld. These welds are typically placed with two sets of passes, each extending from the flange tips and terminating near the bottom access hole.

Structural conditions, due to the geometry of the connection, may affect the distribution of stress within certain elements of SMRF connections. As discussed by Blogdett (1995), the bottom weld region is highly restrained through the length and the transverse direction of the column flanges, thereby, leading to a multiaxial state of tensile stress during girder positive bending. For an element subjected to multiaxial strains, a high state of triaxial tension may lead to brittle fracture prior to ductile yielding (AISC, 1993).

Yang and Popov (1995) have also investigated the possibility of a triaxial stress state at the interface of the backup bar and welded bottom girder-column connection. This condition occurs because the notch or crack creates a geometric discontinuity (a sudden change in cross section) which prevents substantial shear flow of the material to

occur. If such a condition exists in the directions orthogonal to the direction of loading, large stresses in all three directions may result (United States Steel, 1971).

Under the guidance of the SAC Joint Venture, a substantial amount of computational and experimental research, literature review, and forensic investigation of damaged steel moment connections has been conducted since the 1994 Northridge earthquake. In 1996, the SAC Joint Venture concluded (based on their investigations and from independent researchers) that the damage sustained by steel frame buildings during the Northridge earthquake was attributed to a variety of factors. These factors, some of which have been previously mentioned, are now summarized.

In recent years, it has been common practice to design relatively few lateral load-resistant frames to resist seismic forces in steel frame buildings (SAC, 1996b). This philosophy of optimization has led to the construction of connection and member sizes which were larger than what has been tested in laboratories. In terms of quality-control, substandard welding workmanship during the construction process has led to unacceptable weld joints at critical sections of the connections. Also, a lack of consistency in material strength of hot-rolled shape members has been detected. The utilization of low toughness weld metal at the CJP welds of girder flange-to-column connections may have been a significant metallurgical factor affecting the performance of connections.

Several structural phenomena were also concluded to be significant contributors to the damage of steel MRF connections (SAC, 1996b). For instance, high levels of inelastic deformation and a variety of stress concentrations were observed at the girder flange-to-column connection regions due to current detailing procedures. More specifically, the welded girder flange-to-column connections possessed notches or stress risers (i.e., the presence of backup bars), while a triaxial state of strain possibly existed near the center of the weld region. The design of panel zone regions with relatively low strength and stiffness properties resulted in the generation of large, secondary stresses at the girder flange-to-column connections. The research conducted at the University of Minnesota and reported herein has focused on the performance of welded steel moment

connections predominantly due to the effects of composite floor slabs, as well as most of structural phenomena mentioned above.

1.4 Research Objectives

The objectives of this research are to determine if the pre-Northridge moment connection failures occurred partly or predominantly due to various structural phenomena, primarily the presence of composite floor slabs (Leon et al., 1997a). The effect of composite floor slabs is investigated for two primary reasons. First, the presence of shear studs and slab reinforcement most likely activate different force-transfer mechanisms at the top and bottom girder flanges at the girder-column interface. Second, a significant portion of the girder positive moment is transferred into the concrete slab; therefore, a substantial increase in stiffness and strength occurs at the top of the girder due to the presence of the slab, resulting in the concentration of large strains at the bottom welded girder-to-column connection (Leon et al., 1997a).

The placement of the shear tab along the cross section of the girder is also investigated, since it may partially contribute to large strains within the bottom girder-to-column connection. Furthermore, to simulate the large vertical accelerations which occurred during the 1994 Northridge Earthquake, the performance of the specimen connections are observed when the column is subjected to axial tension.

The presence of backup bars at the base of the CJP welds are discussed, since they are believed to contribute to poor weld root penetration and to a triaxial state of stress within the CJP weld. In addition, local bending and shearing of the girder flange near the column flange surface is addressed. A state of triaxial tensile strain is studied at the regions near the girder flange base material near the access holes and the weld material within the complete joint penetration (CJP) welds. Due to restraint by the girder web, a sudden change in cross section exhibited by the access holes, and the presence of column axial tension, a reduction in shear flow or ductility (and thus yielding) within these regions

may be prominent. Finally, the participation of the concrete slab under tension during low drift cycles of girder negative bending is discussed.

1.5 Research Approach

To accomplish the objectives of the research, both an experimental and a corroborating computational research program were undertaken at the University of Minnesota. The computational research was performed partly by employing macro-level finite element frame analyses, which investigated the effects of the earthquake at a building-system level (Hajjar et al, 1995). In addition, continuum finite element analyses, along with the experimental research, were used to study the behavior of pre-Northridge interior MRF joints. This research discusses the results of the experimental study and the micro-level computational results (see also Carlson, 1997; Leon et al., 1997a).

The experimental research entailed the testing of three full-scale, interior moment-resisting moment frame assemblies subjected to cyclic, quasi-static loading as well as constant column axial tension loading. Two of the specimens contained girders with composite floor slabs, while the other specimen contained only bare steel girders. The two composite specimens were designed to be partially composite, with Specimen 2 and 3 exhibiting 55% and 35% levels of composite action, respectively.

Three primary types of experimental data were collected and analyzed in order to investigate the behavior of the specimens: strain behavior, displacements and rotations, and acoustic emission events. Strains were measured at various locations on each specimen, particularly near the girder-to-column connection region. Displacements and rotations of several specimen elements were measured to synthesize hysteresis behavior of the girders and panel zone regions of the specimens as well as to measure composite slip within the composite girder sections. Acoustic emission equipment was utilized in order to detect the location and type of localized fracturing or cracking occurring within the connection region. To supplement the experimental results, forensic studies were

conducted on the East girder cross section of Specimen 3 regarding a possible reduction in material hardness within the girder web-flange junction region of the girder cross section.

1.6 Organization of Report

Chapter 2 describes the various procedures required to perform the experiment. Such procedures include the description of the test specimens, load frame, and testing equipment as well as the instrumentation of various measuring devices. It also summarizes the material properties of the test specimens, which are either assumed or measured.

Chapter 3 summarizes the load history and describes the behavior of each test specimen. Specifically, maximum plastic rotation and moment values are summarized as well as when and where the specimen failures occur. Also, the various types of analyses and tools used to describe and interpret the behavior of the specimens are provided.

Chapter 4 presents the validation of the experimental results based on such procedures as the regeneration of the girder tip deflection components and studies on the effects of friction within the load pin assemblies. This chapter also evaluates the level of composite action occurring within the composite girders of Specimens 2 and 3.

Chapter 5 describes and interprets the behavior of the test specimens and discusses the corroborating computational results.

Chapter 6 outlines the conclusions drawn from the interpretation of the results. Specifically, structural phenomena contributing to the fractures at the bottom connection regions of the specimens are discussed.

Chapter 2

Experimental Procedure

This chapter outlines several aspects of the design and description of the test specimens. Also, key material properties of the test specimens are reported and the testing procedure and layout are described. For the descriptions in this report, note that the loading assemblies are positioned in the laboratory so that the longitudinal axis of the specimens are oriented in the East and West directions, so that the major axis of column and girder bending lies in the North-South direction.

2.1 Design and Description of Specimens

The test specimens are designed to simulate interior moment-resisting connections that existed in steel structures in the Northridge, California region prior to the 1994 earthquake. The three test specimens are based on typical member sizes and connection details found in the lateral-load resisting frames of the Borax corporate headquarters building located in Valencia, California (Figures 2.1 and 2.2) (Hajjar et al., 1995). As discussed in Chapter 1, this structure experienced substantial damage to nearly seventy-five percent of its steel moment-resisting frame connections during the earthquake. The two primary failure mechanisms of these connections were a pull-out of the girder flange from the column and column flange fracture.

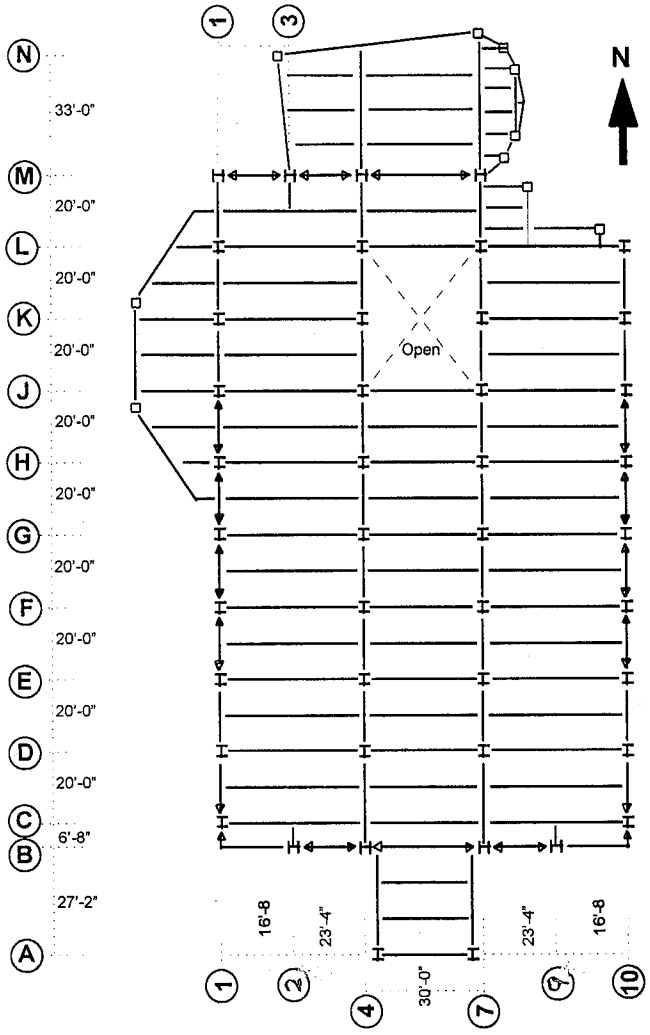

Figure 2.1: Borax Corporate Headquarters (Typical Floor Plan) (Hajjar et al., 1995)

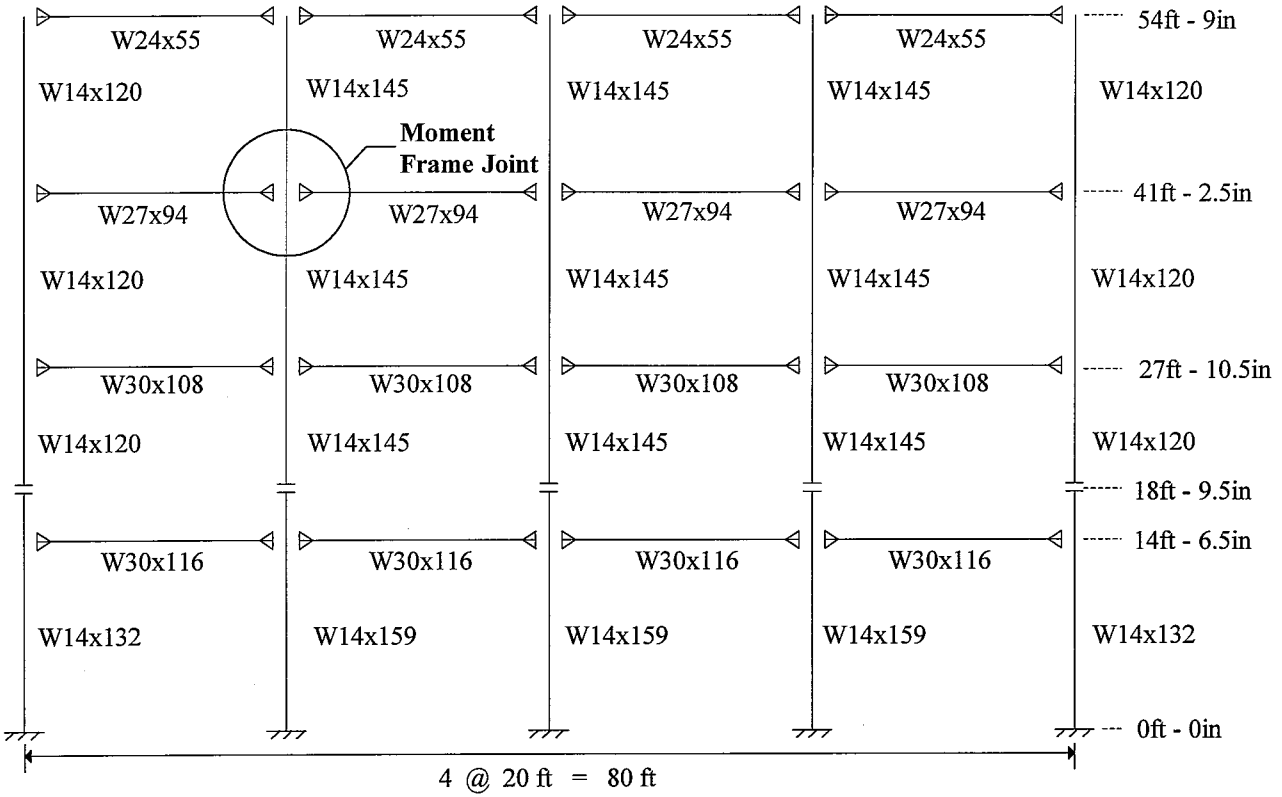

Figure 2.2: West N-S Moment Frame Elevation [after (Hajjar et al., 1995)]

To investigate these modes of failure, which occurred primarily near the bottom welded girder-to-column connections, the specimens have been designed so as to isolate failure within this region of the connections. A strong column-weak girder design criterion and a relatively rigid panel zone region have been emphasized in the design. A relatively strong column is used to ensure that the girders can initiate the development of plastic hinge mechanisms during cyclic loading before significant deformation or damage develops in the column. Also, incorporating a rigid panel zone region significantly reduces the contribution of panel zone shear deformation to the mode of failure. Thus, the column size was moderately increased from the W14X145 section located at a typical joint on which the specimen design was based (Figure 2.2; circled joint, third floor). All three specimens are moment-resisting frame connections comprised of two W27X94 steel girders that are framed into a W14X211 column, which is oriented to provide strong-axis bending during loading (see Figures 2.3 and 2.4).

2.1.1 Girder and Column Design

The W27X94 girders are composed of ASTM A36 steel and are 180 inches in length (see Figures 2.3 and 2.4). The effective length, L_b, measured from the face of the column to the point of applied load, is 132 inches. The length L_b was selected to ensure that the steel girders achieved both extensive girder yielding and large inelastic rotations before the maximum load or stroke (154 kips and +/- 6 inches, respectively) of the actuators was exceeded. The W14X211 columns are composed of ASTM A572 Grade 50 steel and are 171 inches in length, measured from center-to-center of the top and bottom load pins.

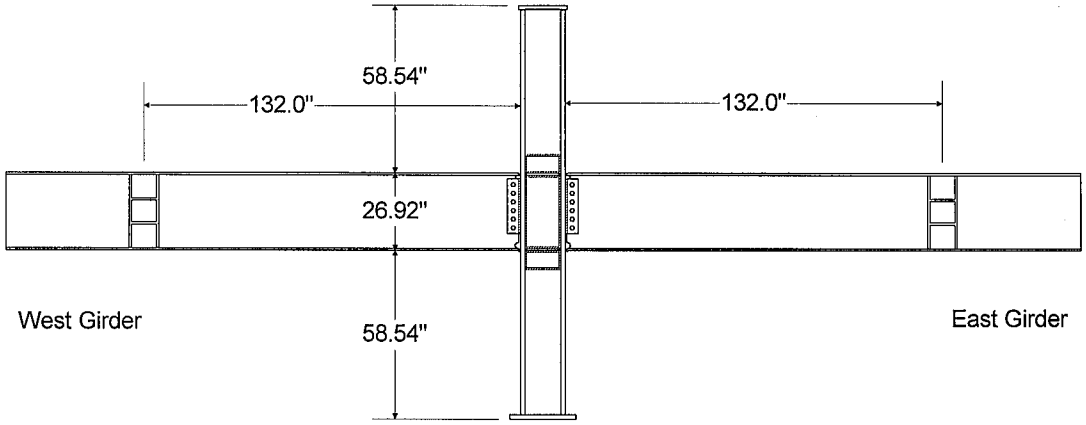

Figure 2.3: Specimen 1

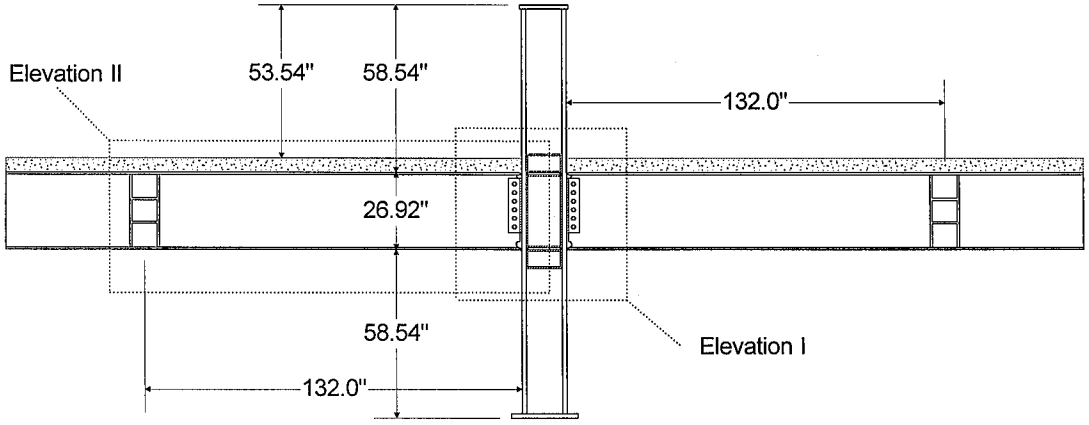

Figure 2.4: Specimens 2 and 3

2.1.2 Connection Design

Figures 2.5 through 2.11 illustrate the dimensions and detailing of the three specimen connection regions. With the exception of the retention of the backup bars, the connection details are identical for all three specimens. The panel zone region incorporates four continuity plates that provide the required tensile capacity to resist the two girder flange forces (AISC, 1993). The continuity plates extend to the edge of the column face, which is a typical detail incorporated in pre-Northridge connections. The panel zone region also includes two 5/8" doubler plates which extend 6 inches above and below the continuity plates (see Figures 2.5 and 2.6). This extension of panel zone rigidity ensures that minimal panel zone shear deformation occurs, which forces a substantial portion of the deformation to occur near the welded girder-to-column connection.

A shear tab plate is fastened to the column flange with a 5/16" fillet weld on each side of the plate (see Figures 2.6 and 2.7). Since the girder flanges provided 70.08% of the nominal flexural strength of the girder, the shear tab is only bolted to the girder web (no weld is required) with six, 1 inch diameter, A325 hex headed bolts.

Several elements of the connection region are connected using various welding details (see Figures 2.7-2.11). The top and bottom of the doubler plate are attached to the column web with two 3/8" fillet welds, while its sides are welded to the column flange-web junction with two 5/8" groove welds. Each continuity plate is welded to the doubler plate with two 5/16" fillet welds and to the column flanges with a 5/8" complete joint penetration (CJP) weld. Finally, the top and bottom girder flanges are welded to the column flange with a 5/8" CJP weld. All welds were placed using AWS 5.20-79/E70T-1 welding electrodes, with the exception of the complete joint penetration welds connecting the girder flanges to the column flanges, which were placed using AWS 5.20-79/E70T-7 welding electrodes. Section 2.2.1 provides a summary of the material properties of these weld metals.

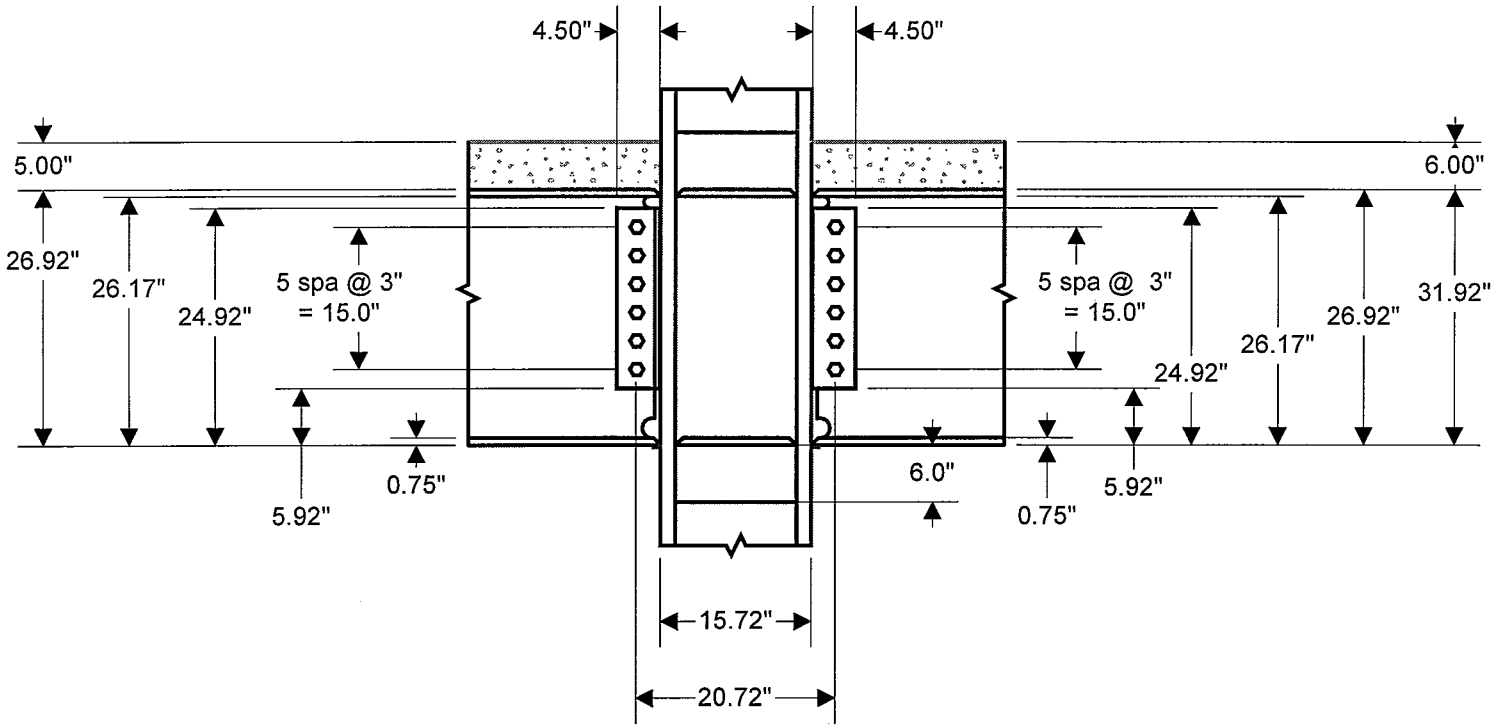

Figure 2.5: Elevation I: Connection Dimensions

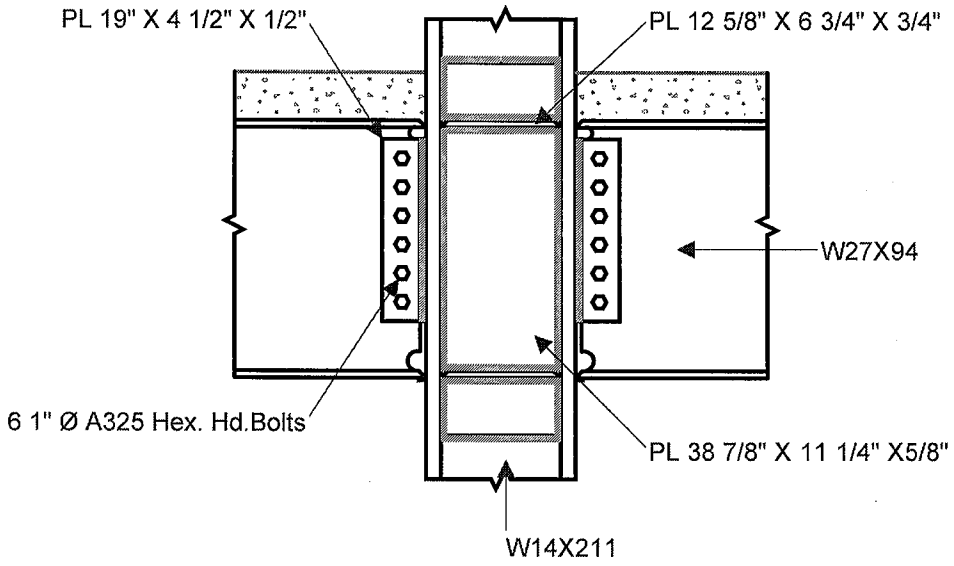

Figure 2.6: Elevation I: Connection Elements

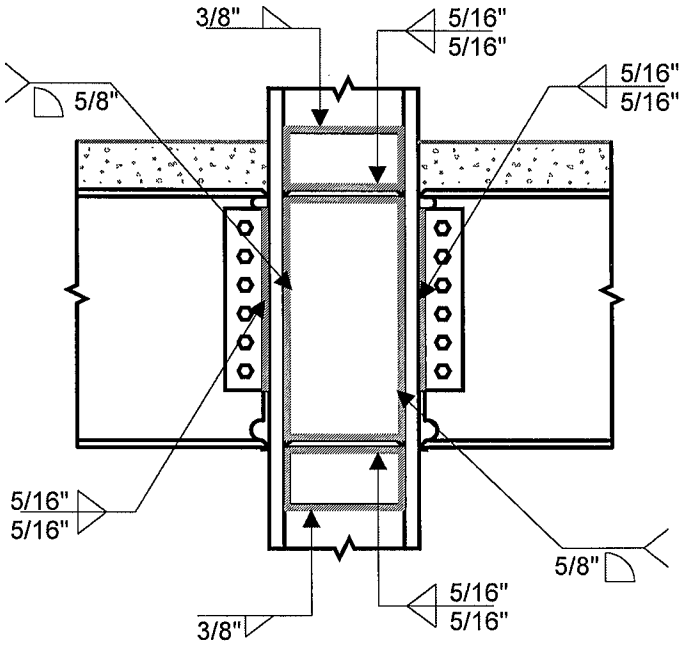

Figure 2.7: Elevation I: Connection Welds

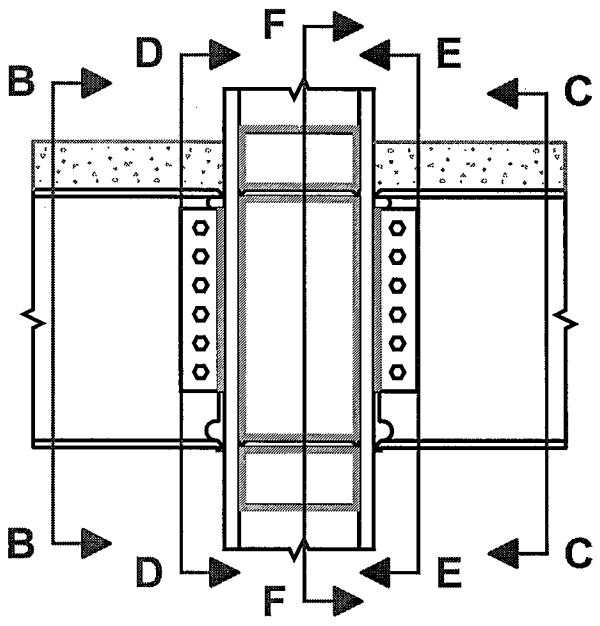

Figure 2.8(a): Elevation I: View Locations of South Connection

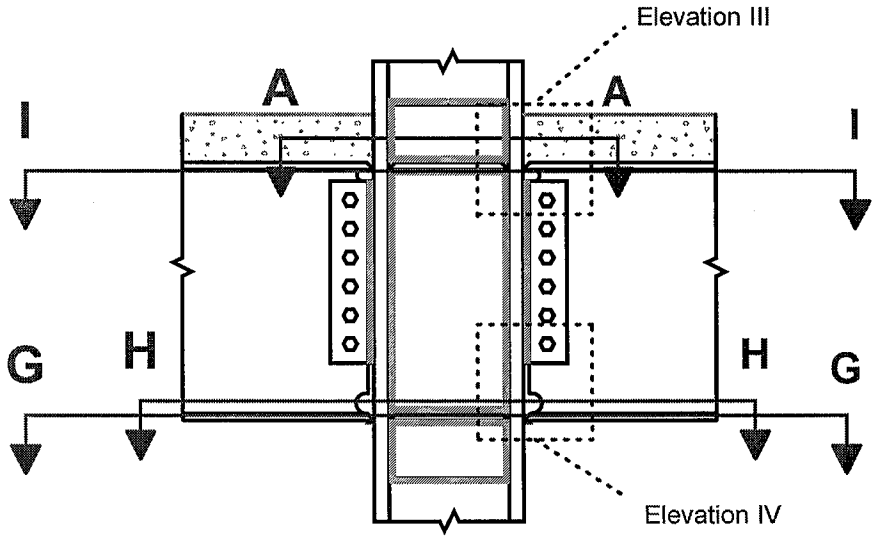

Figure 2.8(b): Elevation I: View Locations of South Connection

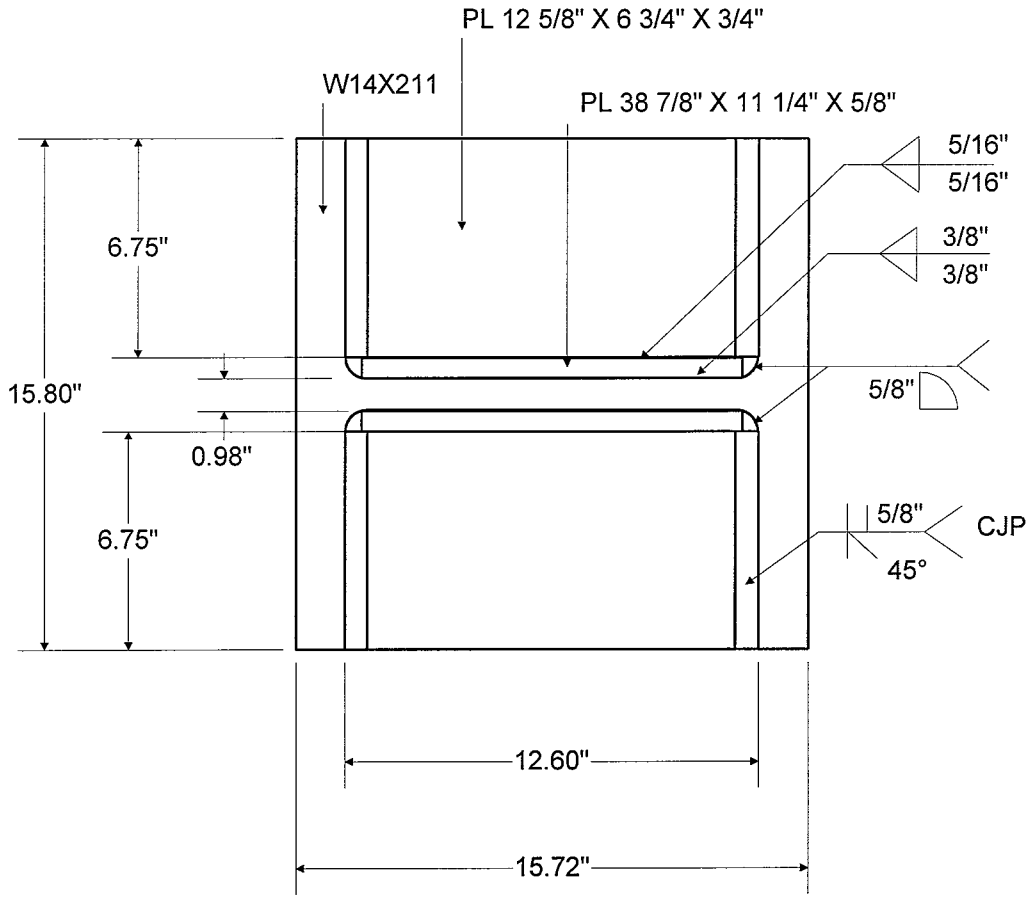

Figure 2.9: Section A-A : Top of Column

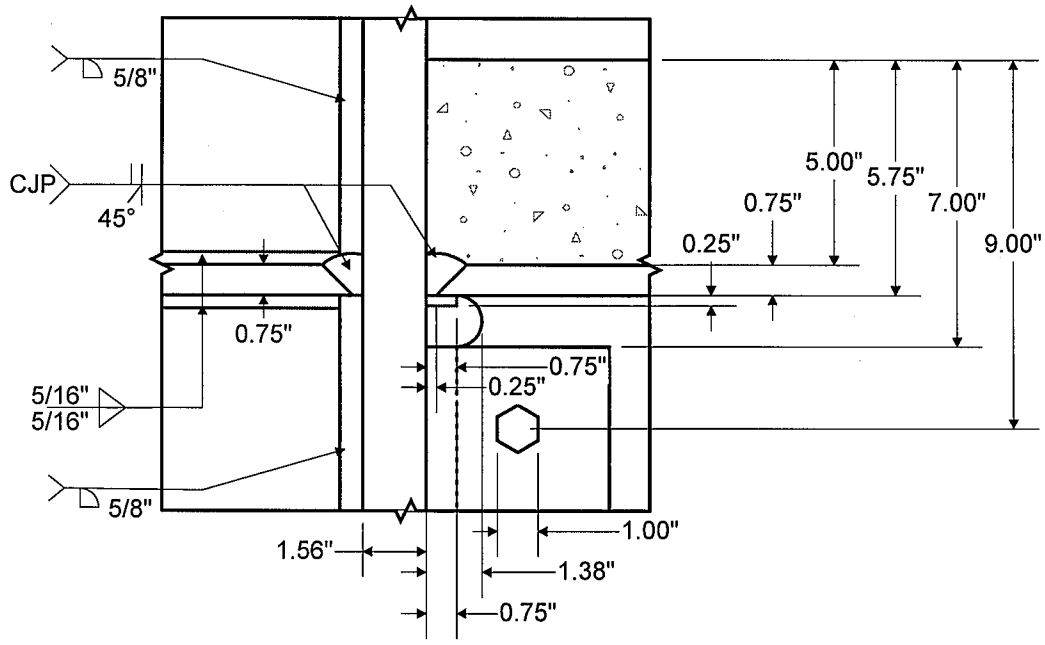

Figure 2.10: Elevation III: Top Access Hole Region

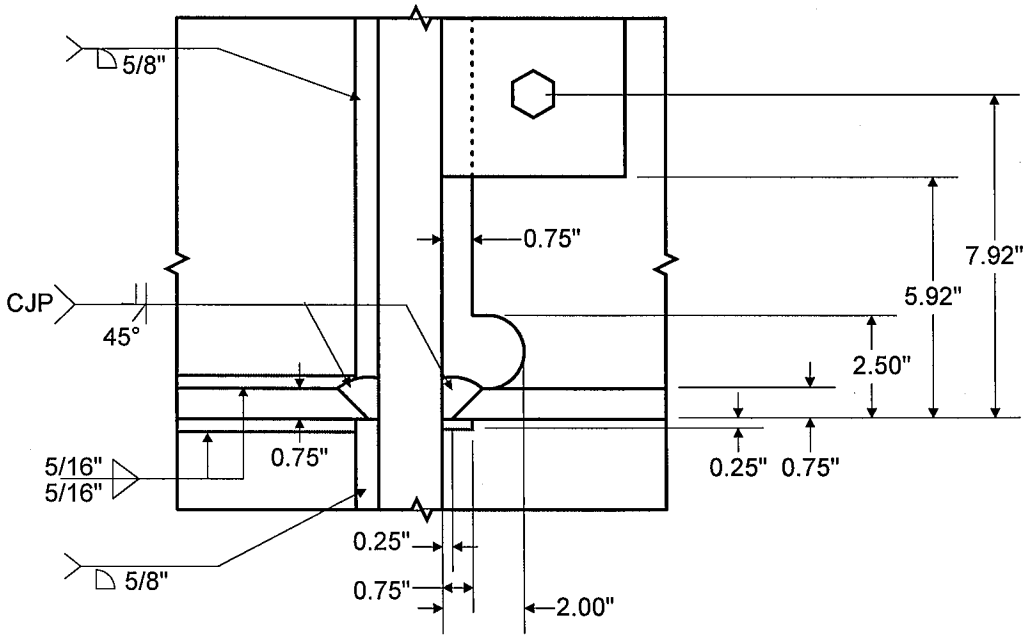

Figure 2.11: Elevation IV: Bottom Access Hole Region

When placing this type of weld, it is a common practice to tack-weld a backup bar on the underside of the top and bottom girder flanges in order to facilitate forming of the weld pool. This procedure was followed when initially fabricating the 12 girder flange-to-column welds of the specimens. However, due to the detection of slag inclusions during ultrasonic testing, six of the backup bars were removed and had the root of their respective CJP weld ground, followed by the passing of a fillet weld. Table 2.1 indicates which girder flange-to-column CJP welds have backup bars remaining. These differences in the presence of the backup bars permit investigation of the effects of backup bars on the behavior of moment-resisting connections. No end tabs were used for these welds.

Table 2.1: Existence of Backup Bars on Final Specimen Connections

	Specimen 1	**Specimen 2**	**Specimen 3**
East/Top CJP Weld	YES	NO	NO
East/ Bottom CJP Weld	NO	YES	NO
West/ Top CJP Weld	YES	YES	NO
West/ Bottom CJP Weld	YES	YES	NO

2.1.3 Composite Girder Design

To investigate the effects of composite floor slabs on moment-resisting connections, one specimen is bare steel and two specimens incorporate composite girders. The girders of Specimens 2 and 3 consist of a 3 inch normal weight concrete slab on a 2 inch metal deck, running parallel to the girder, with an effective width of 60 inches (Figure 2.12). The slabs are placed over the entire length of the girders (180" in length). Note that the slab width is limited by the load frame. However, it is appropriate for the scale of this test

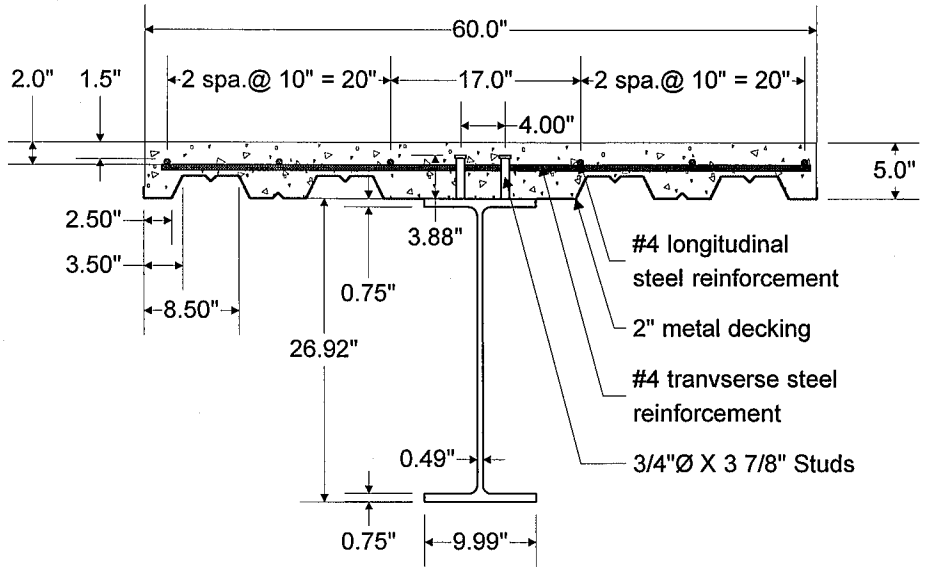

Figure 2.12: Section B-B: Composite Girder Cross Section

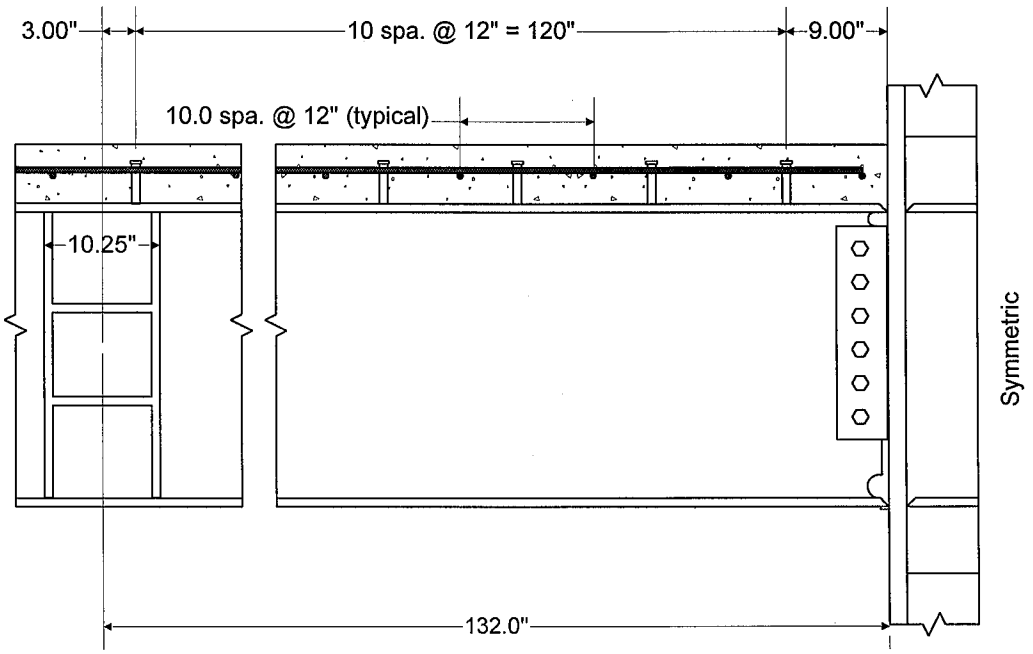

Figure 2.13: Elevation II: Shear Stud Locations

(2*132"+15.72" column depth = 280"; 280"/4 = 70"), and relates well to the 20 foot bay spacing in the Borax facility (see Figure 2.2). In addition, many of the connections that failed during the Northridge Earthquake also incorporated the use of girders that were deeper than the girders used in this experiment (or in the Borax facility). Therefore, the effects of the composite floors slabs on these connections are believed to be representative of typical pre-Northridge MRF connections.

Specimen 2 and 3 are designed to achieve different levels of composite action from their composite girders. Partially composite action is used for both specimens, as this is typical for girders in lateral-load resistance systems. Note that due to a relatively small effective slab cross section, the fully composite failure mode is governed by crushing of the concrete slab, not yielding of the steel girder. The strength provided by the partially composite sections are quantified as the strength provided by the shear studs divided by the tensile strength of the steel girder (see Appendix B1). The girders of Specimen 2, which attain 55% composite interaction, each employ twenty-two 3/4" diameter headed shear stud connectors between the column face and the point of applied load (see Figures 2.12 and 2.13). The studs are welded in pairs to the top surface of the top flange at 12" spacing along the girder, starting 9" from the column face and ending 3" from the point of applied load.

The girders of Specimen 3, which attain 35% composite interaction, each utilize fourteen headed shear stud connectors over the effective length of the girder. The studs are welded to the top surface of the girder top flange at 12" spacing, starting 9" from the column face and ending 39" from the point of applied load. Continuing from this point, three sets of studs are placed in pairs up to 3" from the point of applied load (129" from the column face). The minimum specified tensile strength of one shear stud connector, F_u, is equal to 60 ksi and the cross-sectional area of a 3/4" shear stud connector, A_{sc}, is equal to 0.442 in^2.

The concrete slab was also provided with longitudinal and transverse Grade 60 steel reinforcement (Figures 2.12 and 2.13). Starting 1.5" from the column face, #4 non-

epoxy coated, steel reinforcing bars were placed transversely at 12" spaces over the entire length of the concrete slab and are located 2.0" below the top surface of the concrete. Six rows of #4, reinforcing bars were placed longitudinally along the length of the girders and through the panel zone region. With a concrete top and side cover of 1.5", the reinforcement is spaced at 10" on each side of the column.

2.2 Material Properties

Ancillary tests were performed to measure the strength and hardness of the materials used in fabricating the specimens. Other properties, such as the modulus of elasticity of steel and concrete were either assumed or calculated. The A36 and A572 Grade 50 steel members were produced at Nucor-Yamato Steel Co. All the girders were produced from a single heat, as were all the columns. The members appeared to have been straightened prior to shipment. The concrete used in placing the concrete slabs was a product of Cemstone Products Co.

2.2.1 Steel Properties

Several material properties of the steel, including the lower yield stress, F_{ly}, the ultimate tensile stress, F_u, and the modulus of elasticity of steel, E_s, were obtained from tensile coupon tests and by referencing Certified Mill Test Reports. These material properties are used to calculate various strength and stiffness parameters of the test specimens (see Appendices). The steel girder material properties (A36 structural steel) were determined by performing 12 tensile coupon tests. Table 2.2 summarizes the identification, location, and material properties of these coupons. The first letter and number identify the girder (see also "Location") while the third and fourth letters identify the location of the test coupon along the girder cross section (i.e., F or W and N or S, correspond to flange or web and North or South, respectively). The test coupons of the

girder flange were removed approximately 1.5" from the flange tip, while the test coupons of the upper and lower girder web regions were extracted at distances approximately 9" (T) and 13" (B) from the top flange of the steel girder, respectively. Note that the Certified Mill Test Report from the steel producer indicated F_{ly} and F_u values of 48.5 ksi and 62.5 ksi, respectively.

Table 2.2: A36 Structural Steel Lower Yielding Stress, Ultimate Tensile Stress, and Modulus of Elasticity

Coupon	Location	F_{ly} (ksi)	F_u (ksi)	E_s (ksi)
G1FN	Specimen 1/ East Girder Flange	38.0	58.6	*
G1FS	Specimen 1/ East Girder Flange	36.7	58.1	*
G2FN	Specimen 1/ West Girder Flange	39.3	59.2	*
G3FN	Specimen 2/ West Girder Flange	39.6	65.0	*
G4FN	Specimen 2/ East Girder Flange	38.6	58.6	28,700
G4FS	Specimen 2/ East Girder Flange	37.8	60.4	29,600
G4WB	Specimen 2/ East Girder Web	42.0	60.0	28,300
G4WT	Specimen 2/ East Girder Web	37.0	58.6	29,060
G6FN	Specimen 3/ East Girder Flange	*	57.6	28,000
G6FS	Specimen 3/ East Girder Flange	*	59.5	*
G6WB	Specimen 3/ East Girder Web	40.9	59.8	30,000
G6WT	Specimen 3/ East Girder Web	*	58.3	28,100
Average		38.9	59.6	28,940

* No value was recorded

The coupons were fabricated by beginning with a large section of steel that was removed from the specimen with a blowtorch and then sawed to a 9.0" X 1.0" dimension block. An effective area of 0.5" X 0.375" was then established over a 3.0" length at midspan of each coupon. Coupon G3FN was tested with two strain gages and no

extensometer in accordance to ASTM E8-81 and E8-91. The other coupons were tested in accordance to SSRC Technical Memorandum No. 7 (1986). The average values of F_y, F_u, and E_s of the girder and column sections of the specimens which were used in various analyses in this research are summarized in Table 2.3.

Table 2.3: ASTM A36 and A572/50 Structural Steel and AWS Weld Metal Properties

Steel Grade	F_y (ksi)	F_u (ksi)	E_s (ksi)	CVN (ft*lbs)
ASTM A36 (measured; averages)	38	59	29,000	20 @ 20°C (68°F) (minimum required)
ASTM A572/50 (mill test)	57.5	77.0	29,000	24.7 @ -4°C (25°F) (measured)
AWS E70T-1 (nominal)	60.0	72.0	-----	20 @ -18°C (-0.4°F) (minimum required)
AWS E70T-4 (nominal)	58.0	70.0	-----	15 - 20 @ 20°C (68°F) (typical range; no minimum required)
AWS E70T-7 (nominal)	60.0	72.0	-----	15 - 30 @ 20°C (68°F) (typical range; no minimum required)

The experimental lower yield and ultimate tensile stresses of the A572/50 specimen steel (from the W14X211 column section) were obtained from the Certified Mill Test Report from the steel producer (see Table 2.3). The material toughness of the steel was determined using a Charpy V-Notch Toughness (CVN) testing procedure in accordance to ASTM A370 and A673. These tests were performed by the steel producer and were observed to exceed the minimum CVN values of 15 ft-lbs at 40°F or 20 ft-lbs at 70°F (AISC, 1995).

All welds were placed using AWS 5.20-79/ E70T-1 (F_y = 60 ksi, F_u = 72 ksi) welding electrodes, with the exception of the CJP welds connecting the girder flanges to the column flanges, which were placed using AWS 5.20-79/ E70T-7 (F_y = 60 ksi, F_u = 72 ksi) welding electrodes, 3/32" in diameter (see Table 2.3). In accordance with AWS A5.20-79 requirements, E70T-1 minimum weld toughness corresponds to a Charpy V-notch (CVN) value of 20 ft-lbs at -18° C. E70T-7 weld metal toughness, though not required per AWS A5.20-79, is typically in the range of 15 to 30 ft-lbs based on Charpy-V-notch tests performed at 20° C (Lincoln Electric, Co., 1997). Note that the AWS E70T-7 weld metal has similar strength and toughness properties to AWS E70T-4 weld metal (F_y = 58 ksi, F_u = 70 ksi, CVN = 15 to 20 ft-lbs based on typical test results performed at 20° C). However, Kaufmann and Fisher (1997) have found that E70T-7 weld metal often actually has somewhat better toughness properties than E70T-4 weld metal. E70T-4 weld metal is typically specified in the construction and assembly of pre-Northridge CJP welds (Kaufmann et al., 1996).

2.2.2 Steel Material Hardness Properties

Hardness is a measure of the material's resistance to penetration by a hardened steel ball or diamond indentor and may be used to evaluate the strength of a material (Barrett et al., 1973). It is not possible to quantitatively compare various hardness readings measured by different hardness tests on the same material; however, for a given class of materials (e.g., low-carbon steel) the hardness numbers can be correlated with the ultimate tensile strength, F_u.

The measurement of hardness along the girder cross section was performed using a Wilson Rockwell Hardness Testing Machine. The accuracy and reliability of this machine was first verified using two, Scale B standardized testing blocks. These testing blocks (a 69.1 H_{avg} and 98.7 H_{avg}) were used to substantiate the operation of the tester in accordance with ASTM E18. The testing machine meets both the repeatability and error

criteria set forth in the standard. Since the specimens were composed of low-carbon steel, a type B scale test was performed using a 1/16" ball penetrator and a 100 kg load.

The test specimens were prepared by first removing a three inch cross section from the end of the East girder of Specimen 3 with a blowtorch. To eliminate any effects due to excessive heating from the blowtorch, approximately 2" of the cross section immediately adjacent to the cutting edge was removed with a bandsaw. This cross section, approximately 1.2" in thickness, was cut into four sections, keeping intact the top and bottom flanges and flange-web junction regions, and then milled to a thickness of 1.0" with a No. 65 surface finish. Hardness measurements were taken at 327 locations along the flange, web, and flange-web junction regions (see Figure 2.14). The reliability of the testing machine was checked throughout the test by performing calibration checks with the standardized test blocks after every 25 hardness readings.

A contour illustration of the hardness distribution across the observed steel section is shown in Figure 2.15. Starting near the center of the cross section, the web region shows relatively consistent hardness values up to within 2 and 1.5 inches from the top and bottom flange-web junction, respectively. Then, extending along the fillet region (also defined as the "k"-area) of the flange-web junction towards the flange region, an increase in hardness is prominent. When observing the bottom flange region, the hardness numbers decrease at various locations across the bottom flange. This hardness pattern in the bottom flange-web junction is not as evident in the top flange-web junction. In fact, a small portion of the top region shows an increase in hardness near the center of the top flange. In summary, it may be concluded that no significant variation in material hardness was observed within the top or bottom web-flange junction regions of the steel girder section. However, the increase in hardness near the top and bottom "k"-areas is significant, and may correspond to locations of low fracture toughness (Tide, 1997) (see also Sections 5.4.2 and 6.2.5).

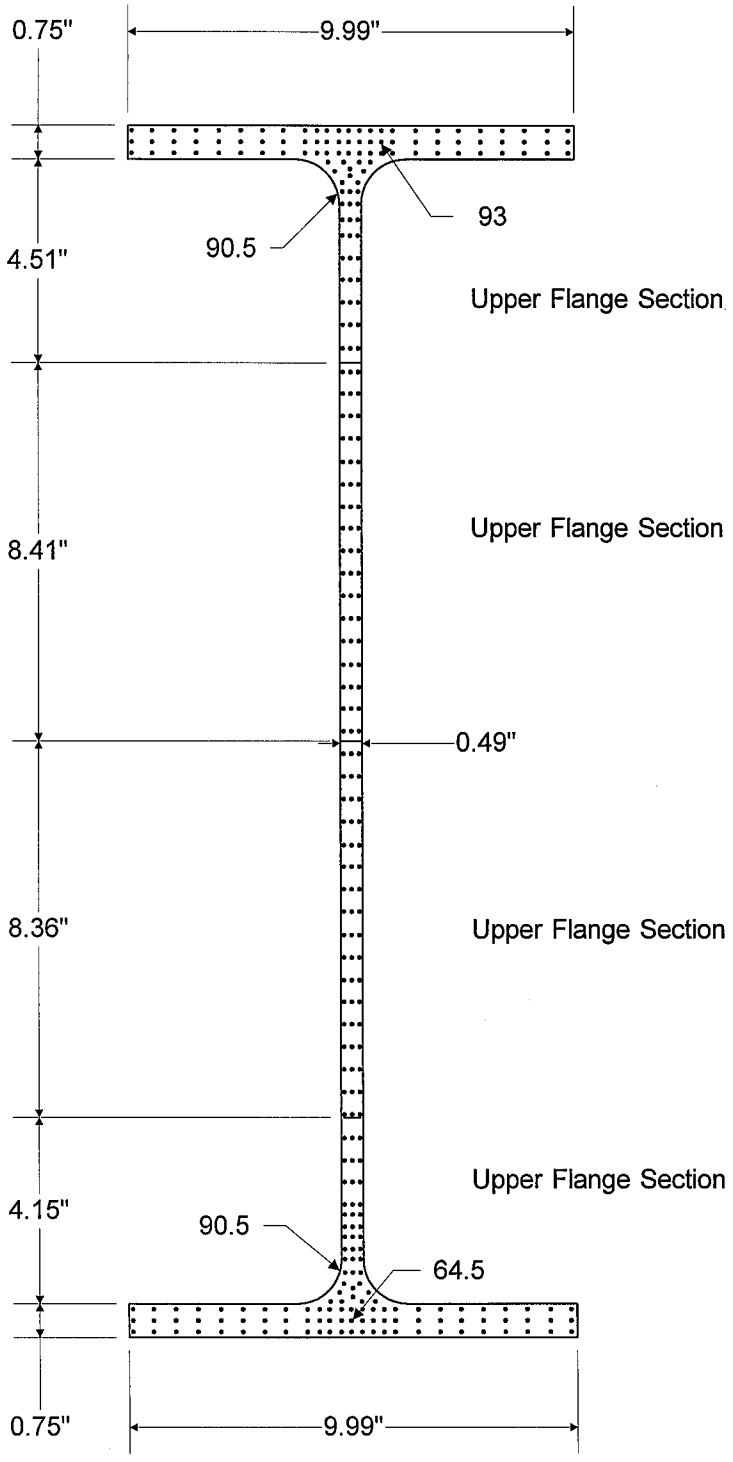

Figure 2.14: Rockwell Hardness Test Locations
(East Girder Cross Section of Specimen 3)

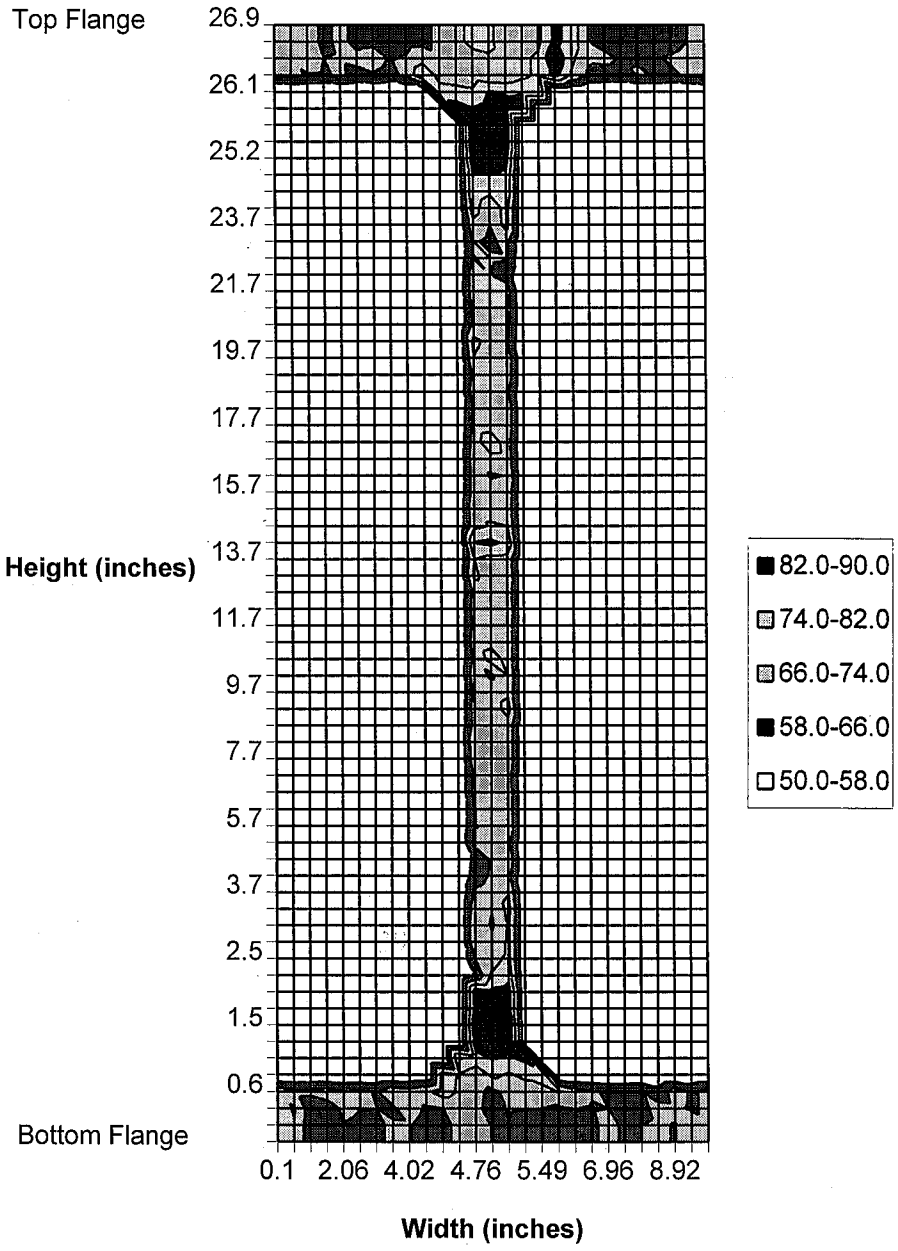

Figure 2.15: Hardness Distribution
(East Girder Cross Section of Specimen 3)

2.2.3 Concrete Properties

The concrete slabs for the two specimens were cast from the same concrete batch, which exhibited 7 day and 28 day compressive strengths equal to 3730 psi (cylinder #1) and 4910 psi (cylinder #4), respectively. The concrete was normal weight (145 pcf). For Specimen 2, an average compressive strength of f_c' = 4910 psi was obtained from compressive strength tests performed on the primary day of testing (8 November 1995, 56 curing days), while for Specimen 3, an average compressive strength of f_c' = 4436 psi was obtained from compressive strength tests performed on the primary day of testing (4 March 1996, 173 curing days) (see Table 2.4):

Table 2.4: Concrete Compressive Strength and Concrete Modulus

Parameter	Source	Specimen 2	Specimen 3
f_c' (psi)	Cylinders #2/ #5	4910	4572
f_c' (psi)	Cylinders #3/ #6	4910	4300
avg f_c' (psi)	calculated	4910	4436
E_c (psi)	calculated ($E_c = 57{,}000\sqrt{f_c'}$)	3.994×10^6	3.796×10^6

Since the concrete deck of Specimen 3 was cast after that of Specimen 2, the lower f_c' measured for the concrete deck of Specimen 3 may be due to the addition of a small amount of water and/or segregation of aggregate of the concrete mix towards the end of the pour, when the Specimen 3 cylinders were cast (#5 and #6). Each average compressive strength value was determined by performing uniaxial compression tests on two, 6"x12" cylinders using a Model QC-400F-LC1 400 kip capacity testing machine manufactured by Forney. The deck was moist cured for seven days and dry cured thereafter. The cylinders were cured in their molds for seven days, and dry cured outside of their molds thereafter.

The concrete modulus for Specimens 2 and 3 is calculated as 3994 ksi and 3796 ksi, respectively, in accordance with AC1 8.5.1 (ACI, 1995) (see Equation in Table 2.4). The results of the average compressive strengths and the calculated modulus of the concrete are summarized for Specimens 2 and 3 in Table 2.4. These material properties are used to calculate various strength and stiffness parameters of the composite girders of the test specimens (see Appendices).

2.3 Monotonic and Cyclic Loading Systems

The specimens were loaded simultaneously using an MTS hydraulic testing machine and four MTS hydraulic actuators (see Figure 2.16). The MTS testing machine, which is capable of applying 600 kips of load, was used to apply a constant tensile axial load (using load control) of 550 kips to the column of the specimen. The actuators, each possessing maximum load and stroke capacities of 77 kips and +/- 6.0", respectively, applied quasi-static antisymmetric, cyclic loading to the girder tips. The actuators incorporated a load controlled, master/slave loading program. Load pin and load frame assemblies were utilized in order to minimize horizontal displacement while permitting free rotation at the ends of the column so as to accurately model the testing scheme as a pinned-pinned cruciform.

2.3.1 Structural Laboratory

The testing of the specimens was conducted in the Structural Laboratory of the Civil Engineering Building at the University of Minnesota. The lab has a clear height of 45', while its base, located on the third floor below grade, has a clear area of 40' X 80.' A 15 ton overhead crane is installed at the ceiling of the lab and is used to transport large loads within the lab complex and in from the loading dock located on ground level. A control room is located on the second floor below grade at the South end of the lab. This

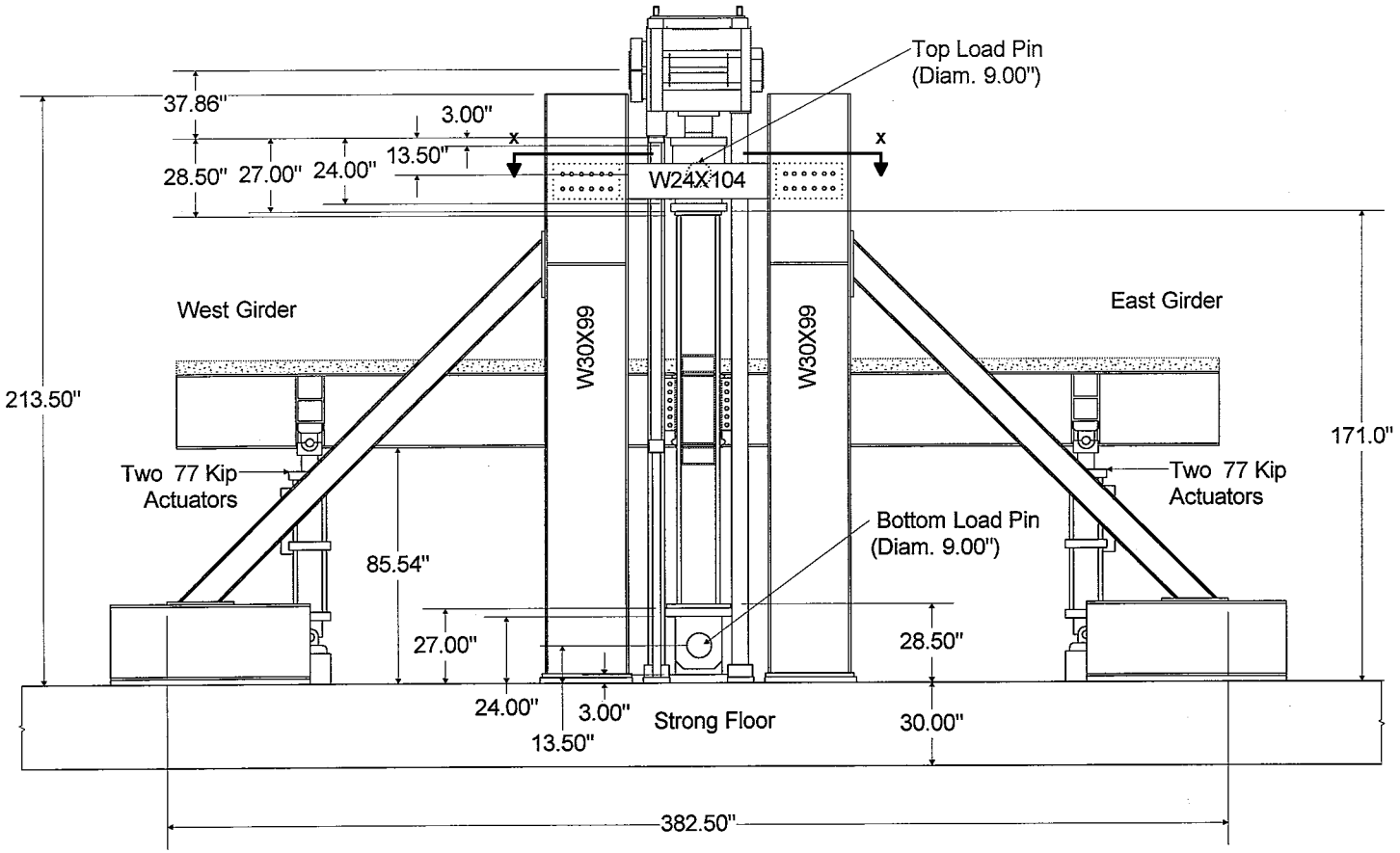

Figure 2.16: Load Frame Assembly With Specimen

facility contains the Digital Equipment Corporation (DEC) test controller computer, hydraulic pump controls, actuator controllers, and data acquisition systems. The strong floor at the base of the structural lab is 30" thick, is coated on the top surface with an epoxy paint, and contains pairs of 2" diameter tie down openings which are spaced at 40" on center. These openings, which are oriented both longitudinally and transversely across the strong floor, are rated for a load capacity of 100 kips per pair of holes.

2.3.2 Load Frame Assembly

The load frame assembly employed for cyclic loading was comprised of several load frame members designed to transfer large shear forces from the top load pin assembly into the strong floor. This was done to restrict horizontal deflections of the top load pin assembly to less than a quarter of an inch. The top load pin assembly was restrained by four C14X40 channels which, in turn, transfer shear forces through two sets of W24X104 braces and into W30X99 vertical members (see Figures 2.16 and 2.17). Forces were then passed into four diagonal braces and into the strong floor.

Girder braces were also attached to the diagonal braces to prevent out-of-plane displacements of the girders due to lateral-torsional buckling (see Figure 2.18). These braces were located at a distance of 84" from the column face. Note that the limiting unbraced length for full plastic bending capacity, L_p, was calculated as 103" for a W27X94 W-shaped section ($L_p = 300 r_y / \sqrt{F_y}$). Two actuator brackets were welded on each side of each girder web at a distance of 132" from the column flange surface. Also, the bottom end of each set of actuators was bolted to a reaction block which was anchored to the strong floor with four, 2.0" diameter high-strength steel ties.

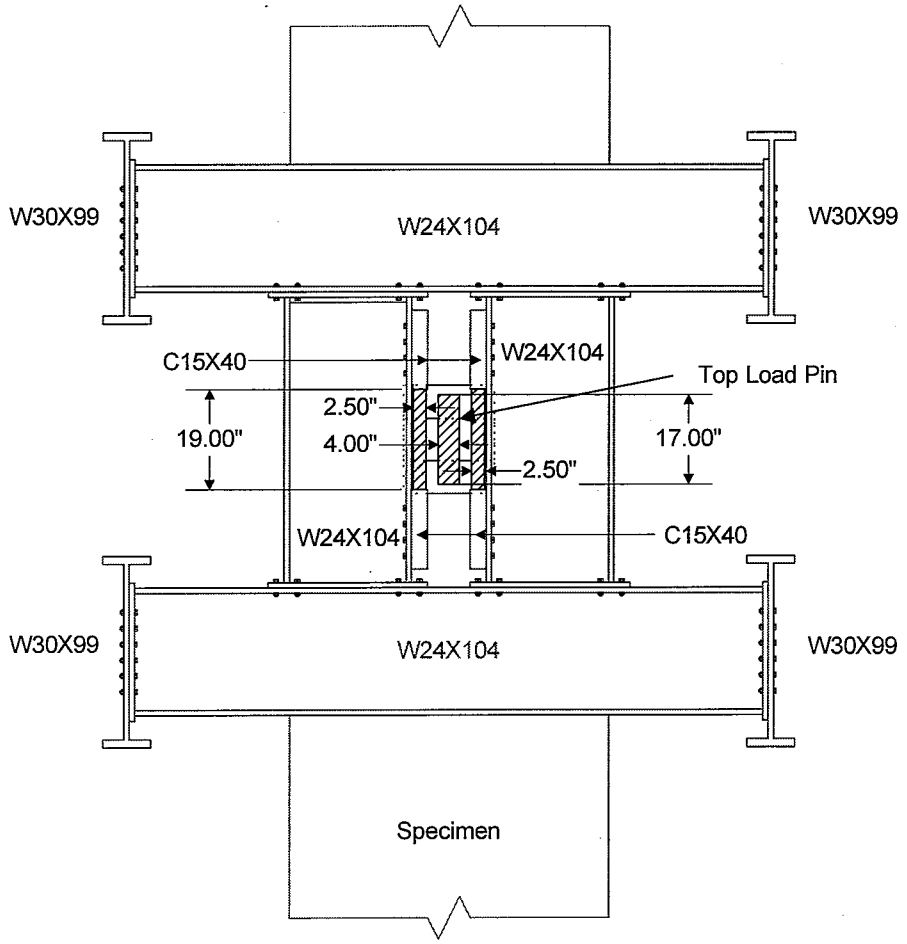

Figure 2.17: Section X-X: Top View of Load Frame and Top Load Pin Assemblies

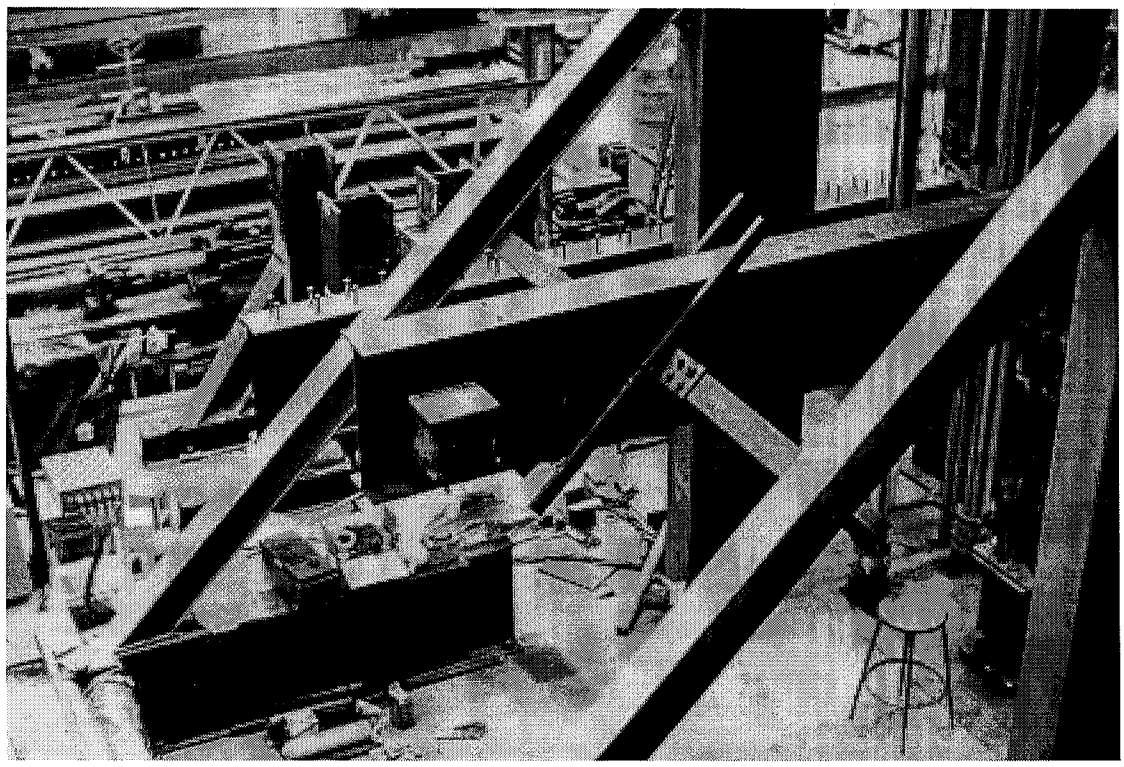

Figure 2.18: Lateral-Torsional Buckling Braces

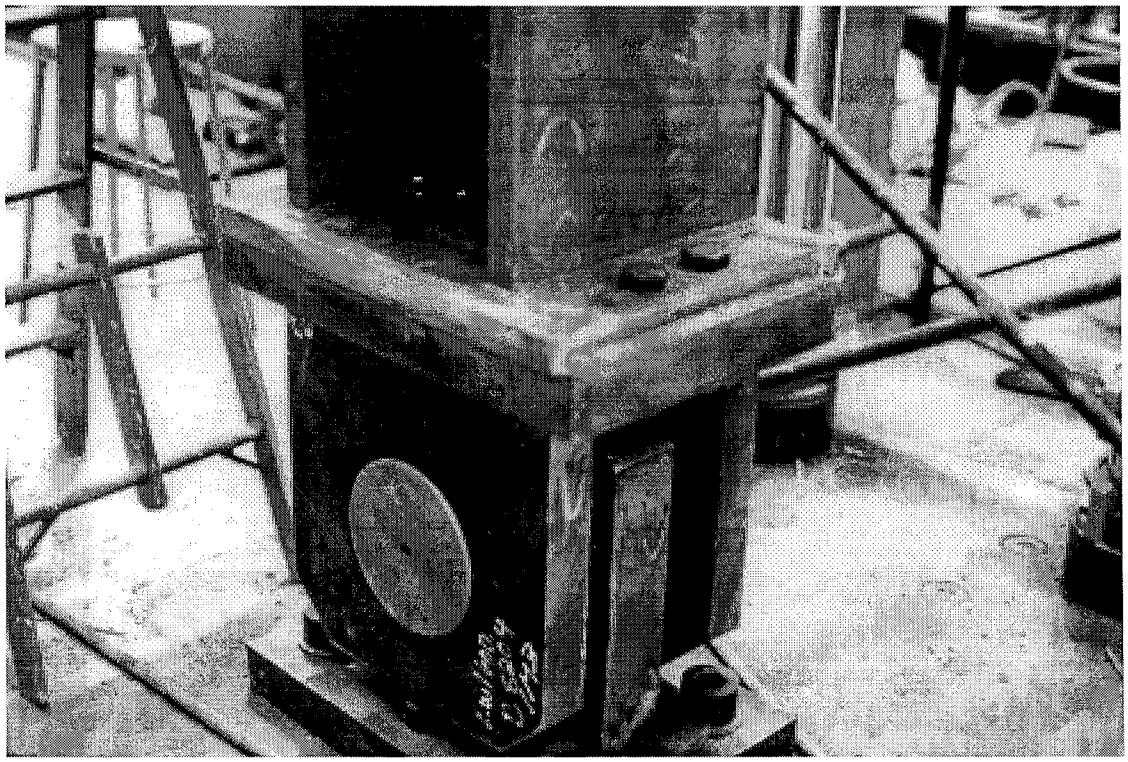

Figure 2.19: Bottom Load Pin Assembly

2.3.3 Load Pin Assemblies

Two load pins were used to allow rotation of the column ends during cyclic loading. The top load pin was connected to the MTS 600 kip testing machine to allow an axial load to be applied to the specimens. The bottom load pin assembly was anchored to the laboratory strong floor with several 1.5" and 2.0" diameter, high-strength steel bolts (see Figure 2.19). The top and bottom load pins were bolted and welded with stitch welds to Specimens 1 and 2. During the testing of Specimen 2, however, the stitched welds at the top load pin cracked. As a result, Specimen 3 was bolted and welded with continuous fillet welds to the top and bottom load pins. To reduce the effects of load pin friction during cyclic testing, the pins were packed with grease prior to the testing of Specimen 1. Based on data analysis, it has been determined that effects of load pin friction were negligible (see Section 4.1.1).

2.4 Instrumentation

Four main types of instrumentation, including an inclinometer, linear variable differential transformers (LVDTs), strain gages, and acoustic emission transducers were employed to measure rotations, displacements, strains, and microfracturing and cracking of various elements of the three test specimens. Various types of LVDTs and strain gages were used to instrument the specimens, depending upon the purpose or function of the instrument.

2.4.1 Inclinometer

An inclinometer was utilized to measure rotation of the connection region relative to the strong floor (see Figure 2.20). This device can measure changes in rotations between +/- 0.5° with a resolution of +/- 0.0001°. The inclinometer was attached to the

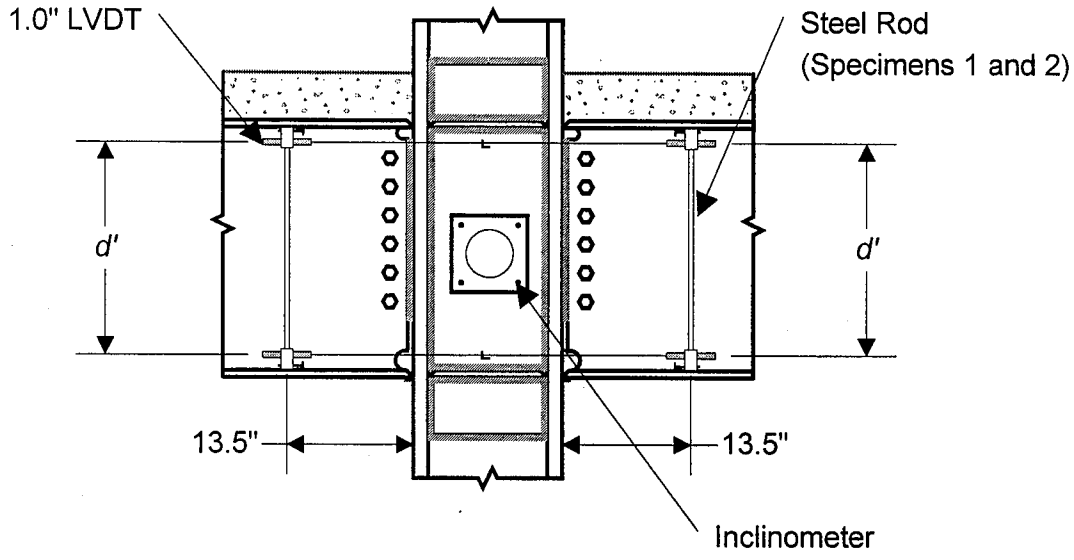

Figure 2.20: LVDT Locations of North Connection Region

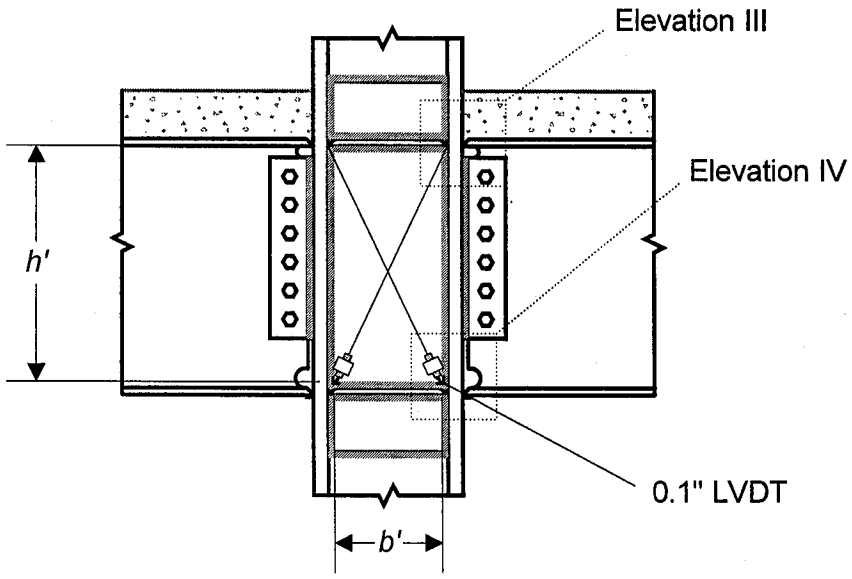

Figure 2.21: LVDT Locations of South Connection Region

center of the North panel zone region with four, 1/4" diameter steel bolts which were tack welded to the surface of the doubler plate. It was operated with a DC power supply and possessed an internal conditioner. Output readings were read with a voltmeter and recorded by the data acquisition system. The inclinometer was a Model 800 Tiltimeter manufactured by Applied Geomechanics Inc.

2.4.2 Linear Variable Differential Transformers

Several Linear Variable Differential Transformers (LVDTs) were used to measure changes in displacement which, in turn, were used to establish changes in connection rotation, distortion, and composite slip. Also, an LVDT measured the horizontal displacement (in the East-West direction) of the top load pin assembly relative to the strong floor. The two LVDT HR Series models utilized in the tests [100 HR (0.1") and 1000 HR (1")] possessed a tolerance of 0.25% and were manufactured by Schaevitz.

The LVDTs measuring panel zone deformation and girder-to-column rotation were each held in place by an LVDT suspension assembly composed of a plastic clamp, 1/2" steel angles, and 1/4" steel threaded rods (see Figures 2.20 to 2.23). This assembly was tack welded to the steel specimen. The ends of the LVDT displacement rods were screwed into free-rotational clamps which were then fastened to the specimen or to a bracket with an epoxy adhesive.

To measure rotation of the girder relative to the column, four 1000 HR (1.0") LVDTs were located on the South side of the specimens (Figure 2.20). The LVDTs were located at the top and bottom flanges of the East and West girders. The LVDTs were connected to the inside surface of the flanges at a distance of 13.5" from the column face, and to the center of the column web. For Specimens 1 and 2, a 1/2" diameter steel rod was used to connect the top and bottom LVDTs for each girder; this rod was removed for Specimen 3 as it was deemed unnecessary. The distances measured between the

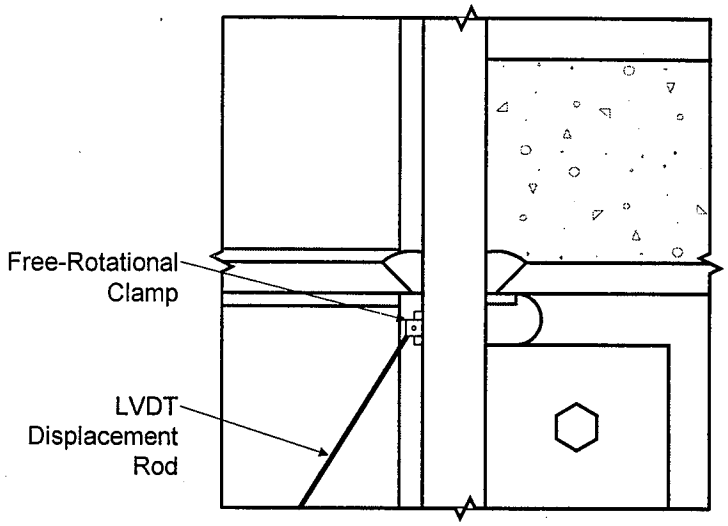

Figure 2.22: Elevation III: LVDT Locations of South Connection Region

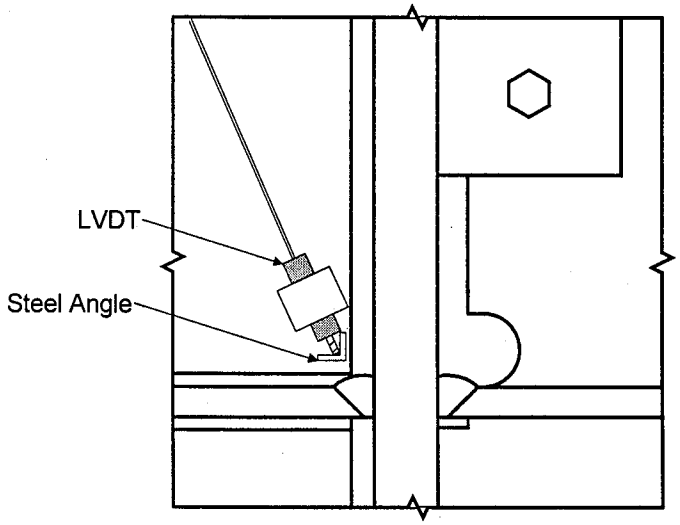

Figure 2.23: Elevation IV: LVDT Locations of South Connection Region

center of the top and bottom LVDTs for the East and West girders, *d'*, and the calculation of the girder-to-column rotations using this parameter is shown in Appendix B.

Two 100 HR (0.1") LVDTs were installed at the South end of the panel zone at the bottom/West and the bottom/East intersection of the column flange and the bottom continuity plate (see Figures 2.21-2.23). The LVDTs were oriented to measure changes in displacement relative to the corner of panel zone that was located diagonally opposite from the LVDT. The vertical and horizontal distances between the LVDT assemblies within the panel zone region, *h'* and *b'*, are provided in Appendix B.

For all the specimens, a 1000 HR (1.0") LVDT was installed to the outside casing of the MTS testing machine (top load pin assembly) and to a column that was connected to the strong floor. This LVDT, which measured displacement of the top load pin assembly relative to the strong floor in the East-West direction, is used to calculate the contribution of load frame deformation to the girder tip deflection (see Appendix F).

During the testing of Specimen 1, a 1000 HR (1.0") LVDT was installed vertically to the East column flange and East girder top of bottom flange. This was done to measure possible "double-curvature" effects and vertical shearing phenomena within this region. Also, Specimen 3 incorporated the use of two 100 HR (0.1") LVDTs that measured the change in displacement in the longitudinal direction of the specimen between the concrete slab and the steel girder sections. For the East and West girders, both end components of each LVDT were located at a distance of 126" from the face of the column. The LVDT suspension assembly was anchored into the bottom side of the slab, where the metal decking was locally removed.

2.4.3 Strain Gages

Three types of strain gages were employed to measure strains at various locations on the specimens: TML Post-Yield Gages (Series TFL), TML Foil Gages (Series F), and TML rosette strain gages (Series PMR-60 and WFRA-6). These gages possessed a

tolerance of 0.05% and were manufactured by Tokyo Sokki Kenyuto Co. Ltd. Figures 2.24 to 2.34 illustrate the locations of these strain gages on the specimens, while Figures 2.8(a) and 2.8(b) provide the locations of the various sections viewed. In conjunction with these figures, Tables 2.5 to 2.8 summarize the locations of the strain gages on the three specimens.

The nomenclature used to identify the strain gages was based on the type of gage and its location on the specimen. Each strain gage label is classified based on its location on the specimen relative to the laboratory (North, South, East, and West directions) and the element on which it is installed (beam, column, or concrete slab). Also, each strain gage label contains a number, individually identifying each strain gage at a specific location on an element. For the post-yield (or high-elongation) strain gages, the labels are preceded with the letter *h*.

Twelve post-yield strain gages were used to measure strains that reached large magnitudes near the girder-to-column interface of the specimens (see Figures 2.24-2.25, 2.28-2.29 and 2.31-2.33). In addition, two rosettes, along with the post-yield strain gages, were also utilized to study a triaxial state of tensile strain near the bottom girder-to-column weld region (see Appendix I).

Fourteen foil gages located along the steel girder sections at a distance of approximately 13.5" from the column face (Figures 2.24 to 2.27). These strain gages were used to calculate the position of the neutral axis and the curvature of the girder sections and, therefore, the girder moments and strains (see Appendix H).

Twenty foil strain gages and two internal concrete rosette strain gages were placed in the concrete slab for Specimens 2 and 3 (see Figure 2.34). The foil strain gages were placed in four rows of five gages, located at a distance of 1.5" and 13.5" from the column face on each side of the column, and were attached to the top side of the #4 longitudinal steel reinforcing bars. The concrete rosette strain gages were placed approximately 4" away from the column face and were placed in the concrete at a depth of approximately 1.5". The strain gages located in the concrete slab at a distance of 13.5" from the column

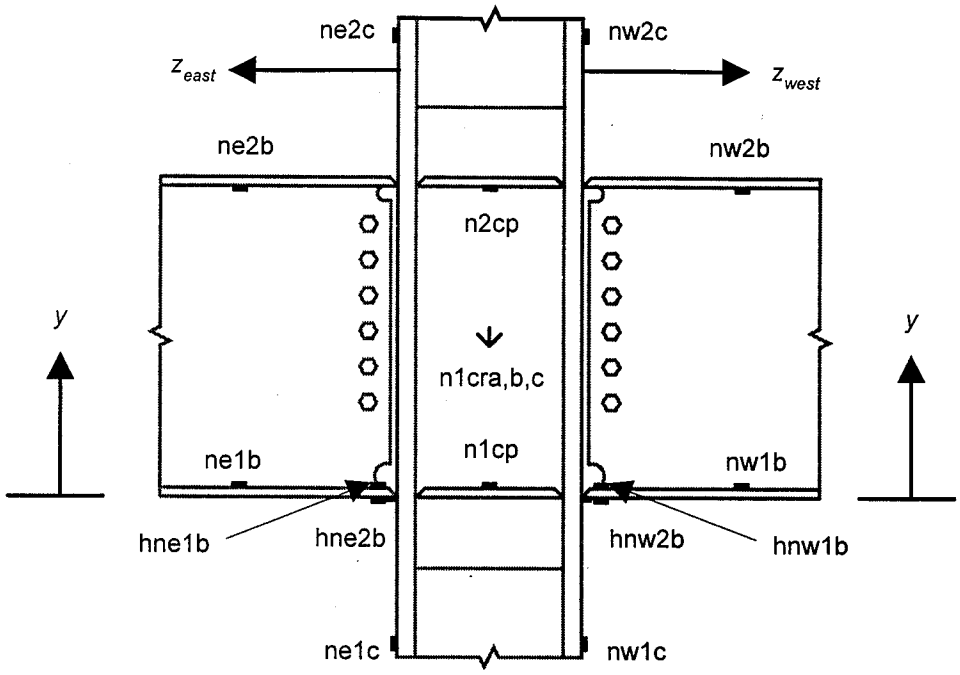

Figure 2.24: Strain Gages of North Connection Region

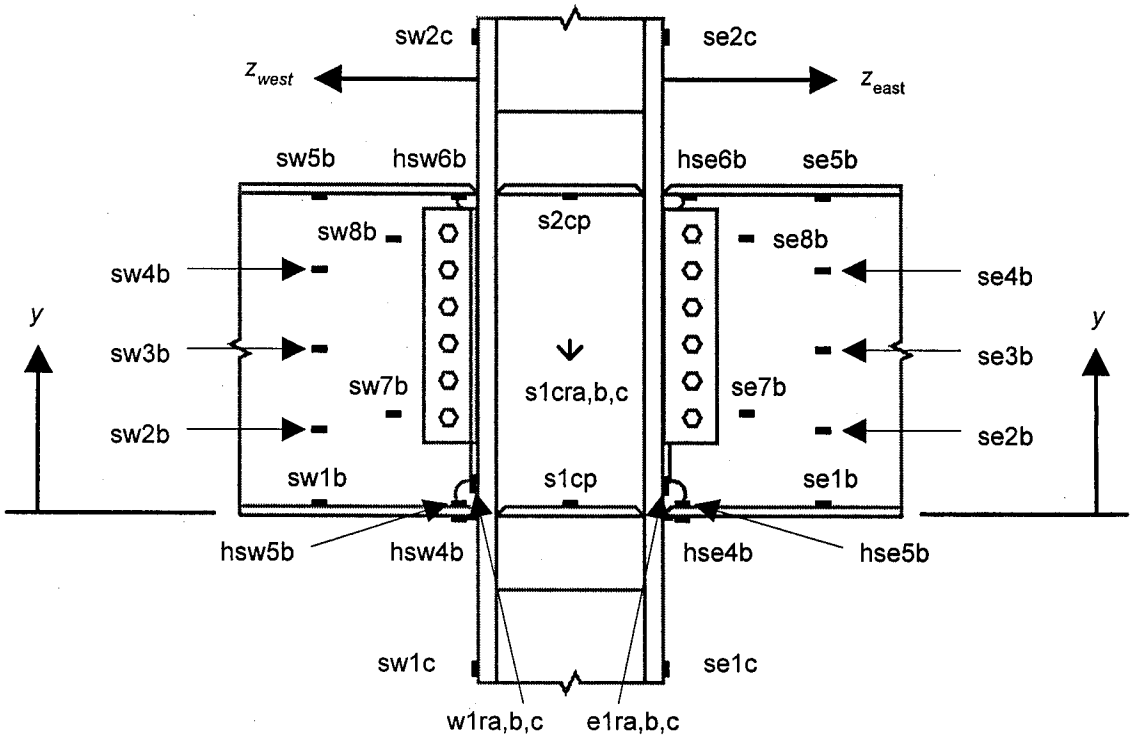

Figure 2.25: Strain Gages of South Connection Region

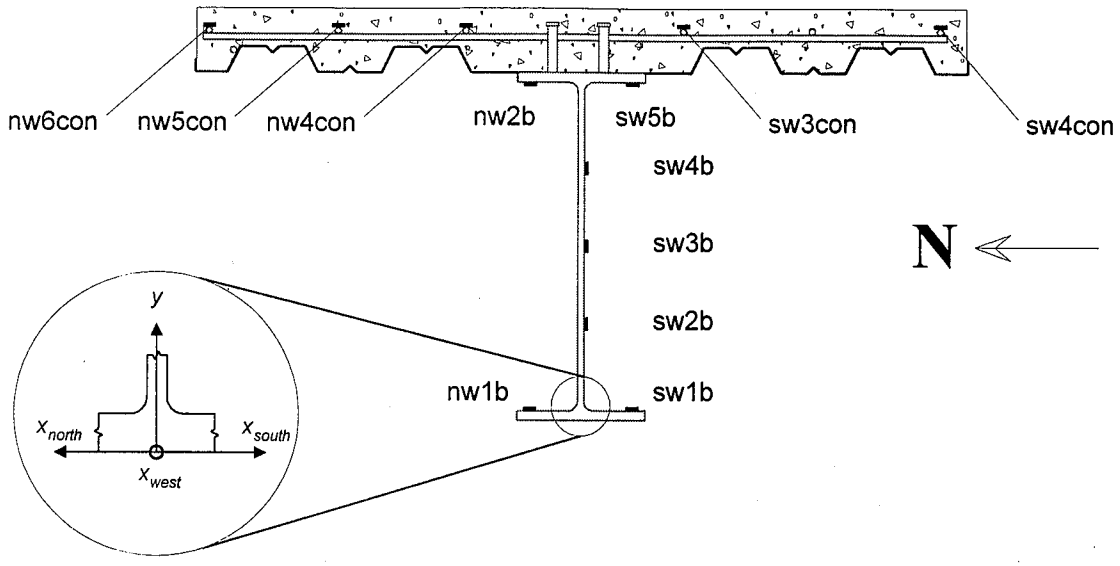

Figure 2.26: Section B-B: Strain Gages of West Girder Cross Section

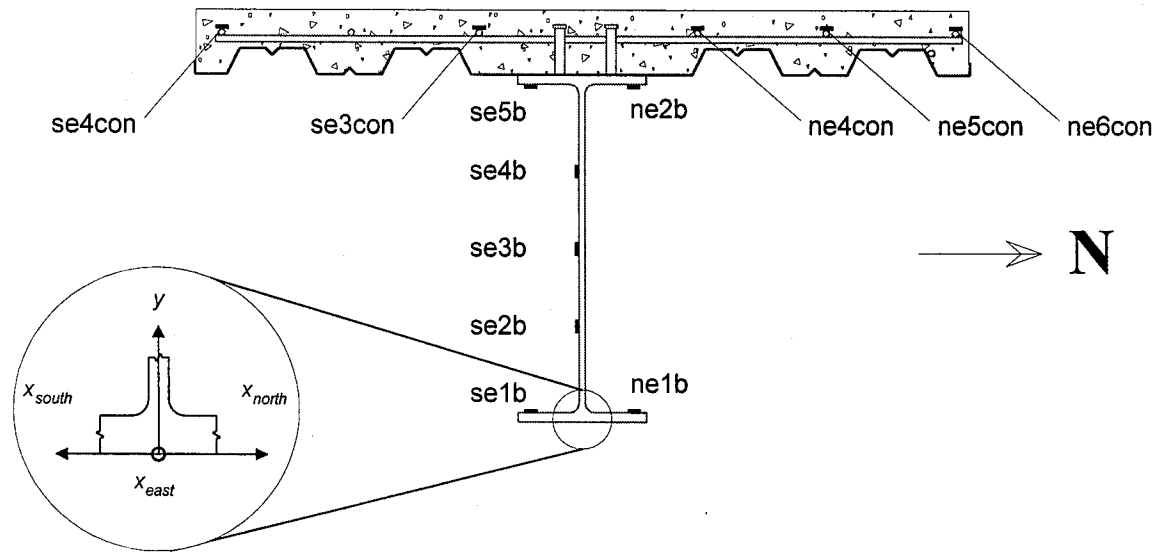

Figure 2.27: Section C-C: Strain Gages of East Girder Cross Section

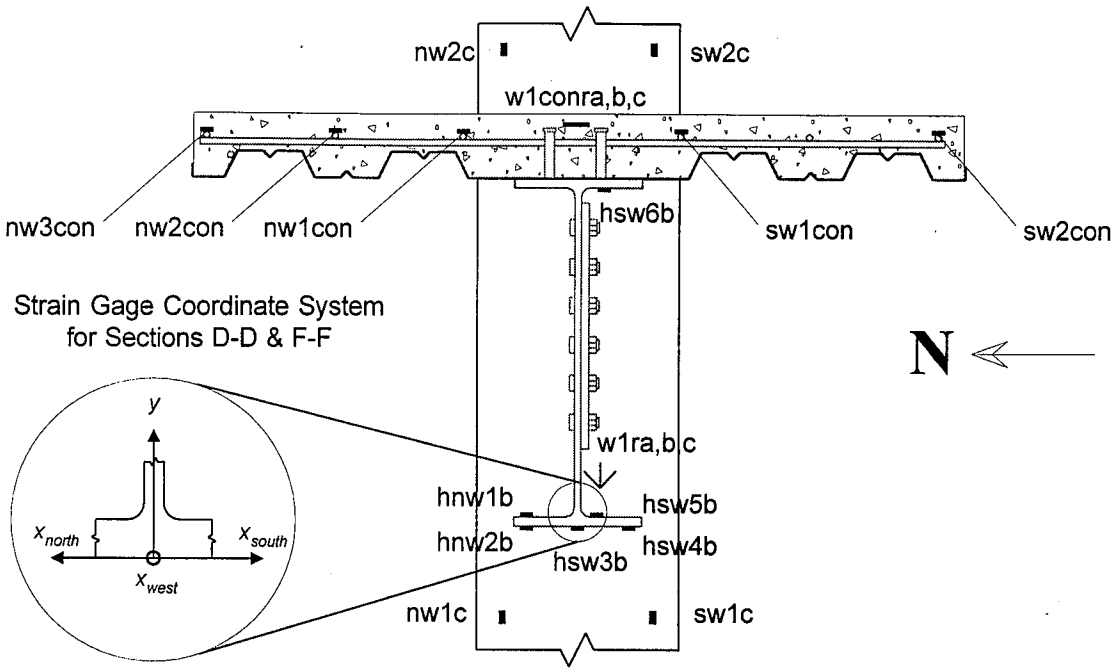

Figure 2.28: Section D-D: Strain Gages of West Girder Cross Section

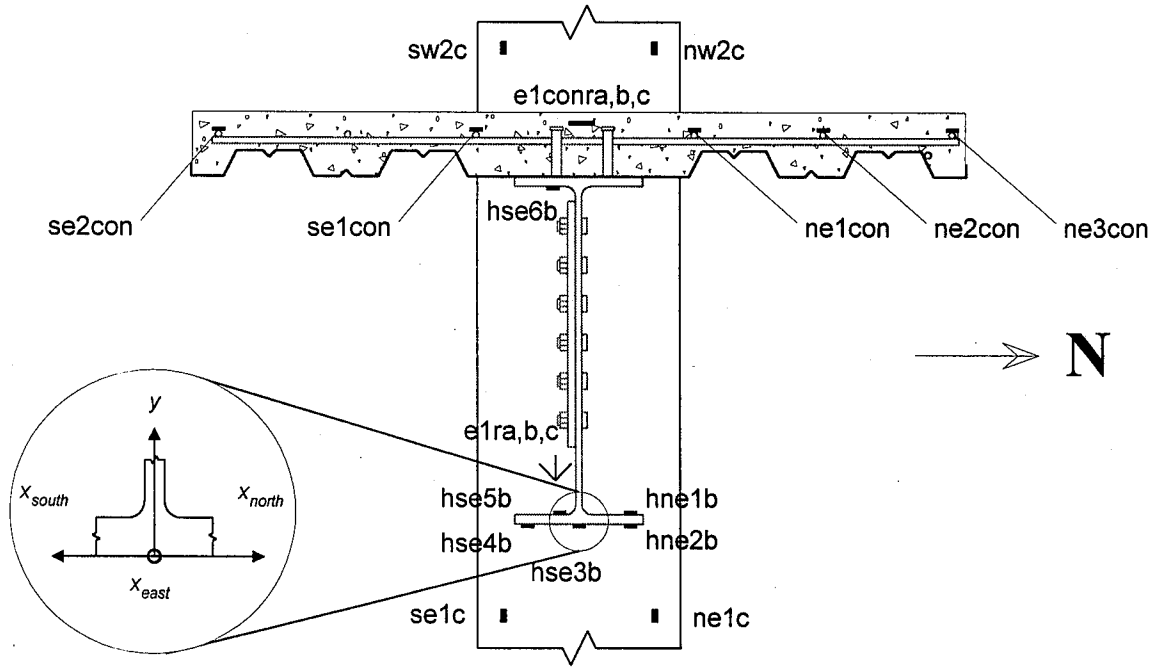

Figure 2.29: Section E-E: Strain Gages of East Girder Cross Section

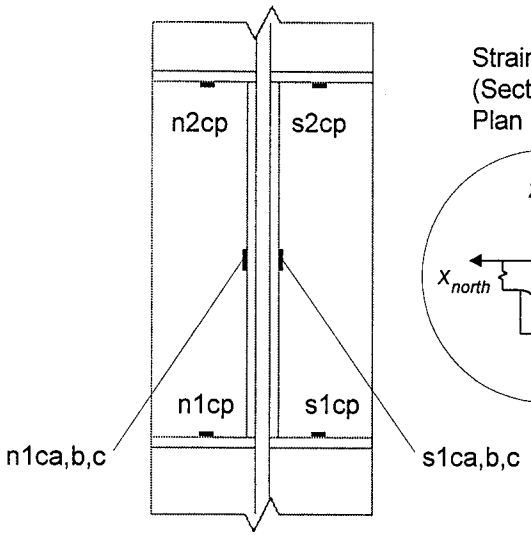

Figure 2.30: Section F-F: Strain Gages of Panel Zone Cross Section

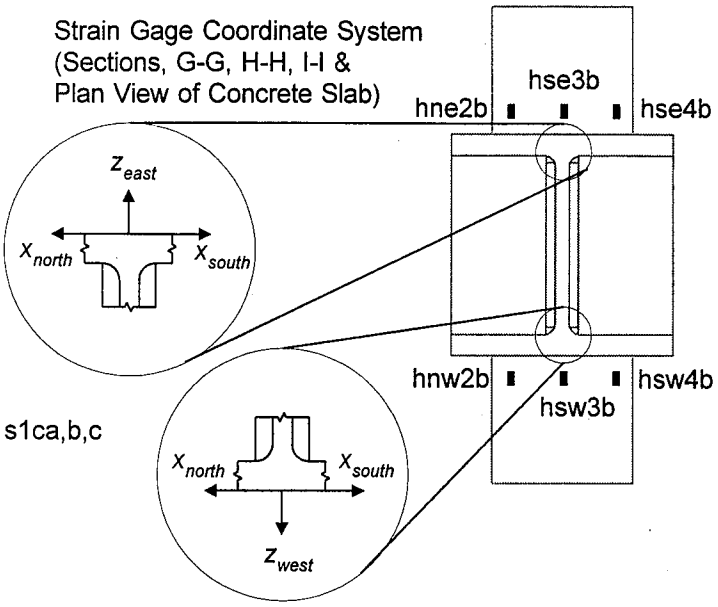

Figure 2.31: Section G-G: Strain Gages of Bottom of Bottom Girder Flanges

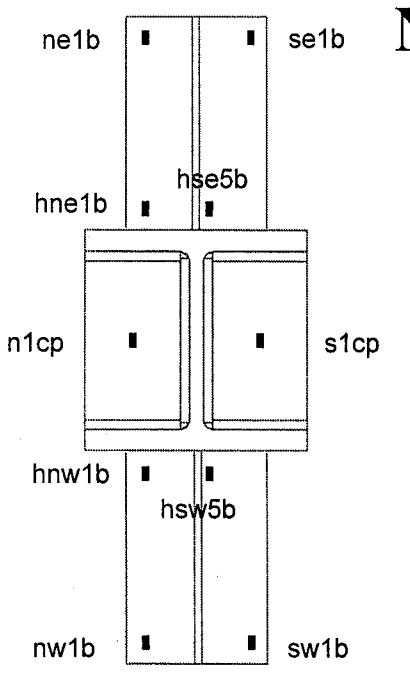

Figure 2.32: Section H-H: Strain Gages of Top of Bottom Girder Flanges

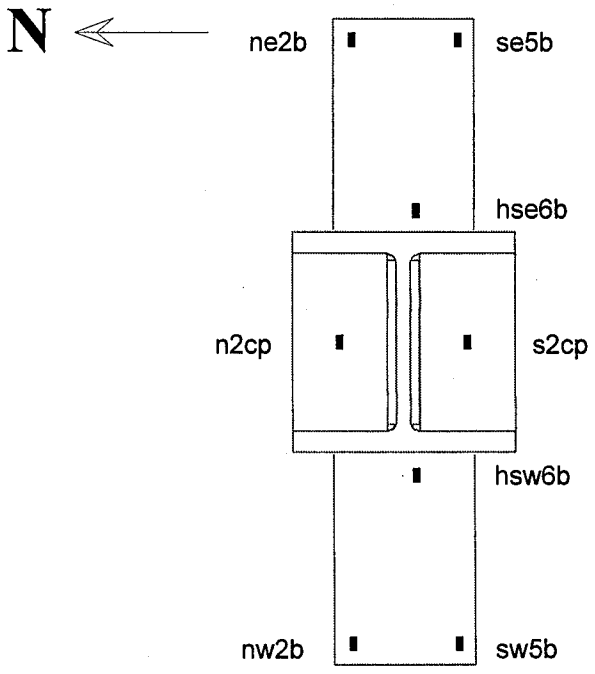

Figure 2.33: Section I-I: Strain Gages of Bottom of Top Girder Flanges

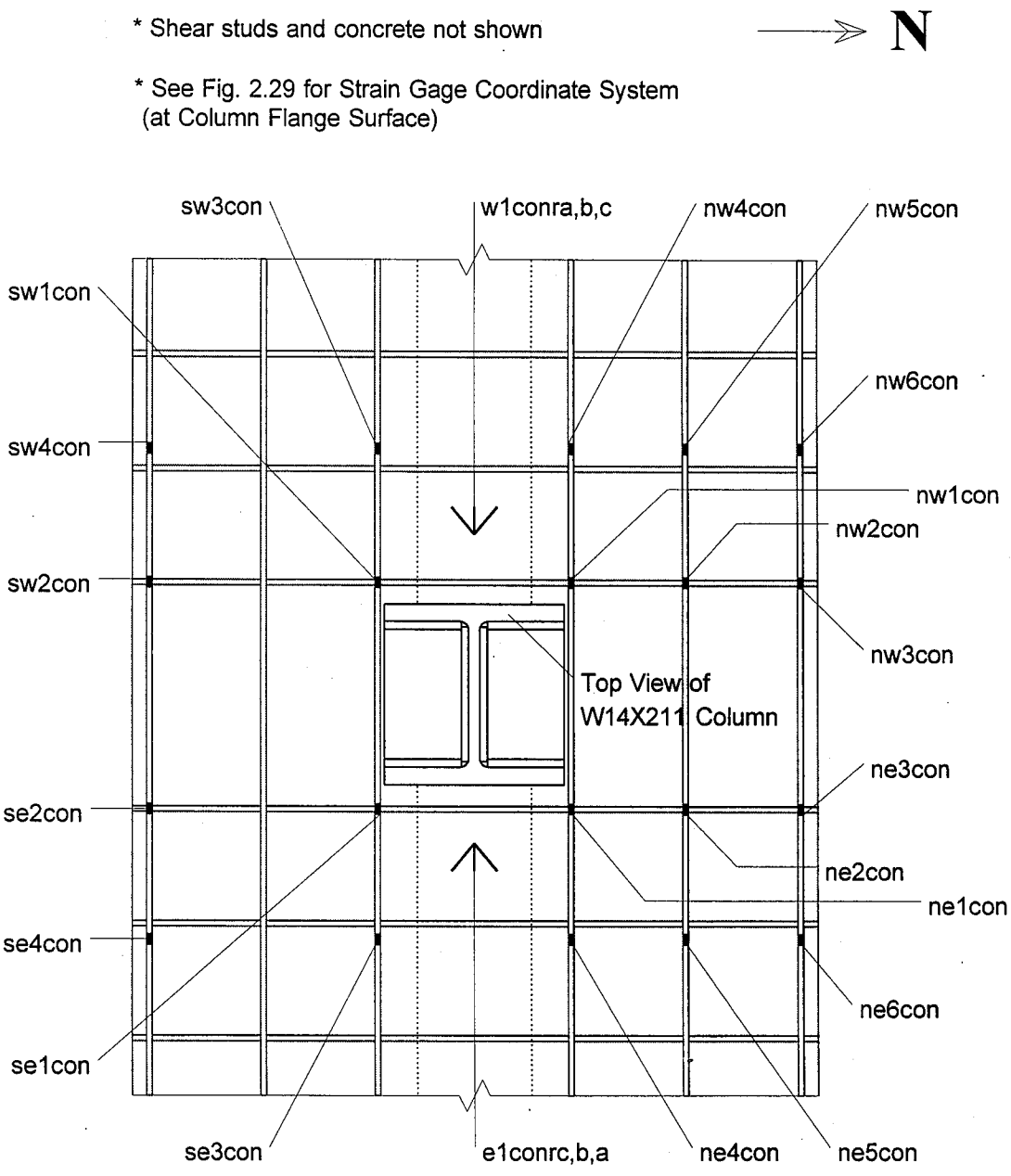

Figure 2.34: Strain Gages of Concrete Slab (Plan View)

Table 2.5: Strain Gage Locations (Northeast Region of Specimens)

Strain Gages	Strain Gage Locations (inches)											
	Nominal			Specimen 1			Specimen 2			Specimen 3		
NE Region	x_{north}	y	z_{east}	x_{north}	y	z_{east}	x_{north}	y	z_{east}	x_{north}	y	z_{east}
hne1b	2.75	0.75	1.50	2.50	0.75	1.25	2.50	0.75	1.25	1.50	0.75	2.75
hne2b	2.75	0.0	1.50	2.88	0.0	1.50	1.50	0.0	2.75	1.50	0.0	2.75
ne1b	2.75	0.75	13.5	2.75	0.75	13.5	2.75	0.75	13.5	2.82	0.75	13.6
ne2b	2.75	26.1	13.5	2.62	26.1	13.8	2.75	26.1	13.6	2.56	26.1	13.5
ne1c	4.88	*-12.5*	0.0	4.88	*-12.5*	0.0	4.88	*-12.0*	0.0	4.88	*-12.4*	0.0
ne2c	1.88	39.4	0.0	1.88	39.4	0.0	4.88	38.4	0.00	5.00	40.6	0.0
ne1con	8.50	30.4	1.50	8.50	30.4	1.50	8.50	30.4	1.50	8.50	30.4	1.50
ne2con	18.5	30.4	1.50	18.5	30.4	1.50	18.5	30.4	1.50	18.5	30.4	1.50
ne3con	28.5	30.4	1.50	28.5	30.4	1.50	28.5	30.4	1.50	28.5	30.4	1.50
ne4con	8.5	30.4	13.5	8.5	30.4	13.5	8.5	30.4	13.5	8.5	30.4	13.5
ne5con	18.5	30.4	13.5	18.5	30.4	13.5	18.5	30.4	13.5	18.5	30.4	13.5
ne6con	28.5	30.4	13.5	28.5	30.4	13.5	28.5	30.4	13.5	28.5	30.4	13.5
e1conrc,b,a	0.0	30.4	4.0	0.0	30.4	4.0	0.0	30.4	4.0	0.0	30.4	4.0

* Note: Italicized values are measured in the negative x, y, or z directions.

Table 2.6: Strain Gage Locations (Northwest Region of Specimens)

Strain Gages	Strain Gage Locations (inches)											
	Nominal			Specimen 1			Specimen 2			Specimen 3		
NW Region	x_{north}	y	z_{west}	x_{north}	y	z_{west}	x_{north}	y	z_{west}	x_{north}	y	z_{west}
hnw1b	2.75	0.75	1.50	2.34	0.75	1.5	2.5	0.75	1.25	2.25	0.75	1.50
hnw2b	2.75	0.0	1.50	2.83	0.0	1.5	2.83	0.0	1.50	2.83	0.0	1.50
nw1b	2.75	0.75	13.5	2.63	0.75	13.5	2.75	0.75	13.5	2.88	0.75	13.5
nw2b	2.75	26.1	13.5	2.63	26.1	13.5	2.75	26.1	13.5	2.81	26.1	13.5
nw1c	4.88	*-12.5*	0.0	4.88	*-12.5*	0.0	4.88	*-12.5*	0.0	4.88	*-12.5*	0.0
nw2c	1.88	39.4	0.0	1.88	39.4	0.0	1.88	39.4	0.0	1.88	39.4	0.0
n1cp	4.50	0.75	*-7.8*	4.50	0.75	*-7.8*	4.50	0.75	*-7.8*	4.50	0.75	*-7.8*
n2cp	4.50	26.1	*-7.8*	4.50	26.1	*-7.8*	4.50	26.1	*-7.8*	4.50	26.1	*-7.8*
n1cra,b,c	1.13	13.4	*-7.9*	1.13	13.4	*-6.9*	1.13	13.4	*-6.9*	1.13	13.4	*-7.0*
nw1con	8.50	30.4	1.50	8.50	30.4	1.50	8.50	30.4	1.50	8.50	30.4	1.50
nw2con	18.5	30.4	1.50	18.5	30.4	1.50	18.5	30.4	1.50	18.5	30.4	1.50
nw3con	28.5	30.4	1.5.0	28.5	30.4	1.50	28.5	30.4	1.50	28.5	30.4	1.50
nw4con	8.5	30.4	13.5	8.5	30.4	13.5	8.5	30.4	13.5	8.5	30.4	13.5
nw5con	18.5	30.4	13.5	18.5	30.4	13.5	18.5	30.4	13.5	18.5	30.4	13.5
nw6con	28.5	30.4	13.5	28.5	30.4	13.5	28.5	30.4	13.5	28.5	30.4	13.5
w1conra,b,c	0.0	30.4	4.00	0.0	30.4	4.00	0.0	30.4	4.00	0.0	30.4	4.00

* Note: Italicized values are measured in the negative x, y, or z directions.

Table 2.7: Strain Gage Locations (Southeast Region of Specimens)

Strain Gages	Strain Gage Locations (inches)											
	Nominal			Specimen 1			Specimen 2			Specimen 3		
SE Region	x_{south}	y	z_{east}	x_{south}	y	z_{east}	x_{south}	y	z_{east}	x_{south}	y	z_{east}
hse3b	0.0	0.0	1.50	*-0.13*	0.0	1.50	*-0.25*	0.0	1.50	*-0.13*	0.0	1.50
hse4b	2.75	0.0	1.50	2.88	0.0	1.50	2.75	0.0	1.50	2.75	0.0	1.50
hse5b	1.50	0.75	1.50	1.50	0.75	1.13	1.50	0.75	1.50	1.44	0.75	1.44
hse6b	1.50	26.1	1.50	2.00	26.1	1.00	1.81	26.1	1.38	1.50	26.1	1.63
e1ra,b,c	1.50	2.00	0.0	1.50	2.00	0.0	1.50	2.00	0.0	1.44	2.94	.0
se1b	2.75	0.75	13.5	2.75	0.75	13.5	2.75	0.75	13.5	2.75	0.75	13.5
se2b	0.25	6.75	13.5	0.25	6.88	13.6	0.25	6.75	13.5	0.25	6.88	13.4
se3b	0.25	13.5	13.5	0.25	13.8	13.6	0.25	13.5	13.5	0.25	13.4	13.4
se4b	0.25	20.3	13.5	0.25	20.5	13.6	0.25	20.4	13.6	0.25	20.3	13.4
se5b	2.75	26.1	13.5	2.75	36.1	13.5	2.75	26.1	13.5	2.63	26.1	13.5
se7b	0.25	7.88	6.00	0.25	7.88	6.00	0.25	7.75	6.00	0.25	7.75	5.88
se8b	0.25	23.3	6.00	0.25	23.2	6.00	0.25	22.8	6.00	0.25	22.8	5.88
se1c	4.88	*-12.5*	0.0	4.88	*-12.5*	0.0	4.88	*-12.0*	0.0	4.88	*-12.4*	0.0
se2c	4.88	39.4	0.0	4.88	39.4	0.0	4.88	38.4	0.0	5.00	40.6	0.0
se1con	8.5	30.9	1.5	8.5	30.9	1.5	8.5	30.9	1.5	8.5	30.9	1.5
se2con	28.5	30.9	1.5	28.5	30.9	1.5	28.5	30.9	1.5	28.5	30.9	1.5
se3con	8.5	30.9	1.5	8.5	30.9	1.5	8.5	30.9	1.5	8.5	30.9	1.5
se4con	28.5	30.9	1.5	28.5	30.9	1.5	28.5	30.9	1.5	28.5	30.9	1.5

* Note: Italicized values are measured in the negative x, y, or z directions.

Table 2.8: Strain Gage Locations (Southwest Region of Specimens)

Strain Gages	Strain Gage Locations (inches)											
	Nominal			Specimen 1			Specimen 2			Specimen 3		
SW Region	x_{south}	y	z_{west}	x_{south}	y	z_{west}	x_{south}	y	z_{west}	x_{south}	y	z_{west}
hsw3b	0.0	0.0	1.50	0.0	0.0	1.50	*-0.25*	0.0	1.50	*-0.13*	0.0	1.50
hsw4b	2.75	0.0	1.50	2.75	0.0	1.50	2.75	0.0	1.50	2.75	0.0	1.50
hsw5b	1.50	0.75	1.50	1.13	0.75	1.50	1.00	0.75	1.50	1.50	0.75	1.63
hsw6b	1.50	26.1	1.50	1.25	26.1	1.50	1.13	26.1	1.13	1.50	26.1	1.50
w1ra,b,c	1.50	2.00	0.0	1.50	2.00	0.0	1.50	2.00	0.0	1.50	2.00	1.63
sw1b	2.75	0.75	13.5	2.75	0.75	13.5	2.75	0.75	13.4	2.75	0.75	13.5
sw2b	0.25	6.75	13.5	0.25	6.63	13.5	0.25	6.75	13.5	0.25	6.69	13.5
sw3b	0.25	13.5	13.5	0.25	13.4	13.5	0.25	13.5	13.5	0.25	12.8	13.5
sw4b	0.25	20.3	13.5	0.25	20.0	13.5	0.25	20.3	13.5	0.25	20.2	13.5
sw5b	2.75	26.1	13.5	2.38	26.1	13.5	2.75	26.1	13.5	2.81	26.1	13.4
sw7b	0.25	7.88	6.00	0.25	7.88	6.00	0.25	7.50	6.00	0.25	7.81	6.00
sw8b	0.25	23.3	6.00	0.25	22.9	5.88	0.25	23.0	5.88	0.25	22.8	6.00
sw1c	4.88	*-12.5*	0.0	4.88	*-12.5*	0.0	4.88	*-12.4*	0.0	4.88	*-12.4*	0.0
sw2c	4.88	39.4	0.0	4.88	39.4	0.0	4.88	38.9	0.0	4.88	40.6	0.0
s1cp	4.50	0.75	*-7.8*	4.50	0.75	*-7.9*	4.50	0.75	*-7.8*	4.50	0.75	*-7.8*
s2cp	4.50	26.1	*-7.8*	4.50	26.1	*-7.9*	4.50	26.1	*-7.8*	4.50	26.1	*-7.8*
s1cra,b,c	1.13	13.4	*-7.8*	1.13	13.4	*-7.9*	1.13	13.4	*-7.8*	1.13	13.4	*-7.8*
sw1con	8.5	30.9	1.5	8.5	30.9	1.5	8.5	30.9	1.5	8.5	30.9	1.5
sw2con	28.5	30.9	1.5	28.5	30.9	1.5	28.5	30.9	1.5	28.5	30.9	1.5
sw3con	8.5	30.9	1.5	8.5	30.9	1.5	8.5	30.9	1.5	8.5	30.9	1.5
sw4con	28.5	30.9	1.5	28.5	30.9	1.5	28.5	30.9	1.5	28.5	30.9	1.5

* Note: Italicized values are measured in the negative x, y, or z directions.

face and the internal concrete rosettes were also utilized to compute the girder strains and moments (see Appendix H).

Located above and below the panel zone region, eight foil gages located on the outside surface of the column flanges were used to calculate the moments in the top and bottom column sections (Figures 2.25-2.26 and 2.28-2.29). These strain moments (based on strains measured in the column) were compared to the column load moments (based on the applied load to the girder tips and basic statics) in order to determine the amount of friction present in the top and bottom load pins during testing. Also, the behavior of the continuity plates and the panel zone were studied by employing four foil gages and two rosettes located within the panel zone region (Figures 2.24-2.25, 2.30 and 2.32-2.33).

A coordinate system based on the x, y, and z directions is established in order to relate the locations of the strain gages on the specimen. The x-axis is oriented orthogonal to the plane of girder web and lies globally in the North and South directions. The y-axis is oriented vertically, while the z-axis is oriented orthogonal to the plane of the column flanges in the East and West directions.

The coordinate system used is based on defining 5 different axes: x_{north}, x_{south}, y, z_{east}, and z_{west}. Each axis is measured from a specified orthogonal plane. The x_{north} and x_{south} axes begin at the specimen's cross-sectional plane of symmetry (the plane passing through the centerline of the girder and column web). These axes are defined as positive when directed toward the girder flange tip (Figures 2.24 - 2.29). The y axis originates at the bottom surface of the bottom girder flange, and is defined as positive and negative when directed towards the top and bottom of the specimen, respectively.

The z_{east} and z_{west} axes start at the outside surface of the East and West column flanges, respectively (Figure 2.31). The z_{east} and z_{west} axes are parallel to the longitudinal axis of the girder and are defined as positive and negative when directed away from and towards the East and West column flange, respectively. The z_{west} axis is utilized in defining locations of strain gages within the panel zone region, where distances are denoted with negative magnitudes. The position of a strain gage on a planar surface of

the specimen may be defined using 3 of the 5 axes, beginning at their respective origins (see Tables 2.5 to 2.8).

2.4.4 Acoustic Emission Transducers

Several acoustic emission transducers were utilized to identify the time and location of events within the connection regions of the specimens. An acoustic emission is a stress-wave within a material originating from a rapid release of strain energy, also referred to as an AE (acoustic emission) event. For this research, AE events are primarily caused by microfractures of the concrete deck or steel. An array of transducers were used in order to isolate the location of the AE events that occurred within the bottom connection regions of the specimens during their load histories.

The AE testing equipment varied for each test. Specimens 1 and 2 employed a Dunegan/Endevco (or DE) Acoustic Emission Preamplifier (Model 1801-170-B) while Specimen 3 utilized a Physical Acoustics Corporation (or PAC) Preamplifier (Model 1220A). Specimens 1, 2, and 3 used a DE: Dunegan 8000, PAC: LOCAN Acoustic Emission Analyzer, and a PAC: MISTRAS 2001 hardware system, respectively. All the specimens incorporated PAC: General Purpose Sensors transducers (Model R15).

The transducers were attached to the outside surface of the column flanges with an adhesive (see Figures 2.35-2.38). The AE transducers and preamplifiers were connected using PAC/EMI (Electro Magnetic Interference) shielded cable and the preamplifiers and the hardware were connected with RG/58 coaxial cable. Note that the East and West connections of Specimen 1 utilized two AE transducers on each connection (see Figures 2.35 and 2.36) while the East connection of Specimen 2 and the East and West connections of Specimen 3 each employed 4 transducers (see Figures 2.37 and 2.38). The West connection of Specimen 2 did not possess AE transducers.

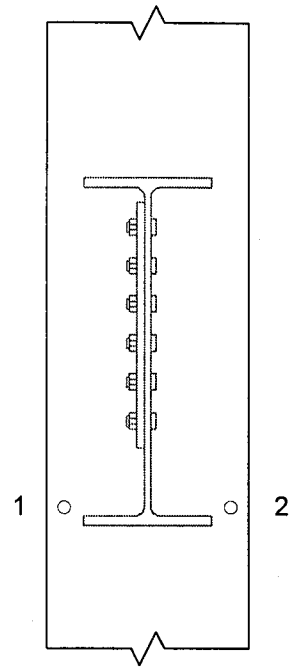

Figure 2.35: AE Transducer Locations (East Connection of Specimen 1)

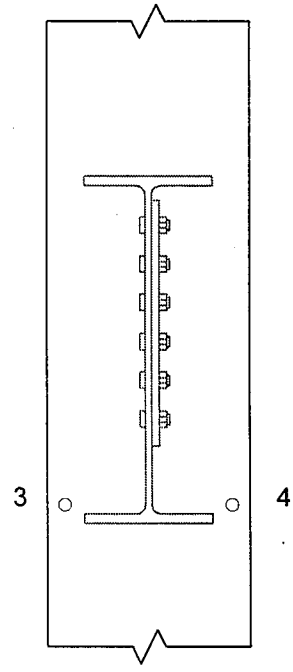

Figure 2.36: AE Transducer Locations (West Connection of Specimen 1)

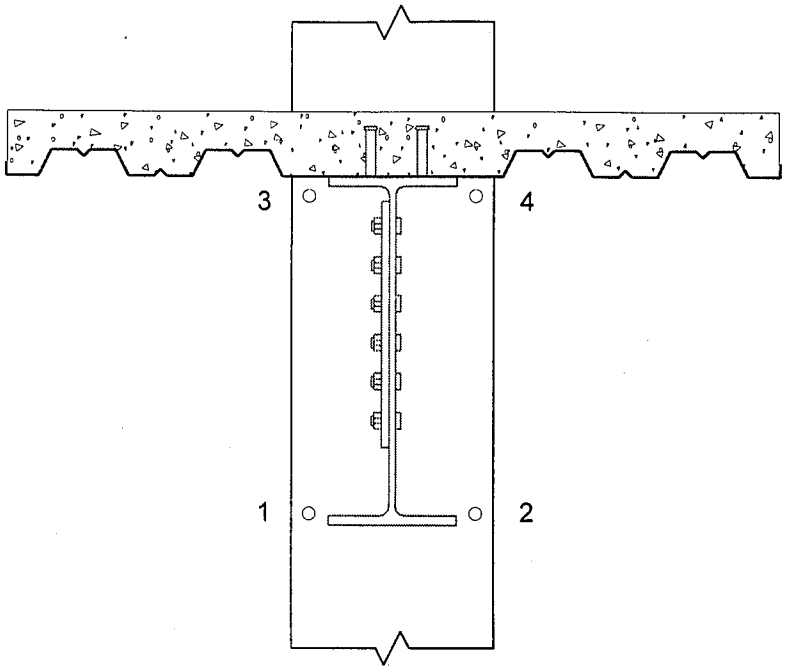

Figure 2.37: AE Transducer Locations (East Connections of Specimens 2 and 3)

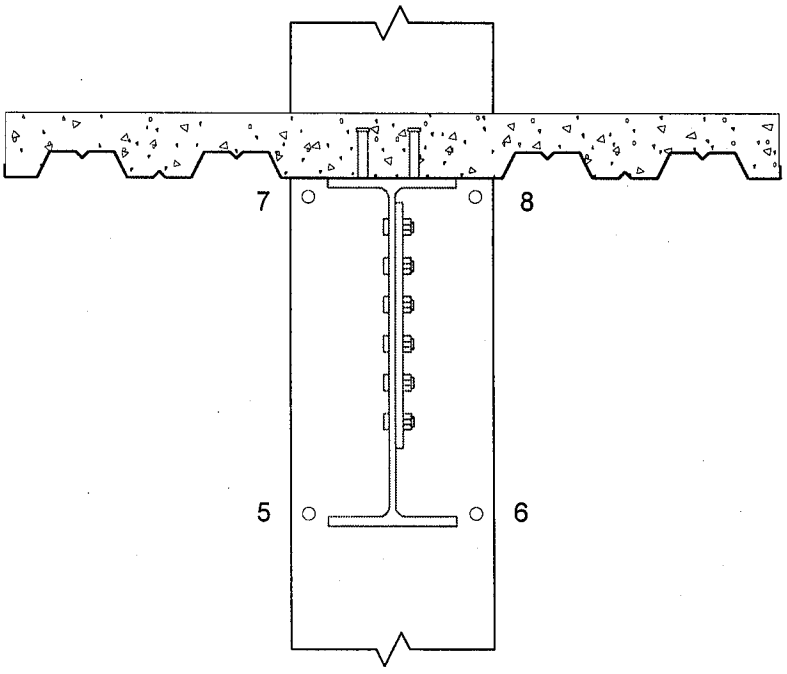

Figure 2.38: AE Transducer Locations (West Connection of Specimen 3)

Chapter 3

Specimen Load Histories and General Behavior

The load histories that were employed can be divided into two phases. First, with no axial load applied to the column, several elastic cycles were conducted in order to measure the elastic behavior of the specimens. Cycling at these lower drift levels also aided in verifying the instrumentation, data acquisition, and load systems of the experiment. Second, 550 kips of axial tension was applied to the column while the specimens were subjected to two cycles at 0.25%, 0.50%, 0.75%, 1.0%, 1.5%, 2.0%, and 3.0% drift cycles. If the specimen exhibited significant deformation after the two cycles at a particular drift level, a third cycle was imposed.

The specimens were loaded based on an interstory drift level percentage. The interstory drift limit is equal to the interstory lateral displacement, Δ_{story}, divided by the interstory height, h_{story} (see Figures 3.1 and 3.2). Furthermore, the interstory drift limit is directly related to $\Delta_{tip}/(L_g + b/2)$, where Δ_{tip}, L_g, and b, are equal to the girder tip deflection, the girder length, and the panel zone effective width, respectively. For example, a girder tip deflection of 1.4" corresponds to a interstory drift level of 1.0% ($L_g + b/2 = 139.9$"). Since the girders of each specimen were subjected to antisymmetric stroke-controlled loading, the girder tip displacements remain equal and opposite for a given loading increment. Tables 3.1 and 3.2 summarize the number and magnitude of drift levels, and the corresponding load stages, subjected to the specimens.

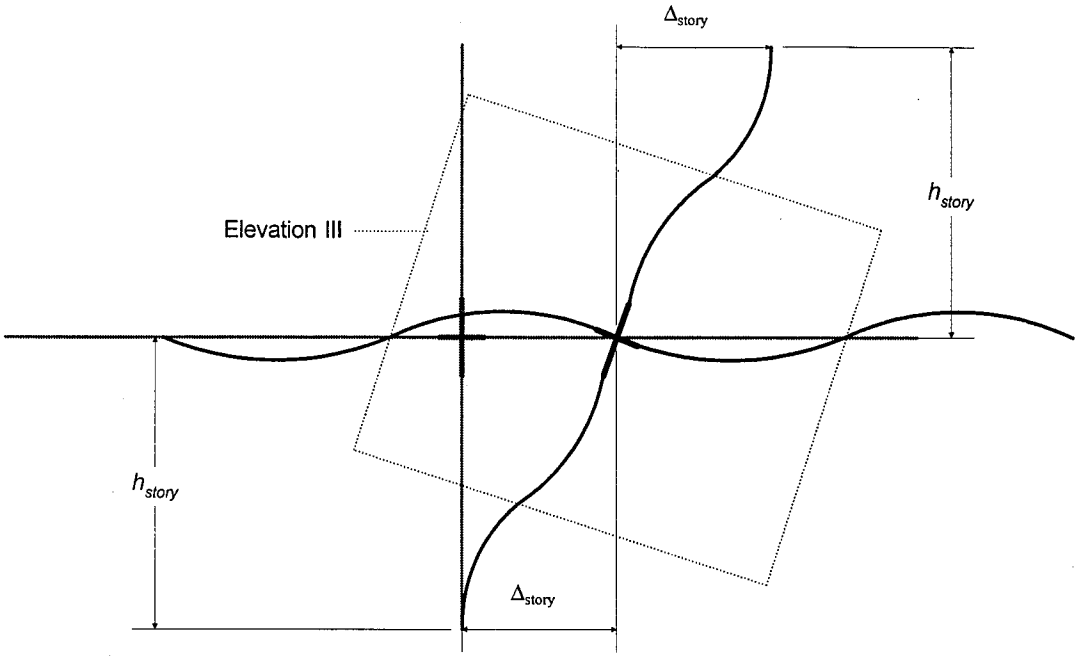

Figure 3.1: Typical Interior Moment Frame (Reverse Curvature Bending)

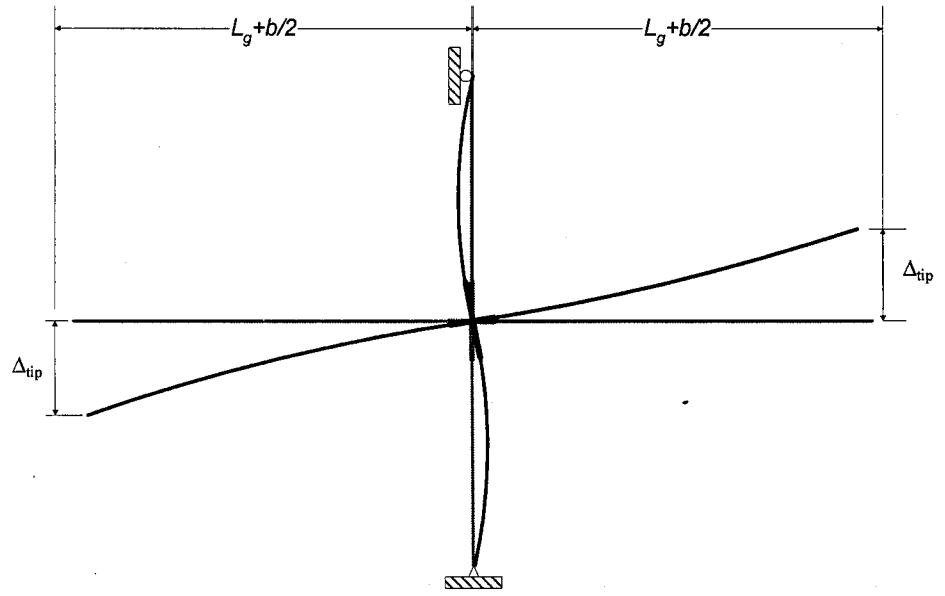

Figure 3.2: Elevation III: Test Specimen (Reverse Curvature Bending)

Table 3.1: Specimen Load Histories: Level and Quantity of Drift Cycles

Drift Cycles (%)	Axial Load (kips)	Specimen 1 (# of cycles)		Specimen 2 (# of cycles)		Specimen 3 (# of cycles)	
		East	West	East	West	East	West
initial[1]	0[2]	5.0	5.0	12.0	12.0	8.0	8.0
0.25	550	2.0	2.0	3.0	3.0	1.0	1.0
0.50	550	2.0	2.0	3.0	3.0	3.0	3.0
0.75	550	2.0	2.0	3.0	3.0	3.0	3.0
1.00	550	2.0	2.0	3.0	3.0	3.0	3.0
1.50	550[3]	3.0	1.5	3.0	3.0	3.0	3.0
2.00	550[3]	3.0	------	1.5	1.5	3.0	3.0
3.00	550[3]	1.0	------	------	------	2.5	2.5

Table 3.2: Specimen Load Stages vs. Drift Cycles

Drift Cycles	Specimen 1 (cycle #)			Specimen 2 (cycle #)			Specimen 3 (cycle #)		
(%)	1	2	3	1	2	3	1	2	3
initial[1]	0 to 457[2]			0 to 604			0 to 610		
axial load	458 to 479			605 to 623			611 to 629		
0.25	480	531	-----	624	673	723	630	-----	-----
	530	576		672	722	768	692		
0.50	577	375	-----	769	853	937	693	741	789
	674	766		852	936	1024	740	788	839
0.75	767	905	-----	1025	1159	1287	840	928	1016
	904	1038		1158	1286	1414	927	1015	1093
1.00	1039	1233	-----	1415	1569	1745	1094	1243	1351
	1232	1437		1568	1744	1832	1242	1350	1444
1.50	1438	1695	1872	1833	1957[3]	2070	1445	1611	1719
	1694	1871	1981	1956	2069	2192	1610	1718	1807
2.00	1982	2091	2167	2193	2266	-----	1808	1959	2067
	2090	2166	2234	2265	2335		1958	2066	2155
3.00	2235	-----	-----	------	------	------	2156	2308	2416
	2335						2307	2415	2463

[1] Initial drift cycles of 0.1% and 0.25% were performed during first phase of testing.

[2] No axial load was applied during the initial cycles with exception to 330 kips of axial compression that was applied to Specimen 1 during the fourth and fifth cycles at 0.25% (at load stage 292 to 332).

[3] Axial load was removed during second cycle at 1.5% drift level for Specimen 2 (at load stage 1984).

3.1 Load Histories of the Specimens

The West and East girders of Specimen 1 were subjected to a total of 14.5 and 20 drift cycles, respectively (see Table 3.1). Figure 3.3 illustrates the East girder deflection history. Note that the specimen was initially tested with five drift cycles at 0.25% and was placed under 330 kips of compression. Then the column was subjected to 550 kips of axial tension while each girder was cycled up to the 1.5% drift levels. After the West connection failed, the West girder actuators were disconnected and the East girder was tested up through the first cycle at the 3.0% drift levels, at which point substantial damage was sustained by the East connection region. Note that Specimen 1 was subjected to a few preliminary cycles at 0.1% drift; however, the effects of these drift levels are assumed to be negligible and, therefore, are not documented in this report.

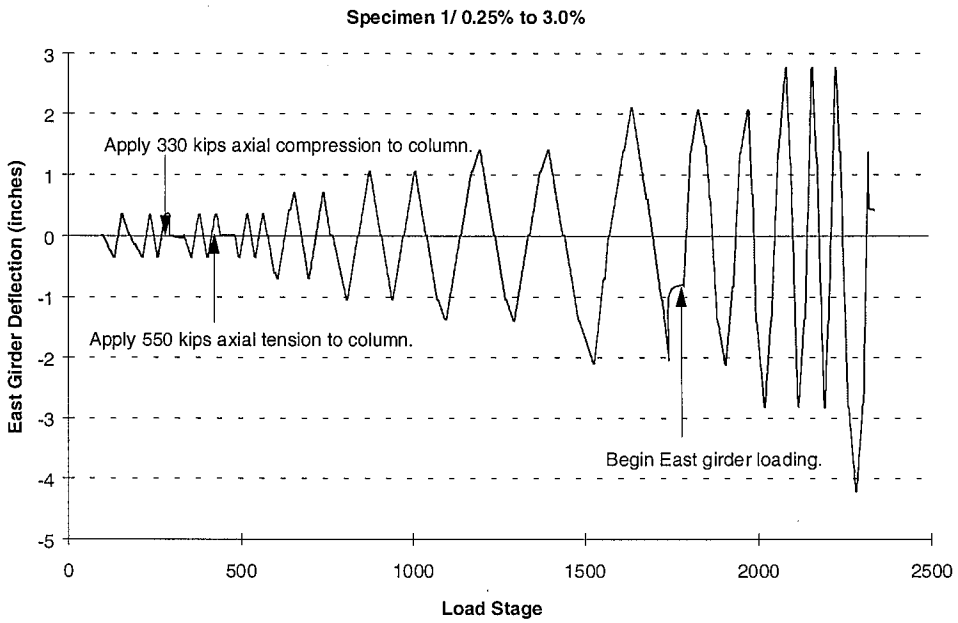

Figure 3.3: Load History of Specimen 1

Specimen 2 was subjected to a total of 28.5 drift cycles, ranging from the 0.1% to 2.0% drift levels (see Table 3.1). Figure 3.4 illustrates the East girder deflection history. Twelve initial cycles at 0.1% and 0.25% drift cycles were administered in sets of three and in an

alternating fashion (see Figure 3.4). After an axial load of 550 kips was applied to the column, Specimen 2 was subjected to 16.5 more cycles, ranging from 0.25% to 2.0%. During the second cycle at 1.5% drift, the 550 kips of axial load was removed from the column due to the interlock on the MTS testing machine being triggered as a result of a large vibration exhibited by the load frame assembly. Despite sustaining substantial damage to the connection regions during the 1.5% drift levels, both girders were cycled up to the 2.0% drift level.

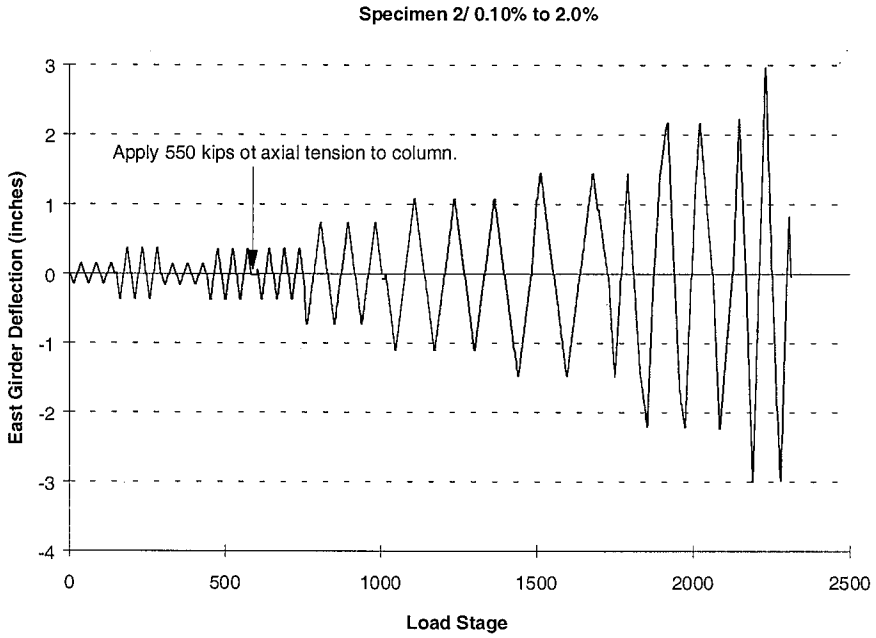

Figure 3.4: Load History of Specimen 2

Specimen 3 was subjected to a total of 26.5 drift cycles, ranging from 0.25% to 3.0% drift levels (see Table 3.1). Figure 3.5 illustrates the East girder deflection history. After 8 initial cycles were conducted at the 0.25% drift levels, an axial load of 550 kips was applied to the column and Specimen 3 was subjected to 18.5 more cycles ranging from the 0.25% to 3.0% drift levels (see Figure 3.5). Cycling of the girders was stopped after the East and West connection regions sustained extensive damage during the 3.0% drift cycles. Note that Specimen 3 was subjected to three preliminary cycles at 0.1% drift; however, the effects of these drift levels are again assumed to be negligible and are not documented in this report.

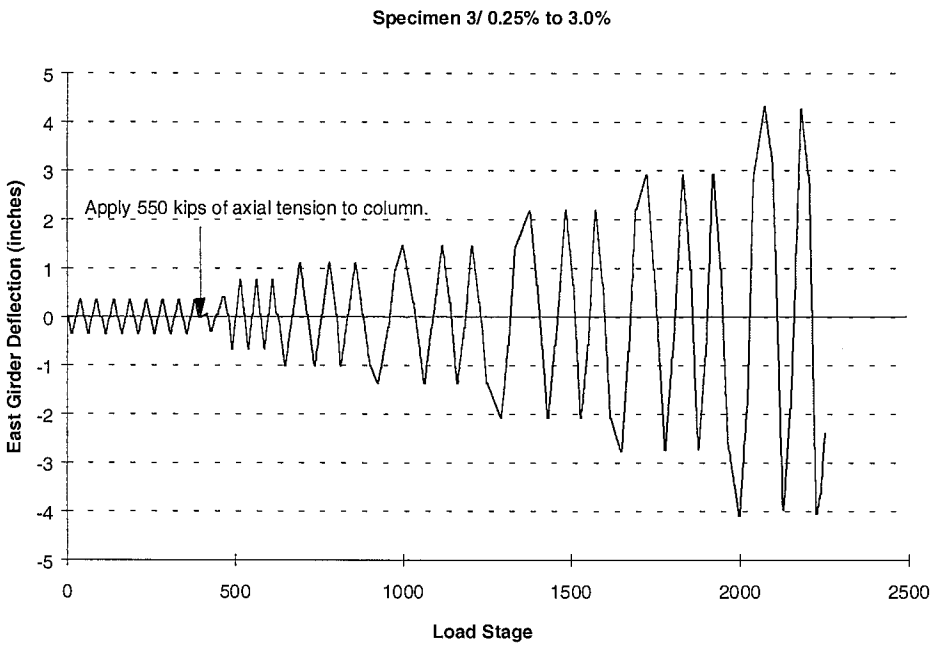

Figure 3.5: Load History of Specimen 3

3.2 Summary of Performance of the Specimens

The performance of the specimens may be summarized by investigating the performance of their girders and the welded girder flange-to-column connections. Table 3.3 reports the computed moment strength, $M_{p\,calc}$, the minimum required strength specified by the SAC Advisory Committee, $0.8M_{p\,calc}$ (SAC, 1996b), the girder moment achieved in the test, $M_{p\,max}$, and the plastic girder-to-column rotation, $\theta_{p\,max}$ for the East and West girders of the specimens. These values are summarized for both positive and negative girder bending. Note that the calculation of $M_{p\,calc}$ and the experimental moment-plastic girder-to-column rotation curves for the three specimens are reported in Appendix B. The moment strength, $0.8M_{p\,calc}$, may be considered an acceptable post-failure strength requirement (i.e., accounting for degradation), particularly if failure occurs by local buckling of the girder flanges (SAC, 1996b). Table 3.4 summarizes the primary mode, location, and time of failure, and may be correlated with the moment and girder-to-column rotations reported in Table 3.3.

The calculated capacities are based on the nominal plastic section modulus and the actual steel yield strength (i.e, for the steel section, $M_{p\,calc}$ = 278 in.^{3} x 38 ksi = 10,560 kip-in.). As such, this value is different from the design moment capacity, which would be based on the nominal yield strength and a resistance reduction factor (0.9 x 278 in.^{3} x 36 ksi = 9,007 kip-in.). However, for discussing the experimental results, the $M_{p\,calc}$ value is appropriate, since the assumption in design is that the connections would develop the full plastic strength of the steel section.

On the other hand, it may be argued that the assumption that the full cross section is effective at the connection is not reasonable for these calculations since the web connection cannot be assumed to be as effective as the solid web in transferring bending forces. This is particularly important for sections such as the W27x94 used in this work, which can transfer only a relatively low amount of the bending through the flanges (70.08% of the plastic moment strength for this section). However, any bolted web contribution is difficult to determine experimentally since it would involve the quantification of friction and bearing forces. Thus, the present calculation for $M_{p\,calc}$, which includes the full web contribution (see Appendix B), remains a reasonable benchmark value to use as a reference in making comparisons.

The performance of each connection may also be studied in Figures 3.6-3.17, which illustrate the girder-to-column moment-plastic rotation curves and failure locations for each of the connections of the specimens. The West connection of Specimen 1 and the East and West connections of Specimen 2 demonstrated a brittle-type failure of the bottom flange welded flange-to-column connection at the weld-to-column interface, each during the second cycle at 1.5% drift (see Figures 3.6-3.11). This type of failure is indicative of girder flange pull-out fractures (Damage Types C2 or W3) documented by the 1995 SAC Interim Guidelines (SAC, 1995) (see Table 1.1). While the West connection of Specimen 1 lost much of its strength after the initial primary fracture across the girder flange width at the second cycle of 1.5% drift (Figure 3.6), the East and West connections of Specimen 2 failed in a two-stage fashion. For the West girder of Specimen 2 (Figure 3.10), the severing of the CJP weld from the column flange initiated during the first cycle at 1.5% drift, as evidenced by a small decrease in moment strength. The primary fracture occurred during the second cycle at 1.5% drift, after which the connection lost much of its strength. In addition, a partial column flange crack occurred,

Table 3.3: Specimen Performance Summary (Girder Strength and Ductility Behavior)

Specimen/ Girder	$M^+_{p\,calc}$ (kip-in)	$0.8M^+_{p\,calc}$ (kip-in)	$M^+_{p\,max}$ (kip-in)	$\theta^+_{p\,max}$ (mrads)	$M^-_{p\,calc}$ (kip-in)	$0.8M^-_{p\,calc}$ (kip-in)	$M^-_{p\,max}$ (kip-in)	$\theta^-_{p\,max}$ (mrads)
Specimen 1 East Girder	10,560	8,450	12,390	12.5	10,560	8,450	12,050	25
Specimen 1 West Girder	10,560	8,450	9,800	5	10,560	8,450	10,000	4.5
Specimen 2 East Girder	16,260	13,010	13,050	18[1]	11,700	9,360	11,800	9.5
Specimen 2 West Girder	16,260	13,010	11,800	17[1]	11,700	9,360	11,000[2]	17.5[2,3]
Specimen 3 East Girder	15,290	12,230	14,000	25	11,700	9,360	12,000	21.3
Specimen 3 West Girder	15,290	12,230	13,770	16.5	11,700	9,360	12,000	32

[1] Approximately 8 milliradians prior to fracture

[2] Maximum value is taken from the reconstructed portion of the hysteresis curve (see Appendix B).

[3] Approximately 7 milliradians prior to fracture

Table 3.4: Specimen Performance Summary (Failure Characteristics)

Specimen/ Girder	Primary Mode of Failure	Location of Failure	Cycle at Ultimate Failure
Specimen 1 East Girder	Low-cycle fatigue rupture	Root of bottom flange access hole	1st cycle at 3.0%
Specimen 1 West Girder	Brittle fracture	Bottom flange weld column interface[1]	2nd cycle at 1.5%
Specimen 2 East Girder	Brittle fracture	Bottom flange weld column interface	2nd cycle at 1.5%
Specimen 2 West Girder	Brittle fracture	Bottom flange weld column interface	2nd cycle at 1.5%
Specimen 3 East Girder	Low-cycle fatigue rupture	Root of bottom flange access hole	2nd cycle at 3.0%
Specimen 3 West Girder	Low-cycle fatigue rupture	Root of bottom flange access hole	3rd cycle at 3.0%

[1] Indicative of a Damage Type C2 or W3 from the SAC Interim Guidelines (SAC, 1995) (see Table 1.1)

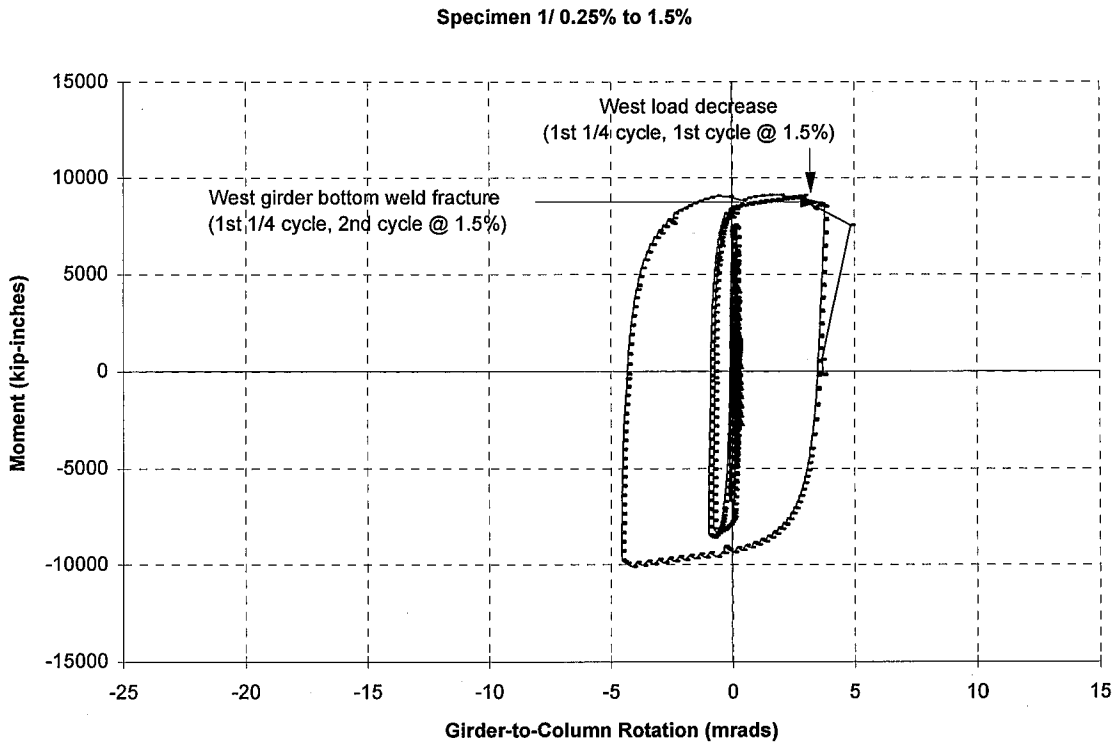

Figure 3.6: Girder-to-Column Moment-Rotation Curve (West Girder of Specimen 1)

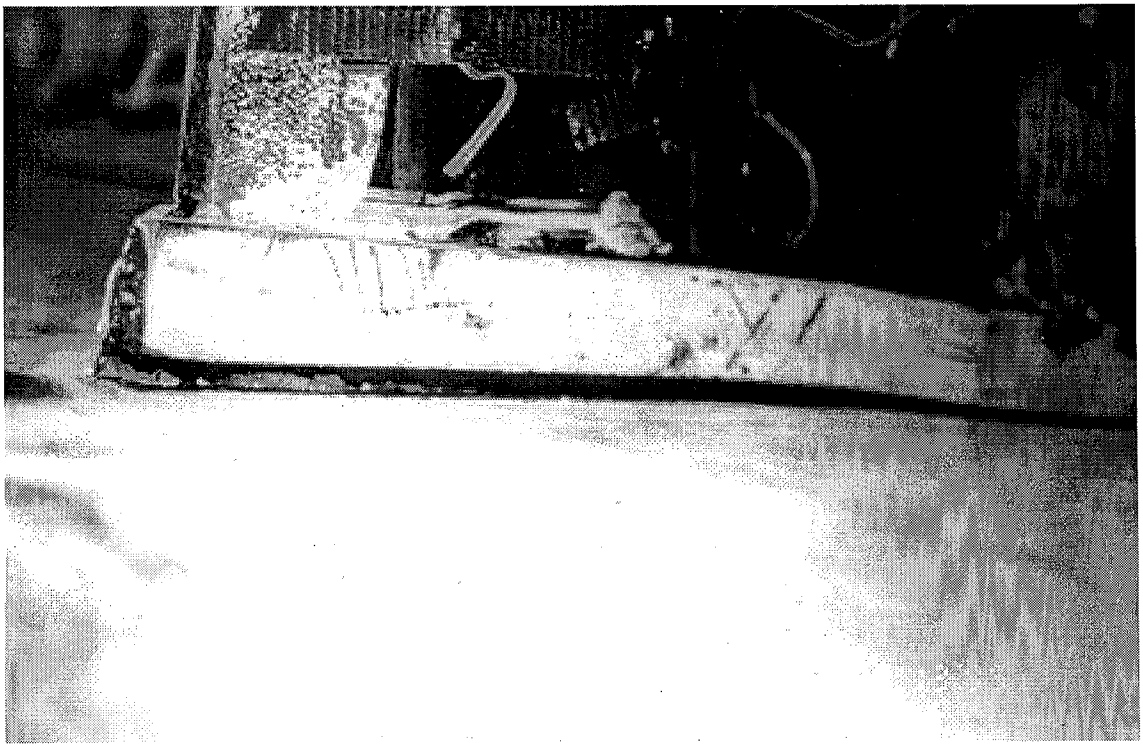

Figure 3.7: Fracture of Bottom CJP Weld (West Girder of Specimen 1)

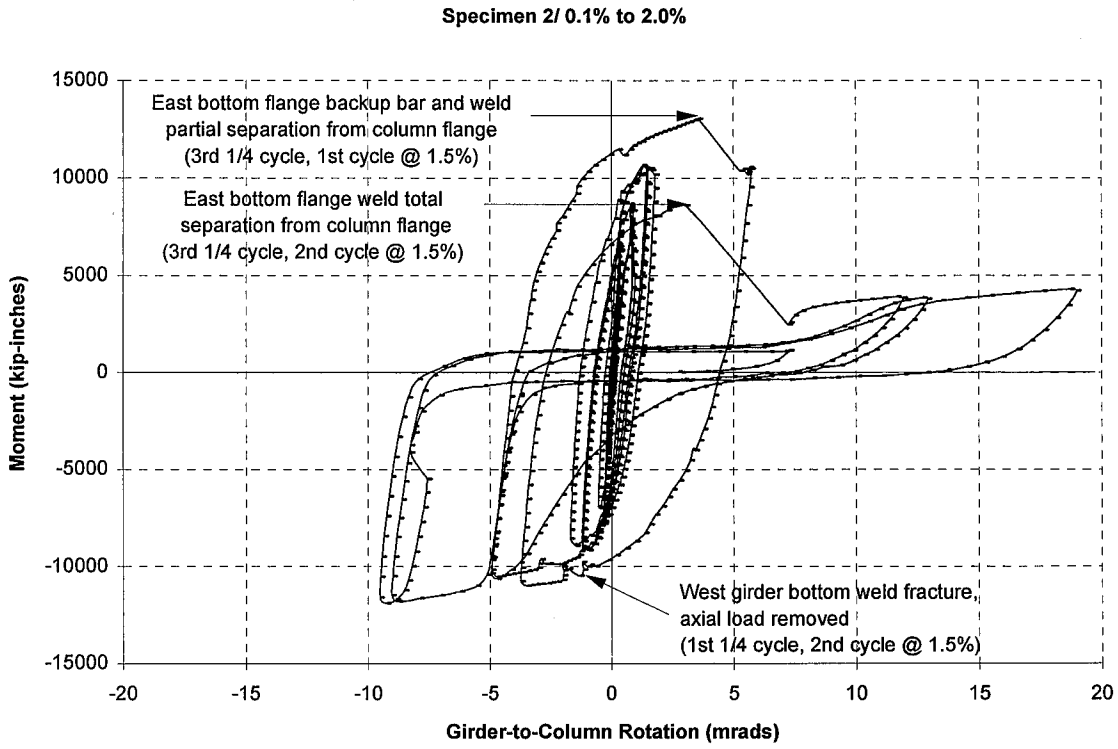

Figure 3.8: Girder-to-Column Moment-Rotation Curve (East Girder of Specimen 2)

Figure 3.9: Fracture of Bottom CJP Weld (East Girder of Specimen 2)

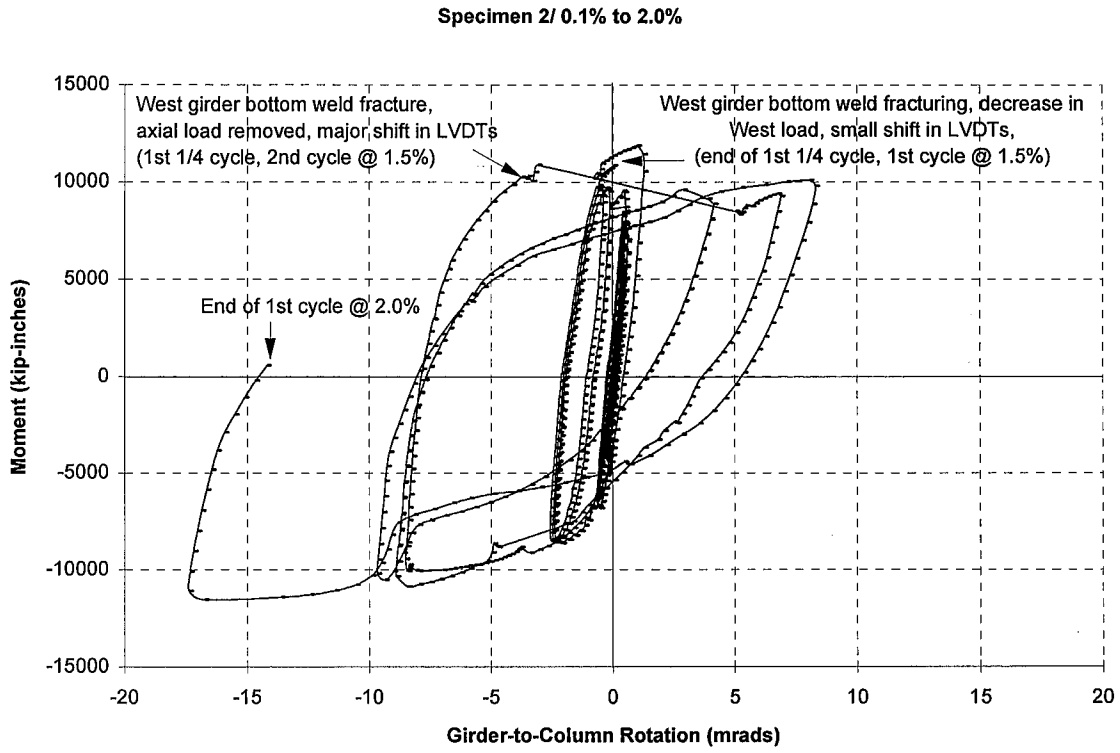

Figure 3.10: Girder-to-Column Moment-Rotation Curve (West Girder of Specimen 2)

Figure 3.11: Pull Out-Type Failure of Column Flange (West Girder of Specimen 2)

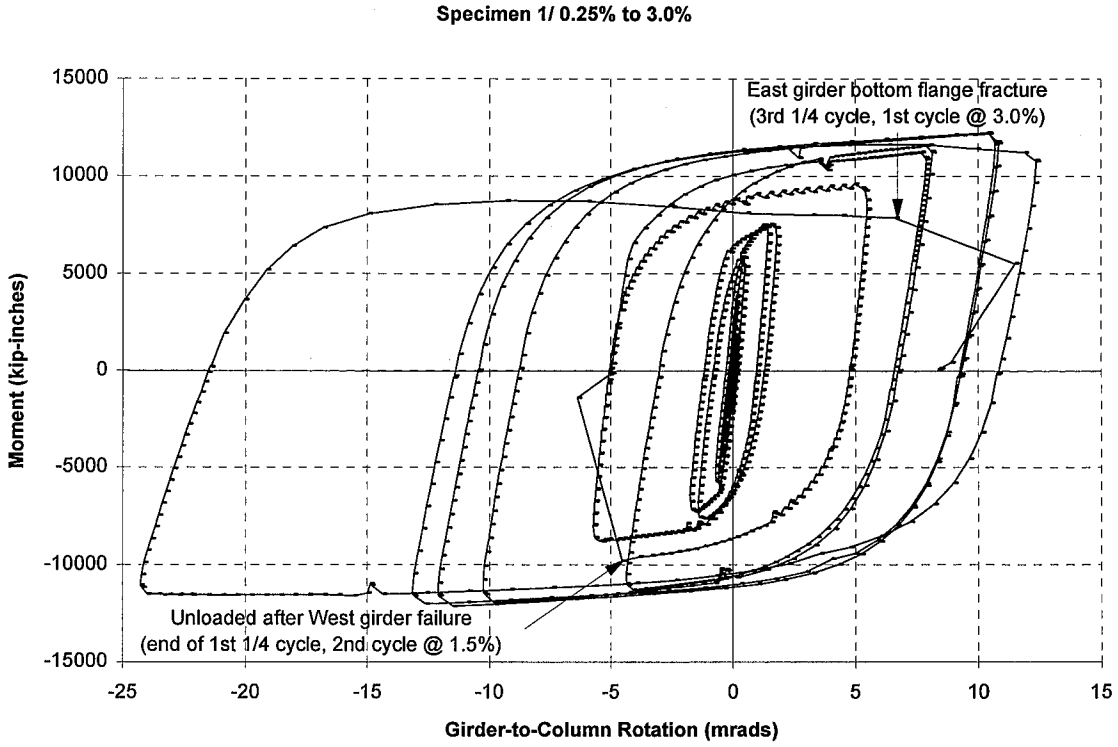

Figure 3.12: Girder-to-Column Moment-Rotation Curve (East Girder of Specimen 1)

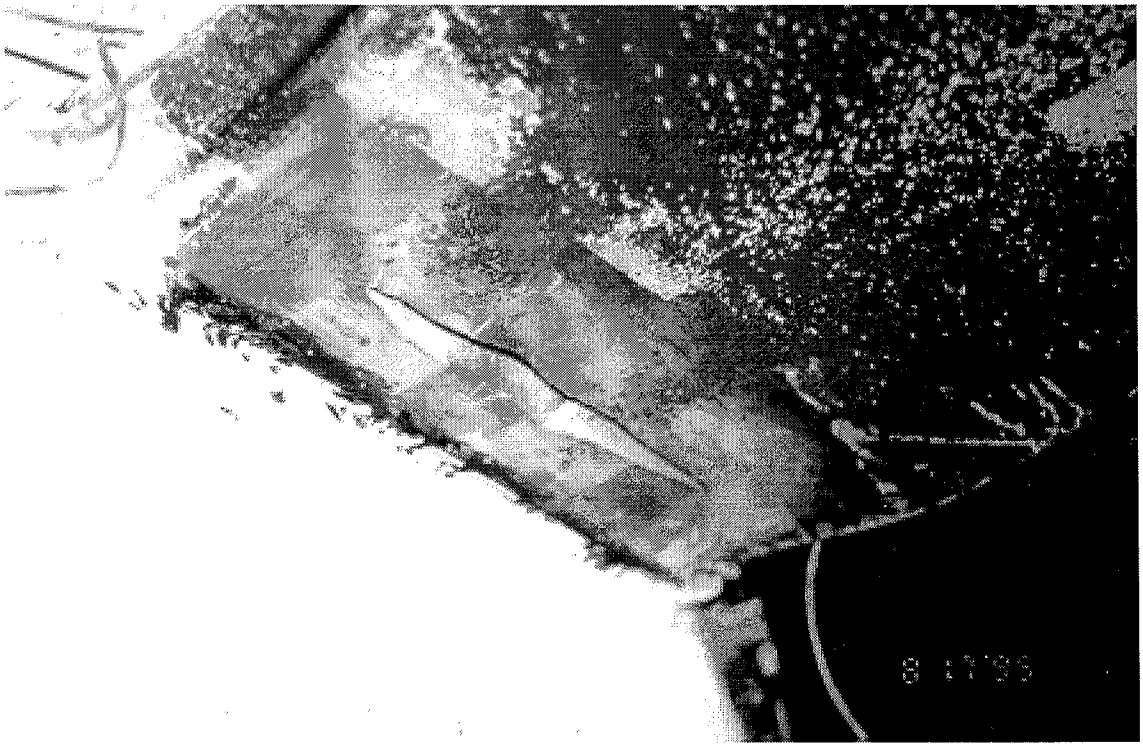

Figure 3.13: Rupture of Girder Bottom Flange (East Girder of Specimen 1)

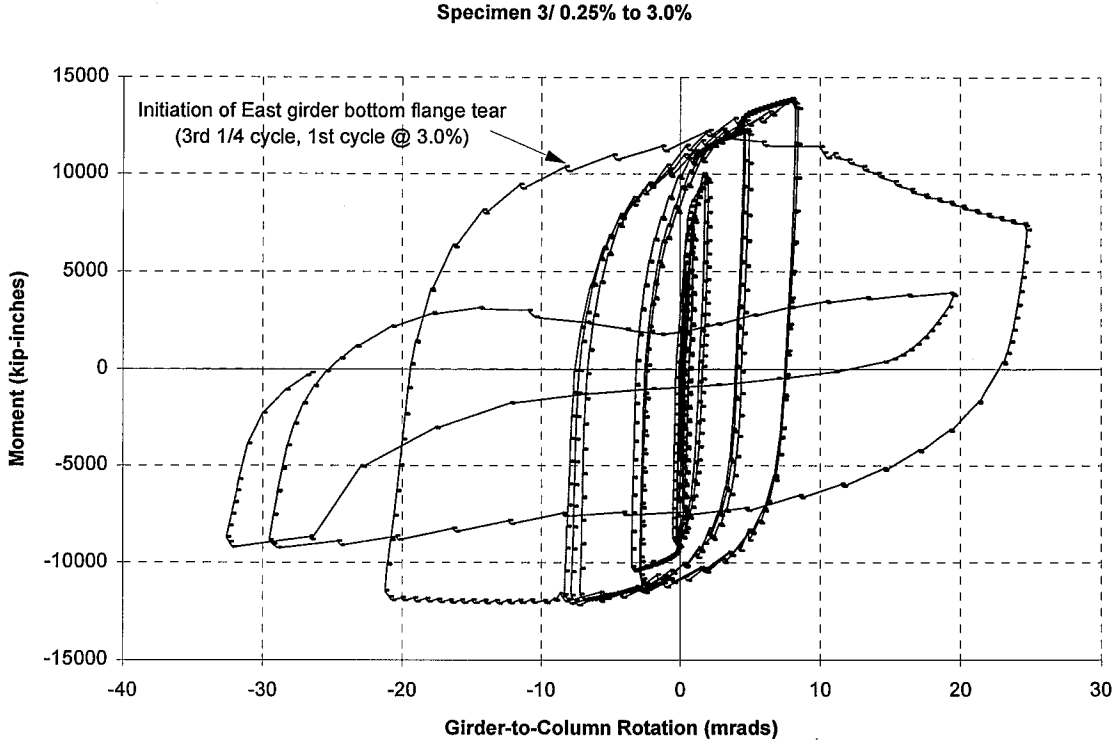

Figure 3.14: Girder-to-Column Moment-Rotation Curve (East Girder of Specimen 3)

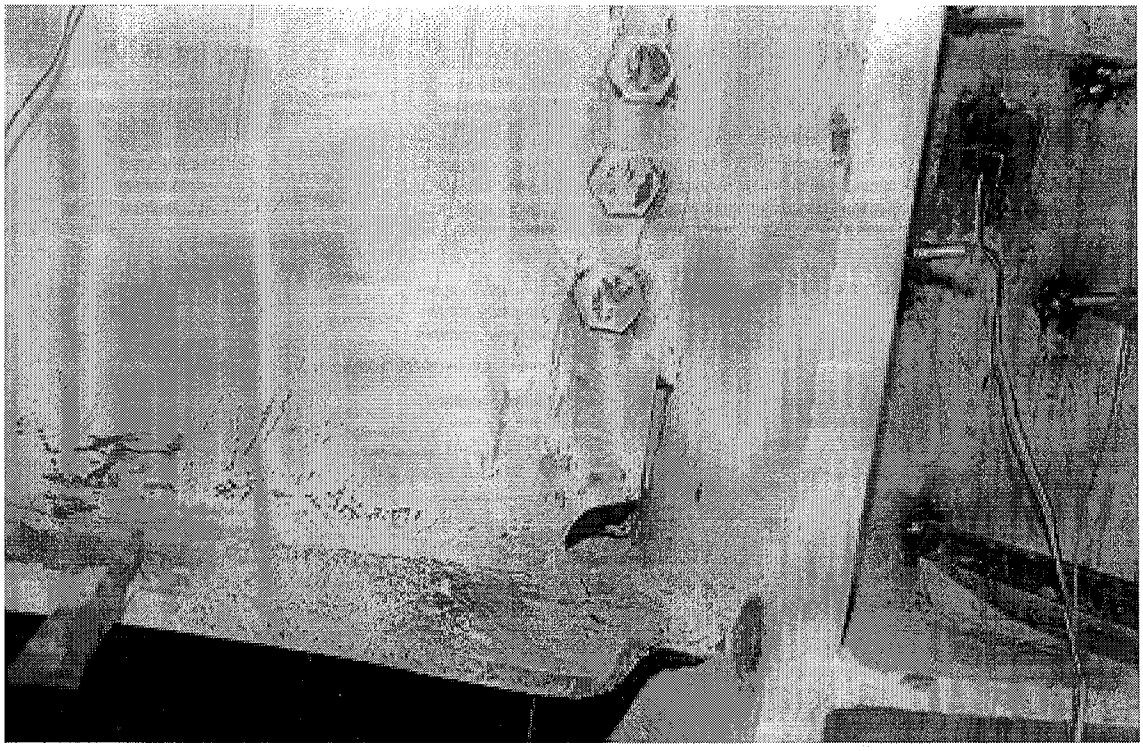

Figure 3.15: Rupture of Girder Bottom Flange (East Girder of Specimen 3)

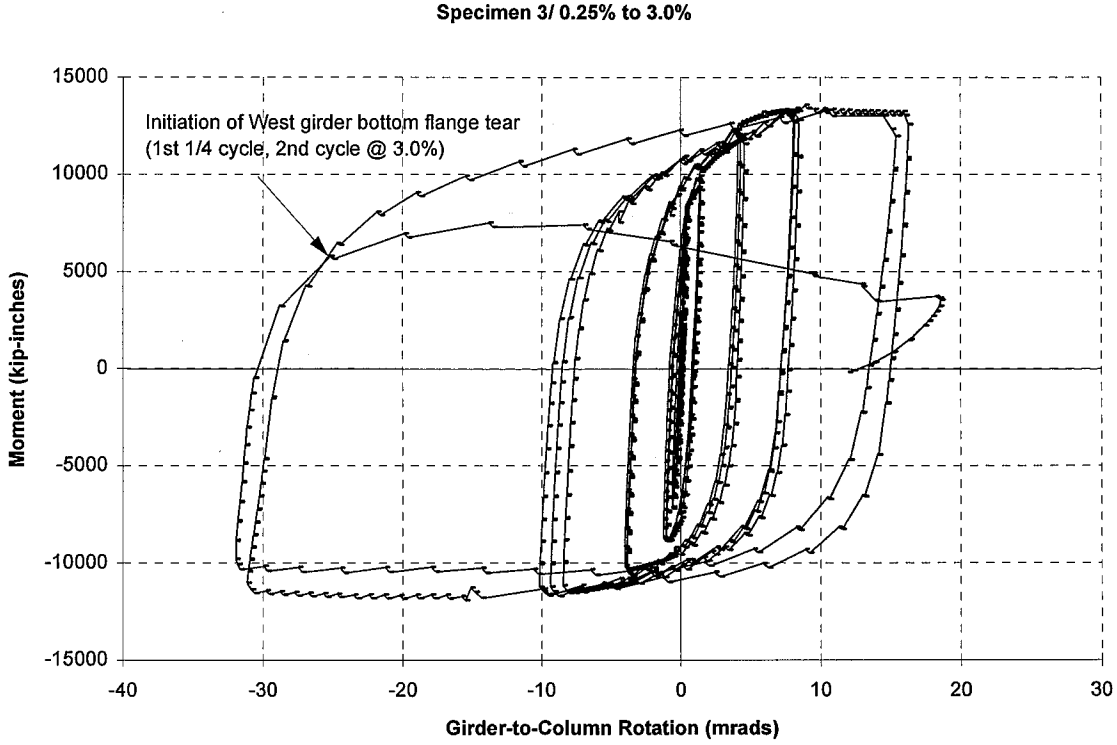

Figure 3.16: Girder-to-Column Moment-Rotation Curve (West Girder of Specimen 3)

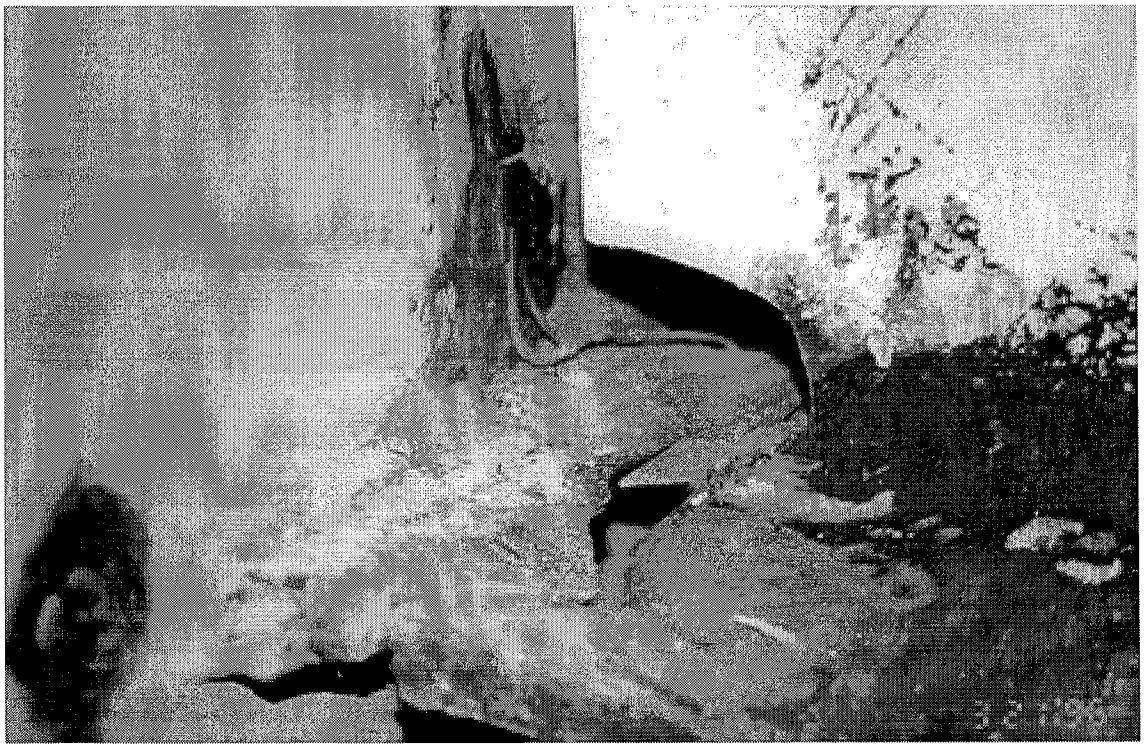

Figure 3.17: Rupture of Girder Bottom Flange (West Girder of Specimen 3)

most likely simultaneously with the severing of the CJP weld from the column flange, during the second cycle at 1.5% drift. This column flange crack propagated to both the North and South halves of the column flange a few inches above the bottom girder flange-to-column weld, and it propagated through the full thickness of the flange at several locations along the column flange width. Figure 3.11 shows the region of the CJP weld of this connection, indicating tearing of the column flange propagating from the tip of the girder flange [indicative of Damage Type C5 documented by the 1995 SAC Interim Guidelines (SAC, 1995)], a column flange fracture towards the center of the column flange [indicative of a combination of Damage Types C2 and C4 documented by the 1995 SAC Interim Guidelines (SAC, 1995)], and substantial flaking of white wash on the column flange. These were the three connections for which a backup bar existed at the bottom girder flange during testing.

Note that immediately after the primary fracture of the West connection of Specimen 2, the LVDTs which measured relative girder-to-column rotation required resetting, and the remaining portion of the moment-plastic rotation curve is reconstructed in Figure 3.10; after this point, relative values of plastic rotation are correct, but absolute values of the rotation relative to the beginning of the test are approximate (see Appendix B).

On the other hand, the East connection of Specimen 1 exhibited a low-cycle fatigue type of rupture of the girder base metal near the bottom access hole during the first cycle at 3.0% drift (see Figures 3.12 and 3.13). The initiation of this tear may have occurred during the third cycle at the 2.0% drift levels, as observed when studying the strain behavior of the bottom girder flange region (see Appendix H). The East and West connections of Specimen 3 also showed low-cycle fatigue type ruptures, in a similar location as the East girder of Specimen 1, during the second and third cycles of 3.0%, respectively (see Figures 3.14-3.17). The initiation of these tears may have occurred during the second cycle at the 2.0% and 3.0% drift cycles, respectively (see Appendix H).

The three connections exhibiting premature, brittle fractures did not perform successfully by any measure. According to SAC (1996b), the minimum recommended

plastic rotation is 30 milliradians for connections utilized in new construction. However, the maximum girder-to-column rotations, $\theta_{p\,max}$, of the connections exhibiting premature fractures were only 6 to 8 milliradians. These connections also achieved poor levels of moment strength. All three connections achieved maximum moment strengths, $M_{p\,max}$, that were generally less than the computed moment strength, $M_{p\,calc}$, especially for positive girder bending (Table 3.3). In addition, for positive girder bending, the achieved moment strengths after failure compare poorly to the minimum required strength, $0.8M_{p\,calc}$ as proposed by SAC (1996b).

Of the three connections exhibiting low-cycle fatigue type failures, only the bare steel girder attained its calculated moment strength in positive bending, and the ductility performance of all three connections was poor (Table 3.3). In addition, the degradation of the composite connections of Specimen 3 was severe after the fractures occurred, and stabilized moment strengths comparable to $0.8M_{p\,calc}$ (SAC, 1996b) were not achieved. The connections did not demonstrate maximum plastic rotations near the recommended value of 30 milliradians (SAC, 1996b) for positive girder bending. Furthermore, the hysteretic behavior of the connections was adequate for only a few cycles at the 3.0% drift levels, until the complete severing of the bottom girder flange occurred. In these connections, local buckling of the bottom flange became noticeable typically at the 2.0% drift levels at a distance of approximately 6" to 12" from the column flange surface. These buckles became very pronounced at 3.0% drift.

All the connections of the specimens failed within the bottom welded girder-to-column region, and the bottom region of the connections of Specimen 2 and 3 sustained significantly more damage compared to the top region (i.e., bottom girder local flange buckling and plastification). In fact, no local flange buckling and only minimal to moderate levels of yielding occurred at the top girder flanges of Specimens 2 and 3. In an effort to explain this excessive straining at the bottom region of the connections (predominantly in the composite specimens), a variety of structural conditions are investigated in the remainder of this report, primarily focusing on the effects of composite floor slabs. This phenomena, along with the location of the shear tab along the girder cross section and the effects of the existence of backup bars on the performance of the connections, will be addressed in Chapters 5 and 6.

Chapter 4

Validation of Experimental Results

Prior to interpreting the experimental results, the measured strains and displacements in this experiment are validated using various data analyses. The effect of load pin friction on the resistance to loading is investigated, as is the validity of the measured girder-to-column rotation and the panel zone shear rotation. Rotations are verified by comparing the sum of the calculated girder tip deflection components to the actual girder tip deflection. In addition, the strains which were measured along the girder cross section at a distance of 13.5" from the column face may be validated by comparing calculated and measured girder moments and strains. This comparison also demonstrates that the girders of Specimen 2 and 3 exhibited partially composite behavior, as was intended.

The computational studies discussed in this chapter are based on linear elastic behavior, since it is felt that such an analysis is sufficient in order to validate the experimental data. However, a more accurate level of data analysis may be performed by incorporating more sophisticated types of computational tools which take into account material and geometric nonlinearities [see (Forcier, 1994)].

4.1 Effects of Load Pin Friction

This section briefly summarizes the contribution of friction in the column load pins to the resistance to loading provided during testing. By using strains measured at

the column flange surface and the load applied to the girder tips, moments calculated from measured strains ("strain moments") and moments calculated directly from the applied loads ("load moments") are computed within the column (see Figures 2.24, 2.25, 2.28, and 2.29 for strain gage locations). These moments are compared to study the effects of column load pin resistance. The procedure for calculating the strain and load moments, along with tabulated results and corresponding figures, are reported in Appendix E.

The differences between the load and strain moments are small during the lower drift cycles for all three tests (see Appendix E). Therefore, it may be concluded that the effects of friction to the resistance of loading during testing is negligible for all three tests. For example, Figures 4.1 and 4.2 illustrate that the differences between the strain and load moments in the bottom and top column regions of Specimen 3 are minimal during the lower drift levels (0.25% to 0.75% drift levels).

Larger differences between the two column moments seen during the higher drift levels (1.0% and 1.5%) may be primarily attributed to the presence of larger shear forces in the column load pins and, therefore, larger levels of load pin friction (see Figures 4.3 to 4.8; see also Appendix E). For Specimens 2 and 3, the effects of friction in both the top and bottom column regions were more significant than they were in Specimen 1 for these higher drift cycles (see Figures 4.5 to 4.8). Furthermore, for all three specimens, differences between the top column region strain and load moments are greater than the differences between the bottom column region strain moments. Nevertheless, it is felt that the effects of load pin friction are in general minimal for these tests.

4.2 Girder Tip Deflection Components

Several components of deflection contribute to the actual tip deflections of the girders of the test specimens (Krawinkler et al., 1971; Forcier, 1994). The deformation components are primarily due to elastic and inelastic behavior in the column, the composite girders, and the panel zone region. In addition, local regions of the connection

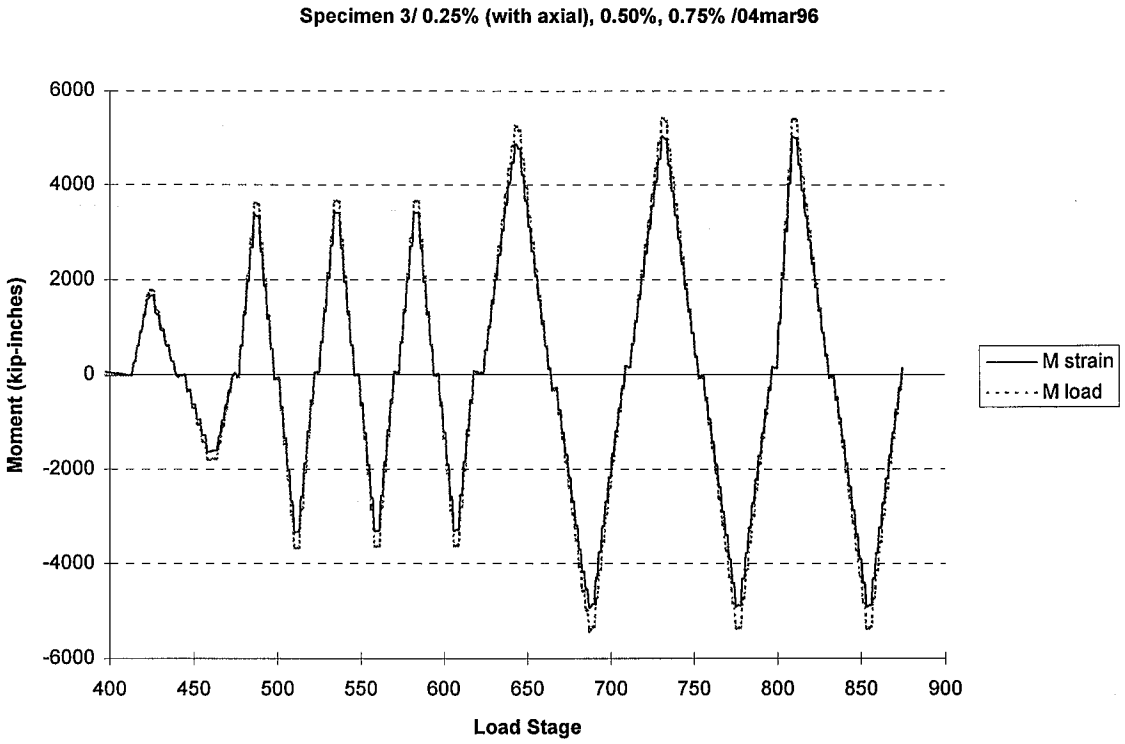

Figure 4.1: Strain Moment vs. Load Moment (Top Column Section of Specimen 3)

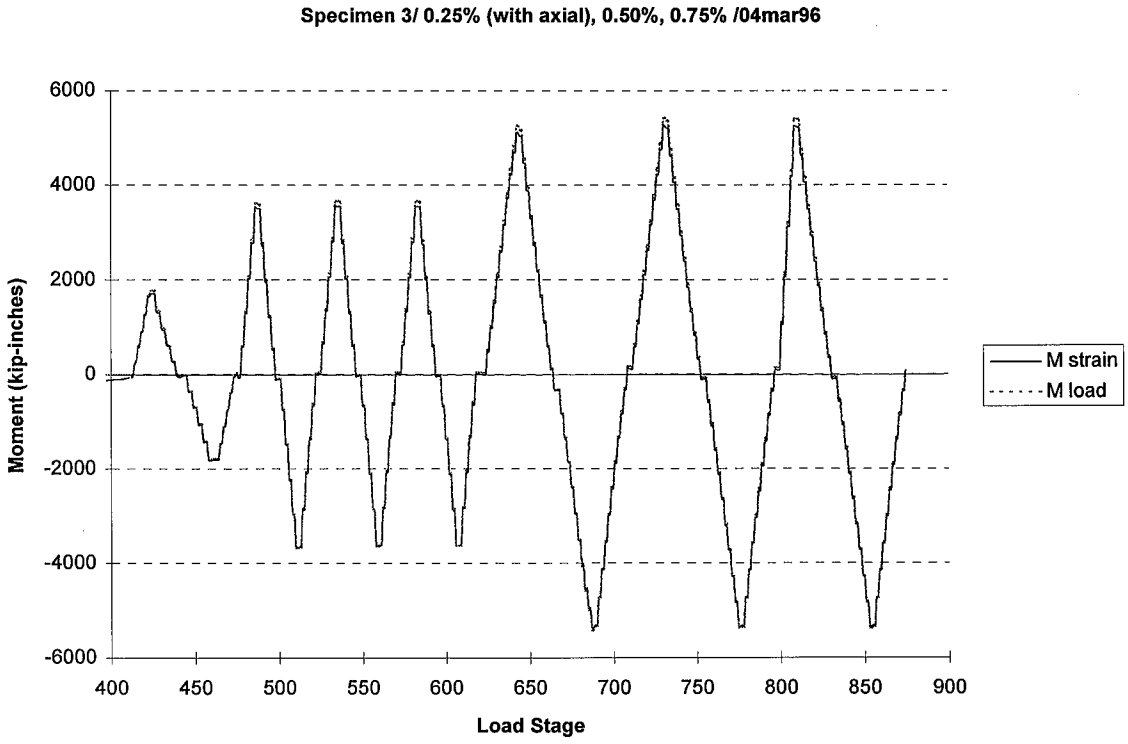

Figure 4.2: Strain Moment vs. Load Moment (Bottom Column Section of Specimen 3)

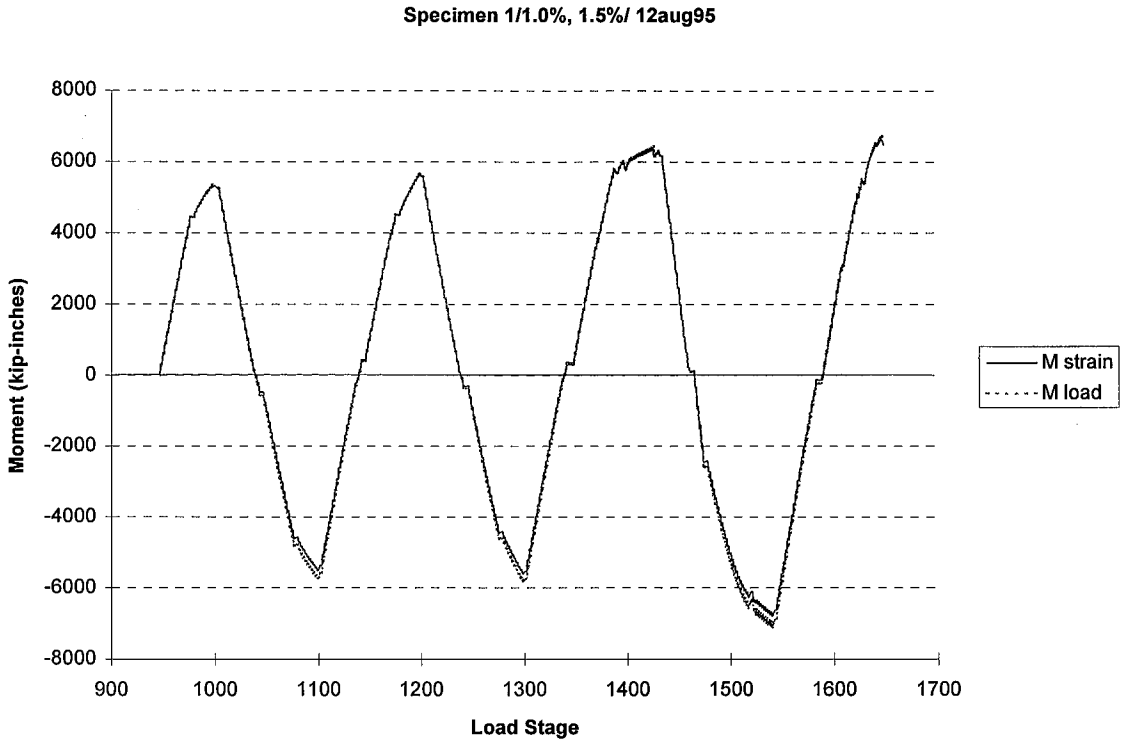

Figure 4.3: Strain Moment vs. Load Moment (Top Column Section of Specimen 1)

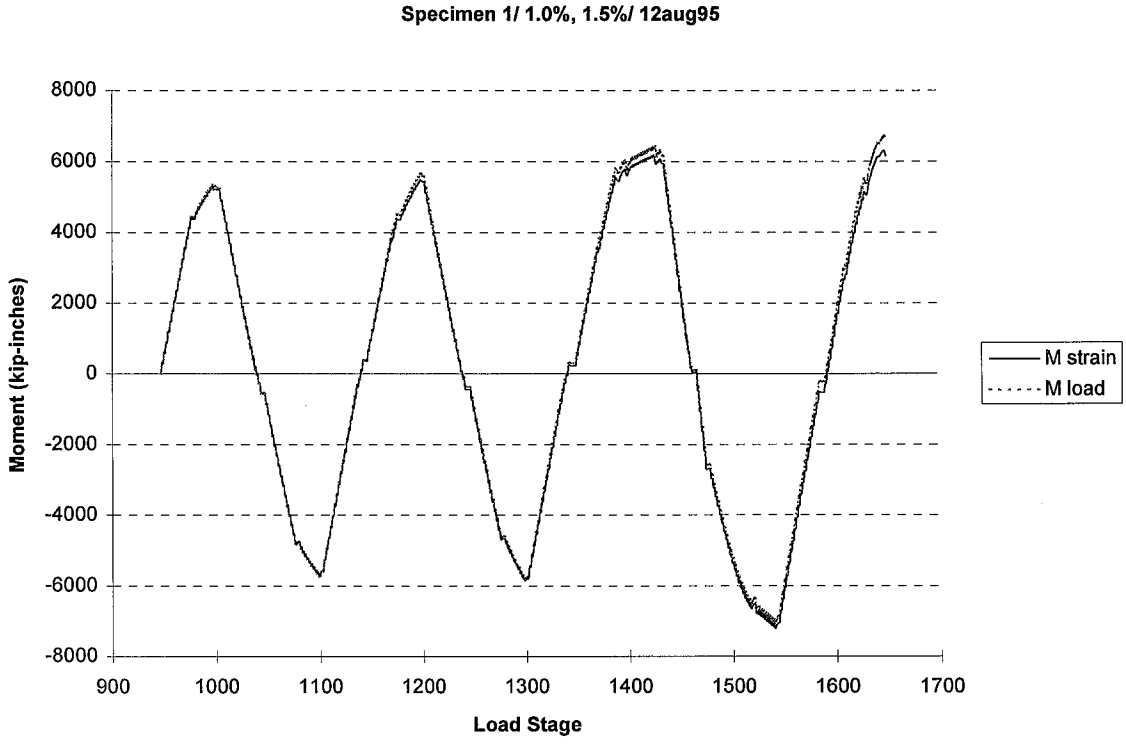

Figure 4.4: Strain Moment vs. Load Moment (Bottom Column Section of Specimen 1)

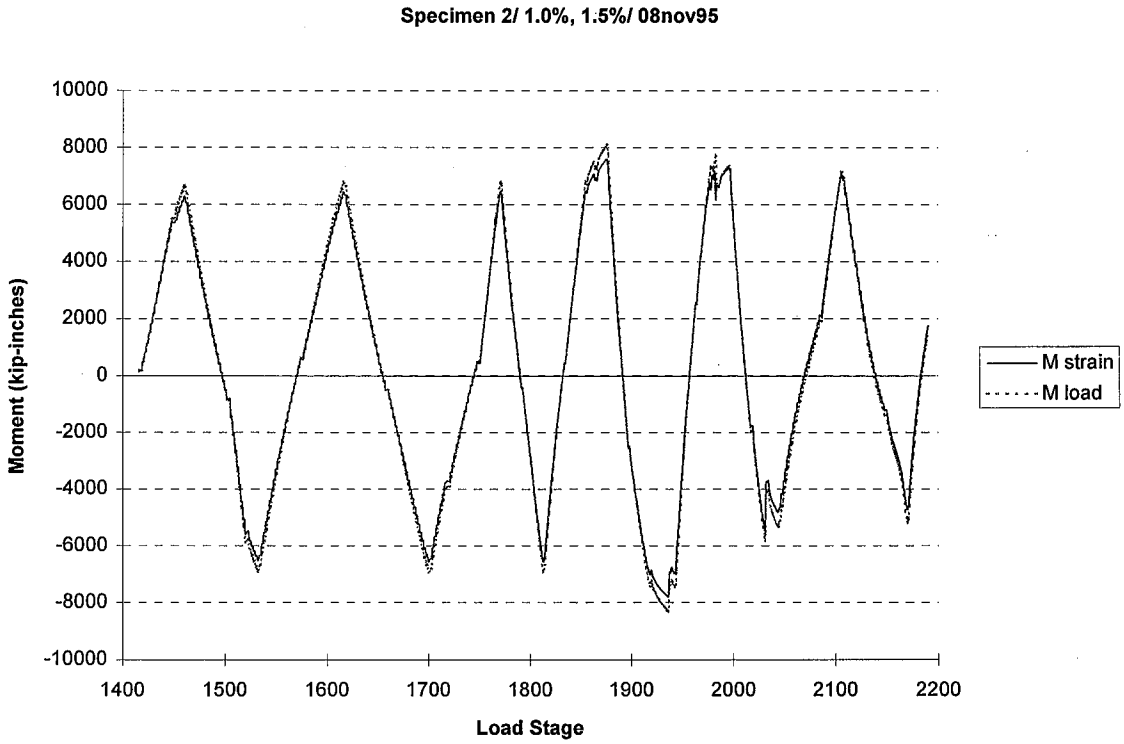

Figure 4.5: Strain Moment vs. Load Moment (Top Column Section of Specimen 2)

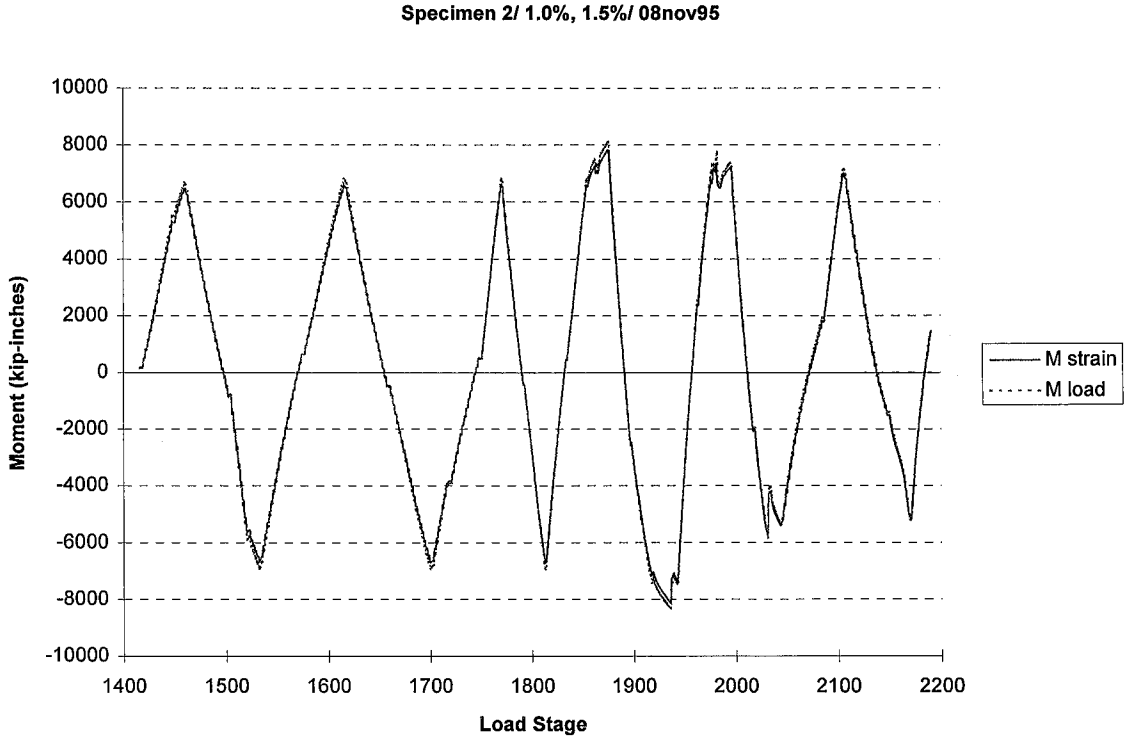

Figure 4.6: Strain Moment vs. Load Moment (Bottom Column Section of Specimen 2)

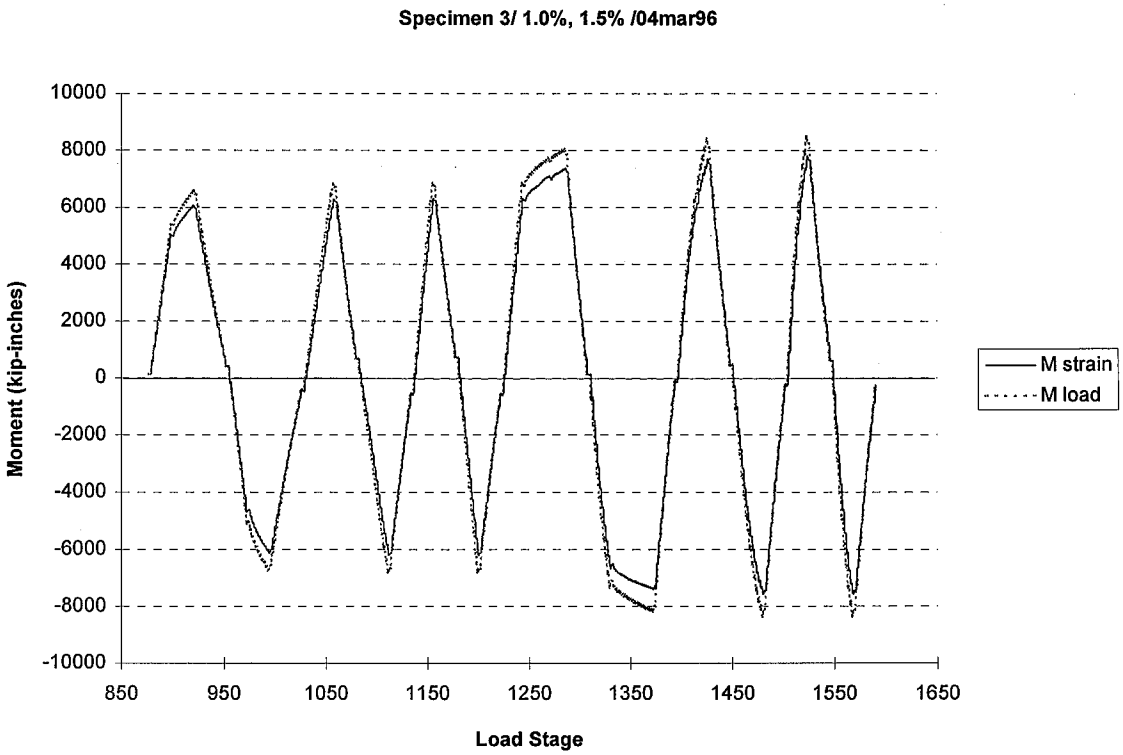

Figure 4.7: Strain Moment vs. Load Moment (Top Column Section of Specimen 3)

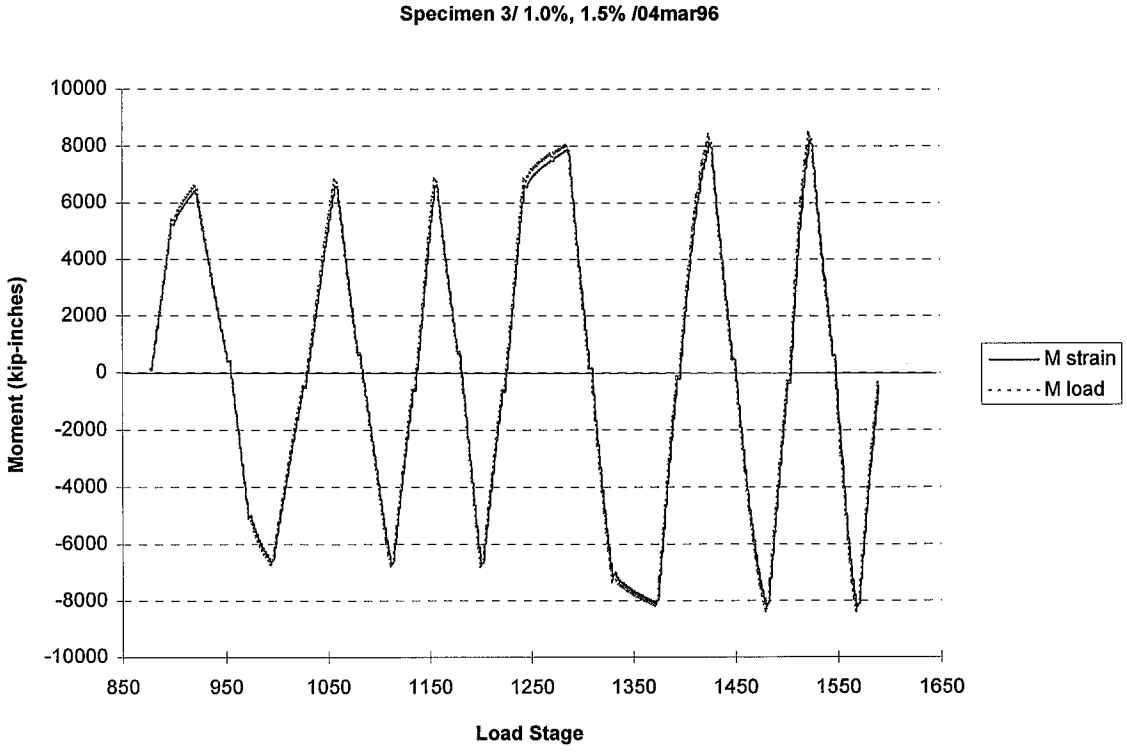

Figure 4.8: Strain Moment vs. Load Moment (Bottom Column Section of Specimen 3)

such as the shear tab bolts and welds and the girder flange-to-column flange welds also contribute to the total deformation. Finally, the deflection of the load frame itself contributes a component to the girder tip deflection.

To capture all of these effects, rotation components have been either experimentally measured or analytically calculated. These components include: panel zone deformation (Δ_{pz}), girder-to-column (relative) rotation (Δ_{rel}), column flexural deformation (Δ_{col}), girder flexural deformation ($\Delta_{gird\,flex}$), girder shear deformation ($\Delta_{\text{gird shear}}$), and deflection of the load frame (Δ_{lf}):

$$\Delta_{calc} = \Delta_{pz} + \Delta_{rel} + \Delta_{col} + \Delta_{gird\,flex} + \Delta_{gird\,shear} + \Delta_{lf} \tag{4.1}$$

In this investigation, only in-plane rotation effects are considered. In addition, second-order effects of the column flexural rotation component due to 550 kips of tension imposed on the column were computed to be negligible; therefore, they are ignored (see Appendix F.8).

Two sets of calculated girder tip deflections are compared to the actual girder tip deflection. The first calculated deflection assumes no rotational resistance in the column supports; therefore, it is referred to as the "calculated girder tip deflection (pinned supports)." The other calculated deflection assumes infinite rotational resistance in the column supports and is referred to as the "calculated girder tip deflection (fixed supports)."

The actual girder tip deflection is bounded by the two calculated girder tip deflections, assuming that some frictional resistance in the column load pins during testing reduced a portion of the moment transferred into the column and panel zone region. Because the amount of resistance present in the load pins is shown to be minimal (see Section 4.1), the actual girder tip deflection will be compared only to the calculated girder tip deflection (pinned supports) for the three specimens. The results from this

comparison, along with the procedure for calculating the girder tip deflection components, are reported in detail in Appendix F.

The top and bottom load pin assemblies may be most accurately modeled as a lateral support (allowing vertical translation) and a pinned support, respectively, with each support possessing a rotational spring (see Appendix D). However, in formulating the column flexural deformation equation and assuming no load pin resistance, a pinned-top and pinned-bottom support condition was utilized. It was verified using matrix structural analysis that this minor deviation in the modeling of the specimen (i.e., restraining vertical translation at the top load pin) was negligible (see Section F.8).

Figures 4.9 to 4.14 compare the actual and calculated girder tip deflections for the West girders of Specimens 1, 2, and 3, respectively, during the 0.25% to 0.75% drift levels. With exception to the 0.25% drift levels without axial loading of the column, the East and West girders of Specimen 1 exhibit actual girder tip deflections that exceed the calculated girder tip deflections by approximately 8% up to when the West connection failed (see Figures 4.9 and 4.10, West girder of Specimen 1). For the East and West girders of Specimen 2 and the East girder of Specimen 3, the actual girder tip deflection values are up to 14% greater than the calculated girder tip deflection values up to the 0.75% drift cycles (see Figures 4.11 and 4.12, West girder of Specimen 2).

The West girder of Specimen 3 demonstrates a strong correlation between the actual girder tip deflections and the calculated girder tip deflections when subjected to negative bending (see Figures 4.13 and 4.14, West girder of Specimen 3). However, when the West girder was subjected to positive bending, the actual girder tip deflection magnitudes exceed the calculated girder tip deflection magnitudes by about 12% to 18%. Note that for all the specimens at the higher drift levels (i.e., at 0.75% drift and higher), the calculated components are assumed to be invalid, due to the effects of material and geometric nonlinear behavior (see Section F.9).

Based on these relatively small peak error percentages during the initial drift cycles (up through 0.50%), it may be concluded that the measured panel zone shear deformation and girder-to-column rotation are valid. A majority of the error between the

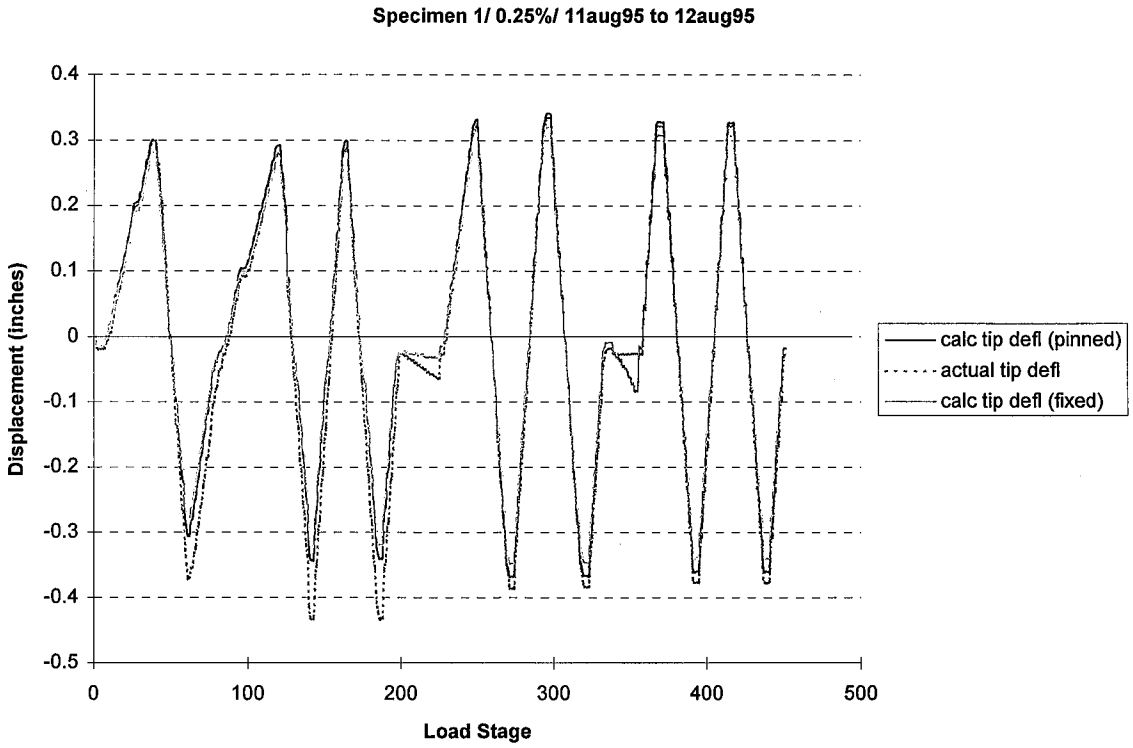

Figure 4.9: Actual vs. Calculated Girder Tip Deflection (West Girder of Specimen 1)

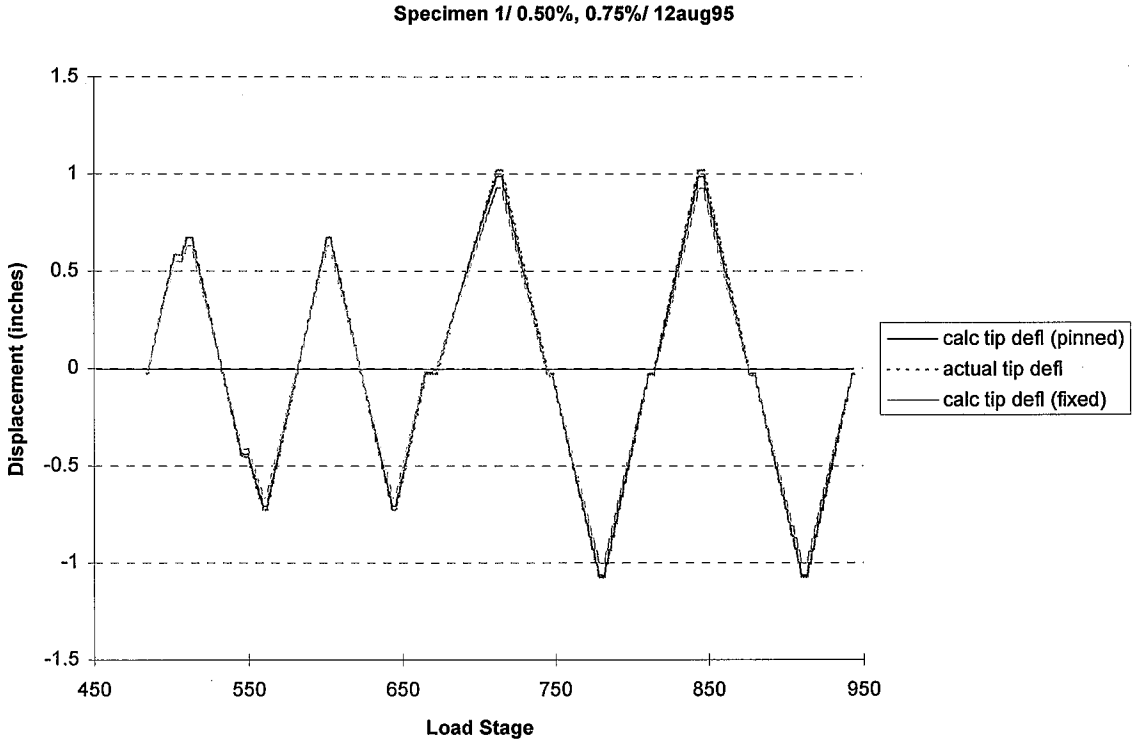

Figure 4.10: Actual vs. Calculated Girder Tip Deflection (West Girder of Specimen 1)

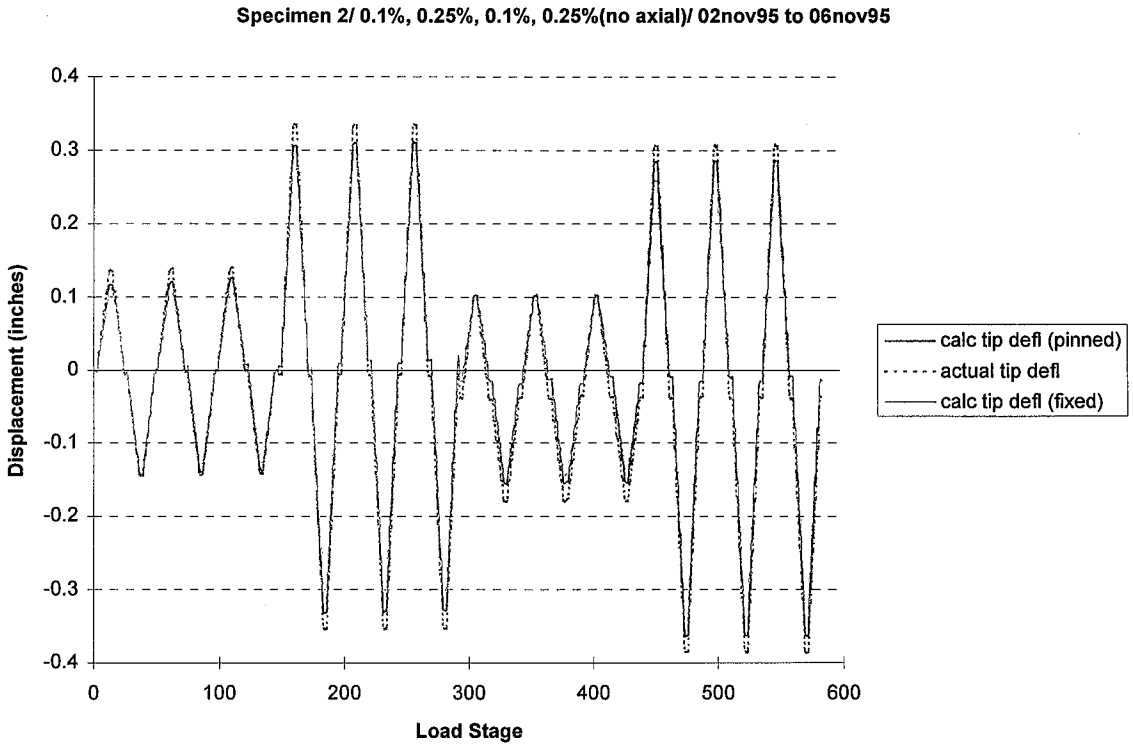

Figure 4.11: Actual vs. Calculated Girder Tip Deflection (West Girder of Specimen 2)

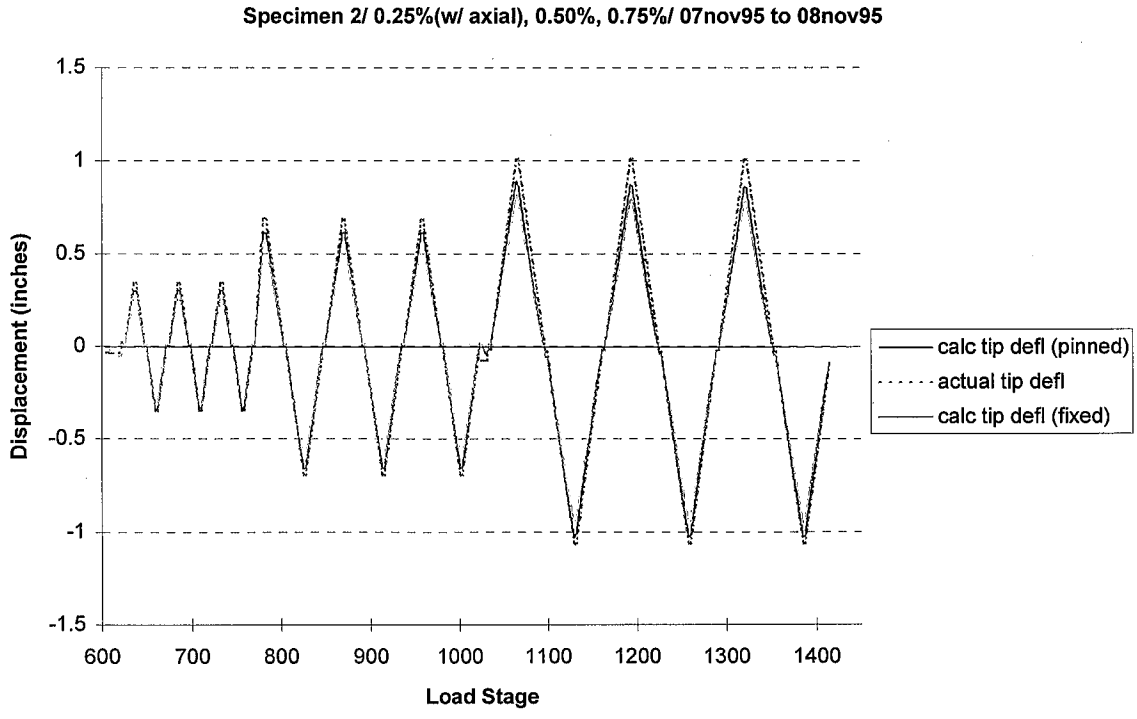

Figure 4.12: Actual vs. Calculated Girder Tip Deflection (West Girder of Specimen 2)

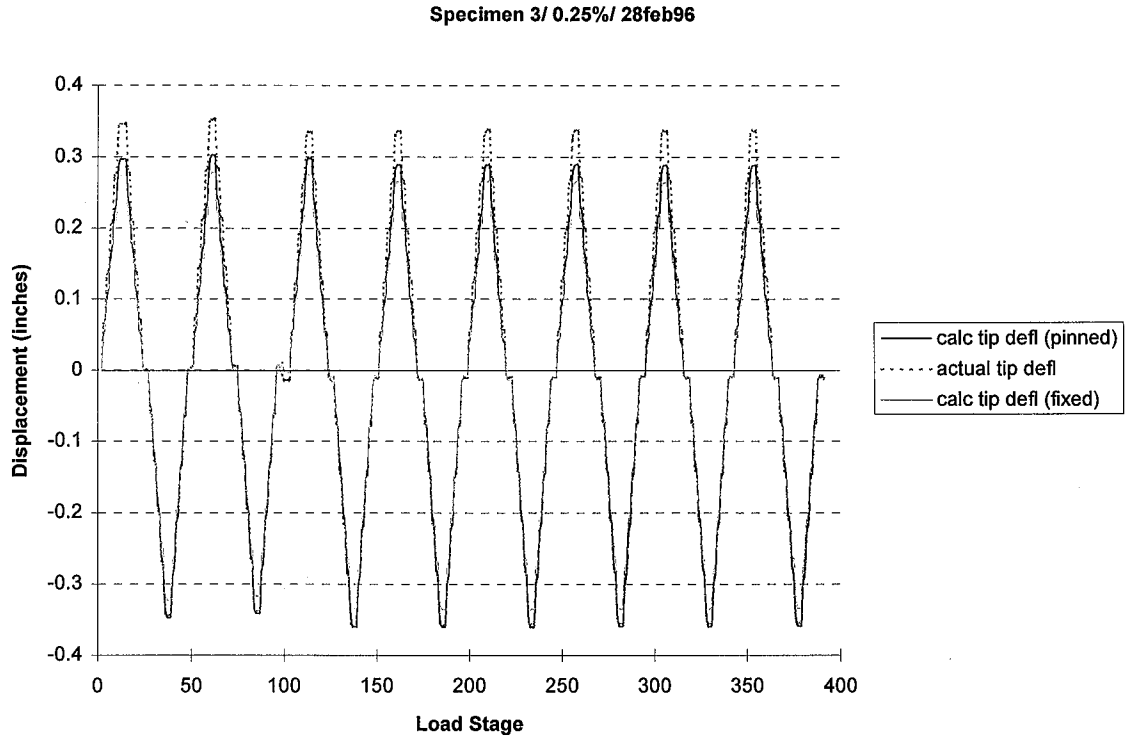

Figure 4.13: Actual vs. Calculated Girder Tip Deflection (West Girder of Specimen 3)

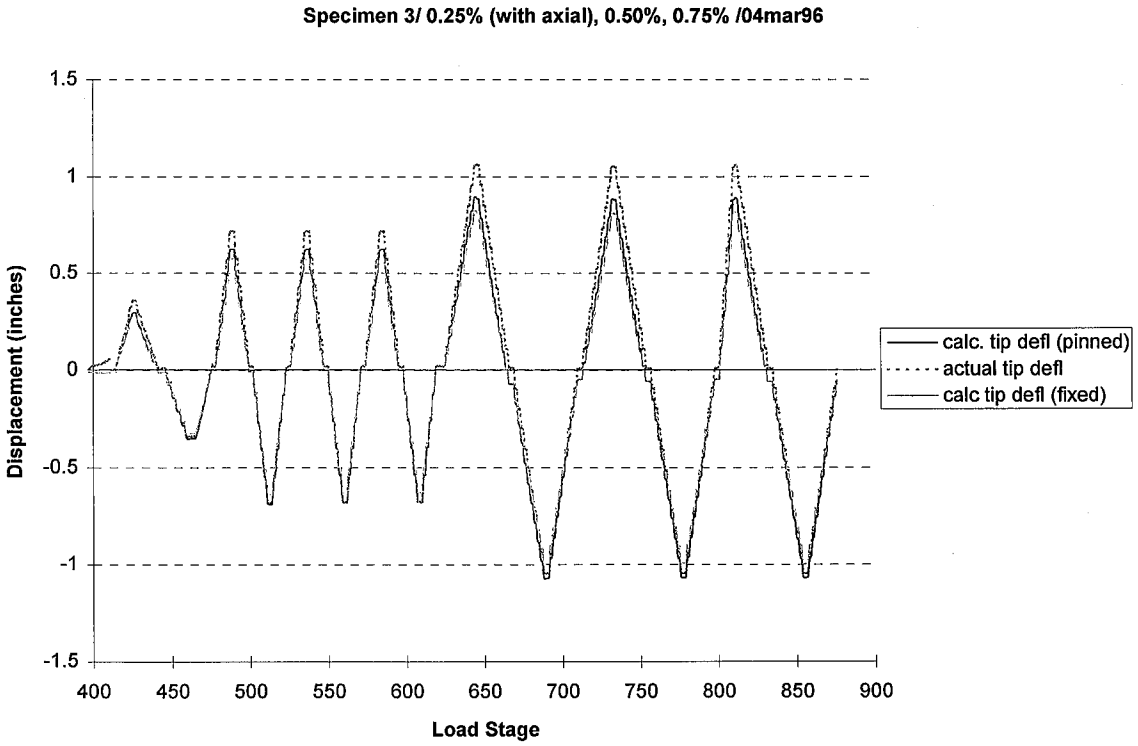

Figure 4.14: Actual vs. Calculated Girder Tip Deflection (West Girder of Specimen 3)

actual and calculated girder tip deflection components occurred during girder positive bending, especially for the West girder of Specimen 3. To address this issue, the effects of composite action on the modeling of the flexural behavior of the girders are more thoroughly discussed in Appendix F. Other conditions contributing to the discrepancies between the two girder tip deflections are also discussed in that appendix.

To illustrate the relationship between the girder tip components that were typically observed for all three tests, Figures 4.15-4.18 compare the six deformation components of the girder tip deflection and the joint rotation component (though not included in the calculated girder tip deflection--see Section F.7) of the West girder of Specimen 3. The girder tip deflection due to girder-to-column rotation, girder flexure, and girder shear deformation are labeled as "gird rel rot", "gird flex", and "gird shear". The joint rotation girder tip deflection component, computed from measurements taken from the inclinometer, is labeled as "connection", and is included for comparison (see Section F.7).

Note that the shear distortion of the panel zone region yields larger values of tip deflection than expected during the lower drift levels, considering it was designed to be relatively rigid. In fact, the panel zone deformation, along with the flexural deformation in the girder, are the primary contributors to the calculated girder tip deflection during the 0.25% to 0.75% drift cycles for all three tests (see Section F.9).

4.3 Actual, Calculated, and Equilibrium Girder Moments and Strains

This section compares the actual girder moments to two calculated girder moments located at a distance of 13.5" from the column face. The actual strains measured in the concrete slab at this location from the column face are also compared to two calculated concrete strains. The purpose of these comparisons is not only to verify that the strains measured along the steel cross section are valid, but also to investigate the presence of slip (between the steel girder and the concrete deck). Also, a nonlinear strain distribution along the girder cross section is investigated. This behavior is primarily due to a longitudinal distortion which varies through the depth of the cross section and is

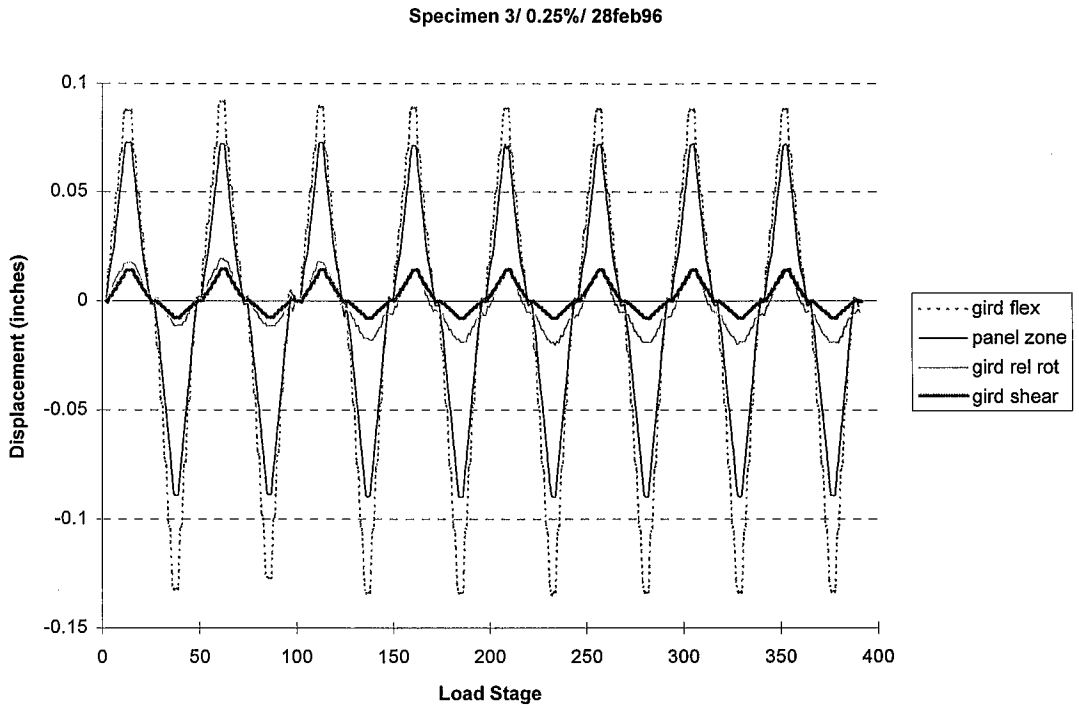

Figure 4.15: Girder and Panel Zone Girder Tip Deflection Components (West Girder of Specimen 3)

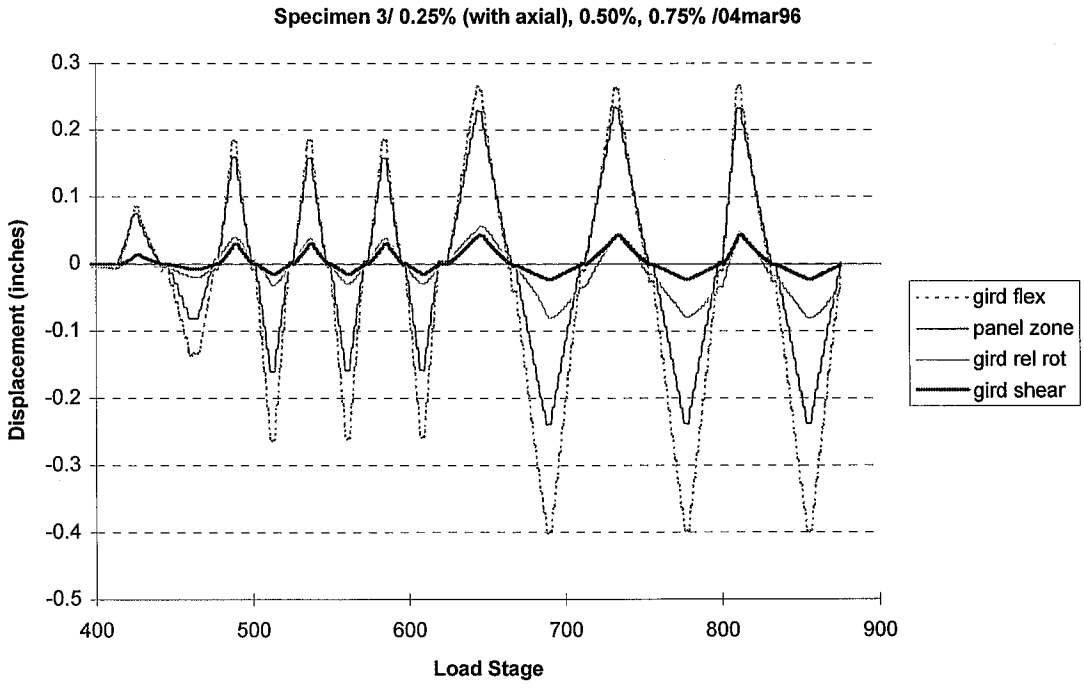

Figure 4.16: Girder and Panel Zone Girder Tip Deflection Components (West Girder of Specimen 3)

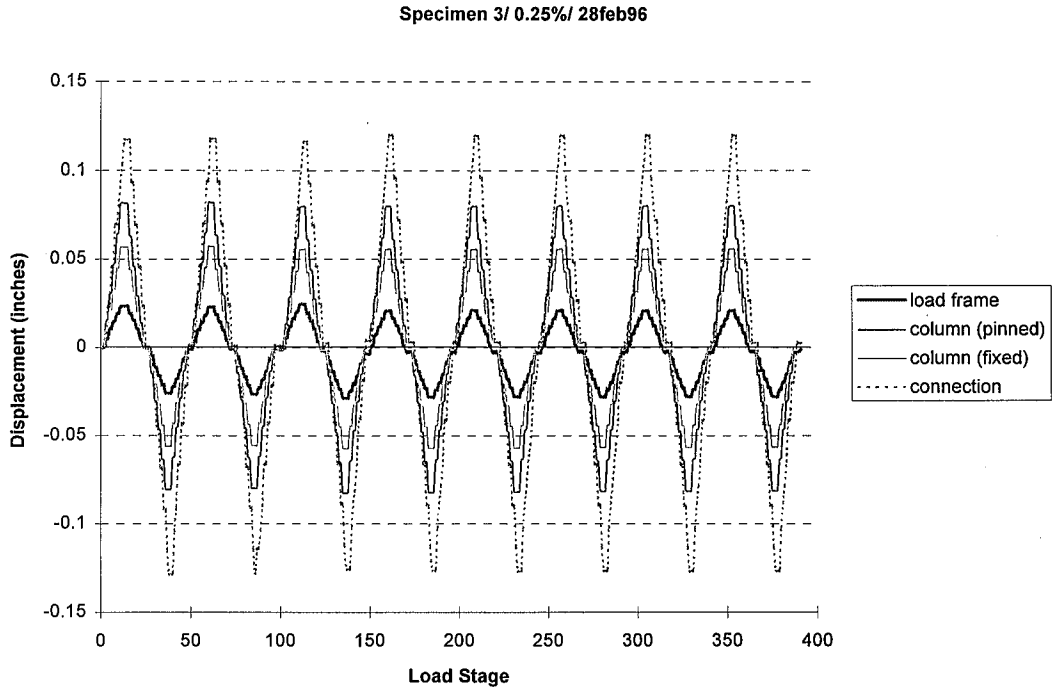

Figure 4.17: Column, Load Frame, and Connection Girder Tip Deflection Components (West Girder of Specimen 3)

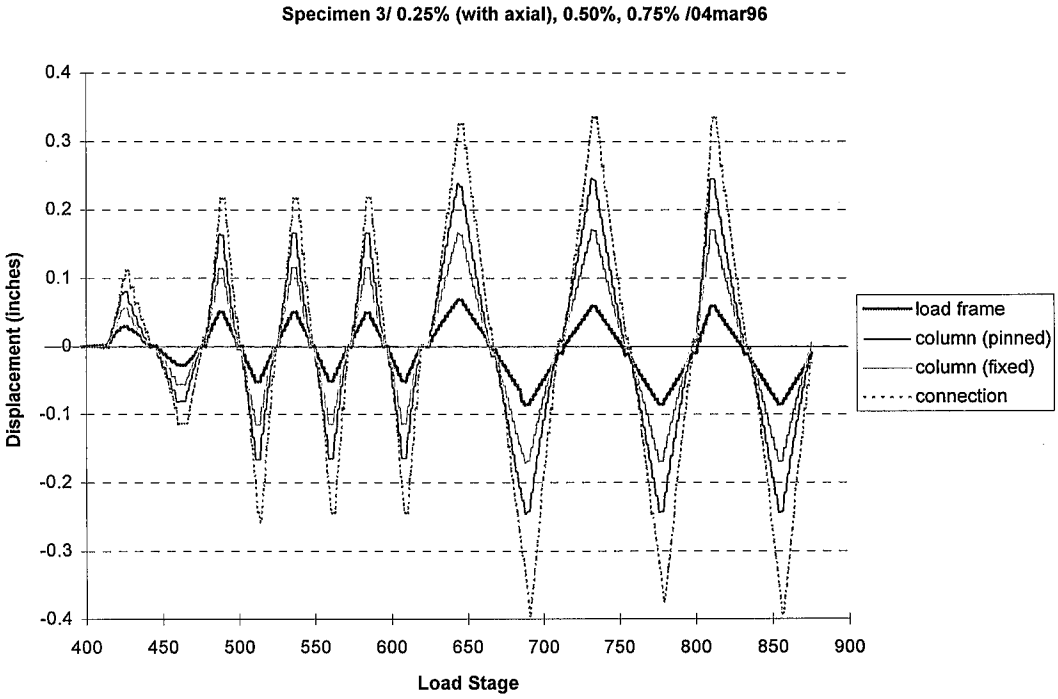

Figure 4.18: Column, Load Frame, and Connection Girder Tip Deflection Components (West Girder of Specimen 3)

most likely uniform through the width of the cross section. Finally, the effect of the accuracy in calculating the concrete modulus is studied. The effects of each condition may be isolated by comparing girder moment and strain values that incorporate different combinations of these conditions in their measurement or calculation (see Table 4.1). Note that this comparative study is based on Euler-Bernoulli beam theory (the effects of elastic shear deformation of the girders is small).

Table 4.1: Conditions Included in the Measurement and Calculation of the Girder Moments and Strains

Conditions	Actual Moment	Calculated Moment	Equilibrium Moment	Actual Strain	Calculated Strain	Equilibrium Strain
Composite Slip	slip	no slip	slip	slip	no slip	slip
Concrete Modulus	actual	calculated	actual	N/A	N/A	calculated
Steel Strain Distribution	nonlinear	linear	linear	nonlinear	linear	linear

The girder moments are determined at a distance 13.5" from the column flange, where a series of seven strain gages were placed on each steel girder so as to locate its neutral axis (see Section 2.4.3). For the composite specimens, five of the six reinforcing bars in the concrete slab were also instrumented with strain gages at this distance from the column flange.

The actual girder moments are determined by multiplying the applied load at the girder tip by the distance between the point of load application and the location of the seven strain gages along the steel cross section. The calculated girder moments are computed by summing girder moment components about the neutral axis of the cross section (see Appendix G for details of these calculations). The girder moment components are computed using five force components located in the upper flange, the

web region below the neutral axis, the web region above the neutral axis, the lower flange, and the concrete slab (see Figure 4.19).

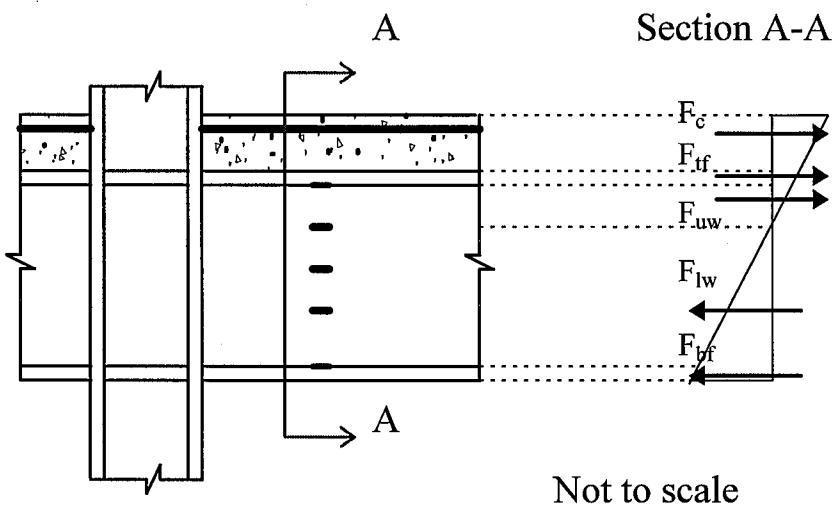

Figure 4.19: Force Components of the Girder Cross Section

The girder moments are calculated in two ways. The first calculated girder moment uses the location of a calculated neutral axis and a calculated curvature of the girder cross section (with the neutral axis location and curvature being calculated based on the measured strains in the cross section; see Appendix G) to estimate strains and forces in the concrete slab. The second calculated girder moment also uses a calculated curvature, but a calculated concrete slab force is determined which satisfies equilibrium of forces in the girder cross section. Using this procedure to obtain the calculated girder moments avoids using a moment of inertia of the composite section, which could vary dramatically throughout the load history.

The actual and calculated girder moments of the East and West girders of Specimen 1 exhibit a strong correlation up through the 0.75% drift levels (see Figures 4.20 and 4.21, West girder of Specimen 1). This is because the calculated girder moment for Specimen 1 is primarily affected by a distortion of the steel cross section and is not dependent upon various effects such as composite slip or concrete modulus variability (see Table 4.1). This is also shown by the actual strain distribution along the steel girder

cross sections at a distance of 13.5" from the column face (see Figure 4.24, West girder of Specimen 1). Based on these results, it may be concluded that the strain measurements along the steel girder cross section are valid for Specimen 1.

For Specimens 2 and 3, the accuracy of the strains along the steel girder cross section can only be speculated, since several conditions (due to the presence of composite floor slabs) exist which complicate the verification of the girder moments and strains. However, these conditions, which include composite slip, concrete modulus variability, and a nonlinear strain distribution along the steel cross section, may be individually addressed to compare the behavior of the steel and composite girders. The results from this study are briefly discussed next, and are more thoroughly investigated in Appendix G.

To study the effects of a nonlinear strain distribution along the steel cross section, the actual and calculated girder moments are compared for Specimen 1 while the actual and equilibrium girder moments are compared for Specimens 2 and 3. As previously mentioned, it is observed that distortion of the steel cross section was minimal for the specimens up through the 0.75% drift levels (see Figures 4.20, 4.21, and 4.24). The East and West girders of Specimen 1 (during both positive and negative girder bending) and of Specimens 2 and 3 (during girder negative bending only) demonstrate minimal nonlinear strain behavior along the steel cross section during drift cycles up to 0.75% (see Figures 4.22 and 4.23, West girder of Specimen 3). The East and West girders of Specimens 2 and 3 (during girder positive bending) maintain linear strain behavior along the girder cross sections up through the 0.50% drift cycles. This is also shown by the actual strain distribution along the steel girder cross sections at a distance of 13.5" from the column face (see Figure 4.25, West girder of Specimen 3).

The amount of slip occurring within the composite girders may be qualitatively studied by comparing the strains measured in the concrete slab to the calculated concrete strains (see Table 4.1). This comparison is valid by assuming that the level of nonlinear behavior across the girder cross section is small and that the measured and calculated concrete strains are not dependent upon the concrete modulus. The East and West

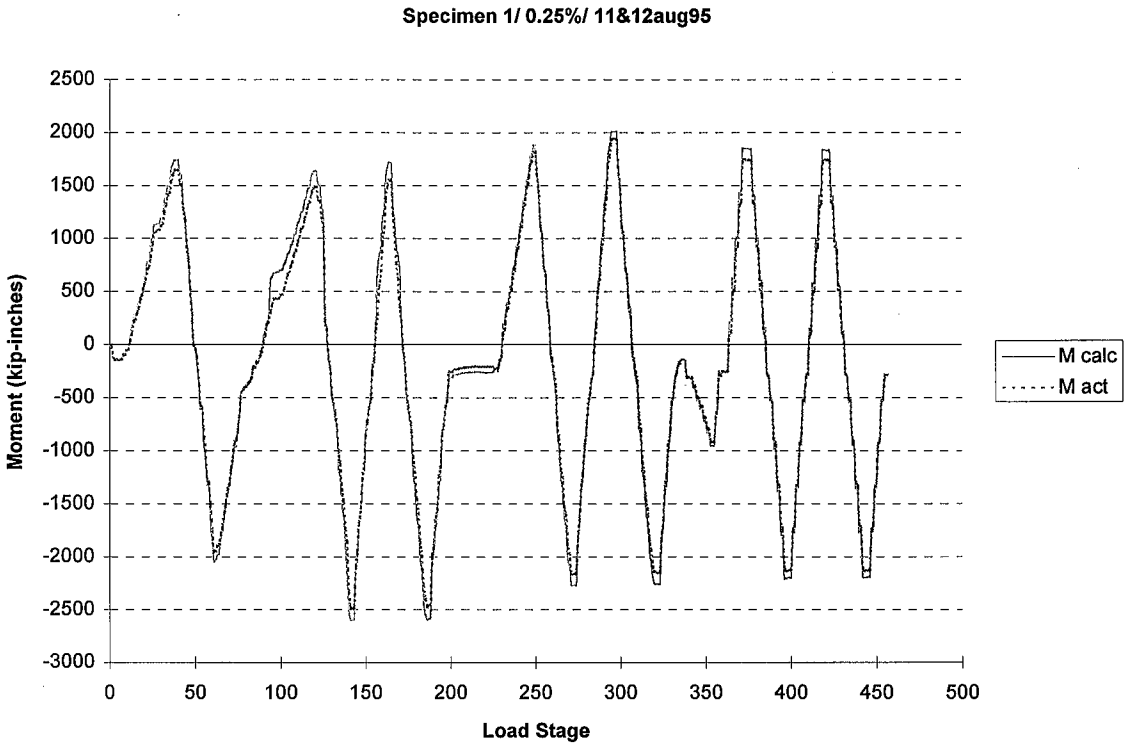

Figure 4.20: Actual vs. Calculated Girder Moment (West Girder of Specimen 1)

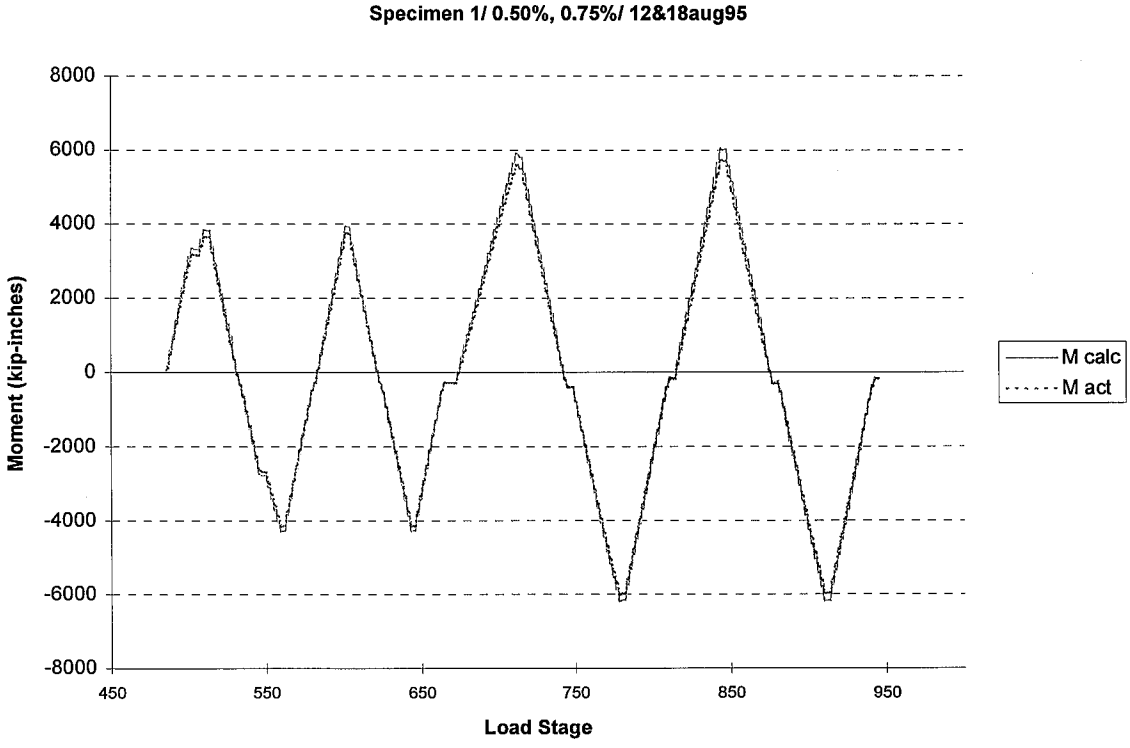

Figure 4.21: Actual vs. Calculated Girder Moment (West Girder of Specimen 1)

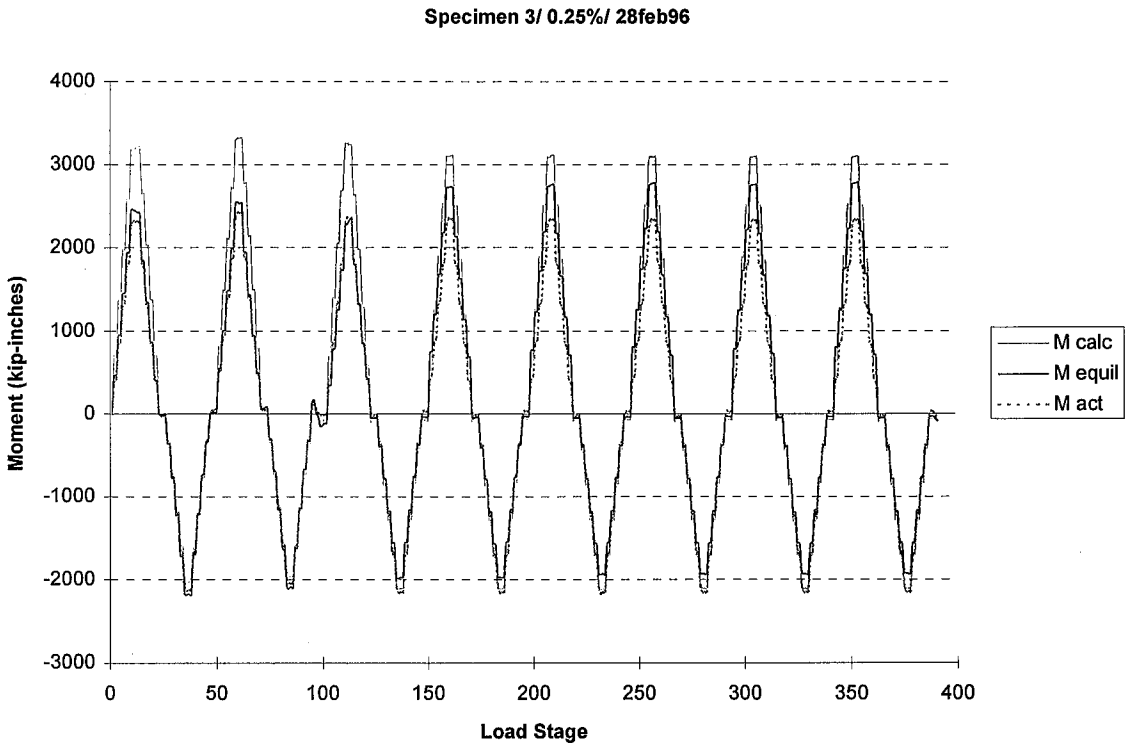

Figure 4.22: Actual vs. Calculated Girder Moment (West Girder of Specimen 3)

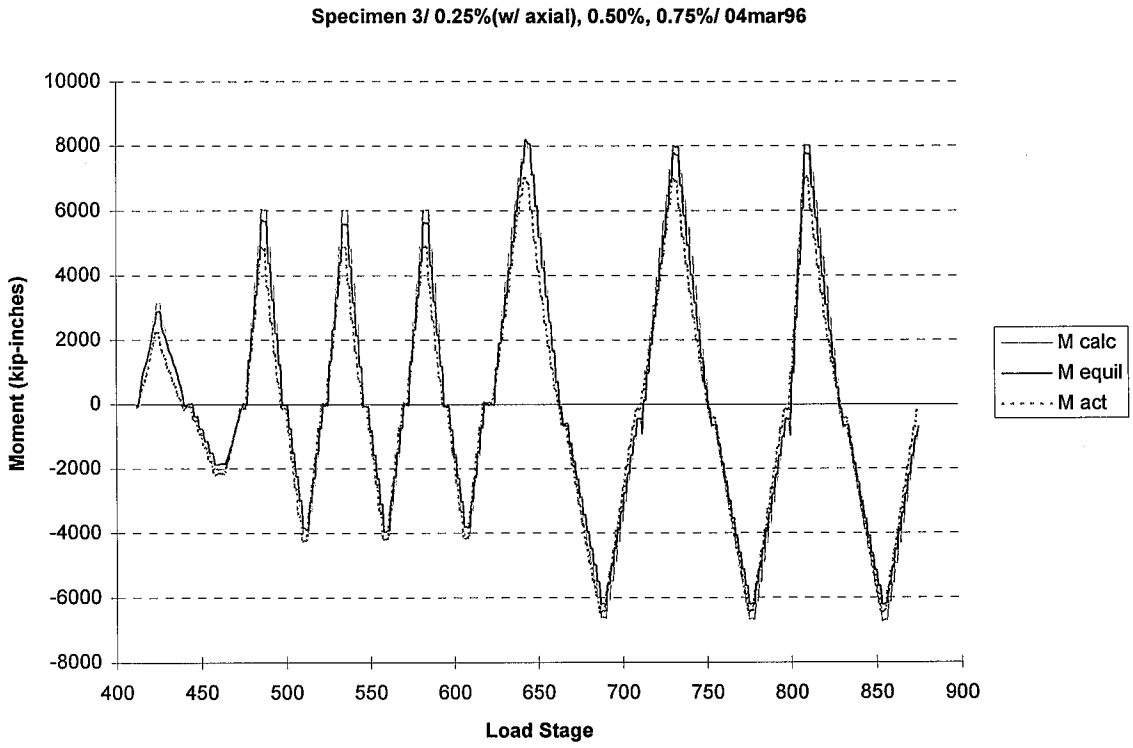

Figure 4.23: Actual vs. Calculated Girder Moment (West Girder of Specimen 3)

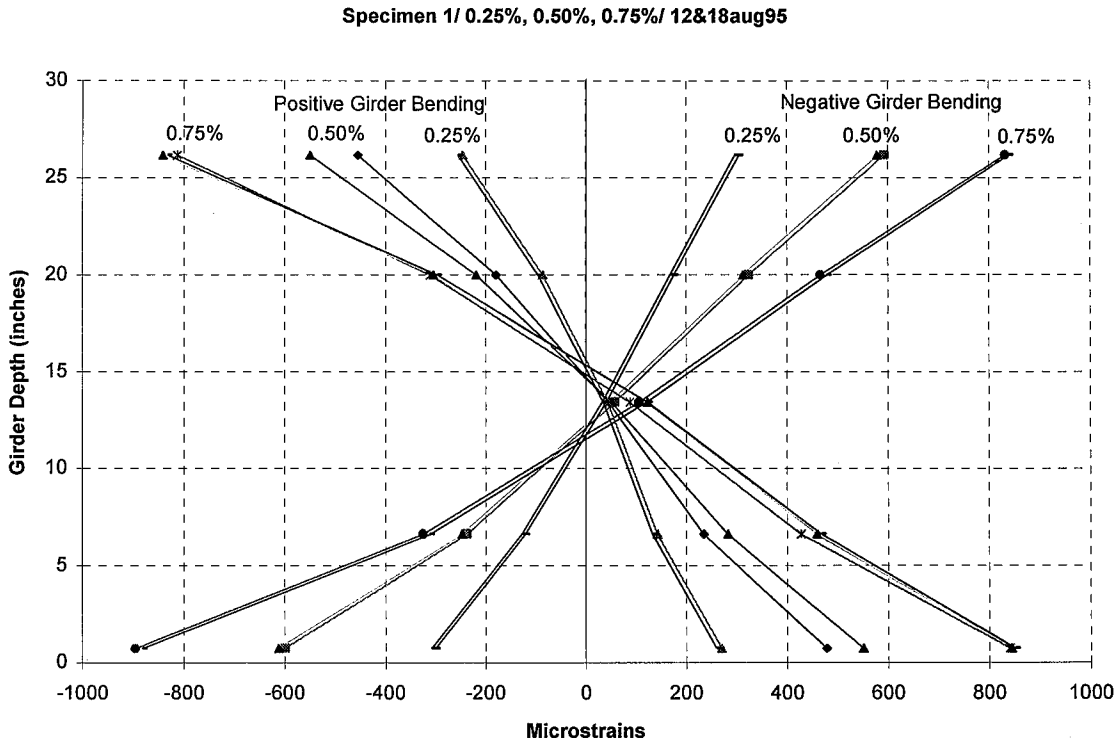

Figure 4.24: Steel Girder Strain Distribution (West Girder of Specimen 1)

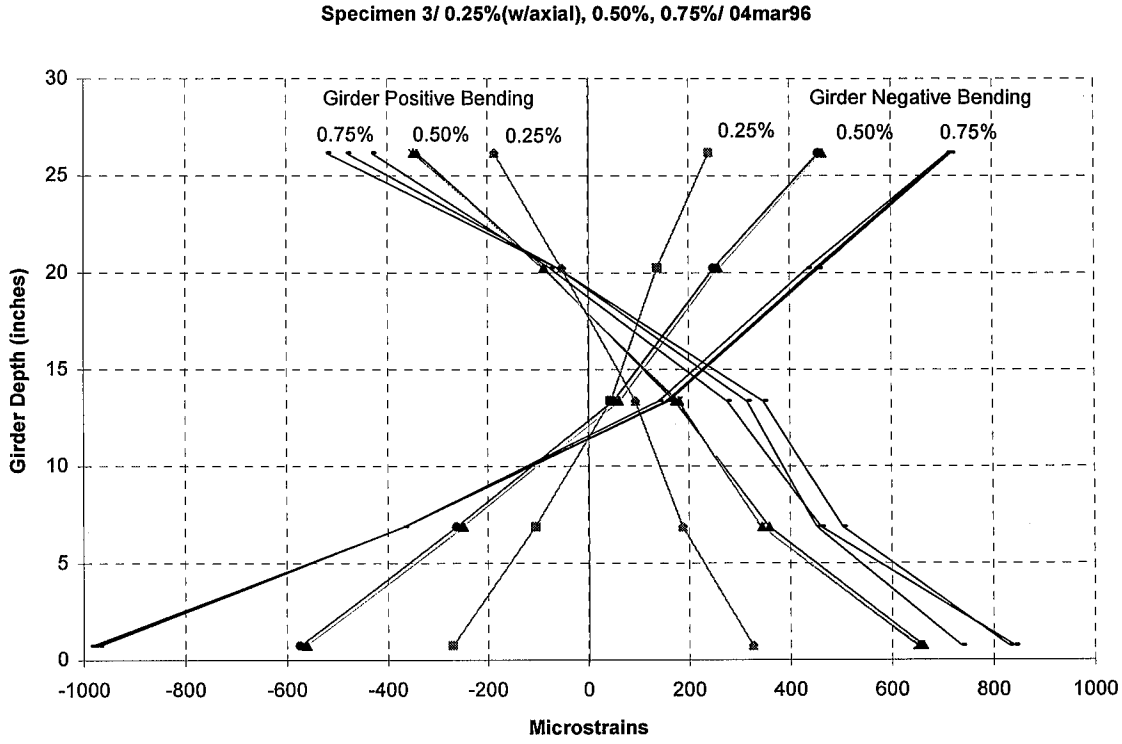

Figure 4.25: Steel Girder Strain Distribution (West Girder of Specimen 3)

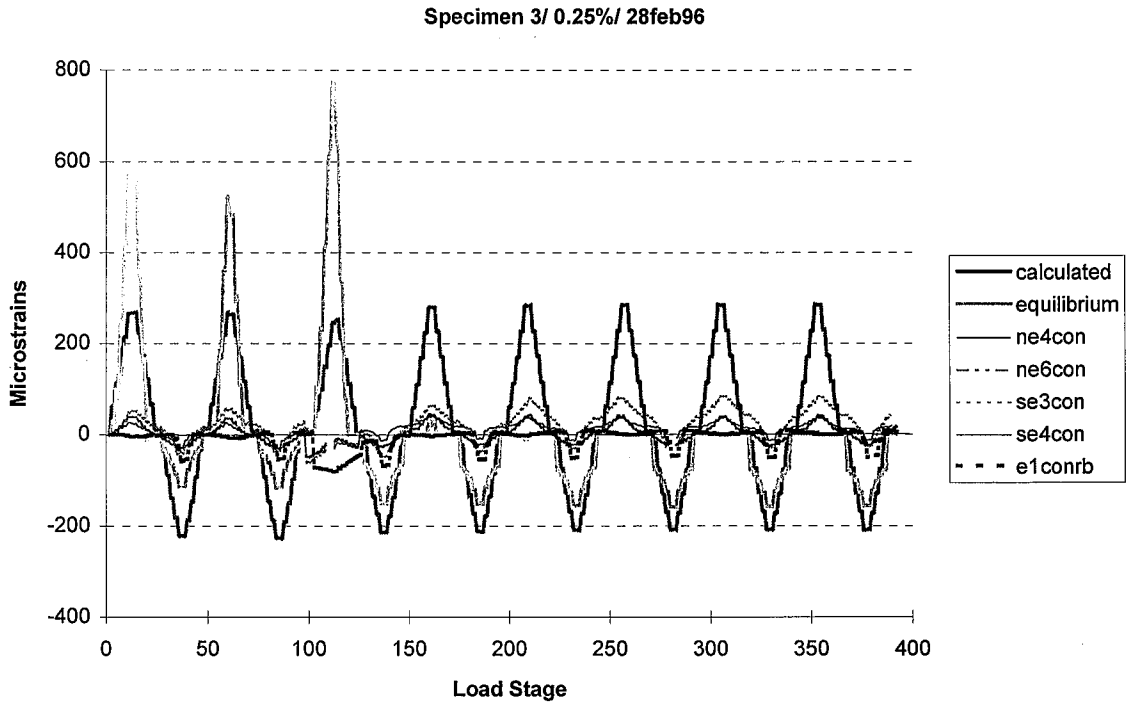

Figure 4.26: Actual vs. Computed Concrete Strains (East Girder of Specimen 3)

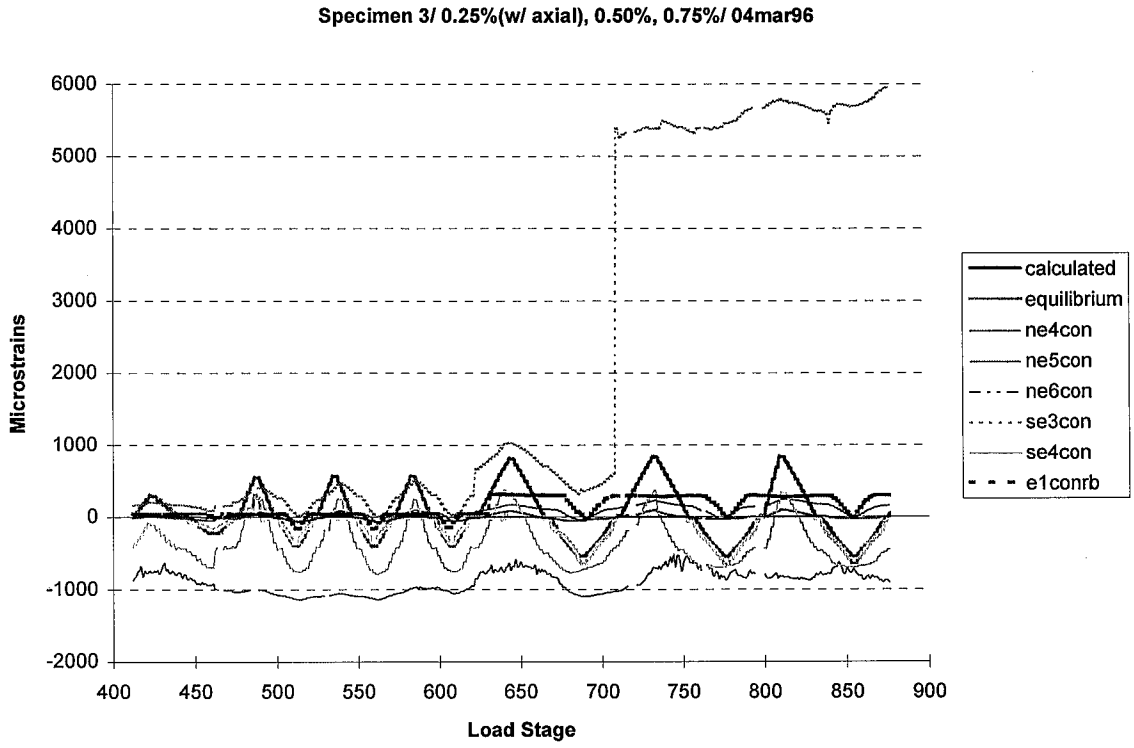

Figure 4.27: Actual vs. Computed Concrete Strains (East Girder of Specimen 3)

girders of Specimen 2 and the East girder of Specimen 3 demonstrate moderate levels of composite slip, evident by larger calculated concrete strains compared to the actual strains measured in the concrete slab (see Figures 4.26 and 4.27, East girder of Specimen 3). However, the West girder of Specimen 3 exhibits minimal amounts of composite slip, since the actual and calculated concrete strains are relatively the same in magnitude (see Figures 4.28 and 4.29, West girder of Specimen 3).

In general, the four composite girders achieve relatively the same levels of composite action. Note that it is expected that the composite girders of Specimen 2 (which exhibit 55% composite action) would have higher levels of composite action than the composite girders of Specimen 3 (which exhibit 35% composite action). Because the East girder of Specimen 3 demonstrates slightly more composite slip than the West girder, the behavior of these two connections may be different (see Chapter 5).

The estimation of the concrete modulus, E_c, is also investigated in Appendix G. By comparing the actual and equilibrium concrete strains (see Table 4.1), it is determined that the calculated concrete moduli provide good approximations of the actual concrete modulus of the East girder of Specimen 2 and the West girder of Specimen 3. However, the West girder of Specimen 2 demonstrates an overestimation of E_c, while the East girder of Specimen 3 exhibits an underestimation of E_c. Other conditions studied in Appendix G include the participation of concrete under tensile loading. It is shown in all four composite girders that some concrete tensile stiffness is evident up through the first few cycles at the 0.25% drift levels.

Other phenomena exist that may contribute to the differences in strain magnitudes between these girder moments and strains. Such conditions include crushing of the concrete slab near the column-concrete slab interface, localized strain behavior within the concrete slab, a changing value of E_s, and the Bauschinger effect. These secondary conditions may be assumed minimal during the lower drift cycles and, therefore, are not directly investigated in this section (i.e., the analyses in this section are based on linear elastic behavior).

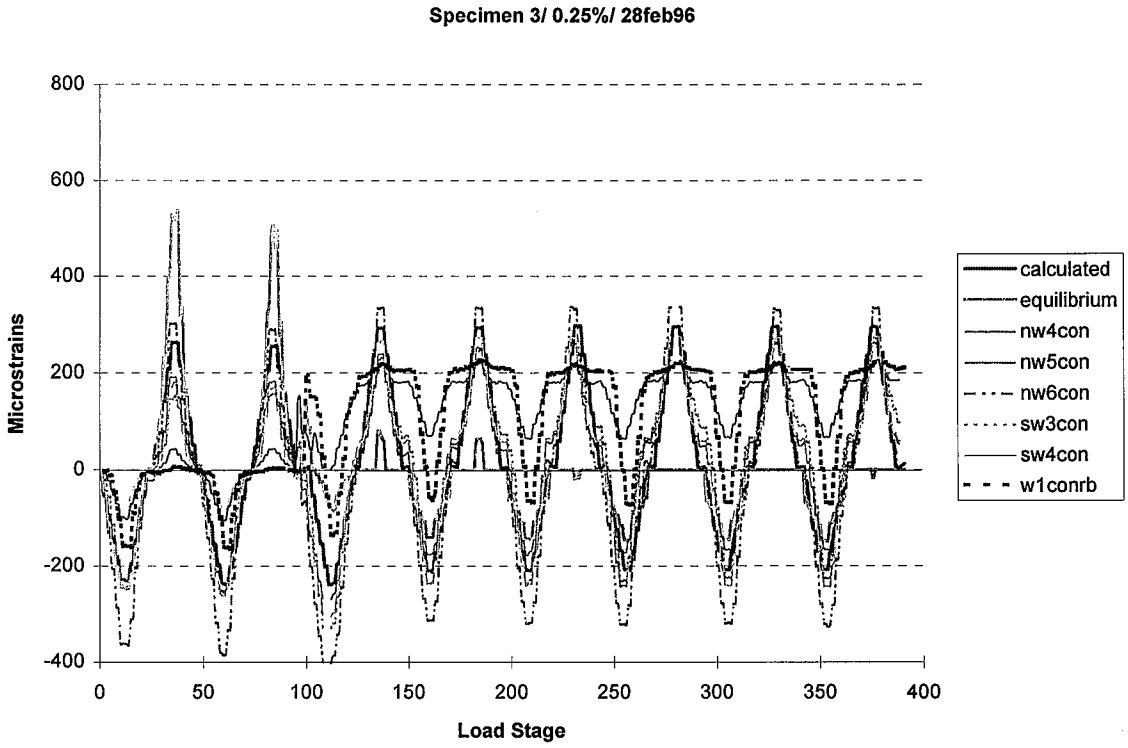

Figure 4.28: Actual vs. Computed Concrete Strains (West Girder of Specimen 3)

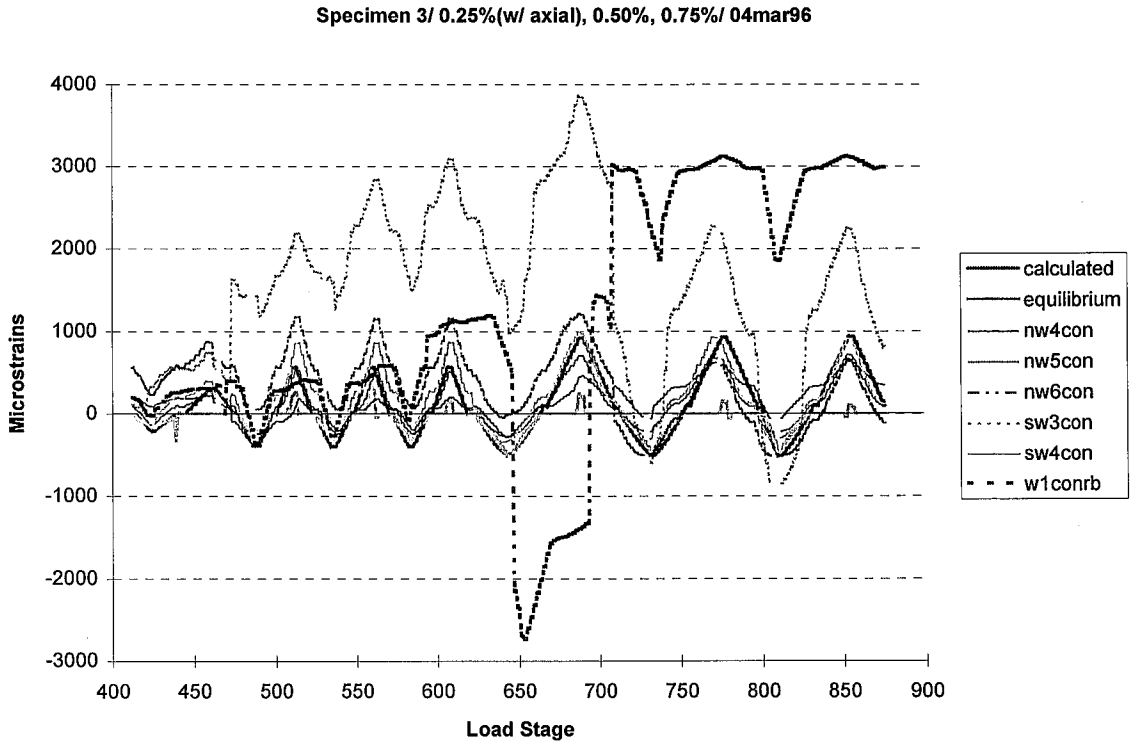

Figure 4.29: Actual vs. Computed Concrete Strains (West Girder of Specimen 3)

Chapter 5

Interpretation of Results

This chapter reports and interprets the experimental results from the testing of the three specimens, along with corroborating computational research. Specifically, several structural phenomena are discussed, particularly the effects of composite floor slabs, which may have contributed to the poor strength and ductility exhibited by the connections of the test specimens. Other geometric conditions addressed are the location of the shear tab along the girder cross section, the existence of backup bars, and strain concentrations near the root of the access holes and the girder flange-to-column welds.

To investigate each one of these structural phenomena effectively, the results are presented in two phases. First, the extensive levels of straining, plastification, and, connection failure at the bottom girder flange region of the connections are associated with the effects of composite floor slabs as well as the placement of the shear tab. Second, the type and location of the connection failures as well as when they occurred are correlated with various structural phenomena, including: the placement of the bottom backup bar at the outside surface of the bottom girder flange, local bending and shearing of the girder flange near the column flange surface, and the potential triaxial tensile strain state caused by restraint in the connection region.

Three primary types of experimental data are utilized to study the behavior of the specimens: strain behavior, displacements and rotations, and acoustic emission activity.

Also, results from continuum finite element analyses are employed to corroborate the experimental study of the specimens.

5.1 The Effect of the Composite Floor Slabs

The effect of the composite floor slabs is investigated for two primary reasons. First, the presence of shear studs and slab reinforcement most likely activate different force-transfer mechanisms at the top and bottom girder flanges at the girder flange-to-column interface. Second, a significant portion of the girder moment is transferred into the concrete slab; therefore, a substantial increase in stiffness and strength occurs at the top of the girder due to the presence of the slab, resulting in the concentration of large strains at the bottom welded girder-to-column connection. This phenomenon occurs only during positive girder bending, assuming that the concrete provides minimal tensile resistance.

This section studies the straining, plastification, and ultimate failure at the bottom and top girder flange regions for Specimens 2 and 3 due to composite action of their girders. Recall that these girders exhibited partially composite behavior as was intended in their design (see Section 4.2). As a result, the effects of composite floor slabs on the performance of Specimens 2 and 3 is believed to be representative of the performance of pre-Northridge connections used in common steel lateral load-resisting frames. These types of frames typically include shear connectors along the length of the girder that are sufficient to induce some partially composite action, although this composite behavior is often neglected in design. Also, addressed are the effects of the placement of the shear tab along the steel girder cross section.

5.1.1 Strain Distribution Along the Girder Cross Section

The distribution of strain along the girder cross sections of the specimens may be studied by comparing the shift in the neutral axis position during positive and negative girder bending. The position of the neutral axis may be evaluated by utilizing the actual strains measured along the girder cross section at a distance of 13.5" from the column face (see Figures 5.1 to 5.2). Using these measured strains, Figures 5.3-5.14 illustrate the strain distributions across the girder cross sections at the peak load point of each cycle through the 1.5% drift cycles. Also, Table 5.1 summarizes the position of the neutral axis of the girders at these peak load points.

For the East and West girders of Specimen 1, the neutral axis is located approximately 15" from the bottom of the bottom girder flange, approximately 1.5" above the elastic centroid of the cross section ($d/2 = 13.46$"), during girder positive bending through the 0.75% drift levels (see Figures 5.3 and 5.4, Table 5.1). This is expected, since the center of the shear tab is located at a distance of 15.4" from the bottom flange of the steel girder, or approximately 2" above the elastic centroid of the steel girder (see Section 2.1.2). During girder negative bending at the same drift levels, the neutral axis is located below the elastic centroid of the steel cross section at a distance of approximately 12" from the bottom girder flange. This deviation of the neutral axis from the elastic centroid of the cross section is unexpected, since the shear tab is located above the elastic centroid of the cross section. Possible explanations for this type of behavior, which relates to the shape of strain profile along the cross section, are discussed later in this section.

A migration of the neutral axis towards the top of the steel section during positive girder bending and towards the bottom of the steel section during negative girder bending is evident during the 1.0% and 1.5% drift cycles for the East and West girders of Specimen 1 (see Figures 5.5 and 5.6). This behavior is primarily due to substantially more yielding of the regions of the girder cross section located farthest away from the

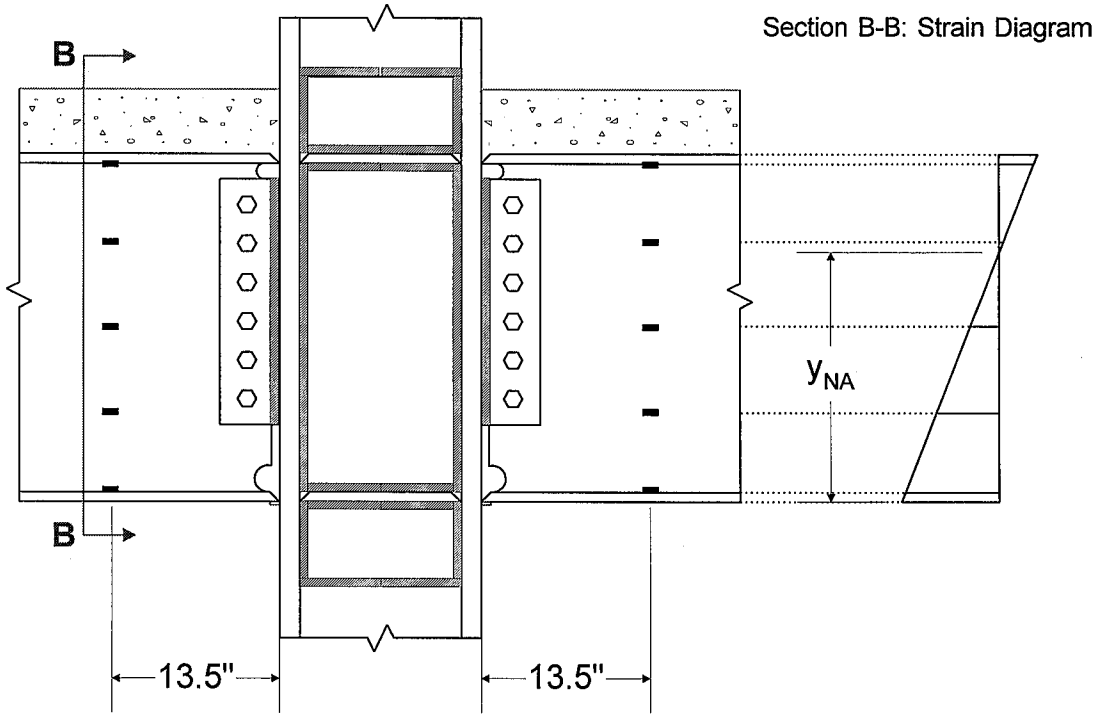

Figure 5.1: Strain Gages Along the Steel Girder Cross Section

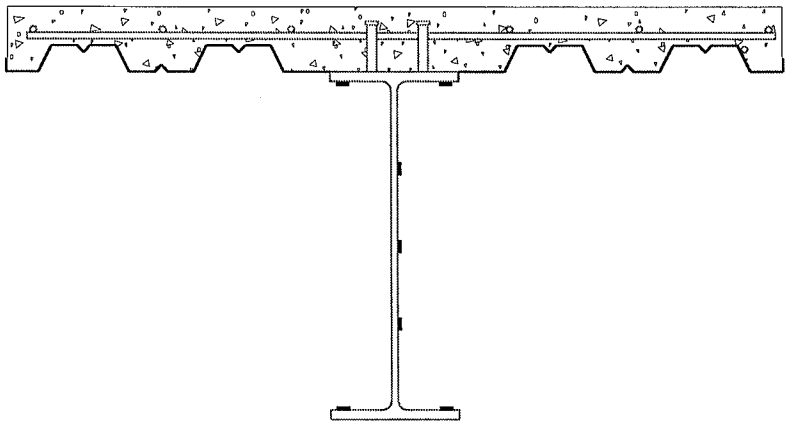

Figure 5.2: Section B-B: Strain Gages Along the Steel Girder Cross Section

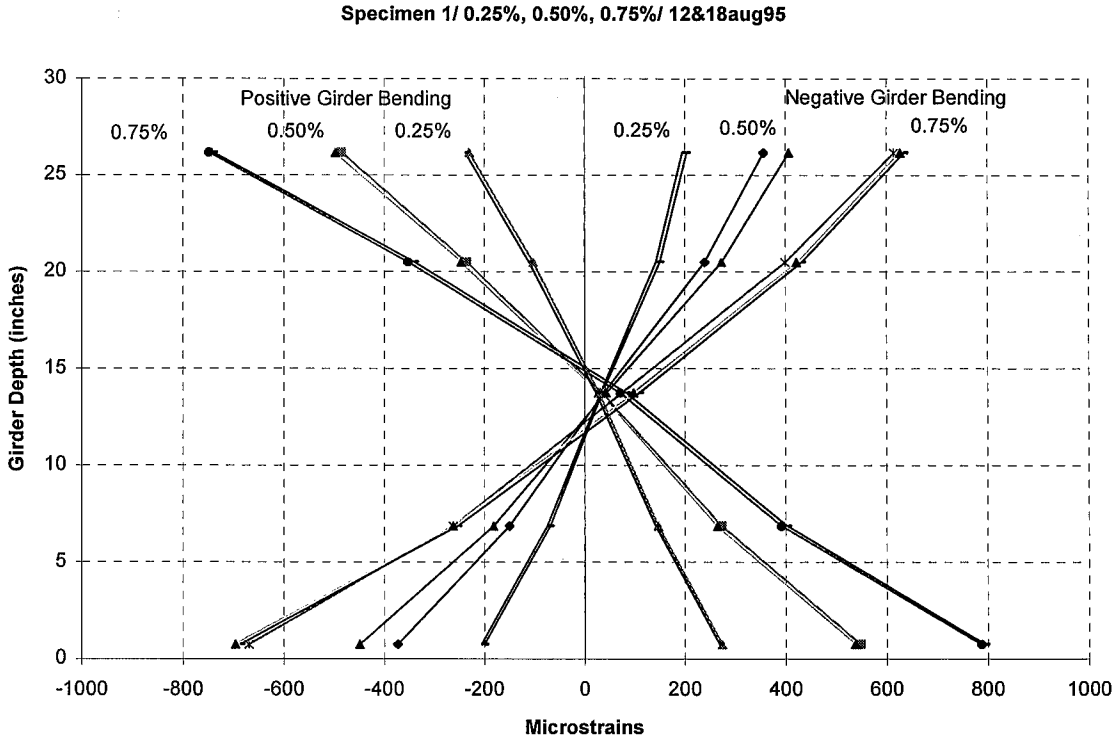

Figure 5.3: Steel Girder Strain Distribution (East Girder of Specimen 1)

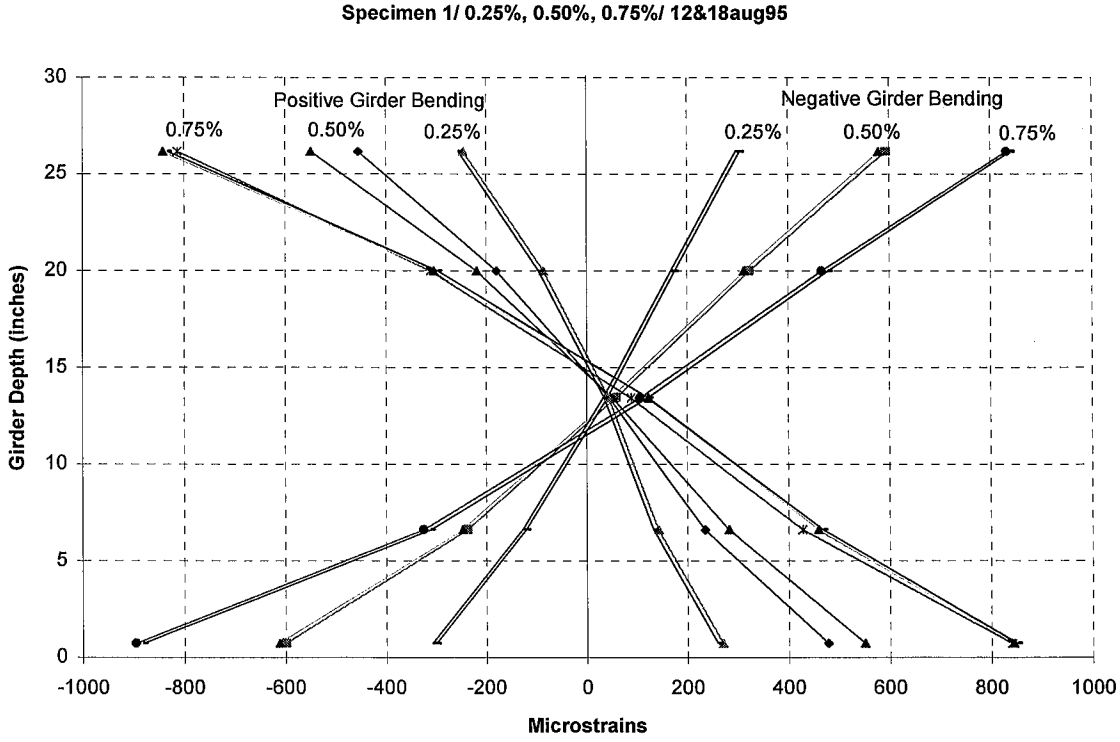

Figure 5.4: Steel Girder Strain Distribution (West Girder of Specimen 1)

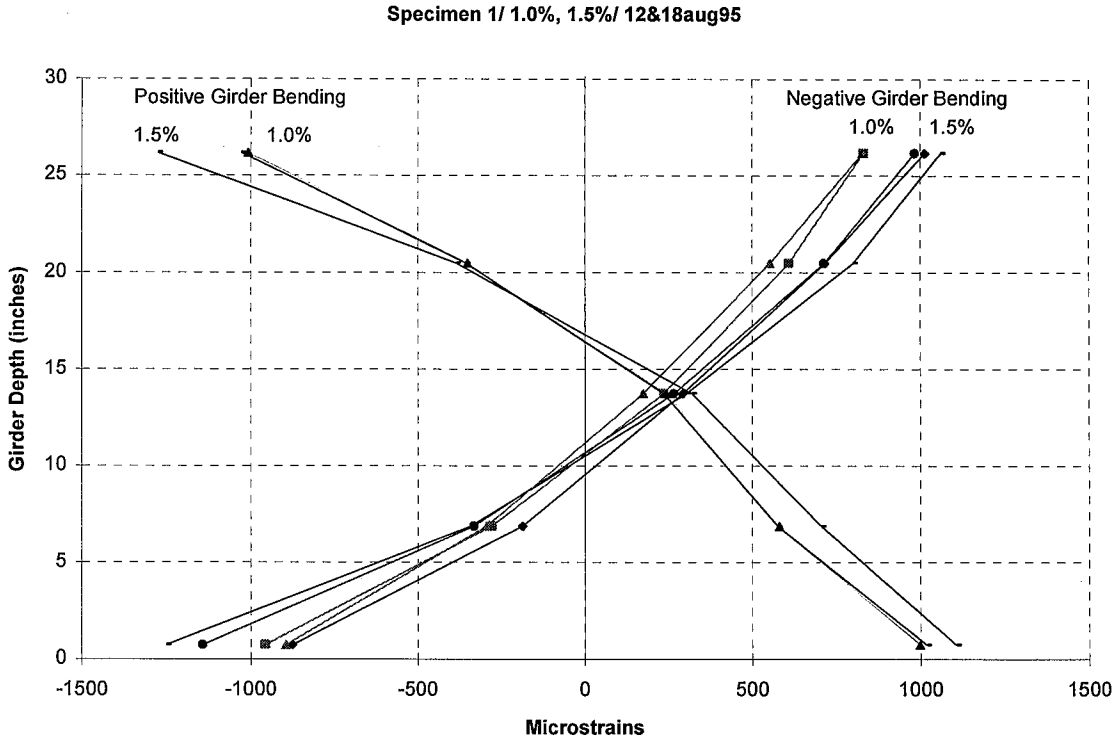

Figure 5.5: Steel Girder Strain Distribution (East Girder of Specimen 1)

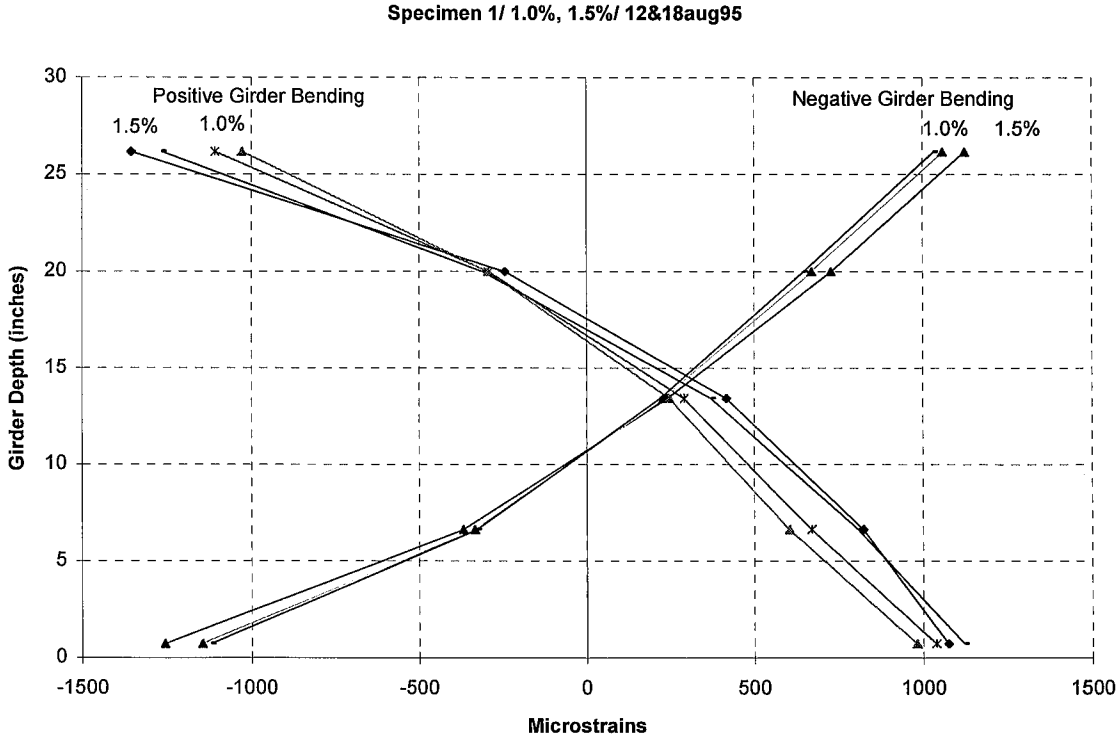

Figure 5.6: Steel Girder Strain Distribution (West Girder of Specimen 1)

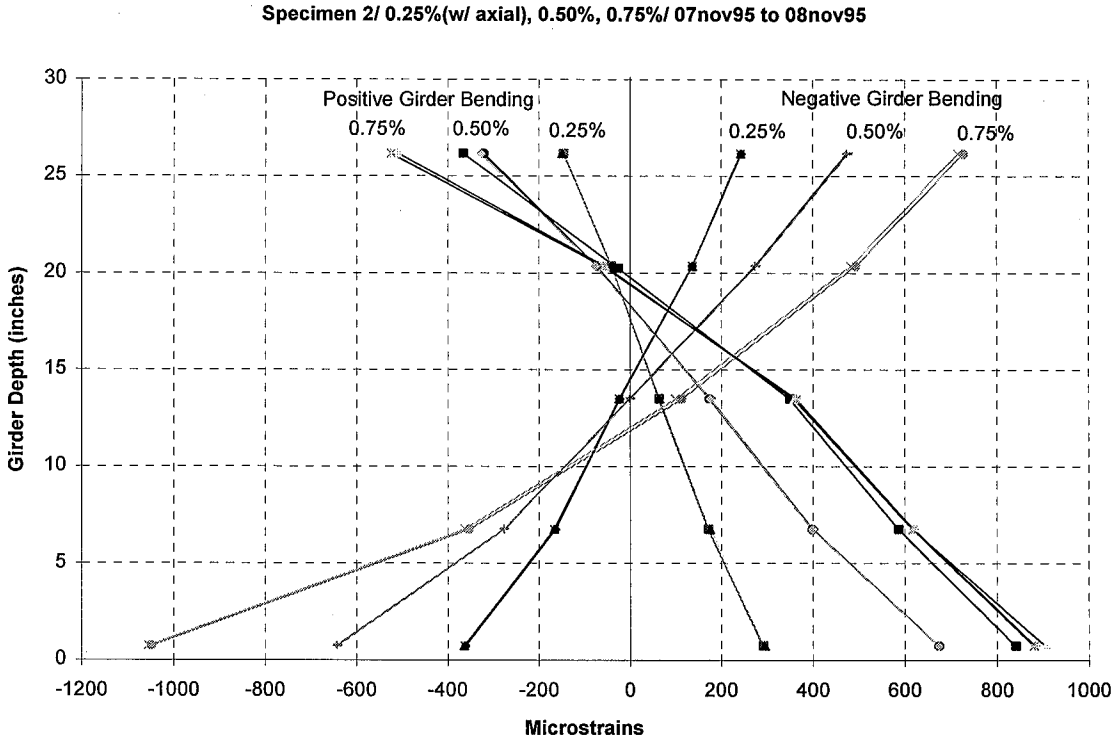

Figure 5.7: Steel Girder Strain Distribution (East Girder of Specimen 2)

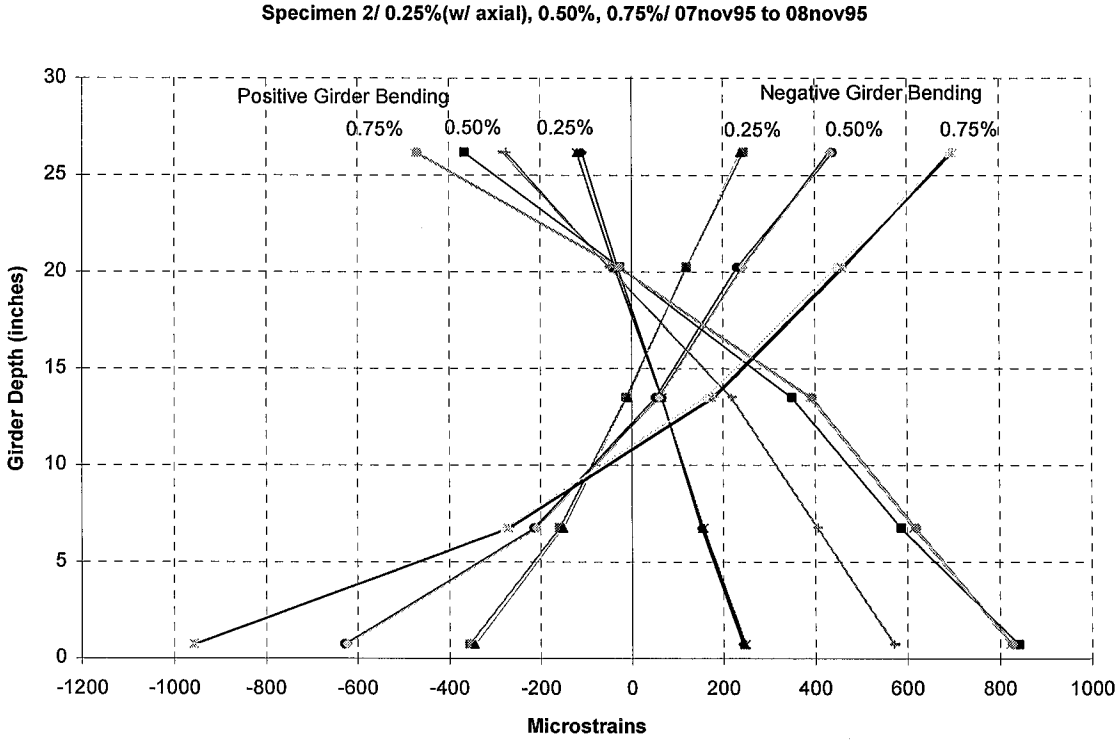

Figure 5.8: Steel Girder Strain Distribution (West Girder of Specimen 2)

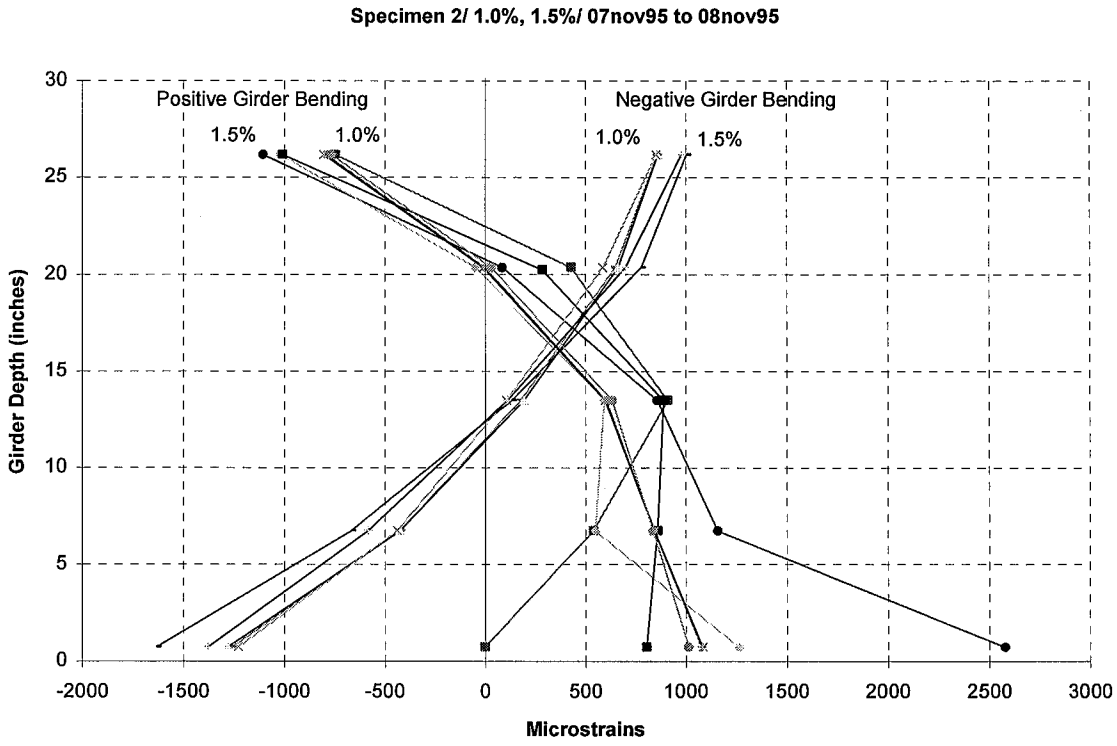

Figure 5.9: Steel Girder Strain Distribution (East Girder of Specimen 2)

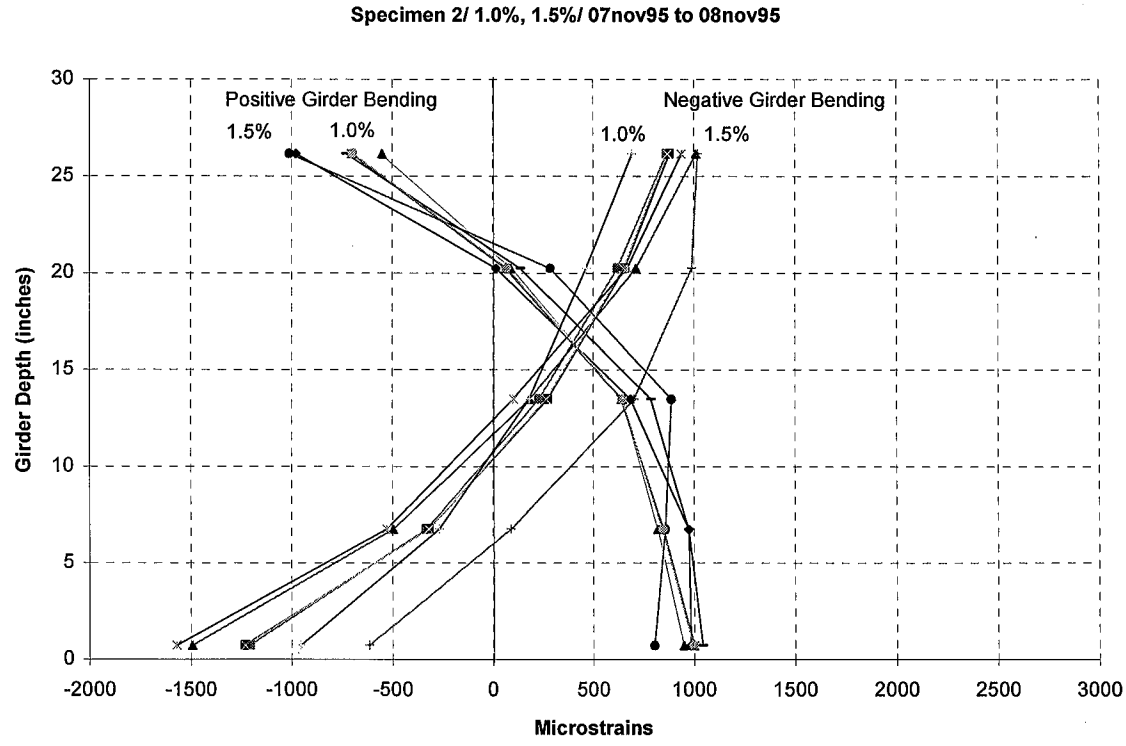

Figure 5.10: Steel Girder Strain Distribution (West Girder of Specimen 2)

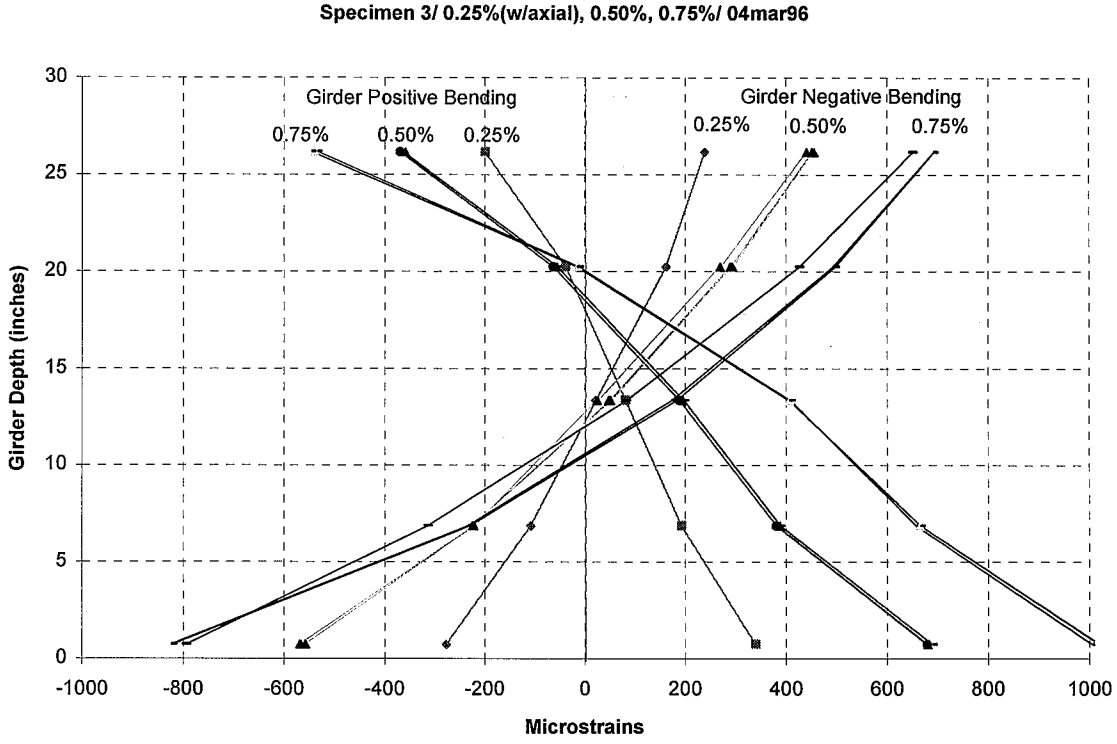

Figure 5.11: Steel Girder Strain Distribution (East Girder of Specimen 3)

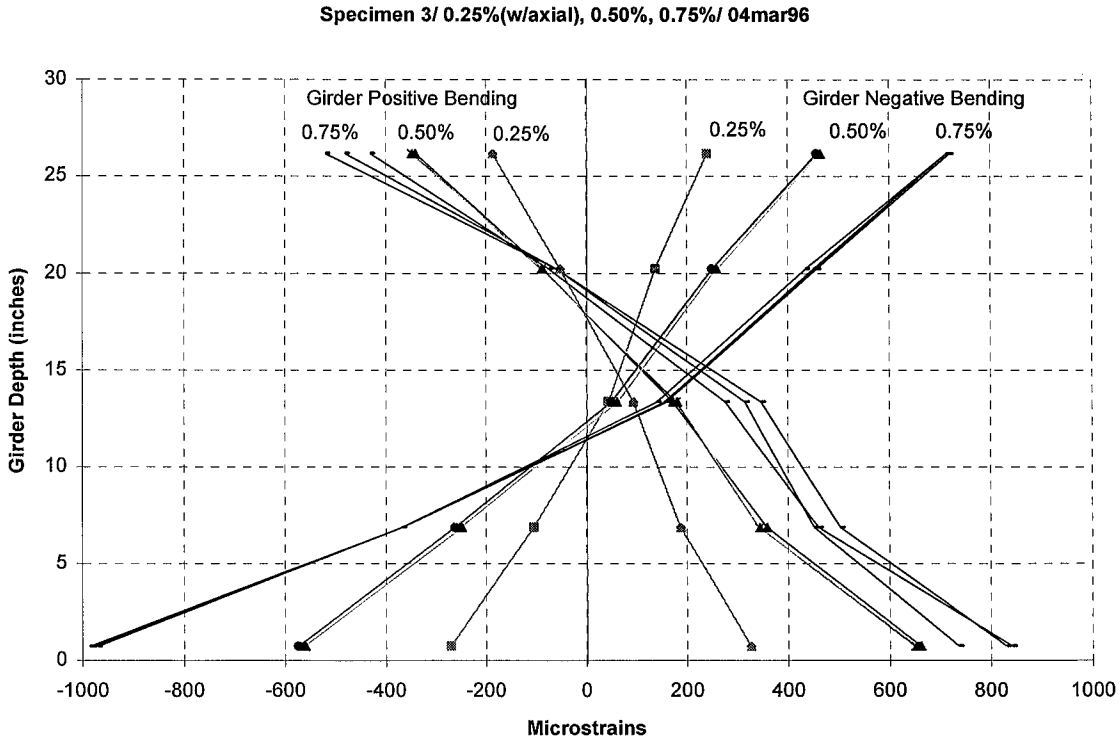

Figure 5.12: Steel Girder Strain Distribution (West Girder of Specimen 3)

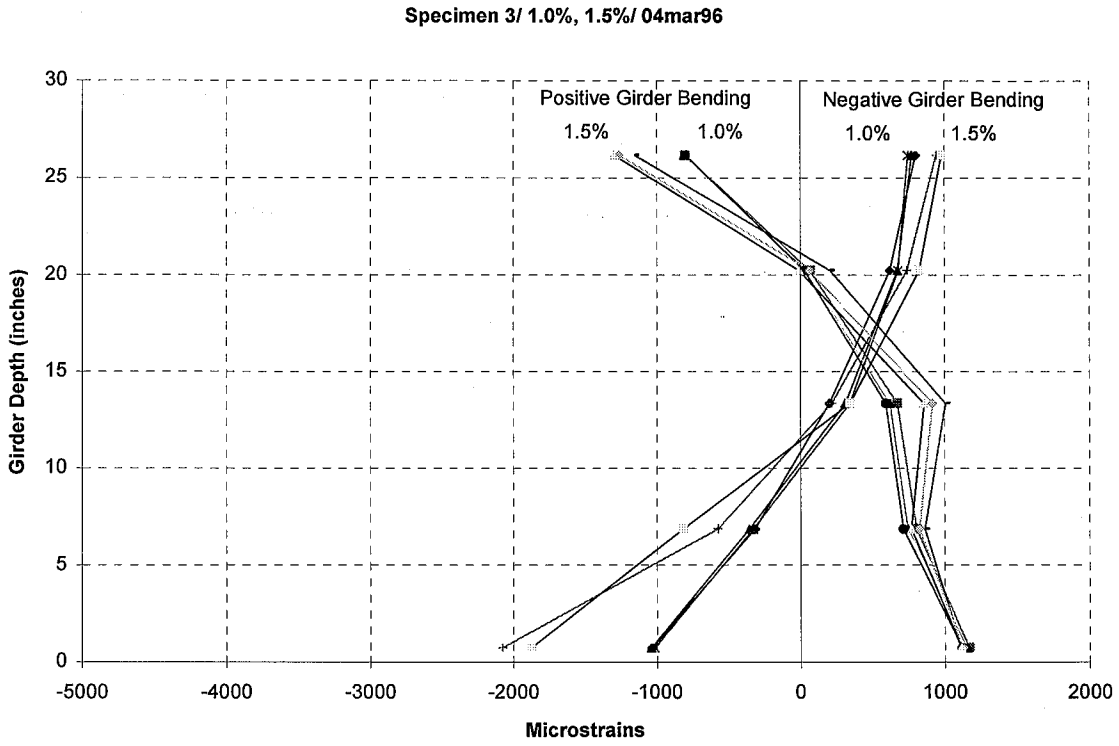

Figure 5.13: Steel Girder Strain Distribution (East Girder of Specimen 3)

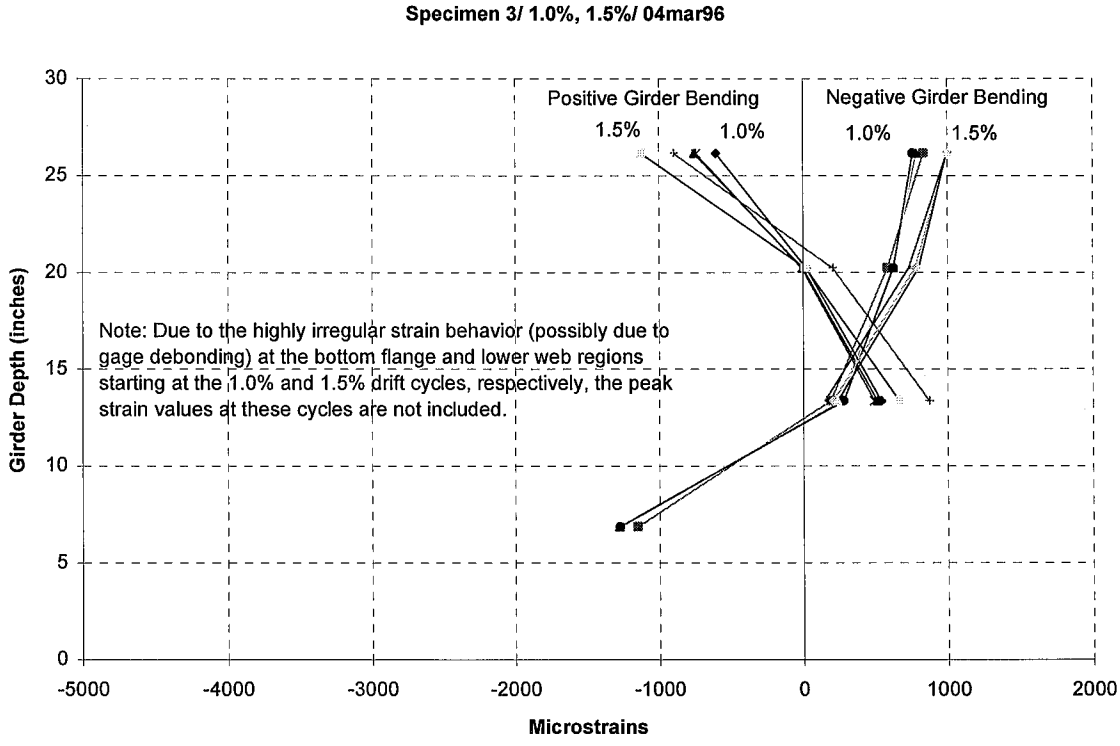

Figure 5.14: Steel Girder Strain Distribution (West Girder of Specimen 3)

elastic centroid, and, therefore, the shifting of the neutral axis away from these inelastic regions in order to maintain the equilibrium of forces within the cross section.

The neutral axis of Specimen 2 is expected to be positioned closer to the concrete slab than the neutral axis of Specimen 3 during girder positive bending, since the composite girders of Specimen 2 include more shear connectors than those of Specimen 3. However, all four composite girders exhibit similar neutral axis locations during the peak loads at the 0.25% through 1.5% drift levels (see Figures 5.7 to 5.14). Furthermore,

Table 5.1: Position of the Neutral Axis Along the Girder Cross Section[1]

Specimen	Girder or Model	Girder Bending	Drift Levels (%)				
			0.25%	0.50%	0.75%	1.0%	1.5%
Specimen 1	East	Positive	15.0	15.0	15.0	16.5	16.8
		Negative	12.0	12.0	12.0	10.5-11.0	9.5-10.5
	West	Positive	15.5	15.0	15.0	16.5-17.0	17.0-17.5
		Negative	12.0	12.0	12.0	10.8	10.8
Specimen 2	East	Positive	18.0	18.5	19.5	20.0-22.5	20.0-21.5
		Negative	14.5	13.5	12.0	11.5-12.5	11.5-12.5
	West	Positive	18.0	19.0	20.0	20.0-20.5	20.0-21.5
		Negative	14.0	12.0	11.0	10.0-12.0	6.0-12.0
Specimen 3	East	Positive	18.0	19.0	20.0	20.0-20.5	20.0-21.0
		Negative	12.0	12.5	11.8	10.0-10.5	10.0-12.0
	West	Positive	18.0	18.0	19.3	20.0	20.0-20.2
		Negative	11.5	12.0	11.5	12.0	----
Bare Steel Model		Positive	----	14.3	----	14.4	13.6
		Negative	----	12.8	----	13.8	13.4
Composite Model		Positive	----	19.6	----	20.3	22.0
		Negative	----	14.3	----	15.3	15.9

[1]Measured from the bottom of the steel girder bottom flange.

the amount of shifting in the neutral axis location between girder positive and negative bending is similar between all four composite girders for a given drift level (see Table 5.1). This behavior implies that the differences in composite action between the girders of Specimens 2 and 3 may be minimal during the initial drift cycles (see Section 4.3).

During the 0.25% to 1.5% drift levels, all four composite girders exhibit a migration of the neutral axis towards the top girder flange during girder positive bending and towards the bottom girder flange during negative girder bending (see Figures 5.5 to 5.14, Table 5.1). This behavior is primarily due to the shifting of the neutral axis away from the yielded regions of the cross section as previously discussed. Also, the loss of tensile resistance provided by the concrete deck may contribute to this behavior during girder negative bending. Since the girders of Specimen 1 do not demonstrate as much neutral axis migration during cycling at increasing levels of drift as the composite girders of Specimens 2 and 3, it may be concluded that the presence of a composite floor increases the level of nonlinear behavior along the girder cross section during girder positive and negative bending as the load history progresses.

Note that the compressive strains at the bottom region of the steel cross section are substantially larger for the composite girders than for the bare steel girders during negative girder bending, especially for the 1.0% and 1.5% drift levels (see Figures 5.5 and 5.6, 5.9, 5.10, and 5.13). This is significant, since this condition may be a major contributor to excessive plastification (due to compressive yielding) of the bottom flange region, along with the extensive amount of straining that occurs within this region during positive girder bending. Note that the peak strains measured along the bottom flange and lower web regions of the West girder of Specimen 3 starting at the first cycles at 1.0% and 1.5% drift levels, respectively exhibited questionable strain behavior (possibly due to problems with the instrumentation), therefore, are not included in Figure 5.14.

The positions of the neutral axes of bare steel girder and composite girder moment connections subjected to positive and negative bending were determined computationally

by employing two three-dimensional geometrically and materially nonlinear continuum finite element models, a bare steel girder specimen model and a composite girder specimen model (see Figures 5.15 and 5.16) (Carlson, 1997). The steel model contained approximately 8300 nodes and 4400 elements and the composite model contained approximately 9400 nodes and 5000 elements. With the exception of the addition of the concrete elements in the composite model, the two models are identical. The models are symmetric about a plane extending through the webs of the girders and columns, which reduces the number of elements required in the analysis by one-half.

The girders extend out 132" from the column face (identical to the effective girder lengths of the test specimens), and are modeled entirely with continuum elements. The columns are modeled with continuum elements from the connection to a distance of 49.5" from the pin supports (well beyond the region of expected plasticity) and the remaining segment of each column is modeled with a cubic interpolation beam element. At the junction between the continuum elements and the girder elements, multi-point constraints were employed to transition from a plane of 3-DOF continuum nodes to a girder node with six DOFs. The multi-point constraints enforce the assumption that a section at the transition point remains planar and perpendicular to the centroidal axis of the column. The beam elements themselves are rectangular in cross section with an effective depth and width chosen to match the moment of inertia and gross area of half (because of symmetry) of the W14X211 column.

The girders, column, welds, concrete slab (with ribs modeled for the decking), reinforcing bars, and key connection elements were modeled after the details, dimensions, and material properties of the three specimens (see Section 2.1 and Appendix A). The steel of the girder and column sections utilized F_y and F_u values of 38 ksi and 58 ksi, and 57.5 ksi and 77 ksi, respectively. The weld metal of the girder flange-to-column CJP welds and the reinforcing bars of the concrete slab both possessed F_y and F_u values of 62.5 ksi and 82 ksi. The composite girders were modeled to attain full composite action; they did not take into account composite slip. The compressive strength, f_c', of the

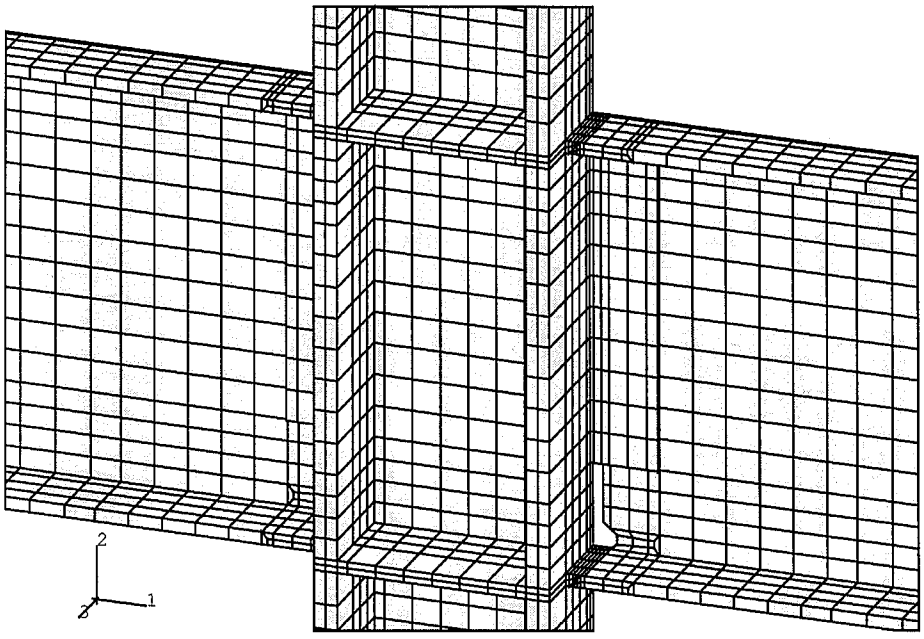

Figure 5.15: Bare Steel Model Discretization

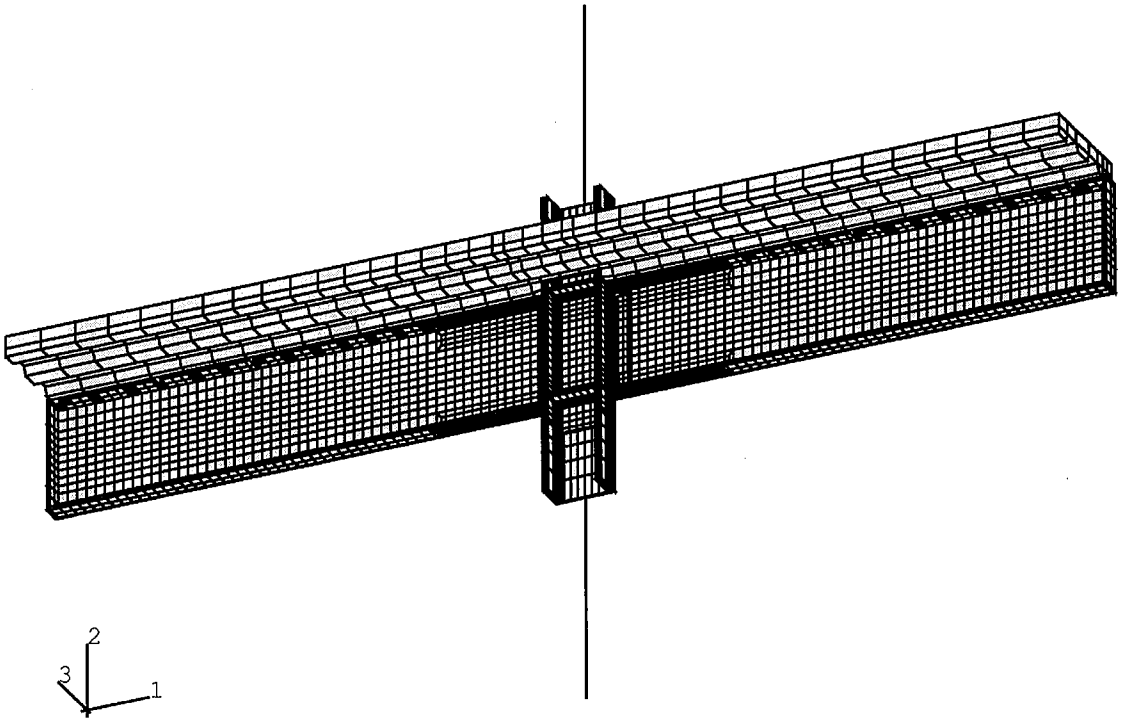

Figure 5.16: Composite Girder Specimen Model Discretization

concrete slab of the composite model was taken as 5000 psi. In addition, the shear tab was assumed to be fully attached to the girder webs (slip between the two elements was not included in the model).

The girders of each model were subjected to antisymmetric monotonic girder tip loads, with the girder tips deflected to specific drift levels up to 3.0% drift. This computational study was performed using the ABAQUS finite element program and the analyses were performed on a Cray C-90 supercomputer (Carlson, 1997).

Figures 5.17 to 5.18 compare the strain distributions along the girder cross section of the bare steel computational model to the East and West girders of Specimen 1. Figures 5.19 to 5.20 compare the strain distributions along the girder cross section of the composite computational model to the East and West girders of Specimens 2 and 3. These strains are measured at 13.5" from the column face during the peak load excursions at the 0.50% and 1.0% drift levels. The strain profiles of the computational models include only one set of peak strains for a given drift level while the strain profiles of the tested girders include the peak strain values for all the cycles tested at a given drift level. In general, the correlation between the computed and measured results is quite good, especially during positive girder bending.

As concluded from investigating the East and West girders of Specimen 1, the finite element analyses indicate that the position of the neutral axis of the bare steel model is above the elastic centroid of the steel girder during girder positive bending, primarily due to the location of the shear tab along the steel cross section (see Table 5.1, Figures 5.17-5.18). Furthermore, during negative girder bending, the neutral axis is located below the elastic centroid of the steel girder as was observed in the test specimens.

The neutral axis position of the composite computational model and composite girders of Specimens 2 and 3 are approximately the same during positive girder bending at the 0.50% and 1.0% drift cycles (see Table 5.1, Figures 5.19-5.20). During girder negative bending, the neutral axis position of the composite computational model is

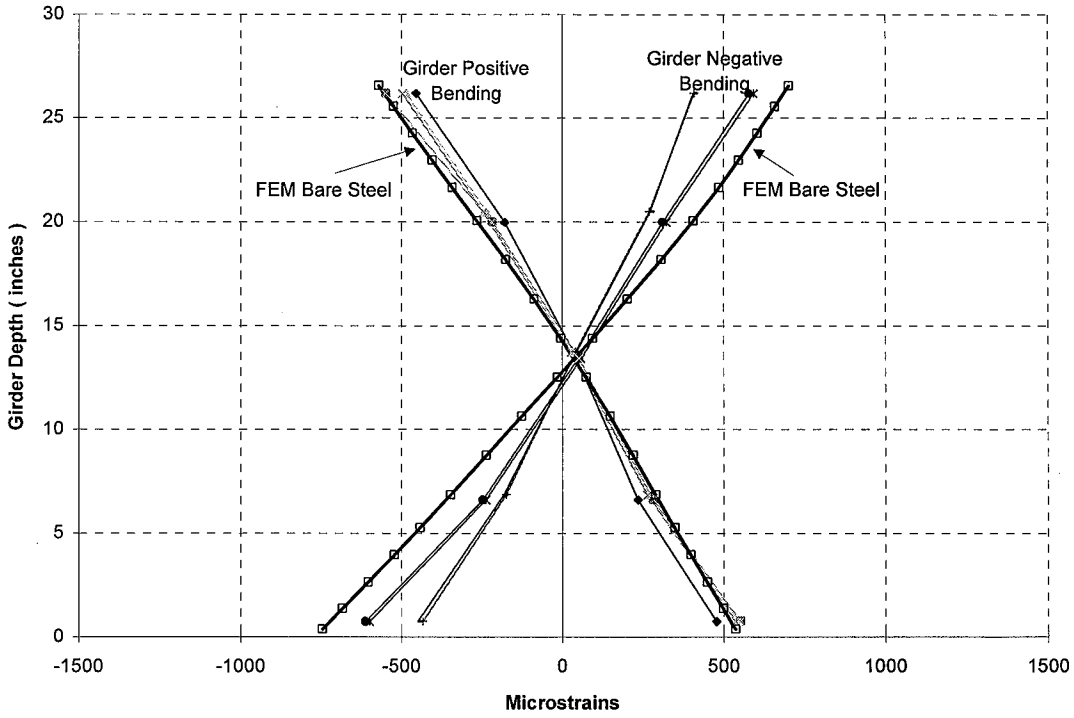

Figure 5.17: Steel Girder Strain Distribution / 0.50% Drift
(Bare Steel Model vs. East and West Girders of Specimen 1)

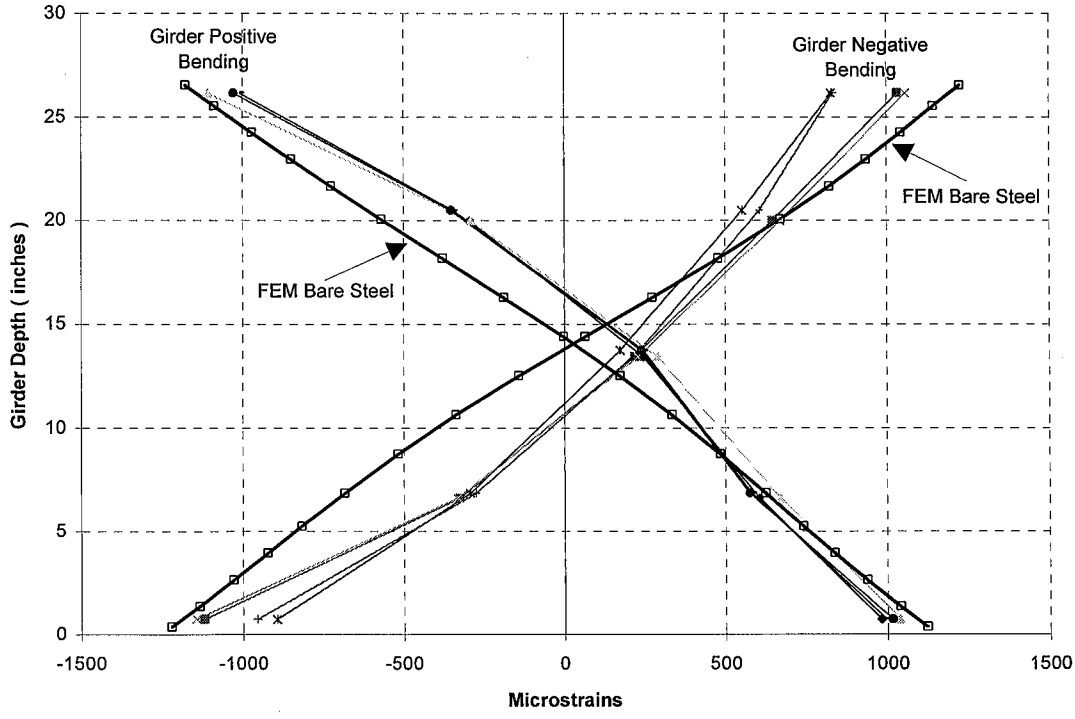

Figure 5.18: Steel Girder Strain Distribution / 1.00% Drift
(Bare Steel Model vs. East and West Girders of Specimen 1)

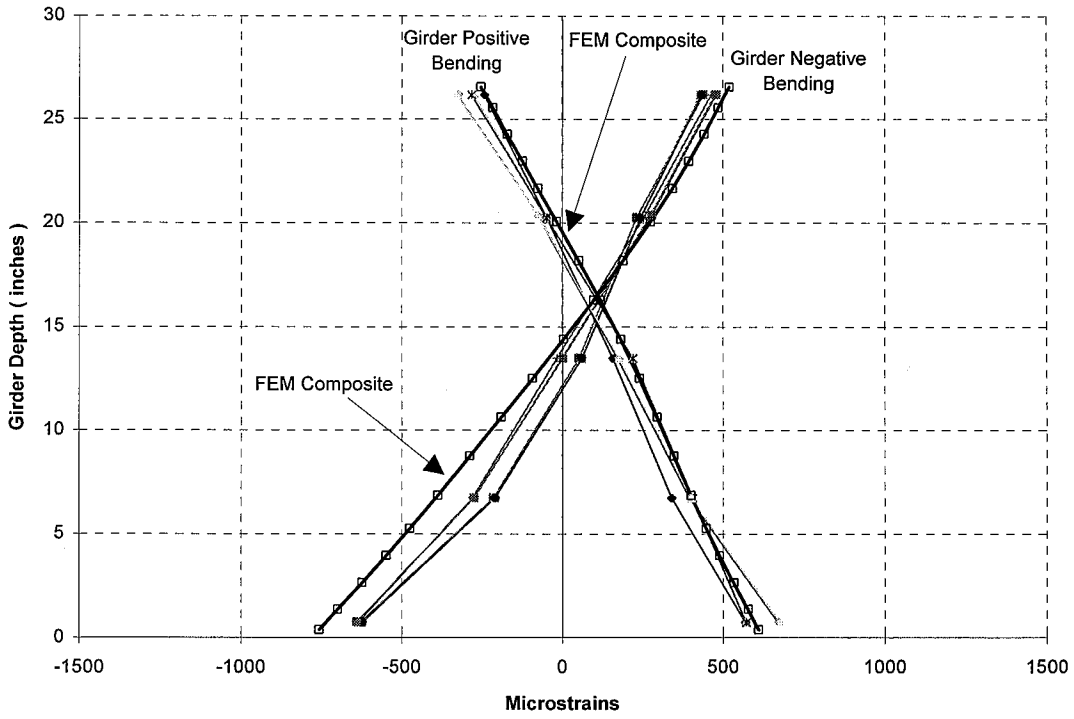

Figure 5.19: Steel Girder Strain Distribution / 0.50% Drift
(Composite Model vs. East and West Girders of Specimens 2 and 3)

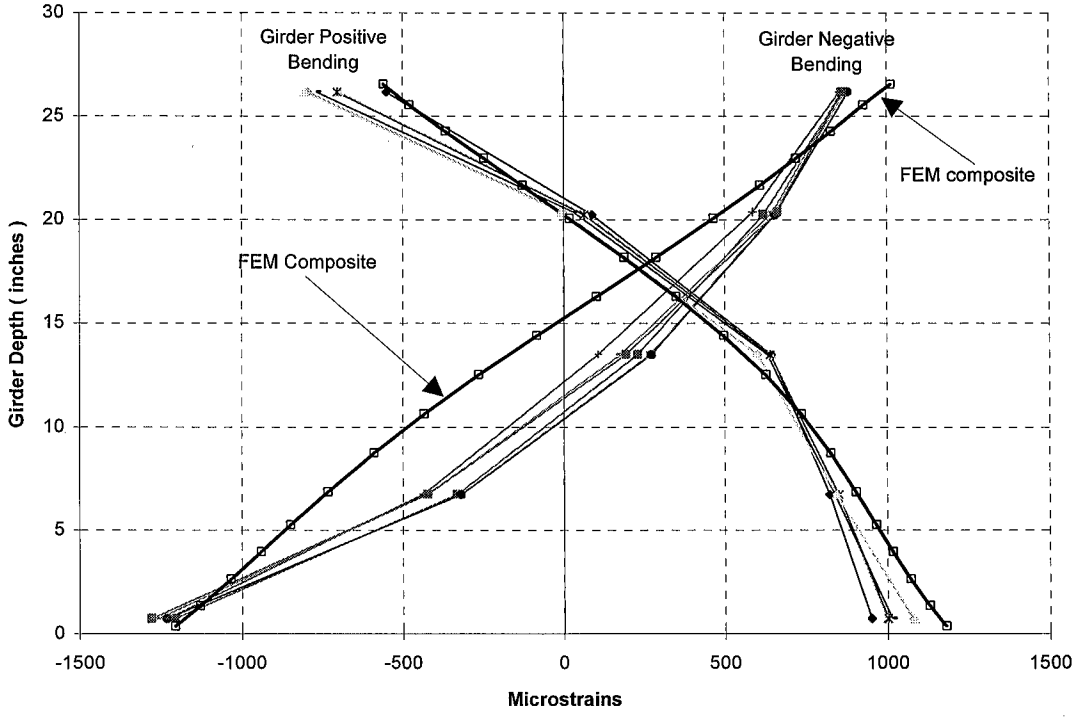

Figure 5.20: Steel Girder Strain Distribution / 1.00% Drift
(Composite Model vs. East and West Girders of Specimens 2 and 3)

located above the elastic centroid of the steel section. This behavior may be due to the tensile resistance of the concrete slab, which may raise the position of the neutral axis up towards the top flange during negative girder bending. Also, the bare steel and composite models show evidence of a migration of the neutral axis towards the top flange during negative girder bending, unlike what was observed in the six tested connections.

The strain distributions along the composite girder cross section of Specimens 2 and 3 and the computational composite model consistently exhibit a distinct nonlinear strain profile during girder positive and negative bending (see Figures 5.5-5.14, 5.17-5.20). This strain profile is distinguished by the fact that the slope of the strain diagram increases (rather than remaining constant) near the bottom girder flange during positive girder bending. The position of the neutral axis along the girder cross section is affected by the shape of this strain profile. This behavior may thus explain why the neutral axis is located below the elastic centroid of the steel section when the girders are subjected to negative girder bending.

This nonlinear strain distribution may be due predominantly to cross section distortion rather than substantial yielding in the bottom girder flange (Goel et al., 1996). Specifically, localized straining of the girder web due to the nearby shear tab may result in additional tensile longitudinal strains within the region of the bottom girder flange during both positive and negative girder bending. Figure 5.21 illustrates this phenomena in the composite girder model. The figure plots the strain oriented along the longitudinal axis of each girder, with the darker colors indicating tensile strain. The location at 13.5" away from the column face is shown in Figure 5.22. Note the strain concentrations in the web near the bottom flange of each girder. This behavior partially contributes to the nonlinear strain diagrams seen in Figure 5.4-5.14 and 5.17-5.20. In addition, small levels of out-of-plane distortion of the girders of the test specimens may contribute to the nonlinear strain profiles [the computational study was based on assuming a symmetric mesh, with out-of-plane deformation restrained, while the girders of the test specimens,

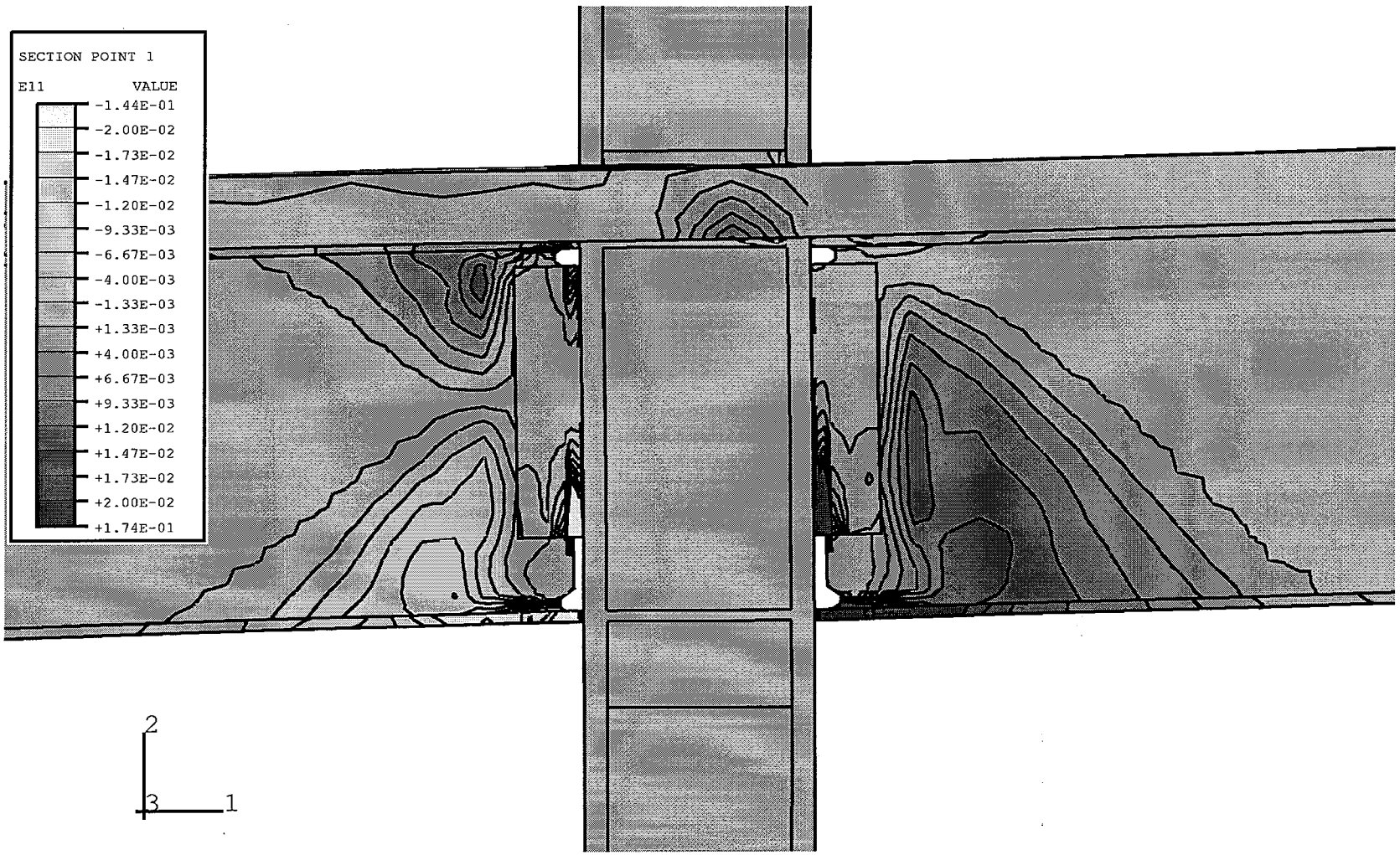

Figure 5.21: Connection Region of Composite Specimen Model/ 3.0% Drift
(Negative Girder Bending on Left; Positive Girder Bending on Right)

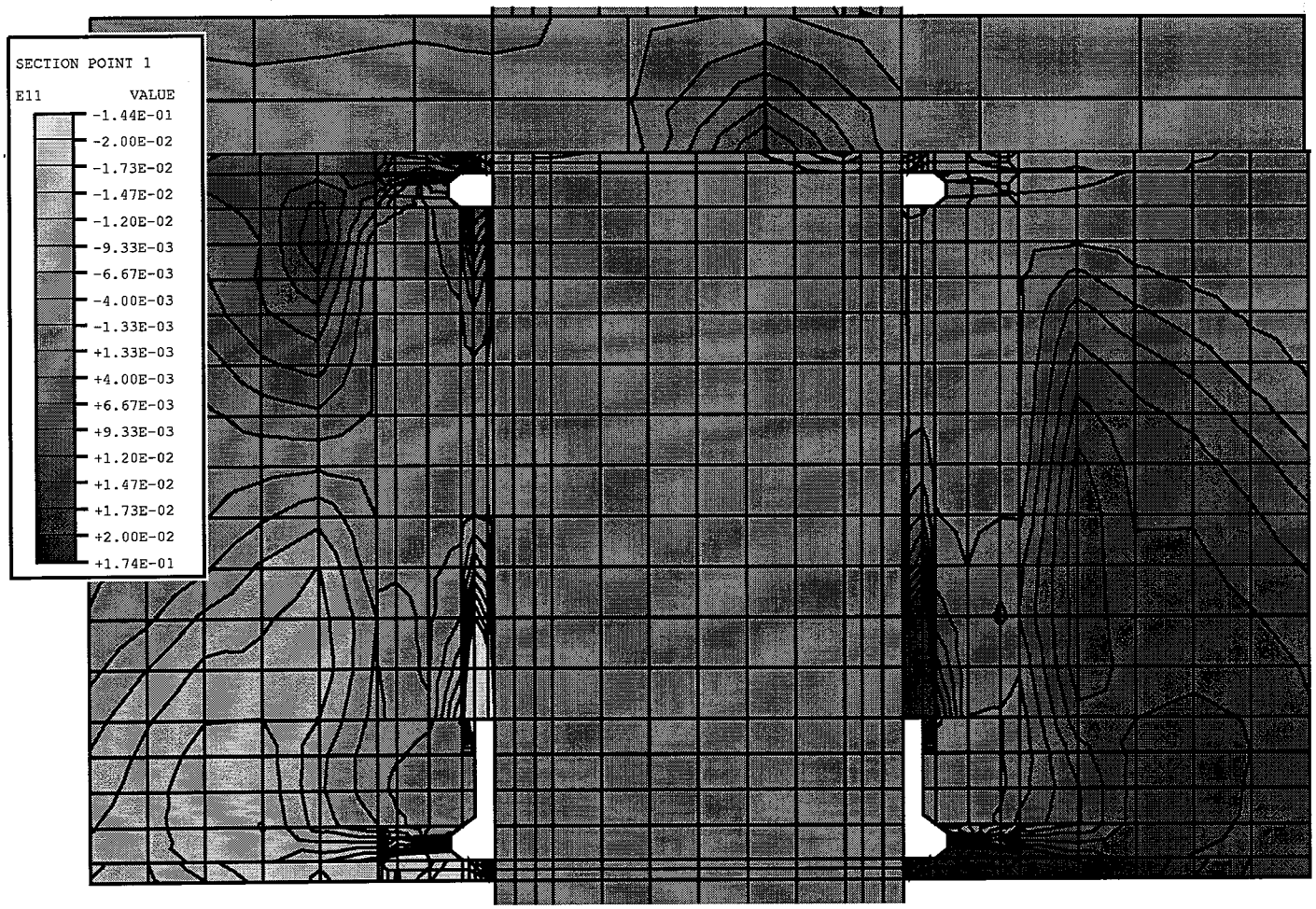

Figure 5.22: Connection Region of Composite Specimen Model/ 3.0% Drift
(Negative Girder Bending on Left; Positive Girder Bending on Right)

although braced along their length (see Figure 2.18), may have experienced small levels of lateral-torsional deformation].

It may also be seen that all six girders exhibited a migration of the neutral axis away from the yielded regions of the cross section (e.g., towards the top girder flange during girder positive bending and towards the bottom girder flange during negative girder bending) as the drift levels increased. Thus, in addition to the effects of the composite slab, the shear tab, and the two-dimensional stress state on the neutral axis location, it is possible that net tensile residuals stresses which precipitated from the placement of the CJP welds resulted in unsymmetrical initial yielding even in the bare steel specimen, with the tension flange tending to yield more than the compression flange in any given cycle. Also, the loss of tensile resistance provided by the concrete deck may have contributed to this behavior during girder negative bending in the composite specimens. As expected, the bare steel girders of Specimen 1 exhibited less variation in the neutral axis location.

The figures also indicate that the compressive strains at the bottom region of the steel cross section were generally 20% to 50% larger for the composite girders than for the bare steel girders during negative girder bending at a given drift level. This is significant, since this may contribute to excessive compressive yielding of the bottom flange region, coupled with the extensive tensile straining that occurs within this region during positive girder bending.

Finally, beginning generally with the 1.5% drift cycles, the strain distributions along the steel cross section of the East girder of Specimen 1 and the East and West girders of Specimen 3 become highly nonlinear due to excessive yielding, cross section distortion, and local buckling (see Figures 5.9, 5.14, 5.23, and 5.24). Note that strains measured near the bottom web and flange regions are highly irregular. These strains were measured from peak load points during the load history and correspond to large localized strain increases within these regions. For example, a large increase in strain was observed near the bottom web region of East girder of Specimen 2 prior to the fracture of the East bottom connection weld during the second cycle at 1.5% drift (see Figure 5.9).

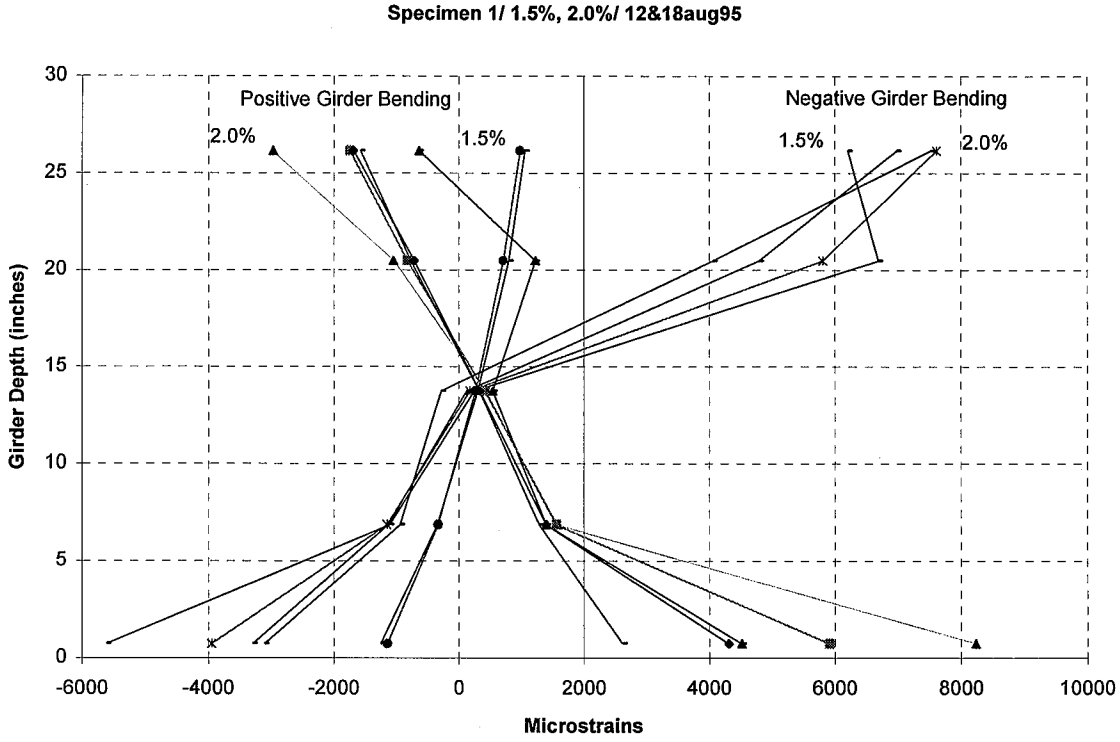

Figure 5.23: Steel Girder Strain Distribution (East Girder of Specimen 1)

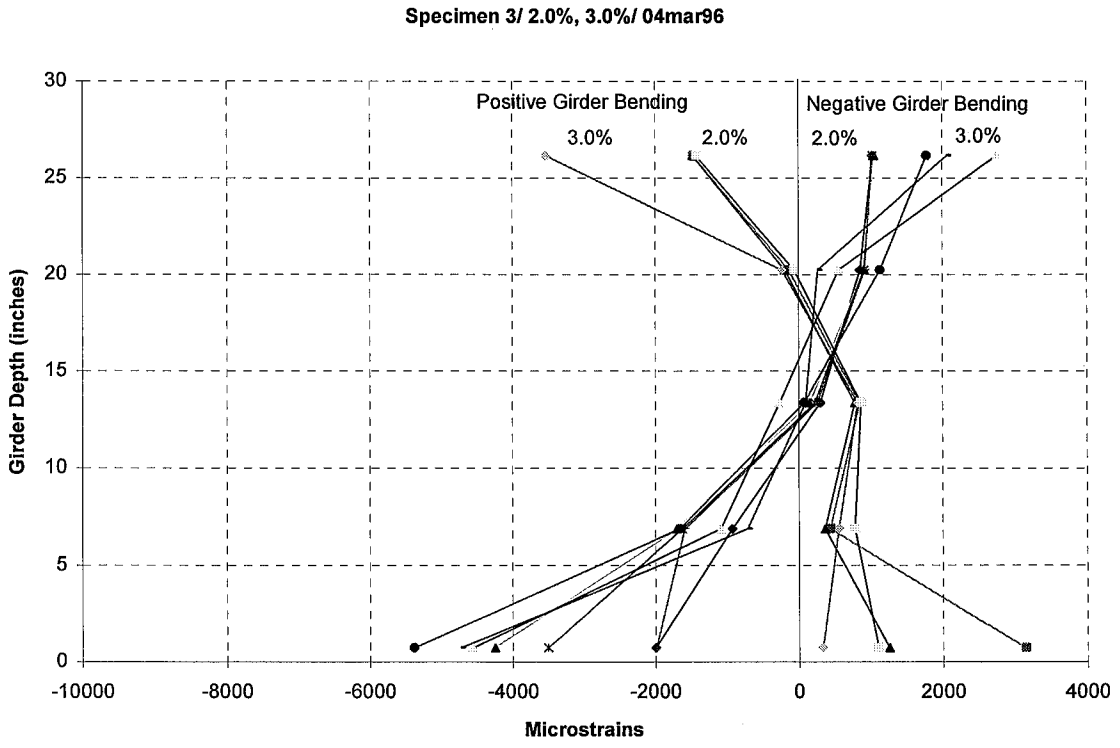

Figure 5.24: Steel Girder Strain Distribution (East Girder of Specimen 3)

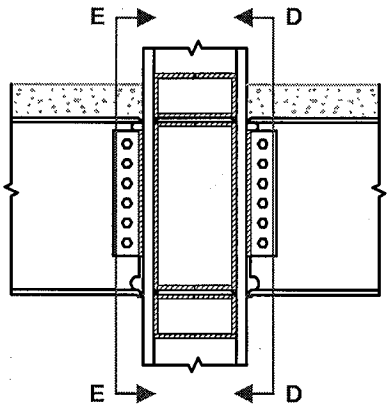

Figure 5.25: Strain Gages of Connection Region (South View)

5.1.2 Comparison of Straining at the Top and Bottom Connection Regions

The distribution of strains along the cross section near the girder flange-to-column connections of Specimens 2 and 3 are investigated in this section In particular, an assessment of the strains at the top and bottom access hole regions is conducted on each connection in order to study the predominance of straining and plastification at the bottom regions of the composite connections. Strains are measured at six locations on the girder flanges at a distance of approximately 1.50" from the column flange surface using post-yielding strain gages (see Figures 5.25 to 5.27; see also Section 2.4.3). The strain gages are oriented so that strains are measured along the longitudinal axis of the girders.

The following discussion refers to the strains measured at these locations along the girder cross section. Note that Figures 5.28 to 5.39, which compare the strains along the cross section of the six connections, highlight only key drift cycles of the load histories for each connection focusing on the predominance of straining near the bottom connection region. The complete load histories of the strain behavior of the connections, along with a corroborating study using acoustic emission activity occurring near the bottom connection, is addressed in Appendix H.

The East and West connections of Specimen 1 exhibit strain amplitudes near the bottom access holes that are approximately 1 to 1.5 times larger than strains near the top

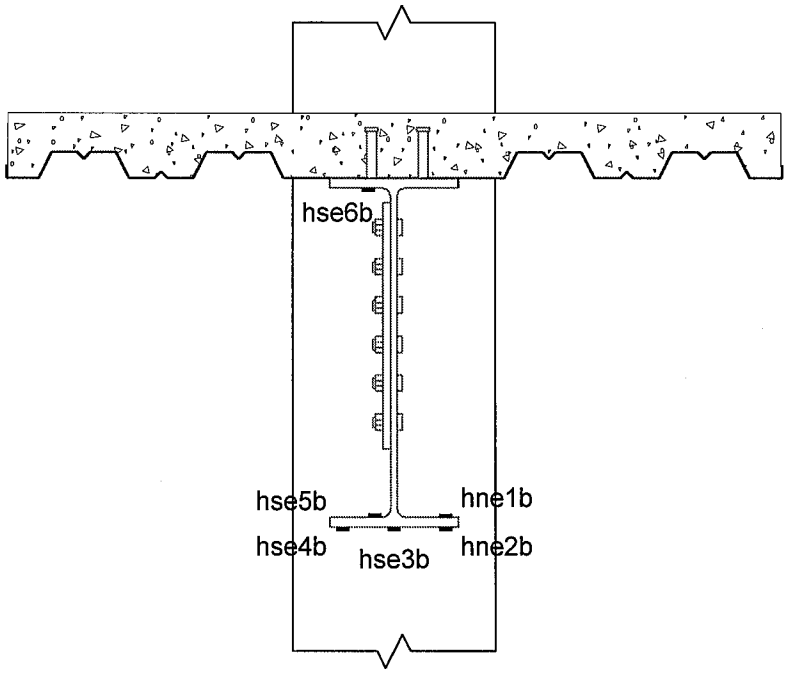

Figure 5.26: Section D-D: Strain Gages of East Connection Region

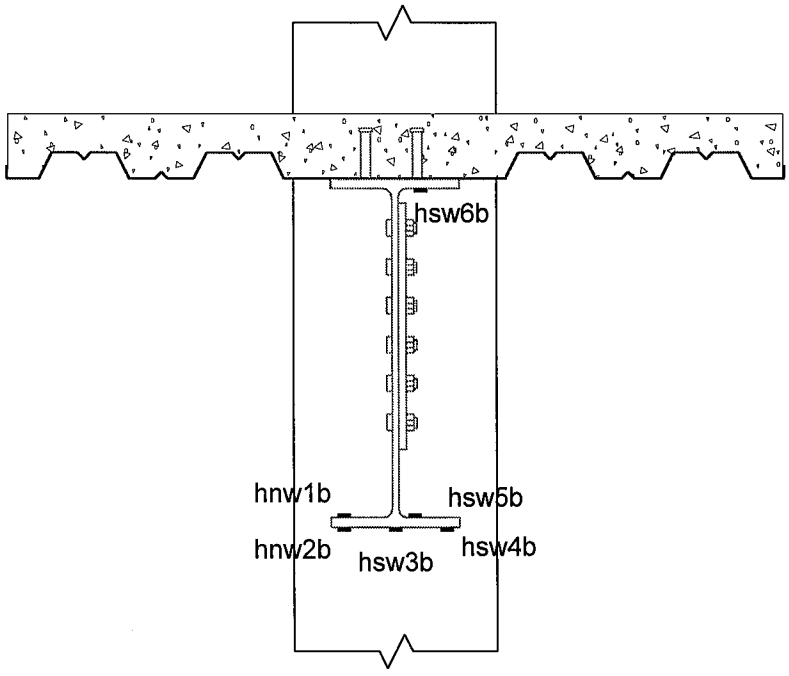

Figure 5.27: Section E-E: Strain Gages of West Connection Region

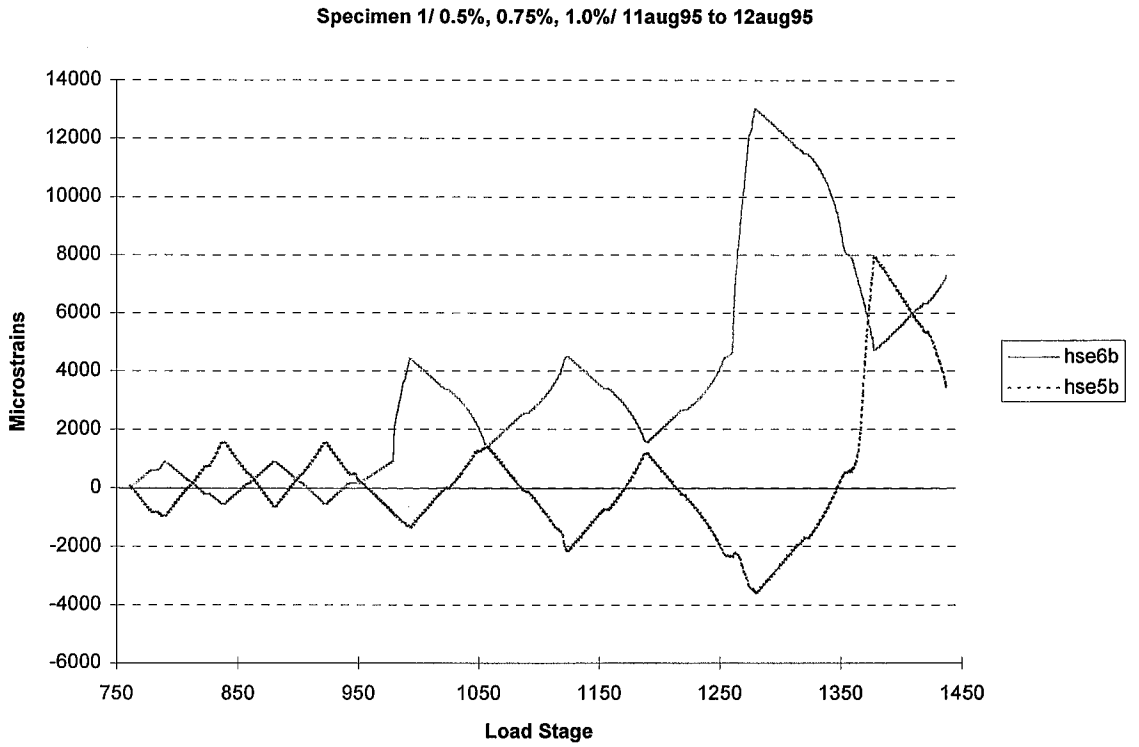

Figure 5.28: Top and Bottom Access Hole Strains (East Girder of Specimen 1)

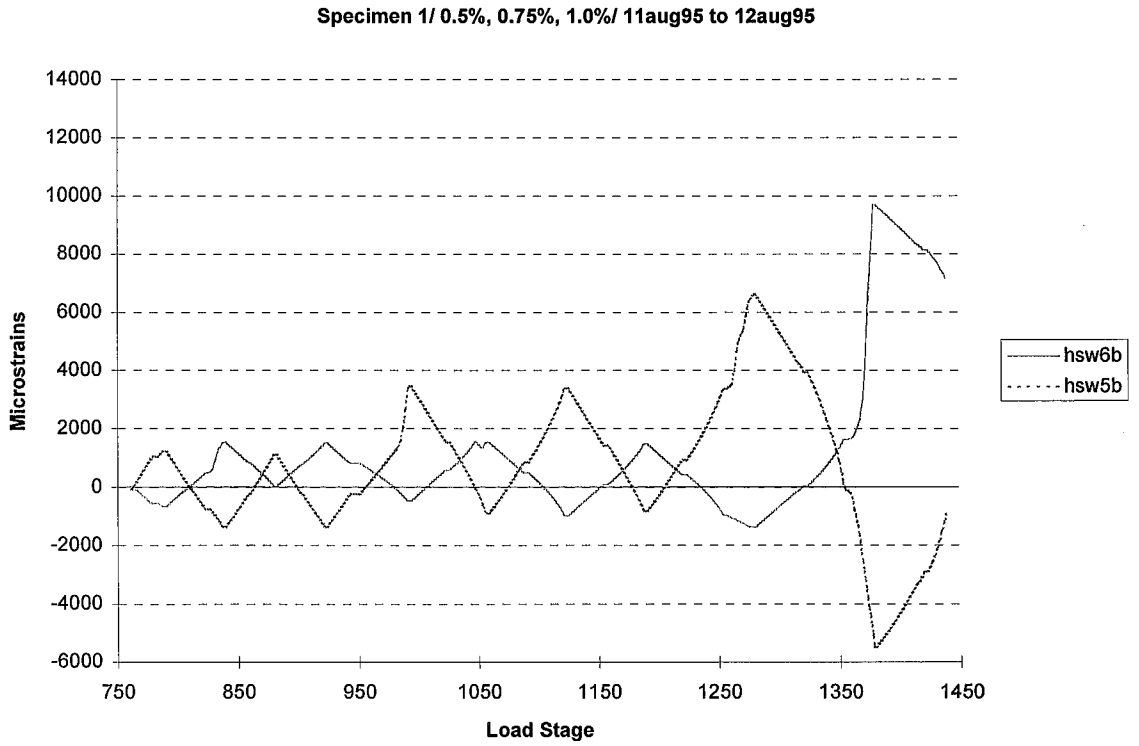

Figure 5.29: Top and Bottom Access Hole Strains (West Girder of Specimen 1)

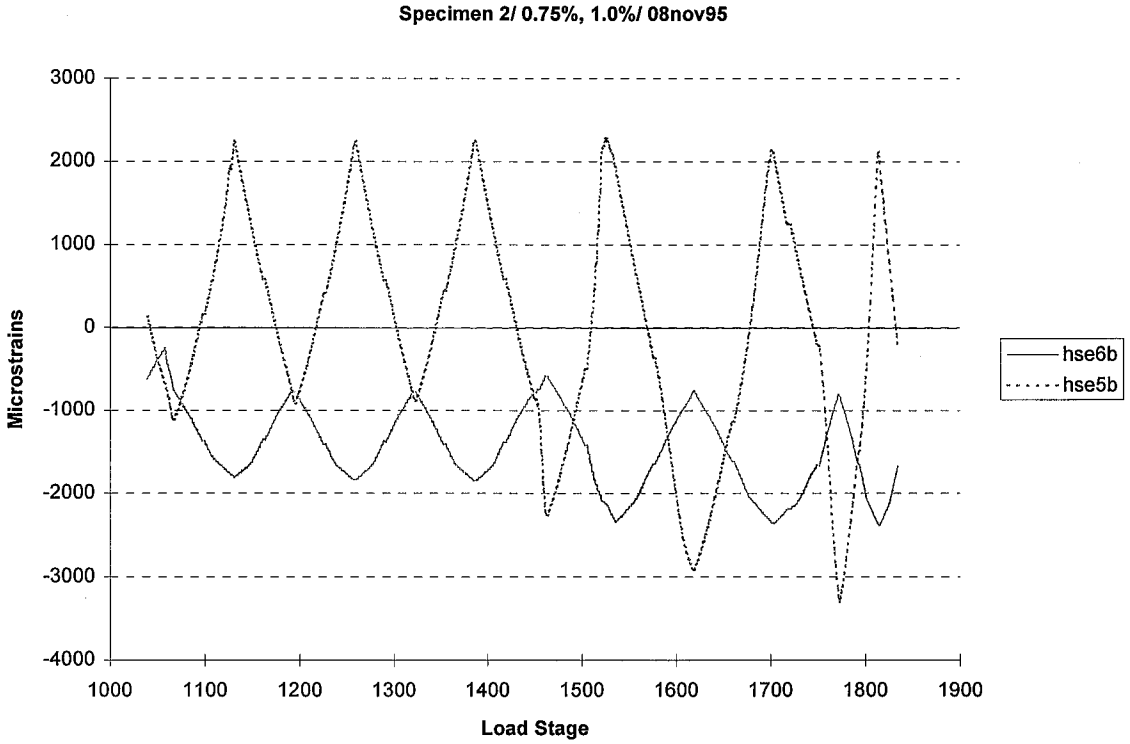

Figure 5.30: Top and Bottom Access Hole Strains (East Girder of Specimen 2)

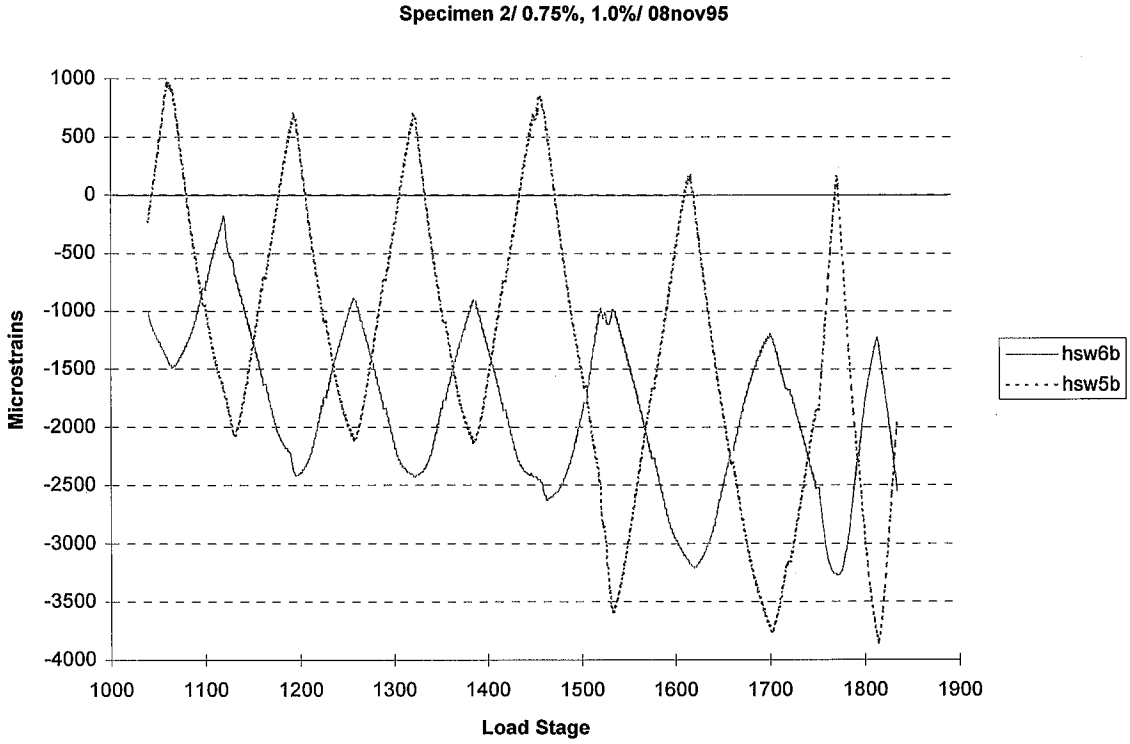

Figure 5.31: Top and Bottom Access Hole Strains (West Girder of Specimen 2)

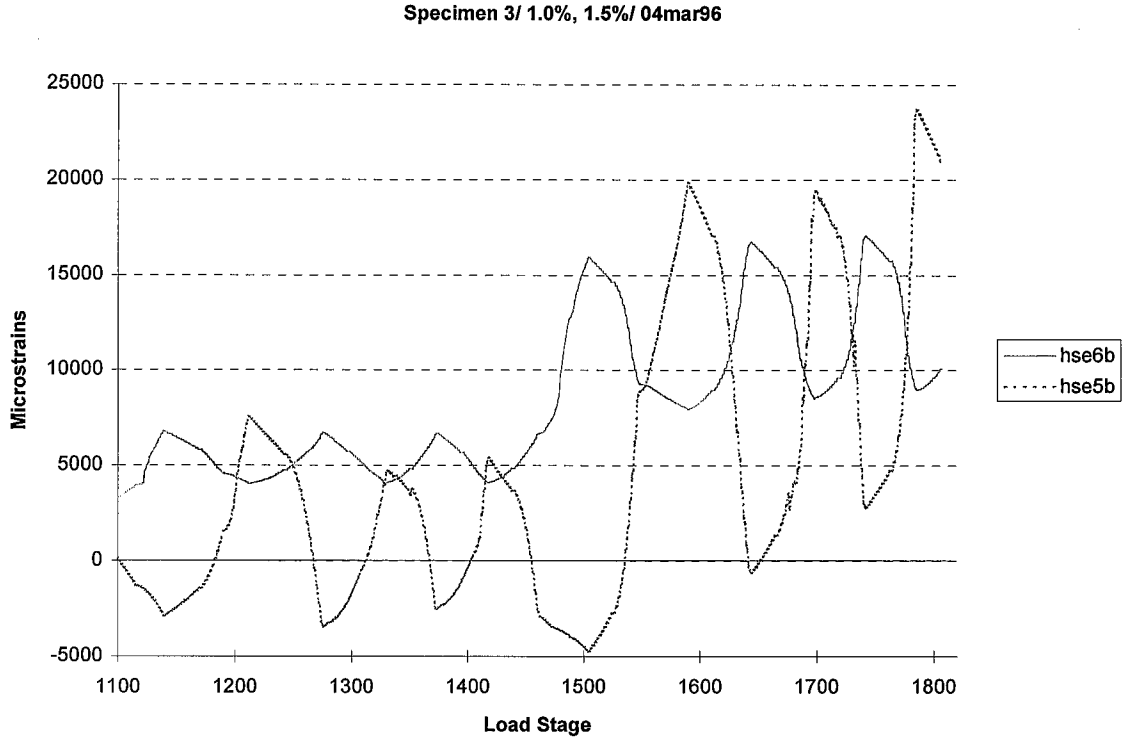

Figure 5.32: Top and Bottom Access Hole Strains (East Girder of Specimen 3)

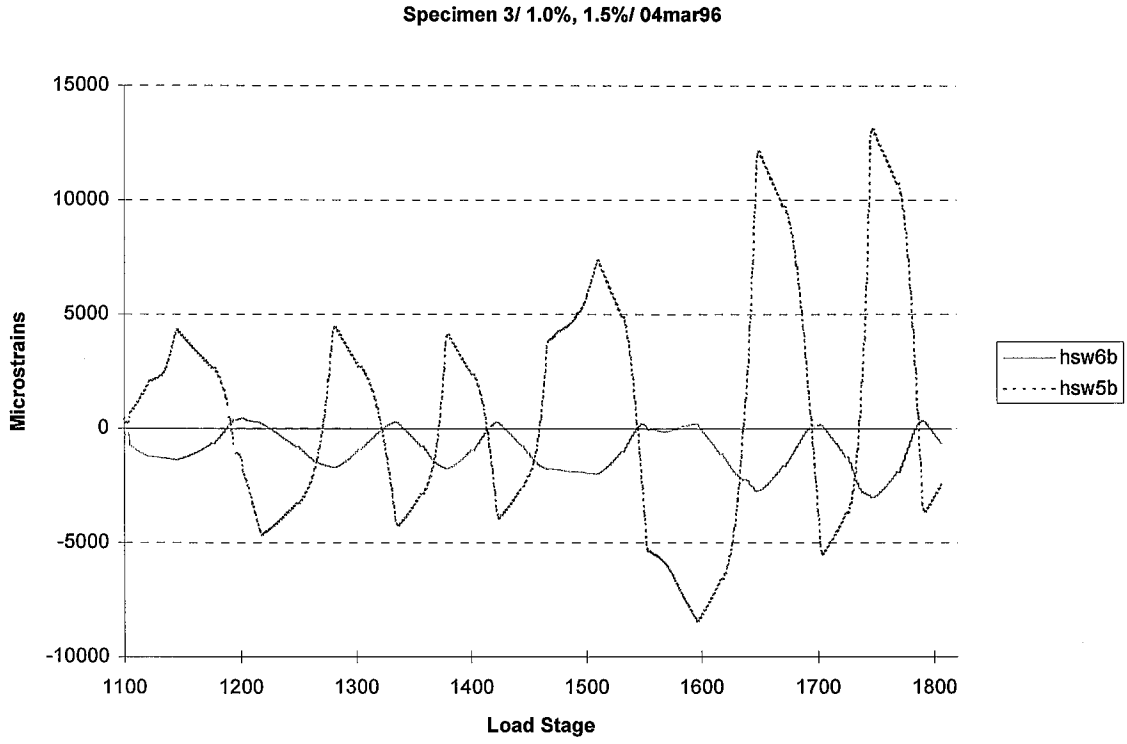

Figure 5.33: Top and Bottom Access Hole Strains (West Girder of Specimen 3)

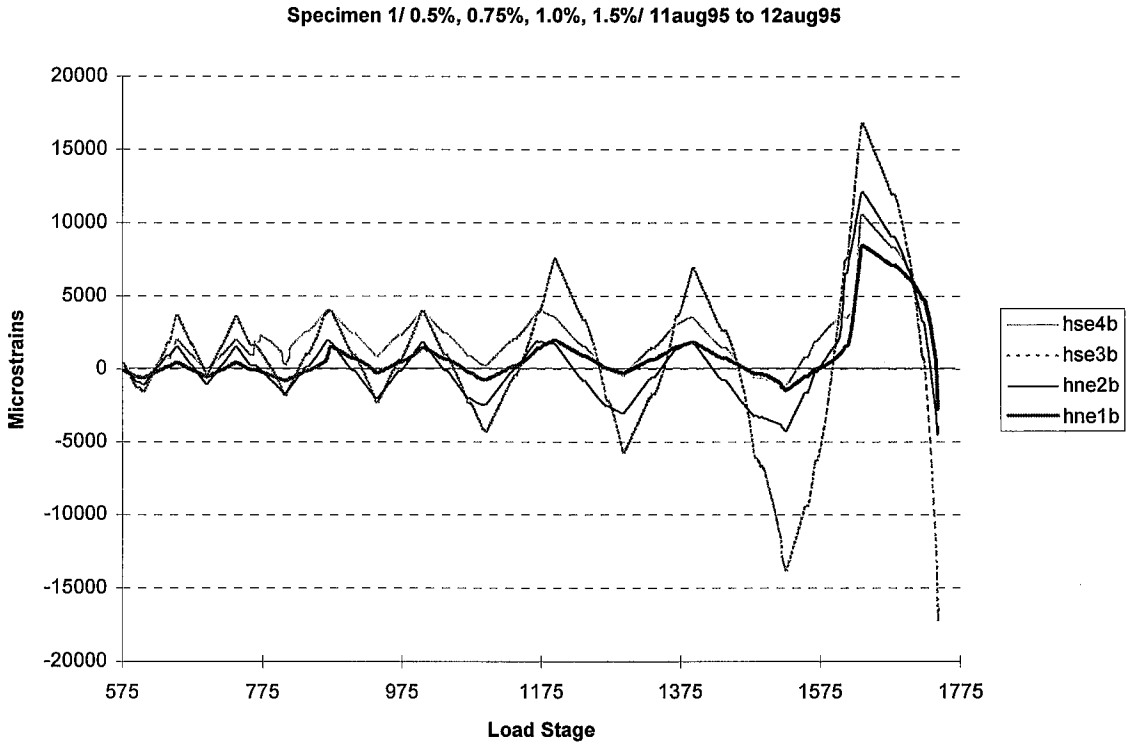

Figure 5.34: Girder Bottom Flange Strains (East Girder of Specimen 1)

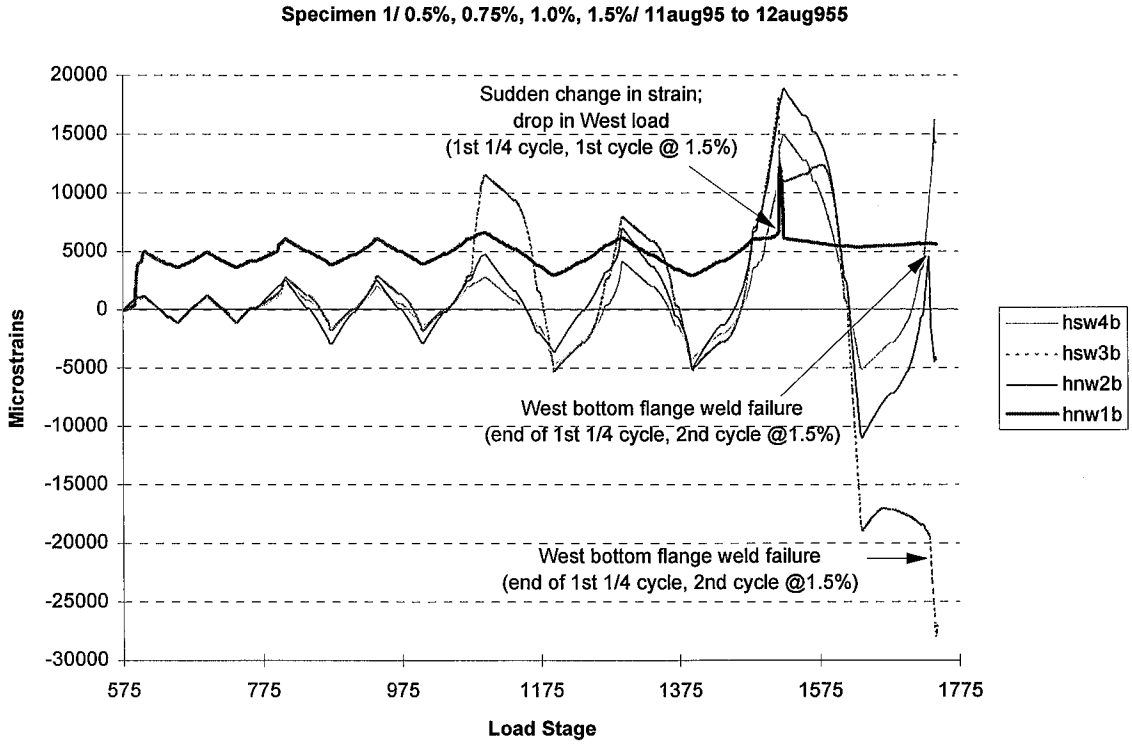

Figure 5.35: Girder Bottom Flange Strains (West Girder of Specimen 1)

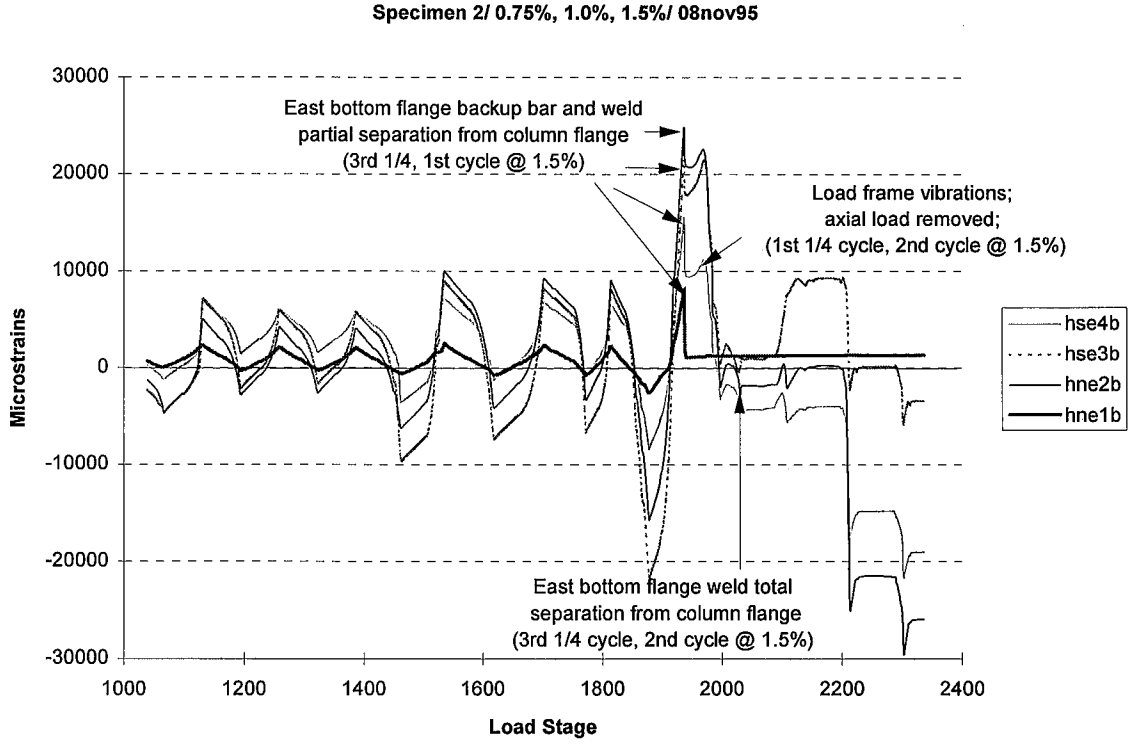

Figure 5.36: Girder Bottom Flange Strains (East Girder of Specimen 2)

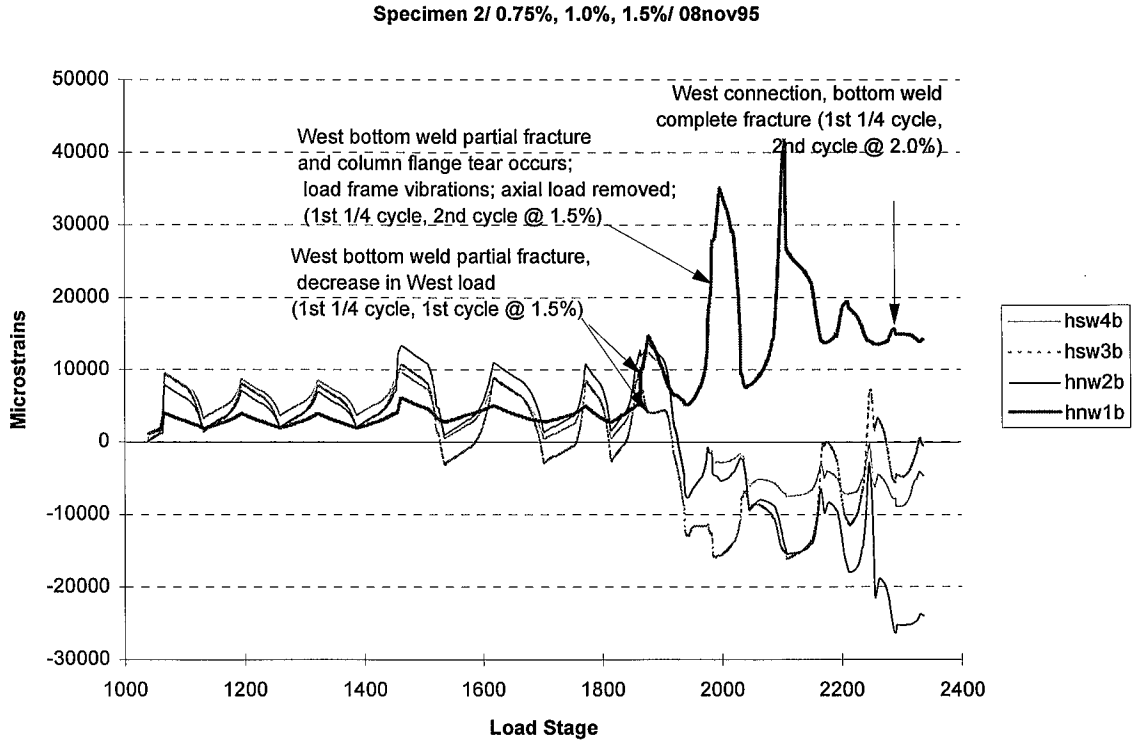

Figure 5.37: Girder Bottom Flange Strains (West Girder of Specimen 2)

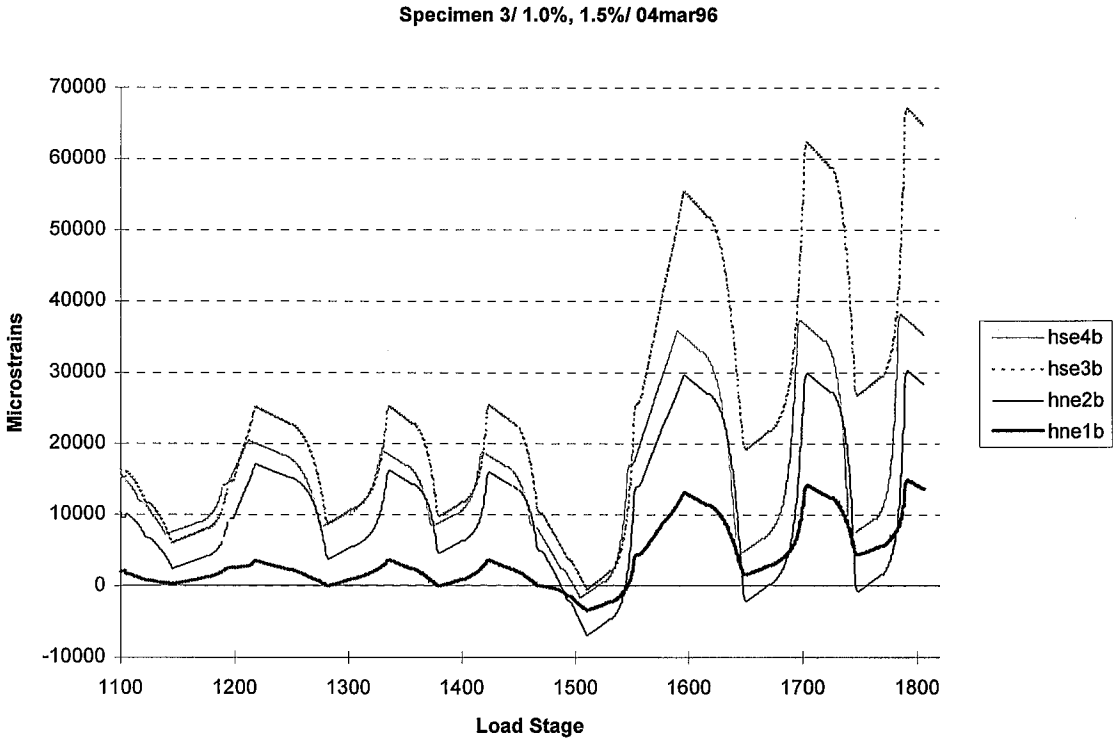

Figure 5.38: Girder Bottom Flange Strains (East Girder of Specimen 3)

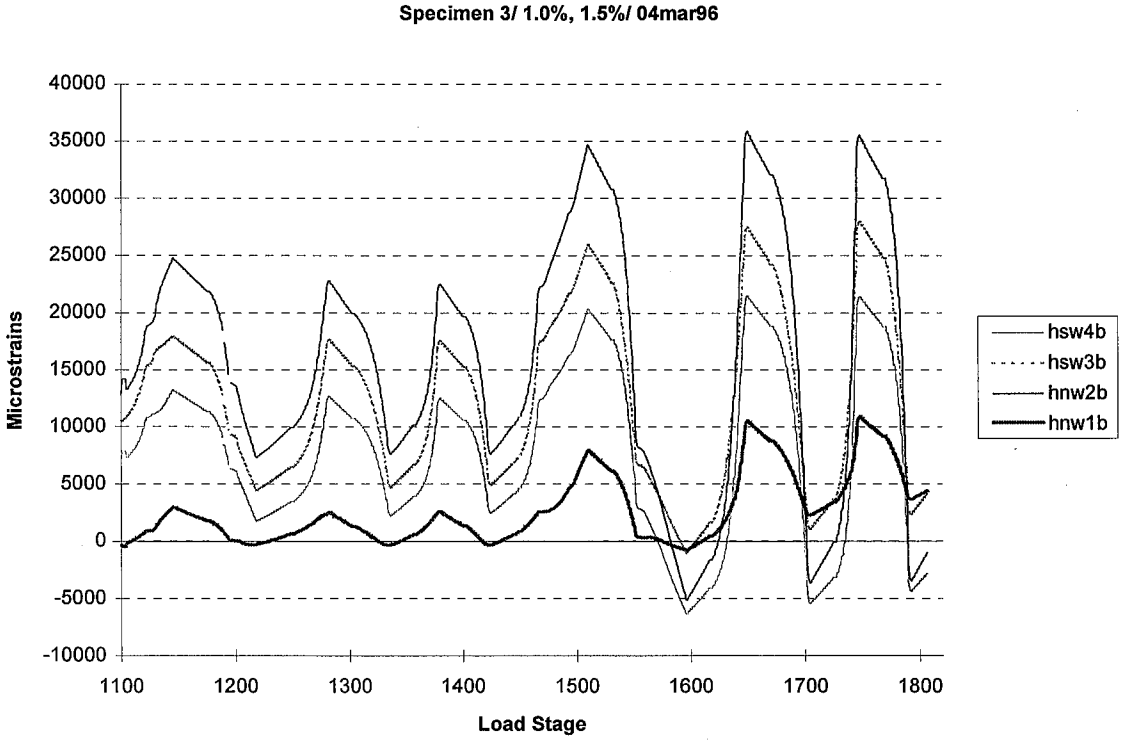

Figure 5.39: Girder Bottom Flange Strains (West Girder of Specimen 3)

access holes (with the exception of the first and ninth quarter cycles at 1.0% drift of the East girder) (see Figures 5.28 and 5.29). The strain behavior, shown here during the 0.50% to 1.0% drift levels, is typical throughout most of the load history of Specimen 1. Because the girders of Specimen 1 are bare steel, the placement of the shear tab is concluded to be the primary source of geometric asymmetry causing this connection behavior.

For the East and West connections of Specimen 2, a significant amount of straining occurs within the bottom regions of the connections compared to the top regions prior to connection failure during the 1.5% drift levels. For example, the strain amplitudes near the bottom access hole of the steel section (gages hse5b, hsw5b) are approximately 2 to 3 times larger than the strains near the top access hole (gages hse6b, hsw6b) during the 0.75% and 1.0% drift levels (see Figures 5.30 and 5.31). It is also observed that strains near both the top and bottom access holes of these connections demonstrate permanent compressive straining through 1.0% drift cycles, especially in the West connection. This behavior, though unexpected, is not significant compared to the tensile and compressive strains exhibited later on in the load history at the 1.5% drift levels.

For the East and West connections of Specimen 3, the strain amplitudes near the bottom access hole of the steel section are approximately 4 to 6 times larger than the strains near the top access hole during the 1.0% and 1.5% drift levels (see Figures 5.32 and 5.33). Note that a significant amount of net tensile straining occurs during the 1.5% drift levels. This behavior may be attributed to plastification of the bottom region of the connection, resulting in a shifting of the neutral axis towards the concrete slab.

The strains at the bottom surface of the bottom flange region in the six connections are shown in Figures 5.34 to 5.39. The strain amplitudes within this region were generally 1.2 to 2 times as large, and sometimes up to five times as large, in the connections of Specimens 2 and 3 compared to the connections of Specimen 1. For example, during the 0.75% drift cycles, a larger amount of net tensile straining typically occurred in the composite girders of Specimen 2 and 3 (e.g., in the range of 10,000 to 25,000 $\mu\varepsilon$) than in the steel girders of Specimen 1 (e.g., in the range of 3,000 to 5,000 $\mu\varepsilon$) during girder positive bending. These higher strains may occur

partially because the stiffer composite specimens may be more likely to rotate inelastically at a given level of interstory drift.

5.1.3 Force Transfer Behavior at the Column-Concrete Slab Interface

The transfer of large compressive forces, and therefore the presence of large compressive strains, may occur near the column-concrete slab interface due to the bearing of the concrete near this region during positive girder bending. Tagawa et al. (1989) have shown that the compressive forces in the concrete slab are affected by the bearing stress of concrete at the column face. These larger than expected forces which are transferred into the concrete slab may contribute to a shifting of the neutral axis along the girder cross section, resulting in large tensile strains at the bottom connection region.

To study this possible condition, longitudinal strains in the concrete slabs of Specimens 2 and 3 were measured at the top surface of the reinforcing bars approximately 1.5" and 13.5" from each face of the column flanges, at a depth of approximately 1.5" from the top surface of the concrete slab (see Figure 5.40; see also Section 2.4.3). The concrete decks for each girder of Specimen 2 and 3 exhibited larger strain magnitudes near the column flange region compared to the edge of the concrete slab during girder positive bending up through the 1.5% drift levels. For example, Figures 5.41 to 5.43 highlight this behavior shown by the West concrete slab of Specimen 2 during the 0.1% to 0.50% drift levels. Also, Figures 5.44 to 5.46 illustrate this phenomenon during the later drift cycles (0.75% to 1.5% drift levels) for the East concrete slab of Specimen 2. Not only are the compressive strains larger near the column-concrete slab interface, but the tensile strains in the concrete slab are generally larger near this region during negative girder bending as well.

Crack patterns along the top surface of the concrete slabs are shown in Figure 5.47 to 5.50 for the East and West concrete slabs of Specimens 2 and 3 after testing. The cracks are identified with a number (i.e., 0.1, 0.25, etc.), which corresponds each crack with the drift cycle at which the crack occurred. It is observed that the majority of the concrete crushing occurs near the column-concrete slab interface. In addition, the concrete cracks typically originate at the column flange tip and extend diagonally away

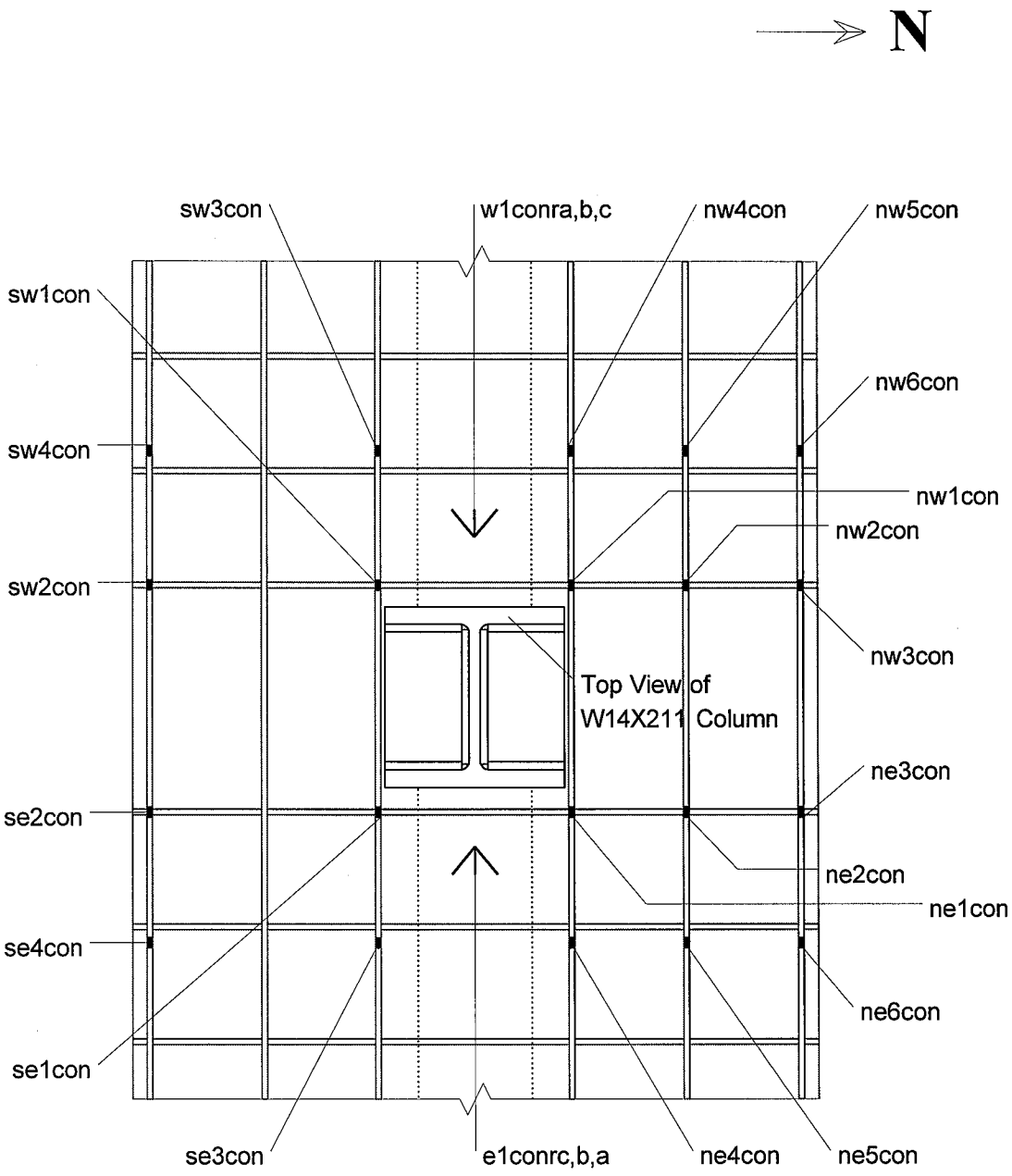

Figure 5.40: Strain Gages of Concrete Slab (Plan View of Specimens 2 and 3)

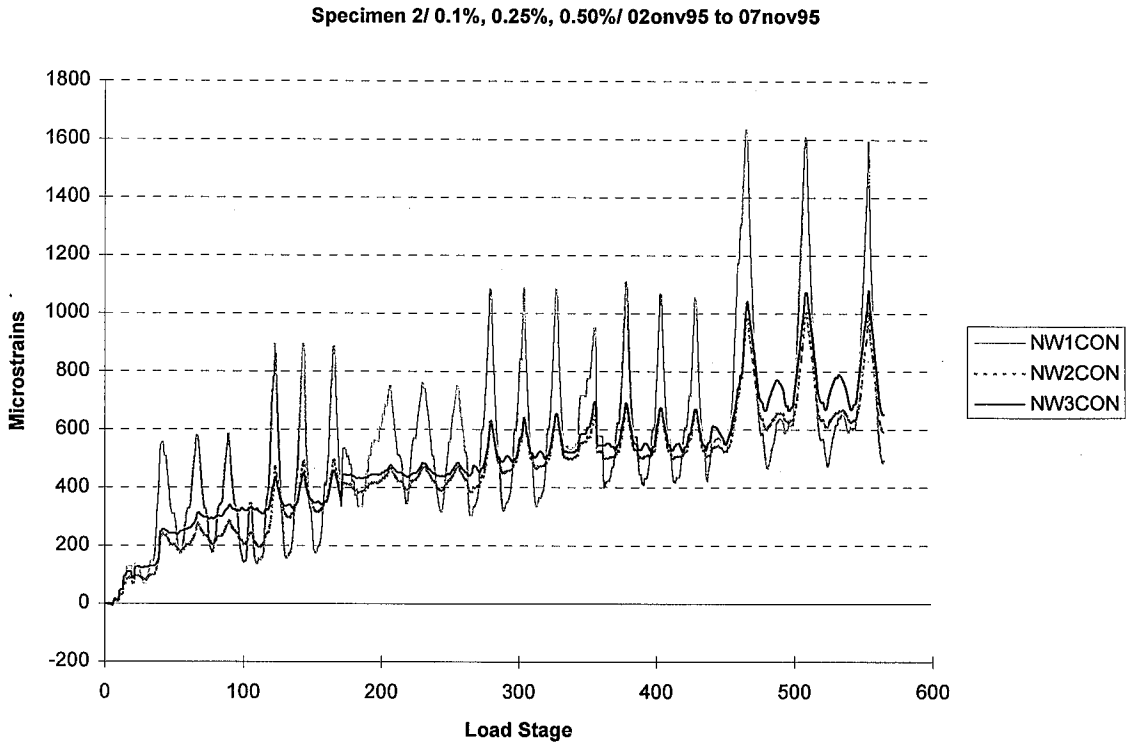

Figure 5.41: NW Concrete Slab Reinforcing Bars Strains (West Slab of Specimen 2)

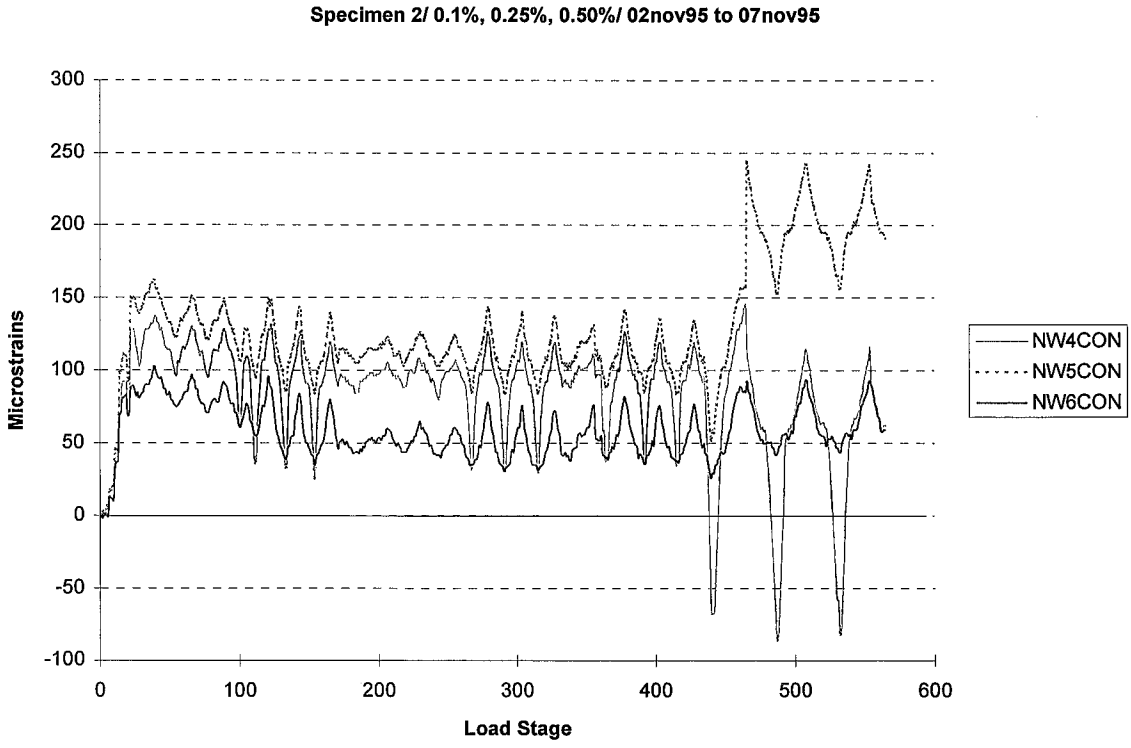

Figure 5.42: NW Concrete Slab Reinforcing Bars Strains (West Slab of Specimen 2)

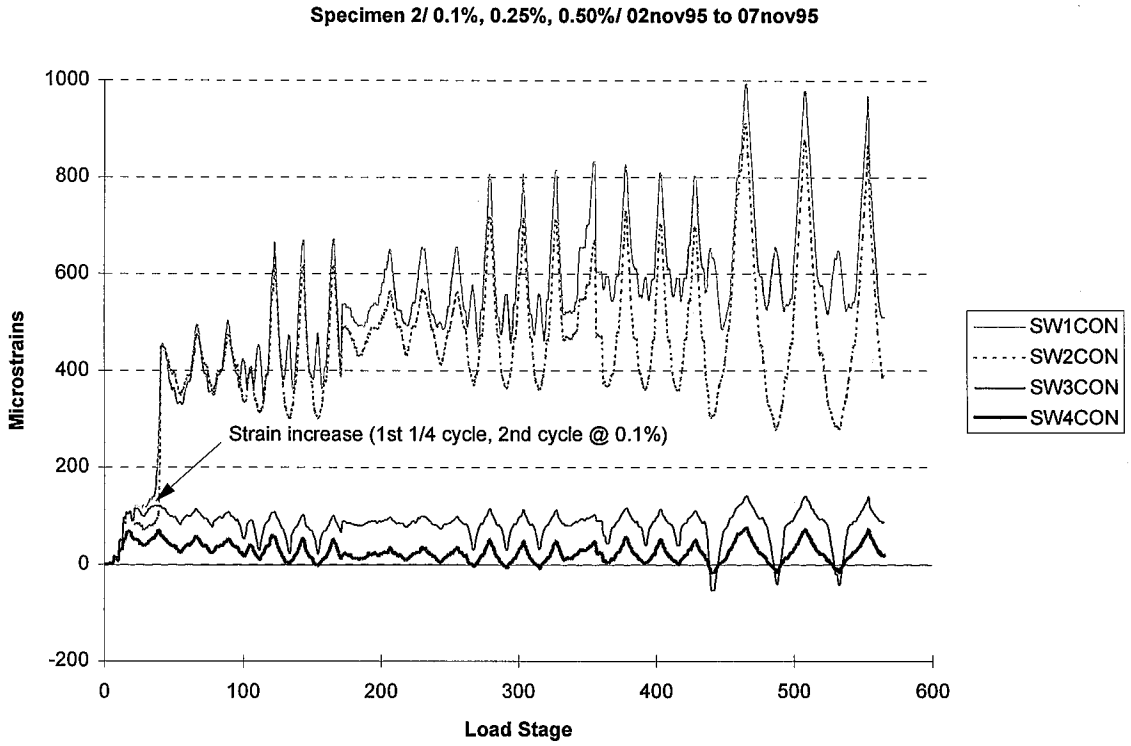

Figure 5.43: SW Concrete Slab Reinforcing Bars Strains (West Slab of Specimen 2)

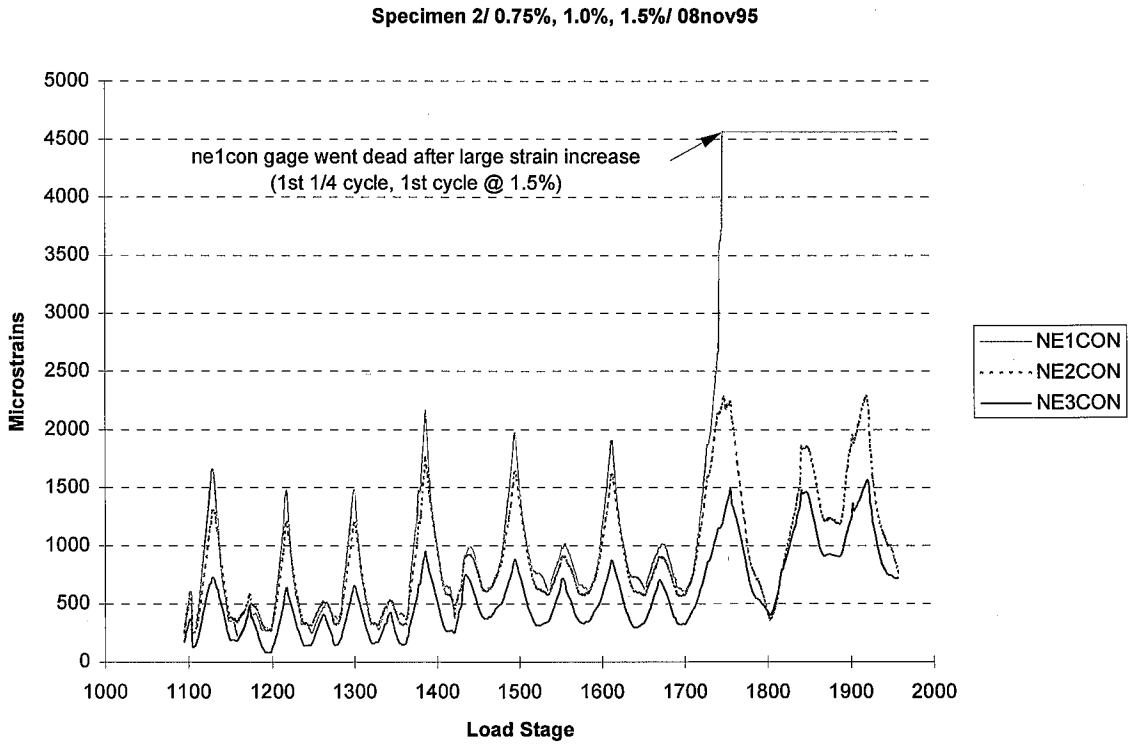

Figure 5.44: NE Concrete Slab Reinforcing Bars Strains (East Slab of Specimen 2)

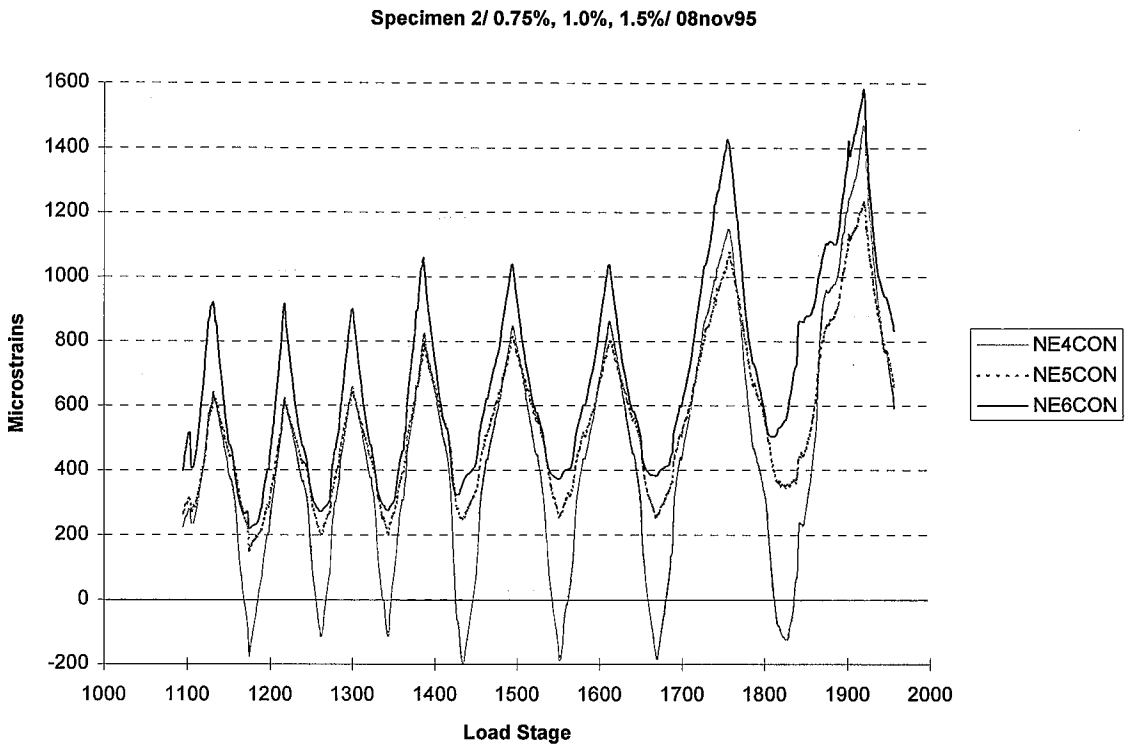

Figure 5.45: NE Concrete Slab Reinforcing Bars Strains (East Slab of Specimen 2)

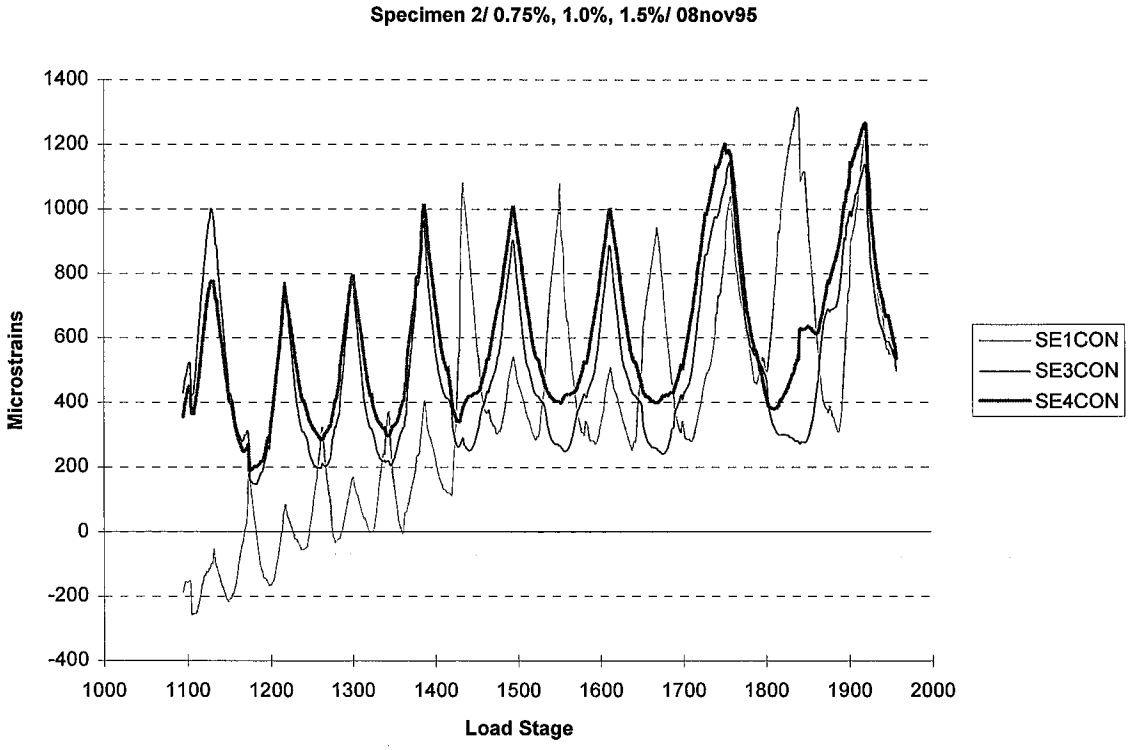

Figure 5.46: SE Concrete Slab Reinforcing Bars Strains (East Slab of Specimen 2)

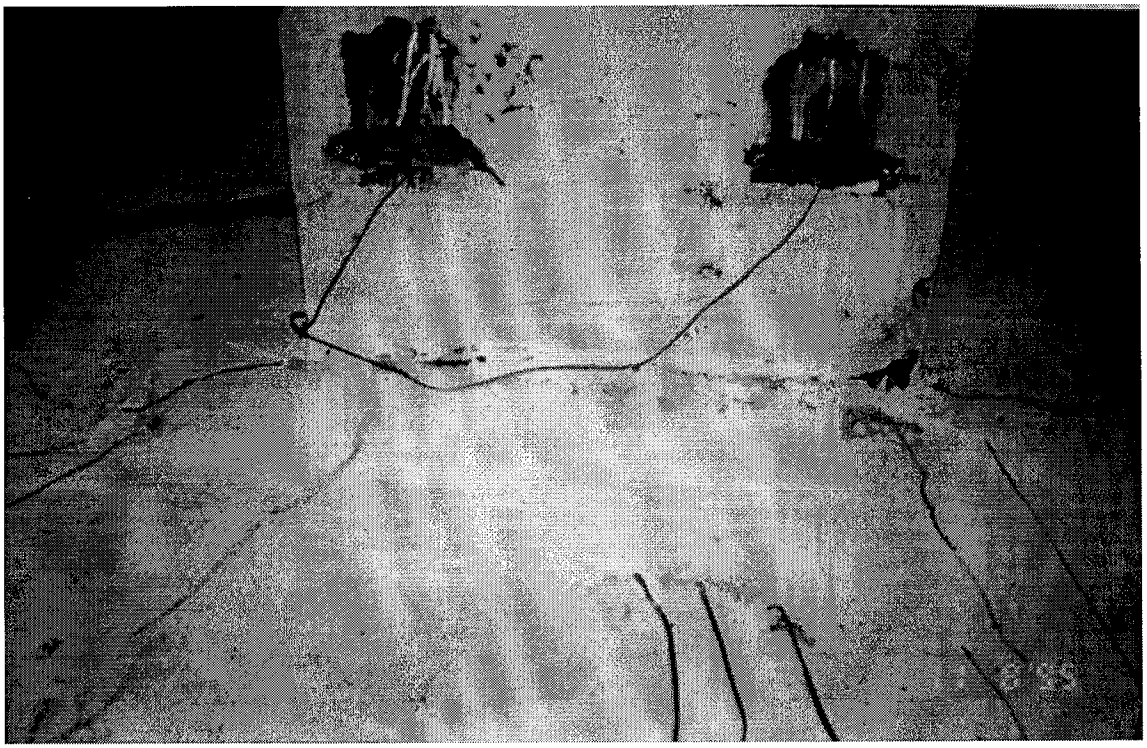

Figure 5.47: Top View of Concrete Slab-Column Interface (East Girder of Specimen 2)

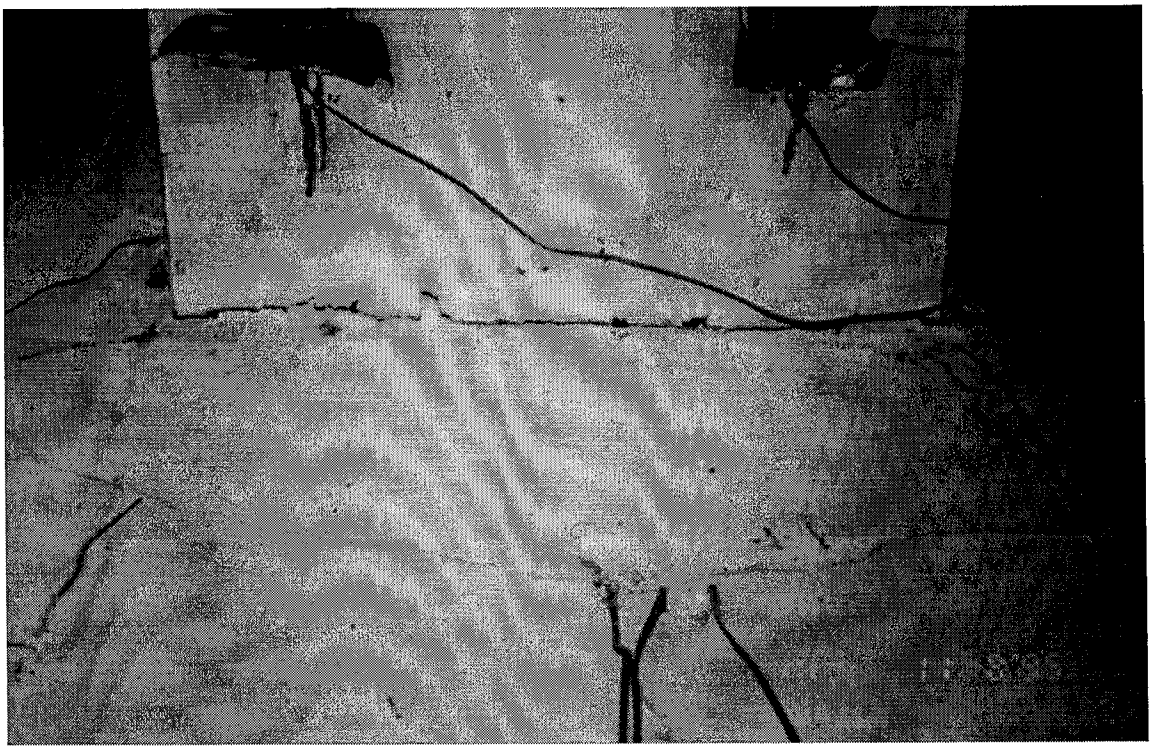

Figure 5.48: Top View of Concrete Slab-Column Interface (West Girder of Specimen 2)

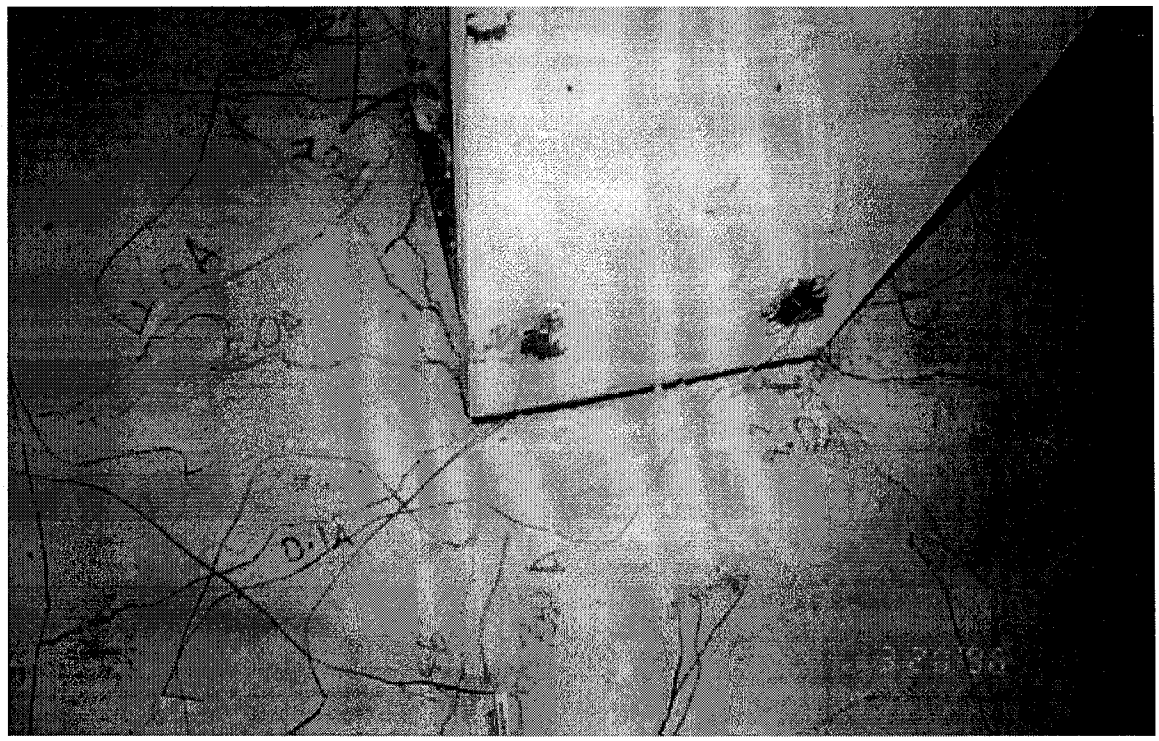

Figure 5.49: Top View of Concrete Slab-Column Interface (East Girder of Specimen 3)

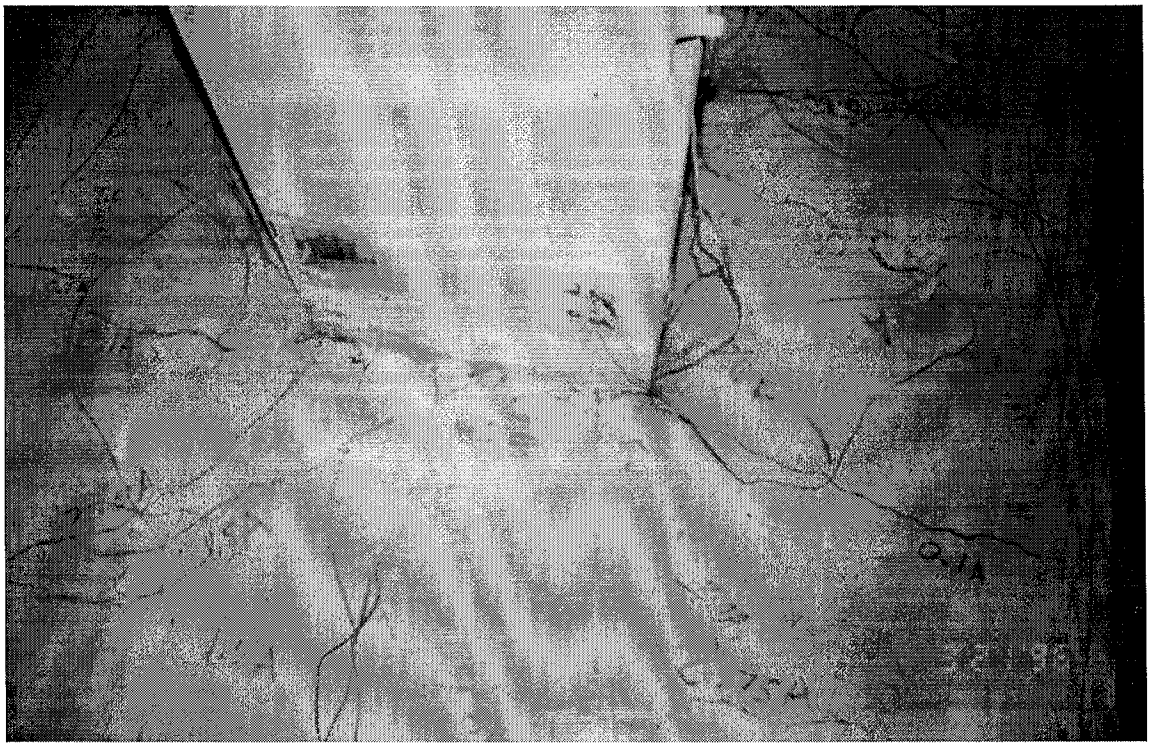

Figure 5.50: Top View of Concrete Slab-Column Interface (West Girder of Specimen 3)

from the column flange towards the edge of the concrete slab, thus showing evidence of compressive stresses focusing towards the column flange, with a resulting tensile principal stress perpendicular to the diagonal cracking.

This type of behavior, along with the evidence of larger strains near the column flange-concrete slab interface, confirms that the bearing, which occurs adjacent to the column flanges, is substantial and may lead to larger tensile strains within the bottom girder flange region during positive girder bending. Note that the West girder concrete slab of Specimen 3 exhibited significantly more cracking and crushing near the column-concrete slab interface than the East girder concrete slab of Specimen 3 during the 0.75% drift levels.

5.1.4 *Comparison of Plastification at the Top and Bottom Connection Regions*

The effects of composite floor slabs on the level of straining and plastification within the bottom region of the composite connections is also verified with visual documentation. Figures 5.51-5.56 illustrate the East and West connection regions of the three specimens after testing. The West girder of Specimen 1 and both girders of Specimen 2 exhibited limited yielding, especially on the bottom flange prior to fracture (see Figure 5.52 to 5.54). Note, however, the high levels of plastic deformation within the bottom girder web and flange regions as well as the formation of plastic hinges due to local flange buckling of the bottom girder flange for the East girder of Specimen 1 and for the composite girders of Specimen 3 (see Figures 5.51, 5.55 and 5.56). Even for Specimen 1, the bottom flange of the East girder showed more extensive yielding and local buckling than the top flange (see Figure 5.51). As discussed in Section 5.1.1., the location of the shear tab may influence this distinct asymmetry in the behavior of this connection.

The top flange of the West girder of Specimen 3 showed extensive yielding, but no fracture or local buckling (see Figure 5.56). The other top flanges of Specimens 2

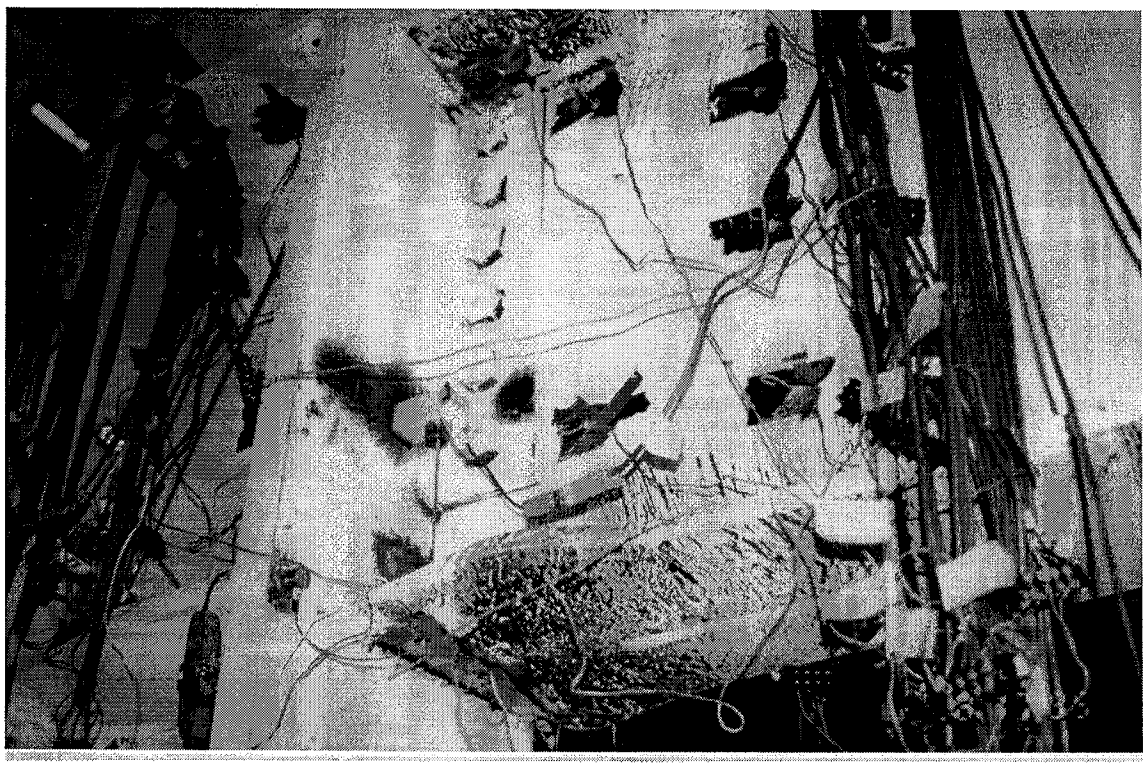

Figure 5.51: SE Connection Region (East Girder of Specimen 1)

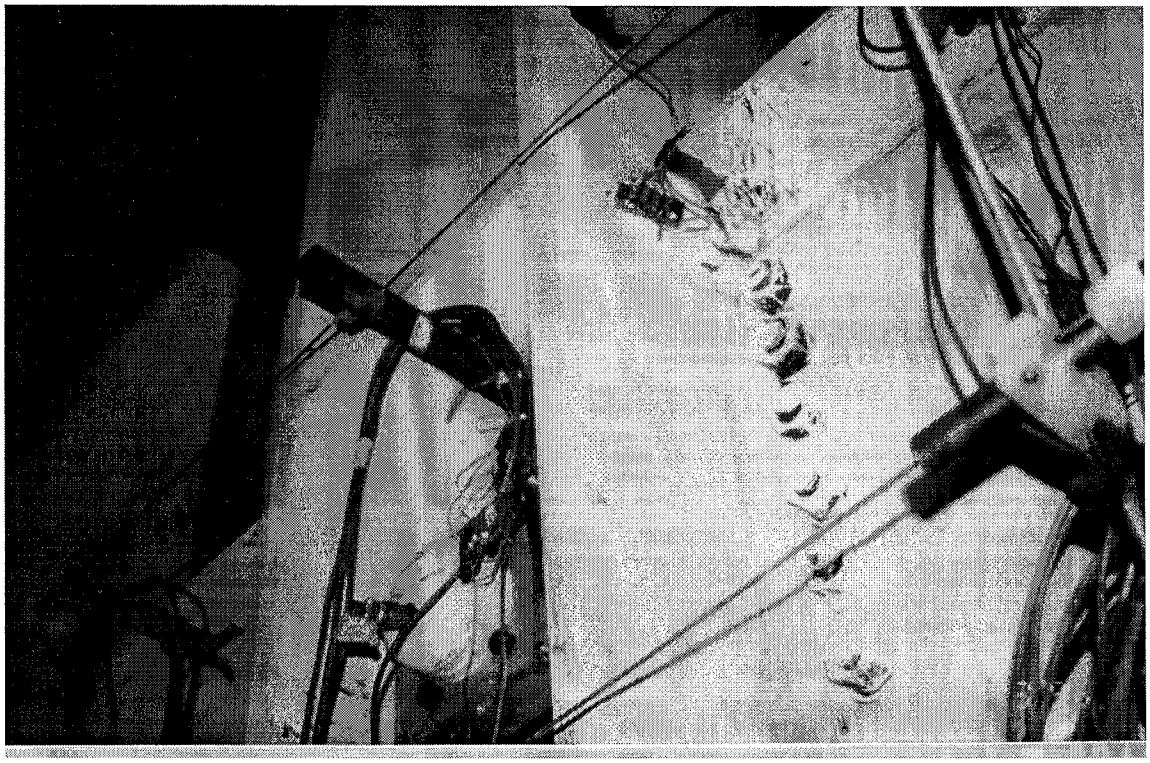

Figure 5.52: NW Connection Region (West Girder of Specimen 1)

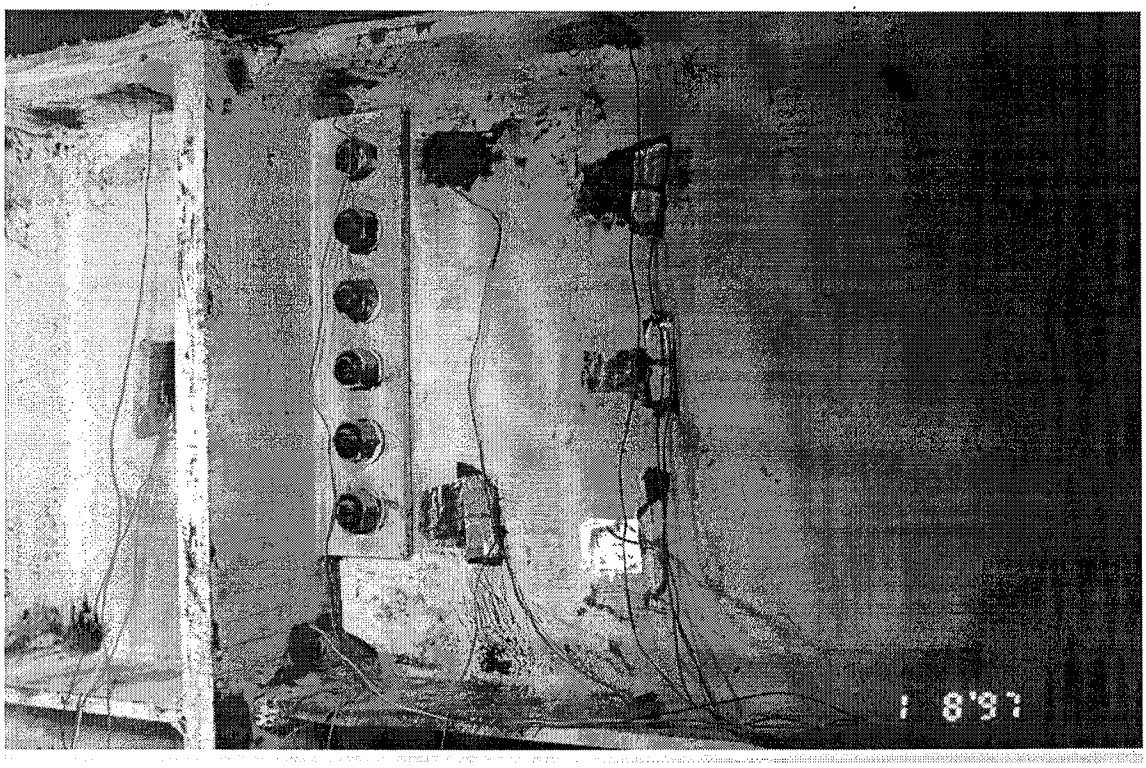

Figure 5.53: SE Connection Region (East Girder of Specimen 2)

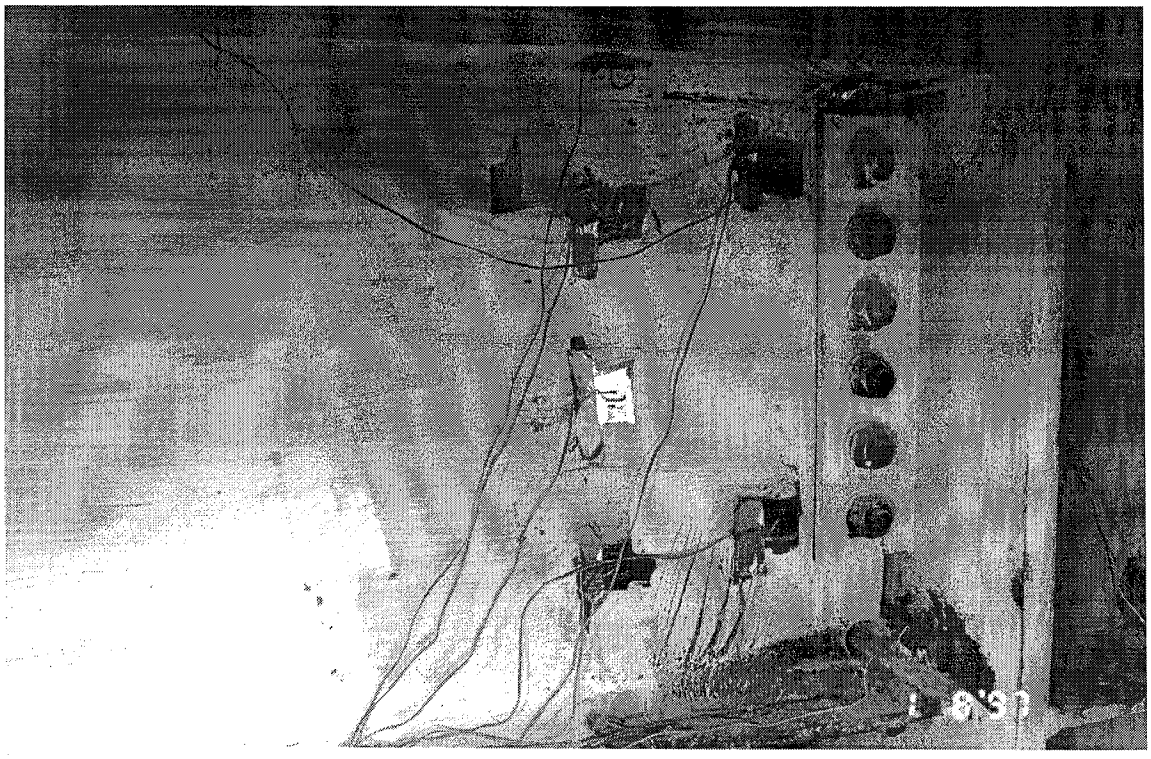

Figure 5.54: SW Connection Region (West Girder of Specimen 2)

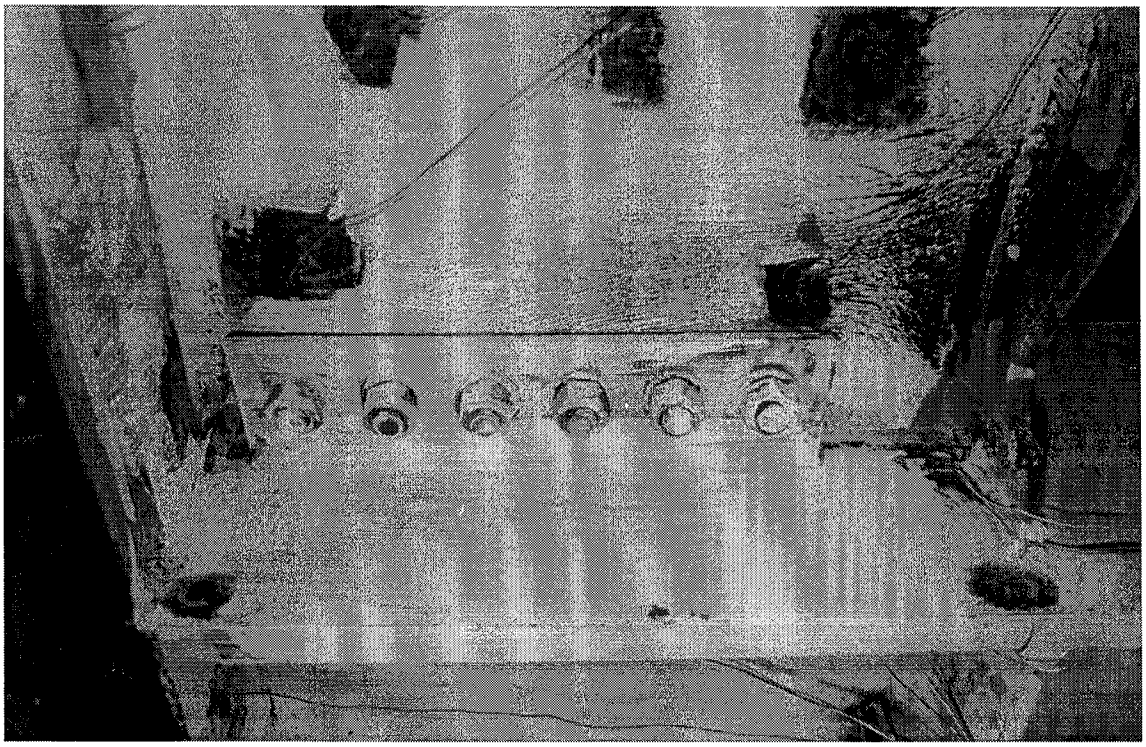

Figure 5.55: SE Connection Region (East Girder of Specimen 3)

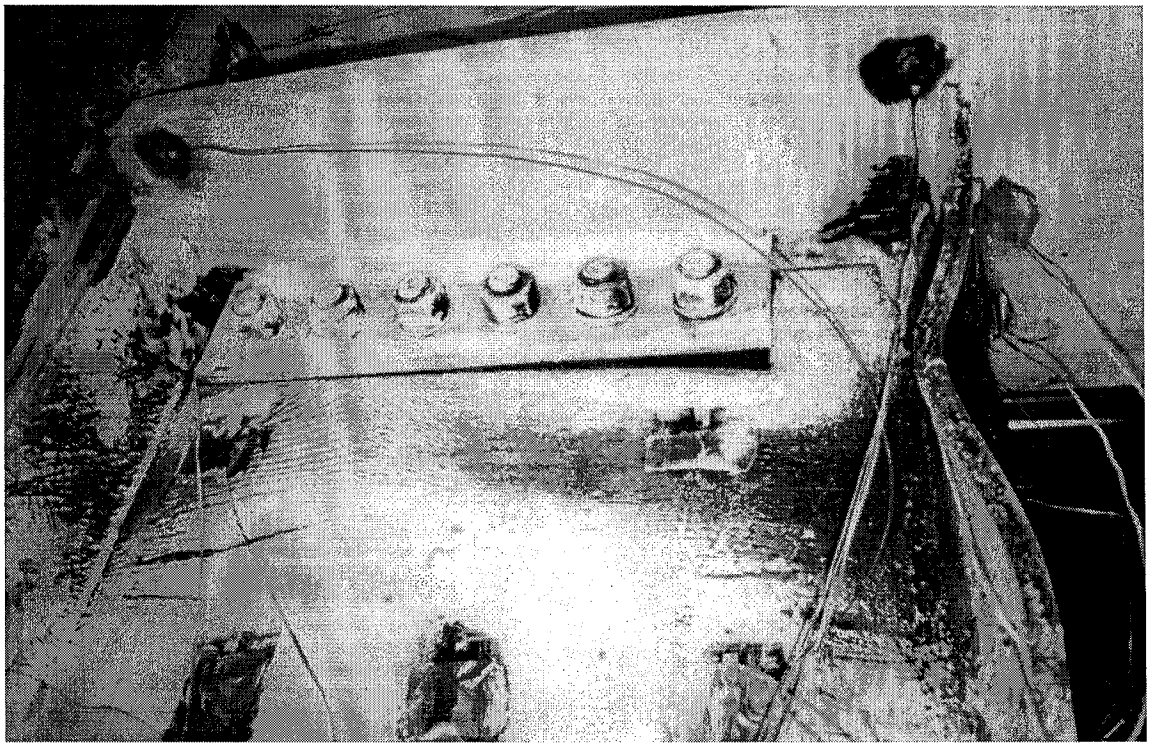

Figure 5.56: SW Connection Region (West Girder of Specimen 3)

and 3 showed little yielding compared to the bottom flanges. Also, recall that all six connections failed at the bottom connection region (see Chapter 3). The connection regions of Specimen 3 ultimately exhibited higher levels of plastic deformation compared with the connections of Specimen 2. This is because the connections of Specimen 2 failed prematurely during the 1.5% drift levels, while the connections of Specimen 3 were cycled up through the 3.0% drift levels until their failure. One possible cause for these premature connection failures during the 1.5% drift levels is the existence of backup bars, a condition which is discussed next.

5.2 The Effect of the Backup Bars

Experimental research and forensic studies have shown that the presence of backup bars at the base of welded girder flange-to-column connections often significantly reduce the ductile performance of the connection (Kaufmann et al., 1996). Specifically, they are believed to contribute to poor weld root penetration, strain concentrations, and crack initiation within the CJP welds at the girder flange-to-column connection. This section compares the connections with and without bottom backup bars based on the hysteretic behavior of the girders, acoustic emission activity, and failure mechanisms. It also provides possible explanations for how backup bars may have contributed to the brittle-type fractures of the welded girder flange-to-column connections studied in this research.

5.2.1 Connection Performance and Failure Mechanisms

The West connection of Specimen 1 and the East and West connections of Specimen 2 failed prematurely by brittle fracture, while the locations of these fractures varied within the HAZ of the weld region (see Section 3.2). These connections all possessed backup bars at the base of the bottom weld, which may have created conditions

which contributed to premature fracture of the bottom welded connection (see Table 5.2; Section 2.1.2). The presence of top backup bars at the top welded girder flange-to-column connections was observed to have an insignificant effect (i.e., none of the connections exhibited any partial or complete failure at or near this region).

Table 5.2: Existence of Backup Bars on Final Specimen Connections

	Specimen 1	**Specimen 2**	**Specimen 3**
East/Top CJP Weld	YES	NO	NO
East/ Bottom CJP Weld	NO	YES	NO
West/ Top CJP Weld	YES	YES	NO
West/ Bottom CJP Weld	YES	YES	NO

Figures 5.57-5.62 illustrate the moment vs. plastic rotation curves of the three connections possessing bottom backup bars (see Appendix B), along with a view of their corresponding failure zones. It is evident that these connections achieved very poor levels of moment strength and plastic girder-to-column rotation (see also Section 3.2). Furthermore, the amount of energy dissipation capacity (evident by the nonlinear hysteretic behavior) is substantially less than expected.

These reductions in girder strength and ductility of the connections possessing bottom backup bars are a direct result of their premature fracturing during the 1.5% drift levels. The fractures occurred at the column flange-bottom CJP weld interface, near the location of the bottom backup bar. The fracture of the West connection of Specimen 2 was significant in that the fracturing of the bottom weld accompanied the fracturing of the West column flange (see Figure 5.62; Section 3.2).

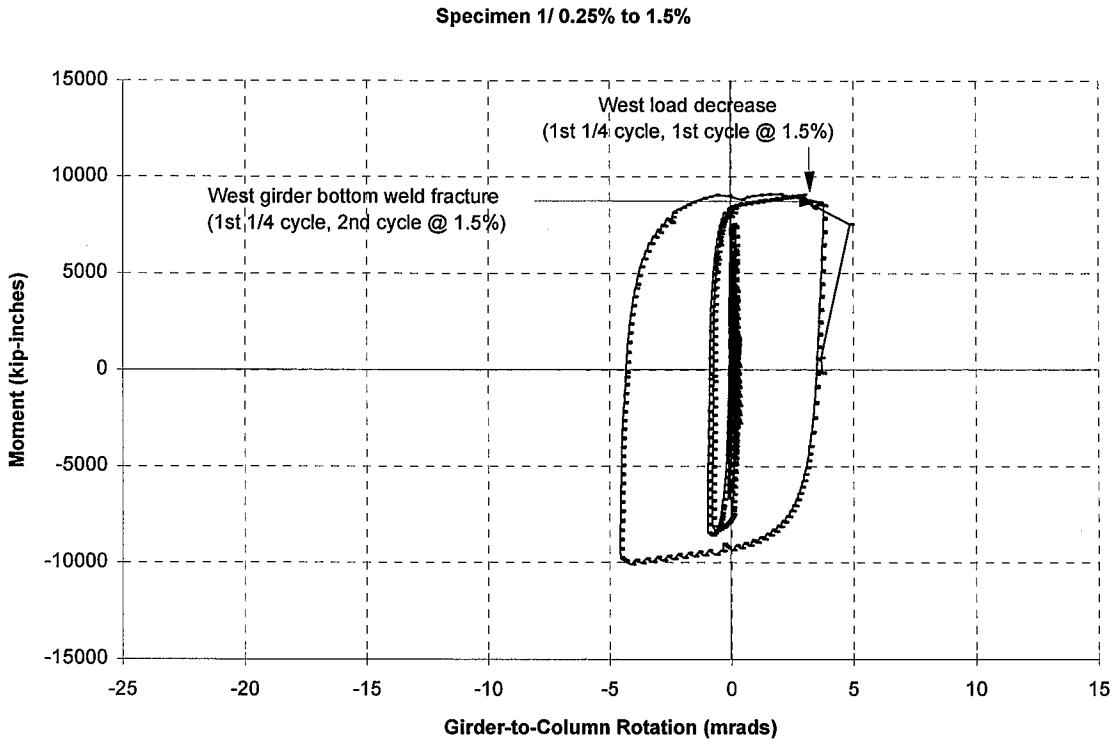

Figure 5.57: Girder-to-Column Moment-Rotation Curve (West Girder of Specimen 1)

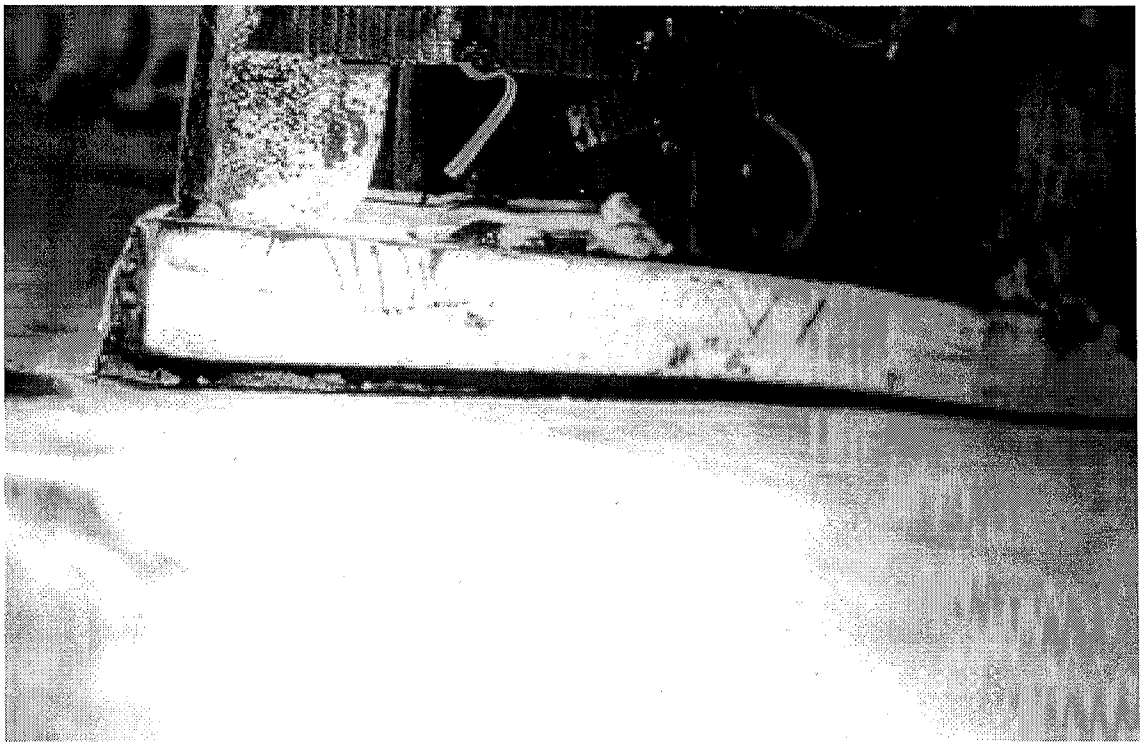

Figure 5.58: Fracture of Bottom CJP Weld (West Girder of Specimen 1)

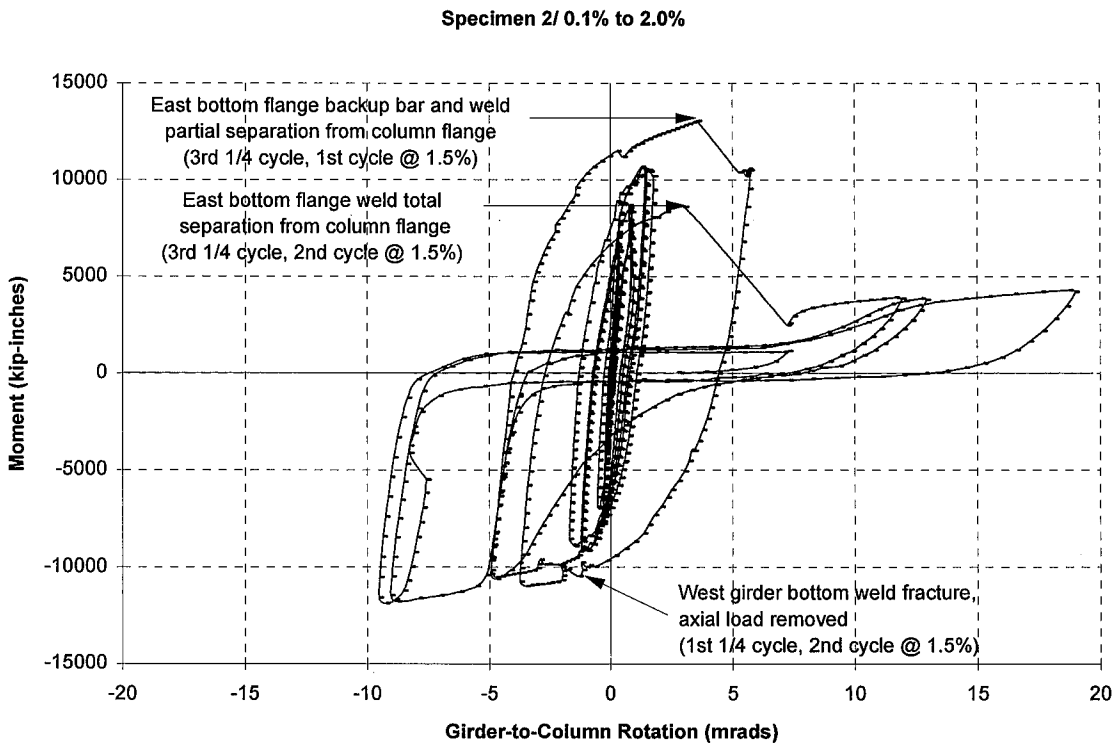

Figure 5.59: Girder-to-Column Moment-Rotation Curve (East Girder of Specimen 2)

Figure 5.60: Fracture of Bottom CJP Weld (East Girder of Specimen 2)

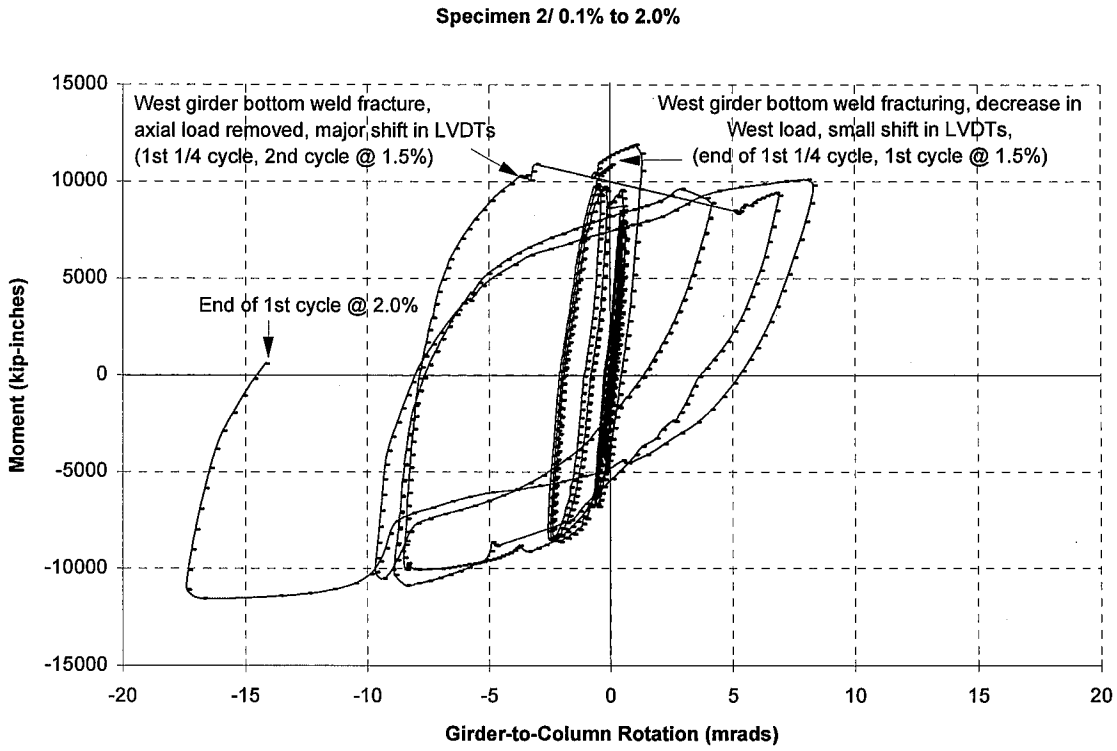

Figure 5.61: Girder-to-Column Moment-Rotation Curve (West Girder of Specimen 2)

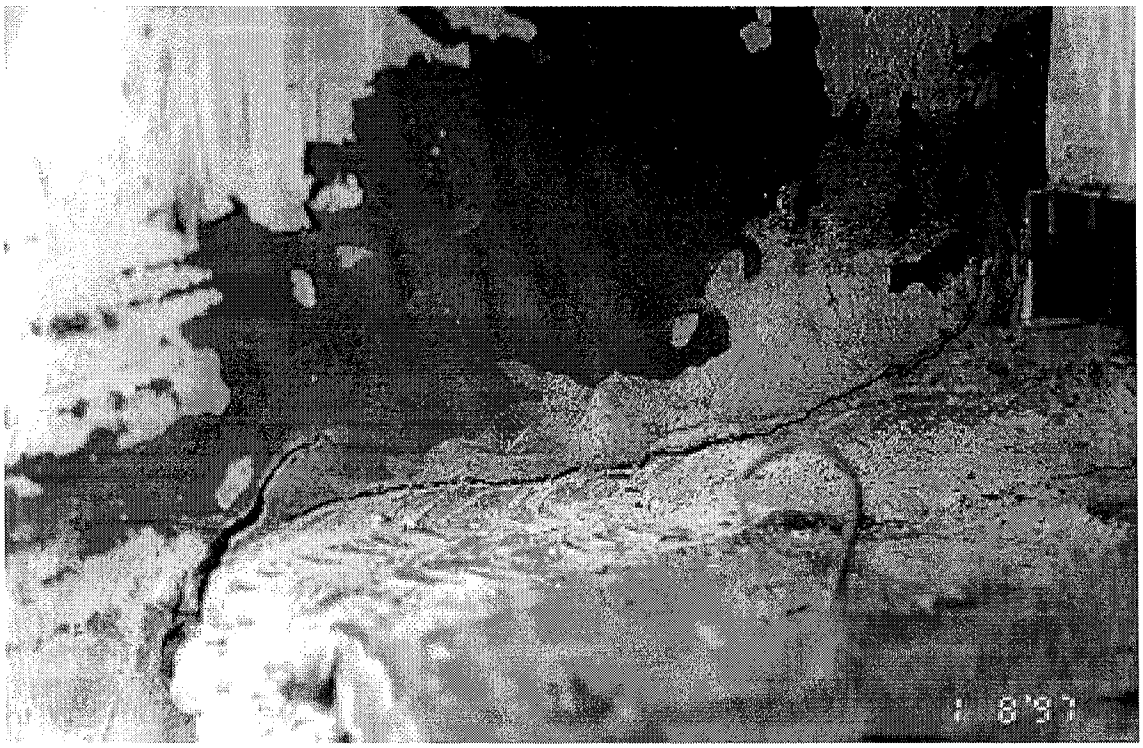

Figure 5.62: Pull Out-Type Failure of Column Flange (West Girder of Specimen 2)

5.2.2 Acoustic Emission Activity Near the Brittle Fracture Zones

The brittle fractures of the three connections possessing bottom backup bars are preceded by evidence of microfracturing, identified by using acoustic emission instrumentation (see Section 2.4.4). Several acoustic emission transducers were employed to identify the time and approximate location of events within the connection regions of the specimens. An acoustic emission is a stress-wave within a material originating from a rapid release of strain energy, also referred to as an AE (acoustic emission) event. For this research, AE events are primarily caused by microfractures of the steel or concrete deck.

The progression of acoustic emission events, or hits, and how often they occur may be corresponded to the brittle or low-cycle fatigue fracture mechanisms (see also Appendix H). Figure 5.63 illustrates that the bottom region of the West connection of Specimen 1 experiences occasional AE events during the 0.25% to 1.0% drift levels and then exhibits a sudden release of energy (as stress waves) across the entire width of the bottom girder flange during the first quarter cycle of the first cycle at 1.5% drift. This event correlates with the event of the bottom girder flange-to-column weld fracture of this connection and is representative of the sudden, brittle-type failure mode exhibited by this connection (see also Figure 5.58).

Figure 5.64 illustrates the presence of microfracturing within the bottom connection region of the East connection of Specimen 2, beginning at the 0.75% drift cycles and steadily intensifying with AE activity through the 2.0% drift levels. This connection, which failed in a two-phase fashion (during the third quarter cycle of both the first and second cycles at 1.5% drift), also possessed a bottom backup bar (see Figure

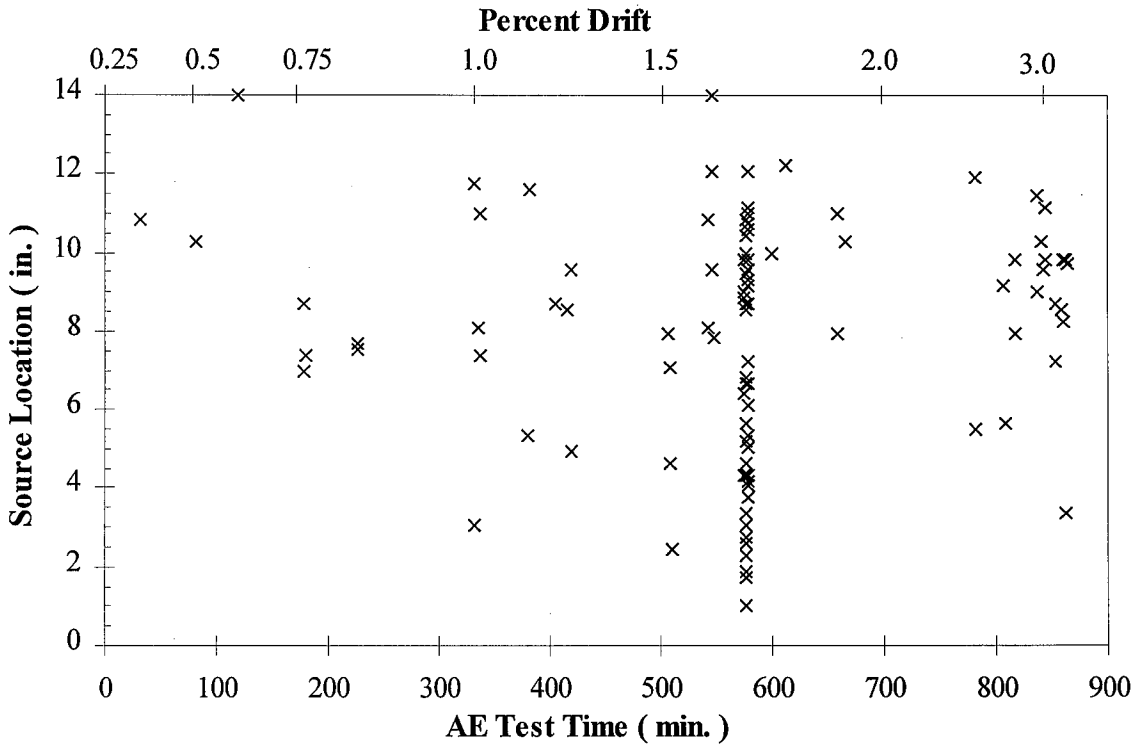

Figure 5.63: AE Event Source Location vs. Time (West Connection of Specimen 1)

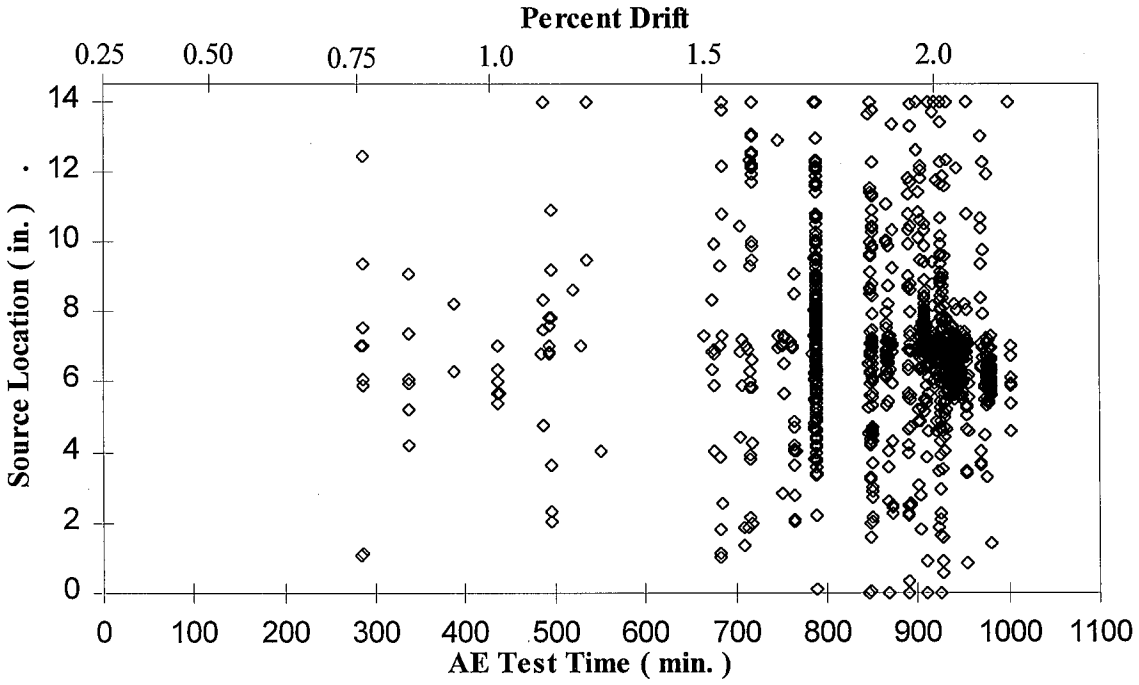

Figure 5.64: AE Event Source Location vs. Time (East Connection of Specimen 2)

5.46). The level of acoustic emission activity (and, therefore, microfracturing of steel within the bottom connection region) is substantial and correlates with localized fracturing that is occurring near the bottom backup bar-CJP weld interface.

5.2.3 The Effects of Localized Girder Flange Bending and Shearing

The West connection of Specimen 1, which possessed both a top and bottom backup bar (see Table 5.3), fractured at the bottom welded girder flange-to-column connection (see Figure 5.57). This connection did not possess a concrete deck and it exhibited similar strains at the top and bottom regions of the connection (see Section 5.1). Consequently, this connection best highlights several other features of the pre-Northridge connection design which accentuated the possibility of fractures occurring in the bottom flange region rather than in the top flange region. In particular, a local bending and shearing of the girder flange near the column flange surface and the placement of the bottom backup bar at the outside surface of the bottom girder flange, coupled with the typical location of the shear tab being near the top flange and the potential triaxial tensile strain state caused by restraint in the connection region, are all structural phenomena which may have led to the premature fracturing of this connection.

A local bending phenomena occurring at the top and bottom girder flange near the girder-to-column interface may cause the strain amplitudes at the bottom surface of the flange to be greater than the strains at the top surface (see Figures 5.65). For example, the strain amplitudes at the top surface of the North bottom flange tips (gages hnw1b and hne1b) are significantly less than the strains at the bottom surface of the North bottom flange tips (gages hnw2b and hne2b) for the East and West connections for all three specimens (Figures 5.34-5.39). These strains were each measured at approximately 1.5" from the column flange.

A local bending anomaly may be addressed by investigating the steel girder and the girder flanges independently as elements experiencing flexural bending (see Figure

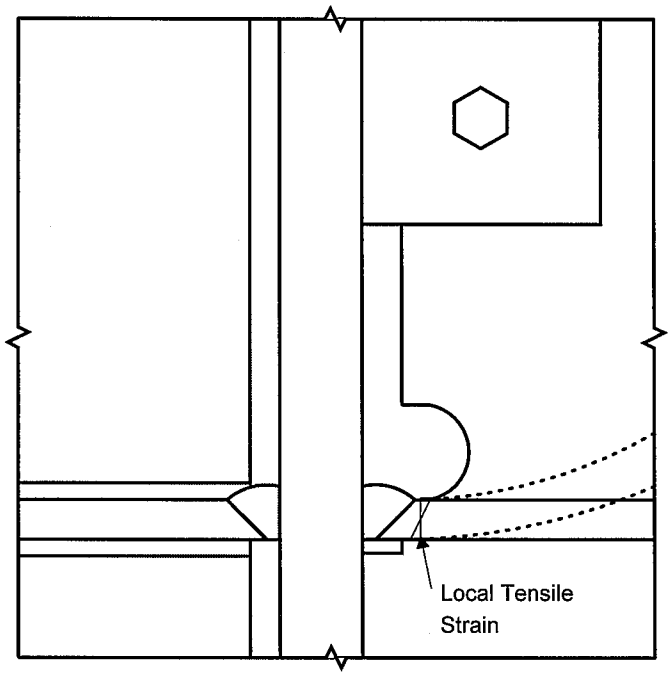

Figure 5.65: Elevation IV: Girder Flange Localized Bending Condition (Positive Girder Bending)

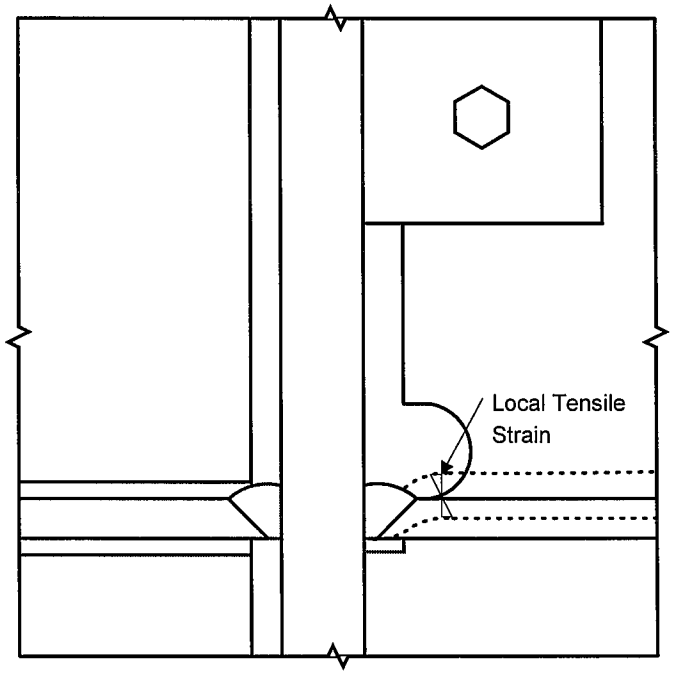

Figure 5.66: Elevation IV: Girder Flange Localized Shear Condition (Positive Girder Bending)

5.65). When observing the bottom surface of the bottom girder flange, the girder flexural and girder flange flexural strain contributions are both tensile during girder positive bending. However, when observing the top surface of the bottom girder flange, the girder flexural strain is tensile, but the girder flange flexural strain is compressive during girder positive bending. Likewise during girder negative bending, the bottom surface of the bottom girder flange experiences compressive strains due to both girder flexure and girder flange flexure. In addition, when studying the top surface of the bottom girder flange, the girder flexural strain is compressive but the girder flange flexural strain is tensile during the girder negative bending.

When investigating the top welded girder-to-column connection, the top surface of the top girder flange experiences the same strain behavior as the bottom surface of the bottom girder flange as described above. However, the top backup bar is located at the base of the top CJP weld; therefore, the backup bar-CJP weld interface (the typical area of fracture initiation) is not subjected to as high of levels of straining as the bottom girder flange backup bar-CJP weld interface (assuming that the forces transferred into the top and bottom girder flanges are relatively equal). Also, the top CJP weld is placed with one continuous weld pass, while the bottom CJP weld is placed with two weld passes; therefore, the bottom CJP weld may be more likely to possess welding imperfections near the center of the bottom girder flange.

Another phenomenon which may contribute to localized straining of the girder flange is reverse curvature bending condition of the girder flange due to the shearing force transferred into the connection from the girder tip load during positive girder bending (see Figure 5.66). This condition was also verified using a finite element continuum analysis (see Figure 5.67 and Section 5.1.1). Note that differences in longitudinal tensile strain between the bottom surface and top surface of the bottom girder flange are significantly larger near the girder web. This is expected, since the shear force is transferred through the girder web into the center region of the girder flange. Since this behavior exists during even the lower drift levels, it is not attributed to

the effects of local flange buckling. Furthermore, this phenomenon is studied approximately 1.5" from the column flange, whereas the local flange buckling regions were observed to start no closer than 5 to 6 inches from the column face. Actual shearing deformation of the East girder flange of Specimen 1 was measured to be minimal in this region using an LVDT; however, the effect of this condition on the strain distribution near the bottom access hole may still be significant.

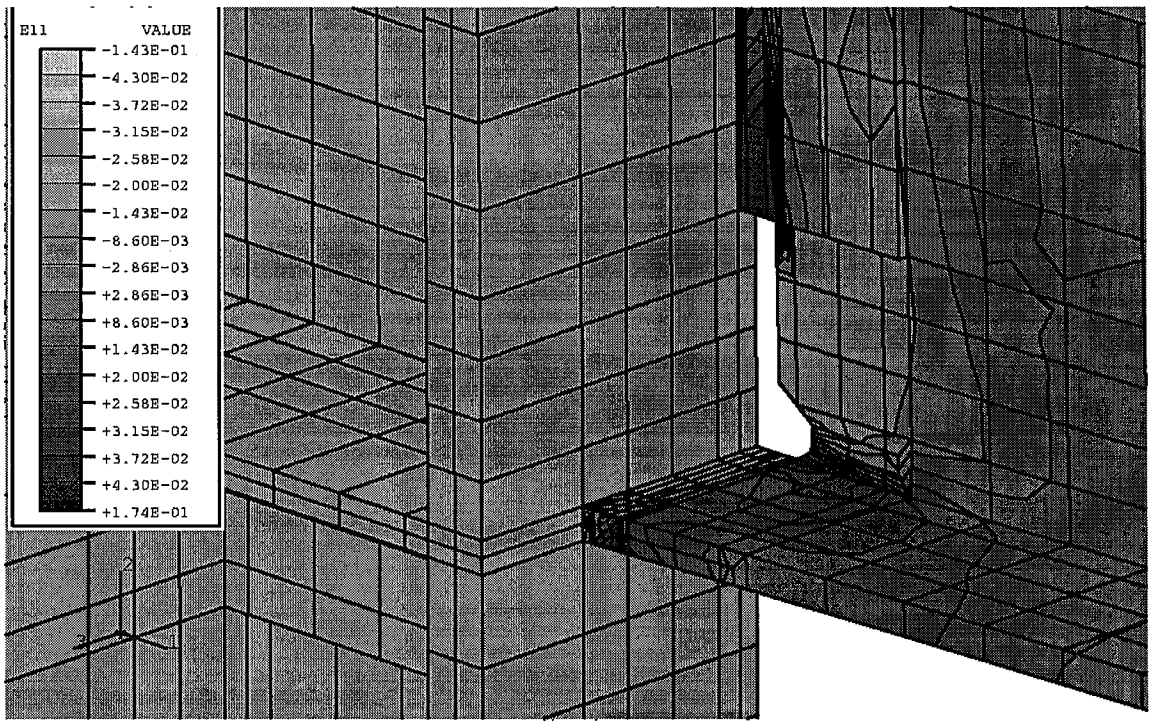

Figure 5.67: Strain Distribution Along Girder Axis at Top of Bottom Girder Flange-to-Column Connection (Composite Girder Specimen Model/ 3.0% Drift)

In summary, a backup bar is typically placed at the bottom side of the bottom girder flange and at the bottom side of the top girder flange. Therefore, it is concluded that the localized bending phenomena described above may have resulted in an additional strain concentration near the root of the bottom CJP weld rather than near the top CJP weld for a given load increment. Furthermore, this strain condition may have

contributed to the premature failure of the bottom CJP welds, not only of the West connection of Specimen 1, but also of the East and West connections of Specimen 2.

5.2.4 Effects of Other Structural and Metallurgical Phenomena

It is possible that the connections with bottom backup bars may have experienced larger strains due to larger bottom flange forces than the connections not possessing bottom backup bars. This scenario may be investigated by comparing the strain amplitudes in the bottom flanges during the 1.5% drift cycles (or the cycles at which premature, brittle connection failures occurred).

It is observed that the largest strain amplitudes in the bottom flanges of the West connection of Specimen 1 and the East and West connections of Specimen 2 are approximately 20,000 με to 30,000 με, 30,000 με, and 15,000 με, respectively, prior to the first event of the fracturing of the bottom welds during the 1.5% drift cycles (Figures 5.35-5.37). Also, the largest strain amplitudes at the bottom of the bottom flanges of the East and West girders of Specimen 3 are approximately 35,000 με and 40,000 με, while the same region of the East connection of Specimen 1 reaches strain amplitudes of 30,000 με during the 1.5% drift cycles (Figures 5.34, 5.38, 5.39). In short, it is shown that the strains that are in the bottom flanges of all six connections demonstrate relatively similar amplitudes prior to the failure of the three connections with bottom backup bars. Therefore, it may be concluded that the premature, brittle failure of the connections with backup bars is not due to an excessive transfer of forces into the bottom flange, at least as may be measured by the strain gages on these specimens.

Past research has investigated the effects of several metallurgical conditions on the performance of welded girder-to-column connections with backup bars. Deficiencies in material toughness and hardness within the HAZ of CJP welds and near the web-flange junction of jumbo-sized W-shape sections have been studied (Tide, 1997). Also, poor welding workmanship and construction limitations have been shown to have an negative

effect on the quality of welds (SAC, 1996b). These studies, though not addressed in this research, are discussed in more detail in Section 1.2.3.

Other structural conditions may have contributed to the premature, brittle fracture of welded girder-column connections that possess backup bars. For example, larger strains may have existed within the HAZ than what is expected in the bottom flange due to a notch or crack that initiates near the root of the weld and backup bar interface. A strain concentration within the bottom weld may have also occurred due to the presence of a triaxial state of tensile strain. This structural phenomena, which may also exist in other regions of the connection, is reported next.

5.3 The Effect of a Triaxial State of Stress Near the Bottom CJP Weld

The effects of the possible existence of a triaxial state of tensile stress and strain in the region of the bottom weld of the bottom girder flange-to-column connection during positive girder bending is studied in this section. The weld region for these types of connections are believed to be highly restrained through the length and the transverse direction of the column flanges, thereby leading to a multiaxial state of both stress and strain (Blogdett, 1995). Furthermore, the columns in these specimens are subjected to axial tension, thereby magnifying a triaxial stress condition. Using a finite element continuum model of Specimen 1, a triaxial strain condition may be observed by the strain concentrations that are generated at the girder flange-to-column interface (see Figure 5.67). Such a strain condition may have contributed to a brittle-type failure mode of the weld, due to the minimization of plastic shear flow (i.e., ductile yielding) prior to fracture.

A triaxial stress and strain condition was investigated in these tests by comparing the strain conditions of two elements, identified as Elements A and B (Figure 5.68). Element A is located on the top surface of the bottom CJP weld at the column flange-bottom weld interface. Element B is located approximately 1.5" away from the column

flange on the top surface of the girder bottom flange. By using strains measured in three orthogonal directions within the vicinity of these elements, normal strains and principal strains are estimated for Elements A and B. In addition, triaxial stresses are obtained assuming linear elastic behavior, which is valid near the connection for only the earliest cycles in each test. A detailed description of the data reduction procedure, the assumptions incorporated into the analysis of these strains, and the interpretation of the results are discussed in Appendix I. A summary of these results is outlined below.

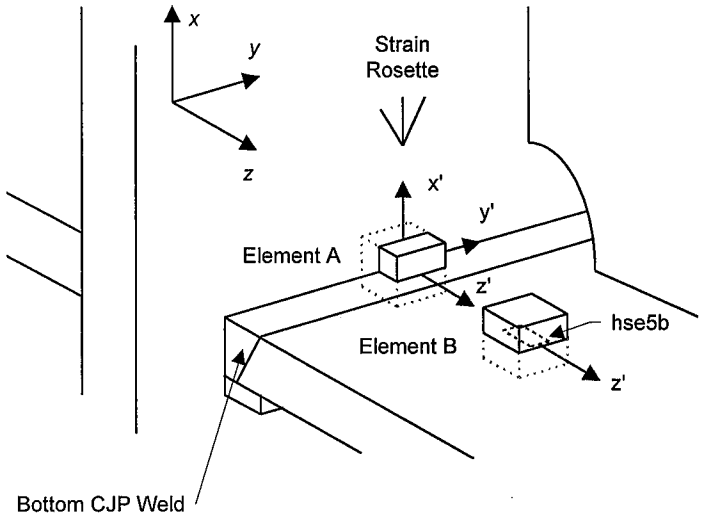

Figure 5.68: Elements A and B (Typical View of Bottom CJP Weld Region)

Based on an analysis of the experimental data in Appendix I, it is observed in all three tests that a triaxial state of stress is present within the proximity of the SE and SW bottom girder flange-column flange welds. This is demonstrated by comparing the three normal stresses of Element A, $\sigma_{x'}$, $\sigma_{y'}$, and $\sigma_{z'}$, (as calculated from the measured strains within the vicinity of Element A) to the uniaxial tensile stress in Element B, σ_t, that is oriented along the z'-axis (as calculated from a longitudinal strain measured at Element B). For example, the East bottom weld regions of Specimens 2 and 3 exhibit magnitudes of stress in the z'-direction (at Element A) that are significantly greater than the

magnitudes of uniaxial tensile stress (at Element B) during the 0.25% and 0.50% drift levels (see Figures 5.69 and 5.70, respectively). This behavior, shown for the East connections of Specimens 2 and 3, is also representative of the behavior of the other connections of the three specimens (see Appendix I.)

The application of 550 kips of axial tension to the column increases the three normal stresses at Element A; however, due to the relatively small amount of applied axial load to the column, this stress increase is minimal. For example, the normal stresses for Element A of the West connection of Specimen 1 increase by approximately 5 ksi during application of 550 kips to the column (see Figure 5.71).

The triaxial and uniaxial stress states of Elements A and B, respectively, are compared in order to correlate a triaxial state of stress to a brittle-type mode of failure. It is assumed that the fracture strength may be approximated by the ultimate tensile stress. When Element B is subjected to uniaxial loading, a ductile failure may occur; that is, the element's shear yield stress may be attained by the maximum shear stress before the element's ultimate tensile stress is breached by the maximum normal stress, σ_t (see Figure 5.72). However, when Element A is subjected to multiaxial strains, a high state of triaxial tension may lead to brittle fracture prior to ductile yielding. This is because the ultimate tensile stress may be reached by the maximum normal stress, σ_z, before its shear yield stress is reached by the maximum shear stress (Blodgett, 1995).

However, as shown in Appendix I, no strong correlation is made between the brittle-type fractures of three of the six connections with the stress condition defined above. Nevertheless, it is clear that a triaxial state of tensile stress is evident near the bottom girder flange-to-column weld region of all the connections (shown both computationally and experimentally), and that this condition may have at least resulted in stress and strain concentrations near the bottom CJP weld region.

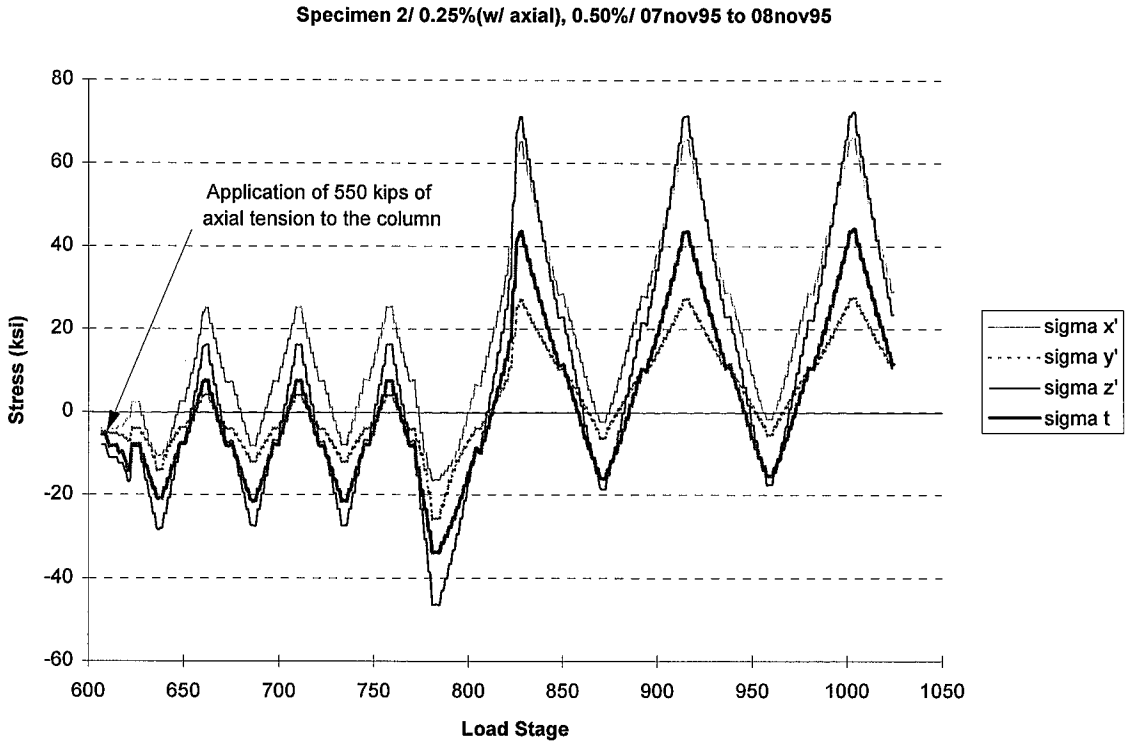

Figure 5.69: Normal Stresses at Elements A and B (SE Connection of Specimen 2)

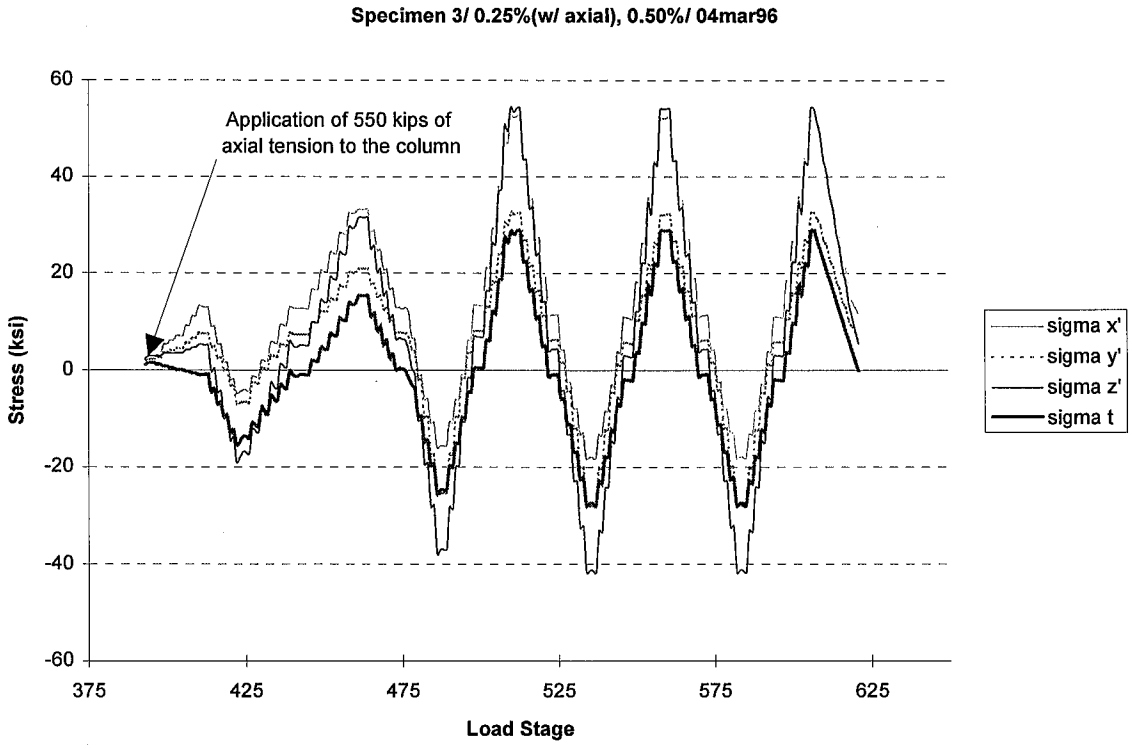

Figure 5.70: Normal Stresses at Elements A and B (SE Connection of Specimen 3)

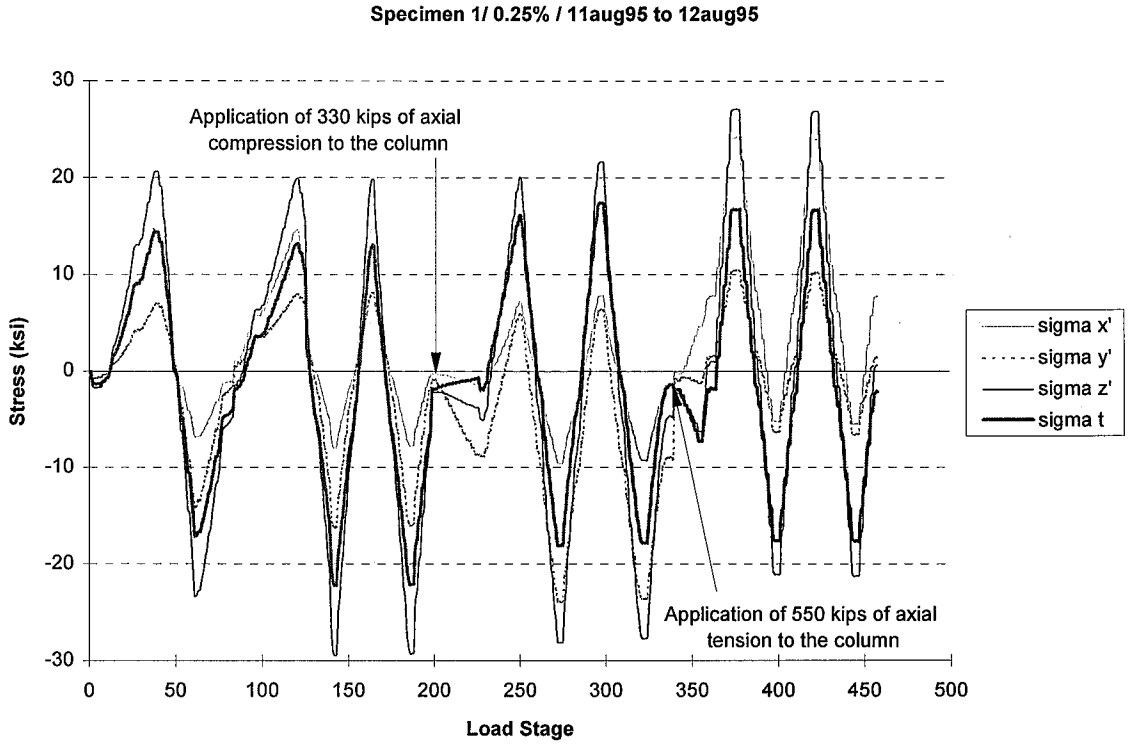

Figure 5.71: Normal Stresses at Elements A and B (SW Connection of Specimen 1)

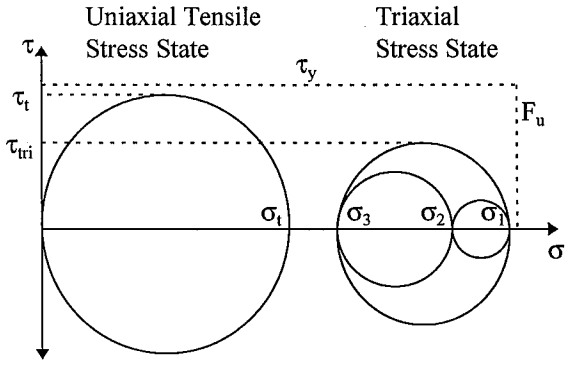

Figure 5.72: Uniaxial Tensile and Triaxial 3-D Stress States Using Mohr's Circle [after (Cook and Young, 1985)]

5.4 The Effect of Strain Concentrations at the Root of the Access Hole

The effects of the geometry of the welded girder flange-to-column connections of the specimens are investigated near the root of the access hole in this section. Specifically, stress and strain concentrations at the root of the bottom access hole are correlated with the locations and types of low-cycle fatigue connection failures seen in the tests. The stress and strain concentrations are caused primarily by the restraint offered by the girder web, column web, and column flange, and by a sudden change in cross section near the access hole. These studies are conducted by employing results from experimental and computational strain distributions and acoustic emission activity.

5.4.1 Connection Performance and Failure Mechanisms

Figures 5.73-5.78 illustrate the girder plastic moment-rotation hysteresis curves of the East connection of Specimen 1 and the East and West connections of Specimen 3, along with a view of their failure zones. These connections, which did not possess bottom backup bars, exhibited low-cycle fatigue type rupture failures during the 3.0% drift levels (see Section 3.2). Each of these failures originated from the propagation of a tear located approximately one inch from the column flange within the bottom flange base metal near the root of the bottom access hole. Each tear ultimately severed the bottom girder flange from the weld region and the column flange.

It is evident that these connections attained higher levels of girder moment strength compared to the three connections that failed at the 1.5% drift cycles (see Section 3.2). However, their attained strength and ductility performance is marginal overall. In fact, the hysteretic behavior of the connections occurs for only a few cycles (one to two) at the 3.0% drift levels. The failure mechanism of these connections (and, therefore, inadequate connection performance) may be attributed largely to the presence of a strain concentration near the root of the bottom access hole.

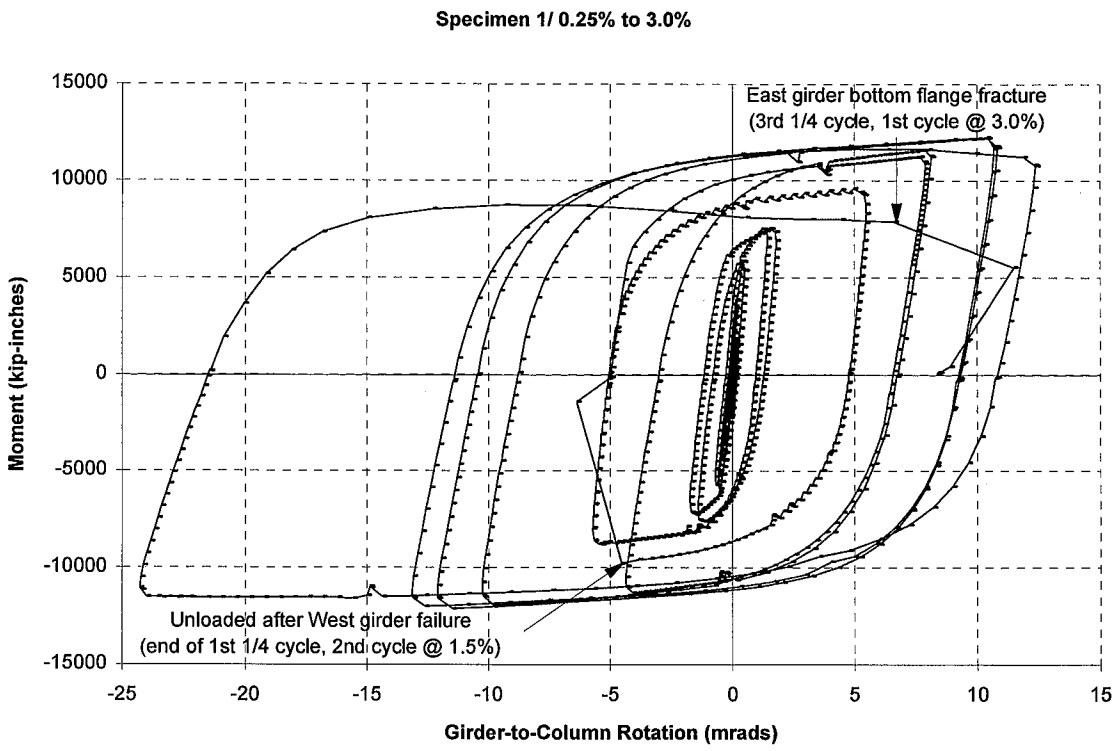

Figure 5.73: Girder-to-Column Moment-Rotation Curve (East Girder of Specimen 1)

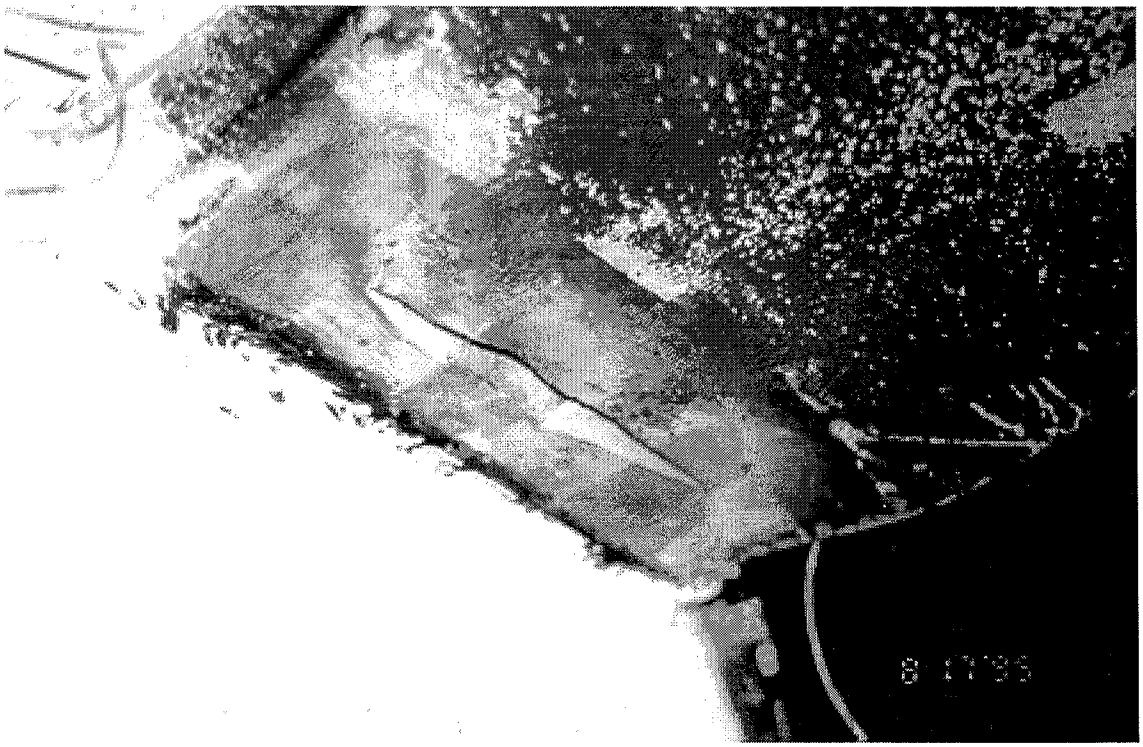

Figure 5.74: Rupture of Bottom Girder Flange (East Girder of Specimen 1)

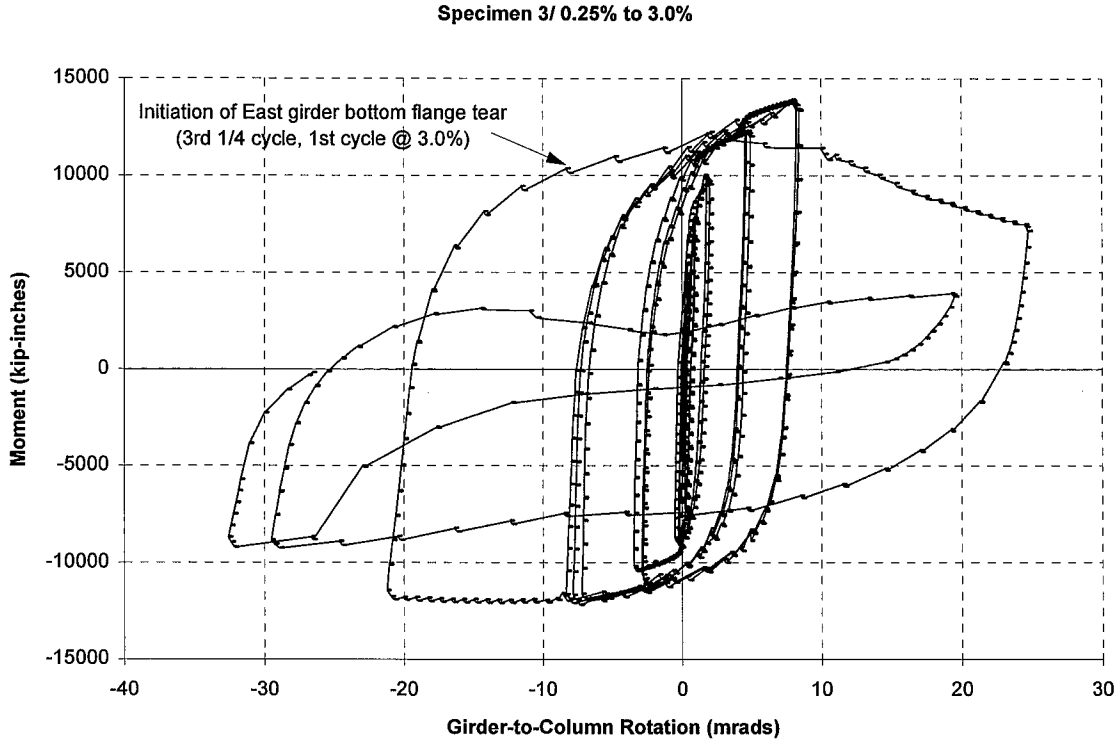

Figure 5.75: Girder-to-Column Moment-Rotation Curve (East Girder of Specimen 3)

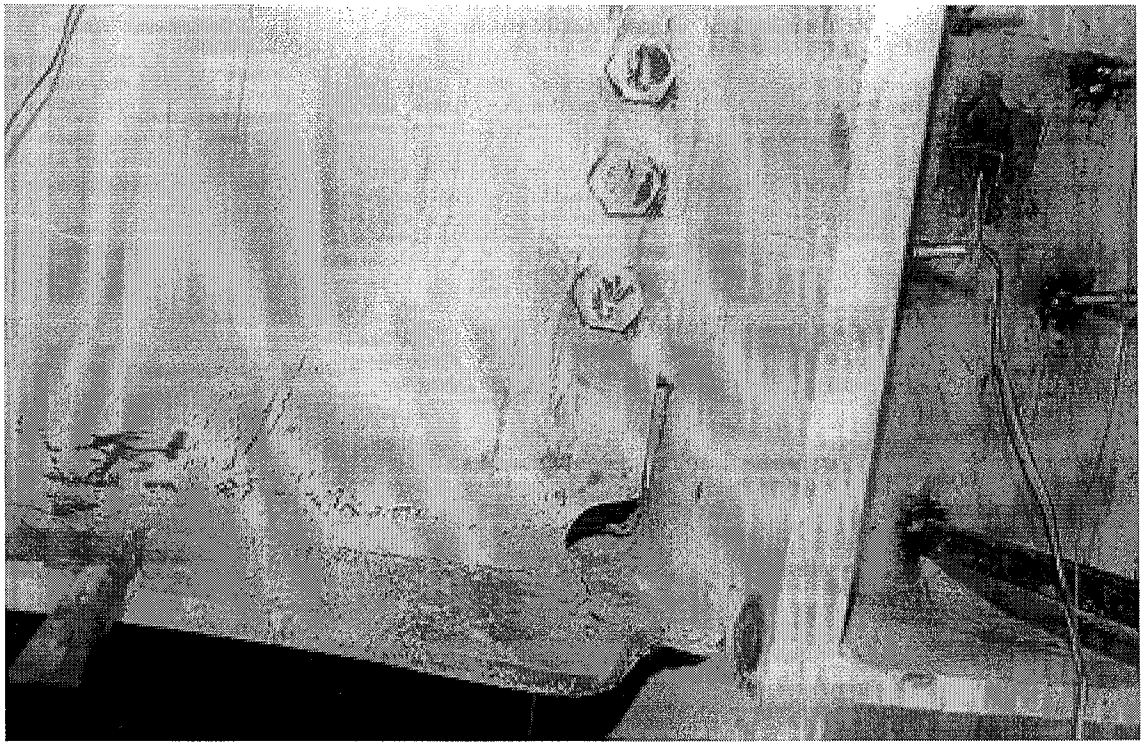

Figure 5.76: Rupture of Bottom Girder Flange (East Girder of Specimen 3)

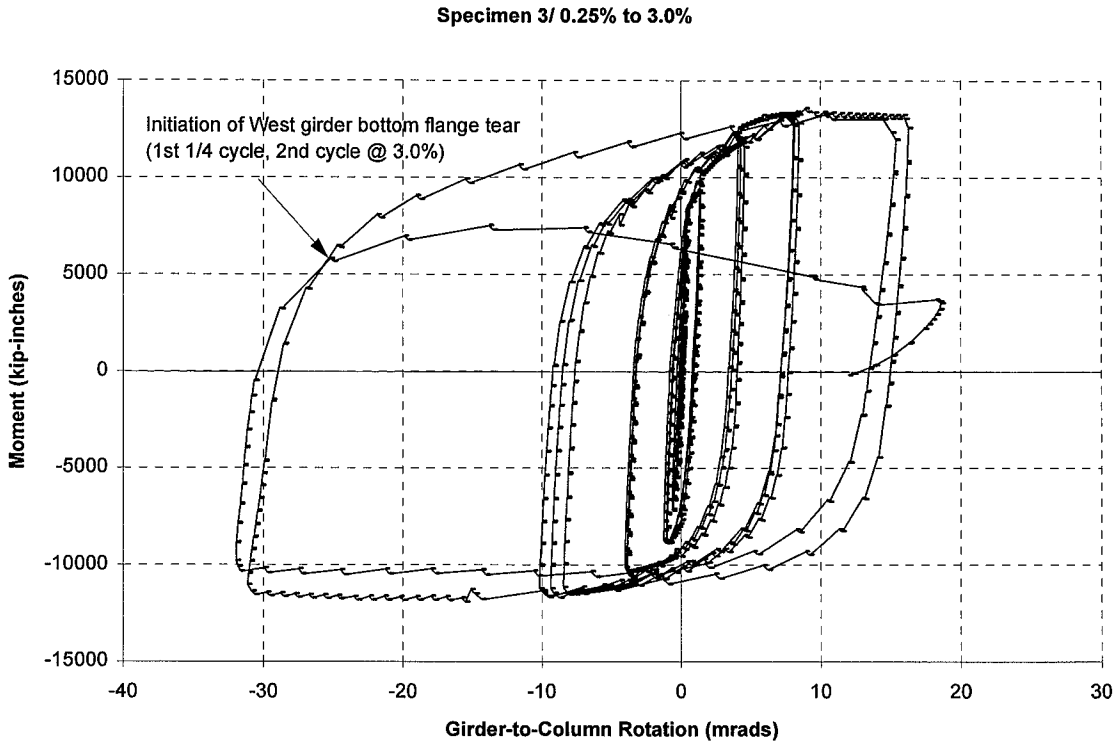

Figure 5.77: Girder-to-Column Moment-Rotation Curve (West Girder of Specimen 3)

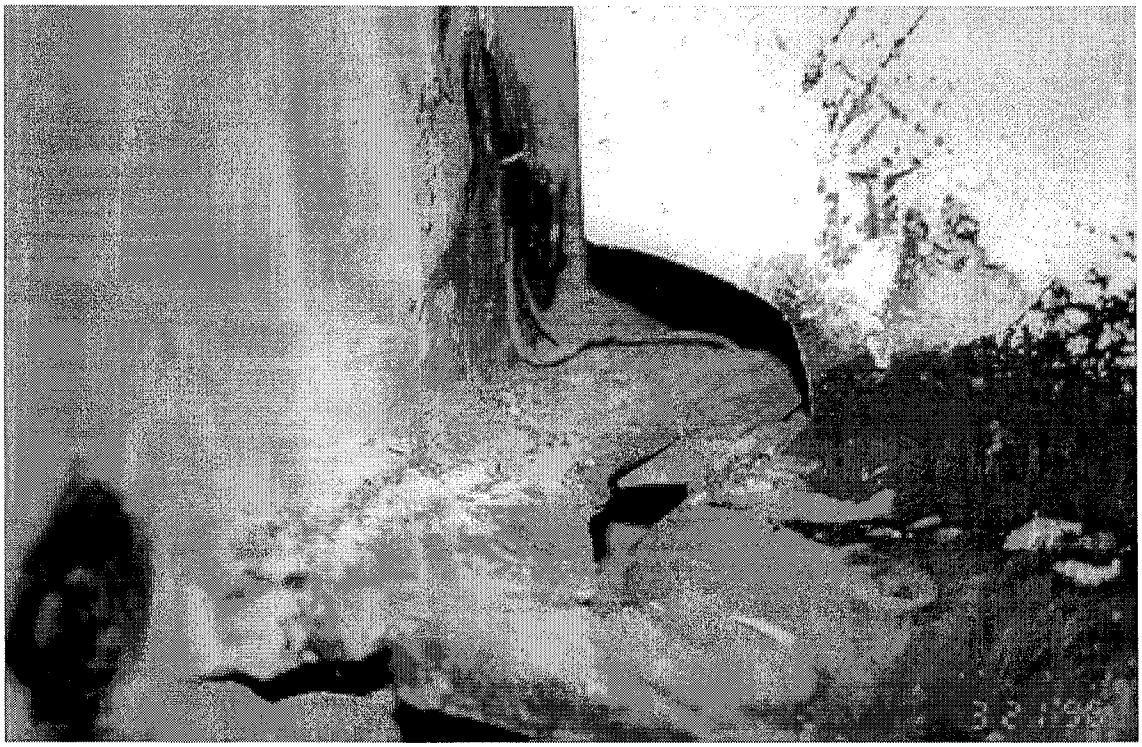

Figure 5.78: Rupture of Bottom Girder Flange (West Girder of Specimen 3)

5.4.2 Strain Concentrations Near the Root of the Bottom Access Hole

Based on a finite element continuum computational study, a strain concentration is seen to be prominent near the root of the bottom access hole. For example, the composite girder model exhibits strains in the longitudinal direction of the girder flange at the root of the access hole that are approximately 20 times greater than the longitudinal strains in the girder flange tips at the same cross section when subjected to positive bending at the 3.0% drift levels (see Figure 5.67).

Also, nearly all the connections of the tests specimens exhibit a strain concentration at the bottom surface of the bottom girder flange (directly below the root of the access hole). Figures 5.34-5.39 and 5.79-5.81 illustrate that the strains along the bottom of the bottom girder flange are substantially larger near the center of the flange (gages hse3b, hsw3b) than near the flange tips (gages hne2b, hnw2b, hse4b, hsw4b) during the 0.75% to 3.0% drift levels. This is despite the presence of continuity plates in all the specimens. The only connection not exhibiting this behavior is the West girder of Specimen 3, which demonstrates larger strain amplitudes at the North flange tip (hnw2b) than near the center of the bottom flange (hsw3b) (see Figure 5.81). Note that the strain amplitudes prior to failure of the East connection of Specimen 1 and the East and West connections of Specimen 3 reach approximately 60,000 $\mu\varepsilon$ during the 3.0% drift levels. A more comprehensive comparison of the strain behavior of the connections (along with a corroborating AE study) and the failure characteristics of the connections is reported in Appendix H.

Recent studies have been conducted in response to the evidence of brittle crack initiations in W-shape sections due to current steel production methodologies (Tide, 1997). It is shown that regions near the "k"-area (near the web fillet region) of steel W-shapes possess high material hardness numbers, while exhibiting low fracture toughness properties and relatively high yield to tensile ratios (nominally exceeding 0.90). As shown in this research, the East girder of Specimen 3 exhibited larger hardness numbers

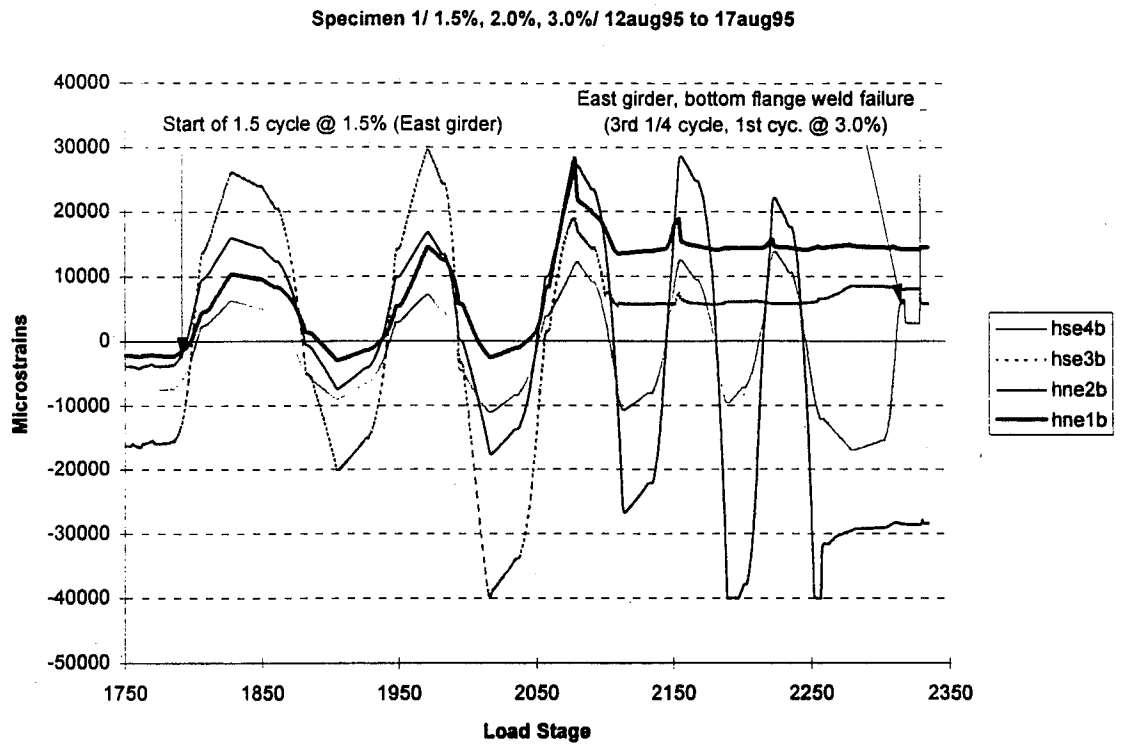

Figure 5.79: Girder Bottom Flange Strains (East Girder of Specimen 1)

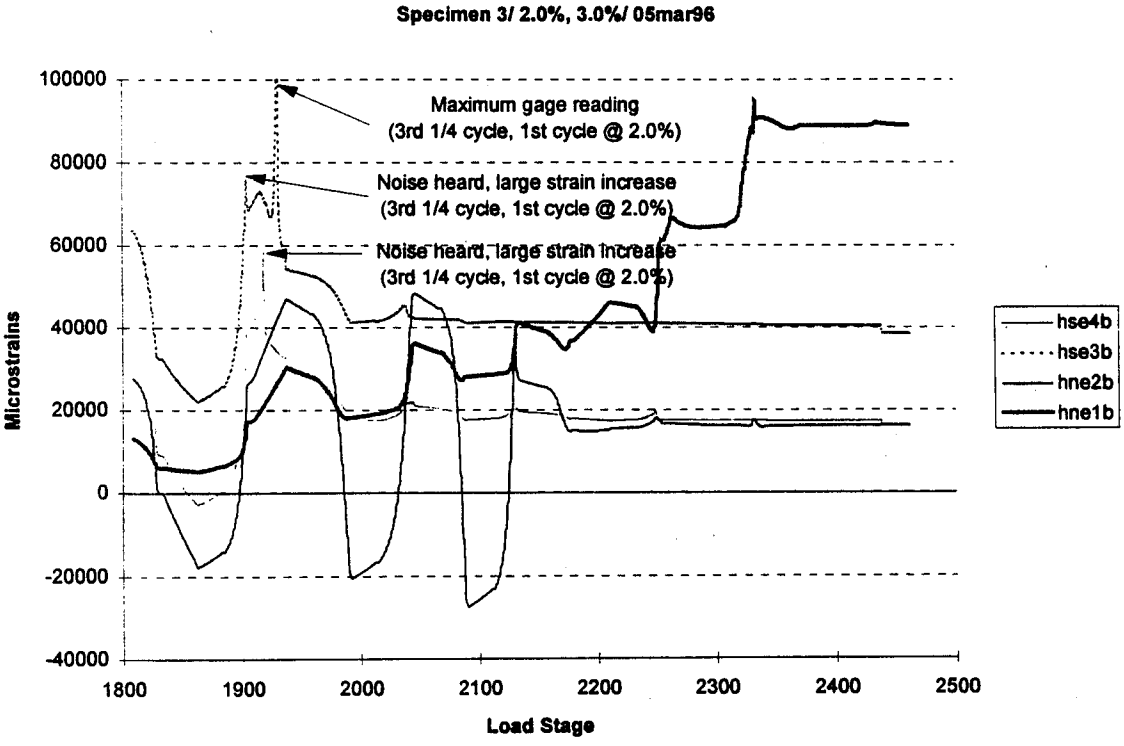

Figure 5.80: Girder Bottom Flange Strains (East Girder of Specimen 3)

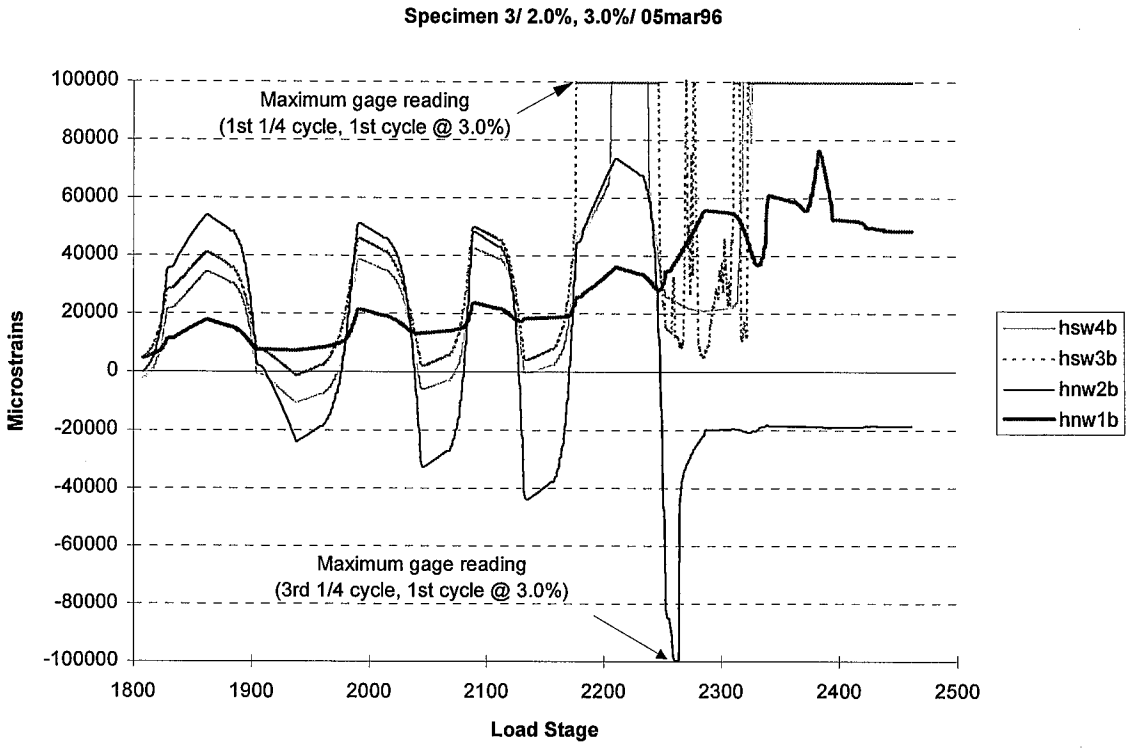

Figure 5.81: Girder Bottom Flange Strains (West Girder of Specimen 3)

near the "k"-area of both the top and bottom fillet regions (see Section 2.2.2). Furthermore, the region of increased hardness at the bottom fillet region is located at the root of the bottom access hole, where large stress concentrations were shown to exist, and where the initiation of fracture occurred for three of the six connections.

5.4.3 Acoustic Emission Activity Near Low-Cycle Fatigue Connection Failures

Acoustic emission activity occurs within the bottom girder flanges, especially near the center, in the East connection of Specimen 1 (see Figure 5.63 after a time of 700 seconds) and in the East and West connections of Specimen 3 prior to failure (see Figures 5.82-5.83). These events begin primarily during the 1.5% drift levels and increase in

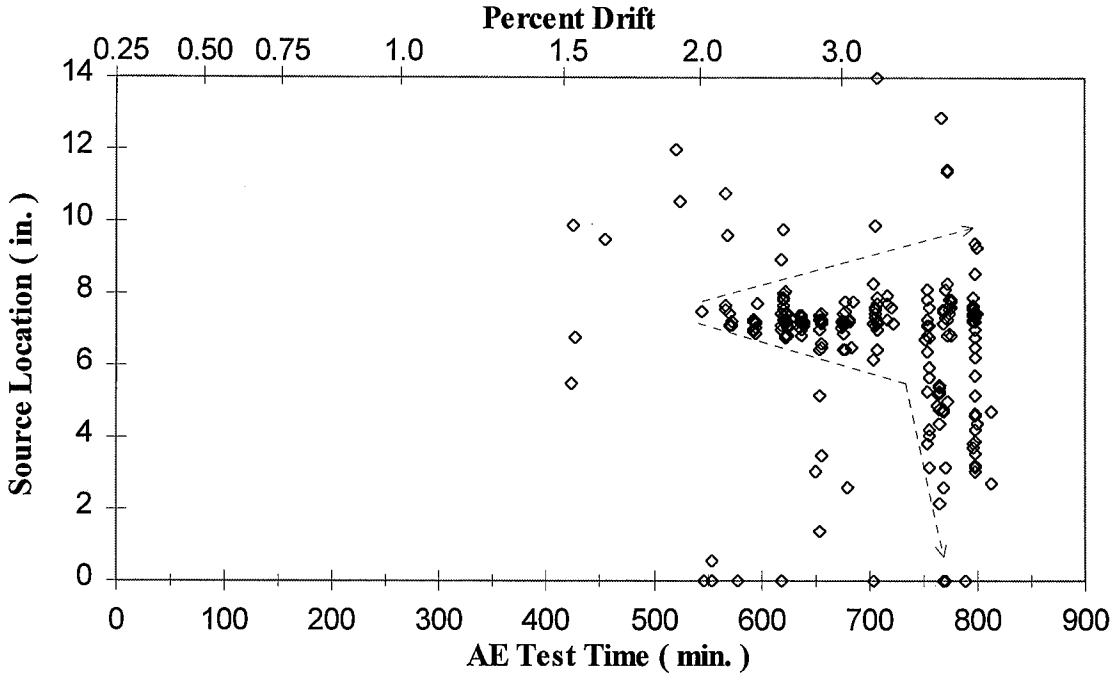

Figure 5.82: AE Event Source Location vs. Time (East Girder of Specimen 3)

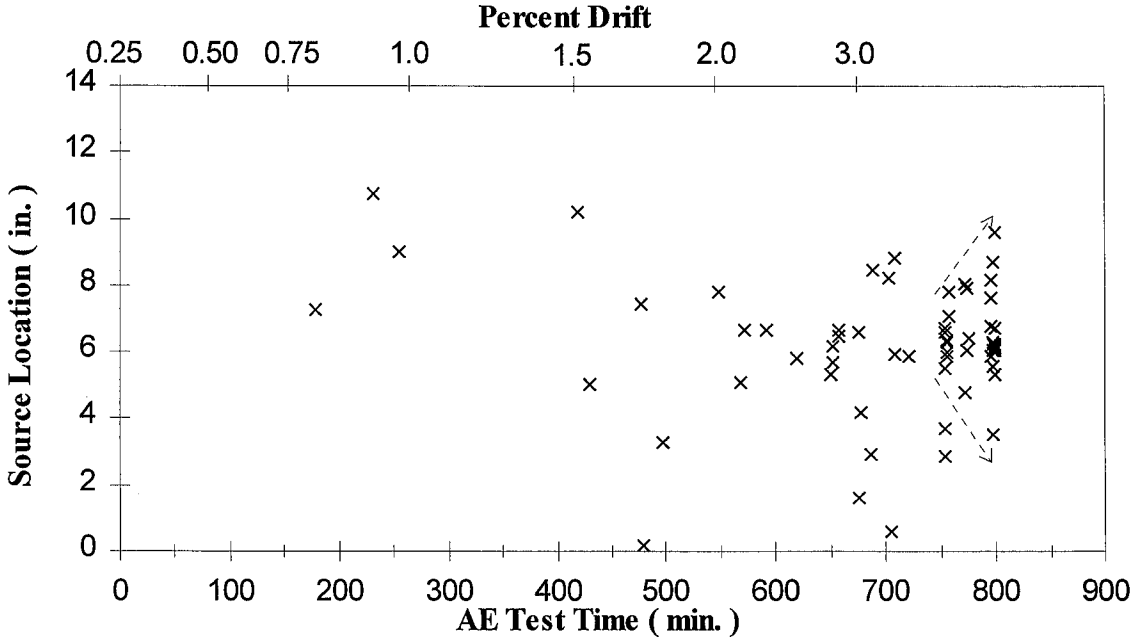

Figure 5.83: AE Event Source Location vs. Time (West Girder of Specimen 3)

frequency and spread across the girder flange width as the load histories progress. This type of behavior correlates with the low cycle fatigue type ruptures of the bottom girder flange metal of these connections, which initiate near the center of the bottom girder flanges and propagate out towards the flange tips.

Note that these connections, which did not possess bottom backup bars, demonstrate relatively less AE activity than the connections possessing bottom backup bars (see also Figures 5.82 and 5.83). It may be concluded that the failure of the connections exhibiting low-cycle fatigue type ruptures initiated early on in the load history (during the 1.5% drift levels), but did not demonstrate ultimate failure until the 3.0% drift levels. A more comprehensive study of the acoustic activity and strains measured along the cross section of each connection is reported in Appendix H and in (Carlson, 1997).

Chapter 6

Conclusions

The objectives of this research are to determine if the failure of pre-Northridge steel moment-resisting frame connections during the Northridge, California earthquake of January 17, 1994, occurred partly due to various structural characteristics of the connection. The connection failures occurred predominantly in the regions of the girder bottom flanges. Structural phenomena which may have contributed to the failures include the presence of composite floor slabs, the location of the shear tab along the girder cross section, the placement of a backup bar at the outside surface of the bottom girder flange, local bending and shearing of the bottom girder flange near the access hole, and the potential triaxial tensile strain or stress state caused by restraint in the connection region.

To accomplish the objectives of the research, both an experimental and a corroborating computational research program were undertaken at the University of Minnesota. The experimental research entailed the testing of three full-scale specimens representing interior steel moment-resisting frame subassemblies subjected to cyclic, quasi-static loading as well as to column axial tension loading. Two of the specimens possessed composite floor slabs (having 35% and 55% partially composite action), while the other specimen had bare steel girders. The computational research included three-dimensional geometrically and materially nonlinear continuum finite element analyses of the test specimens. Two computational models were employed, including a model of the bare steel girder specimen and of the composite girder specimen.

All six connections in this research failed in the region of the bottom girder flange by fracture, three by a brittle failure at the weld-column interface and three by a low cycle fatigue fracture of the base metal of the girder flange emanating from the root of the access hole. In addition, the bottom region of the connections in the composite specimens generally sustained significantly more damage compared to the top region (as evidenced by local flange buckling and extensive plastification at the bottom flange, and by the relative strain levels of the top and bottom flange regions).

The connections which failed by brittle fracture did so at an interstory drift of 1.5%, with plastic rotations in the range of 6 to 8 milliradians. The connections which failed by the low cycle fatigue fracture achieved 3.0% drift prior to fracture, but they sustained at most 3 cycle at this drift level, and they achieved plastic connection rotations of at most 25 milliradians. Only the bare steel strength was achieved by these three connections---the composite specimens did not achieve their nominal partially composite strength (based on measured material properties) computed as per (AISC, 1993). Thus, even though the three connections exhibiting low-cycle fatigue failures attained higher levels of girder moment strength and ductility than the three connections exhibiting premature, brittle fracture, their overall performance was marginal.

It is important to note that the nominal moment strength of the partially composite beams (AISC, 1993), assumes that the entire cross section of the steel beam participates in the transfer of forces into the column flange, whereas the girder shear tabs in the specimens are only bolted to the girder web (see Section 2.1.2). The moment strengths achieved by the composite girders may be compared to a computed girder strength which includes the resistance provided only by the girder flanges and the concrete slab. A calculation such as this may provide a better lower bound estimate of the nominal moment strength; however, other approaches for assessing nominal moment strength of these connections for comparison with the experimental results are possible as well, and should be the subject of future research.

Regardless of the method of calculation of a comparative value of moment strength, explanations for the inadequate performance of the connections may be

attributed partially to the presence of composite floor slabs, along with several other structural characteristics, which are discussed in the following sections.

6.1 Classification of Various Structural Phenomena Contributing to Connection Failure

The experimental results of this research, along with the corroborating computational results, verify that several structural phenomena resulted in extensive levels of straining and connection failure at the bottom connection regions of the test specimens. These structural conditions are related to vertical asymmetry through the girder cross section and in the connection, and are primarily due to the presence of a composite floor slab, and partially due to the location of the shear tab along the girder cross section, as well as other minor asymmetries (see Table 6.1).

Table 6.1: Structural Characteristics Affecting the Performance of the Test Specimens

Structural Characteristics	*Effect on Connection Performance*
Existence of Composite Floor Slab	Excessive straining at the bottom of the connection region
Location of the Shear Tab	
Existence of Bottom Backup Bars	Stress or strain risers at bottom backup bar-CJP weld interface
Restraint of the CJP Weld By the Column Flange and Girder Web	Triaxial state of tensile stress or strain near the bottom CJP weld
Restraint of the Girder Bottom Flange and a Sudden Change in Cross Section	Stress or strain concentrations near the root of the bottom access hole

Other structural characteristics may also contribute to the type and location of the connection failures, as well as to when the failures occurred (see Table 6.1). These structural conditions include the placement the bottom backup bar at the outside surface of the bottom girder flange, local bending and shearing of the girder flange near the

column flange surface, and the potential triaxial tensile stress state caused by restraint in the connection region. Furthermore, the application of axial tension to the column of steel moment frame connection may accentuate the effect of a state of triaxial tensile stress near these critical elements of the connection.

It may be concluded that the structural phenomena reported in Table 6.1 are primary contributors to the poor-to-marginal ductile performance of the connections and to the ultimate failure at the bottom flange region of the connections. The significance of each of these conditions is presented next by briefly correlating the experimental and computational results with these phenomena.

6.2 The Effect of Various Structural Phenomena on the Performance of the Specimens

6.2.1 The Presence of the Composite Floor Slabs

The presence of composite floor slabs may have a significant effect on the local behavior of steel moment-resisting frame connections. The strains and forces sustained by the key connecting elements of the connection (i.e., the full penetration welds in the case of SMRFs) depend upon how the slabs contribute to the transfer of forces into the connections. Therefore, the number of shear studs, along with friction and bearing of the slab against the column flange, all contribute to the behavior of SMRF connections.

Both the experimental and computational results clearly demonstrate a significant increase in straining in the bottom flange region of the connections possessing composite floor slabs (see Section 5.1). As indicated in the experimental results, the strains near the bottom access hole connection regions in the composite girders of Specimens 2 (55% composite) and 3 (35% composite) were up to six times higher than the strains near the top access hole connection regions during their load histories. This behavior may also be observed by noting the significant shift of six to eight inches in the neutral axis along the

girder cross section of the composite girders during positive bending at a distance of 13.5" from the column face. The predominance of strain concentrations near the bottom flanges of the composite girders is confirmed by the finite element continuum computational study and by visual documentation.

A noticeable increase in compressive straining near the column flange-concrete slab interface is evident during positive girder bending due to bearing of the slab, based on strains measured along several locations within the concrete slabs of Specimens 2 and 3. Also, it was observed that the majority of the concrete crushing occurred near the column-concrete slab interface, and that for each specimen, concrete cracks originated at the column flange tip and extended diagonally away from the column flange towards the edge of the concrete slab. These results help to explain the predominance of bottom flange failures during the earthquake, and they indicate that unintended composite floor action should be considered in the design of these types of connections.

It is interesting to note that the location of the neutral axis along the girder cross section at 13.5" from the column face was similar between the composite girders of Specimen 2 (designed as 55% partially composite) and of Specimen 3 (designed as 35% partially composite) during girder positive bending. In addition, based on studying the strains and moments at this same position along the girder cross section (see Section 4.3), the composite girders of Specimens 2 and 3 are shown to exhibit similar levels of composite action. This similarity in attained composite action may be related to the relatively small difference between the computed girder moment strengths of the two specimens (they differed by only approximately 6%; see Table 3.3). Also, the estimated flexural rigidities of the girders of the composite specimens, $I_{eff}E_s$, were relatively similar (the effective moments of inertia differed by only approximately 9%; see Appendix A).

It is also shown from the girder tip deflection calculations, which verified a portion of the experimental results (see Section 4.2), that the calculation of the effective moment of inertia of partially composite girders may be overestimated using current design methodologies (AISC, 1993), just as may the composite moment strength (see Section B.1). Finally, evidence of the participation of the concrete slab under tension

was observed during girder negative bending during the low drift cycles for the composite girders (see Section G.2.5).

6.2.2 The Location of the Shear Tab Along the Girder Cross Section

The location of the shear tab along the cross section is another characteristic of asymmetry which affects the structural behavior of the connection. For example, the bare steel girders of Specimen 1 demonstrated somewhat larger strains in the bottom flange than in the top flange close to the CJP welds (up to 1 to 1.5 times in magnitude) and exhibited yielding and local buckling predominantly at the bottom girder flange region. This implies that the placement of the shear tab on the web, the only predominant asymmetry in the specimen, may have a moderate effect on the transfer of moment along the girder cross section, though not nearly as significant as the presence of composite floor slabs.

6.2.3 The Existence of Bottom Backup Bars

The presence of backup bars at the base of the CJP welds is believed to lead to crack initiation in the region and to poor weld root penetration. Since there are several conditions which may have contributed to how and when the connections in this research failed, it can be only speculated as to what effect the presence of backup bars may have had on the failure mechanisms of the six connections. However, the West connection of Specimen 1 (bare steel specimen) and the East and West connections of Specimen 2 all failed prematurely by brittle fracture, although the locations of these fractures vary within the HAZ of the weld region. These connections all possessed backup bars at the bottom flange, which may have created conditions which contributed to the premature fractures of the bottom welds.

In the pre-Northridge connections, a backup bar is typically placed at the bottom side of the girder bottom flange and at the bottom side of the girder top flange. It was

observed that the strains at the bottom surface of the girder bottom flange were significantly larger than the strains at the top surface of the girder bottom flange for all three specimens during girder positive bending (see Section 5.2.3). This condition, which may be attributed to local phenomena such as a shearing or bending effect of the girder bottom flange during positive girder bending, is not as accentuated at the top welded girder-to-column connection (see Section 5.2.3). Therefore, it is concluded that the localized bending phenomenon may have resulted in a larger strain concentration near the root of the bottom CJP weld rather than near the top CJP weld for a given displacement increment.

There are other possible conditions that may have contributed to the premature, brittle fracture of welded girder-column connections that possess backup bars. For example, it is possible that a higher strain condition may have existed within the HAZ than what was shown by the strains in the bottom girder flange, due to a notch or crack that initiated near the root of the weld. This geometric discontinuity would occur due to the presence of a backup bar at the base of the welded girder-to-column connection and may contribute to the explanation as to why the three connections with bottom backup bars fractured brittlely, while the three connections without bottom backup bars did not. It is also possible that the strains within the HAZ were represented by the strains measured in the bottom flange, but that the fracture toughness within the HAZ was substantially lower than the weld and base metal surrounding it (Fisher et al., 1995).

6.2.4. The Restraint of Critical Connection Elements

Due to restraint by the girder web, a change in cross section exhibited by the access holes, and the presence of column axial tension, a reduction in shear flow (and thus yielding) may be prominent near critical elements of the connections in the region of the girder bottom flange. In particular, the effects of the possible existence of a triaxial state of tensile stress or strain in the region of the bottom weld of the girder bottom flange-to-column connection during positive girder bending was investigated in this

research. The weld region for these types of connections is believed to be highly restrained through the length and the transverse direction of the column flanges, thereby potentially leading to a multiaxial state of both stress and strain (Blogdett, 1995). Furthermore, the columns in these specimens are subjected to axial tension, thereby magnifying a triaxial stress condition. Such a triaxial state of tensile stress may have contributed to the brittle failure modes of the weld in these specimens, due to the minimization of plastic shear flow (i.e., ductile yielding) prior to fracture.

Based on an analysis of the strains near the bottom CJP weld of the connection, it was observed in all three tests that a triaxial state of stress appears to be present within the proximity of the SE and SW girder bottom flange-column flange welds (see Section 5.3). Strain concentrations near this region of the connection were also verified computationally with a finite element continuum model. The application of 550 kips of axial tension to the column appeared to have a minimal effect on the state of stress and strain near the bottom CJP weld, due partially to the relatively small magnitude of the applied load ($P/P_y = 0.15$). The column axial stress, increased several ksi due to the axial load, but no substantial change in behavior in the weld region was seen. Also, no correlation was made between the three connections exhibiting brittle failure modes and the existence of a triaxial state of tensile stress (i.e., to a possible breaching of the ultimate tensile stress prior to breaching of the shear yield stress) near the bottom CJP weld region.

The presence of large stress concentrations near the girder flange base material and the access hole of the bottom connection is also evident, primarily due to the change in geometry of the access hole (see Section 5.4). This conclusion is based on the results of both experimental and computational studies of the strain behavior near this region. Based on the strains measured at various locations along the girder cross section and the acoustic emission analysis data that was measured in the connections, the connections which failed by low cycle fatigue fracture initiated failure near the bottom access hole within the base metal of the girder bottom flange. It was also evident that the strains near the access holes were, in general, much larger than those near the flange tips.

In addition, during the earliest cycles of loading, these strains close to the column face were consistently seen to be several times higher than the strains calculated due strictly to flexure of the girder assuming Euler-Bernoulli beam theory. This indicates a concentration of strains within the flanges of the connection (Goel et al., 1996). From a practical standpoint, these strain concentrations mean that it is possible that the full plastic moment capacity cannot be reached for beams near the 70% flange moment capacity limit, even considering the effect of strain hardening. This was clearly seen in the poor performance of all three test specimens in positive bending.

6.2.5 Construction Limitations and Metallurgical Phenomena

It is important to note that other conditions may have contributed to the failures within the bottom connection regions. For example, deficiencies in welding workmanship may have occurred near the bottom access hole, where it is the most difficult to effectively place the weld. These welds are placed with two passes, each generally extending from the flange tips and terminating below the bottom access hole. These termination points may act as locations of substandard root penetration, resulting in crack initiations and poor weld ductility (Kaufmann et al., 1996).

Past research has investigated the effects of several metallurgical conditions, such as deficiencies in material toughness and hardness within the HAZ of CJP welds and near the web-flange junction of jumbo-sized W-shape sections (Yura and Ulloa, 1994; Fisher et al., 1995). These studies have also been conducted in response to the recent evidence of brittle crack initiations in W-shape sections due to current steel production methodologies (Tide, 1997). It is shown that regions near the "k"-area (near the web fillet region) of steel W-shapes possess high material hardness numbers, while exhibiting low fracture toughness properties and relatively high yield to tensile ratios (nominally exceeding 0.90). The W27X94 girder employed in the design of the specimens in this research, which possesses a relatively thin through thickness, also exhibited larger hardness numbers near the "k"-area of both the top and bottom fillet regions (see Section 2.2.2). Furthermore,

the region of increased hardness at the bottom fillet region is located at the root of the bottom access hole, where large stress concentrations exist, and where the initiation of fracture occurred for three of the six connections.

6.3 Closing Remarks

Due to the damage sustained to steel-framed structures during the 1994 Northridge earthquake, it is apparent that changes must be made to the current design provisions for designing steel moment-resisting frame connections in seismic zones. Such changes would take into account several factors, including structural and metallurgical conditions unique to these type of connections. The structural phenomena investigated in this research, especially the presence of composite floor slabs, were shown to have a significant effect on the behavior, strength, ductility, and failure mechanisms of the tested connections. While the specific connection failure modes themselves correlated best with the presence of a backup bar at the bottom girder flange, the behavior of the connections in general, and of the bottom girder flange in particular, clearly showed the influence of the structural phenomena discussed in this report, and led to the marginal performance of even the most well-behaved of the connections tested.

Despite the possible effects on various connection responses, the effects of composite floor slabs are currently not included in the design of lateral-load resistant steel frame systems in the U.S. Some of the other structural phenomena discussed in this research have been addressed in current design methodologies recommended by the SAC Advisory Committee (SAC, 1996b). For example, the removal of backup bars from critical regions of moment-resisting connections is stated in order to minimize potential stress risers and notch effects (note, however, that this research indicates that the removal of the backup bar alone may be insufficient for eliminating fracture from these connection details). Also, weld filler metals with rated toughness values are suggested. In addition, an appropriate proportioning of column-girder connections is desired such that inelastic behavior occurs at a location away from the column face. Ultimately, however, the research reported here in indicates that it is prudent to establish a connection design which, at a minimum, takes into account the inherent asymmetries in the connection region due to the presence of a concrete floor slabs.

Appendix A

Effective Moment of Inertia

Because the testing procedure simultaneously loaded one composite girder in positive bending while loading the other in composite girder in negative bending, different moments of inertia are exhibited by each girder for a given loading ramp. The moment of inertia of each girder is used in several studies related to this research and is referred to in several of the following appendices.

To simulate a typical composite floor slab used in interior frame systems, a partially composite design procedure (AISC, 1993) was followed to compute the positive bending effective moment of inertia for both Specimens 2 and 3. Note that for these specimens the term "fully composite action" does not imply that the section will attain full plastification of the steel section due to positive bending moment (i.e., the slab properties controlled the strength calculation for fully composite action, although the percent composite is still computed relative to $A_s F_y$ of the steel section). The modulus of the concrete slab is calculated as $E_c = 57{,}000(f_c')^{1/2}$(ACI, 1995). Using compressive strengths, f_c', from the day of testing, the modulus of concrete for Specimens 2 and 3 was calculated as 3994 ksi and 3796 ksi, respectively (see Section 2.2.3).

In this procedure, an elastic centroidal distance, y_e, is first determined for a transformed moment of inertia for a fully composite section. The position of the elastic neutral axis is dependent upon the compressive resistance of the concrete and the steel reinforcement, and the tensile resistance of the steel girder:

$$y_e = \frac{ab_e\left(d + t_s - \frac{a}{2}\right) + A_s n\frac{d}{2} + N_{bars}\frac{1}{4}\pi d_{bar}^2(d + t_s - cover)n}{ab_e + A_g n + N_{bars}\frac{1}{4}\pi d_{bar}^2 n} \quad \text{(A.1)}$$

where a = effective thickness of concrete slab (in.)

b_e = width of effective concrete slab (in.)

d = depth of steel section (in.)

d_{bar} = diameter of #4 steel reinforcement (in.)

n = modular ratio = E_s/E_c

$cover$ = top concrete cover of steel reinforcement (in.)

t_s = thickness of slab measured from the top of the concrete slab to the top of the steel girder (in.)

A_s = gross area of steel section (in^2)

E_s = modulus of elasticity of steel

N_{bars} = number of reinforcement bars

Values for the parameters a, b_e, d, d_{bar}, $cover$, t_s, A_s, E_s, and N_{bars} are taken as 4.0", 60", 26.92", 0.50", 1.5", 5.0", 27.7", 29,000 ksi, and 6, respectively (see also Appendix K). For Specimens 2 and 3, the value of n is equal to 7.26 and 7.64, respectively. The elastic neutral axis during girder positive bending is equal to 22.57" and 21.27" for Specimens 2 and 3, respectively, measured from the bottom of the girder.

The transformed moment of inertia, I_{tr}, for a fully composite section is then calculated using the strong axis bending moment of inertia, I_{xx}, for a W27X94 steel section to obtain Eq. A.2:

$$I_{tr} = I_{xx} + A_s\left(y_e - \frac{d}{2}\right)^2 + N_{bars}\frac{1}{4}\pi d_{bar}^2(d + t_s - cover - y_e) + \frac{1}{12n}a^3 b_e + ab_e\left(d + t_s - \frac{a}{2} - y_e\right)^2 \quad \text{(A.2)}$$

The transformed moment of inertia for positive bending of the girders is equal to 7471 in^4 and 7378 in^4 for Specimens 2 and 3, respectively.

The horizontal shear capacity at the steel-concrete interface of each composite girder is required before calculating an effective moment of inertia. For Specimen 2, twenty-two 3/4" diameter headed shear stud connectors were welded in pairs spaced evenly along the top flange of each girder, between the column face and the point of applied load (see Section 2.1.3). For Specimen 3, fourteen shear connectors were welded to the steel girder. The shear capacity of one shear stud connector, Q_n, is expressed in kips as (AISC, 1993):

$$Q_n = \min\begin{Bmatrix} 0.5A_{sc}\sqrt{E_c f_c'} \\ A_{sc}F_{uc} \end{Bmatrix} \tag{A.3}$$

The minimum specified tensile strength of one shear connector, F_{uc}, is equal to 60 ksi and the cross-sectional area of a 3/4" shear stud connector, A_{sc}, is equal to 0.442 in^2. Q_n is equal to 26.51 kips for both Specimens 2 and 3 since the nominal strength of one shear connector governed in Eq. A.3 for both specimens. The compressive force in the concrete slab (in kips), C, is governed by the smallest of three cases: steel section yielding, concrete slab compression crushing, and shear stud yielding (AISC, 1993):

$$C = \min\begin{Bmatrix} Q_n N_{sc} \\ A_s F_y \\ 0.85A_c f_c' \end{Bmatrix} \tag{A.4}$$

The number of shear connectors, N_{sc}, is equal to 22 and 14 for Specimens 2 and 3, respectively, and F_y = 38 ksi, based on tensile coupon tests (see Section 2.2.1). The effective concrete area, A_c, is equal to 240 in^2 for Specimens 2 and 3. A_c is equal to the product of the effective width, b_e, of 60", and the maximum effective thickness, a, of 4".

For both Specimens 2 and 3, yielding of the shear connectors governs the value of C from Eq. A.4. For Specimens 2 and 3, C is equal to 583.2 kips and 371.1 kips, respectively.

The effective moment of inertia for a partially composite section loaded in positive bending can be expressed using the section shear stud capacity, the moment of inertia for the steel section, the transformed moment of inertia (Eq. A.2) and the compressive force in the concrete slab (Eq. A.4) (AISC, 1993):

$$I_{eff} = I_{xx} + \sqrt{\frac{Q_n N_{sc}}{C}}(I_{tr} - I_{xx}) \tag{A.5}$$

For Specimens 2 and 3, the effective moment of inertias for positive bending are equal to 6476 in^4 and 5901 in^4, respectively.

The negative bending moment of inertia design for Specimens 2 and 3 includes only tensile and compressive forces from the steel reinforcement and the W27X94 steel section (i.e., tensile forces in the concrete are ignored). The position of the elastic neutral axis is calculated as:

$$y_e = \frac{A_s n \frac{d}{2} + N_{bars} \frac{1}{4} \pi d_{bar}^2 (d + t_s - cover) n}{A_s n + N_{bars} \frac{1}{4} \pi d_{bar}^2 n} \tag{A.6}$$

For negative girder bending, the elastic neutral axis is equal to 14.15" for both Specimens 2 and 3.

The transformed moment of inertia during girder negative bending is given by:

$$I_{tr} = I_{xx} + A_s \left(y_e - \frac{d}{2} \right)^2 + N_{bars} \frac{1}{4} \pi d_{bar}{}^2 (d + t_s - cover - y_e) \tag{A.7}$$

During girder negative bending, I_{tr} is equal to 3595 in^4 for both Specimens 2 and 3. The parameters in Eqs. A.6 and A.7 were previously defined in the moment of inertia procedure for girder positive bending. All values calculated with Eqs. A.1 through A.7 are tabulated in Table A.1 for Specimens 2 and 3. Note that * terms represent values that governed as minimum values for Eqs. A.3 and A.4.

Table A.1: Composite Girder Strength and Stiffness Parameters

Parameter	Girder Bending	Equation	Specimen 2	Specimen 3
f_c' (psi)	Positive/Negative	measured	4910	4436
E_c (psi)	Positive/Negative	$57{,}000\sqrt{f_c'}$	4.901X10^6	3.994X10^6
y_e (in.)	Positive	Eq. A.1	22.57	21.27
I_{tr} (in^4)	Positive	Eq. A.2	7471	7378
Q_n (kips)	Positive	Eq. A.3	26.51	26.51
	Positive	$0.5A_{sc}\sqrt{E_c f_c'}$	30.95	28.68
	Positive	$A_{sc}F_{uc}$	26.51*	26.51*
C (kips)	Positive	Eq. A.4	583.2	371.1
	Positive	$Q_n N_{sc}$	583.2*	371.1*
	Positive	$A_s F_y$	1053	1053
	Positive	$0.85A_c f_c'$	1002	904.9
Composite Action (%)	Positive	$C/A_s F_y$	55	35
I_{eff} (in^4)	Positive	Eq. A.5	6476	5901
y_e (in.)	Negative	Eq. A.6	14.15	14.15
I_{tr} (in^4)	Negative	Eq. A.7	3595	3595

* Governing values for the given parameter

Appendix B

Girder-to-Column Plastic Moment and Rotation

This appendix discusses the procedures followed to generate experimental girder moment and rotation values from measured loads and LVDT displacements. These values are used to study the behavior of the connection based on the strength and ductility performance of the girders. The maximum girder strength achieved during testing is also compared to the computed moment strength for each girder (see Chapter 3).

B.1 Computed Girder Moment Strength

The nominal plastic moment strengths of each girder for girder positive and negative bending are calculated in this section as $M_p^{+}{}_{calc}$ and $M_p^{-}{}_{calc}$, respectively (AISC, 1993). For the bare steel girders of Specimen 1, the plastic modulus of a W27X94 W-shaped steel section, $Z_x = 278$ in^3, and the yielding stress of the steel, $F_y = 38$ ksi (see Section 2.2.1), are used such that:

$$M_{p\,calc} = Z_x F_y \tag{B.1}$$

and $M_{p\,calc}$ is equal to 10,560 kip-in.

For the partially composite girders of Specimens 2 and 3, the calculation of $M_p^{+}{}_{calc}$ and $M_p^{-}{}_{calc}$ involves several steps (AISC, 1993). First, the tensile strength of the upper flange region, P_{yf}, is calculated:

$$P_{yf} = \frac{1}{2}\left[P_y - (d - 2t_f)t_w F_y\right] \tag{B.2}$$

where d = depth of W27X94 steel section (in.)

t_f = thickness of flange of W27X94 steel section (in.)

t_w = thickness of web of W27X94 steel section (in.)

F_y = yielding strength of W27X94 steel section (ksi)

$P_y = A_s F_y$ = tensile strength of the steel section (kips)

Values for the variables in Eq. B.2 are summarized in Appendix K. The value of P_{yf} is 289.5 kips.

The location of the plastic neutral axis for positive girder bending, y_p, is then calculated within the top flange or within the web by using expressions that sum the forces along the girder cross section (see Figure B.1):

$$y_p = \left\{ \begin{array}{l} \dfrac{(P_y - C)t_f}{2P_{yf}} \quad if\, y_p \le t_f \\ \dfrac{2t_f t_w F_y + P_y - C - 2P_{yf}}{2F_y t_w} \quad if\, y_p \ge t_f \end{array} \right\} \tag{B.3}$$

Note that y_p is measured from the top of the top flange towards the bottom flange of the steel section. Values for C, the compression force in the concrete slab, are summarized in Appendix A. For the composite girders of Specimen 2 and 3 subjected to positive girder bending, y_p is computed as 0.604" (located in the top flange) and 3.50" (located in the web), respectively.

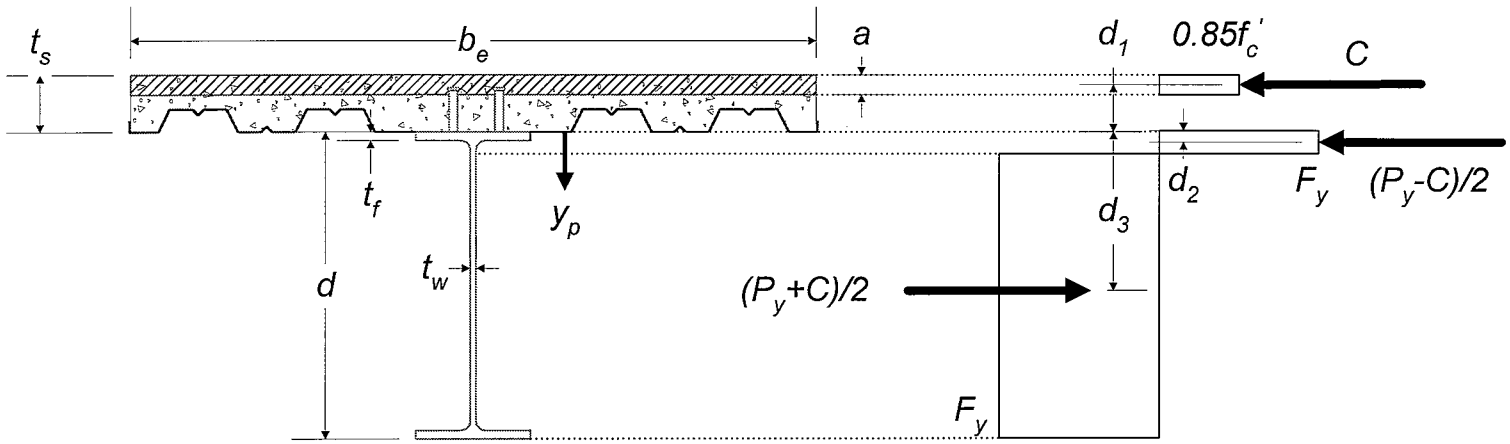

Figure B.1: Composite Girder Plastic Stress Distribution (Positive Bending) [after (AISC, 1993)]

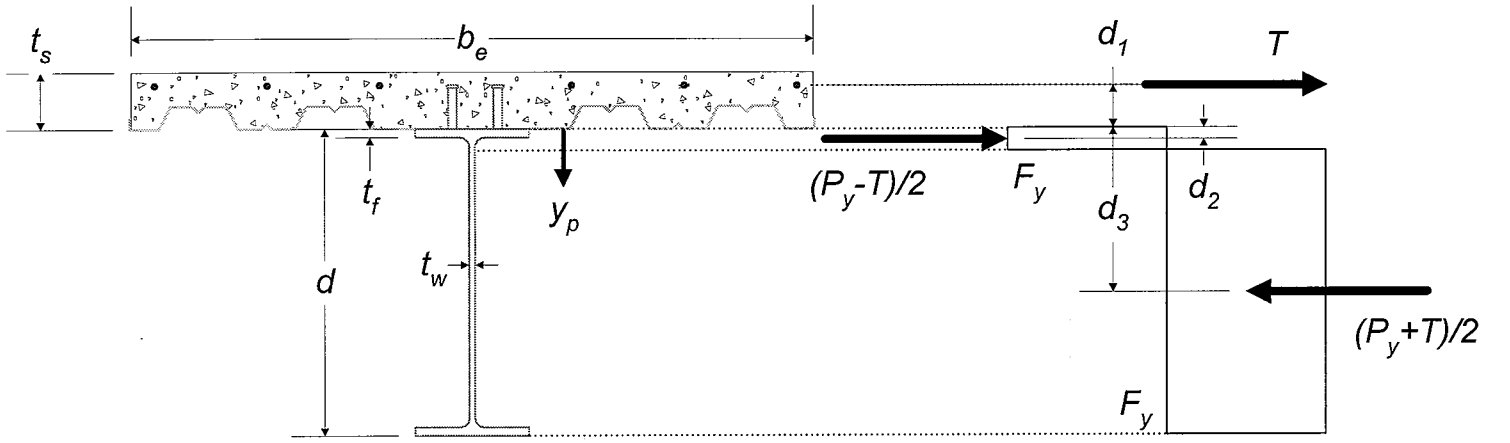

Figure B.2: Composite Girder Plastic Stress Distribution (Negative Bending) [after (AISC, 1993)]

Next, the effective depth of the concrete slab, a, is computed using the compression force in the concrete slab (in kips), C, the effective width of the concrete slab (in inches), b_e, and the compressive strength of the concrete (in ksi), f_c' (see Appendix A):

$$a = \frac{C}{0.85 f_c' b_e} \tag{B.4}$$

This depth is then used to calculate the distance from the centroid of the compression force, C, (acting at the mid-depth of the effective depth) to the top of the steel section:

$$d_1 = \left(t_s - \frac{a}{2} \right) \tag{B.5}$$

where t_s = thickness of concrete slab measured from the top of the concrete slab to the top of the steel section (in.)

Finally, the nominal plastic moment strength of each partially composite girder, $M_p^+{}_{calc}$, is computed for positive girder bending (AISC, 1993):

$$M_{p\,calc}^{+} = C(d_1 + d_2) + P_y(d_3 - d_2) \tag{B.6}$$

where d_2 = distance from the centroid of the compression force in the the steel section to the top of the steel section (in.)

d_3 = distance from P_y to the top of the steel section (in.), or *d/2*

For the composite girders of Specimens 2 and 3 subjected to positive girder bending, the nominal plastic moment strength is calculated to be 16,260 kip-in. and 15,290 kip-in., respectively.

The location of the plastic neutral axis for girder negative bending, y_p, is calculated as either within the top flange or within the web by using expressions that sum the forces along the girder cross section (see Figure B.2):

$$y_p = \begin{Bmatrix} \dfrac{(P_y - T)t_f}{2P_{yf}} & if\, y_p \le t_f \\ \dfrac{2t_f t_w F_y + P_y - T - 2P_{yf}}{2F_y t_w} & if\, y_p \ge t_f \end{Bmatrix} \tag{B.7}$$

Note that y_p is measured from the top of the top flange towards the bottom flange of the steel section. The tension force in the concrete slab, T, is equal to the minimum of the yielding tensile resistance provided by the reinforcing bars or the ultimate tensile resistance provided by the shear connectors (see Appendix A) (AISC, 1993):

$$T = \min\begin{Bmatrix} A_r F_{ry} \\ N_{sc} Q_n \end{Bmatrix} \tag{B.8}$$

where A_r = cross sectional area of reinforcing bars (in^2)

F_{ry} = yielding stress of reinforcing bars (ksi)

N_{sc} = number of shear studs per girder

Q_n = shear capacity of one shear stud connector (kips)

For the composite girders of Specimen 2 and 3 subjected to negative girder bending, the tension force, T, is governed by the strength of the steel reinforcing and equals 70.69 kips, and y_p is computed as 11.56" (located in the web).

The distance, d_1, is measured from the centroid of the tension force, T, (acting at the centroid of the steel reinforcement in the concrete slab) to the top of the steel section:

$$d_1 = \left(t_s - cover - \frac{1}{2} d_{bar} \right) \tag{B.9}$$

where d_{bar} = diameter of #4 steel reinforcement (in.)

cover = top concrete cover of steel reinforcement (in.)

Finally, the nominal plastic moment strength of each partially composite girder for negative girder bending, $M_{p\,calc}^{-}$, is computed (AISC, 1993):

$$M_{p\,calc}^{-} = C(d_1 + d_2) + P_y(d_3 - d_2) \tag{B.10}$$

where d_2 = distance from the centroid of the tension force in the the steel section to the top of the steel section (in.)

d_3 = distance from P_y to the top of the steel section (in.), or *d/2*

For the composite girders of Specimens 2 and 3 subjected to negative girder bending, the nominal plastic moment strength is calculated to be 11,700 kip-in.

B.2 Experimental Girder Moment Strength

The maximum girder moment achieved during testing is equal to the product of the maximum applied load (in kips) at the girder tip , P_{max}, and the length measured from the location of applied load at the girder tip to the face of the column, L_g:

$$M_{p\,\max} = P_{\max} L_g \tag{B.11}$$

For each girder, the applied load is equal to the sum of the loads applied by two actuators. Figures B.3-B.8 illustrate the uncorrected girder load-displacement curves for the East and West girders of Specimens 1, 2, and 3.

B.3 Experimental Girder-to-Column Moment-Rotation

This section describes how girder-to-column rotation of the connections (i.e., rotation of the girder relative to the column) was measured and how girder-to-column plastic rotation is calculated during the testing of Specimens 1, 2, and 3. Girder-to-column plastic rotation refers to the amount of girder rotation due only to plastic deformation in the girder and the connection components (shear tab, bolts, and welds). In this appendix, three methods of quantifying girder-to-column rotation are discussed: the use of the uncorrected girder-to-column rotation, the calculation of girder-to-column plastic rotation from the uncorrected girder-to-column rotation, and a back-calculated girder-to-column plastic rotation using the components of the girder tip deflection.

B.3.1 Uncorrected Girder-to-Column Moment-Rotation

Rotation of the girder relative to the column was measured using two LVDTs that were situated near the top flange and bottom flange (see Figures B.9 and B.10 and Section 2.4.2 for their measured locations). The LVDTs measured displacements Δ_{top} and Δ_{bot} between the girder (at a location 13.5" from the column flange) and the center of the panel zone (at the column centerline). Relative rotation of the girder was calculated using these displacements and the vertical distance, d', between the LVDTs.

$$\theta_{uncorr} = \frac{|\Delta_{top}| + |\Delta_{bot}|}{d'} \tag{B.12}$$

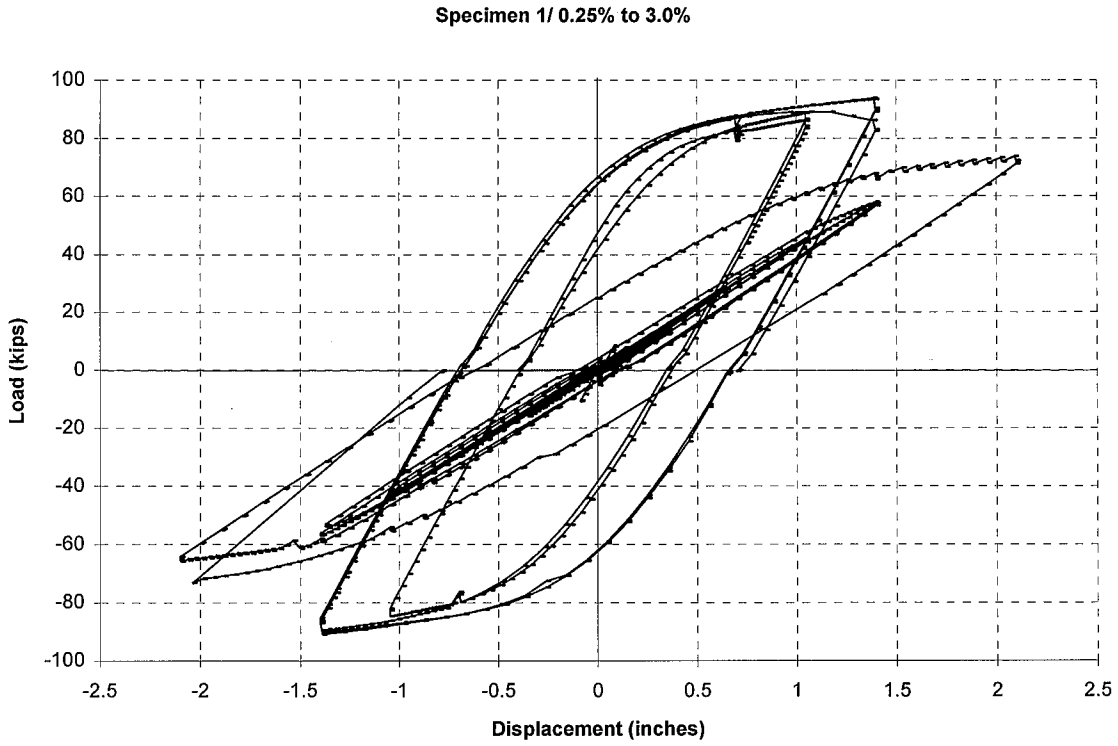

Figure B.3: Load vs. Displacement (East Girder of Specimen 1)

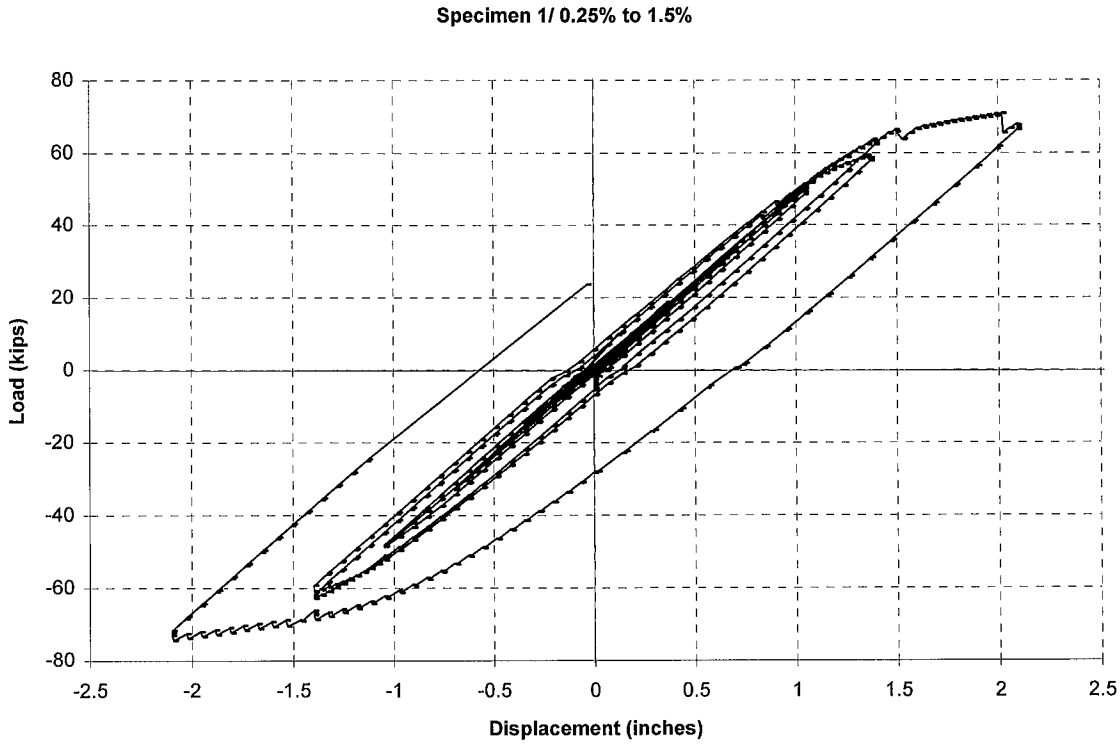

Figure B.4: Load vs. Displacement (West Girder of Specimen 1)

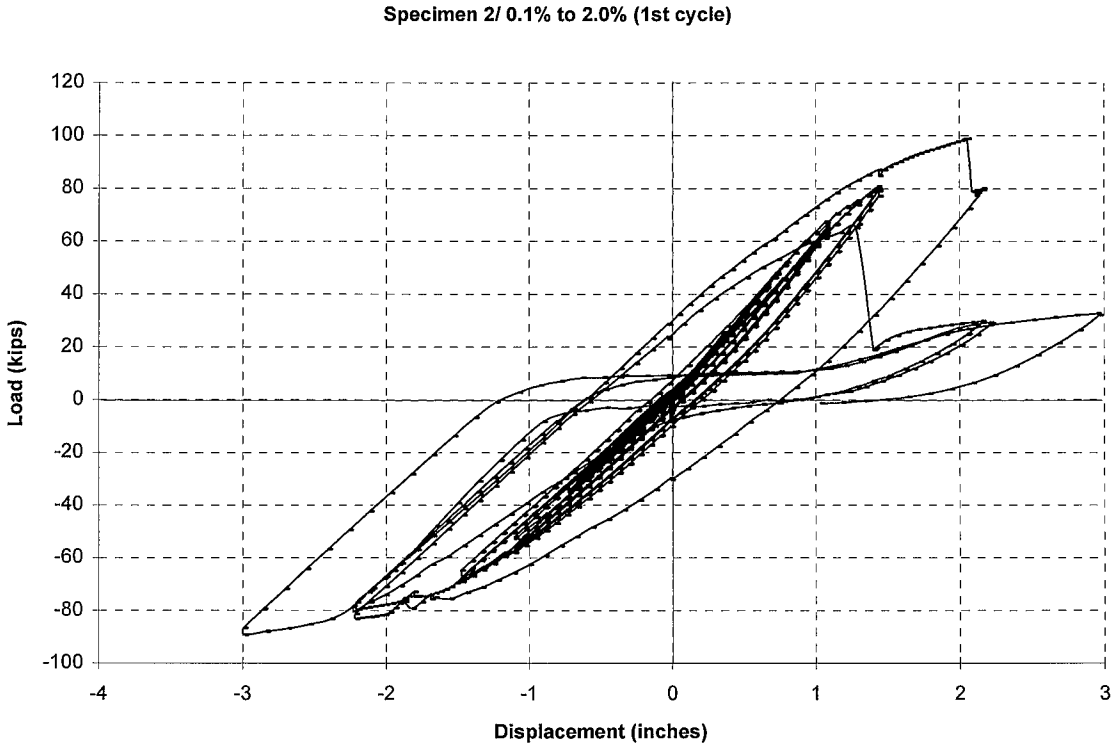

Figure B.5: Load vs. Displacement (East Girder of Specimen 2)

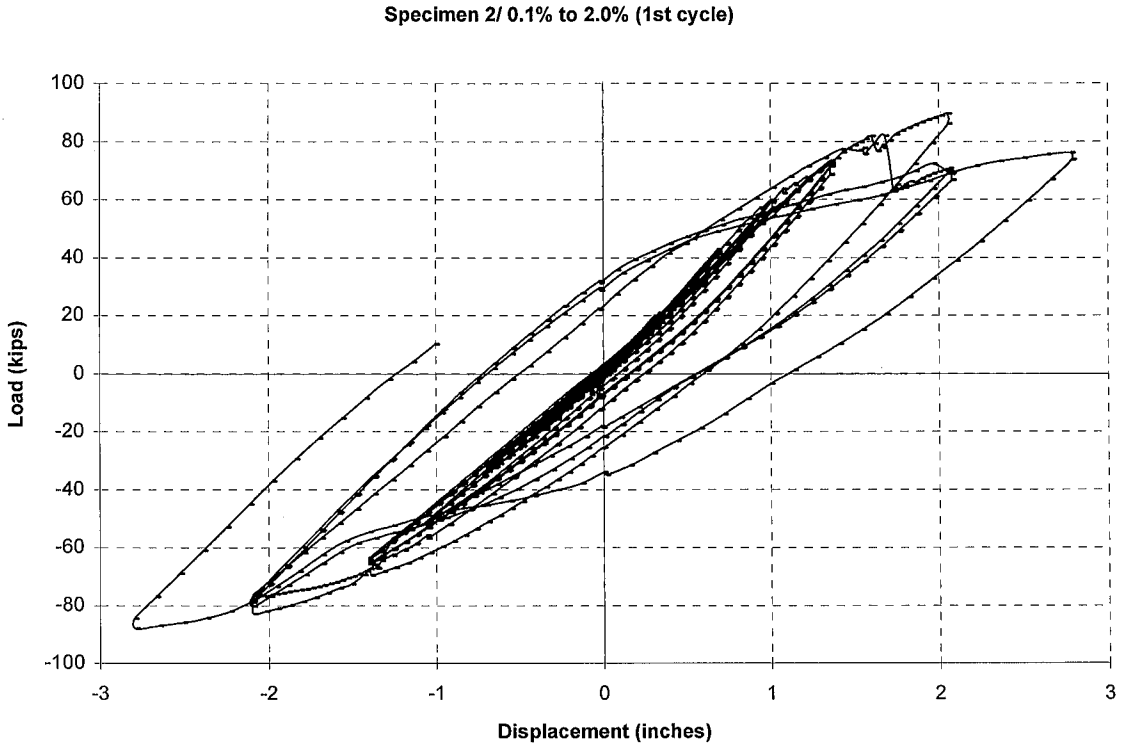

Figure B.6: Load vs. Displacement (West Girder of Specimen 2)

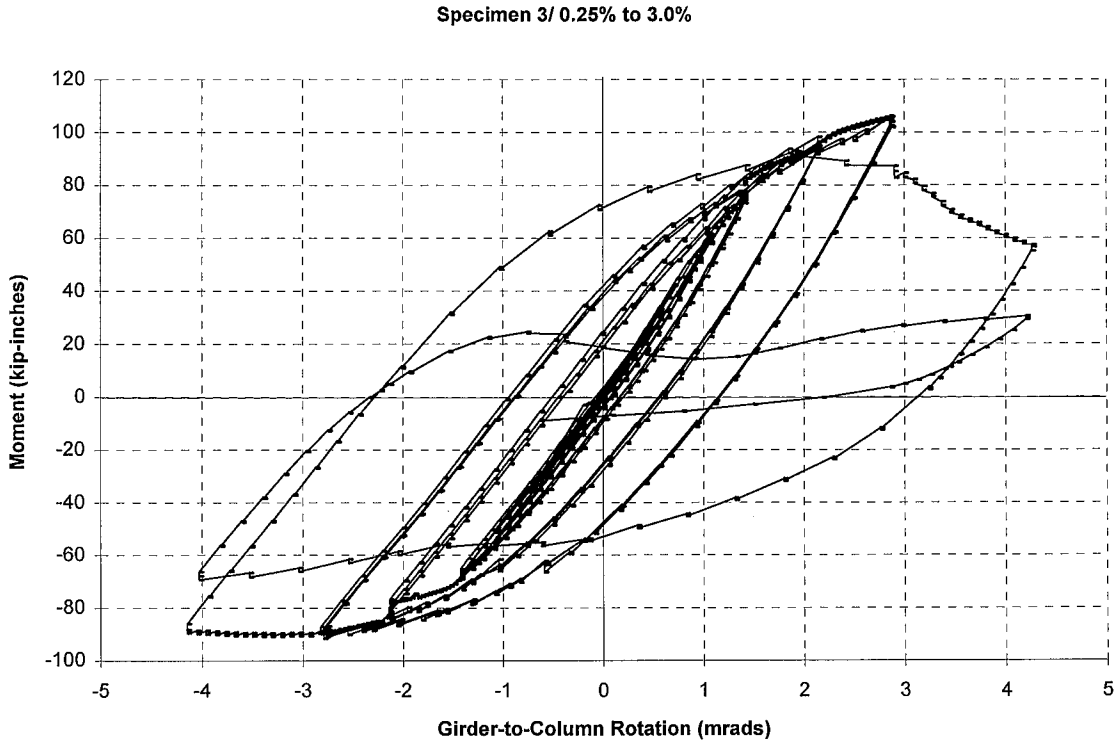

Figure B.7: Load vs. Displacement (East Girder of Specimen 3)

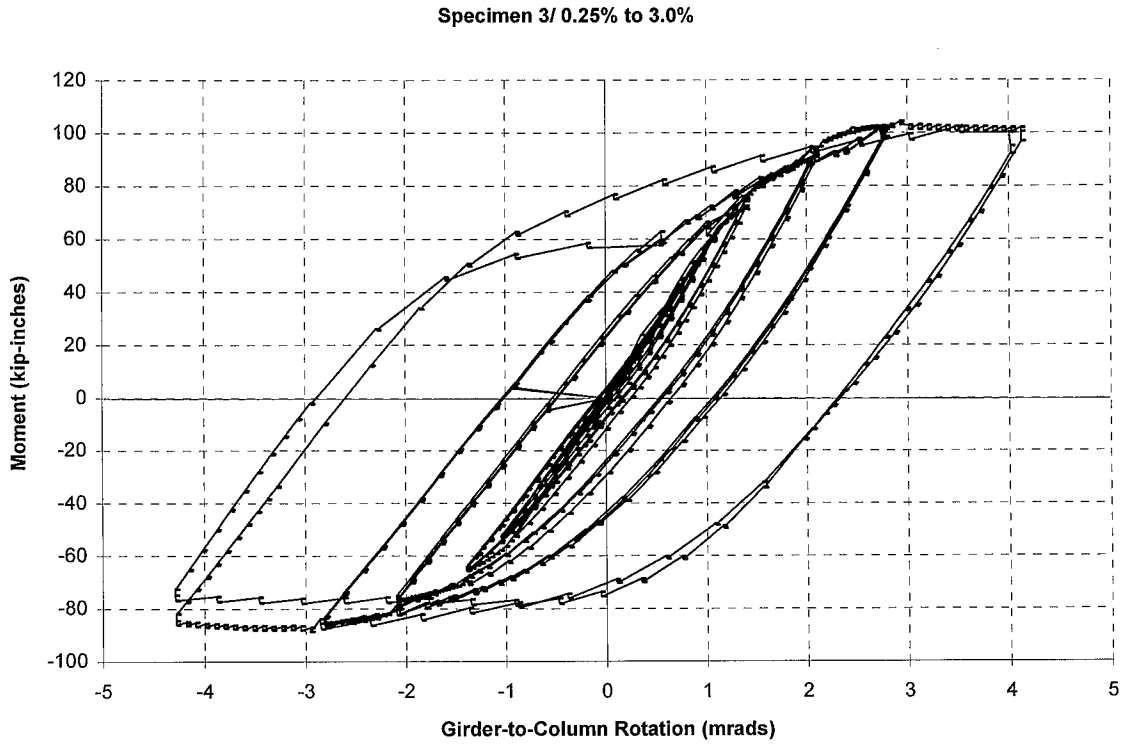

Figure B.8: Load vs. Displacement (West Girder of Specimen 3)

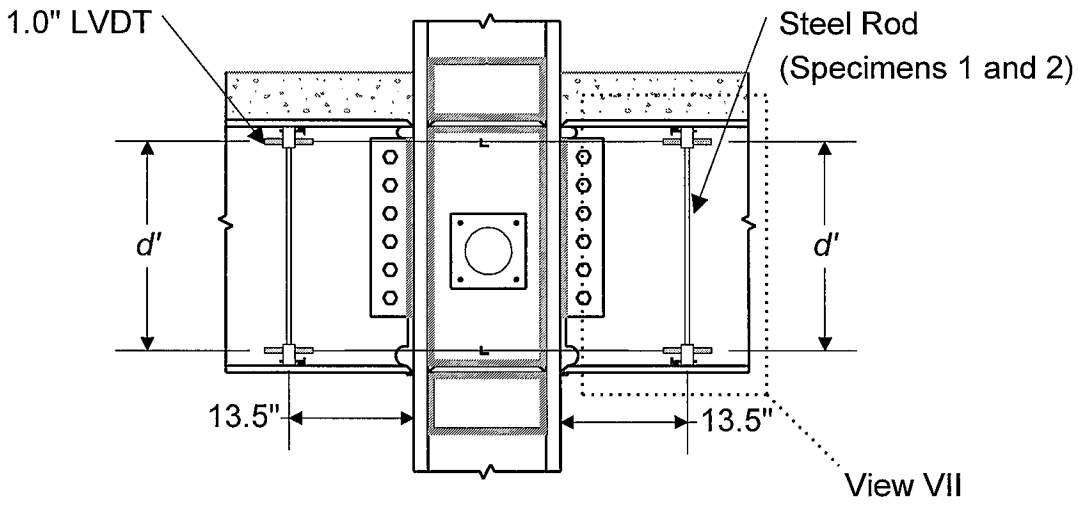

Figure B.9: Girder Relative Rotation LVDT Configuration (North Connection Region)

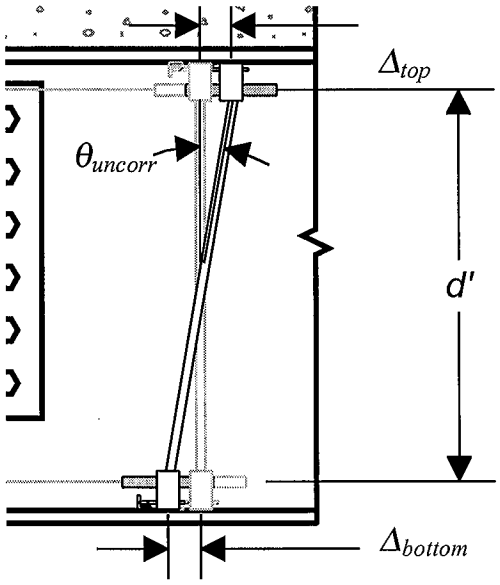

Figure B.10: View VII: Measured Girder-to-Column Rotation

where d' = depth measured from top to bottom girder-to-column rotation LVDTs (in.)

Δ_{top} = horizontal displacement measured at top girder-to-column rotation LVDT position (in.)

Δ_{bot} = horizontal displacement measured at bottom girder-to-column rotation LVDT position (in.)

This rotation, defined as the uncorrected girder-to-column rotation, represents the girder-to-column rotation due to elastic and plastic deformation in the connection components that are within 13.5 inches from the column face. For the East girders of Specimens 1, 2, and 3, d' is equal to 21.11", 22.00", and 21.32", respectively, and for the West girder of Specimens 1, 2, and 3, d' is equal to 21.17", 21.75", and 21.19", respectively. Figures B.11-B.16 illustrate the uncorrected girder-to-column rotation behavior for the East and West girders of the specimens.

B.3.2 Girder-to-Column Moment-Plastic Rotation

The girder-to-column plastic rotation is computed by subtracting the component of rotation due to elastic flexural within the 13.5" (L_a) of the girder from the uncorrected girder-to-column rotation:

$$\theta_p = \theta_{uncorr} - \frac{PL_a(2L_g - L_a)}{2E_s I_{eff}} \tag{B.13}$$

The force P is equal to the load applied to the girder tip, E_s is equal to Young's modulus of steel (see Section 2.2.1) and L_a is equal to the distance between the column face and the relative rotation LVDTs or 13.5". The effective moment of inertia, I_{eff}, that is utilized varies between girders and between girder positive and negative bending (see Appendix A). With the elastic flexural component removed, the remaining rotation

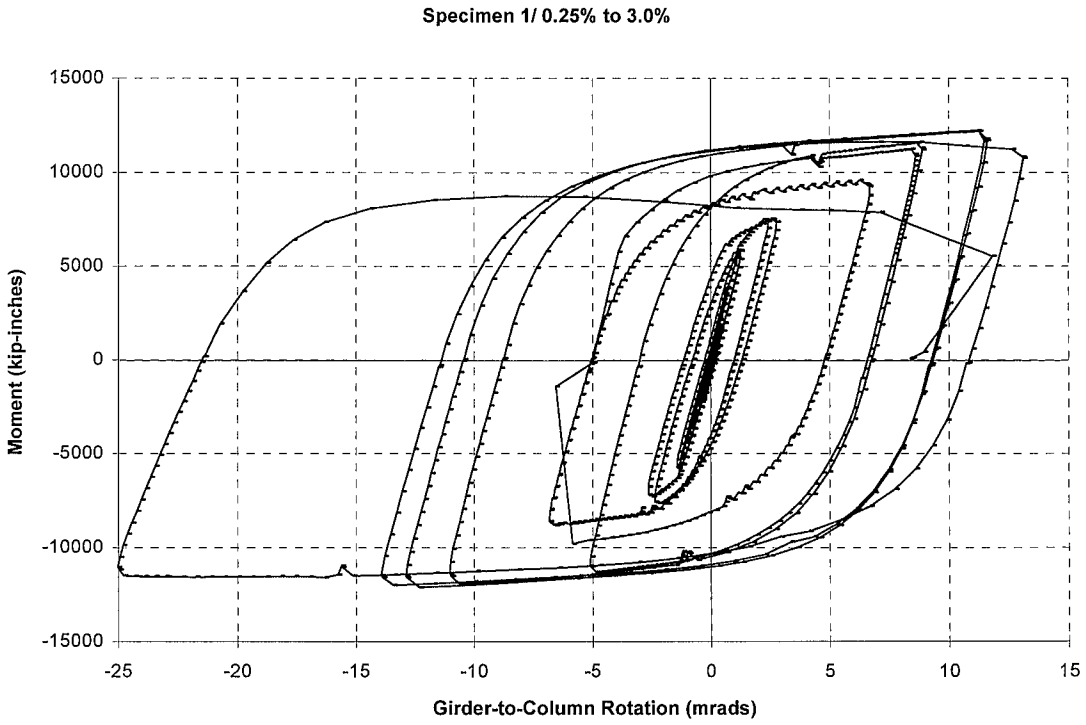

Figure B.11: Uncorrected Girder-to-Column Moment-Rotation
(East Girder of Specimen 1)

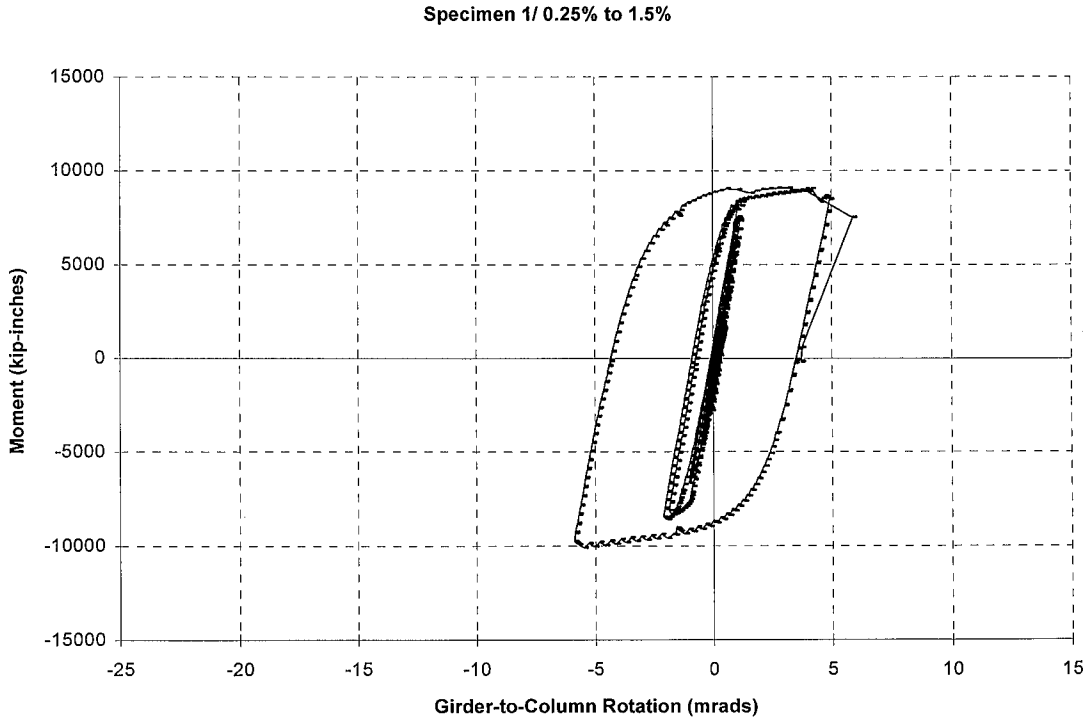

Figure B.12: Uncorrected Girder-to-Column Moment-Rotation
(West Girder of Specimen 1)

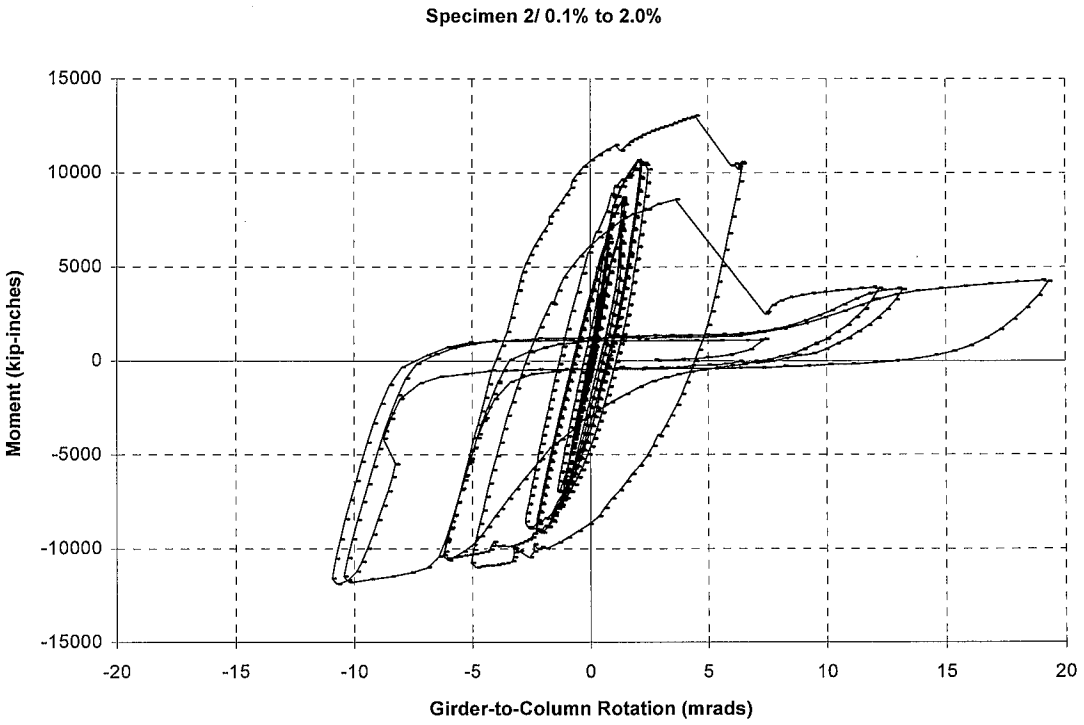

Figure B.13: Uncorrected Girder-to-Column Moment-Rotation
(East Girder of Specimen 2)

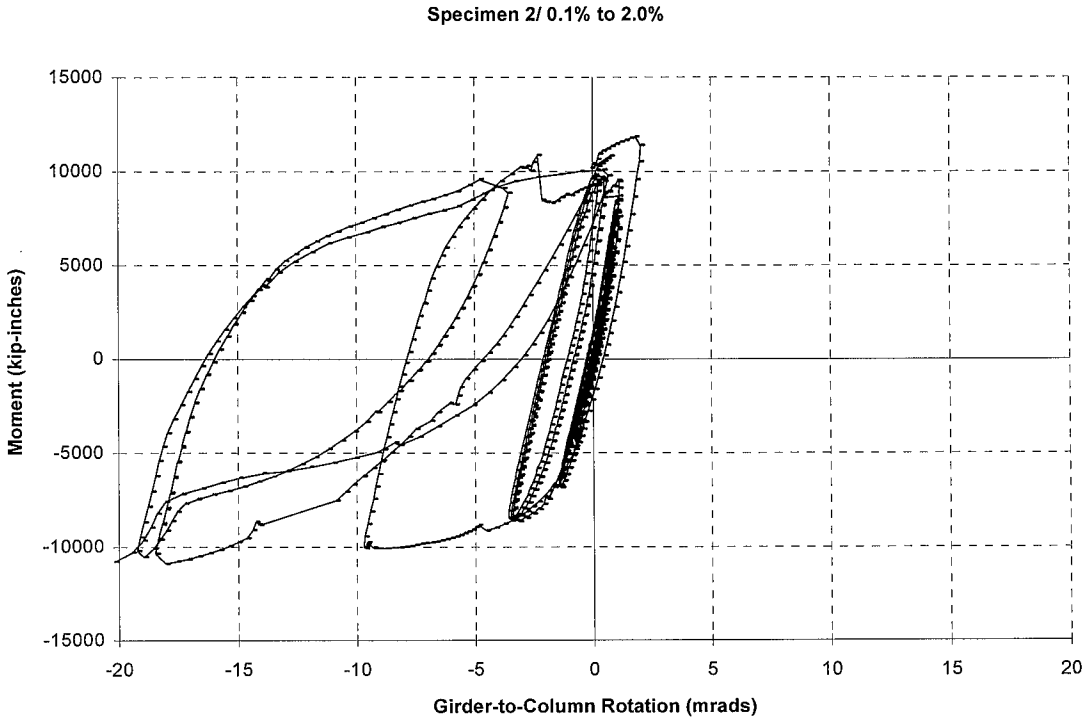

Figure B.14: Uncorrected Girder-to-Column Moment-Rotation
(West Girder of Specimen 2)

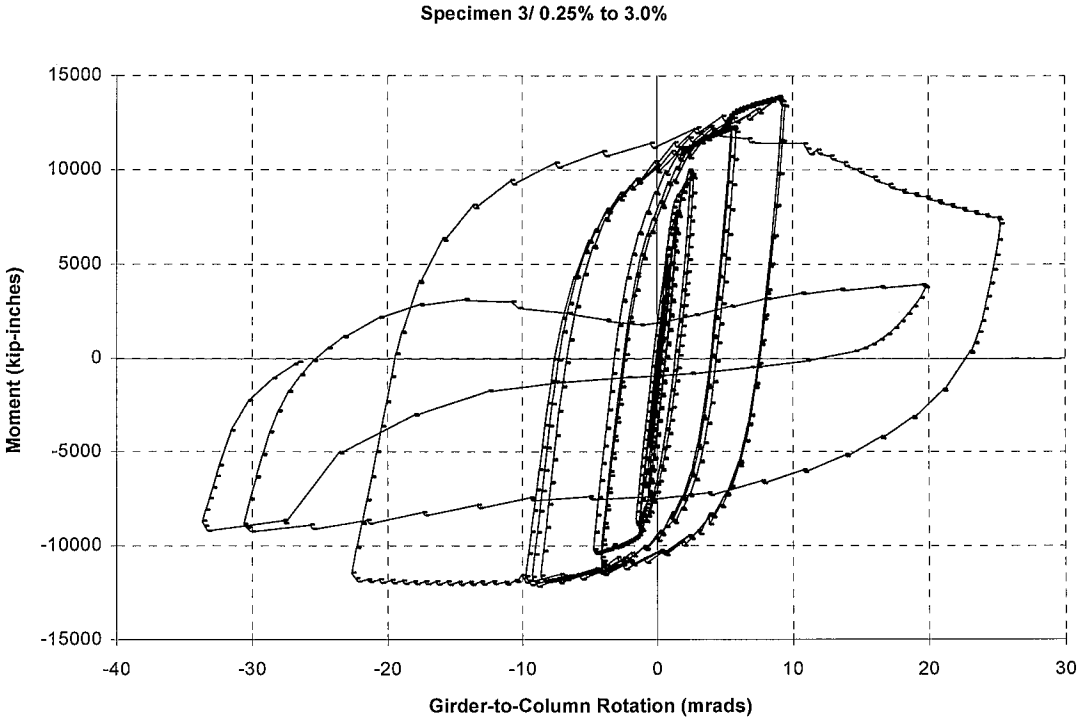

Figure B.15: Uncorrected Girder-to-Column Moment-Rotation
(East Girder of Specimen 3)

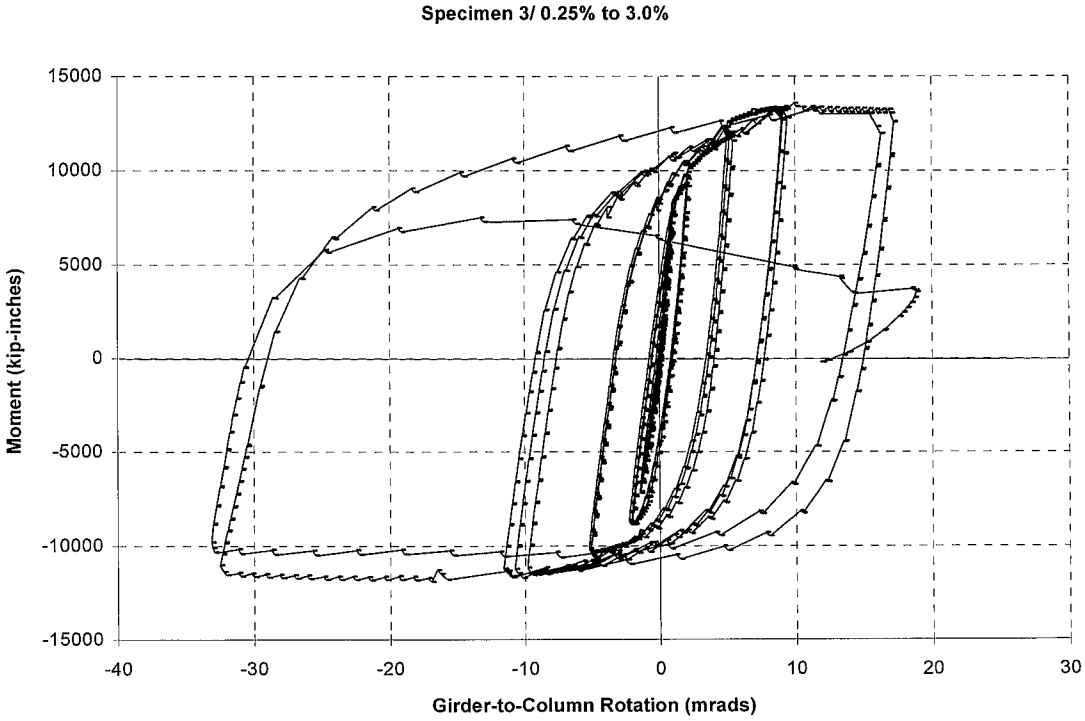

Figure B.16: Uncorrected Girder-to-Column Moment-Rotation
(West Girder of Specimen 3)

represents the rotation due almost exclusively to plastic deformation of the connection region and girder within 13.5 inches from the column face.

Equation B.13 is only valid if one assumes a rigid panel zone and neglects elastic deformation of the connection components (shear tabs, bolts, and welds), since the flexural component expression (second term in Eq. B.13) represents the rotation for a fixed end cantilever. Figures B.17-B.22 illustrate the girder-to-column plastic rotation behavior for the East and West girders of the specimens. Note that the vertical slope of the moment-rotation curve signifies that minimal girder-to-column plastic rotation occurs during the lower drift levels, and that the elastic deformation of the connection components is minimal, as expected.

B.3.3 Back-Calculated Girder-to-Column Moment-Plastic Rotation

Near the end of the second cycle at 1.5% drift of Specimen 2, sudden load frame and specimen vibrations, due to weld fracture, severely shifted the West girder LVDTs. The LVDTs remained out of range until they were adjusted during the first ramp of the third cycle at 1.5% drift cycles. Due to this temporary period of LVDT failure, it is not possible to completely reconstruct the LVDTs' behavior for this section of the loading history. This affects the moment-rotation curves of this girder (see Figure B.20). Therefore, the girder-to-column plastic rotation for the West girder of Specimen 2 is also calculated here based on knowledge of the components which contributed to the girder tip deflection (labeled as "back calculated" plastic rotation), and is used to reconstruct a portion of the West girder's moment-plastic rotation response for Specimen 2. For comparison, the moment-rotation behavior of the other girders is also calculated in this fashion in this section.

For this calculation, the actual girder tip deflection is employed, along with the calculated components which contribute to this tip deflection (see Appendix F). These components represent flexural deformations of the column and girders as well as deformations in the panel zone region and the load frame. The girder-to-column rotation

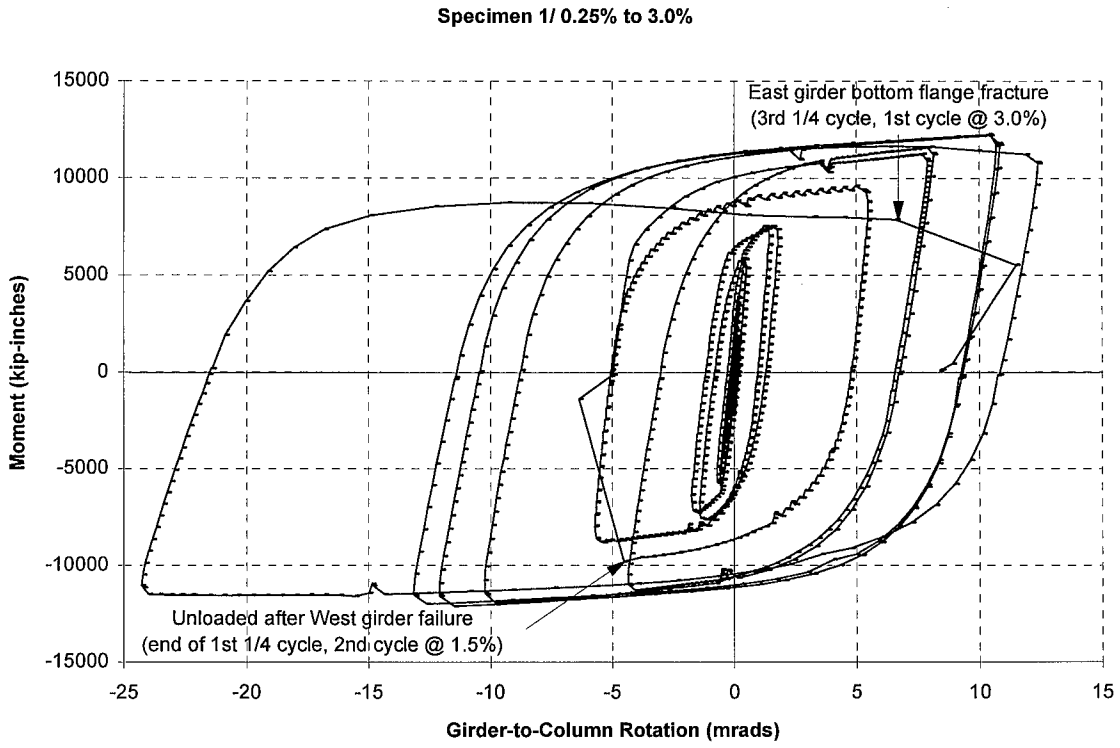

Figure B.17: Girder-to-Column Moment-Plastic Rotation (East Girder of Specimen 1)

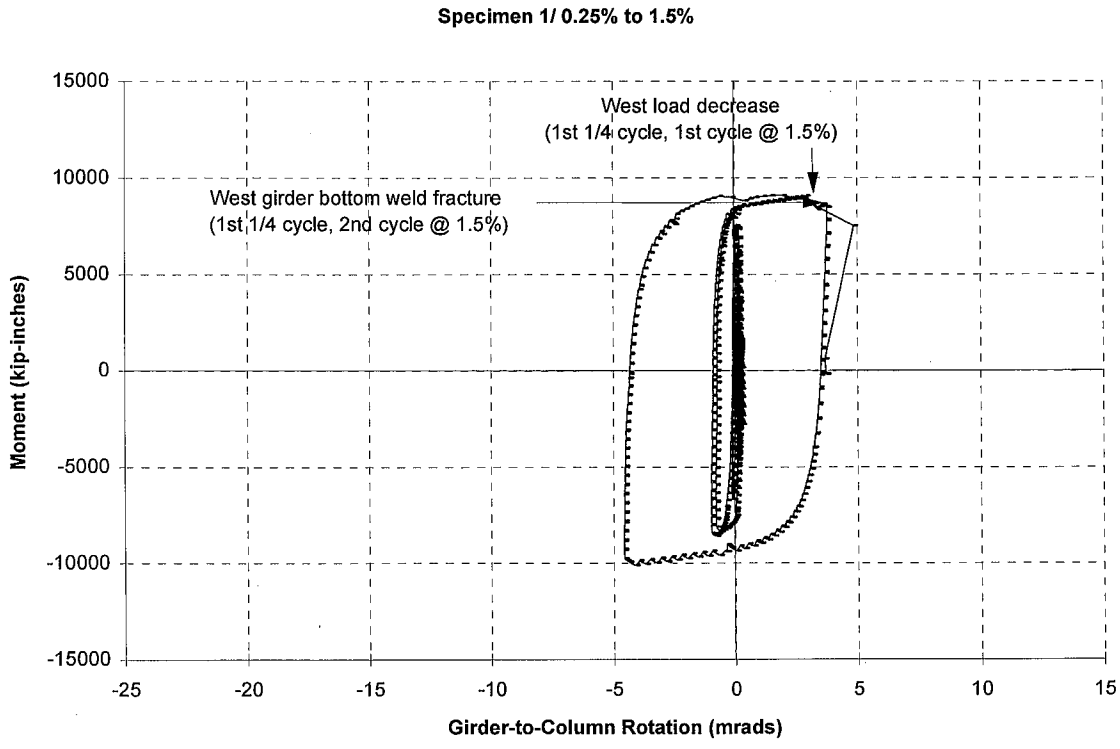

Figure B.18: Girder-to-Column Moment-Plastic Rotation (West Girder of Specimen 1)

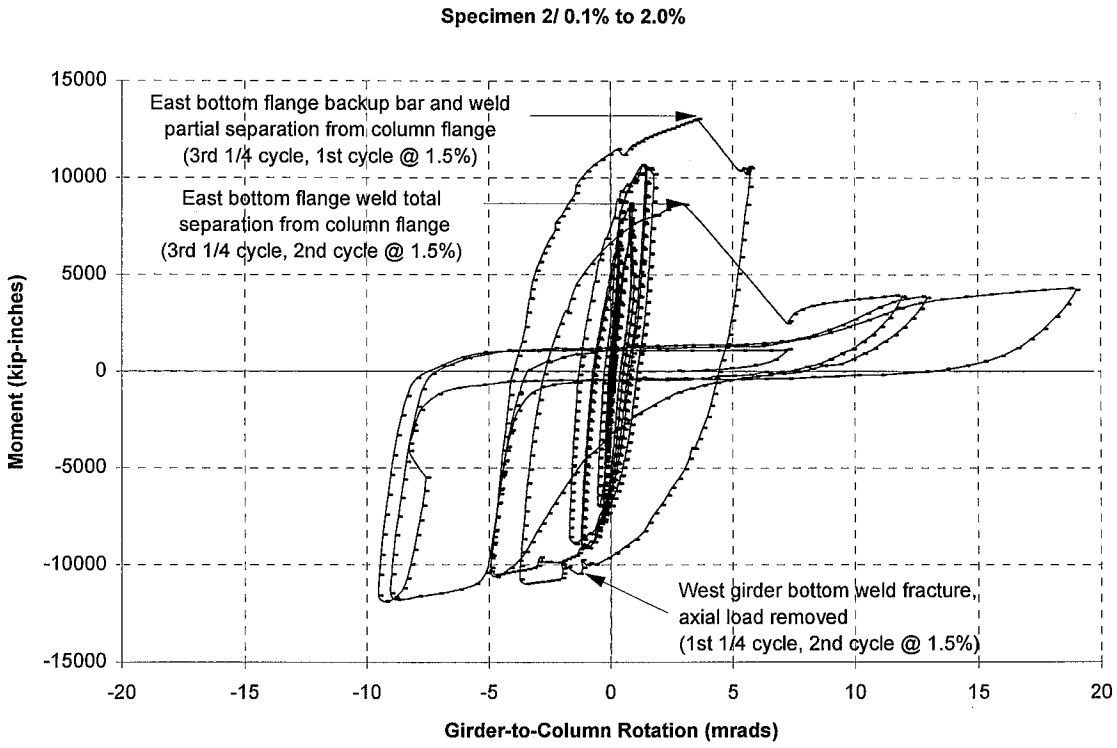

Figure B.19: Girder-to-Column Moment-Plastic Rotation (East Girder of Specimen 2)

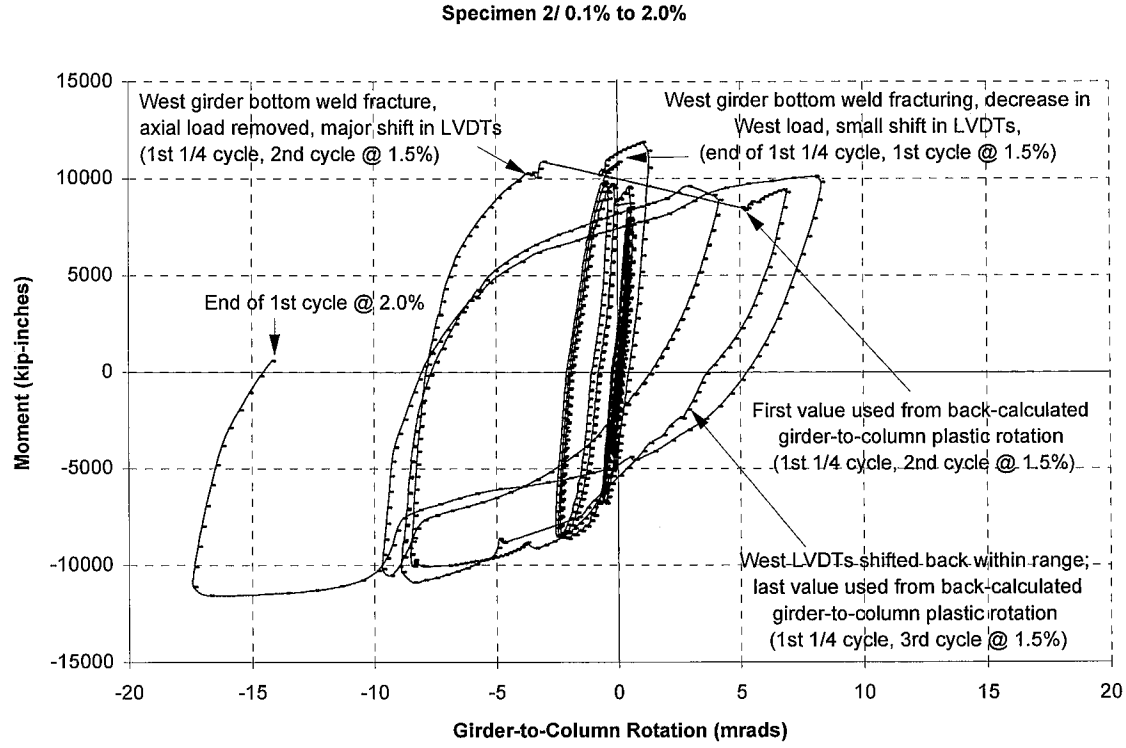

Figure B.20: Girder-to-Column Moment-Plastic Rotation (West Girder of Specimen 2)

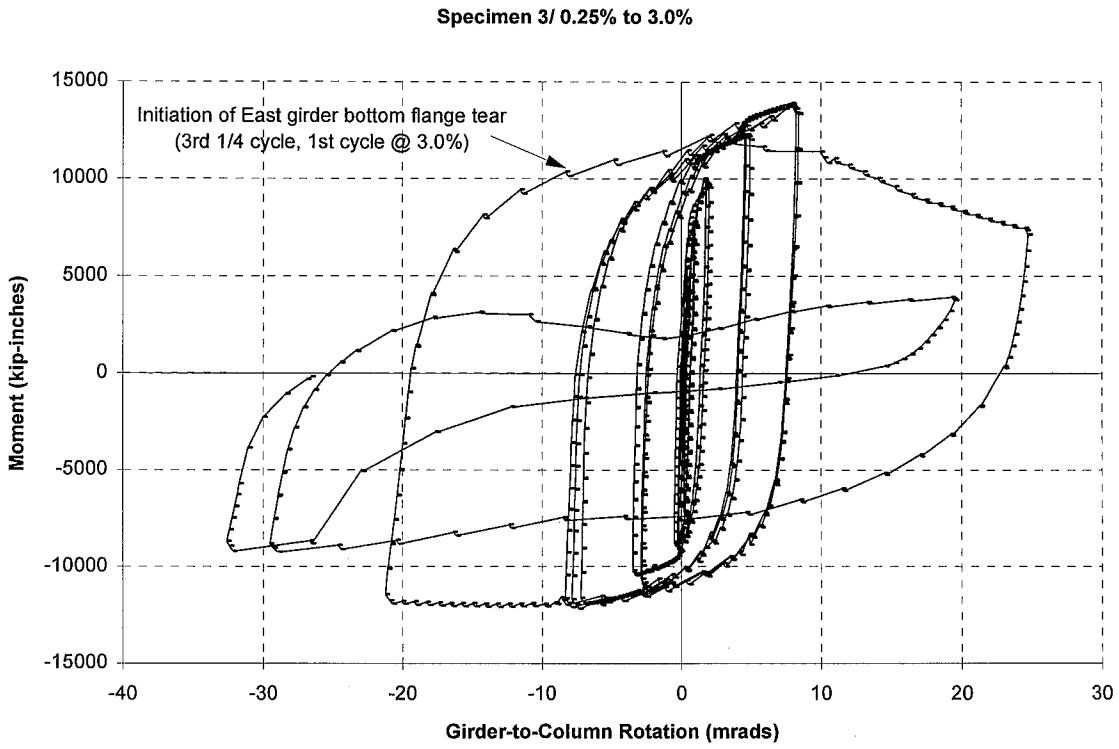

Figure B.21: Girder-to-Column Moment-Plastic Rotation (East Girder of Specimen 3)

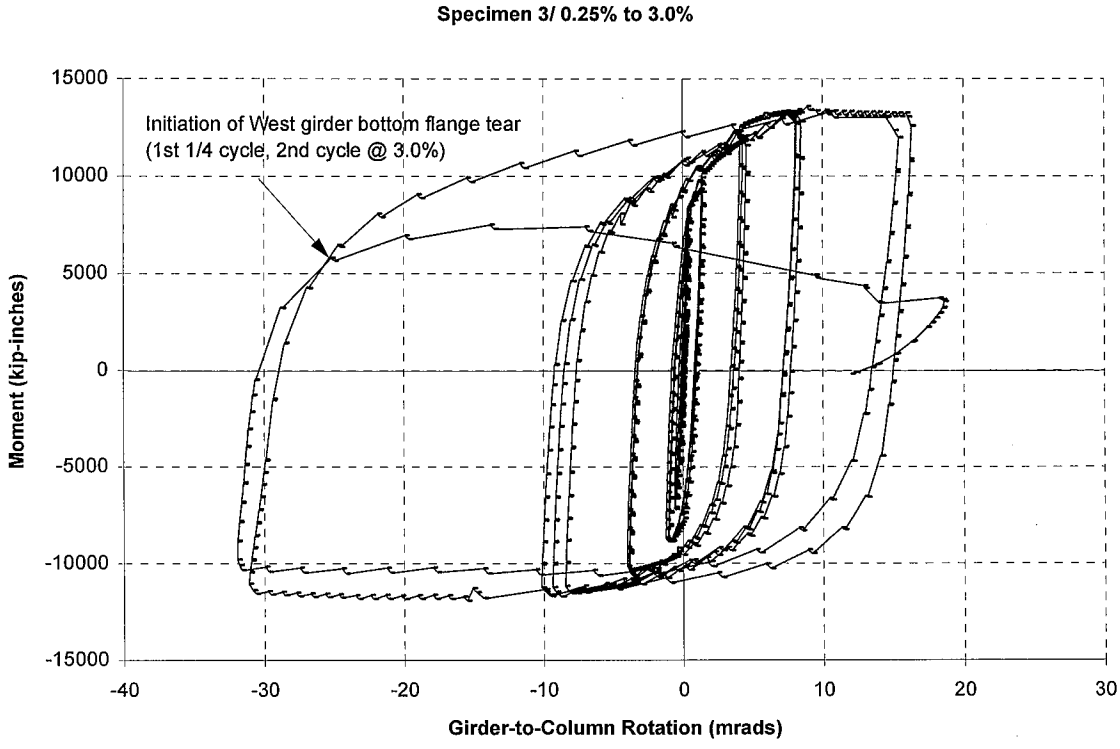

Figure B.22: Girder-to-Column Moment-Plastic Rotation (West Girder of Specimen 3)

is computed by subtracting all components of the tip deflection from the actual tip deflection, and then dividing by the length of the girder:

$$\theta_{back\_calc} = \frac{1}{L_b}\left(\Delta_{back\_calc}\right) = \frac{1}{L_b}\left(\Delta_{act} - \Delta_{girder} - \Delta_{column} - \Delta_{pz} - \Delta_{lf}\right) \qquad \text{(B.14)}$$

where Δ_{act} = average measured displacement of the two actuators at the girder tip (in.)

Δ_{col} = girder tip deflection due to column flexural deformation (in.)

Δ_{gir} = girder tip deflection due to girder flexural deformation (in.)

Δ_{lf} = girder tip deflection due to load frame deformation (in.)

Δ_{pz} = girder tip deflection due to panel zone deformation (in.)

L_b = length of girder measured from column face to applied load at the girder tip (in.)

The back-calculated girder-to-column moment-plastic rotation curves are illustrated in Figures B.23-B.28 respectively. The results from this calculation provide an interesting contrast to the girder-to-column moment-plastic rotation curves (see Figures B.17-B.22). Note that the panel zone and load frame components of the girder tip deflection are based directly on measured quantities, but that the column and girder flexural deformation contributions are calculated (see Appendix F). Therefore, the assumptions made in these calculations must be considered when evaluating the reliability of the back-calculated girder-to-column plastic rotation.

A portion of the back-calculated girder-to-column plastic rotation is used to reconstruct the girder-to-column plastic rotation of the West girder of Specimen 2 (see Figure B.20). This correction was performed starting at the end of the third 1/4 cycle, second cycle at 1.5% drift, and ending during the first 1/4 cycle, third cycle at 1.5% drift. As previously mentioned, the West LVDTs were shifted out of range during this time period.

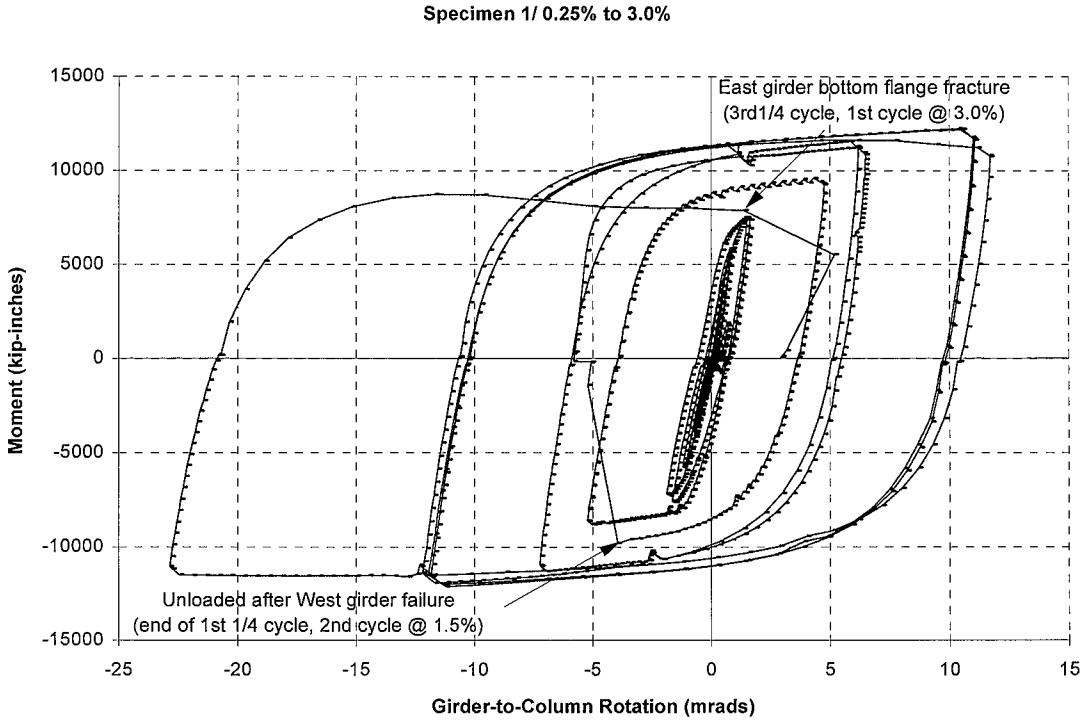

Figure B.23: Back Calculated Girder-to-Column Moment-Plastic Rotation (East Girder of Specimen 1)

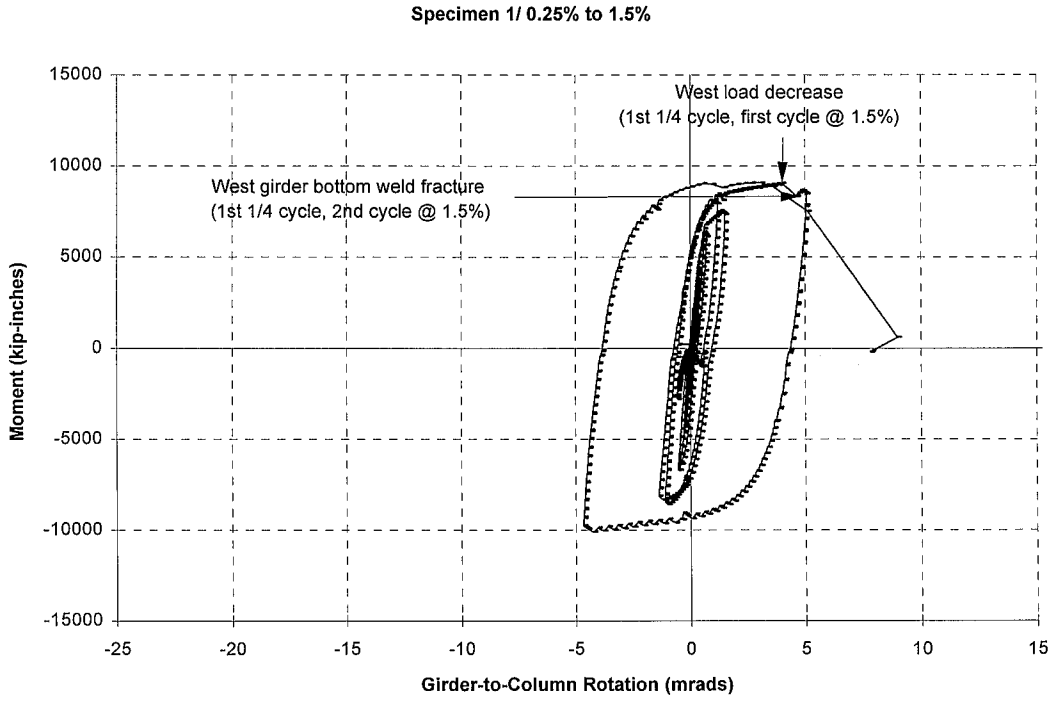

Figure B.24: Back Calculated Girder-to-Column Moment-Plastic Rotation (West Girder of Specimen 1)

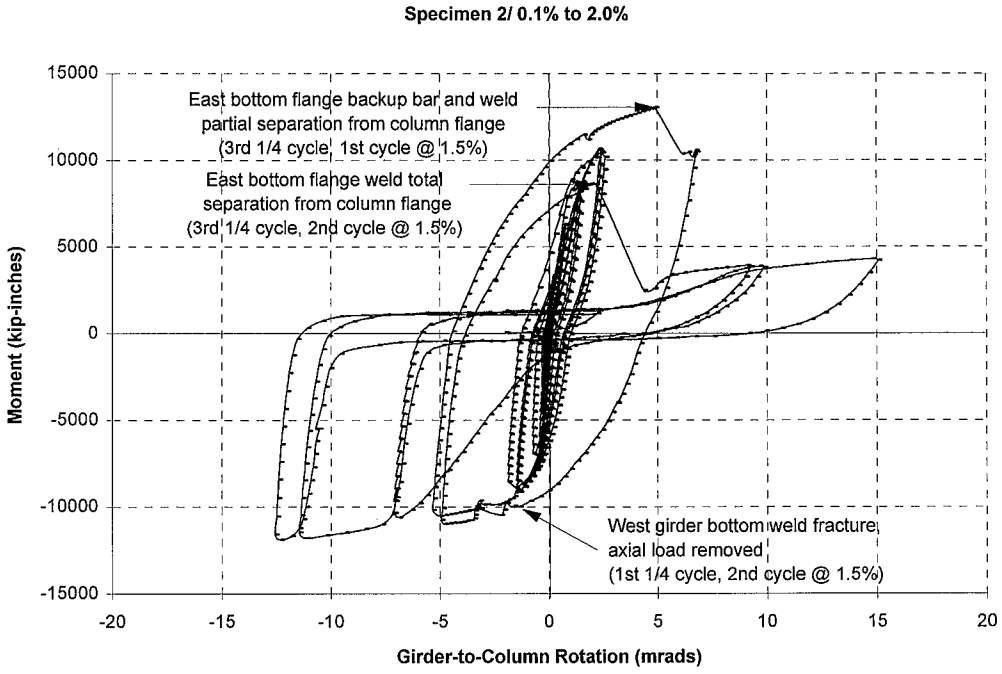

Figure B.25: Back Calculated Girder-to-Column Moment-Plastic Rotation (East Girder of Specimen 2)

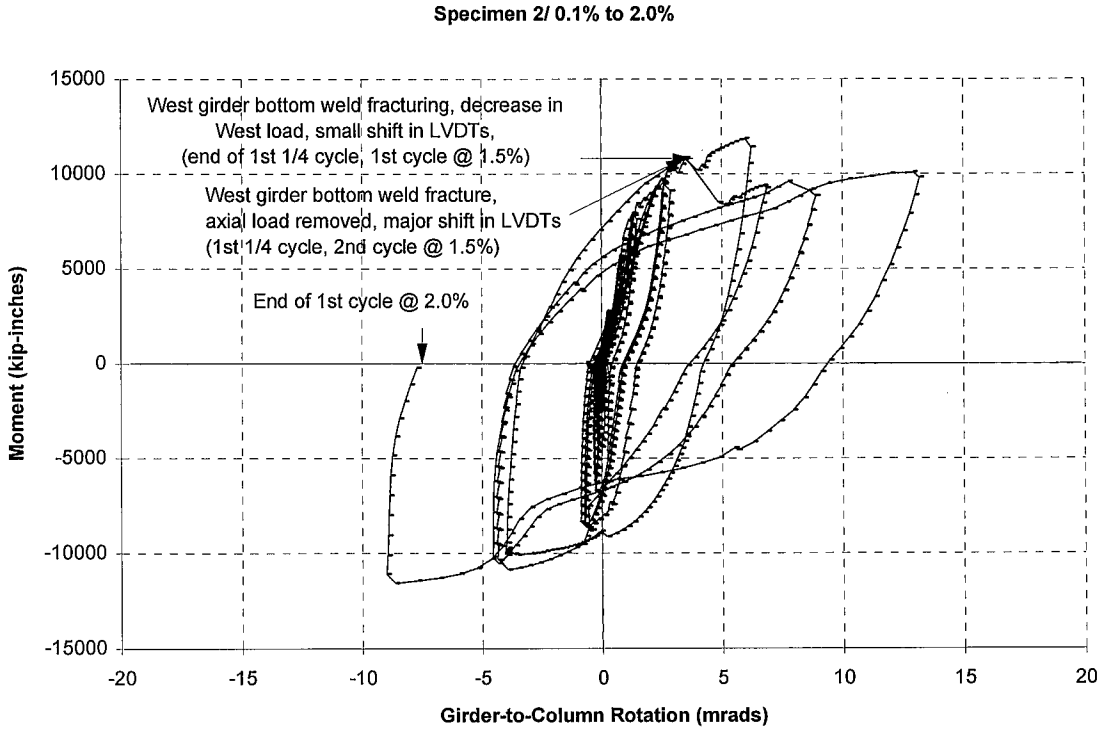

Figure B.26: Back Calculated Girder-to-Column Moment-Plastic Rotation (West Girder of Specimen 2)

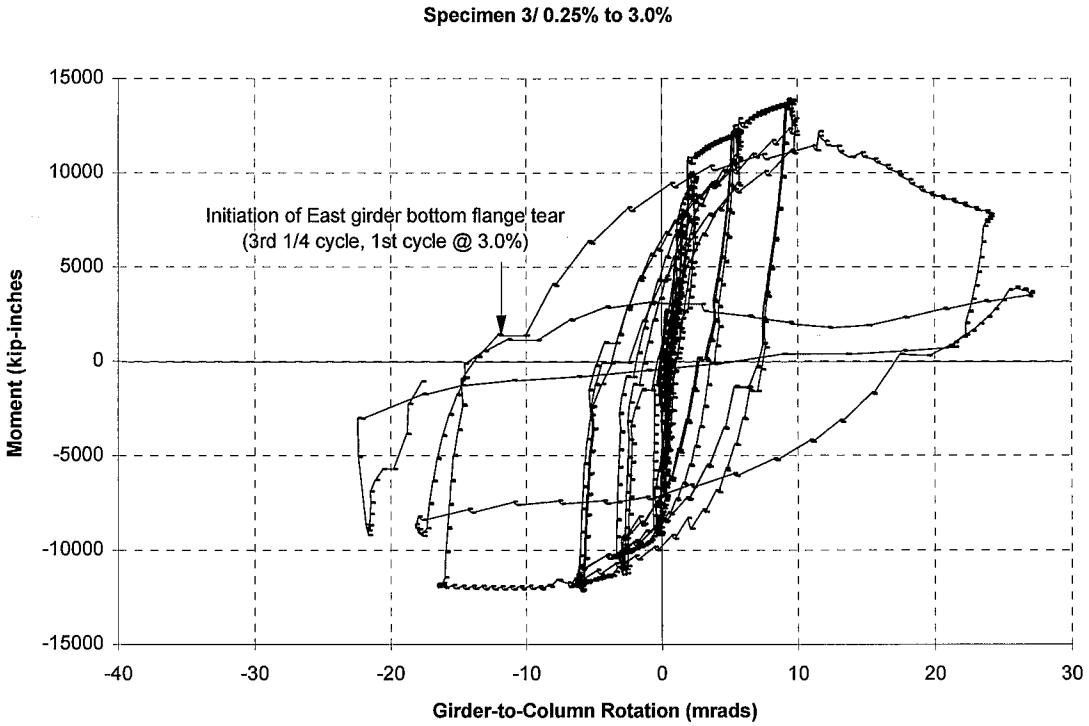

Figure B.27: Back Calculated Girder-to-Column Moment-Plastic Rotation (East Girder of Specimen 3)

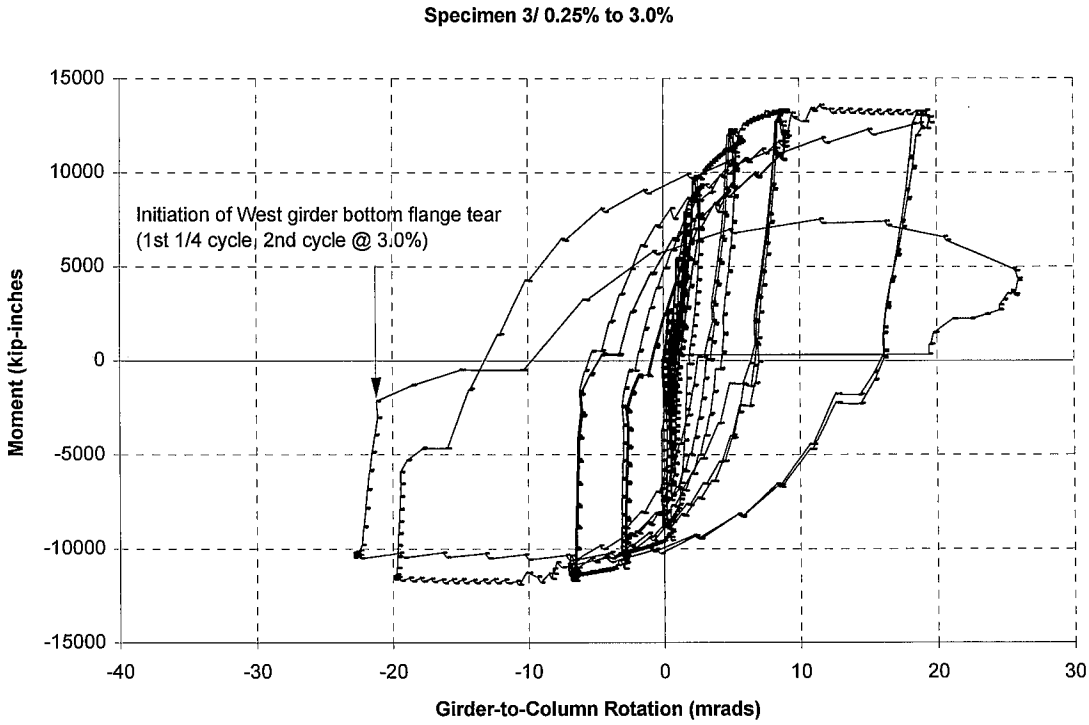

Figure B.28: Back Calculated Girder-to-Column Moment-Plastic Rotation (West Girder of Specimen 3)

For these drift cycles following this time period, the girder-to-column plastic rotations of the West girder are not quantitatively correct. This is because when the West LVDTs were shifted back within range, they were not adjusted to a known position. The girder-to-column plastic rotations are, however, qualitatively accurate, that is, the change in rotation relative to the girder rotation measured once the West LVDTs were readjusted is valid. Therefore, for those drift cycles following the readjusting of the West LVDTs, the girder-to-column plastic rotation is reconstructed by adding the change in the girder-to-column plastic rotation to the last back-calculated girder-to-column plastic rotation value.

Even though the later portion of the girder-to-column plastic rotation of the West girder of Specimen 2 can only be investigated qualitatively, some interesting behavior is observed. After the East and West girders fractured during the second and third cycles at 1.5% drift cycles, respectively, the West girder continued to show substantial energy dissipation capacity while the East girder did not. Also, visual and written documentation during the test confirmed continued yielding of the West girder connection region during 2.0% drift cycles.

Appendix C

Panel Zone Shear Distortion

This appendix describes how the panel zone shear distortion was measured for each connection, and it presents the results of the panel zone shear distortion. Deformation in the panel zone region was measured in milliradians using two 0.1 inch LVDTs. The LVDTs recorded the change in length, Δ_1 and Δ_2, between the bottom East/top West corners and the bottom West/top East corners of the panel zone, respectively (recall that the plane of the panel zone is oriented in the East and West directions). Figure C.1 illustrates the setup of the two LVDTs, while Figure C.2 shows a closer view of the panel zone distortion occurring at the bottom East corner of the panel zone.

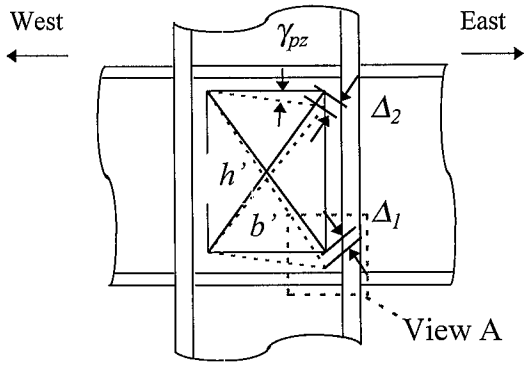

Figure C.1: Measurement of Panel Zone Shear Distortion
[after (Krawlinker et al., 1971)]

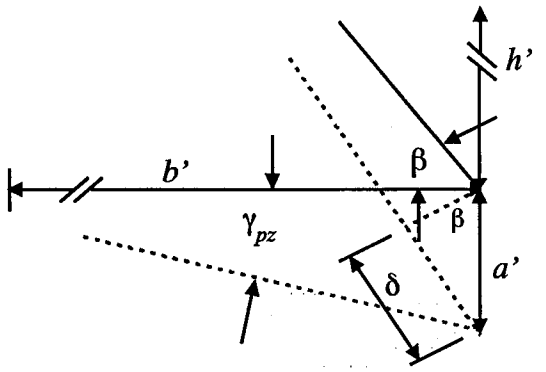

Figure C.2: View A: East Bottom LVDT on Panel Zone [after (Krawlinker et al., 1971)]

C.1 Calculation of Panel Zone Shear Distortion

The terms h' and b' represent the height and base dimensions, respectively, between the LVDT end points. The expression is derived from three trigonometric relations that are obtained from the geometry illustrated in View A (Krawinkler et al., 1971). First, the diagonal length of the panel zone is calculated with Pythagorean's Theorem, using the panel zone height and base, h' and b'. The angle δ is equal to the average of the LVDT changes in displacement, Δ_1 and Δ_2, while the angle β is defined as the inverse sine of δ divided by the angular panel zone distortion arc length, a'. By combining the expression $a' = tan(\gamma_{pz})b'$ with the expression defining β, and assuming that $tan(\gamma_{pz}) = \gamma_{pz}$, an equation is formulated that represents the angular panel zone distortion in radians:

$$\gamma_{pz} = \frac{|\Delta_1| + |\Delta_2|}{2} \frac{\sqrt{b'^2+h'^2}}{b'h'} = \delta \frac{\sqrt{b'^2+h'^2}}{b'h'} \qquad \text{(C.1)}$$

For Specimens 1 and 2, b' and h' are equal to 10.05" and 24.25", respectively, and for Specimen 3, b' and h' are equal to 9.00" and 22.00", respectively (see also Appendix K).

C.2 Moment-Panel Zone Shear Distortion Curves

The panel zone shear distortion is illustrated in Figures C.3-C.8, versus both the girder moments of the East and West girders of Specimens 1, 2, and 3. All the specimens exhibit relatively low levels of panel zone inelastic deformation. When investigating the three connections cycled up to the 1.5% drift levels, the panel zone of Specimen 2 (East and West girder moments) demonstrates larger amounts of both deformation and strength than the panel zone of Specimen 1 (West girder moment). Because the specimens were tested under stroke-control and flexure of the composite girders contributes less to the girder tip deflection, it is possible that the panel zone deformation of Specimen 2 is required to contribute a larger portion to the girder tip deflection. Furthermore, Specimen 3 exhibits a higher level of panel zone rotation and strength when the West girder was subjected to positive bending compared to negative bending.

Specimen 2 shows jumps in panel zone rotation during the 1.5% and 2.0% drift levels due to fractures occurring within the bottom girder flange-to-column connections (Figures C.3 and C.4). Note that the stiffness changes during the 1.5% drift levels when using the East girder moment of Specimen 1. This is because only the East girder was tested during a portion of the 1.5% drift levels up through the 3.0% drift levels.

It may concluded that the level of panel zone shear distortion is minimal for all three specimens, as was intended. Also, the relatively rigid behavior exhibited by the panel zone region simplifies the modeling of the specimens, in that the panel zone region may be assumed to possess a very high rigidity. The structural idealization and modeling of three specimens is discussed in the next appendix.

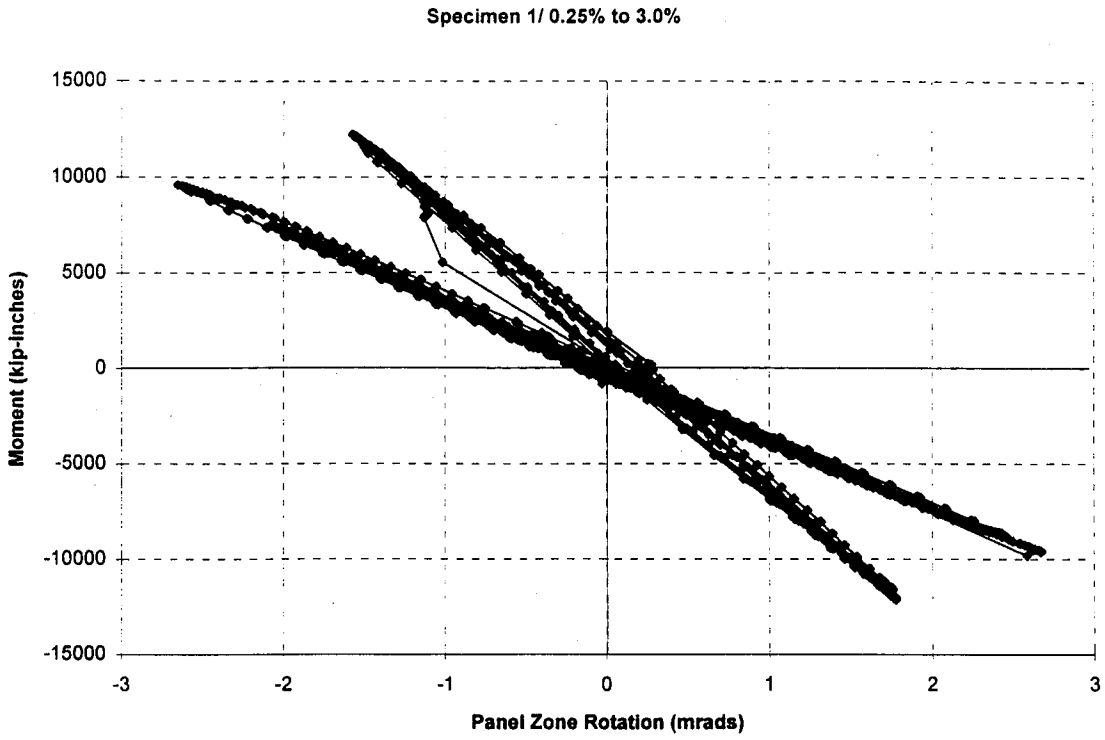

Figure C.3: Panel Zone Shear Rotation (East Girder of Specimen 1)

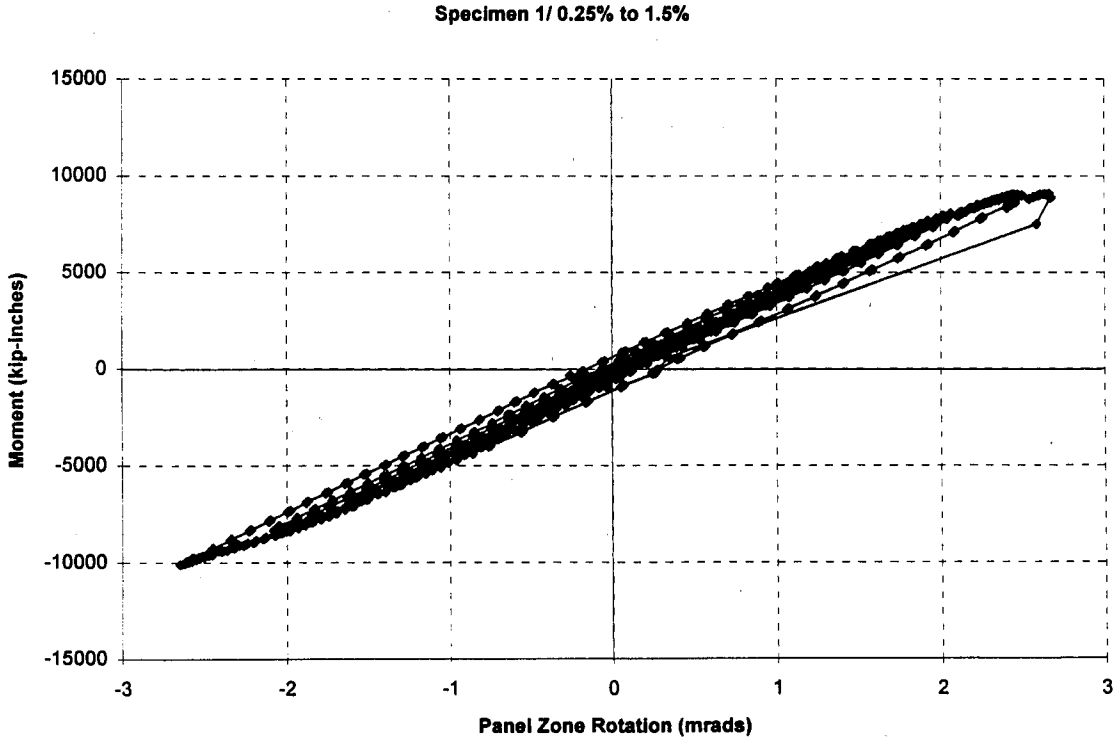

Figure C.4: Panel Zone Shear Rotation (West Girder of Specimen 1)

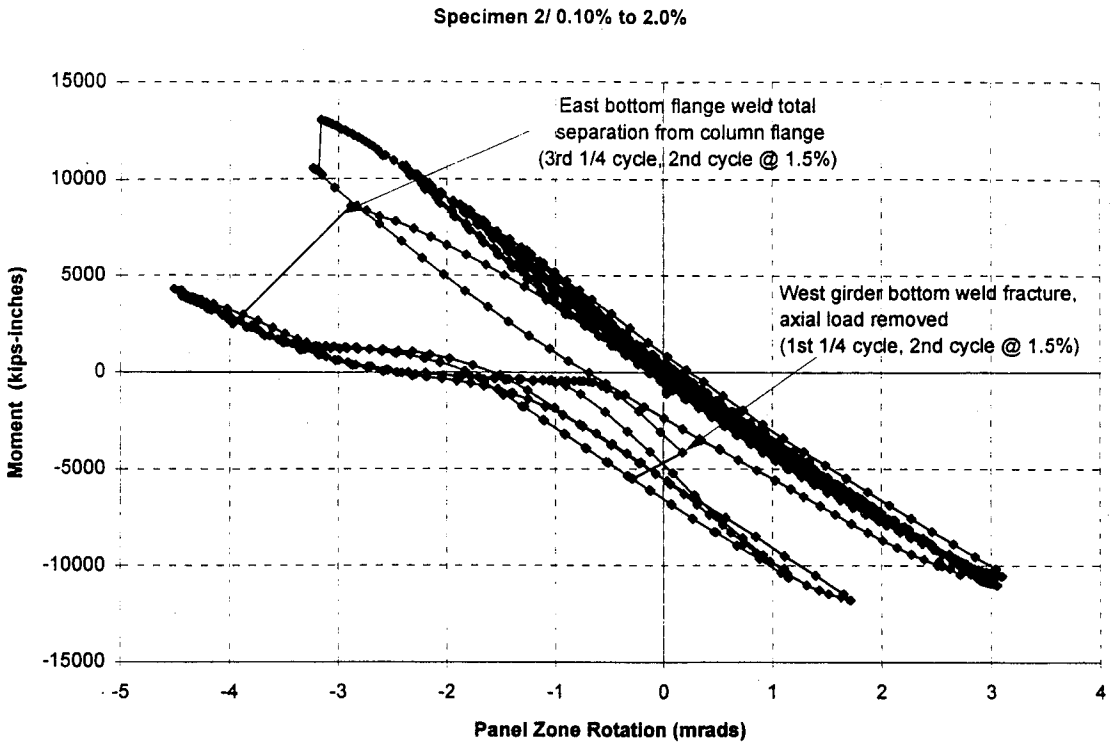

Figure C.5: Panel Zone Shear Rotation (East Girder of Specimen 2)

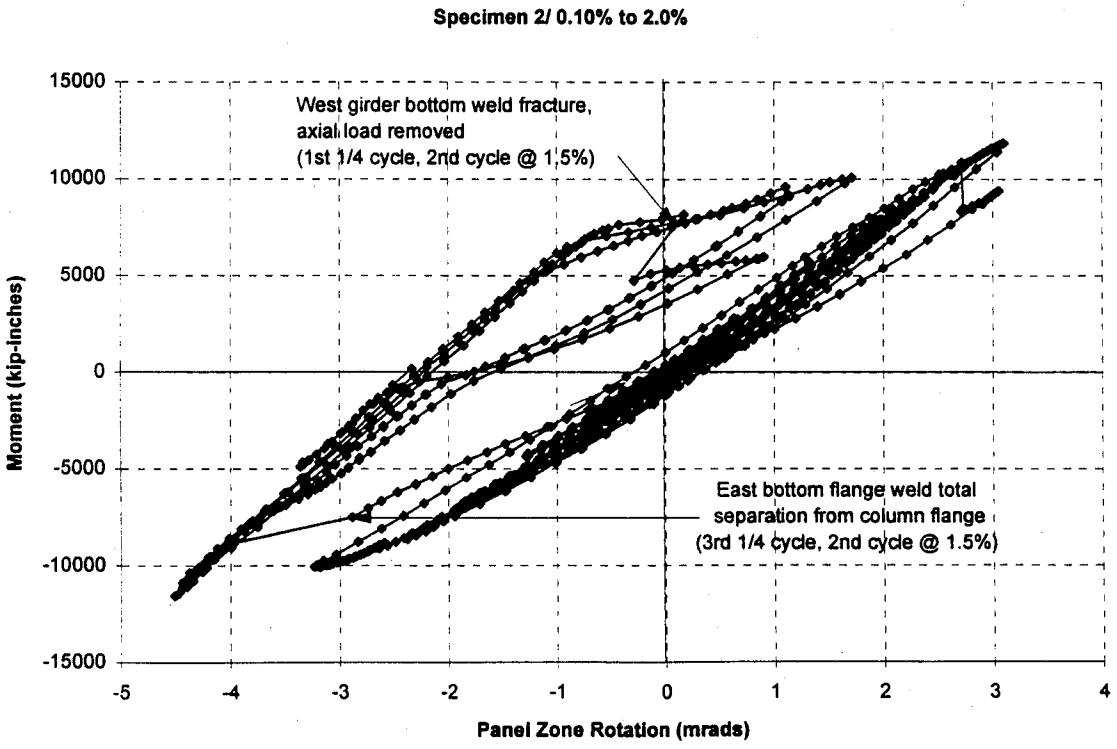

Figure C.6: Panel Zone Shear Rotation (West Girder of Specimen 2)

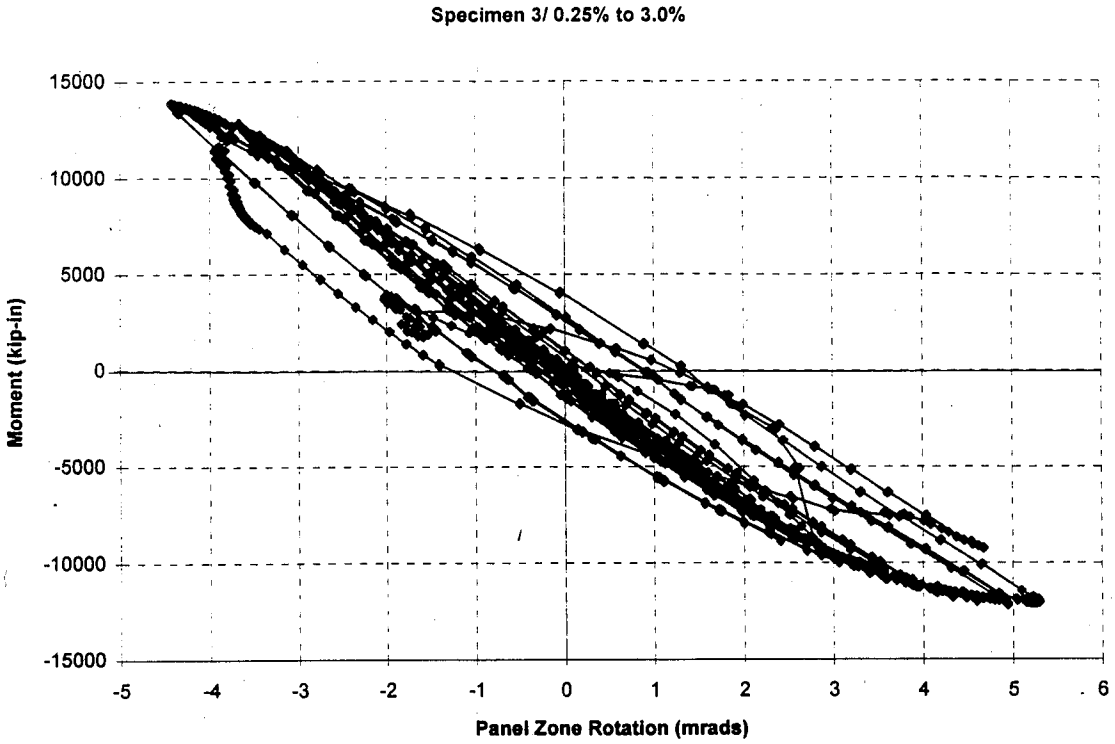

Figure C.7: Panel Zone Shear Rotation (East Girder of Specimen 3)

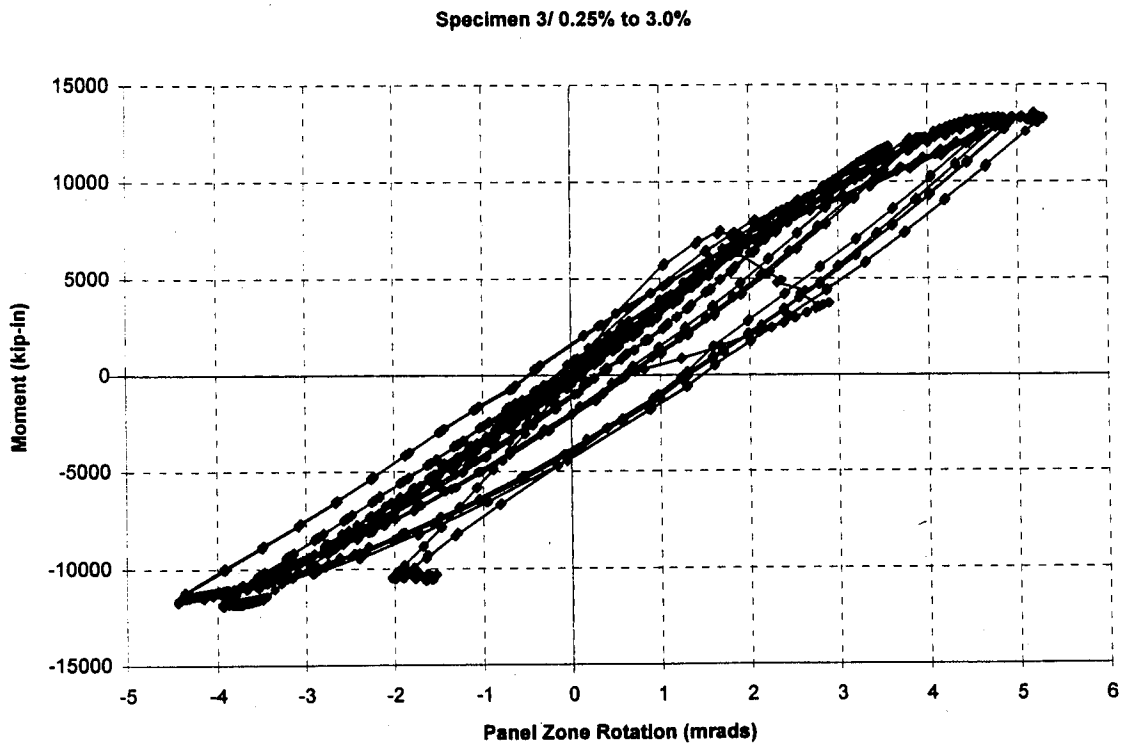

Figure C.8: Panel Zone Shear Rotation (West Girder of Specimen 3)

Appendix D

Structural Idealization of Specimens

Elastic finite element analysis of the specimens was required for several of the calculations performed for data reduction. This appendix describes the structural idealization model used in these data reduction processes, and reports the assumptions made that determine the material and geometric properties of the model which are representative of the specimens. The cross sections of the elements of the specimens are assumed to remain plane during loading (Euler-Bernoulli beam theory is assumed). Also, the specimen model incorporates an infinitely rigid panel zone region and is valid for only linear elastic behavior.

D.1 Modeling of Reaction Components and External Loads

The specimen is modeled as having a pinned bottom and a laterally supported, pinned top, with both pins having rotational springs with stiffness values of k (Figures D.1 and D.2). The top load pin is supported only in the horizontal position since the MTS load machine, which is attached to the top load pin, is free to displace vertically. Note that for the calculation of the column flexural deformation component of the girder tip deflection, the top load pin is assumed to be restrained in the vertical direction [i.e, the top load pin is assumed to be a pinned support (see Section 4.2 and Appendix F)].

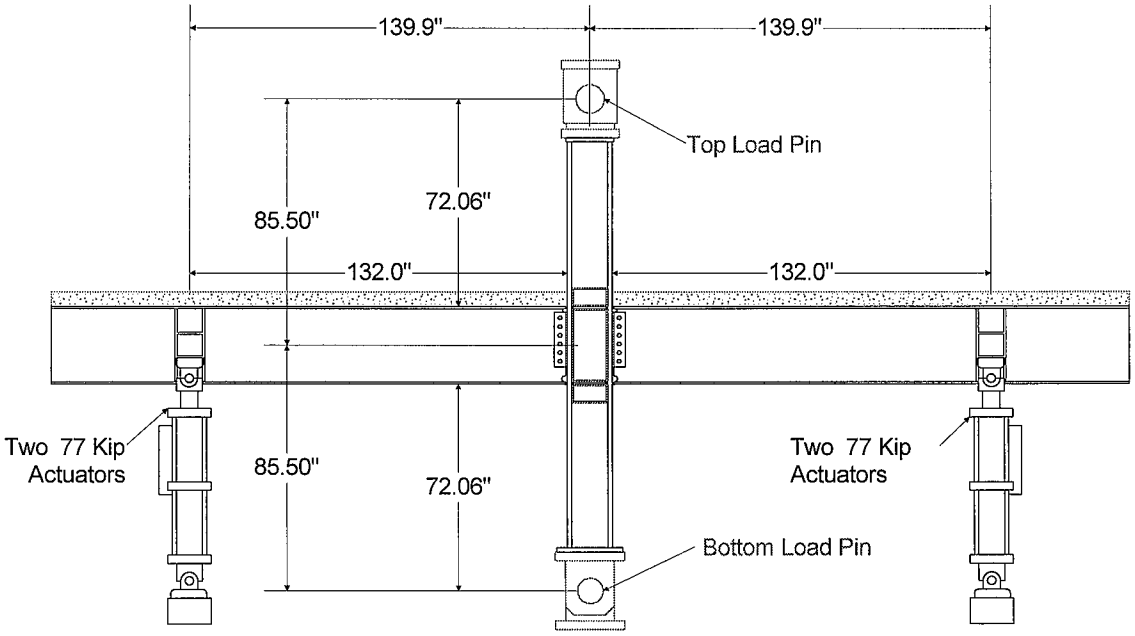

Figure D.1: Actual Specimen Loading Scheme

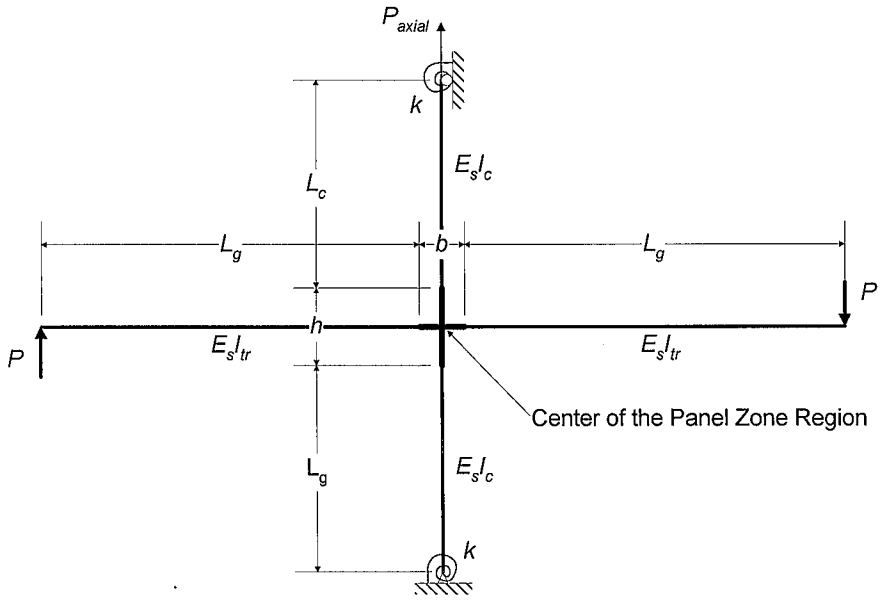

Figure D.2: Structural Idealization of Specimen Loading Scheme

However, it is shown in Appendix F that the effects of this assumption have a minimal effect on the calculation of the column flexural deformation.

Rotational springs are incorporated at the supports because there is an undetermined amount of rotational resistance due to the effects of load pin friction. The significance of these effects is discussed in Section 4.1.1 and in Appendix E. The load, P, for each girder is equal to the sum of the loads of the two actuators loading the girder tip, while the applied axial load to the column, P_{axial}, is equal to 550 kips tension.

D.2 Modeling of Specimen Geometric and Material Properties

The elements of the idealized models are modeled to possess linear elastic material properties and to exhibit geometric linearity. The panel zone region of each specimen, defined by the region within the continuity plates, h, and the column flanges, b, is assumed to be infinitely rigid. Note that the height of this rigid section does not include the entire doubler plate, which extends 6" beyond the top and bottom continuity plates. It is assumed that the doubler plate does not provide substantial flexural rigidity beyond the continuity plates. The length of the girder, L_g, is measured from the column face to the point of applied load. Similarly, the length of the column, L_c, is measured from the center of the load pin to the nearest continuity plate. Values for these dimensions are shown in Figure D.1 and are provided in Appendix K.

The column employs a constant flexural rigidity value of E_sI_c, where E_s and I_c are equal to the modulus of elasticity of steel and the moment inertia of a W14X211 steel member (strong axis bending), respectively. It is assumed that the load pin assembly, which connects the load pin to the top of the column, possesses flexural rigidity properties that are similar to those of the column. Therefore, the parameter, E_sI_c, is assumed to be valid over the entire effective length of the column L_c. For Specimen 1, the transformed moment of inertia of the girder, I_{tr}, is equal to moment of inertia of a W27X94 steel section (strong-axis bending), since the girders of Specimen 1 do not

possess a concrete deck. For Specimens 2 and 3, the estimation of the transformed moment of inertia takes into account the level of composite action between the steel girder and the concrete slab (see Appendix A). Finally, the stiffness of each girder varies between girder positive and negative bending. Values for these parameters are provided in Appendix K.

Appendix E

Effects of Load Pin Resistance

This appendix investigates the effect of load pin friction to the resistance to loading provided during testing by performing linear elastic computational studies of the specimens. As discussed in Section 2.3.3, two load pins were utilized to allow rotation of the column ends during cyclic loading. The bottom load pin assembly was anchored to the laboratory strong floor while the top load pin was connected to the MTS 600 kip testing machine to allow an axial load to be applied to the specimens. The top and bottom load pins were bolted and welded with stitch welds to Specimens 1 and 2, but were bolted and welded with continuous fillet welds to the top and bottom load pins for Specimen 3. By representing the resistance due to load pin friction as a rotational spring with a stiffness, k, a structural idealization of the specimens and the loading system may be constructed (see Appendix D).

E.1 Calculation of Load and Strain Moments

In this section, the load pin friction is studied directly by comparing the "load moment" and the "strain moment." The load moment is the moment in the column calculated based on the actuator loads, while the strain moment is the internal moment

that is calculated using strain measurements in the column. The load moment, M_{load}, is determined by considering static equilibrium in the specimens assuming a pinned support at the bottom load pin and only a lateral support at the top load pin (see Figure E.1). Horizontal reaction forces, H at the top and bottom of the column section are calculated by taking the moment about the center of the panel zone region:

$$\sum M_{pz} = H\left(L_c + \frac{h}{2}\right) + H\left(L_c + \frac{h}{2}\right) - P_{east}\left(L_b + \frac{b}{2}\right) - P_{west}\left(L_b + \frac{b}{2}\right) = 0 \qquad \text{(E.1)}$$

$$H = \frac{\left(P_{east} + P_{west}\right)\left(L_b + \frac{b}{2}\right)}{2L_c + h} \qquad \text{(E.2)}$$

where b = width of panel zone region (in.)

h = height of panel zone region (in.)

L_b = length of girder measured from girder tip to column face (in.)

L_c = length of column measured from top of panel zone region to center of load pin (in.)

P_{east} = load applied to the East girder tip (kips)

P_{west} = load applied to the West girder tip (kips)

Values for the parameters h, b, L_c, and L_b are specified in Appendix K.

The top and bottom column moments are calculated at approximate locations of 13.75" and 12.38" above the top continuity plate and below the bottom continuity plate, respectively. These locations, which represent points at which strains in the column flanges were measured for Specimens 1, 2, and 3, are documented in Section 2.4.3.

The horizontal reaction forces at the top and bottom of the column are equal and opposite due to symmetry. Matrix structural analysis was used to verify calculations when considering unequal girder stiffnesses (see Appendix F.8). Using the horizontal

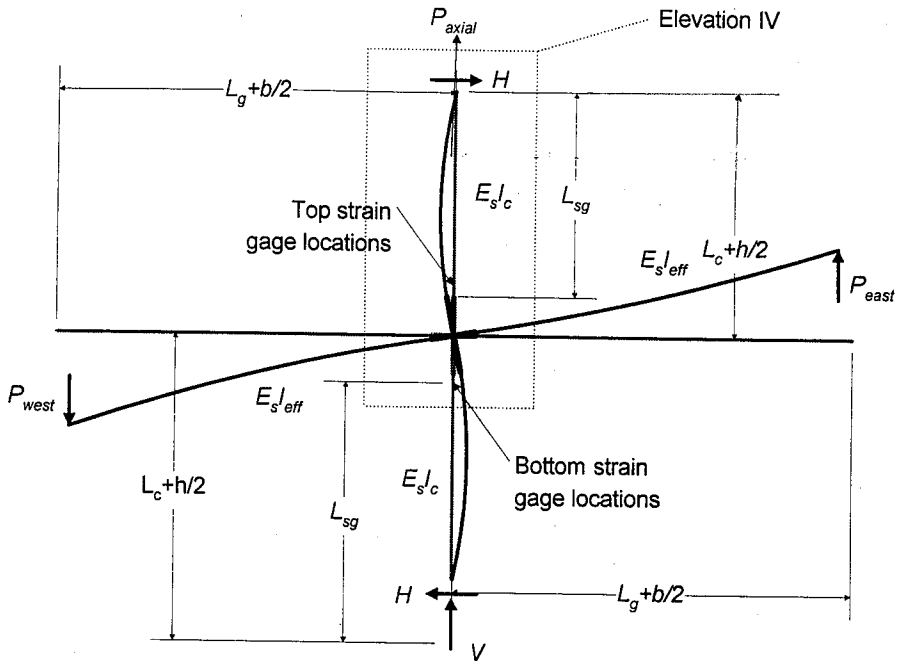

Figure E.1: Free Body Diagram of Test Specimen

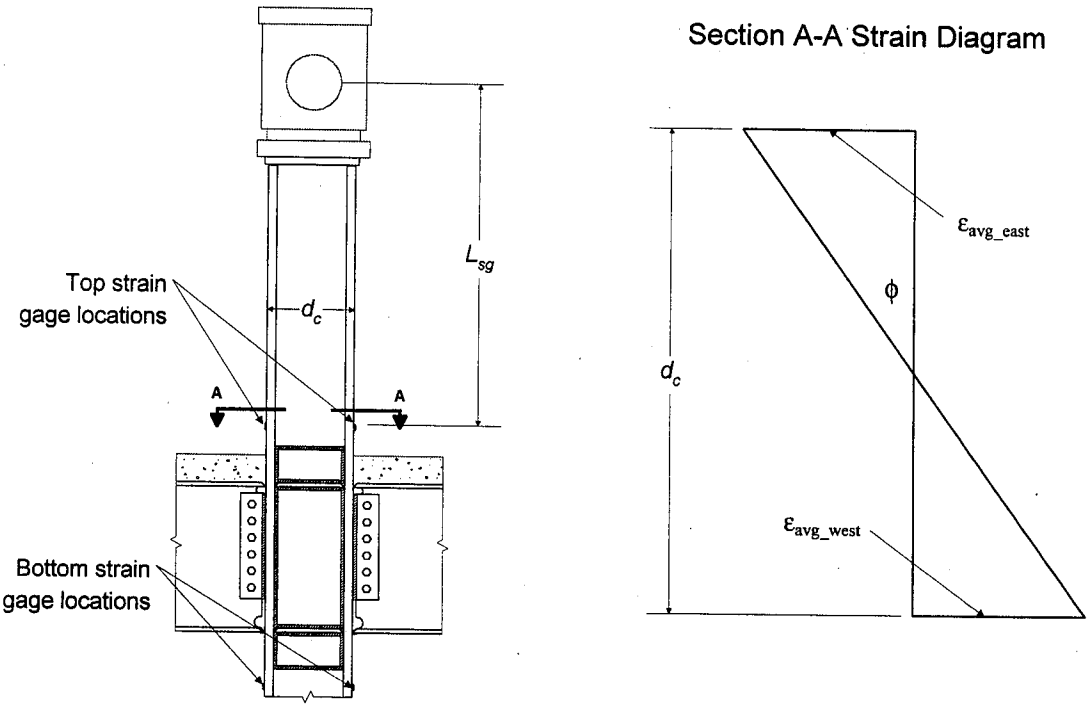

Figure E.2: Elevation IV: View of Top Load Pin Assembly and Connection Region

reaction forces at the top and bottom load pins, column moments located above and below the panel zone region are each calculated at distance L_{sg}, which is the distance between the center of a load pin and the location of the column strain gages (see Figure E.2, top load pin only):

$$M_{load} = HL_{sg} \tag{E.3}$$

where L_{sg} = length measured from center of load pin to column strain gage location (in.)

The strain moment is computed by first using strain measurements of the column to determine the curvature in the column at a distance L_{sg} from the center of a load pin:

$$M_{strain} = -E_s I_c \phi_{col} \tag{E.4}$$

where E_s = modulus of elasticity of steel (ksi)

I_c = moment of inertia of a W27X94 steel section (strong-axis bending) (in^4)

The curvature, ϕ_{col}, is determined by using four strain measurements and the depth of the column, d_c. Two strain measurements are taken from each column flange surface and averaged (for locations of the strain gages, see Section 2.4.3). Curvature of the column is then set equal to the sum between the averaged strains of the column flanges divided by the distance between the strain measurements (i.e., the depth of the column):

$$\phi_{col} = \frac{(\varepsilon_{avg\_east} - \varepsilon_{avg\_west})}{d_c} \tag{E.5}$$

The calculated moment in either the top or bottom column section is defined in terms of the strains in the column flanges, the flexural rigidity (E_s = 29,000 ksi; I_c = 2660 in^4 for the strong axis of a W14X211 section), and the depth of the column:

$$M_{strain} = -E_s I_c \frac{(\varepsilon_{avg\_east} - \varepsilon_{avg\_west})}{d_c} \tag{E.6}$$

This expression is valid assuming elastic material behavior and a linear strain distribution across the column cross-section.

E.2 Comparison of Results

Figures E.3 through E.20 compare the strain moment and load moment in the top and bottom sections of the column. Tables E.1, E.2, and E.3 summarize the percentage errors between the actual and calculated girder tip deflections of the East and West girders for Specimens 1, 2, and 3, respectively. Each tabulated error percentage value is equal to the average of all error percentages for a specific interstory drift level. The error percentages are calculated at the peaks of each cyclic ramp (maximum girder tip deflections). These values are also referred to as peak error percentages.

The drift cycles are also labeled with the corresponding axial load applied to the column. Negative error percentages represent strain moments that are greater in magnitude than the load moments. Also, table cells that contain dashed lines infer that a specific loading excursion did not occur.

For Specimen 1, the effects of friction in the load pins appear to be negligible up to the 1.5% drift levels (Figures E.3 to E.8, Table E.1). The peak error percentages occur in the top column region during negative bending of the West girder, with the error reaching 9%. For Specimen 2, the effects of friction are also negligible in the bottom portion of the column (Figures E.10, E.12, and E.14; Table E.2). For the top portion of the column of Specimen 2, the load moment is much as 11.6% greater than the strain

Table E.1: Percent Error of Strain Moment vs. Load Moment (Specimen 1)

			% Drift / (# of Cycles)									
Column	**West Bending**	**Avg & Std Dev**	**0.25[1] (3)**	**0.25[2] (2)**	**0.25[3] (2)**	**0.50[3] (2)**	**0.75[3] (2)**	**1.0[3] (2)**	**1.5[3] (1.5)**	**1.5[3] (1.5)**	**2.0[3] (3)**	**3.0[3] (1)**
Top	positive	avg	-4.98[4]	-0.33	-3.40	-1.26	-0.38	-0.02	1.08	5.78	6.66	7.60
		std dev	0.17	0.36	0.11	0.06	0.10	0.17	0.93	0.06	0.26	0.00
Top	negative	avg	8.11	2.59	9.00	5.94	4.37	3.81	4.38	-0.32	0.64	------
		std dev	0.34	0.11	0.00	0.03	0.07	0.19	0.00	0.53	0.29	------
Bottom	positive	avg	-8.05	-3.20	-1.54	-0.15	0.51	2.25	5.25	-0.87	1.28	3.07
		std dev	0.23	0.05	0.47	0.45	0.31	0.84	1.33	0.23	0.81	0.00
Bottom	negative	avg	7.83	2.75	1.62	1.55	1.35	-0.06	-1.48	5.67	4.23	------
		std dev	0.08	0.15	0.10	0.06	0.09	0.66	0.00	0.30	0.31	------

[1] Column loaded with no axial load during interstory drift cycle.
[2] Column loaded with 330 kips of axial compression during interstory drift cycle.
[3] Column loaded with 550 kips of axial tension during interstory drift cycle.
[4] Negative percentage values represent load moments that are less in magnitude than strain moments.

Table E.2: Percent Error of Strain Moment vs. Load Moment (Specimen 2)

			% Drift / (# of Cycles)									
Column	**West Bending**	**Avg & Std Dev**	**0.10[1] (3)**	**0.25[1] (3)**	**0.10[1] (3)**	**0.25[1] (3)**	**0.25[2] (3)**	**0.50[2] (3)**	**0.75[2] (3)**	**1.0[2] (3)**	**1.5[2] (3)**	**2.0[2] (1.5)**
Top	positive	avg	3.47	3.26	-4.95[3]	-5.37	-0.37	1.36	2.24	5.34	2.76	2.65
		std dev	0.19	0.05	9.09	0.08	0.02	0.15	0.16	0.29	2.39	0.33
Top	negative	avg	6.10	4.44	11.6	11.4	2.76	6.27	5.13	5.36	7.00	8.30
		std dev	0.42	0.32	9.00	0.14	8.39	0.18	0.20	0.22	1.29	0.00
Bottom	positive	avg	2.76	-2.09	3.74	2.72	3.01	3.63	3.99	2.83	2.49	2.55
		std dev	0.17	0.23	0.30	0.08	0.35	0.38	0.44	0.11	0.59	0.13
Bottom	negative	avg	0.50	1.51	-0.24	1.35	3.09	3.16	3.37	3.24	0.91	0.43
		std dev	0.11	0.05	0.24	0.05	0.03	0.11	0.26	0.31	1.80	0.00

moment when the West girder is subjected to negative bending. However, these errors occur only occasionally in the peaks. Figures E.9, E.11, and E.13 show an excellent correlation between the strain and load moments in the top column region of Specimen 2.

For Specimen 3, Figures E.16 to E.18 demonstrate a good correlation between the load and strain moments in the early cycles (i.e., 0.25% to 0.50% drift levels). The error percentages between the strain and load moments in the top column are most significant starting at 0.75% drift cycles (Figures E.19 and E.20, Table E.3). However, plasticity may have occurred within this range, thus invalidating Equations E.1 through E.3. Nevertheless, the effects of load pin friction are deemed to be small for all three specimens.

Table E.3: Percent Error of Strain Moment vs. Load Moment (Specimen 3)

			% Drift / (# of Cycles)							
Column	**West Bending**	**Avg & Std Dev**	**0.25[1] (8)**	**0.25[2] (1)**	**0.50[2] (3)**	**0.75[2] (3)**	**1.0[2] (3)**	**1.5[2] (3)**	**2.0[2] (3)**	**3.0[2] (2.5)**
Top	positive	avg	6.34	6.35	6.99	12.43	11.84	7.72	7.72	9.12
		std dev	0.50	0.00	0.21	3.50	1.87	0.17	0.17	1.94
Top	negative	avg	-9.48[3]	9.76	9.23	14.33	12.51	9.52	9.52	4.62
		std dev	0.46	0.00	0.03	2.74	1.68	0.23	0.23	0.41
Bottom	positive	avg	5.49	3.27	2.93	8.07	6.90	3.27	3.27	4.75
		std dev	0.73	0.00	0.24	4.11	2.76	0.76	0.76	1.16
Bottom	negative	avg	-3.04	-1.31	0.74	7.13	7.42	1.52	1.52	0.97
		std dev	0.29	0.00	0.20	3.07	1.57	0.36	0.36	0.27

[1] Column loaded with no axial load during interstory drift cycle.

[2] Column loaded with 550 kips of axial tension during interstory drift cycle.

[3] Negative percentage values represent load moments that are less in magnitude than strain moments.

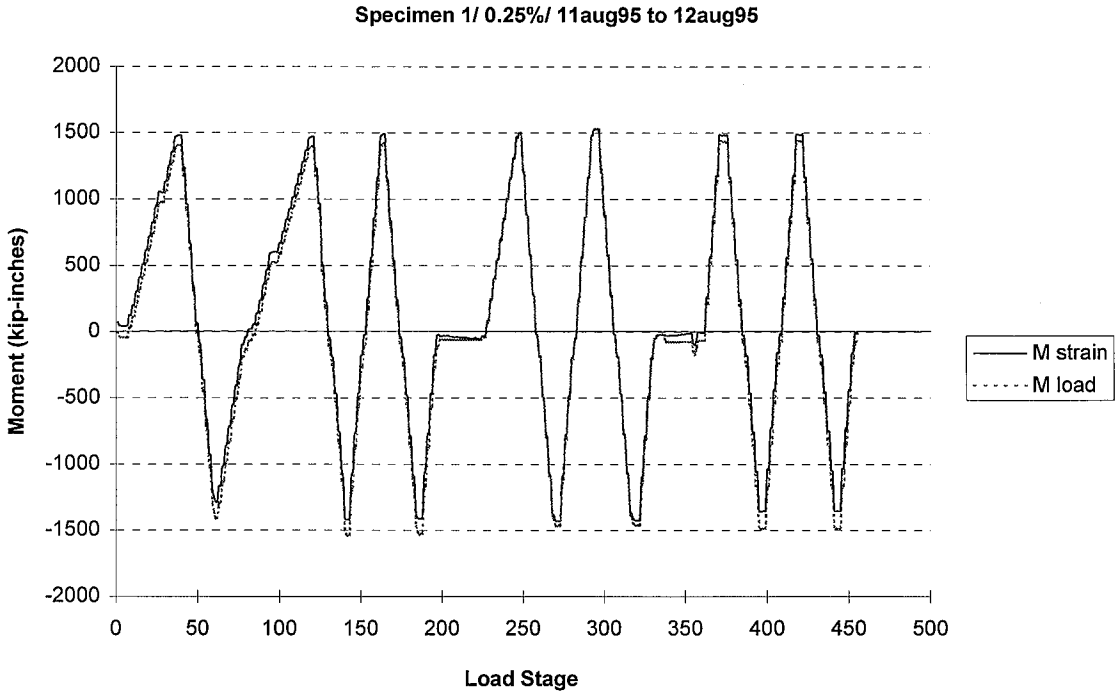

Figure E.3: Strain Moment vs. Load Moment (Top Column Section of Specimen 1)

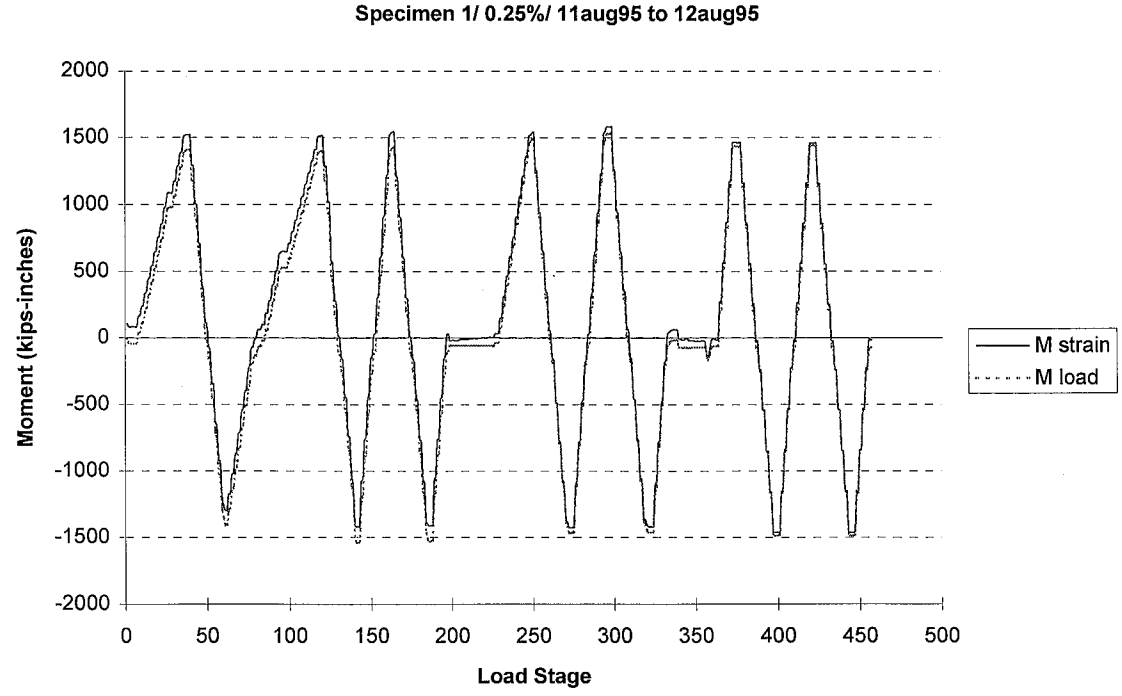

Figure E.4: Strain Moment vs. Load Moment (Bottom Column Section of Specimen 1)

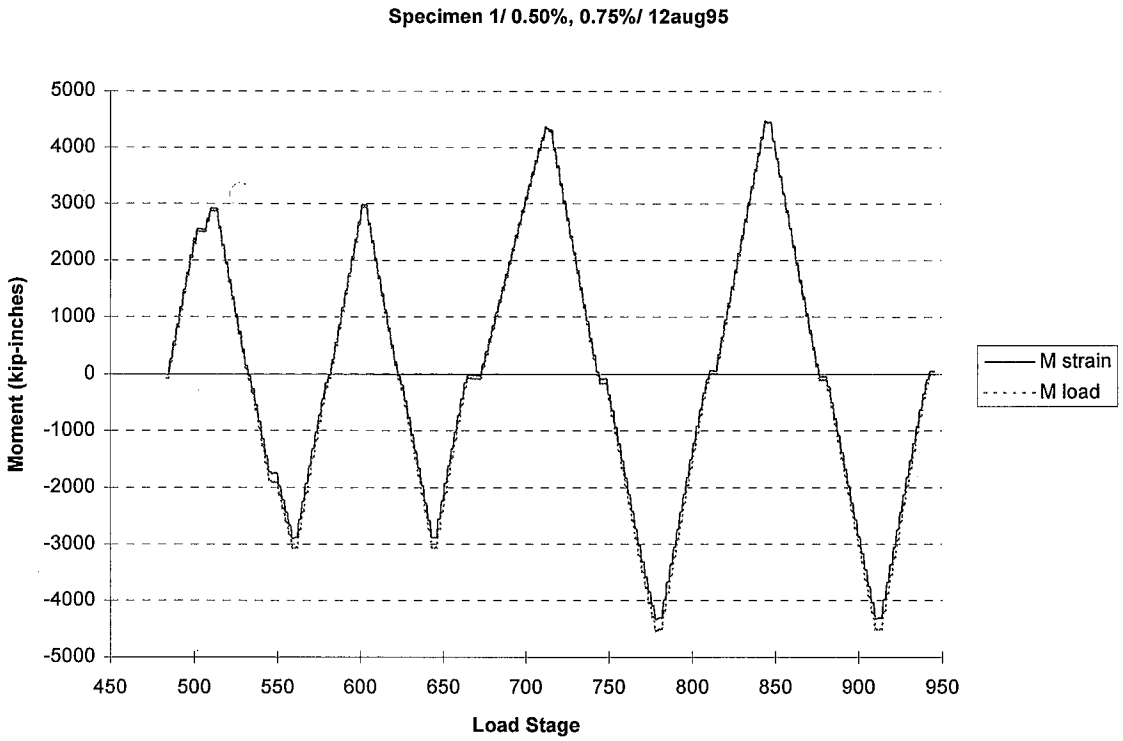

Figure E.5: Strain Moment vs. Load Moment (Top Column Section of Specimen 1)

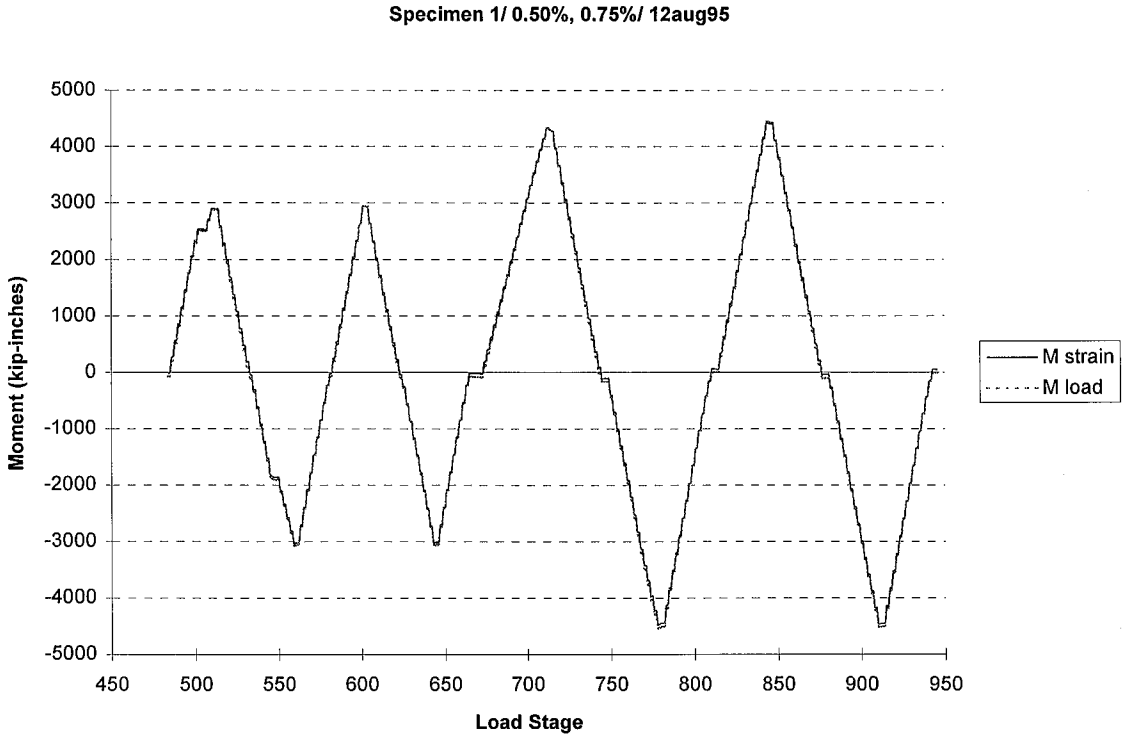

Figure E.6: Strain Moment vs. Load Moment (Bottom Column Section of Specimen 1)

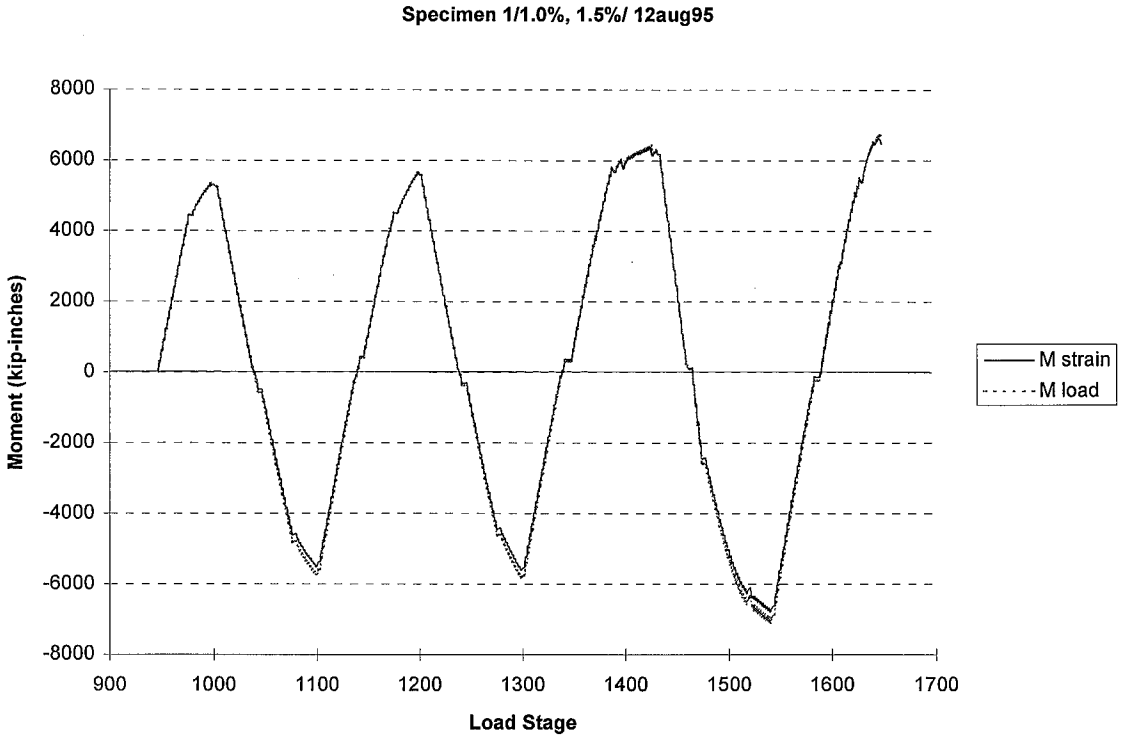

Figure E.7: Strain Moment vs. Load Moment (Top Column Section of Specimen 1)

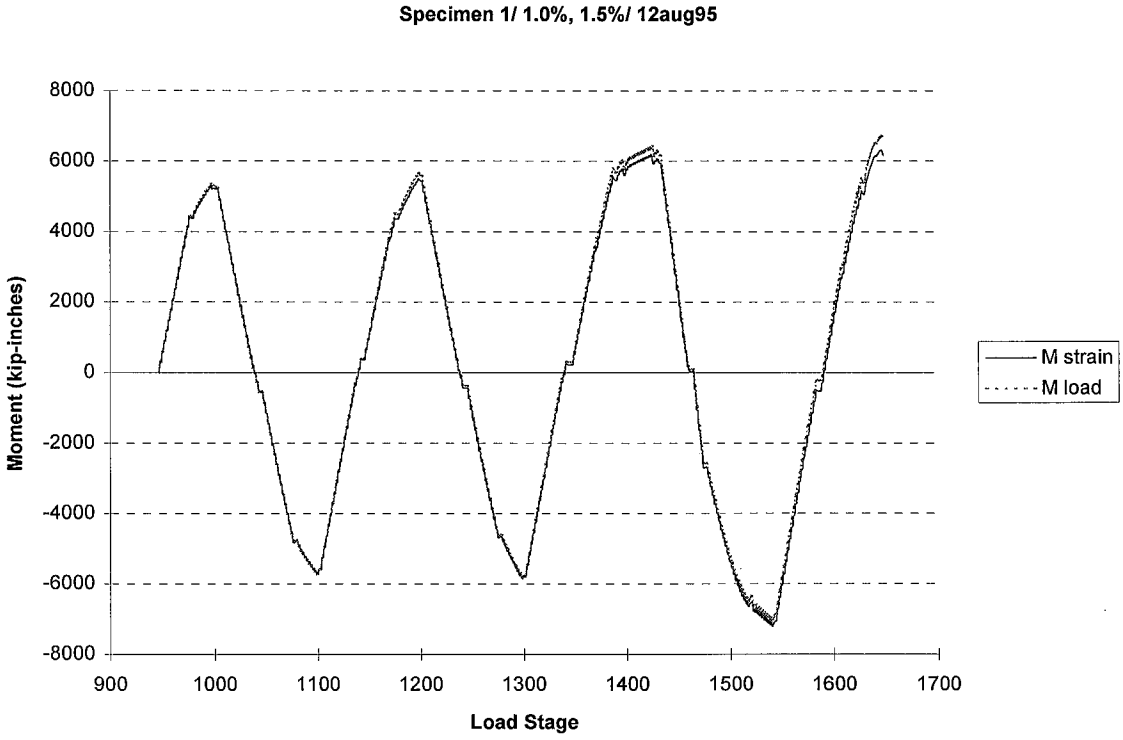

Figure E.8: Strain Moment vs. Load Moment (Bottom Column Section of Specimen 1)

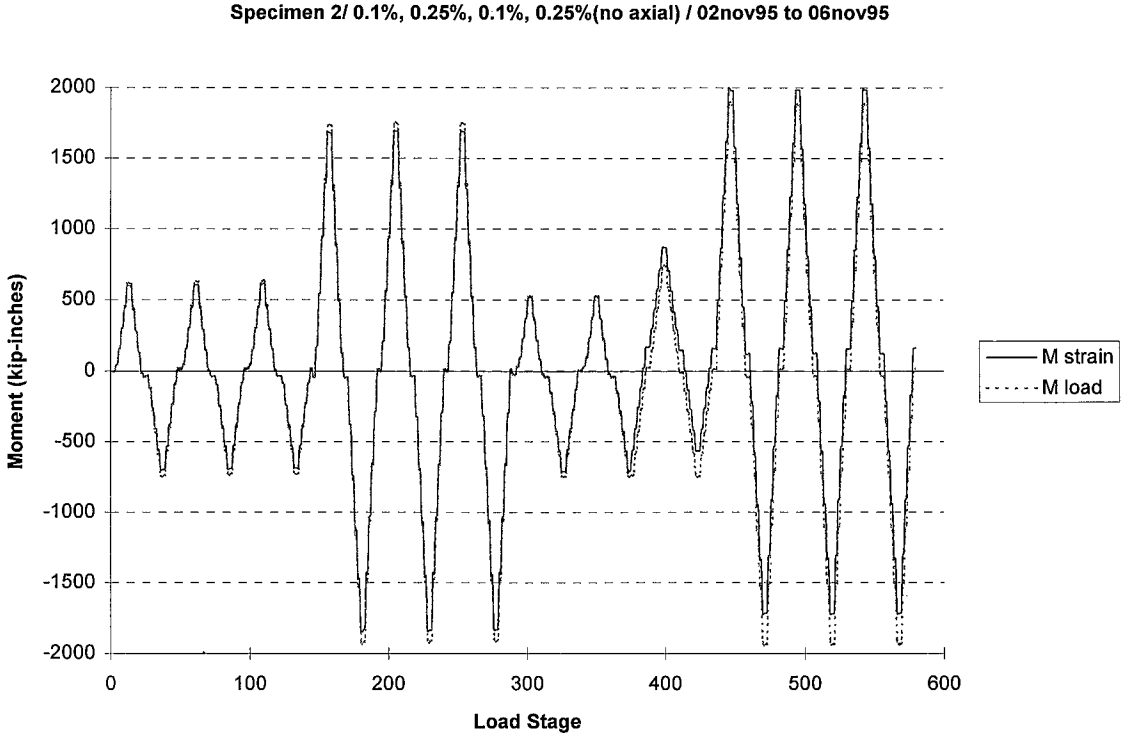

Figure E.9: Strain Moment vs. Load Moment (Top Column Section of Specimen 2)

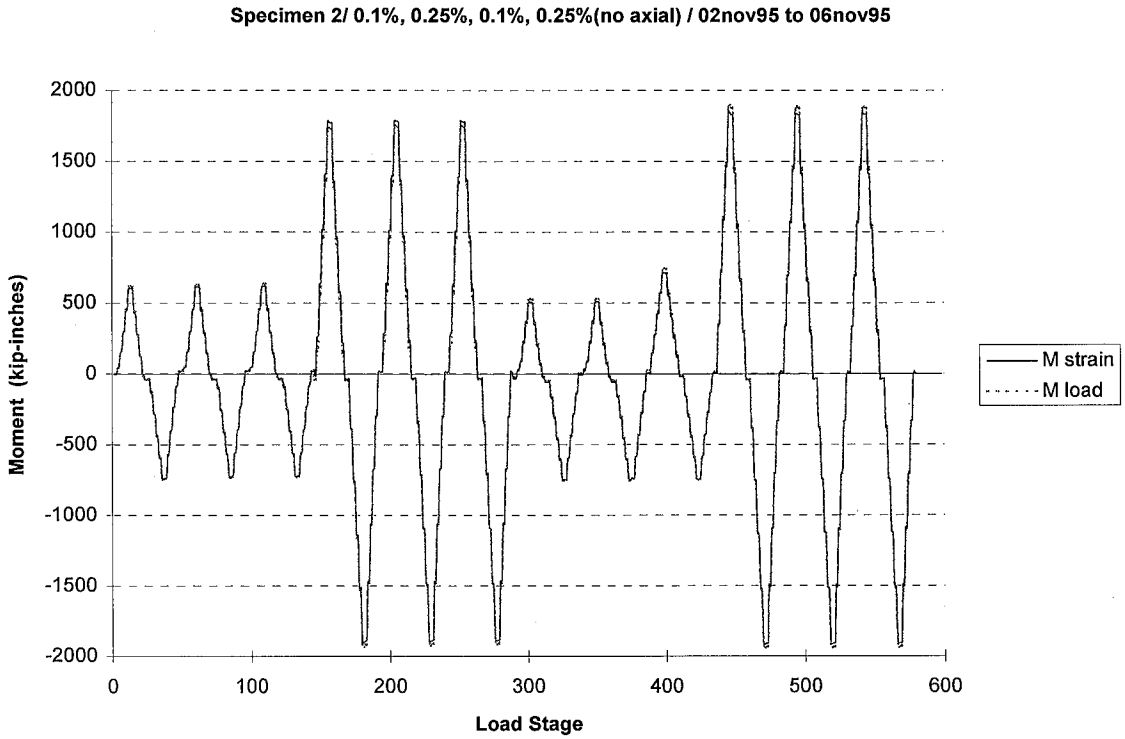

Figure E.10: Strain Moment vs. Load Moment (Bottom Column Section of Specimen 2)

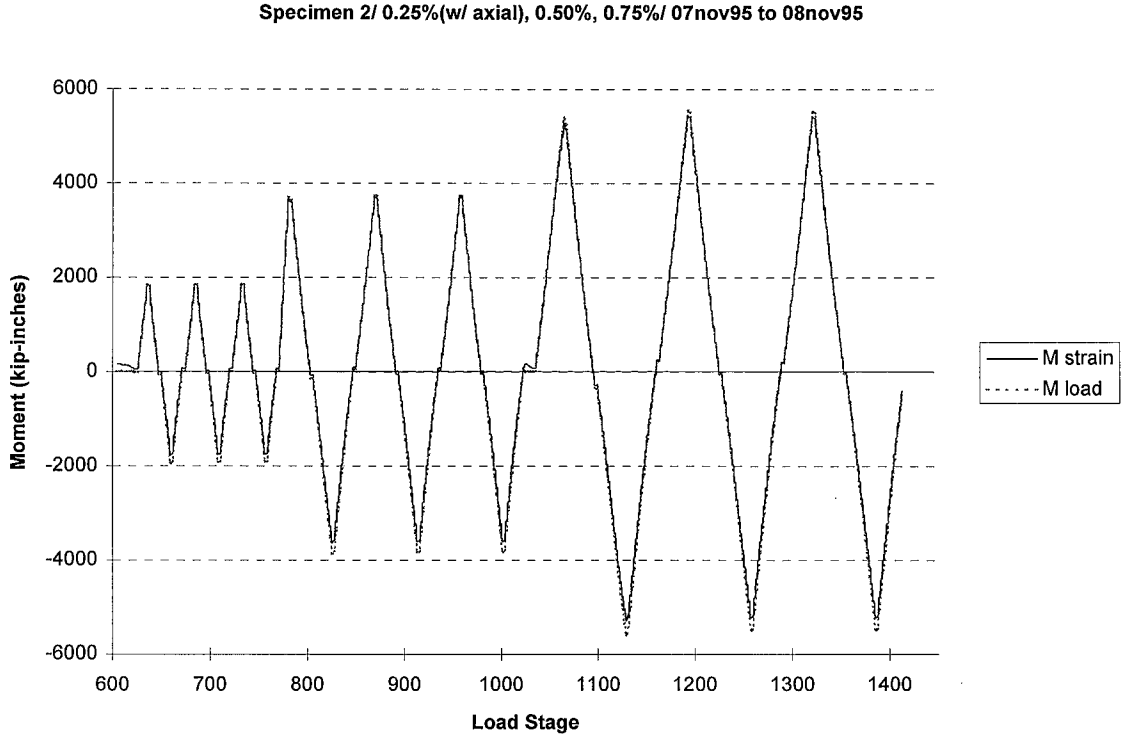

Figure E.11: Strain Moment vs. Load Moment (Top Column Section of Specimen 2)

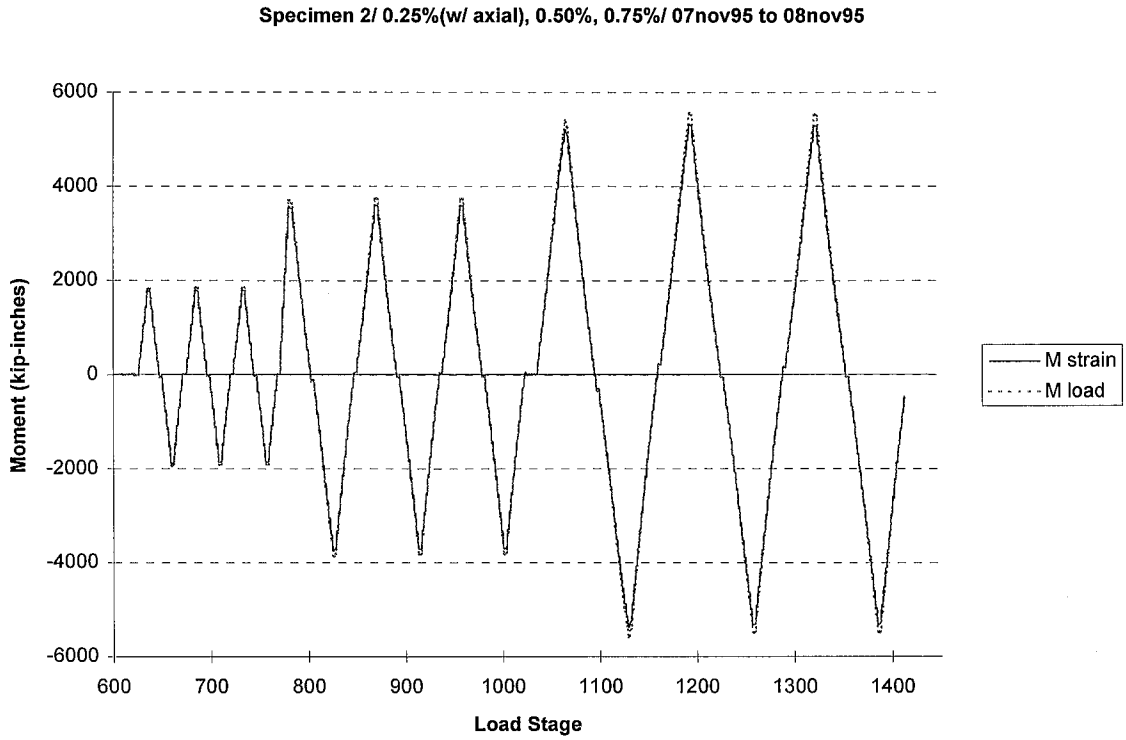

Figure E.12: Strain Moment vs. Load Moment (Bottom Column Section of Specimen 2)

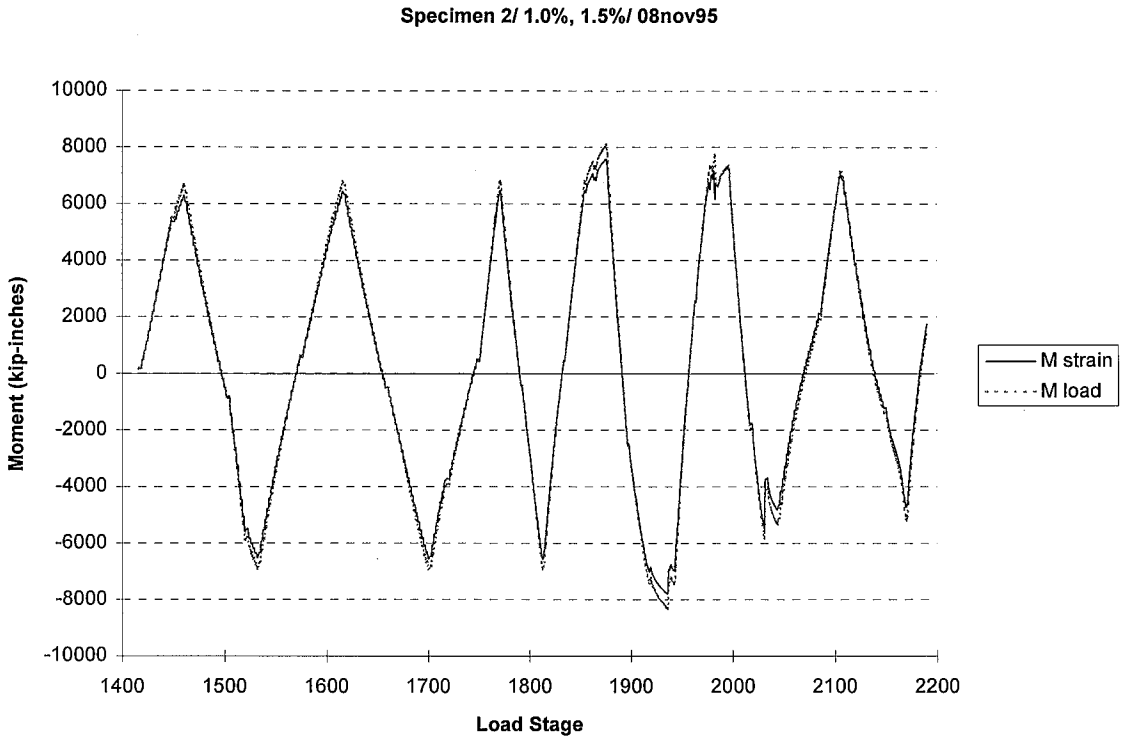

Figure E.13: Strain Moment vs. Load Moment (Top Column Section of Specimen 2)

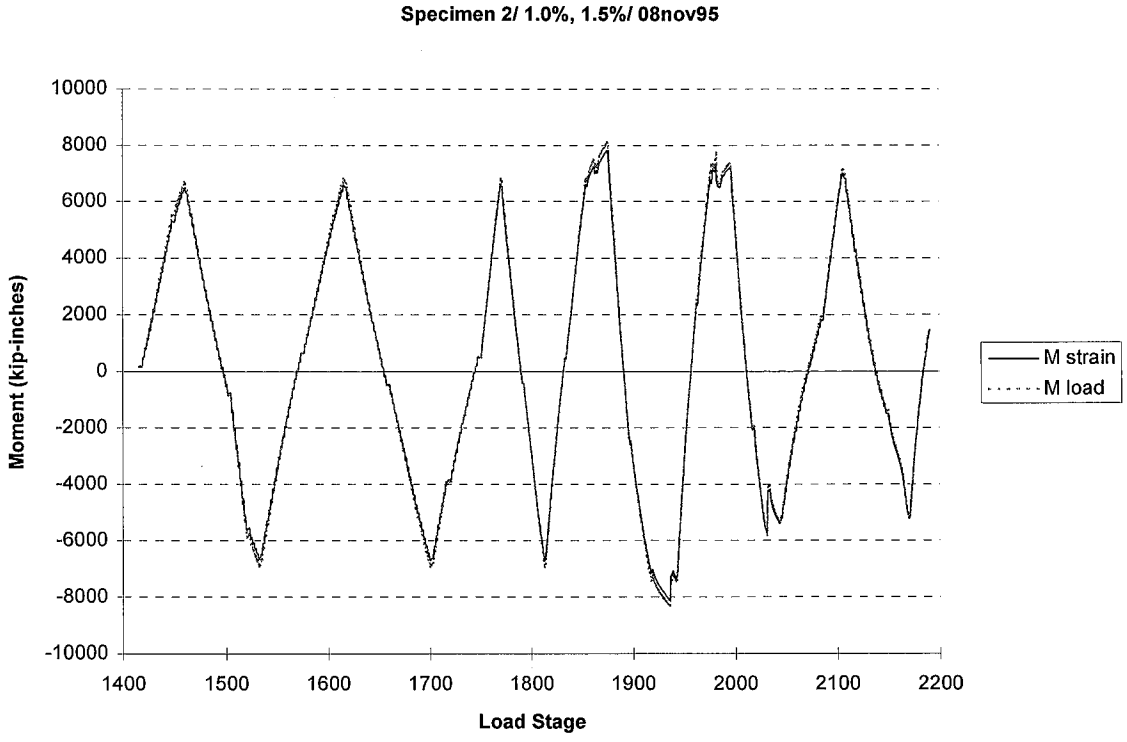

Figure E.14: Strain Moment vs. Load Moment (Bottom Column Section of Specimen 2)

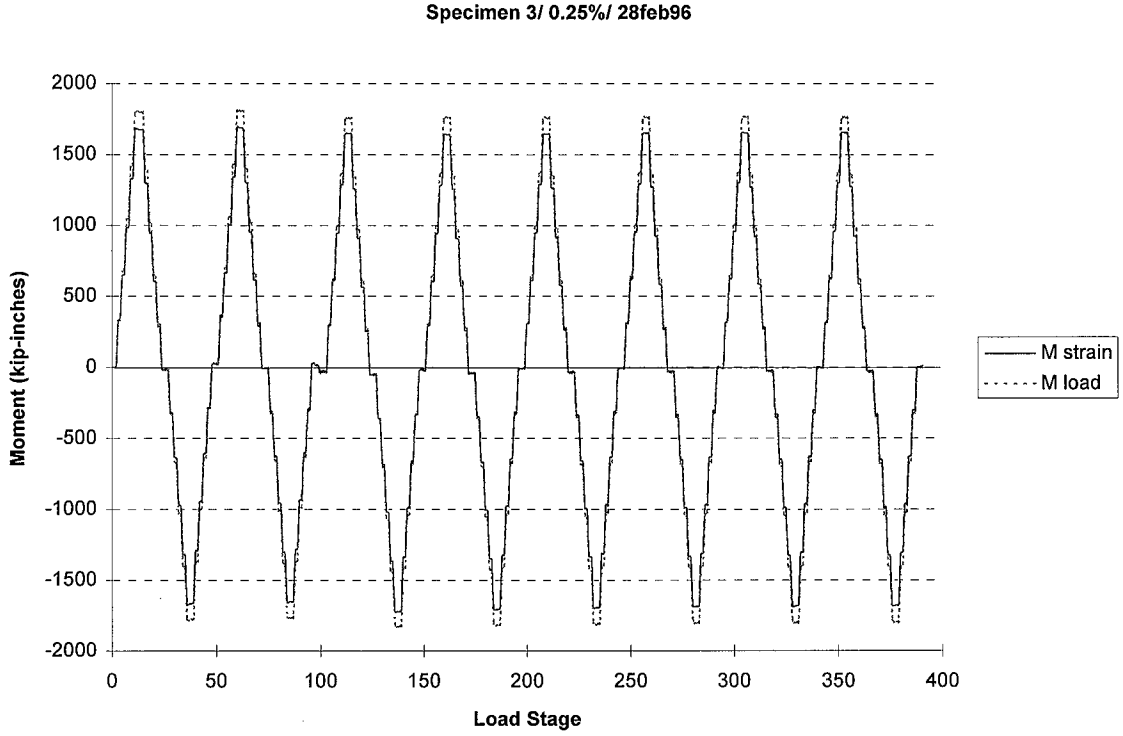

Figure E.15: Strain Moment vs. Load Moment (Top Column Section of Specimen 3)

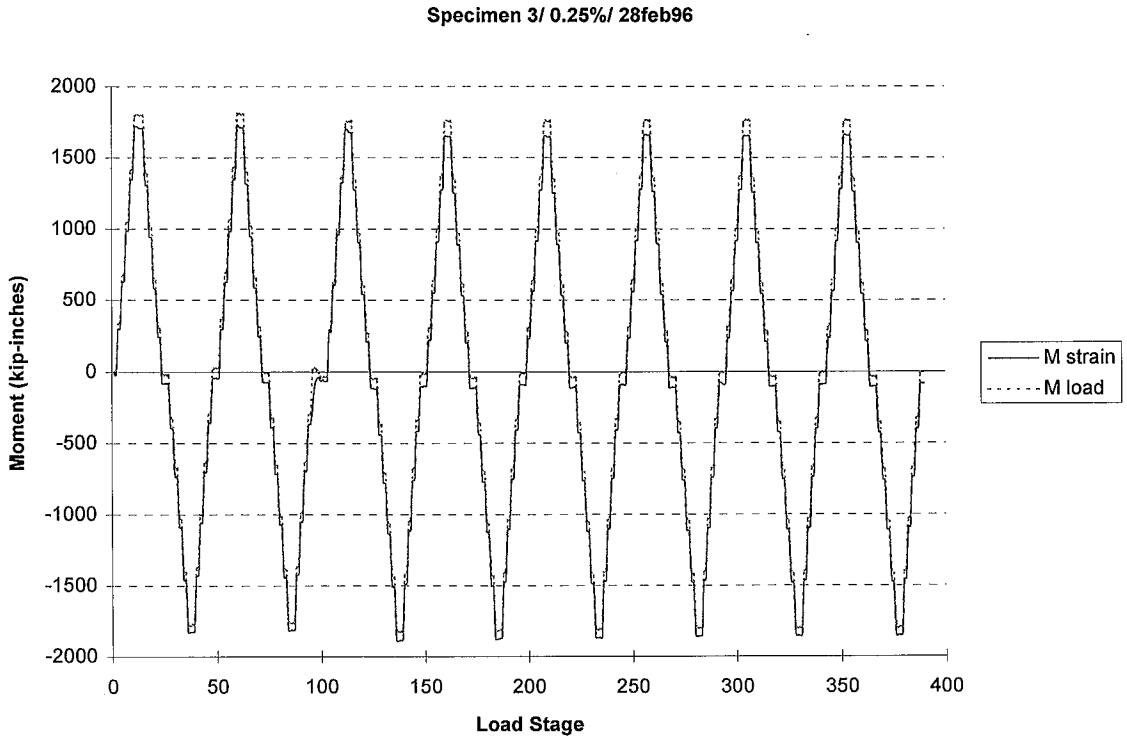

Figure E.16: Strain Moment vs. Load Moment (Bottom Column Section of Specimen 3)

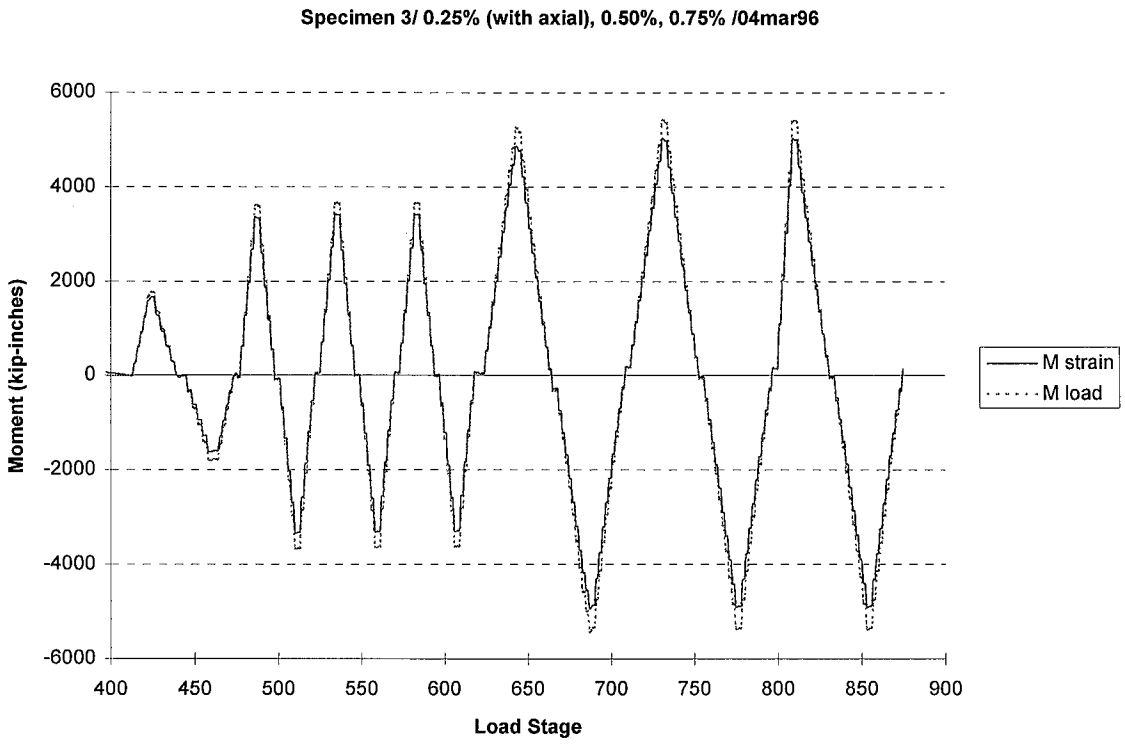

Figure E.17: Strain Moment vs. Load Moment (Top Column Section of Specimen 3)

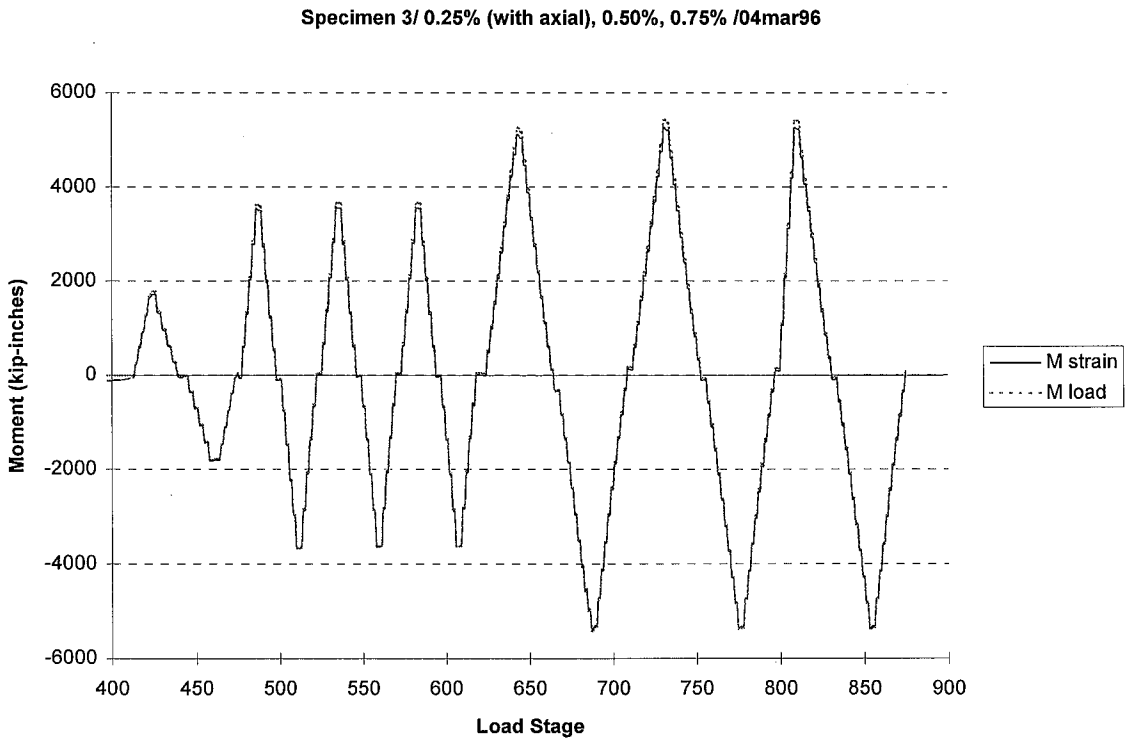

Figure E.18: Strain Moment vs. Load Moment (Bottom Column Section of Specimen 3)

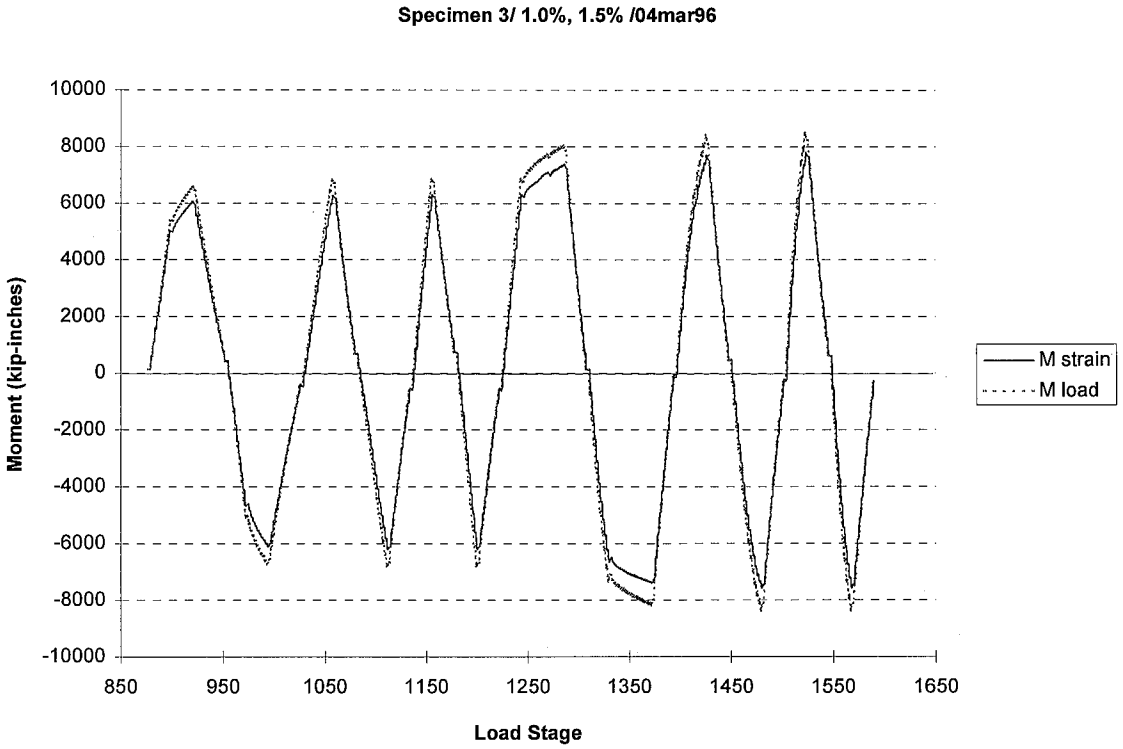

Figure E.19: Strain Moment vs. Load Moment (Top Column Section of Specimen 3)

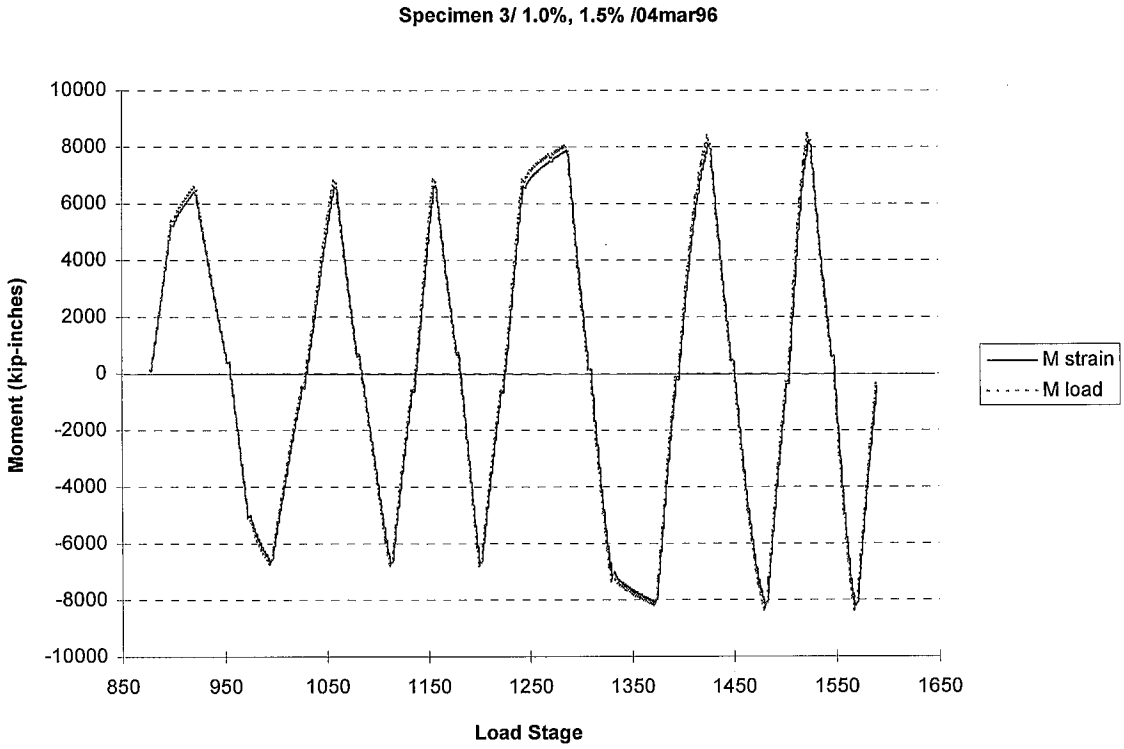

Figure E.20: Strain Moment vs. Load Moment (Bottom Column Section of Specimen 3)

Appendix F

Girder Tip Deflection Components

This appendix discusses the calculation of the five components contributing to the girder tip deflection of the specimens. These components include: panel zone deformation (Δ_{pz}), girder-to-column (relative) rotation (Δ_{rel}), column flexural deformation (Δ_{col}), girder flexural deformation ($\Delta_{gird\,flex}$), girder shear deformation ($\Delta_{\text{gird shear}}$), and deflection of the load frame (Δ_{lf}):

$$\Delta_{calc} = \Delta_{pz} + \Delta_{rel} + \Delta_{col} + \Delta_{gird\,flex} + \Delta_{gird\,shear} + \Delta_{lf} \qquad \text{(F.1)}$$

Results from the comparison of the actual and calculated girder tip deflections are reported along with various conditions which may have generated errors between the two deflections. Such effects include the calculation of effective moment of inertia of the composite girders and the accuracy of the instrumentation.

F.1 Panel Zone Shear Distortion Component

The specimens were intentionally designed with relatively rigid panel zone regions so as to ensure minimal yielding of the panel zone prior to a connection failure at

the welded girder-to-column connection. Even though the panel zone was designed to constitute only a small percentage of the overall specimen deformation, panel zone shear distortion still occurred and was thus measured. It is transformed here into a girder tip deflection component.

Given a measured value of the angular panel zone distortion, γ_{pz}, determined in Appendix C, the girder tip deflection component due to distortion of the panel zone may be computed (Leon, 1983). Figure F.1 shows the panel zone before and after its deformed state.

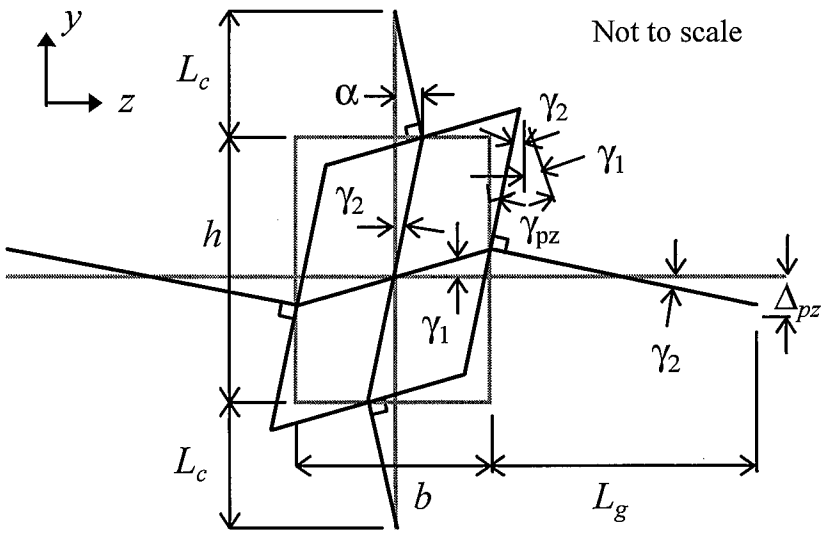

Figure F.1: Girder Tip Deflection Component Due to Panel Zone Shear Distortion [after (Leon, 1983)]

The angular panel zone distortion is decomposed into two components, γ_1 and γ_2:

$$\gamma_{pz} = \gamma_1 + \gamma_2 \tag{F.2}$$

These two components represent the distortion of the panel zone with respect to the horizontal direction (z-axis) and the vertical direction (y-axis), respectively. The angle γ_1 is expressed (in units of radians) in terms of γ_2, h, and L_c as:

$$\gamma_1 = \gamma_2 \left(\frac{h}{2L_c} \right) \tag{F.3}$$

This equation is formulated by representing the displacement of the top or bottom edge of the panel zone, α, in terms of γ_1, γ_2, h, and L_c. L_c denotes the length of the column from the center of the load pin to the edge of the panel zone and h is equal to the height of the panel zone. Equation F.2 and Equation F.3 are combined to create an expression for the angle, γ_2, in radians:

$$\gamma_2 = \gamma_{pz} \left(\frac{L_c}{L_c + \frac{h}{2}} \right) \tag{F.4}$$

Again referring to Figure F.1, the contribution of panel zone distortion to the girder tip deflection may be expressed in terms of the two panel zone components:

$$\Delta_{pz} = \gamma_2 L_g - \gamma_1 \frac{b}{2} \tag{F.5}$$

Note that the panel zone distortion in the vertical direction, γ_1, actually negates a portion of the girder tip deflection due to distortion of the panel zone. Equations F.4 to F.6 are combined to define the panel zone distortion component of the girder tip deflection in units of inches:

$$\Delta_{pz} = \left[\frac{\gamma_{pz} L_c L_g}{\left(L_c + \frac{h}{2} \right)} - \frac{\gamma_{pz} h}{(2L_c + b)} \frac{b}{2} \right] \tag{F.6}$$

where b = width of panel zone (in.)

h = height of panel zone (in.)

L_g = length of girder measured from point of applied girder tip load to column face (in.)

L_c = length of column measured from center of load pin to panel zone edge (in.)

Several assumptions are made in order to formulate Eqs. F.3 through F.6. First, it is assumed that the center of the panel zone experiences only shear distortion. In addition, the top and bottom edges of the panel zone and the East and West edges of the panel zone each remain parallel to one another during panel zone distortion. Finally, the column and girders remain orthogonal to the panel zone edges and the column and girder elements are assumed to be infinitely rigid for this calculation.

F.2 Girder Flexural Deformation Component

A major portion of the girder tip deflection is due to flexural deformation of the girder. This contribution to the girder tip deflection is defined using Euler-Bernoulli beam theory (Gere and Timoshenko, 1990):

$$\Delta_{gird\ flex} = \frac{PL_g^{\ 3}}{3E_s I_{eff}} \tag{F.7}$$

where P = applied load at the girder tip (kips)

E_s = modulus of elasticity of steel (ksi)

I_{eff} = effective girder moment of inertia (in^4)

Equation F.7 is formulated by assuming that the girder behaves as a fixed cantilever, assuming a rigid panel zone region, and was verified using matrix structural analysis (see Section F.8).

The length of the girder, L_g, is measured from the column face to the point of applied load to the girder tip. The load, P, for each girder is equal to the sum of the loads of the two actuators loading the girder tip. For Specimen 1, the effective moment of inertia, I_{eff}, is equal to the strong-axis moment of inertia of a W27X94 steel section. For Specimens 2 and 3, the effective moments of inertia include the effects of a partially composite slab. Because the testing procedure simultaneously loaded one composite girder in positive bending while loading the other in composite girder in negative bending, different moments of inertia are used for the composite girders for a given load excursion in Eq. 7. The calculation of the effective moment of inertias for the composite girders are reported in Appendix A. Based on a comparison between a computational model of Specimen 3 and the equations used to generate the flexure components of girder tip deflection, it is concluded that Eq. 7 is a good approximation of the girder flexure component of the girder tip deflection (see Section F.8).

F.3 Column Flexural Deformation Components

Two expressions for the girder tip deflection due to elastic flexural deformation of the column were derived from slope deflection equations: one assuming pinned column supports (zero resistance to column rotation) and the other assuming fixed column supports (infinite resistance to column rotation). These expressions represent upper and lower bounds to the actual column flexural deformation (assuming linear elastic behavior of the column) and were verified using matrix structural analysis (see Section F.8). Also, the occurrence of vertical deflection at the top load pin was assumed negligible when formulating the column flexural deformation components (see Section F.8).

F.3.1 Pinned Column Supports

An expression for column flexural rotation is derived using slope deflection equations (Eqs. F.8 and F.9), assuming no rotational resistance at the column supports and no vertical displacement of the column supports (see Figure F.2).

$$M_{ab} = \frac{2E_s I_c}{L_c}\left(2\theta_a + \theta_b - \frac{3\Delta}{L_c}\right) \tag{F.8}$$

$$M_{ba} = \frac{2E_s I_c}{L_c}\left(2\theta_b + \theta_a - \frac{3\Delta}{L_c}\right) \tag{F.9}$$

where θ_a = column rotation at top pinned support (radians)

θ_b = column rotation at top of panel zone (radians)

Δ = column horizontal deflection of point A relative to B (in.)

I_c = moment of inertia of W14X211 steel section (strong-axis bending) (in^4)

To isolate the contribution of column flexure to the girder tip deflection, the structural idealization model employs a rigid panel zone of width b and depth h, and two rigid girder lengths, L_g (see Appendix D). It is also assumed that the column rotation at the top edge of the panel zone, θ_b, is equal to the column rotation at the bottom edge of the panel zone, θ_c (see Figure F.3). Defining h as the height of the panel zone, the relative horizontal deflection between points A and B, Δ, may be defined as (assuming a small rotation θ_b):

$$\Delta = \left(\frac{h}{2}\tan(\theta_b)\right) \approx \frac{-h\theta_b}{2} \tag{F.10}$$

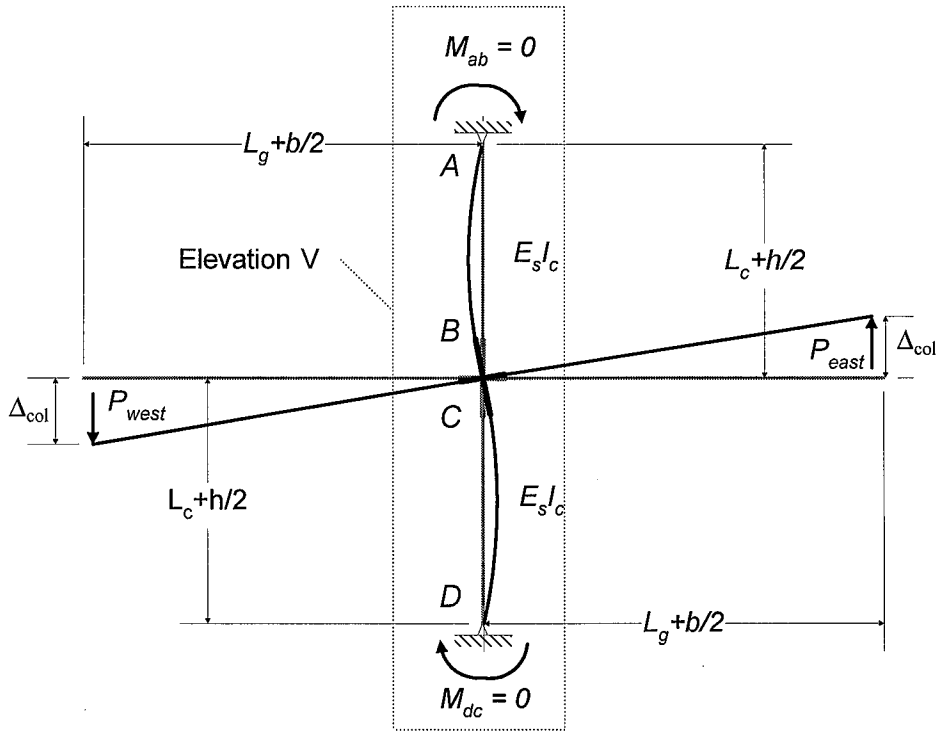

Figure F.2: Specimen Structural Idealization (Pinned Column Supports)

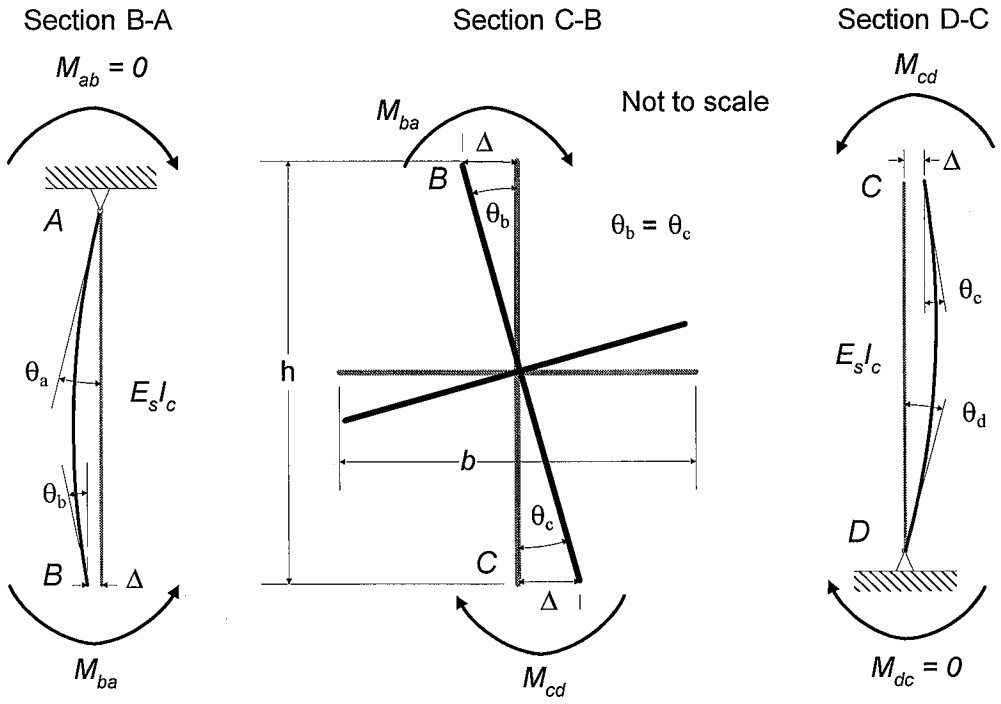

Figure F.3: Elevation V: Column and Panel Zone Sections B-A, C-B, and D-C

The fixed-end moments, M_{ab} and M_{dc}, at the top and bottom column supports, respectively, are assumed equal to zero for this calculation. Using the slope deflection equation defining M_{ab} (Eq. F.8), the column rotation at the top column support is expressed in terms of the column rotation at the top edge of the panel zone, θ_b:

$$\theta_a = \frac{-\theta_b}{2}\left(1+\frac{3h}{2L_c}\right) \tag{F.11}$$

Substituting this expression into Eq. F.9 gives an expression of M_{ba} in terms of the column rotation, θ_b:

$$M_{ba} = \frac{2E_sI_c}{L_c}\theta_b\left(\frac{3}{2}+\frac{3h}{4L_c}\right) \tag{F.12}$$

M_{ba} may also be expressed in terms of the applied loads at the girder tips, P_{east} and P_{west}, using static equilibrium equations:

$$M_{ba} = \left(\frac{P_{east}\left(L_g+\frac{b}{2}\right)+P_{west}\left(L_g+\frac{b}{2}\right)}{2L_c+h}\right)L_c = \left(\frac{P_{tot}\left(L_g+\frac{b}{2}\right)}{2L_c+h}\right)L_c \tag{F.13}$$

Note that $P_{tot} = P_{east} + P_{west}$ (assuming antisymmetric loading causes both forces to have the same sign) and that when calculating the reaction forces at the column supports, the moment arm lengths used include the column and girder lengths as well as the panel zone dimensions (see Figure F.2). Equations F.12 and F.13 are combined to express the flexural column rotation θ_b in terms of P_{east}, P_{west}, and the dimensions of the specimen:

$$\theta_b = \frac{P_{tot} L_c^2 \left(L_g + \frac{b}{2} \right)}{2E_s I_c (2L_c + h) \left(\frac{3}{2} + \frac{3h}{4L_c} \right)} \tag{F.14}$$

Finally, the flexural column rotation contribution to the girder tip deflection (pinned column supports) is calculated by multiplying the flexural column rotation, θ_b, by the distance measured from centerline of the panel zone to the point of applied load at the girder tip:

$$\Delta_{col} = \theta_b \left(L_g + \frac{b}{2} \right) = \frac{P_{tot} \left(2L_g + b \right)^2 L_c^2}{8E_s I_c (2L_c + h) \left(\frac{3}{2} + \frac{3h}{4L_c} \right)} \tag{F.15}$$

F.3.2 Fixed Column Supports

An expression for column flexural rotation is derived using slope deflection equations, assuming infinite rotational resistance at the column supports and no vertical displacement of the column supports (see Figure F.4). As was previously shown for the pinned column support case, the panel zone region and girders are assumed infinitely rigid and θ_b is assumed equal to θ_c (see Figure F.5). The fixed-end moments, M_{ab} and M_{ba}, are defined at points A and B respectively. In order to relate the fixed-end moments and column rotations, slope deflection equations are again created for region AB:

$$M_{ab} = \frac{2E_s I_c}{L_c} \left(2\theta_a + \theta_b - \frac{3\Delta}{L_c} \right) \tag{F.16}$$

$$M_{ba} = \frac{2E_s I_c}{L_c} \left(2\theta_b + \theta_a - \frac{3\Delta}{L_c} \right) \tag{F.17}$$

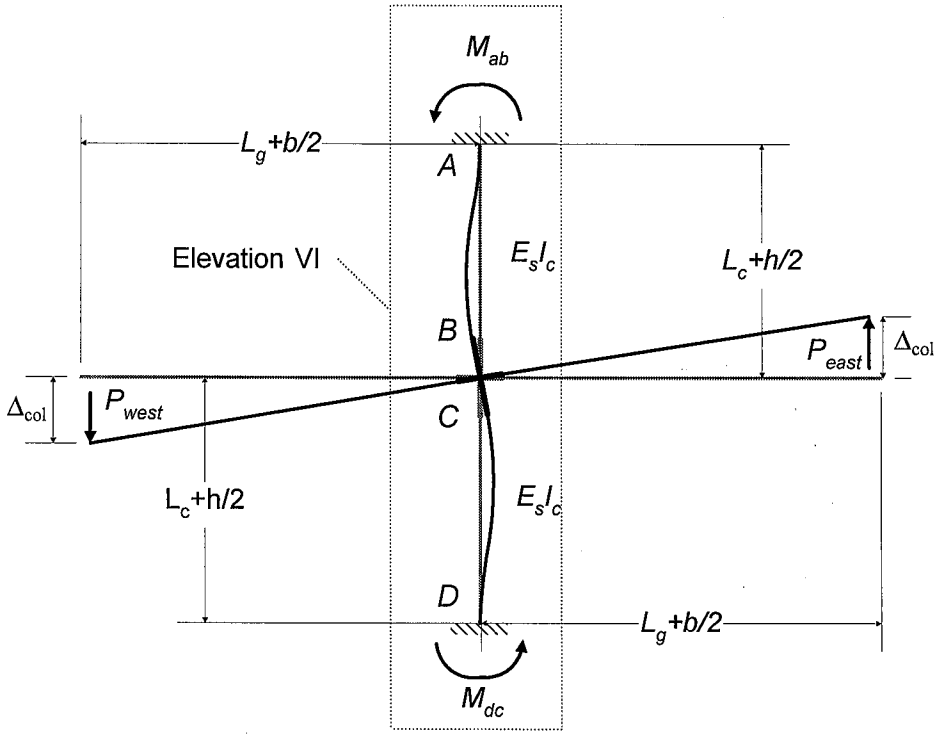

Figure F.4: Specimen Structural Idealization (Fixed Column Supports)

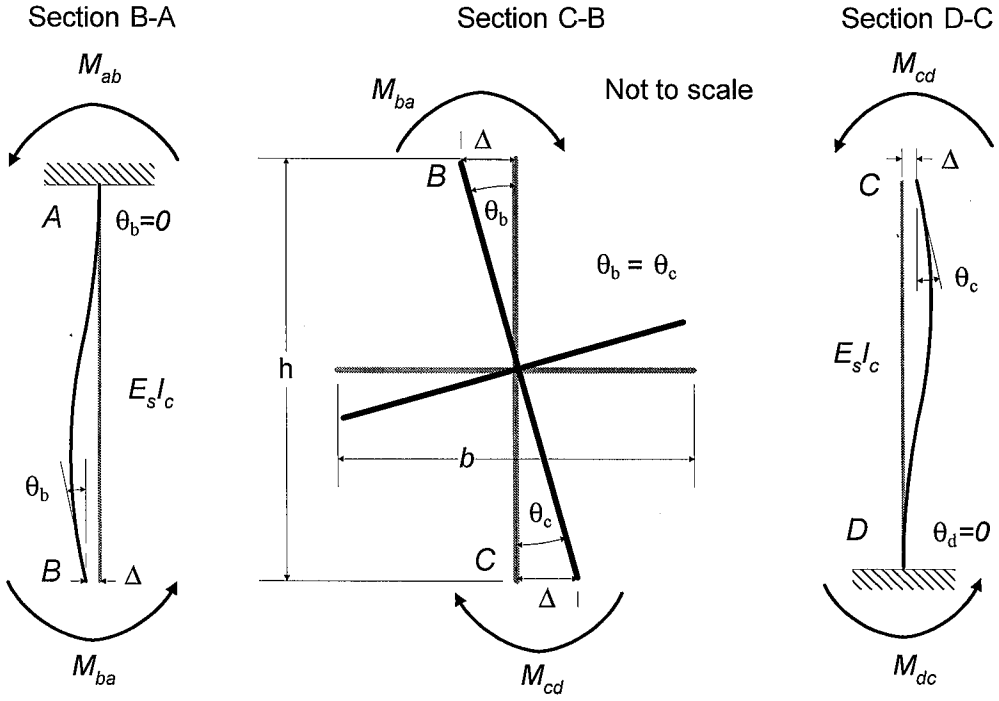

Figure F.5: Elevation VI: Column and Panel Zone Sections B-A, C-B, and D-C

Similar to the pinned column supports case, the relative horizontal deflection, Δ, represents the change in horizontal deflection between points A and B:

$$\Delta = \left(\frac{h}{2}\tan(\theta_b)\right) \approx \frac{-h\theta_b}{2} \tag{F.18}$$

When combining Eqs. F.16 to F.18, and assuming that θ_a is equal to zero, the expressions for the fixed-end moments M_{ba} and M_{ab} are:

$$M_{ab} = \frac{2E_sI_c}{L_c}\theta_b\left(1+\frac{3h}{2L_c}\right) \tag{F.19}$$

$$M_{ba} = \frac{2E_sI_c}{L_c}\theta_b\left(2+\frac{3h}{2L_c}\right) \tag{F.20}$$

The moment M_{ba} is computed in terms of the fixed-end moment M_{ab} by combining Eq. F.19 and F.20:

$$M_{ba} = M_{ab}\left(\frac{4L_c+3h}{2L_c+3h}\right) \tag{F.21}$$

M_{ba} may also be expressed in terms of the applied loads at the girder tips, P_{east} and P_{west}, using static equilibrium equations:

$$M_{ba} = \left(\frac{P_{east}\left(L_g+\frac{b}{2}\right)+P_{west}\left(L_g+\frac{b}{2}\right)}{2L_c+h}\right)L_c = \left(\frac{P_{tot}\left(L_g+\frac{b}{2}\right)}{2L_c+h}\right)L_c \tag{F.22}$$

Equations F.21 and F.22 are combined to express the moment M_{ab} in terms of P_{west}, P_{east}, and the dimensions of the specimen:

$$M_{ab} = \frac{P_{tot} L_c \left(L_g + \frac{b}{2} \right) (2L_c + 3h)}{(2L_c + h)(4L_c + 3h)} \tag{F.23}$$

The flexural column rotation at the top edge of the panel zone, θ_b, is defined when setting Eq. F.19 equal to Eq. F.23:

$$\theta_b = \frac{P_{tot} \left(L_g + \frac{b}{2} \right) L_c^3}{E_s I_c (2L_c + h)(4L_c + 3h)} \tag{F.24}$$

Finally, the flexural column rotation contribution to the girder tip deflection (fixed column supports) is calculated by multiplying the flexural column rotation, θ_b, by the distance measured from centerline of the panel zone to the point of girder applied load:

$$\Delta_{col} = \theta_b \left(L_g + \frac{b}{2} \right) = \frac{P_{tot} \left(2L_g + b \right)^2 L_c^3}{4E_s I_c (2L_c + h)(4L_c + 3h)} \tag{F.25}$$

F.4 Girder-to-Column Rotation Component

Slip in the moment frame connection (i.e., the bolted shear tab connection) and inelastic deformation in the connection region contribute to the girder tip deflection. For all three specimens, the inelastic connection deformation constituted the largest component of the girder tip deflection starting at interstory drift cycles of 1.5%. To accurately capture this critical component, plastic rotation of the girder relative to the column, θ_p, was measured using two LVDTs that were situated near the top flange and

bottom flange and by subtracting out a girder flexural component (see Appendix B). The corresponding tip deflection component is determined by multiplying the girder-to-column rotation, θ_p, by the length of the girder, L_g:

$$\Delta_{rel} = \frac{\theta_p L_g}{1000\ mrads / 1\ radian} \tag{F.26}$$

F.5 Girder Shear Deformation Component

Elastic shear deformation of the girder cross section is a contributor to the girder tip deflection of the specimens. The effects of this type of deformation to the deflection of a girder is typically minimal compared to the girder deflection due to flexure. Since the girder length, L_g, of the specimens is relatively short compared to the depth of the girder cross section, elastic shear deformation of the girder represents approximately 4% to 6% of the girder tip deflection during the elastic drift levels, and is included in the girder tip deflection calculations for completeness. For the calculation of the elastic shear deformation component to the girder tip deflection for Specimens 2 and 3, it is assumed that the composite girders exhibit fully composite action.

To compute this contribution to the girder tip deflection, the area of the composite girder section must first be transformed into an equivalent steel section area, A_{tr}:

$$A_{tr} = A_s + \frac{1}{n} A_c + N_{bars} \frac{\pi}{4} d_{bar}^2 \tag{F.27}$$

where d_{bar} = diameter of #4 steel reinforcement (in.)
n = modular ratio = E_s/E_c
A_c = effective area of concrete slab (in^2)
A_s = gross area of steel section (in^2)
N_{bars} = number of reinforcement bars

The transformed area of the girder cross sections of Specimens 2 and 3 is equal to 61.93 in^2 and 58.72 in^2, respectively. For the steel girders of Specimen 1, A_{tr} is equal to A_s, or 27.7 in^2. Values for parameters addressed in Eq. F.27 are also reported in Appendices A and K.

The first moment areas of the girder cross section may then be determined along five regions of the girder cross section: the bottom flange (Q_{bf}), lower web (Q_{lw}), upper web (Q_{uw}), top flange (Q_{tf}), and the concrete slab (Q_{slab}). Note that the upper web, top flange, and concrete slab regions are located above the elastic neutral axis, y_e, of the girder cross section, while the lower web and bottom flange regions are located below y_e. As in Appendix A, the elastic neutral axis is measured from the bottom of the steel girder. The first moments may be computed as functions of y, the distance varying along the depth of the cross section (measured from the bottom of the steel girder). A first moment area is equal to the cross sectional area located between y and the adjacent extreme fiber of the cross section times the distance measured from the elastic neutral axis, y_e, to the centroid of the respective cross sectional area (Gere and Timoshenko, 1990):

$$Q_{bf} = b_f y\left(y_e - \frac{y}{2}\right) \tag{F.28}$$

$$Q_{lw} = t_w(y - t_f)\left(y_e - t_f - \frac{1}{2}(y - t_f)\right) + b_f t_f\left(y_e - \frac{t_f}{2}\right) \tag{F.29}$$

$$\begin{aligned} Q_{uw} = {} & t_w(d - t_f - y)\left(\frac{1}{2}(d - y + t_f) - y_e\right) + b_f t_f\left(d - y_e - \frac{t_f}{2}\right) \\ & + A_{tr\,slab}\left(d + t_s - \frac{a}{2} - y_e\right) \end{aligned} \tag{F.30}$$

$$Q_{tf} = b_f(d-y)\left(d - y_e - t_f - \frac{1}{2}(d-y)\right) + A_{tr\,slab}(d + t_s - \frac{a}{2} - y_e) \quad \text{(F.31)}$$

$$Q_{slab} = b_e(d-y+t_s)\left(d + t_s - y_e - t_f - \frac{1}{2}(d-y+t_s)\right) + A_{tr\,slab}(d + t_s - \frac{a}{2} - y_e) \quad \text{(F.32)}$$

where a = effective thickness of concrete slab (in.)

b_e = width of effective concrete slab (in.)

b_f = width of girder flange (in.)

d = depth of steel section (in.)

t_f = thickness of girder flange (in.)

t_s = thickness of slab measured from the top of the concrete slab to the top of the steel girder (in.)

t_w = thickness of girder web (in.)

y_e = elastic neutral axis (in.)

$A_{tr\,slab}$ = transformed area of concrete slab (in^2)

The extra area near the fillet regions of the steel section may be assumed to be negligible in the calculation of the first moments and, therefore, is not included in Eqs. F.28 to F.31. The transformed area of the concrete slab, $A_{tr\,slab}$, is equal to sum of the transformed concrete area, A_c/n, plus the area of the reinforcing steel, and is equal to 34.34 in^2 and 31.02 in^2 for the concrete slabs of Specimens 2 and 3, respectively. The effective concrete slab thickness, a, is taken as 4", since these calculations assume fully composite action between the steel girders and the concrete slabs. Values for other parameters specified in Eqs. F.28 to F.32 are reported in Appendix K.

Next, the shear form factor, f_s, is defined. This value is a dimensionless parameter which may be calculated for a composite girder section by integrating along the girder cross section as follows:

$$f_s = A_{tr}\frac{1}{I_{tr}^2}\left[\int_0^{t_f} Q_{bf}^2\frac{1}{b_f}dy + \int_{t_f}^{y_e} Q_{lw}^2\frac{1}{t_w}dy + \int_{y_e}^{d-t_f} Q_{uw}^2\frac{1}{t_w}dy + \int_{d-t_f}^{d} Q_{tf}^2\frac{1}{b_f}dy + \int_{d+t_s-a}^{d+t_s} Q_{slab}^2\frac{1}{b_e}dy\right]$$

(F.33)

where I_{tr} = transformed moment of inertia (in^4)

Q_{bf} = first moment area within bottom girder flange (in^3)

Q_{lw} = first moment area within lower girder web (in^3)

Q_{uw} = first moment area within upper girder web (in^3)

Q_{tf} = first moment area within top girder flange (in^3)

Q_{slab} = first moment area within the concrete slab (in^3)

The transformed moment of inertia is equal to 7471 in^4 and 7378 in^4 for Specimens 2 and 3, respectively (see Appendix A). The shear form factor for the steel girders of Specimen 1 (when subjected to positive and negative girder bending) and the composite girders of Specimen 2 and 3 (when subjected to positive girder bending) is computed to be 2.08, 3.73 and 3.49, respectively. For negative girder bending, it is assumed that the shear form factor of the composite girders is equal to the shear form factor of a steel girder section ($f_s = 2.08$) (it is assumed that the contribution of the concrete slab to the shear deformation of the composite girders is minimal during negative girder bending). When calculating the shear form factor for a bare steel section, the first moment area term for the concrete slab, Q_{slab}, is equal to zero and I_{tr} is equal to I_{xx} (3270 in^4 -- see Appendix A). Note that by setting $t_w = b_f$, $y_e = d/2$ (the centroidal axis of a rectangular section), $A_{tr} = b_f d$, $A_{tr\ slab} = 0$, $I_{tr} = b_f d^3/12$ (the moment of inertia for a rectangular section) and by defining Q_{slab} to be zero, Eq. F.33 reduces to the shear form factor for a rectangular section, or 1.2 (therefore, the accuracy of Equation F.33 may be substantiated).

The girder tip deflection component due to girder elastic shear deformation, $\Delta_{gird\ shear}$, may be calculated by assuming that the girder behaves as a fixed cantilever and by assuming a rigid panel zone region:

$$\Delta_{gird\,shear} = \frac{PL_g}{GA_{tr}} f_s \qquad \text{(F.34)}$$

where A_{tr} = transformed area of the girder cross section (in^2)

f_s = form factor for shear

G = shear modulus of steel (ksi)

This expression is obtained from the unit-load equation which equates the external work with the internal work of the girder when subjected to a point load, P, to the girder tip. The shear modulus of steel, G, is taken as $E_s/2(1+\nu)$, or 11,154 ksi.

F.6 Load Frame Deformation Component

All the previously mentioned components of the girder tip deflection have been due to deformations within the specimens. However, large shear forces were transferred through the column into the load frame assembly and generated small lateral displacements at the top of the load frame, resulting in a contribution to the girder tip deflection. Load frame displacement in the East-West direction, Δ_{ew_lf}, was measured relative to the laboratory's strong floor. This was done using an LVDT located on the North side of the MTS testing machine and oriented horizontally and parallel to the specimen (see Figure F.6). Note that the horizontal deflection of the specimen and top load pin relative to the MTS crosshead were measured to be infinitesimal.

To focus only on the contribution of load frame deformation to the girder tip deflection, a structural idealization model is used which assumes that the test specimen is infinitely rigid when subjected to cyclic loading (see Figure F.7). Therefore, when the top load pin is deflected laterally (measured by lateral displacement of the MTS testing machine), the specimen rotates as a rigid member about the bottom load pin assembly. The load frame horizontal displacement, Δ_{ew_lf}, divided by the distance from the bottom

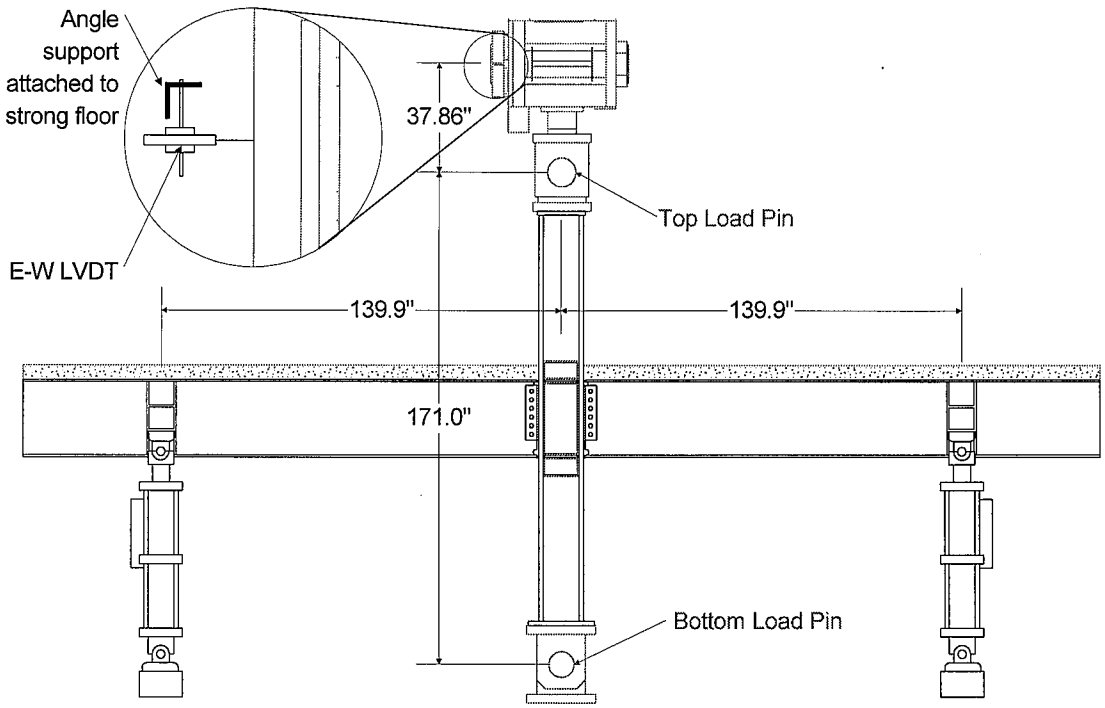

Figure F.6: Specimen and MTS Testing Machine

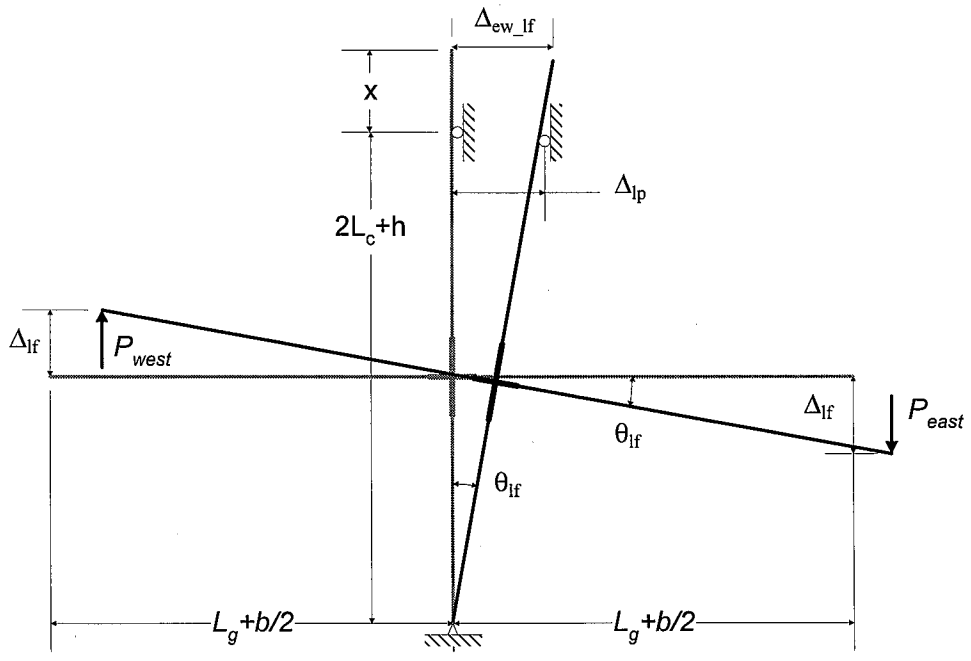

Figure F.7: Structural Idealization of Load Frame Deformation

column support to the LVDT denotes the load frame rotation, θ_{lf}. The contribution of the load frame rotation to the girder tip deflection is:

$$\Delta_{lf} = \theta_{lf}\left(L_g + \frac{b}{2}\right) = \left(\frac{\Delta_{ew\_lf}}{(2L_c + h) + x}\right)\left(L_g + \frac{b}{2}\right) \tag{F.35}$$

where x = distance measured between center of top load pin to East-West LVDT (in.)

The load frame deformation was computed by assuming $tan(\theta_{lf}) \approx \theta_{lf}$ and neglecting vertical displacements of the specimen when rotated.

F.7 Measured Joint Rotation

The rotation of the connection region, referred to as joint rotation, was also measured for each of the specimens. This rotation, though not used in the calculation of the girder tip deflections for the specimens, may be compared to five components contributing to the girder tip deflection. To measure joint rotation, an inclinometer was installed in the center of the panel zone region (see Section 2.4.1). This device measured the absolute rotation of the connection region. For this research, the joint rotation refers to the rotation of the joint relative to the specimen. Therefore, the load frame deflection contribution to joint rotation was subtracted out from the measured joint rotation. The contribution (see Section F.5) of joint rotation to the girder tip deflection is defined using the measured joint rotation, θ_{joint}, the load frame girder tip deflection component, Δ_{lf}, and the distance from the center of the connection region to the girder tip:

$$\Delta_{joint} = \theta_{joint}\left(L_g + \frac{b}{2}\right) - \Delta_{lf} \tag{F.36}$$

where θ_{joint} = rotation of connection region measured at center of panel zone (radians)

Δ_{lf} = girder tip deflection due to load frame deformation (in.)

The contribution of joint rotation to girder tip deflection is directly related to the flexural deformation of the column. This is because the joint rotation is actually measured on the column (within the panel zone region). In fact, the contribution of the joint rotation to the girder tip deflection should be equal to the girder tip deflection component due to flexural deformation of the column. However, this is valid only when assuming that no joint rotation occurs due to panel zone shear deformation. In these tests, the panel zone did distort from the shape of a rectangle to the shape of a parallelogram, but may have contributed negligibly to any rotation of the joint itself. In addition, some joint rotation due to panel zone distortion may be measured due to the distortion of the bolts which attach the inclinometer to the center of the panel zone. However, this effect is also assumed to be negligible. In addition, it is assumed that no kinking of the column occurs at the panel zone boundaries.

In summary, the joint rotation relative to the specimen is directly related to the rotation of the column section (Section F.3). Therefore, the amount of joint rotation, though not included in the calculation of the girder tip deflection, can be qualitatively represented by the amount of column rotation.

F.8 Verification of Calculated Girder Tip Deflection Components

A matrix structural analysis program (Visual Analysis 2.5, 1994) was used to verify the integrity of four equations used to formulate girder tip deflection components. These components were due to flexural deformation of the girders (Eq. F.7) and the column (Eq. F.15 and F.25), and deformation of the load frame (Eq. F.35). Note that second-order effects were not taken into account in this analysis, since second-order

analysis (Gourley and Hajjar, 1994) was used to determine that the significance of column axial tension on the flexural deformation of the column was negligible.

The properties of Specimen 3, along with the dimensions specified in Appendix D, were used in this study to generate a structural idealization model of Specimen 3. Also, the model was analyzed by applying girder tip loads monotonically, with the girder tip loads equaling the peak loads attained in the first cycle at 0.25% drift of Specimen 3 (P_{east} = 19.51 kips, P_{west} = -18.22 kips) (see Figure F.8). Because the East girder of Specimen 3 was subjected to negative bending during this load excursion, I_{eff} = 3595 in^4 (see Appendix A). Similarly, the West girder was subjected to positive bending; therefore, I_{eff} = 5901 in^4. The column was modeled as a W14X211 steel section, and the flexural and axial stiffnesses of the panel zone region were modeled as being very high to simulate infinite stiffness (represented by five struts which minimize rotation relative to one another) (see Figure F.8).

F.8.1 Verification of Girder and Column Flexural Deformation Equations

The girder and column flexural deformation equations (see Eqs. F.7, F.15, and F.25) are verified simultaneously, along with investigating the pinned column support and the fixed column support conditions separately. For the pinned column support condition, the girder tip deflection due to column and girder flexure (using Eqs. F.7 and F.15) is compared to the girder tip deflection that is determined using a computational model that assumed pinned column supports (the top and bottom supports were allowed to rotate). For the fixed column support condition, the girder tip deflection due to column and girder flexure (using Eqs. F.7 and F.25) is compared to the girder tip deflection that is determined using a computational model that assumed fixed column supports (the top and bottom supports were fixed against rotation). The computational model is monotonically loaded at the girder tips, with loads and girder, column, and panel zone stiffnesses as defined above. To represent the actual support conditions when

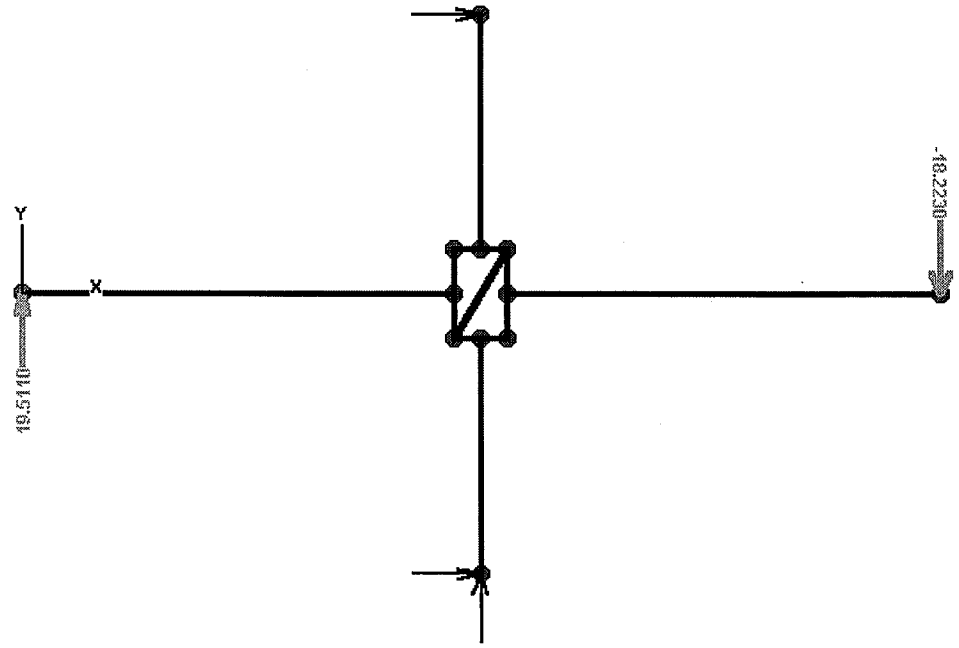

Figure F.8: Computational Model of Specimen 3/ 0.25% Drift Level
(Pinned Bottom Column Support/ Laterally Supported Top Column Support)

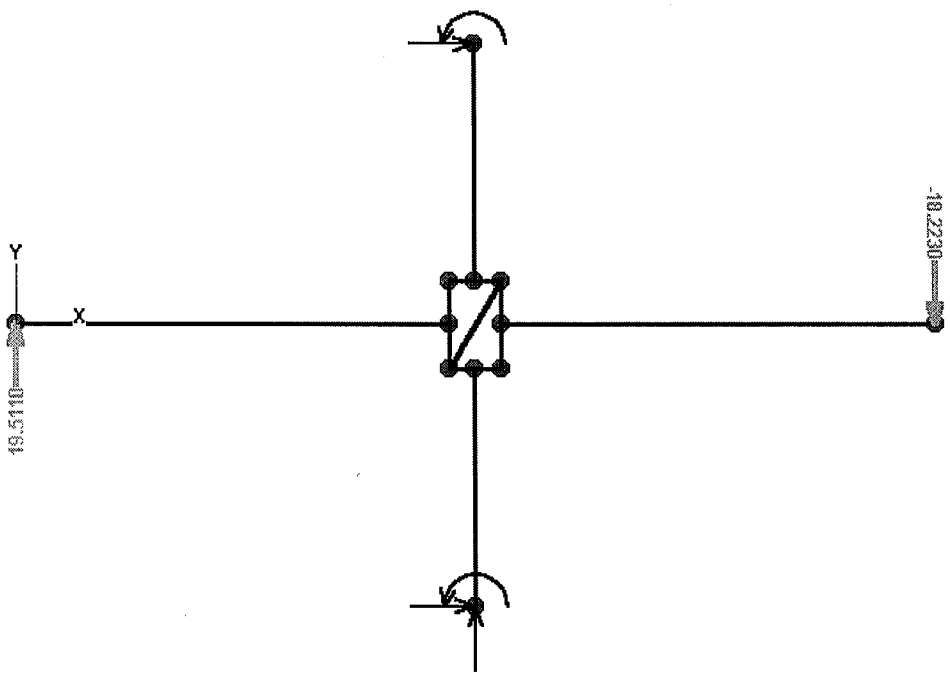

Figure F.9: Computational Model of Specimen 3/ 0.25% Drift Level
(Fixed Top and Bottom Column Supports)

loading the specimens, the top load pin is assumed to be not supported in the vertical direction (see Figures F.8 and F.9).

Table F.1 summarizes the results of the matrix structural analysis procedure and the calculations using the derived flexural equations (see Equations F.7, F.15, and F.25). Note that the parameter, Δ_{flex}, refers to the sum of the girder tip deflection components due to column and girder flexure. The error percentages are small as compared either to equations assuming pinned (Equations F.7 and F.15) or fixed column supports (Equations F.7 and F.25). It is also concluded that modeling the top load pin assembly as pinned, rather than only laterally-supported, is an acceptable approximation in deriving the flexural component equations.

Table F.1: Verification of Girder and Column Flexural Components (Specimen 3)

Girder	Column Supports	Load (kips)	I_{tr} (in^4)	E_s (ksi)	Δ_{flex} (in.) (Analysis)	Δ_{flex} (in.) (Equations)	Error (%)
East	Fixed	-18.22	3595	29,000	-0.1876	-0.1907	2.10
	Pinned	-18.22	3595	29,000	-0.2166	-0.2155	0.77
West	Fixed	19.51	5901	29,000	0.1411	0.1441	-0.19
	Pinned	19.51	5901	29,000	0.1702	0.1689	-0.22

F.8.2 Verification of Load Frame Deformation Equation

The calculation of the girder tip deflection component due to load frame deformation, Δ_{lf}, (see Eq. F.35) is verified by comparing the calculated girder tip deflection using Eq. F.35 and to that obtained from a computational model (see Figure F.10). The computational model is monotonically loaded at the girder tips, with the loading condition stated in Section F.8. The model also assumes that the column, girder, and panel zone elements have very high stiffness properties, in order to capture only the

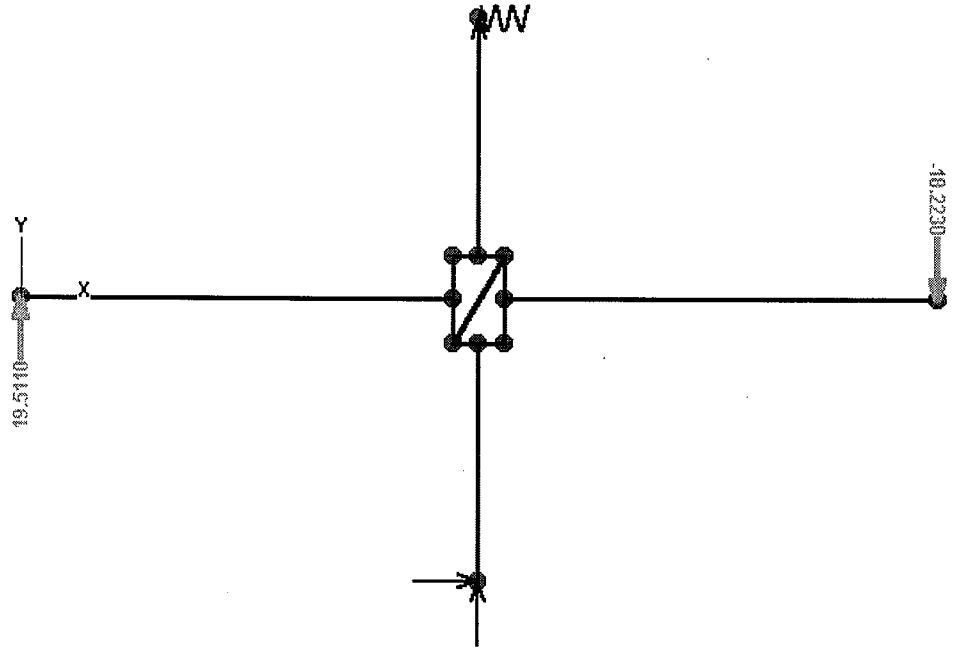

Figure F.10: Computational Model of Specimen 3/ 0.25% Drift Level
(Pinned Bottom Support/ Top Support Laterally Supported With a Translational Spring)

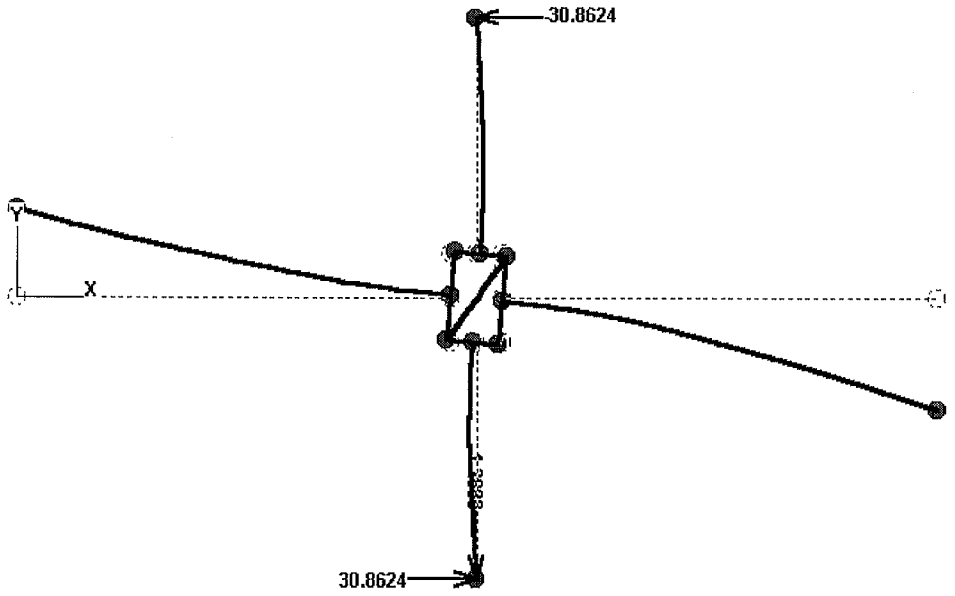

Figure F.11: Loaded Computational Model of Specimen 3/ 0.25% Drift Level
(Pinned Bottom Column Support/ Laterally Supported Top Column Support)

contribution of load frame deformation to the girder tip deflection. The bottom column support is assumed to be pinned, while the top column support is assumed to be laterally supported with a translational spring with stiffness, k_{lf}.

The value for the spring constant, k_{lf}, may be determined by dividing the shear force, H, at the top load pin by the displacement of the top load pin in the East-West direction, Δ_{lp}, or $k_{lf} = H/\Delta_{lp}$. The displacement, Δ_{lp}, is taken as the maximum value measured during the first peak of the 0.25% drift cycles of Specimen 3, and is interpolated at a distance of 194.25" above the center of the bottom load pin using the measured load frame deformation, Δ_{ew_lf} (see Figures F.6 and F.7):

$$\Delta_{lp} = \frac{2(L_c + h)}{2(L_c + h + x)} \Delta_{ew\_lf} \tag{F.29}$$

The shear force transferred into the top load pin, $H = 30.86$ kips, was obtained by employing a computational model of the Specimen 3, assuming a pinned bottom column support and a laterally-supported top column support (see Figure F.11). The loading condition stated in Section F.8 was once again utilized. Note that the shear forces at the top and bottom pins are equal. These forces are assumed equal in the derivation of the column flexural expressions (Eqs. F.15 and F.25) and in the calculation of the moment in the column based on the applied load to the girder (see Appendix E).

Table F.2 reports the values of the calculated girder tip deflection due to load frame deformation using the computational model (see Figure F.10) and Eq. F.35. The resulting girder tip deflection using the computational model correlated within a few percent of the calculated girder tip deflection using Eq. F.35. One source of this error is that only rotational displacement is considered when calculating the deformation of the

load frame. However, these errors are small, thus verifying that the model of the load frame deformation component of the girder tip deflection is accurate.

Table F.2: Verification of Load Frame Deformation Component (Specimen 3)

Δ_{ew_lf} (in.)	Δ_{lp} (in.)	H (kips)	$k_{lf} = H/\Delta_{lp}$ (kips/in.)	Δ_{lf} (in.) (Model)	Δ_{lf} (in.) (Eq. F.27)	Error (%)
0.0324	0.0285	30.86	1082	0.0245	0.0233	4.90

F.8.3 Second-Order Effects of Column Axial Tension on Column Flexure Behavior

The column flexural deformation equations take into account only first-order effects. However, when the column is subjected to 550 kips of axial tension, second-order effects may contribute to the flexural behavior of the column. To determine the significance of this condition and the accuracy of Equations F.15 and F.25, a second-order matrix analysis program, CFTMacro, was employed (Gourley and Hajjar, 1994). The same support conditions and material properties specified in Section F.7.1 were utilized, along with the application of 550 kips of axial tension to the top of column. The top and bottom column regions were each discretized into three equal length elements. The axial load was ramped to 550 kips over 20 load increments and maintained at that value while the East and West girders were ramped to 19.51 kips and -18.22 kips, respectively, over 40 load increments.

The vertical displacement of the top of the column was computed to be 0.0426" using second-order analysis. Using a first-order analysis, where displacement of the column due to axial loading was equal to $P_{axial}(2L_c\text{-}h)/E_sA_c$, the displacement at the top of the column was also equal to 0.0426." The joint rotation (i.e., column rotation, assuming a rigid panel zone region) was equal to 1.47 milliradians and 1.45 milliradians using first-order and second-order analysis, respectively. Therefore, it is concluded that the effects of tensile loading of the column on the flexural deformation of the column were minimal.

F.9 Discussion of Results

Figures F.12-F.23, F.24-F.35, and F.36-F.47 correlate the actual girder tip deflection to the calculated girder tip deflections (pinned support and fixed support) for Specimens 1, 2, and 3, respectively. Also, these figures compare the six calculated and measured girder tip deflection components and the measured joint rotation for the three specimens. The figures include the drift levels up through the 0.75% drift levels. The girder tip deflection due to girder-to-column rotation, girder flexure, and girder shear deformation are labeled as "gird rel rot", "gird flex", and "gird shear". The joint rotation girder tip deflection component, though not included in the calculated girder tip deflection, is also shown in these figures and is labeled as "connection".

Tables F.3, F.4, and F.5 summarize the peak error percentages between the actual and calculated girder tip deflections of the East and West girders for Specimens 1, 2, and 3. Error percentages for 1.0%, 1.5%, 2.0%, 3.0% drift cycles are not included, since the extensive nonlinearity in the specimens voids comparison with the girder tip deflection equations. Each tabulated error percentage value is equal to the average of all error percentages for a specified interstory drift level. The peak error percentages are calculated at the peaks of each load excursion (maximum girder tip deflections). Comparisons between the actual and calculated girder tip deflections are based on calculated girder tip deflections assuming a pinned-pinned column condition, since minimal rotational resistance was observed at the supports during testing (see Section 4.1 and Appendix E).

With the exception of the 0.25% drift levels without axial loading of the column, the East and West girders of Specimen 1 exhibited actual girder tip deflections that exceeded the calculated girder tip deflections by approximately 8% up to the 0.75% drift levels (Table F.3, Figures F.12 and F.13, F.18 and F.19). During the 0.25% drift levels with no axial load applied to Specimen 1, the error percentages between the actual and calculated tip deflections were substantially large for both the East and West girders.

Table F.3:
Percent Error of Calculated Girder Tip Deflection vs. Actual Girder Tip Deflection (Specimen 1)

			% Drift (# of Cycles)				
Girder Bending	**Column Support Condition**	**Avg & Std Dev**	**0.25[1] (3)**	**0.25[2] (2)**	**0.25[3] (2)**	**0.50[3] (2)**	**0.75[3] (2)**
East positive	**pinned**	avg	19.64	7.40	6.97	1.67	2.81
		std dev	5.65	0.06	0.29	0.42	0.16
	fixed	avg	25.69	12.94	12.79	7.43	8.61
		std dev	5.59	0.03	0.28	0.35	0.08
East negative	**pinned**	avg	8.10	0.74	1.17	3.07	0.72
		std dev	1.80	0.22	0.01	0.21	0.07
	fixed	avg	13.64	6.57	6.89	9.10	6.63
		std dev	1.79	0.20	0.01	0.20	0.07
West positive	**pinned**	avg	-3.11[4]	-2.68	-2.13	-0.35	2.88
		std dev	2.04	0.61	0.04	0.22	0.04
	fixed	avg	3.65	3.67	4.04	6.88	8.78
		std dev	1.86	0.55	0.05	1.39	0.16
West negative	**pinned**	avg	19.81	4.43	4.05	2.31	0.44
		std dev	1.65	0.10	0.16	0.13	0.08
	fixed	avg	24.82	9.68	9.50	10.42	6.23
		std dev	1.49	0.10	0.14	2.41	0.08

[1] Column loaded with no axial load during interstory drift cycles.
[2] Column loaded with 330 kips of axial compression during interstory drift cycles.
[3] Column loaded with 550 kips of axial tension during interstory drift cycles.
[4] Negative percentage values represent actual girder tip deflection values that are less in magnitude than the calculated girder tip deflection values.

Table F.4:
Percent Error of Calculated Girder Tip Deflection vs. Actual Girder Tip Deflection (Specimen 2)

		% Drift (# of Cycles)							
Girder Bending	**Column Support Condition**	**Avg & Std Dev**	**0.10[1] (3)**	**0.25[1] (3)**	**0.10[1] (3)**	**0.25[1] (3)**	**0.25[2] (3)**	**0.50[2] (3)**	**0.75[2] (3)**
East positive	**pinned**	avg	7.21	-5.34[3]	-6.29	3.08	11.48	9.48	10.53
		std dev	0.60	0.03	0.42	0..16	0.21	0.33	0.24
	fixed	avg	14.22	13.19	1.41	10.67	18.77	16.54	16.65
		std dev	0.68	0.02	0.44	0.15	0.20	0.23	0.60
East negative	**pinned**	avg	7.35	10.79	24.30	12.04	1.73	10.46	9.60
		std dev	0.81	0.05	0.42	0.29	5.57	0.33	0.63
	fixed	avg	13.40	17.46	29.57	19.00	12.85	17.76	16.65
		std dev	0.85	0.09	0.40	0.31	0.29	0.28	0.60
West positive	**pinned**	avg	12.11	7.77	0.42	6.79	12.03	10.72	13.94
		std dev	1.30	0.70	1.01	0.03	0.73	0.01	1.12
	fixed	avg	18.37	0.42	8.48	15.30	19.46	18.21	21.42
		std dev	1.40	0.65	2.31	0.05	0.70	0.06	1.21
West negative	**pinned**	avg	2.52	6.66	13.48	6.03	3.48	5.88	3.76
		std dev	0.47	0.20	0.40	0.07	0.96	0.32	0.28
	fixed	avg	9.56	14.16	19.23	12.96	11.12	13.45	10.90
		std dev	0.40	0.28	0.40	0.05	093	0.30	0.26

[1] Column loaded with no axial load during interstory drift cycles.
[2] Column loaded with 550 kips of axial tension during interstory drift cycles.
[3] Negative percentage values represent actual girder tip deflection values that are less in magnitude than the calculated girder tip deflection values.

Table F.5:
Percent Error of Calculated Girder Tip Deflection vs. Actual Girder Tip Deflection (Specimen 3)

			% Drift (# of Cycles)			
Girder Bending	**Column Support Condition**	**Avg & Std Dev**	**0.25[1] (8)**	**0.25[2] (1)**	**0.50[2] (3)**	**0.75[2] (3)**
East positive	**pinned**	avg	9.74	5.21	7.55	9.68
		std dev	2.00	0.00	0.72	0.71
	fixed	avg	15.35	12.13	11.61	16.59
		std dev	5.88	0.00	3.66	0.78
East negative	**pinned**	avg	6.78	9.19	9.49	4.79
		std dev	2.60	0.00	4.20	0.40
	fixed	avg	13.24	16.15	13.70	11.85
		std dev	1.49	0.00	0.03	0.37
West positive	**pinned**	avg	14.07	17.60	12.80	15.60
		std dev	1.20	0.00	0.09	0.44
	fixed	avg	21.25	24.42	19.82	22.63
		std dev	1..19	0.00	0.12	0.52
West negative	**pinned**	avg	-0.74[3]	-3.74	-0.31	-2.15
		std dev	0.41	0.00	0.40	0.18
	fixed	avg	6.30	3.53	7.10	4.94
		std dev	0.41	0.00	0.40	0.16

[1] Column loaded with no axial load during interstory drift cycles.
[2] Column loaded with 550 kips of axial tension during interstory drift cycles.
[3] Negative percentage values represent actual girder tip deflection values that are less in magnitude than the calculated girder tip deflection values.

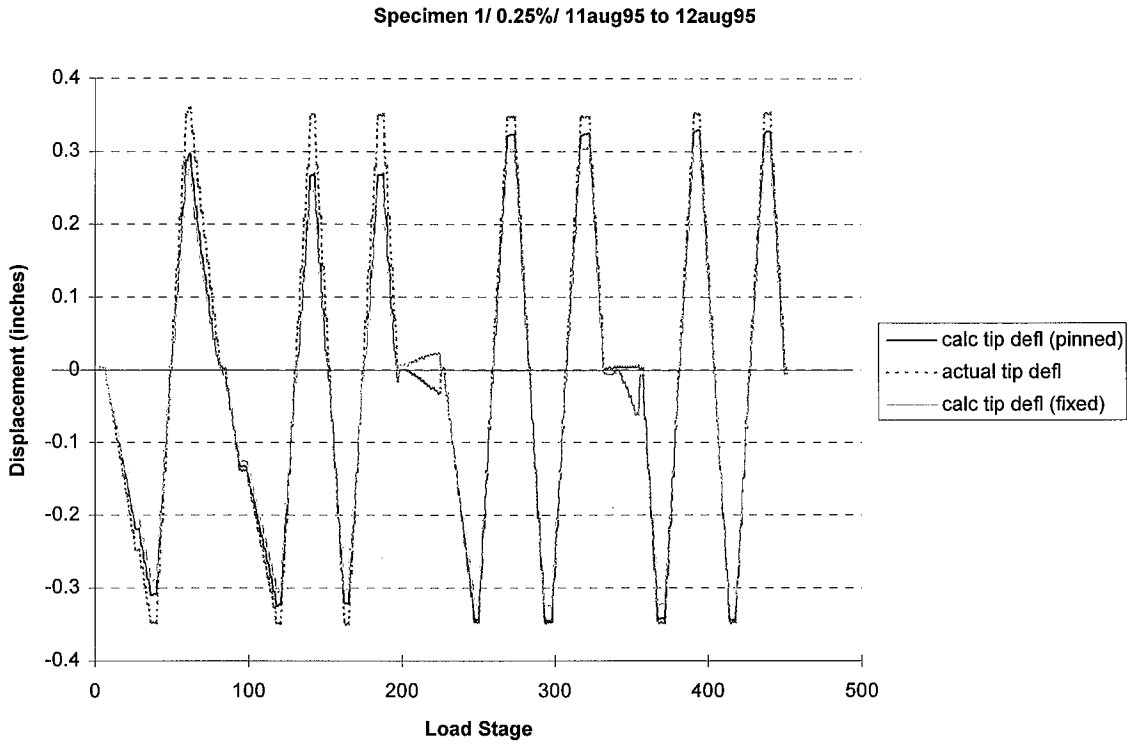

Figure F.12: Actual vs. Calculated Girder Tip Deflection (East Girder of Specimen 1)

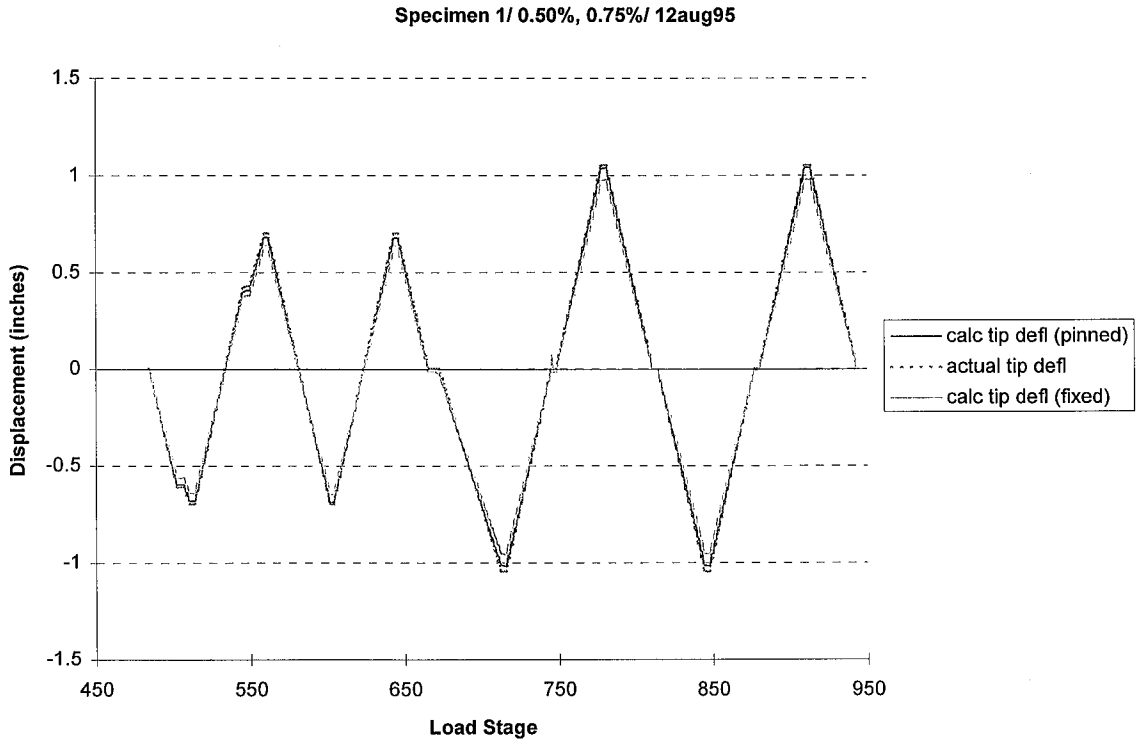

Figure F.13: Actual vs. Calculated Girder Tip Deflection (East Girder of Specimen 1)

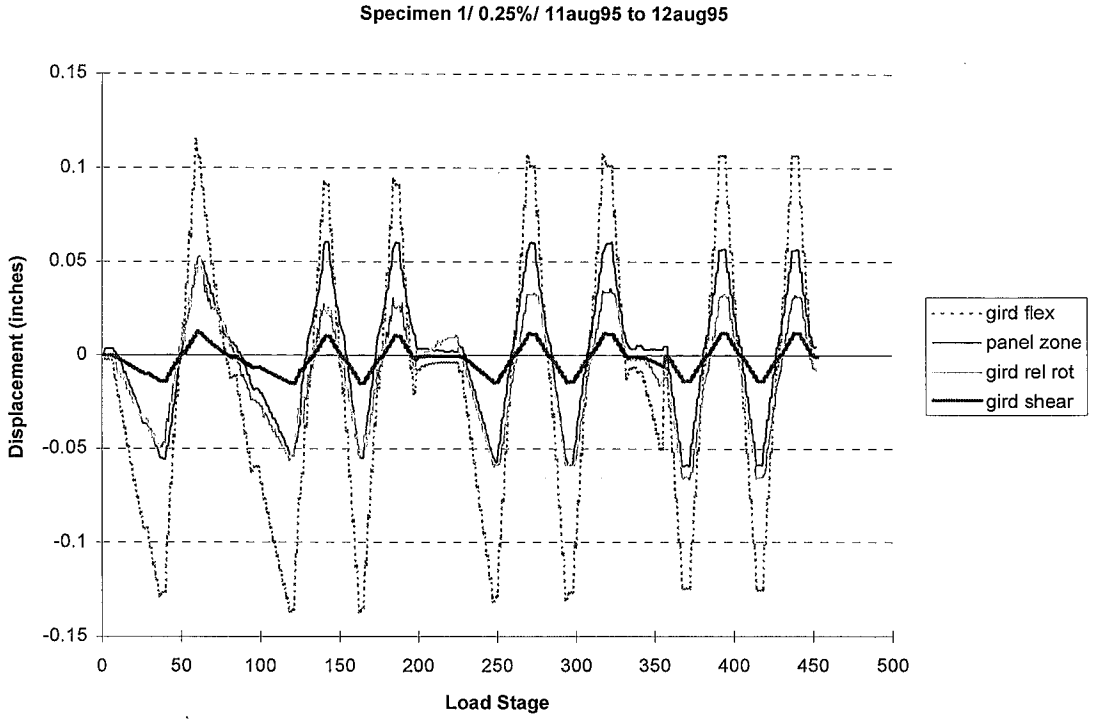

Figure F.14: Girder and Panel Zone Girder Tip Deflection Components (East Girder of Specimen 1)

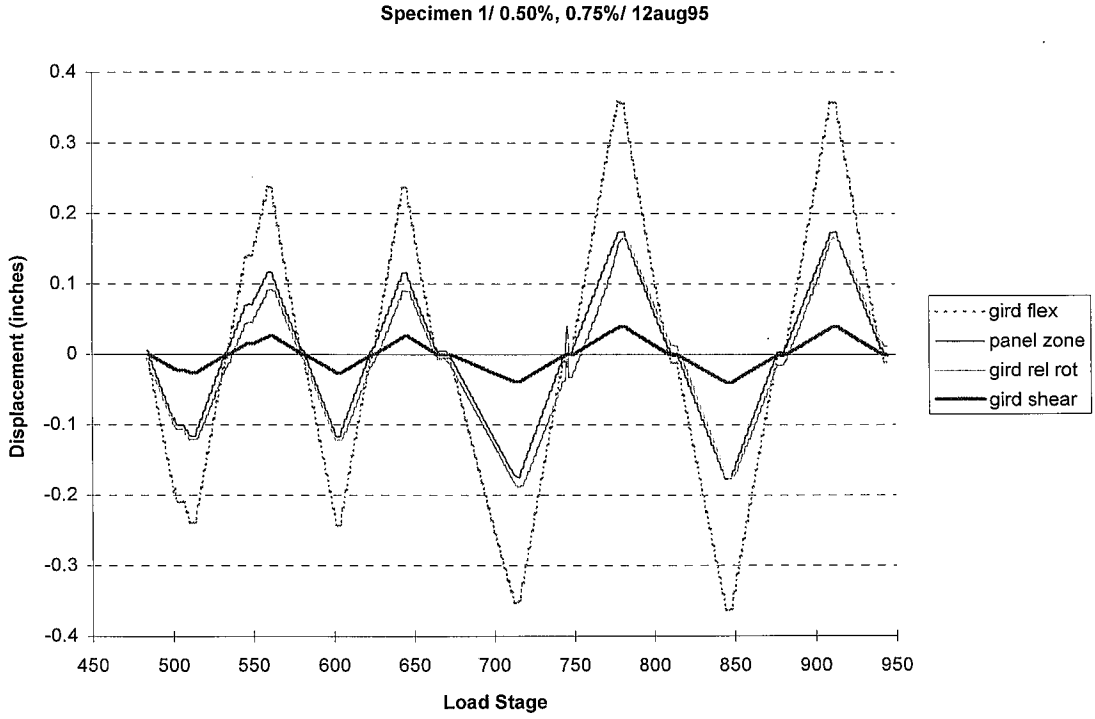

Figure F.15: Girder and Panel Zone Girder Tip Deflection Components (East Girder of Specimen 1)

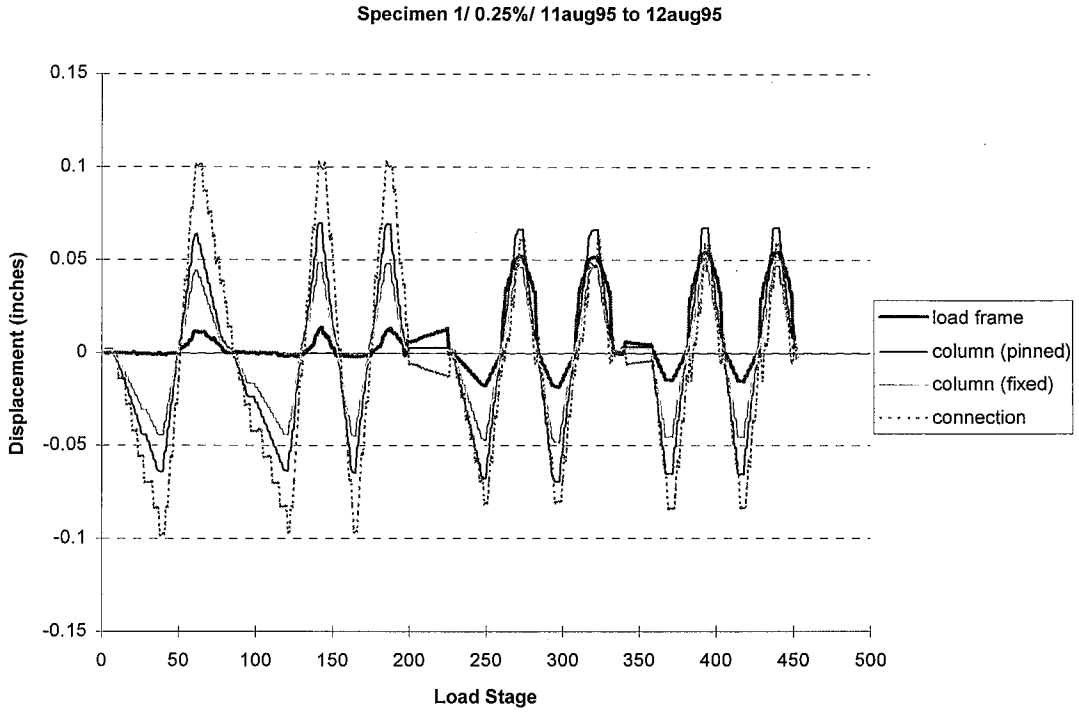

Figure F.16: Column, Load Frame, and Connection Girder Tip Deflection Components (East Girder of Specimen 1)

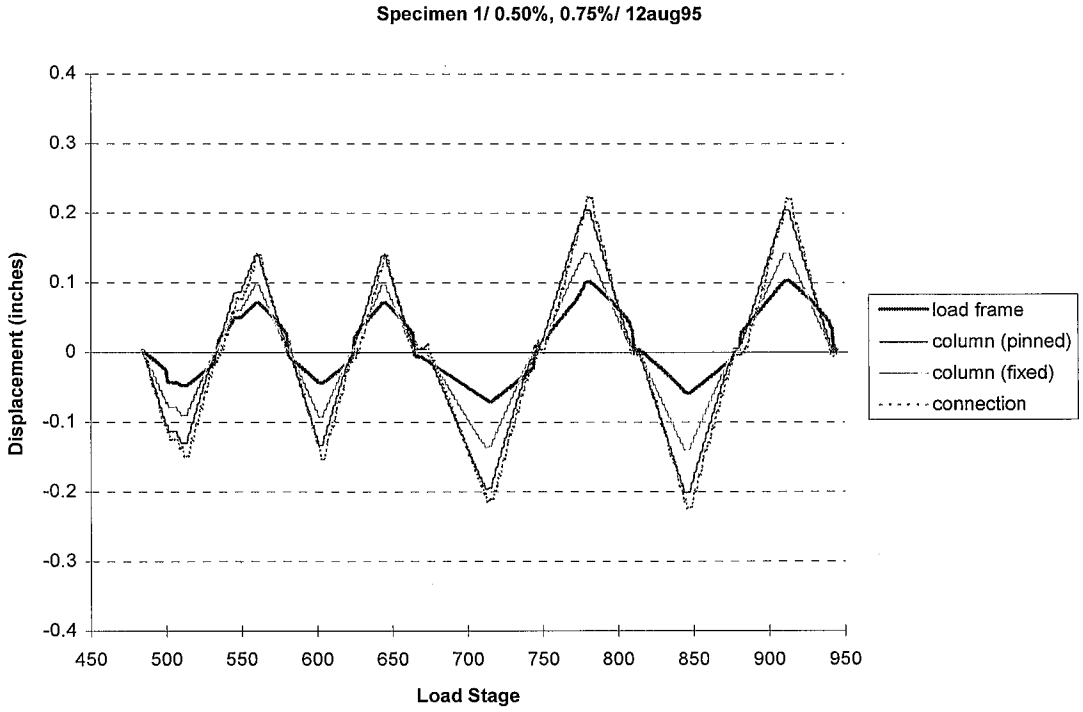

Figure F.17: Column, Load Frame, and Connection Girder Tip Deflection Components (East Girder of Specimen 1)

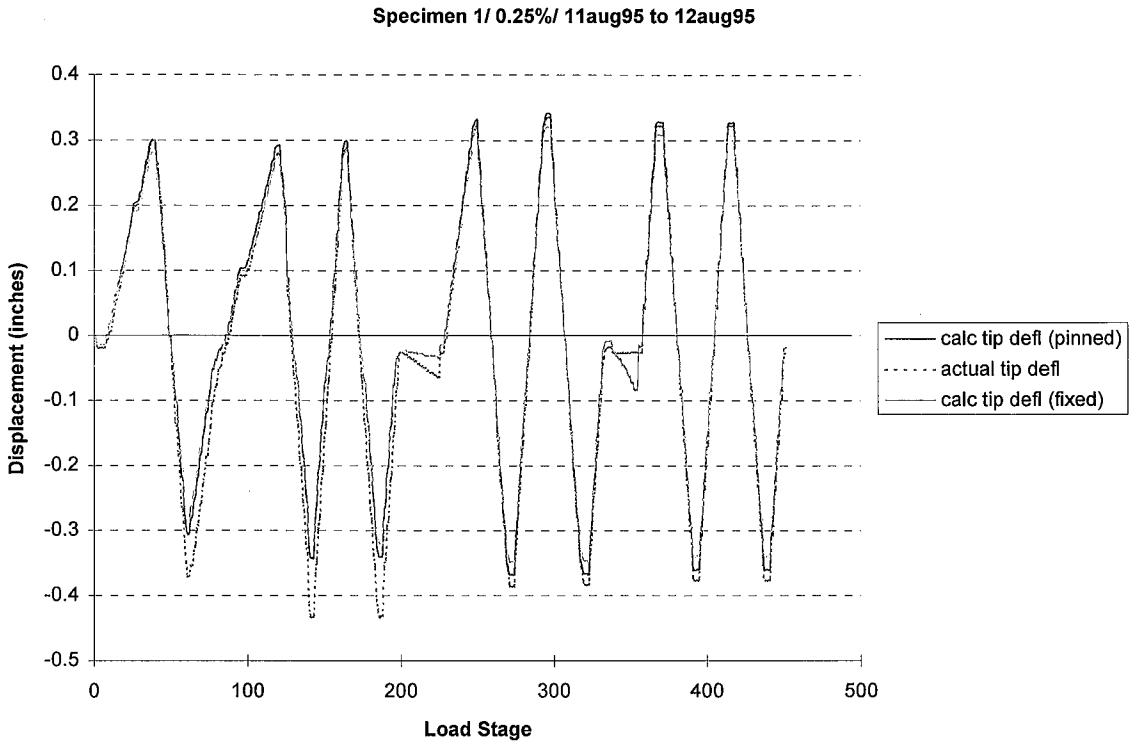

Figure F.18: Actual vs. Calculated Girder Tip Deflection (West Girder of Specimen 1)

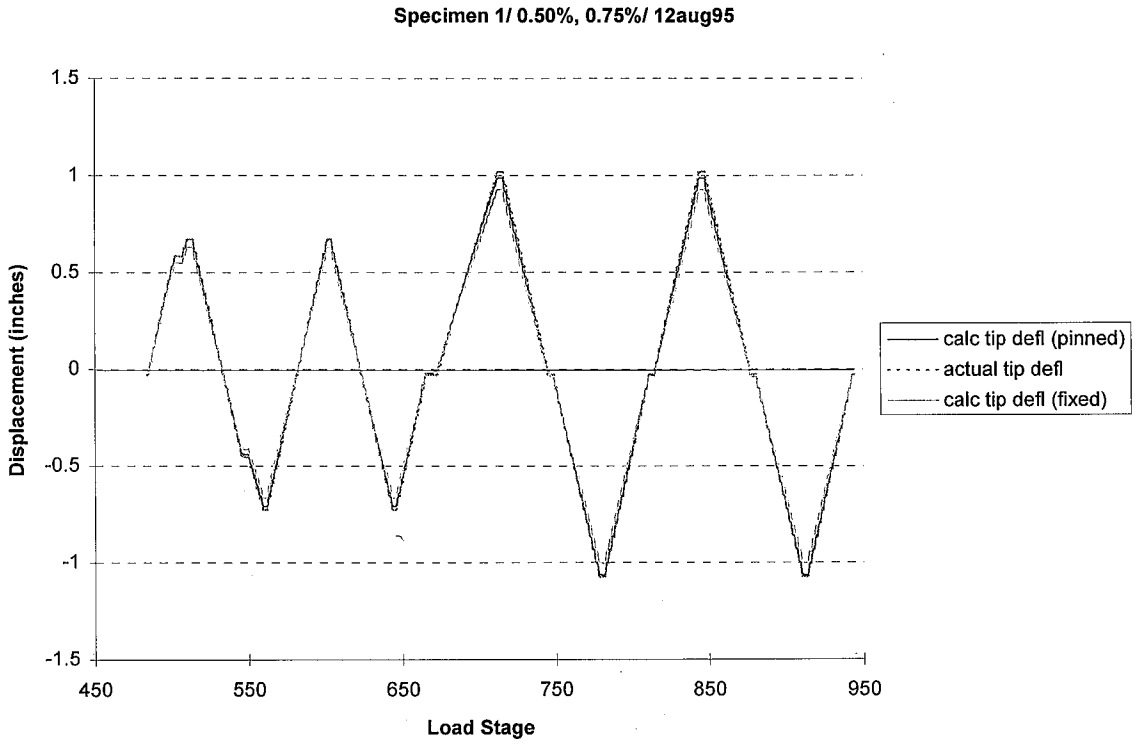

Figure F.19: Actual vs. Calculated Girder Tip Deflection (West Girder of Specimen 1)

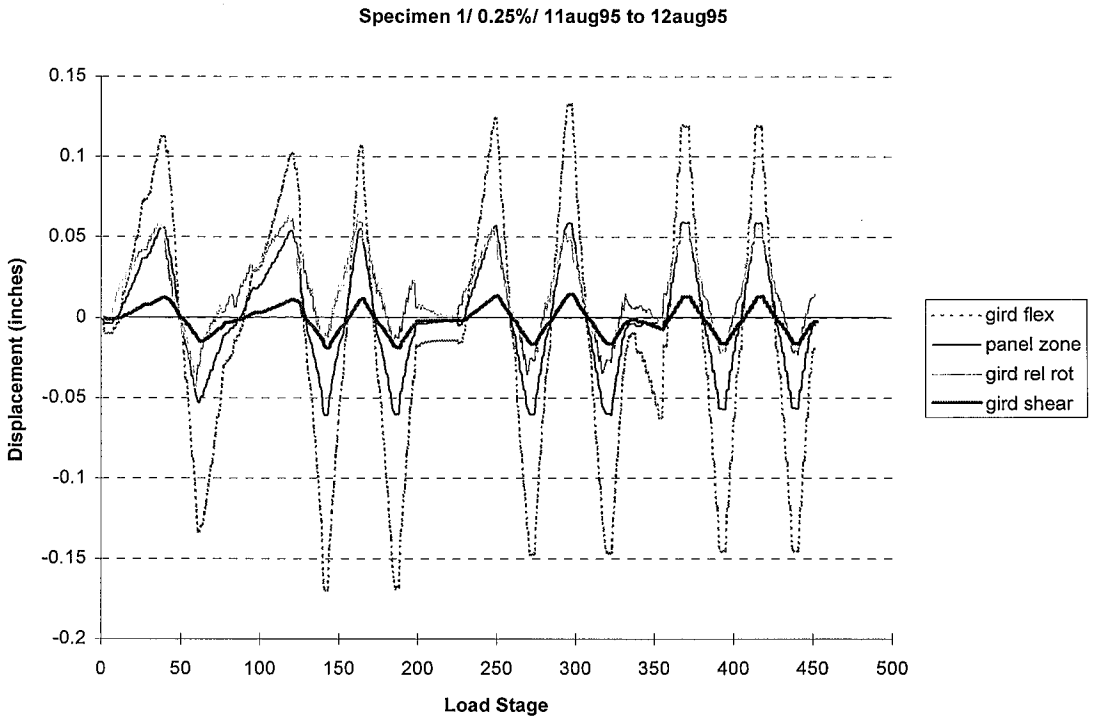

Figure F.20: Girder and Panel Zone Girder Tip Deflection Components (West Girder of Specimen 1)

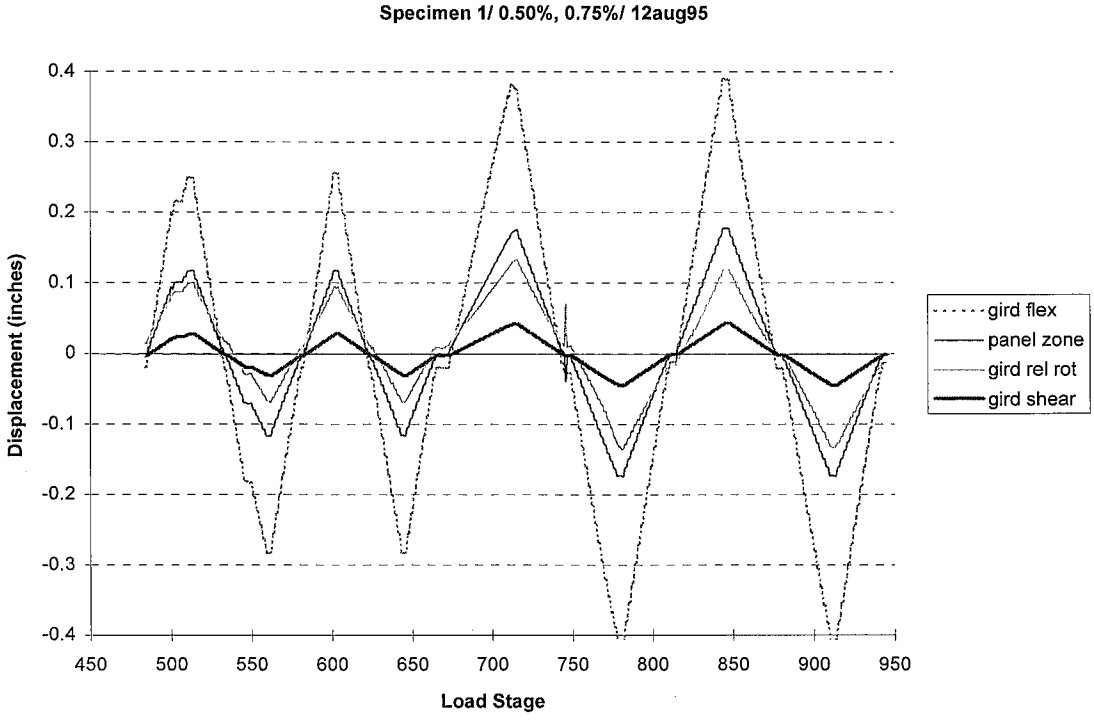

Figure F.21: Girder and Panel Zone Girder Tip Deflection Components (West Girder of Specimen 1)

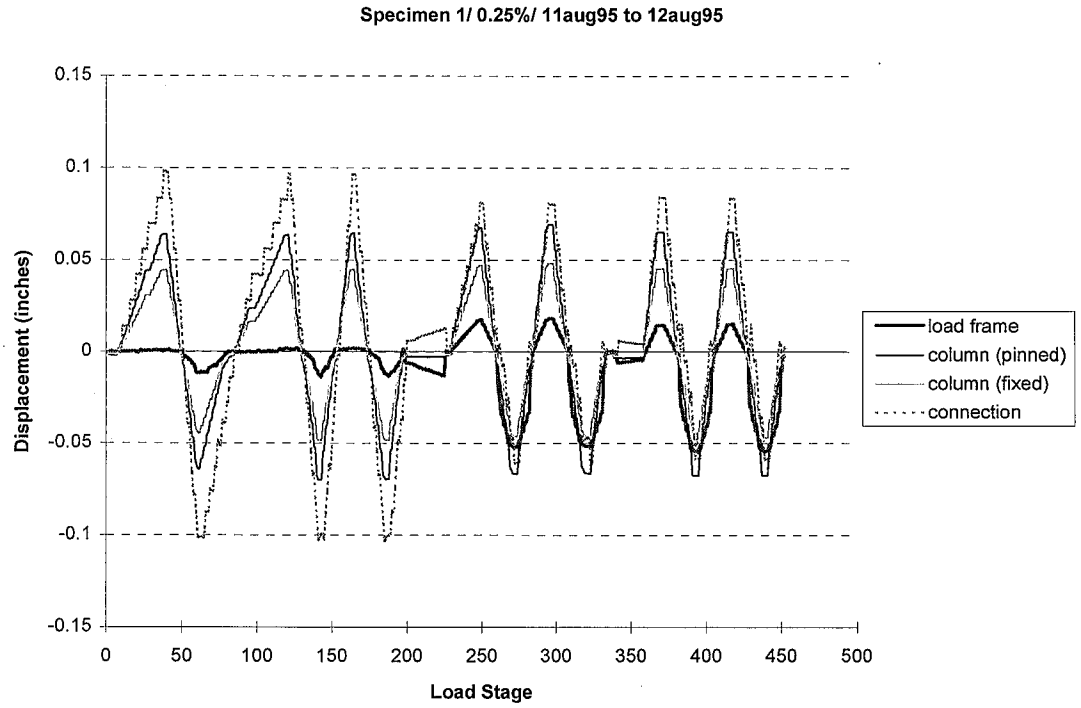

Figure F.22: Column, Load Frame, and Connection Girder Tip Deflection Components (West Girder of Specimen 1)

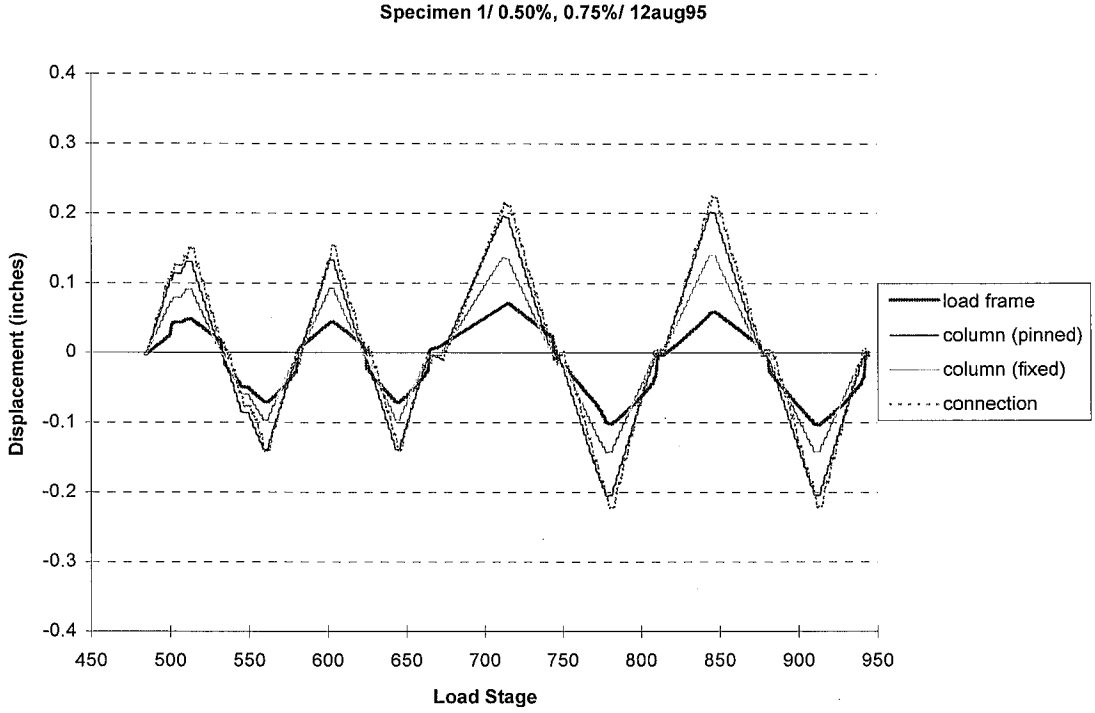

Figure F.23: Column, Load Frame, and Connection Girder Tip Deflection Components (West Girder of Specimen 1)

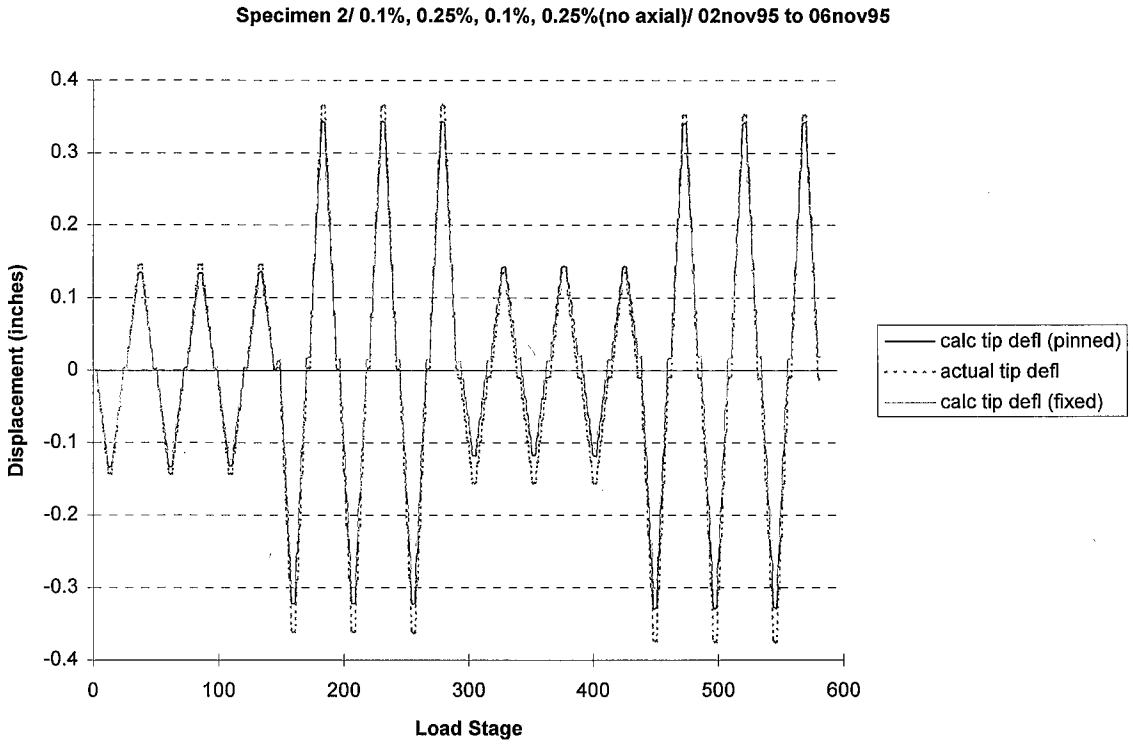

Figure F.24: Actual vs. Calculated Girder Tip Deflection (East Girder of Specimen 2)

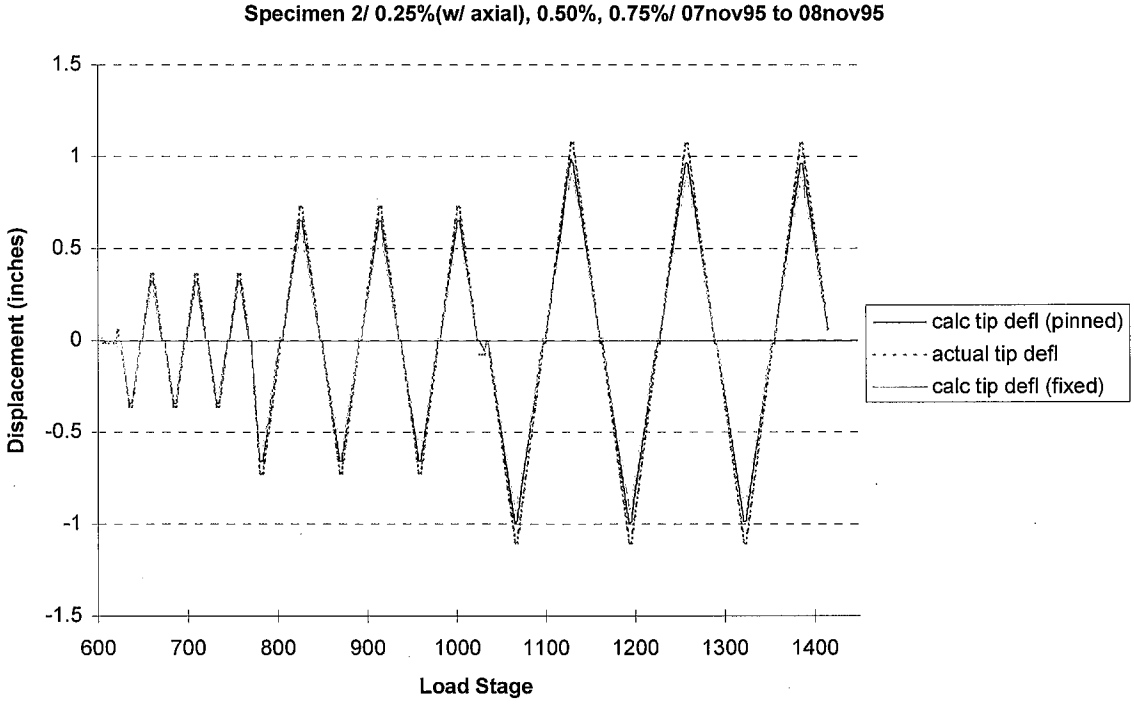

Figure F.25: Actual vs. Calculated Girder Tip Deflection (East Girder of Specimen 2)

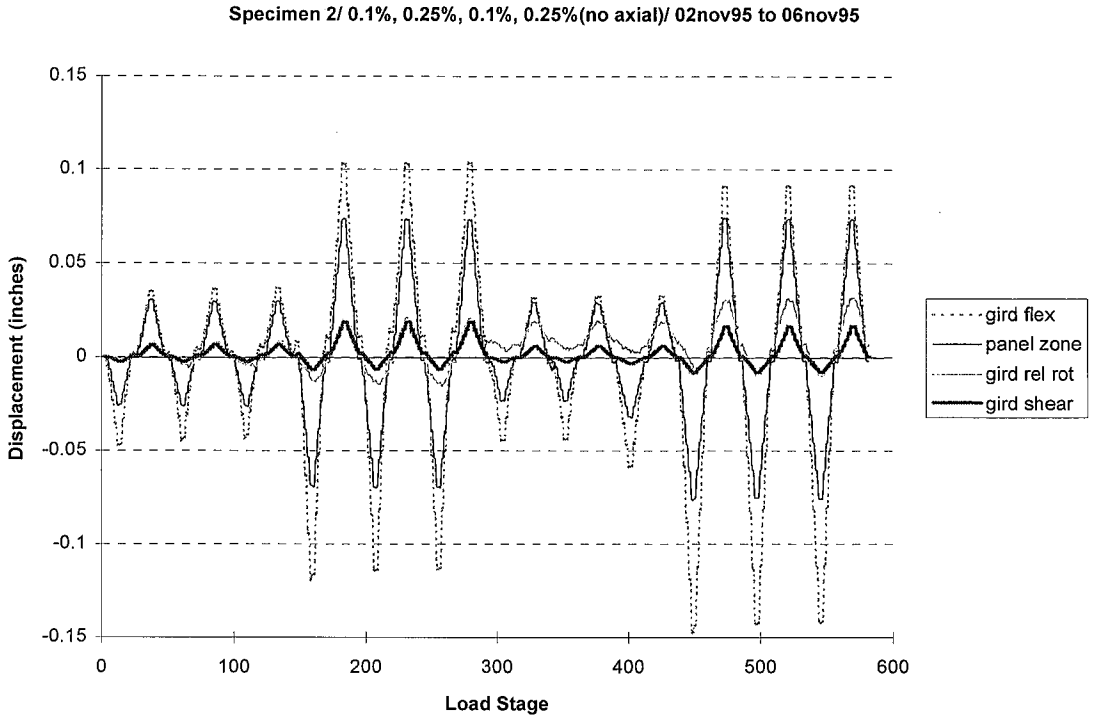

Figure F.26: Girder and Panel Zone Girder Tip Deflection Components (East Girder of Specimen 2)

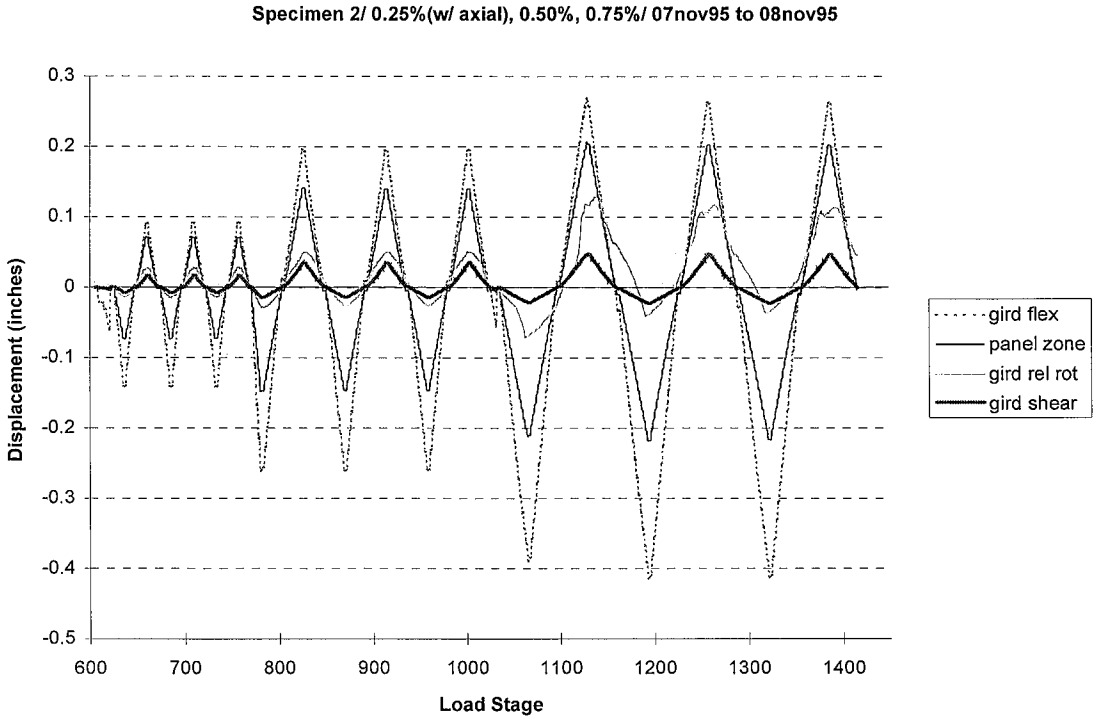

Figure F.27: Girder and Panel Zone Girder Tip Deflection Components (East Girder of Specimen 2)

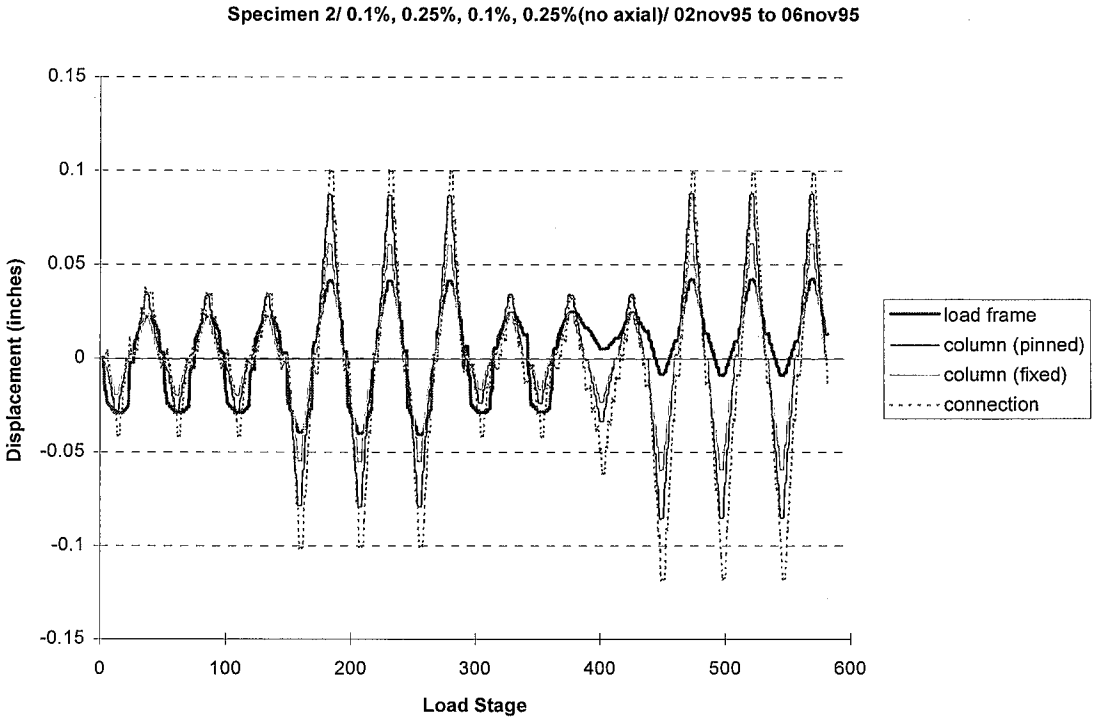

Figure F.28: Column, Load Frame, and Connection Girder Tip Deflection Components (East Girder of Specimen 2)

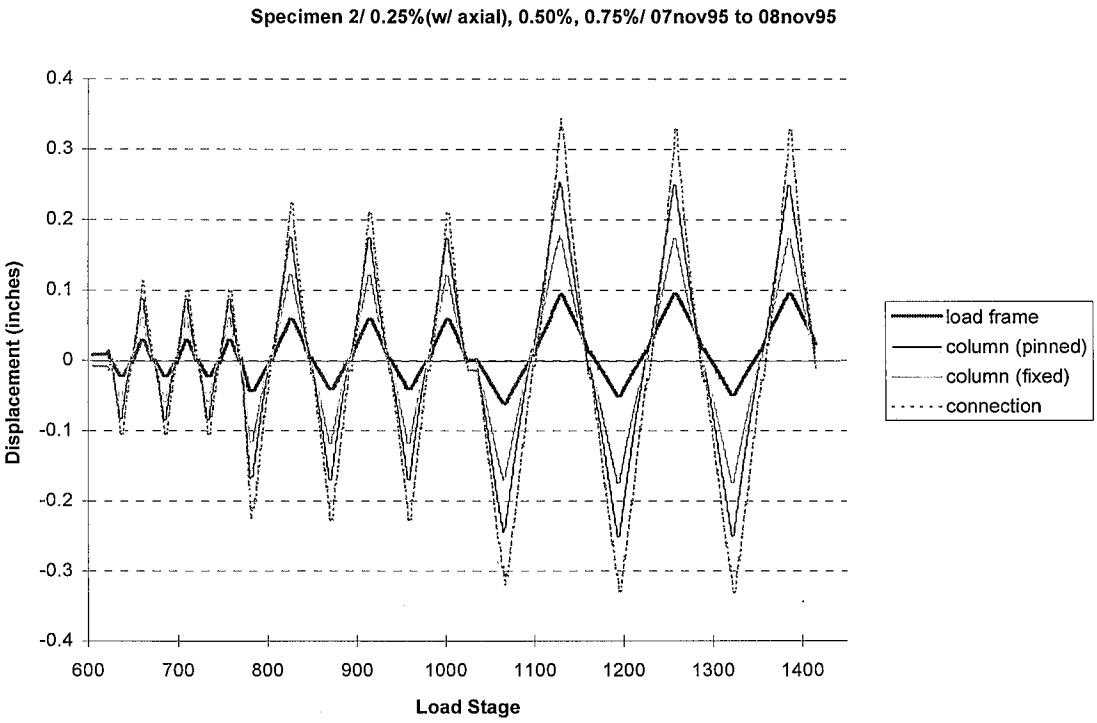

Figure F.29: Column, Load Frame, and Connection Girder Tip Deflection Components (East Girder of Specimen 2)

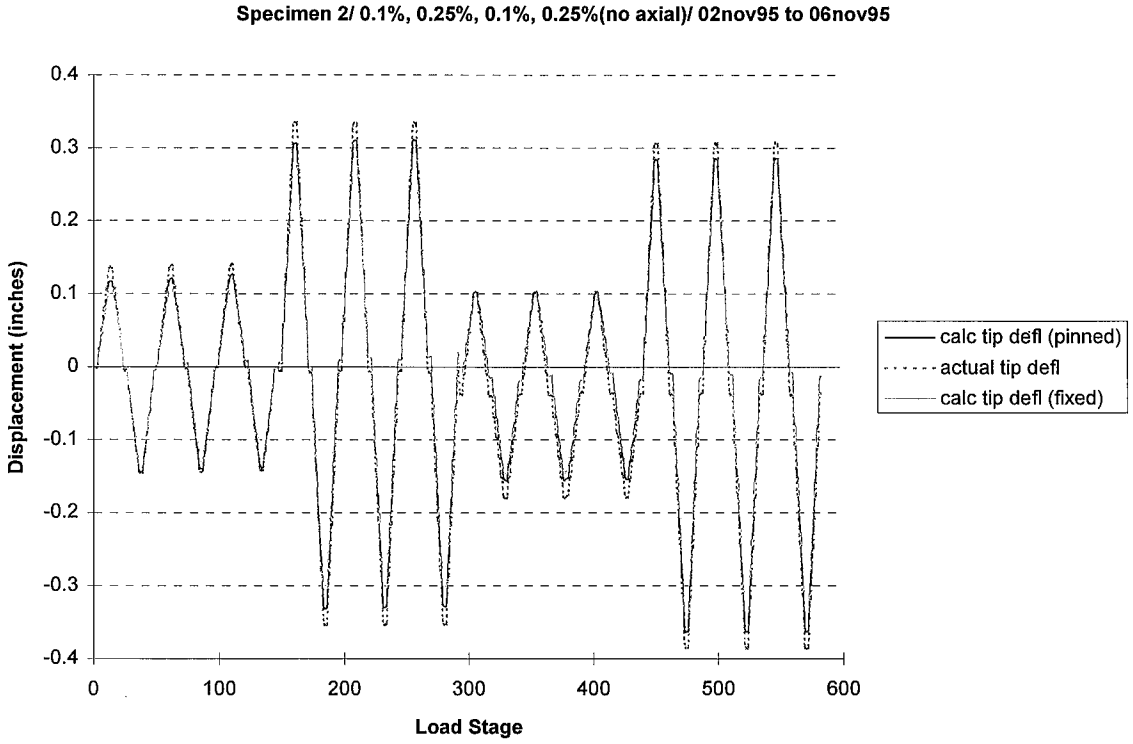

Figure F.30: Actual vs. Calculated Girder Tip Deflection (West Girder of Specimen 2)

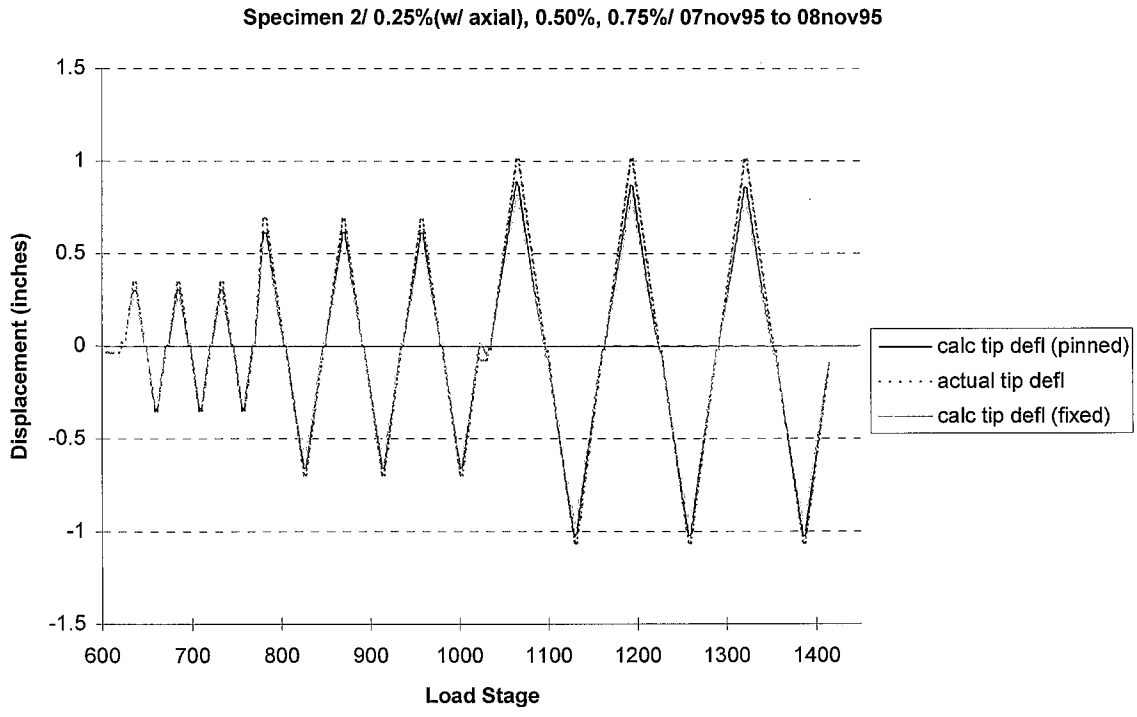

Figure F.31: Actual vs. Calculated Girder Tip Deflection (West Girder of Specimen 2)

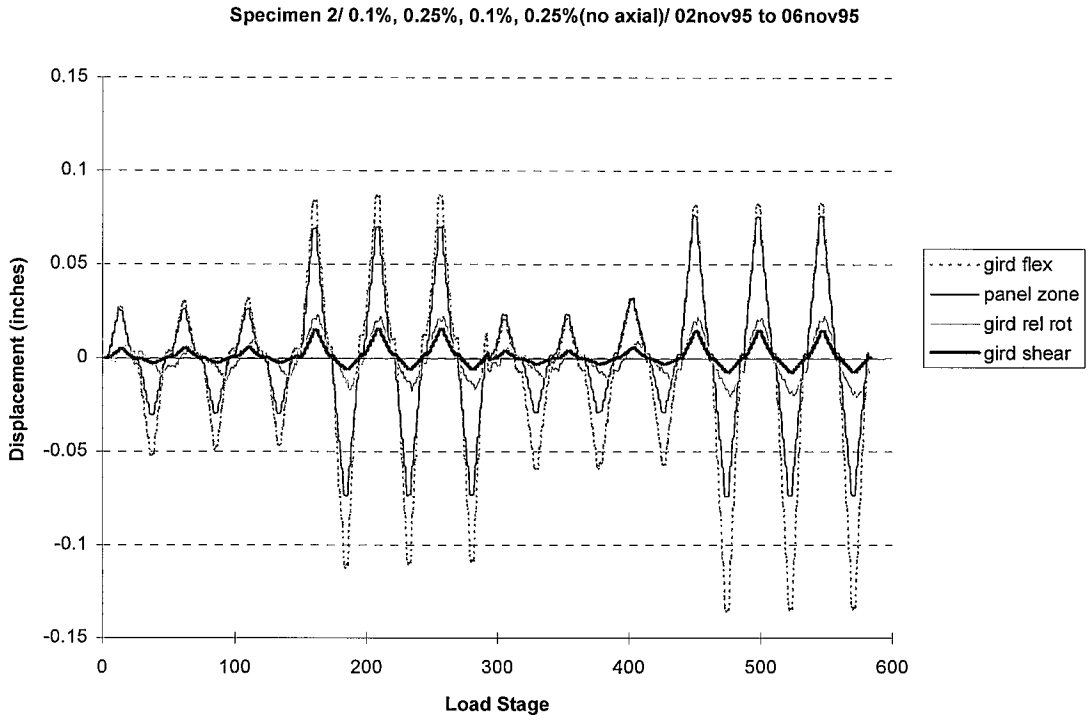

Figure F.32: Girder and Panel Zone Girder Tip Deflection Components (West Girder of Specimen 2)

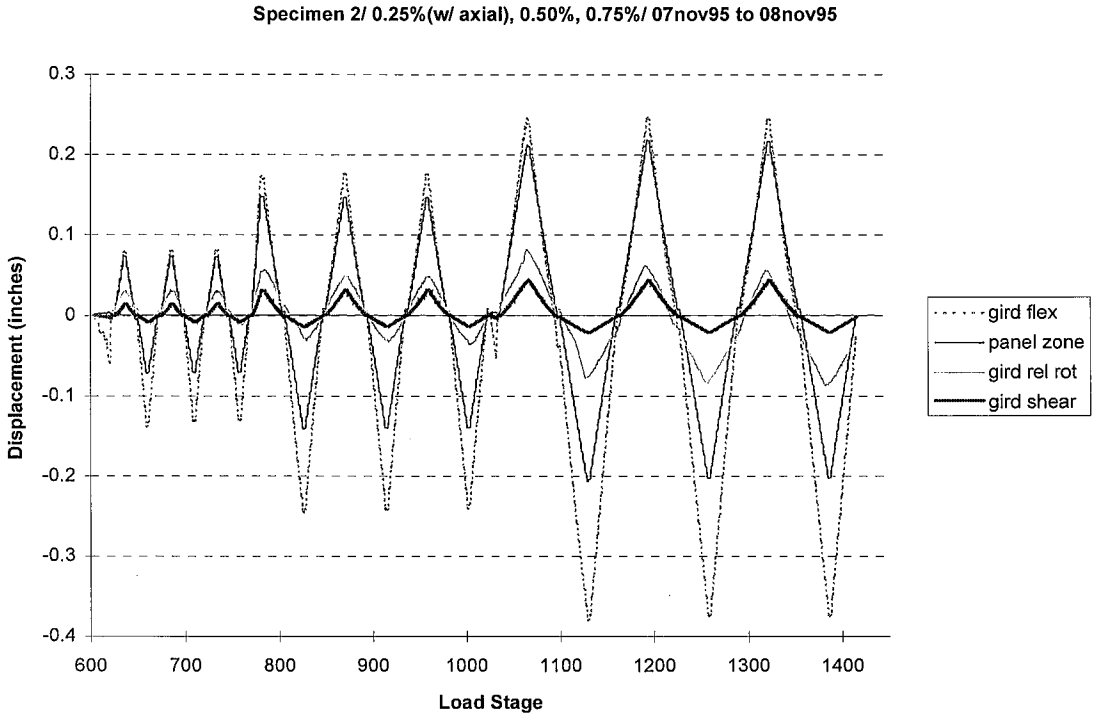

Figure F.33: Girder and Panel Zone Girder Tip Deflection Components (West Girder of Specimen 2)

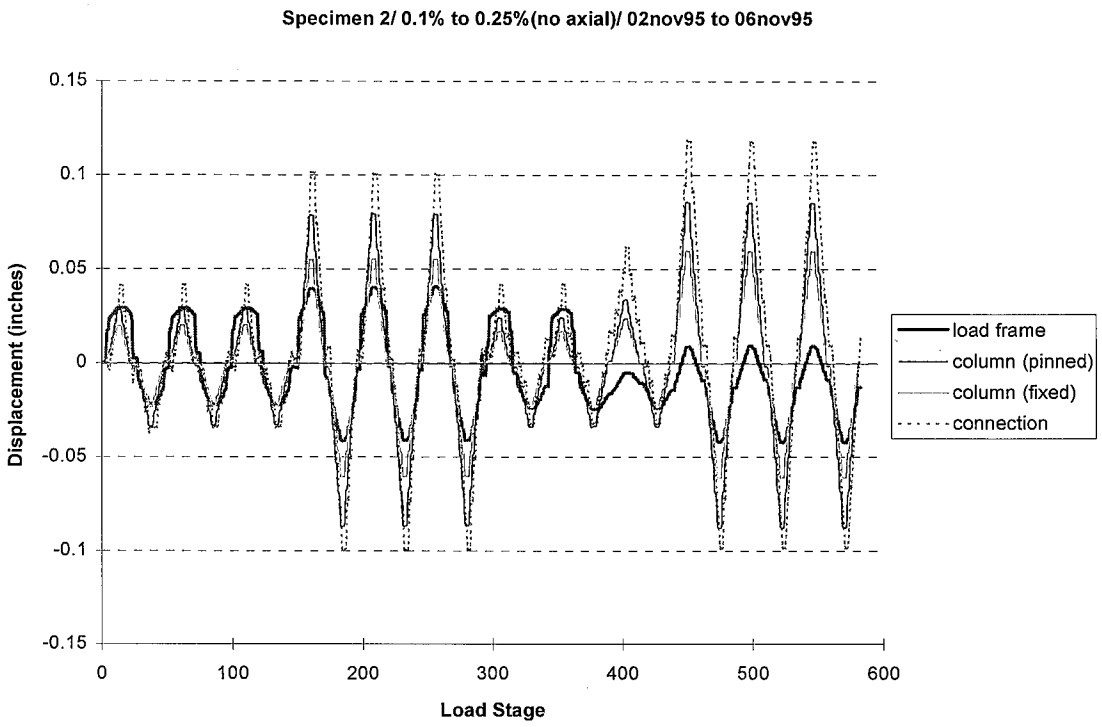

Figure F.34: Column, Load Frame, and Connection Girder Tip Deflection Components (West Girder of Specimen 2)

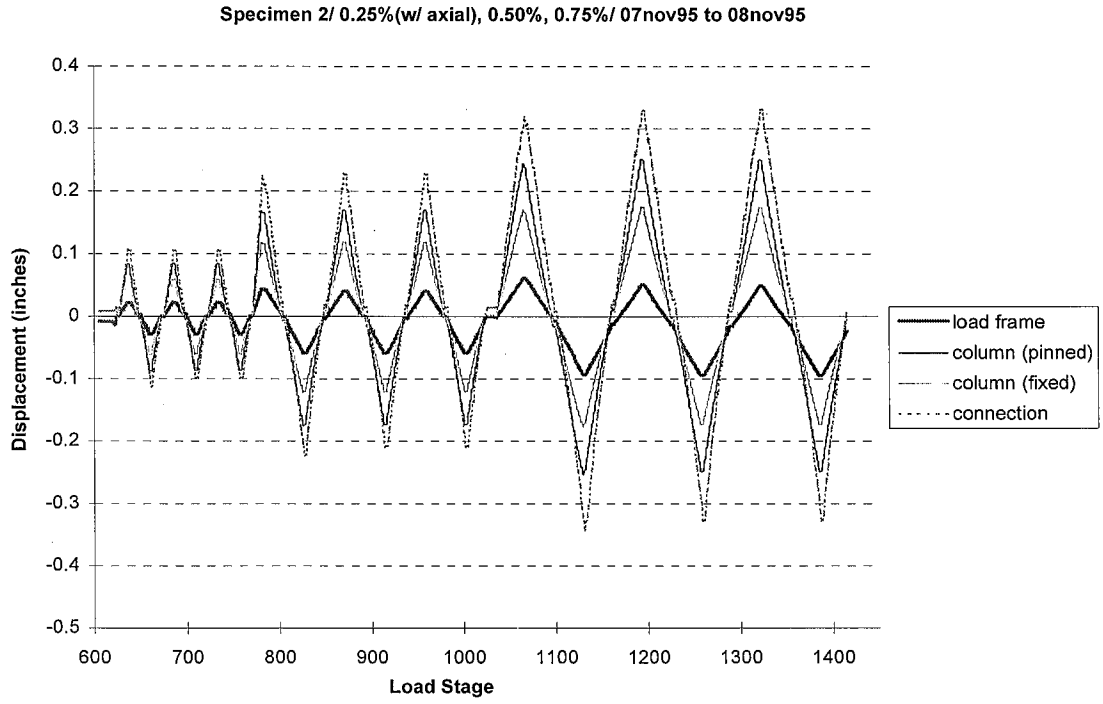

Figure F.35: Column, Load Frame, and Connection Girder Tip Deflection Components (West Girder of Specimen 2)

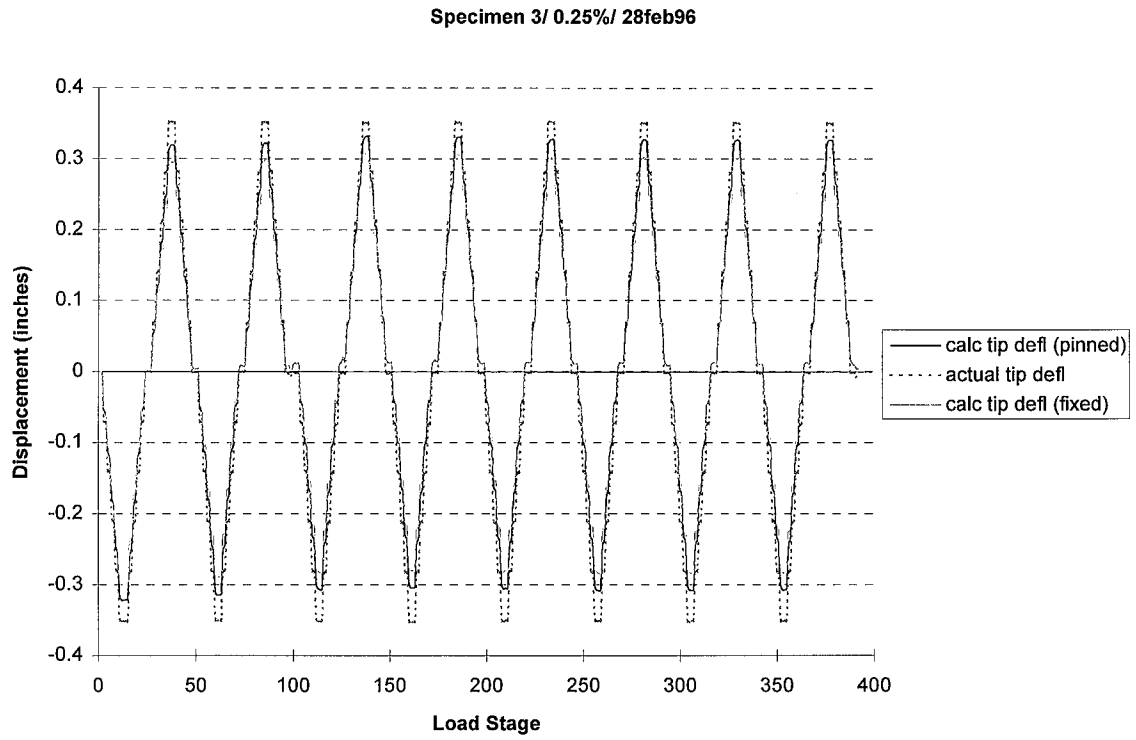

Figure F.36: Actual vs. Calculated Girder Tip Deflection (East Girder of Specimen 3)

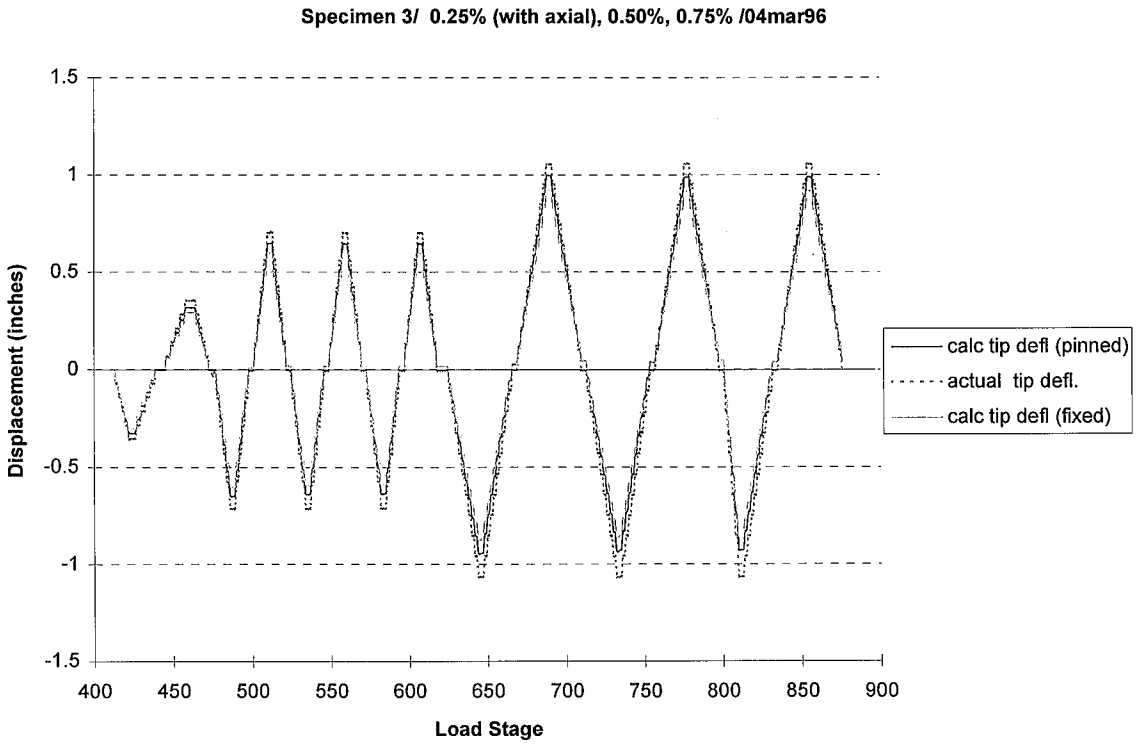

Figure F.37: Actual vs. Calculated Girder Tip Deflection (East Girder of Specimen 3)

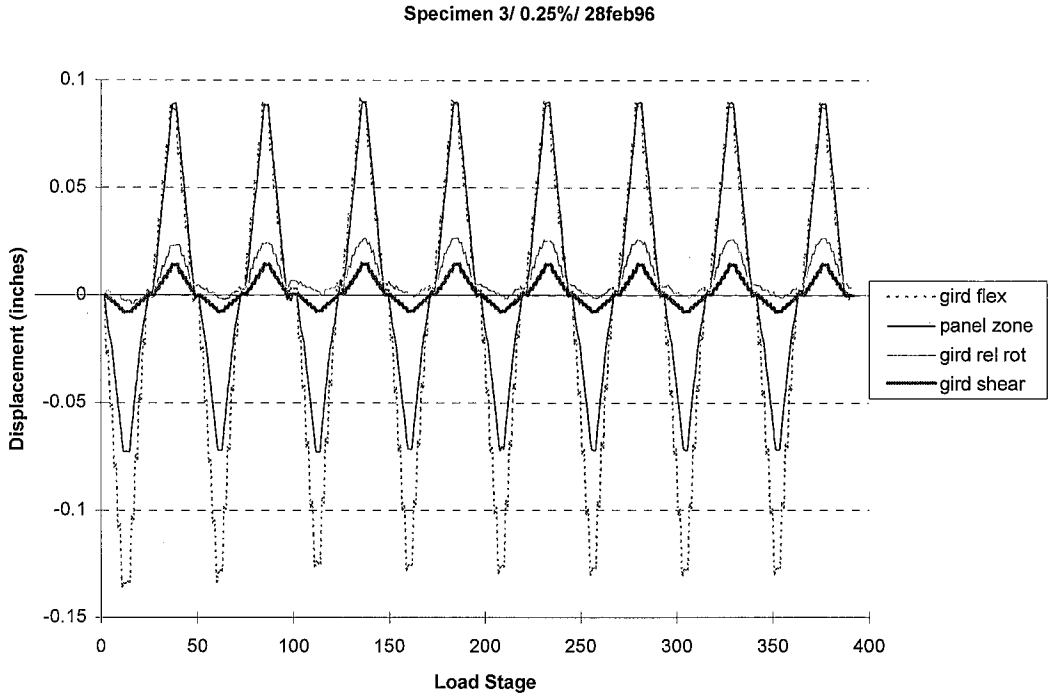

Figure F.38: Girder and Panel Zone Girder Tip Deflection Components (East Girder of Specimen 3)

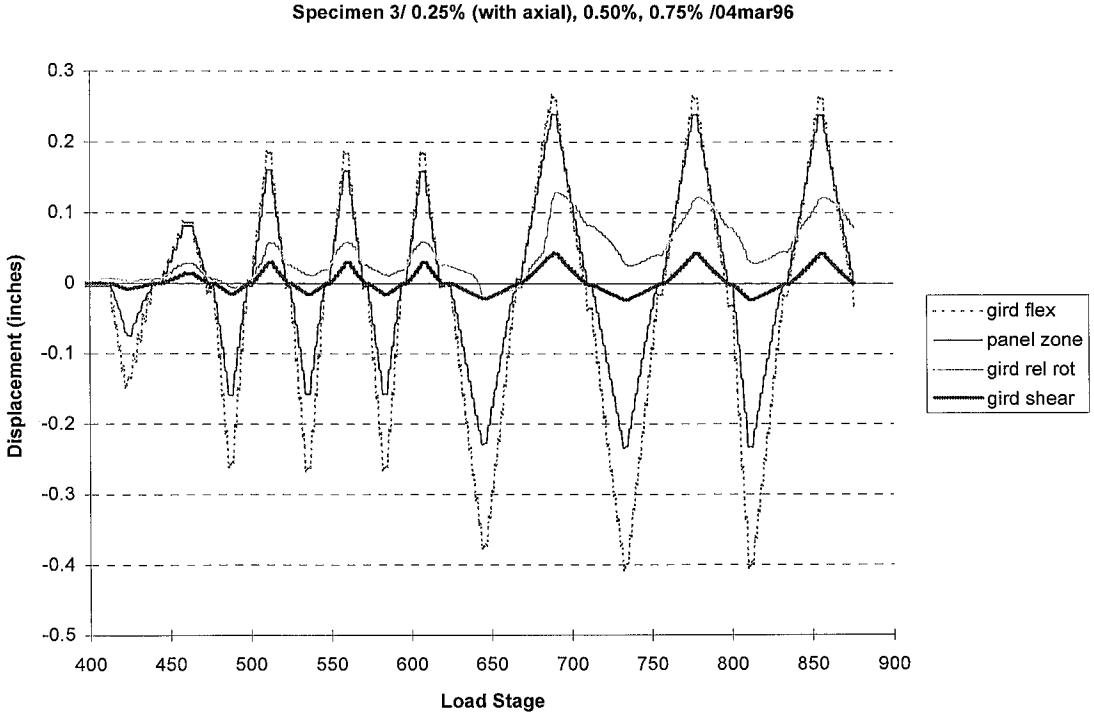

Figure F.39: Girder and Panel Zone Girder Tip Deflection Components (East Girder of Specimen 3)

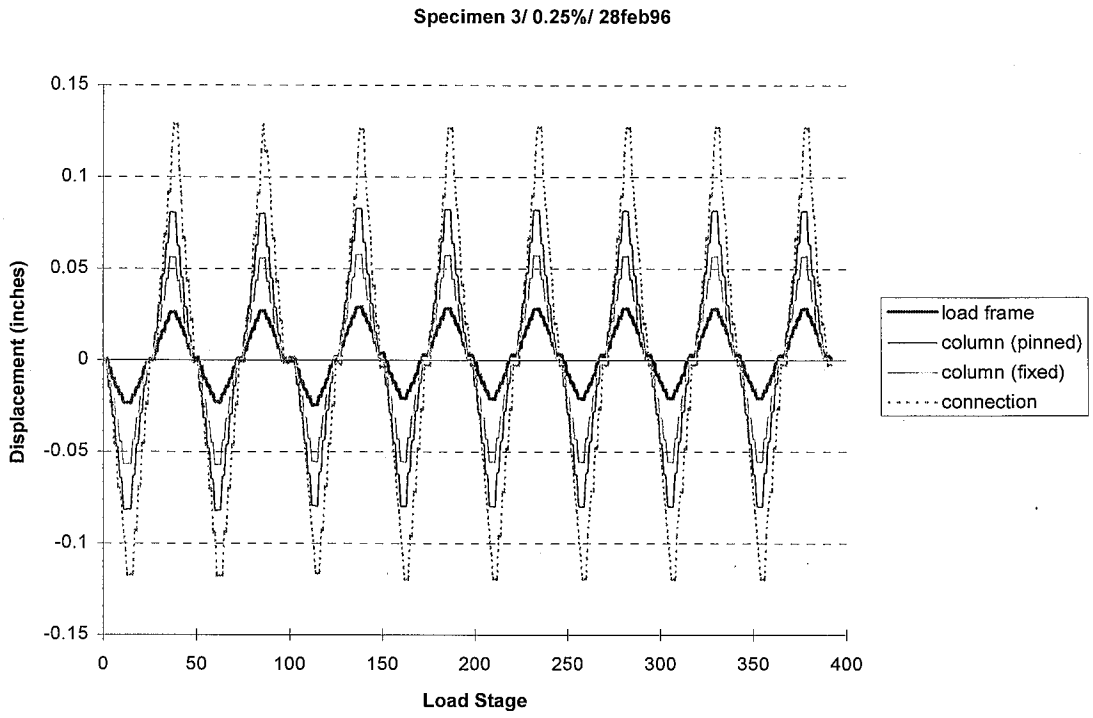

Figure F.40: Column, Load Frame, and Connection Girder Tip Deflection Components (East Girder of Specimen 3)

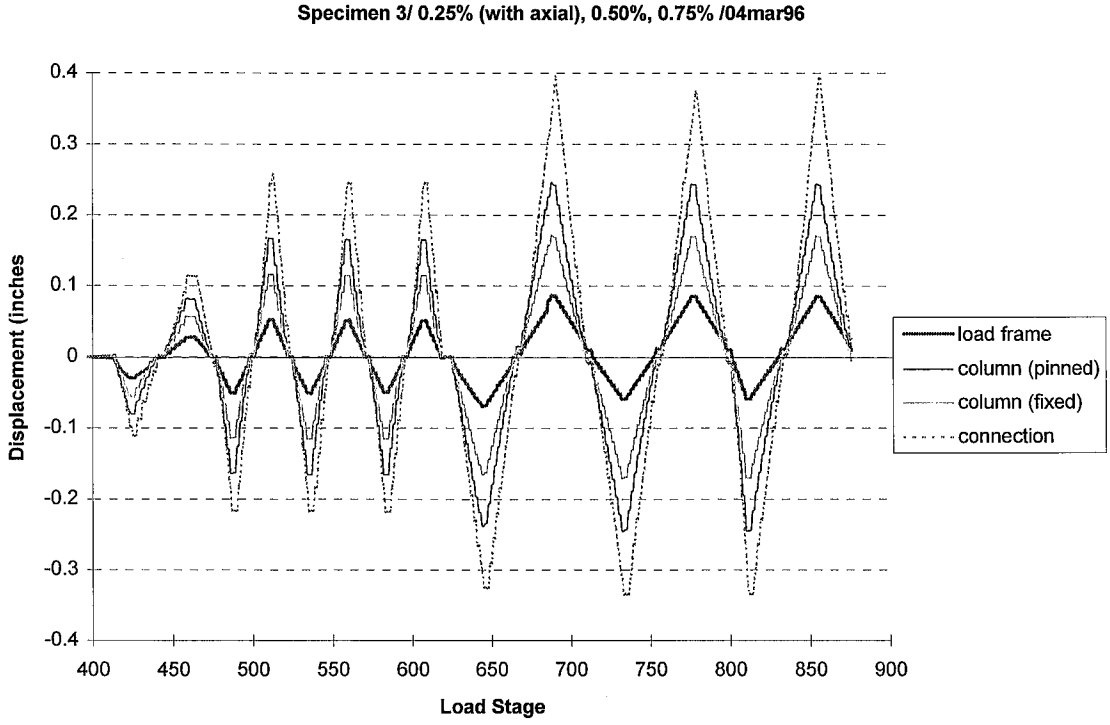

Figure F.41: Column, Load Frame, and Connection Girder Tip Deflection Components (East Girder of Specimen 3)

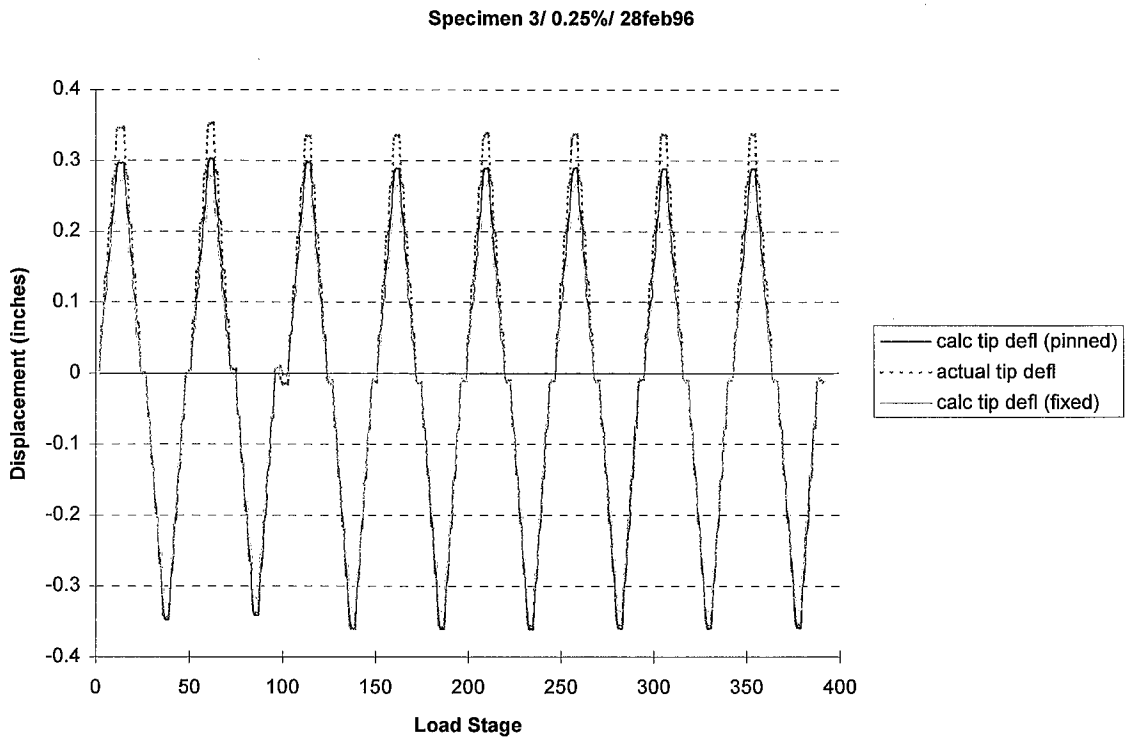

Figure F.42: Actual vs. Calculated Girder Tip Deflection (West Girder of Specimen 3)

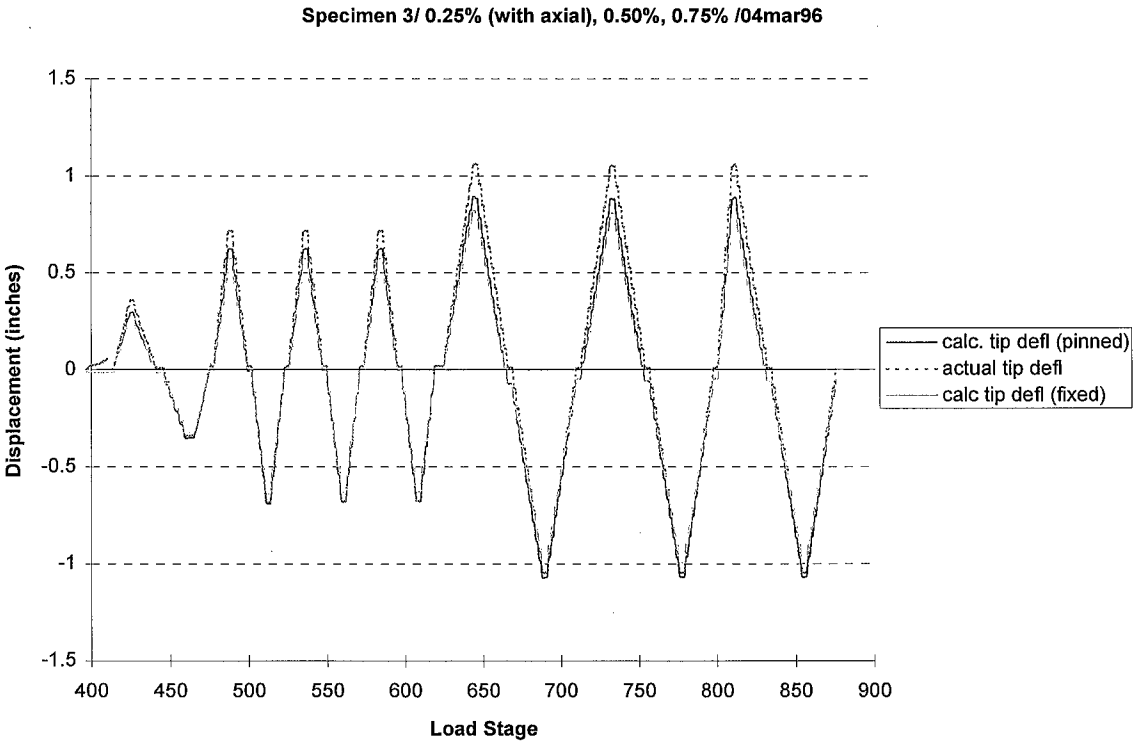

Figure F.43: Actual vs. Calculated Girder Tip Deflection (West Girder of Specimen 3)

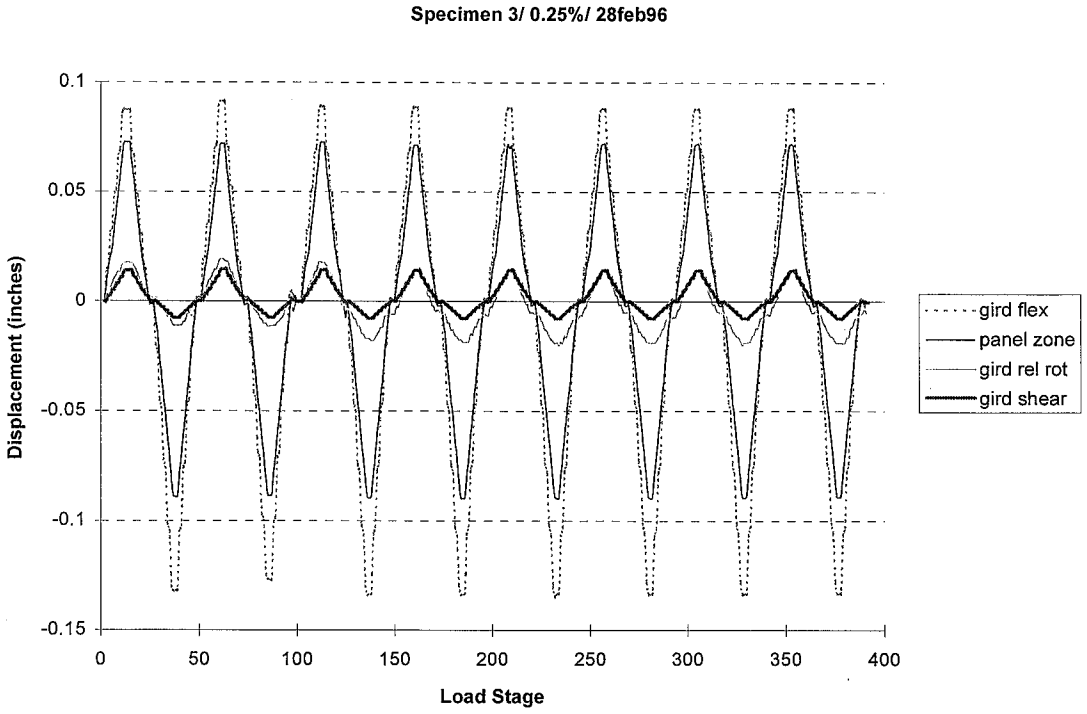

Figure F.44: Girder and Panel Zone Girder Tip Deflection Components (West Girder of Specimen 3)

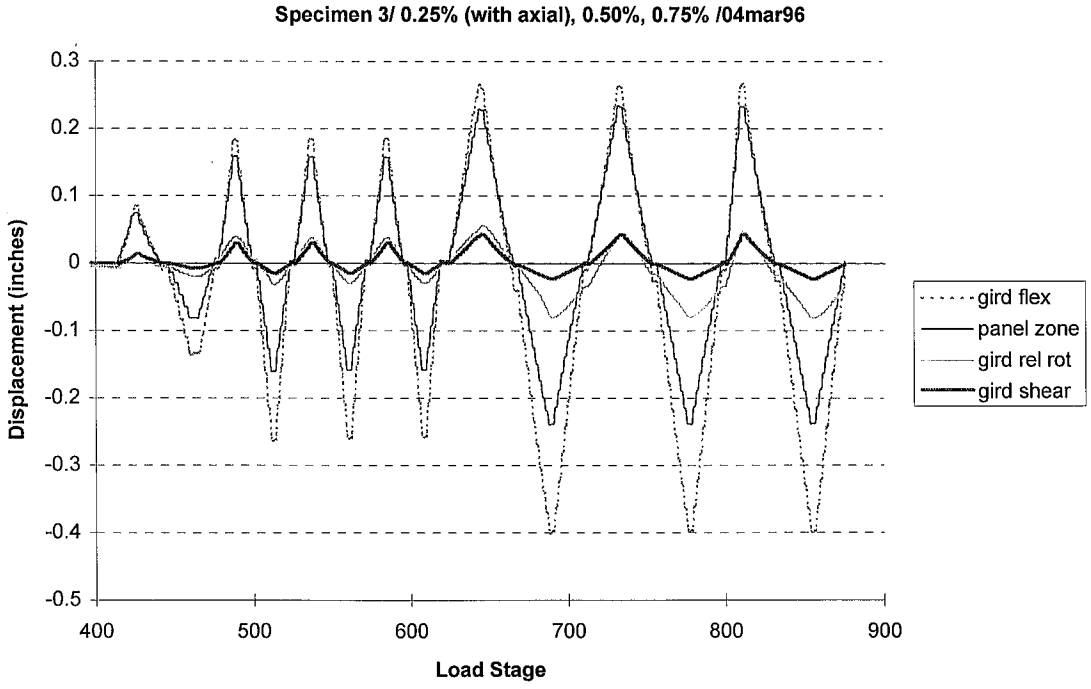

Figure F.45: Girder and Panel Zone Girder Tip Deflection Components (West Girder of Specimen 3)

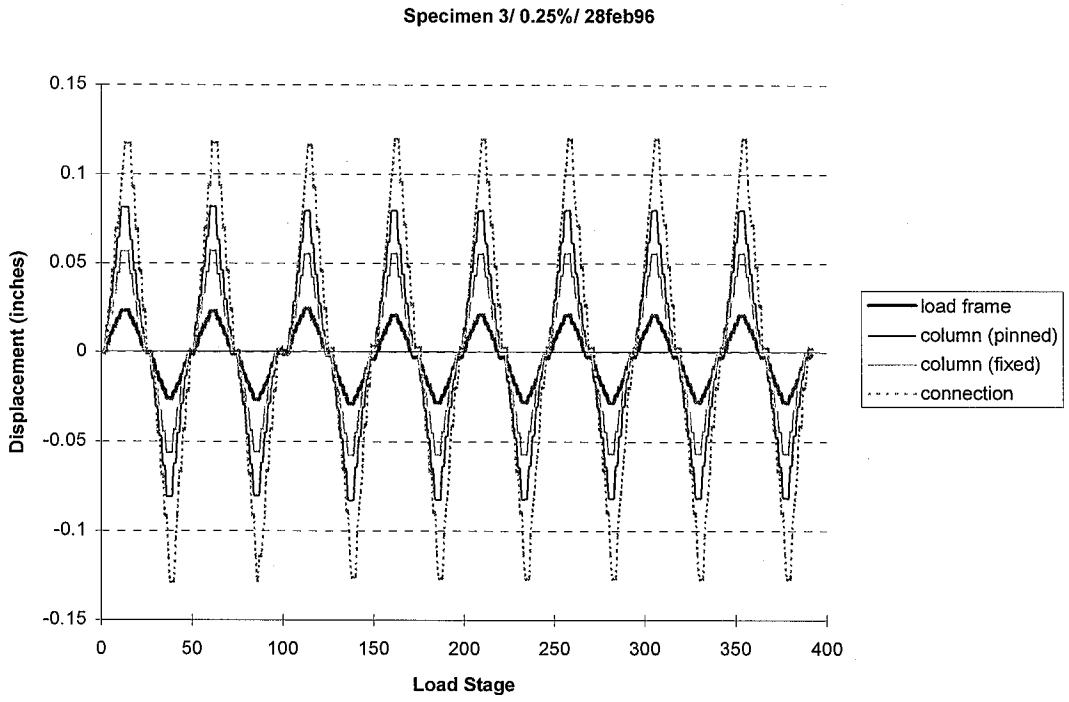

Figure F.46: Column, Load Frame, and Connection Girder Tip Deflection Components (West Girder of Specimen 3)

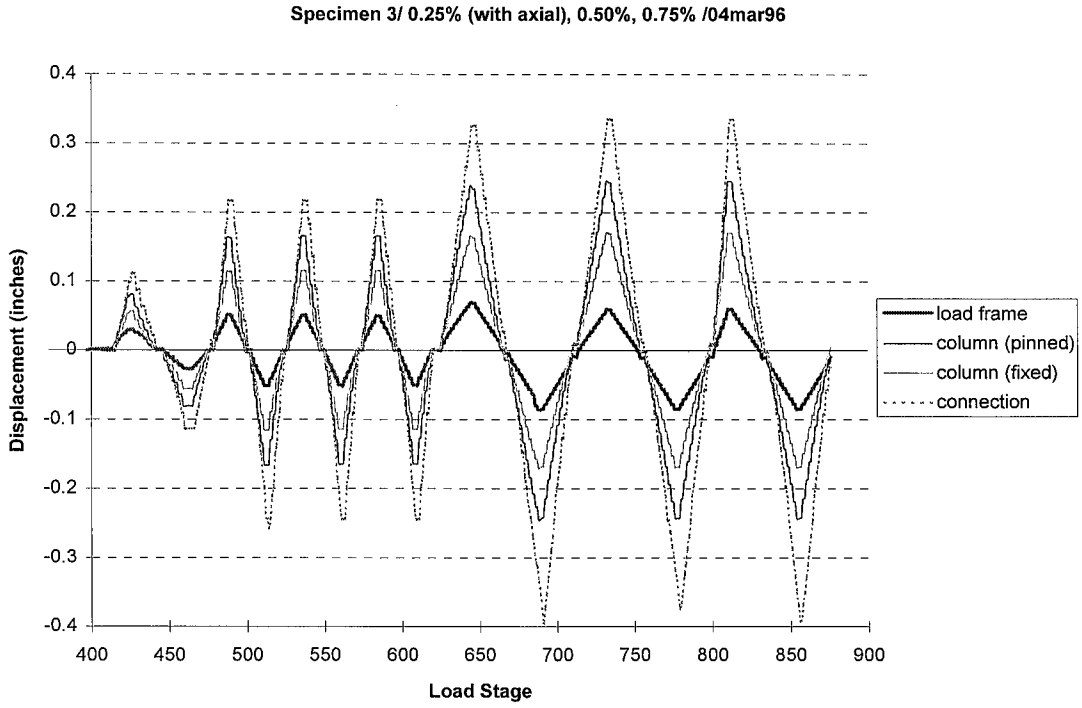

Figure F.47: Column, Load Frame, and Connection Girder Tip Deflection Components (West Girder of Specimen 3)

It is evident from Figures F.16, F.17, F.22, and F.23 that deformation in the East and West direction of the load frame relative to the strong floor was substantially less during the first three cycles at 0.25% when the East girder was subjected to girder positive bending. This may be due to inaccurate LVDT measurements taken during these initial cycles. As a result, the peak error percentages were predominantly due to the load frame contribution to the girder tip deflection. If actual deformation of the load frame during the first 3 cycles at 0.25% was similar to the load frame deformations during the last four cycles of 0.25%, the percentage error differences are reduced significantly.

For Specimen 2, the actual girder tip deflection values were up to 14% greater than the calculated girder tip deflection values up to the 0.75% drift cycles (Table F.4, Figures F.24, F.25, F.30, and F.31). These results are slightly less accurate than Specimen 1 due largely to the difficulty in computing the effects of the concrete slab.

When the East girder of Specimen 3 is subjected to positive and negative girder bending, the actual girder tip deflections are approximately 5% to 10% greater than the calculated girder tip deflections up to the 0.75% drift levels (see Figure F.36 and F.37). The West girder of Specimen 3 demonstrates a strong correlation between the actual girder tip deflections and the calculated girder tip deflections when subjected to negative bending (see Figure F.38 and F.39). However, when the West girder is subjected to positive bending, the actual girder tip deflection magnitudes exceed the calculated girder tip deflection magnitudes by about 12% to 18%.

The panel zone distortion of Specimen 3 was greater when the East girder was subjected to positive bending (compared to negative bending) up through the 0.75% drift levels (see Figures F.38, F.39, F.44, and F.45). This asymmetric behavior of the panel zone may explain the lower calculated girder tip deflection values of the West girder compared to the East girder during girder positive bending and may be a direct result of a relatively smaller I_{eff} exhibited by the West girder of Specimen 3.

For all three tests, the actual and calculated girder tip deflection (assuming pinned-pinned column end support conditions) compare relatively well. Therefore, it is

concluded that the measured girder-to-column plastic rotation and panel zone distortion are valid for all three tests. Possible sources of error that may contribute to the difference between the actual and calculated girder tip deflections include the formulation of the girder and column flexure equations and nonlinear behavior of the steel girders beyond 13.5" from the column face.

It is observed that the peak error percentages between the actual and calculated girder tip deflections are greater during girder positive bending than negative bending for Specimens 2 and 3. Although nonlinear material behavior and elastic shear deformation of the steel girder may contribute to this error, the discrepancy may be partially attributed to an overestimation of the calculated effective moments of inertia of the composite girders, I_{eff}.

The effective moment of inertia is computed based on the modulus of concrete, E_c (see Appendix A). This value is estimated for Specimens 2 and 3 using the compressive strength of the concrete slab and an equation provided by ACI Section 8.5.1 (ACI, 1995). This reference states that the actual E_c can vary up to 20% from a typical estimated E_c. Furthermore, E_c is assumed constant throughout the load history. An underestimation of the modulus of concrete was found in Specimen 3 by comparing the strains measured in the concrete slab and the reinforcing steel of the East and West girder concrete slab (see Section 4.3).

Based on visual documentation of the crack patterns on the top surface of the concrete decks of Specimens 2 and 3, it was evident, especially for the West girder of Specimen 3, that substantial cracking of the concrete occurred (near the column flange-concrete deck interface during and after the 0.50% drift levels). The existence of such conditions may have led to a substantial degradation in concrete modulus and compressive resistance of the composite floor slabs.

The equation used to express I_{eff} may also contribute to the underestimation of the actual I_{eff} of the girders of the specimens, since it is only an estimation of the effective moment of inertia of a partially composite girder (see Appendix A) (AISC, 1993).

Adjusted I_{eff} values (which are utilized in the girder and column flexural deformation components) were computed which resulted in girder tip deflection peak magnitudes similar to the actual girder tip deflection peak magnitudes. For both the East and West girders of Specimen 2, the actual girder tip deflection was bounded by the calculated girder tip deflections with I_{eff} having values of approximately 4200 in^4 to 5000 in^4. For the East girder of Specimen 3, the actual girder tip deflection was bounded by the calculated girder tip deflections with I_{eff} approximately 4200 in^4 to 4500 in^4. For the West girder of Specimen 3, the actual girder tip deflection was bounded by the calculated girder tip deflections with I_{eff} approximately 3500 in^4 to 3700 in^4. These adjusted I_{eff} values are compared to the calculated I_{eff} of Specimens 2 and 3 (5901 in^4 and 6476 in^4, respectively) which are valid for the 0.25% and possibly the 0.50% drift cycles (i.e., for linear behavior) (see Appendix A).

It may be concluded that the effective moments of inertia of the East and West girders of Specimens 2 and 3 are less than that calculated. Discrepancies between the actual and calculated girder tip deflections during negative bending are not as attributable to the difficulty in calculating I_{eff}, because participation of the concrete slab is minimal during negative bending of the East and West girder.

Appendix G

Calculation of Girder Moments and Strains

This appendix discusses the assumptions and calculations used to formulate the girder moments and strains reported in Chapter 4. Girder moments and strains are compared to further verify the experimental measurements. In addition, discrepancies shown between these moments and strains are used to substantiate that partially composite action is occurring within the composite girders. Also, the errors may be qualitatively compared between specimens to investigate the accuracy of the estimated concrete modulus and the effect of a nonlinear strain distribution along the girder cross section (due to longitudinal distortion of the girder cross section along its width) on the calculation of the girder moments and strains. The studies in this section are based on assuming Euler-Bernoulli beam theory (i.e., the effects of elastic shear deformation of the girder is minimal).

G.1 Procedure for Calculating Girder Moments and Strains

A series of seven strain gages were installed along the steel cross section of each girder at a distance 13.5" out from the column flange. Figure G.1 illustrates where three gages were placed on the girder web and a pair of gages were placed both on the bottom of the girder top flanges and the top of the girder bottom flanges (see also Section 2.1.3).

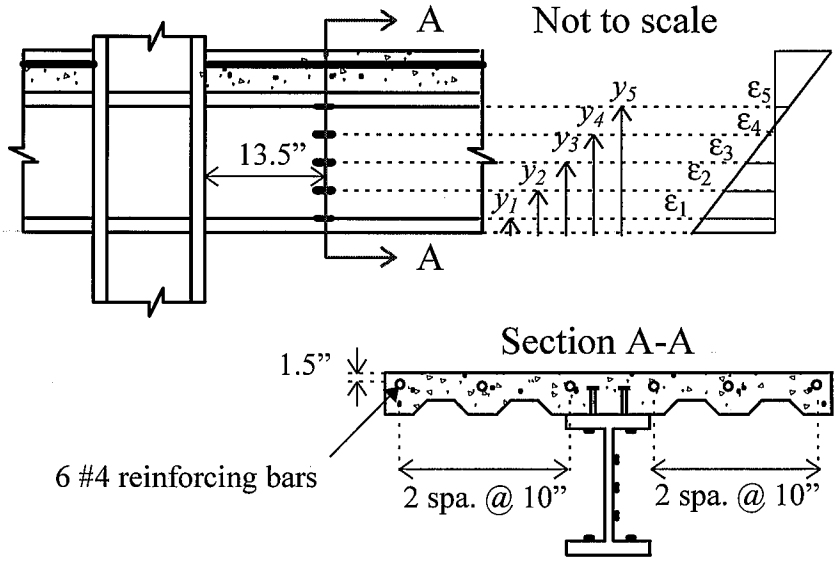

Figure G.1: Strain Gage Locations Along the Girder Cross Section

As seen in the strain diagram in Figure G.1, the strains measured by these gages are defined as ε_1, ε_2, ε_3, ε_4, and ε_5, and represent strains measured parallel to the girder's longitudinal axis and along its steel cross section. Note that the pair of strain gages located on the top and bottom girder flanges are averaged to represent ε_5 and ε_1, respectively. The locations of the strain gages are measured from the bottom surface of the steel girder and are defined as y_1, y_2, y_3, y_4, and y_5:

Table G.1: Position of Steel Cross Section Strain Gages

Specimen	**Girder**	**Strain gage position measured from bottom of steel section (inches)**				
		y_1	y_2	y_3	y_4	y_5
Specimen 1	**East**	0.745	6.87	13.74	20.50	26.18
	West	0.745	6.62	13.43	20.00	26.18
Specimen 2	**East**	0.745	6.75	13.50	20.37	26.18
	West	0.745	6.75	13.50	20.25	26.18
Specimen 3	**East**	0.745	6.87	13.37	20.25	26.18
	West	0.745	6.87	13.37	20.25	26.18

For Specimens 2 and 3, strains in the concrete slab were measured using five strain gages placed on the top side of the reinforcing bars at a distance of 13.5" from the column flange. The reinforcing bars were spaced at 10" across the slab width with 1.5" of concrete cover. Strains in the concrete slab were also measured with one rosette whose intersection point of the three component gages was placed approximately 4" from the column face in each girder's concrete slab, with the three component gages fanning outwards from the column face (see also Section 2.4.3 for strain gage locations).

To calculate the girder moment for a given load stage, the curvature, neutral axis location and forces in the girder sections are used. First, the seven strain measurements in the girder are employed to compute the curvature at the cross section utilizing linear regression. This calculation assumes the bending strain distribution of the steel cross section is linear. By using the methods of least squares, the slope, m, of a linear regression line through the seven strain measurements is calculated using the strain magnitudes and their respective position on the girder cross section (Larsen and Marx, 1981):

$$m = \frac{n\sum_{i=1}^{n} y_i \varepsilon_i - \left(\sum_{i=1}^{n} y_i\right)\left(\sum_{i=1}^{n} \varepsilon_i\right)}{n\sum_{i=1}^{n} (\varepsilon_i)^2 - \left(\sum_{i=1}^{n} \varepsilon_i\right)^2} \qquad \text{(G.1)}$$

The terms n, ε_i, and y_i are equal to the number of strain measurements, the ith strain magnitude, and the ith strain location measured from the surface of the girder bottom flange, respectively.

The slope, m, represents the change in vertical distance along the girder cross section divided by the change in strain. Therefore, the tangent of the curvature of the girder cross section, ϕ, is equal to inverse of m since the curvature represents the change in strain divided by the change in distance between strain gage locations:

$$tan\phi = \frac{1}{m} \tag{G.2}$$

It is important to note that curvatures calculated at peak loads demonstrate less error than those calculated at zero load. The strain values measured at zero load were not exactly zero and their values were small and erratic, leading to erratic values of curvature which are ignored in this procedure.

The position of the neutral axis is needed to calculate the moment in the girder cross section. For a given load stage, the centroidal distance, y_{NA}, is equal to the distance between the bottom of the girder steel section and its neutral axis (see Figure G.2). To calculate y_{NA}, a generalized line equation is used, where Eq. G.1 and a line-intercept value, c, are employed. The parameter c is formulated using the mean of the strain magnitudes, $\bar{\varepsilon}$, and the mean of the strain gage locations, $\bar{Y}$, measured from the bottom flange (Larsen and Marx, 1981):

$$c = \bar{Y} - \frac{\bar{\varepsilon}}{tan\phi} \tag{G.3}$$

The neutral axis may now be located along the girder cross section where the strain, ε_{NA}, is equal to zero:

$$\varepsilon_{NA} = 0 \tag{G.4}$$

$$y_{NA} = m\varepsilon_{NA} + c = \bar{Y} - \frac{\bar{\varepsilon}}{tan\phi} \tag{G.5}$$

The increase in calculated curvature error when approaching zero loading affects the accuracy of the neutral axis calculation. Consequently, near zero load, the neutral

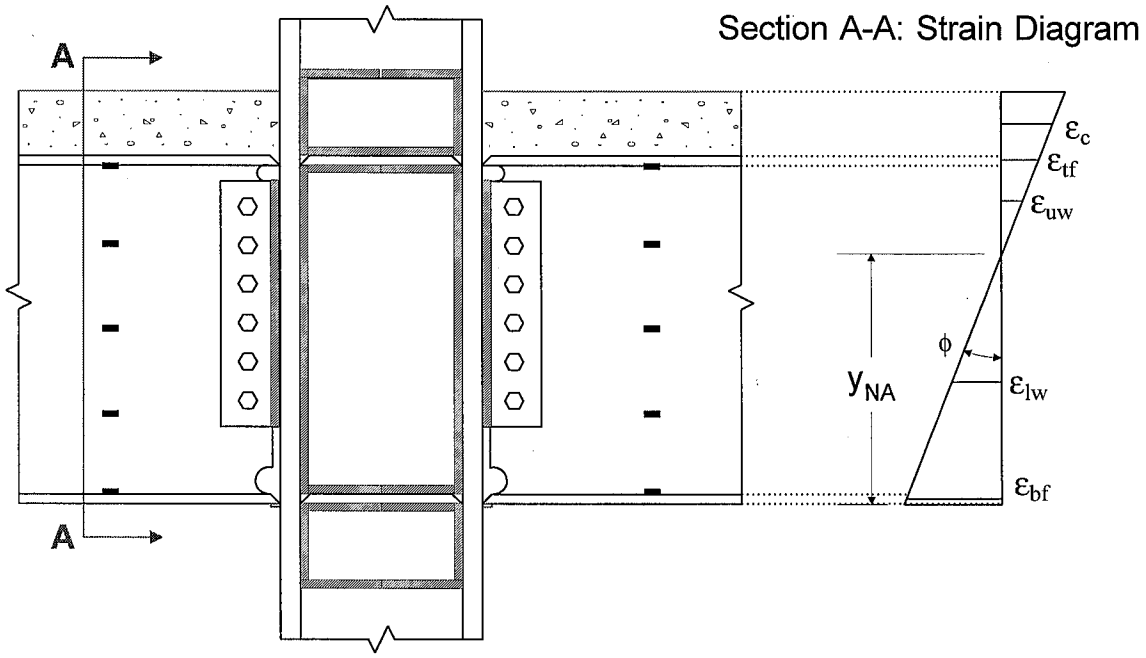

Figure G.2: Calculated Strains Along the Girder Cross Section

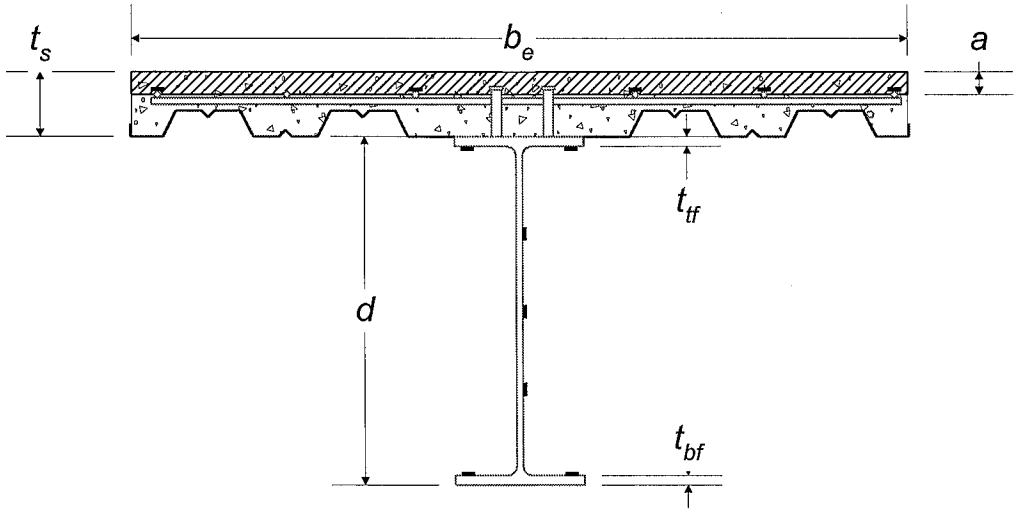

Figure G.3: Dimensions of Girder Cross Section

axis location is set equal to one-half the steel girder depth, *d/2,* or 13.46 inches for all specimens. The actual neutral axis location of a composite girder subjected to near-zero bending loads is not necessarily at *d/2*. However, *d/2* is selected as a lower bound for convenience. Note that information resulting only at peak load magnitudes are considered in this section as providing relevant information.

With the position of the neutral axis known for a given load stage, a resultant strain (or average strain) may be calculated for each component area (Figure G.2). This strain is assumed to represent the strain distribution over a given component area:

$$\varepsilon_c = (d + t_s - \frac{a}{2} - y_{NA}) \tan\phi \tag{G.6}$$

$$\varepsilon_{tf} = (d - \frac{t_{tf}}{2} - y_{NA}) \tan\phi \tag{G.7}$$

$$\varepsilon_{uw} = \frac{1}{2}(d - t_{tf} - y_{NA}) \tan\phi \tag{G.8}$$

$$\varepsilon_{lw} = \frac{1}{2}(y_{NA} - t_{bf}) \tan\phi \tag{G.9}$$

$$\varepsilon_{bf} = (y_{NA} - \frac{t_{bf}}{2}) \tan\phi \tag{G.10}$$

where ε_c = strain measured in the concrete slab (assuming no slip) (in.)

ε_{tf} = strain measured in the top flange region of the steel girder (in.)

ε_{uw} = strain measured in upper web region of the steel girder (in.)

ε_{lw} = strain measured in lower web region of the steel girder (in.)

ε_{bf} = strain measured in top flange region of the steel girder (in.)

a = effective thickness of concrete slab (in.)

d= depth of steel girder section (in.)

t_s = thickness of concrete slab measured from the top of the concrete slab to the top of the steel girder (in.)

The strain distribution is assumed to vary linearly within each area; therefore, the top flange, bottom flange, and concrete slab strain distributions are trapezoidal while the upper and lower web strain distributions are triangular. Equation G.6 is based on the assumption that no slip occurs between the concrete slab and the steel girder section. Figure G.3 illustrates the dimensions of the composite girder cross section. Note that these strains are computed because the actual strains that are measured along the cross section are not located at the center of each area component.

With the strain distribution known for a given applied girder moment, a stress analysis procedure is used to acquire the five force components across the composite cross section. Each force component is the product of the component area and the stress distribution across the component area (see Figure G.4).

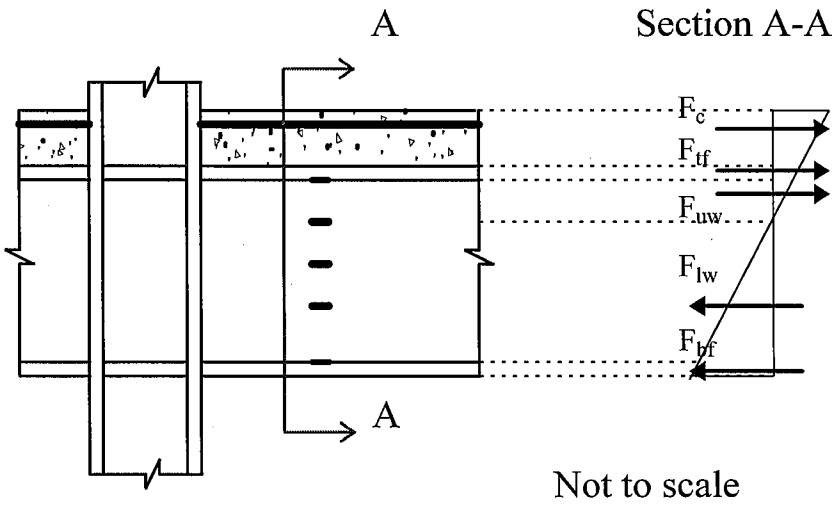

Figure G.4: Force Components Along the Girder Cross Section

$$F_c^+ = \varepsilon_c E_c A_c \tag{G.11}$$

$$F_c^- = \varepsilon_c E_s A_r \tag{G.12}$$

$$F_{tf} = \varepsilon_{tf} E_s A_{tf} \tag{G.13}$$

$$F_{uw} = \varepsilon_{uw} E_s A_{uw} \tag{G.14}$$

$$F_{lw} = \varepsilon_{lw} E_s A_{lw} \tag{G.15}$$

$$F_{bf} = \varepsilon_{bf} E_s A_{bf} \tag{G.16}$$

where A_c = effective cross-sectional area of the concrete slab (in^2)

A_r = cross-sectional area of the reinforcing steel (in^2)

A_{tf} = cross-sectional area of steel top flange of steel girder (in^2)

A_{uw} = cross-sectional area of steel upper web of steel girder (in^2)

A_{lw} = cross-sectional area of steel lower web of steel girder (in^2)

A_{bf} = cross-sectional area of steel bottom flange of steel girder (in^2)

E_c = modulus of concrete (ksi)

E_s = modulus of elasticity of steel (ksi)

F_c^+ = force in concrete slab due to positive girder bending (kips)

F_c^- = force in concrete slab due to negative girder bending (kips)

F_{tf} = force in the top flange of the steel girder (kips)

F_{uw} = force in the upper web of the steel girder (kips)

F_{lw} = force in the lower web of the steel girder (kips)

F_{bf} = force in the bottom flange of the steel girder (kips)

The top and bottom flange widths of the steel section are adjusted slightly to taken into account the steel in the flange-web junction not included when assuming rectangular cross section components. The modulus of concrete was calculated for Specimens 2 and 3 as 3994 ksi and 3796 ksi, respectively. These values were determined by using a modulus equation defined as $E_c = 57{,}000\sqrt{f_c'}$, where f_c' is equal to the compressive strength of the concrete slab measured in units of psi (ACI, 1995).

The modulus of elasticity of steel, E_s, is equal to 29,000 ksi and is held constant throughout the load history for these calculations. These calculations are thus valid only in the range where the materials are elastic. In addition, because the specimens are loaded cyclically, note that the yield strengths in tension and compression of the steel sections may experience a shift due to the Bauschinger effect (Gere and Timoshenko, 1990).

The equation that expresses the compressive force in the concrete slab (Eq. G.11) neglects the contribution of steel reinforcement to the girder stiffness during positive girder bending. The equation expressing tensile forces in the concrete slab (Eq. G.12) ignores the participation of concrete; therefore, only the steel reinforcement area is assumed to provide stiffness during negative bending of the girder. Eq. G.11 and G.12 are ignored when analyzing Specimen 1, since no concrete slab is present.

The effective area of the concrete slab, A_c, is the product of the effective concrete width and thickness, b_e and a, respectively (see Figure G.3). The value a is determined by C, which is the compressive force in the concrete slab (AISC, 1993):

$$a = \frac{C}{0.85 f_c' b_e} \tag{G.17}$$

where b_e = effective width of the concrete slab (in.)

f_c' = compressive strength of the concrete slab (ksi)

C = compressive force in the concrete slab (kips)

This force is governed by one of the three cases: the concrete crushing, the steel girder yielding, or the shear connectors failing. For Specimens 2 and 3, all four composite girders were designed as partially composite; therefore, C is governed by the case of the shear studs yielding (see Appendix A). The term C is equal to 583.2 kips and 371.1 kips for the composite girders of Specimens 2 and 3, respectively. Also, a is equal to 2.33" and 1.64" for the composite girders of Specimens 2 and 3, respectively. Note that if the girders were fully composite, a would be equal to the average concrete thickness of 4.0."

Next, the moment arms for each force component are computed in units of inches. Each moment arm is equal to the distance between the centroid of its stress distribution and the neutral axis location for a given load stage. These distances are shown in Figure G.5 and Eqs. G.18 through G.22:

$$y_c = d + t_s - y_{NA} - a\left(\frac{3y_{NA} - 2a}{6y_{NA} - 3a}\right) \tag{G.18}$$

$$y_{tf} = d - y_{NA} - t_{tf}\left(\frac{3y_{NA} - 2t_{tf}}{6y_{NA} - 3t_{tf}}\right) \tag{G.19}$$

$$y_{tw} = \frac{2}{3}\left(d - y_{NA} - t_{tf}\right) \tag{G.20}$$

$$y_{lw} = \frac{2}{3}\left(y_{NA} - t_{bf}\right) \tag{G.21}$$

$$y_{bf} = y_{NA} - t_{bf}\left(\frac{3y_{NA} - 2t_{bf}}{6y_{NA} - 3t_{bf}}\right) \tag{G.22}$$

The last parenthetical terms in Equations G.18, G.19, and G.22 represent the centroid for a trapezoidal stress distribution in terms of the height of the stress block component and the neutral axis.

The calculated girder moments are computed (in kip-inches) about the neutral axis using the force components and their corresponding moment arms. Two equations are used to compute the calculated girder moments during positive and negative bending of the girders of all the specimens:

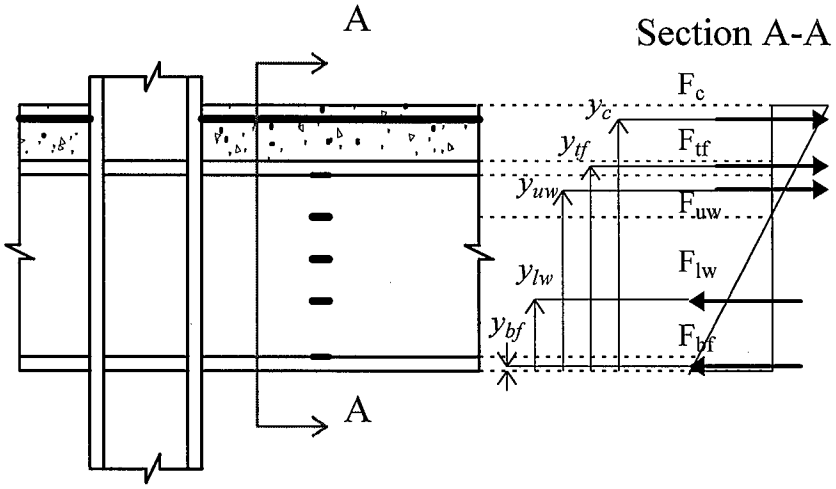

Figure G.5: Centroids of Force Components Along the Girder Cross Section

$$M^{+}_{calc} = F^{+}_{c} y_c + F_{tf} y_{tf} + F_{uw} y_{uw} + F_{lw} y_{lw} + F_{bf} y_{bf} \tag{G.23}$$

$$M^{-}_{calc} = F^{-}_{c} y_c + F_{tf} y_{tf} + F_{uw} y_{uw} + F_{lw} y_{lw} + F_{bf} y_{bf} \tag{G.24}$$

The only difference between the two equations is the concrete slab force component. Since the girders of Specimen 1 are non-composite, its concrete slab force component is zero.

Due to girder composite slip, inaccurate values of the concrete modulus, E_c, or a nonlinear strain distribution in the girder cross section, it is possible that the previous girder moment calculations do not accurately represent the force transferred into the

concrete slab. In fact, Equations G.23 and G.24 do not necessarily comply with force equilibrium across the cross section (i.e., the summation of the tensile forces do not equal the summation of the compressive forces).

In order to decouple these effects from the girder moment, an expression that satisfies force equilibrium is defined that uses the calculated steel girder forces (still assuming a linear strain distribution and elastic behavior of the steel section) to determine the force in the concrete slab during girder positive and negative bending. For a given girder moment, the sum of the compression forces must be equal to the sum of the tension forces in the composite girder cross section at a location 13.5" from the column flange. The force in the concrete slab may thus be expressed (in kips) in terms of the steel girder forces for both positive and negative bending of the composite girder:

$$F_{equil} = F_{bf} + F_{lw} - F_{uw} - F_{tf} \tag{G.25}$$

Using Eq. G.25 to establish the force in the concrete slab, a girder moment equation can be calculated that satisfies force equilibrium at a given applied girder load:

$$M_{equil} = F_{equil} y_c + F_{tf} y_{tf} + F_{uw} y_{uw} + F_{lw} y_{lw} + F_{bf} y_{bf} \tag{G.26}$$

Note that the only difference between Eq. 26 and Eqs. 23 and 24 is the force component that is determined in the concrete slab.

The actual girder moment is equal to the product of the applied load (in kips) at the girder tip , P, and the length measured from the girder tip to the location at which strains were measured along the girder cross section:

$$M_{act} = P(L_b - L_a) \tag{G.27}$$

For each girder, the applied load is equal to the sum of the loads applied by the two actuators.

Finally, a strain in the concrete slab that satisfies equilibrium, or equilibrium concrete strain, may be determined to compare with the actual strain in the concrete slab. The equilibrium concrete strain is calculated using the concrete slab force component that satisfies equilibrium:

$$\varepsilon^{+}_{equil} = \frac{F_{equil}}{E_c A_c} \tag{G.28}$$

$$\varepsilon^{-}_{equil} = \frac{F_{equil}}{E_s A_s} \tag{G.29}$$

Equation G.28 expresses the compressive strains in the concrete slab and neglects the contribution of steel reinforcement to the girder stiffness during positive girder bending. Equation G.29 defines the tensile strains in the concrete slab, and assumes that only the steel reinforcement provides resistance during negative bending of the girder.

G.2 Comparison of Results

A comparative study has been performed with the actual, calculated, and equilibrium girder moments and strains. The purpose of this investigation is not only to validate the strains measured along the steel cross section (see Chapter 4), but also to verify that the composite girders exhibited partially composite behavior as intended. Also, the presence of composite slip and nonlinear strain behavior along the steel cross section are reported and the accuracy of the estimated concrete modulus is studied. These three conditions are the primary contributors to the differences in magnitudes between the actual, calculated, and the equilibrium girder moments and strains. The effects of each condition can be isolated by comparing girder moment and strain values

that incorporate different combinations of these conditions in their measurement or calculation (Table G.2). Note that the actual and calculated strains are not dependent upon the concrete modulus.

It is important to note that other conditions exist that may contribute to the differences in strain magnitudes between these girder moments and strains. Such conditions include crushing of the concrete slab near the column-concrete slab interface, localized strain behavior within the concrete slab, and a changing value of E_s due to the Bauschinger Effect and steel yielding. These secondary conditions may be assumed minimal during the lower drift cycles and, therefore, are not directly investigated in this section.

Table G.2: Conditions Included in the Measurement and Calculation of the Girder Moments and Strains

Conditions	Actual Moment	Calculated Moment	Equilibrium Moment	Actual Strain	Calculated Strain	Equilibrium Strain
Composite Slip	slip	no slip	slip	slip	no slip	slip
Concrete Modulus	actual	calculated	actual	N/A	N/A	calculated
Steel Strain Distribution	nonlinear	linear	linear	nonlinear	linear	linear

Figures G.6 to G.37 illustrate the results from this study for the drift levels up through 0.75% for all three tests. Figures G.6 to G.9 compare the two girder moment cases discussed for the East and West girder of Specimen 1, while Figures G.10 to G.17 compare the three girder moment cases discussed for the East and West girders of Specimens 2 and 3. Also strain profiles of the cross sections of all six steel girders at a distance of 13.5" from the column face are shown in Figures G.18 to G.20. The calculated and actual girder moments and strains in the East and West girder of Specimens 2 and 3 are shown in Figures G.21 to G.31. Finally, Figures G.32 to G.37

Specimens 2 and 3 are shown in Figures G.21 to G.31. Finally, Figures G.32 to G.37 illustrate the change in the neutral axis location along the girder cross section at a distance of 13.5" from the column face for all six girders during their entire load histories.

G.2.1 Effects of a Nonlinear Strain Distribution

A nonlinear strain distribution in the steel cross section may be due to the effects of longitudinal distortion which varies through the depth of the cross section and is, most likely, uniform along its width. However, during lower drift cycles, these effects should be minimal at the girder cross section located 13.5" from the column face. The effects of torsion and warping of the girder sections may also contribute to a nonlinear strain distribution in the steel girder, although these contributions may be assumed to be negligible.

The strain distribution of the East and West girders of Specimen 1 (at a distance of 13.5" from the column face) is observed to remain relatively linear up to 0.75% drift cycles when comparing the actual and calculated girder moments (Figures G.6 to G.9). This is also seen when studying the strain distribution of the East and West girders at 13.5" from the column face at peak loads up to 0.75% (Figures G.18 and G.19). Some error is observed between the calculated and the actual girder moments for the East and West girders subjected to negative bending at the 0.25% drift cycles; however, these errors are minimal.

The equilibrium girder moment for Specimens 2 and 3 implicitly includes the effects of composite slip. Also, it is based on assuming a linear strain distribution within the steel cross-section and, implicitly, on the actual concrete modulus (see Table G.2). The actual girder moment includes the effects of composite slip and is based on the actual concrete modulus and strain distribution. Therefore, for low drift levels in which little yielding has occurred at 13.5" from the column face, the differences between the actual and equilibrium girder moments of Specimens 2 and 3 may be attributed

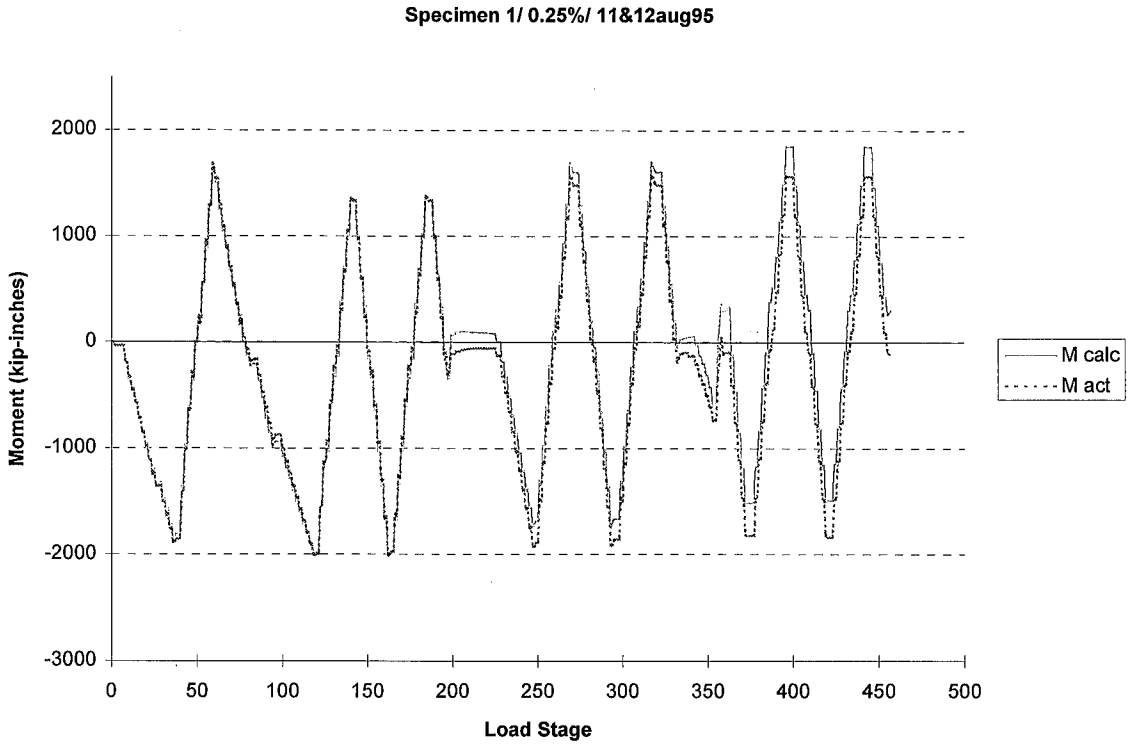

Figure G.6: Actual vs. Calculated Girder Moment (East Girder of Specimen 1)

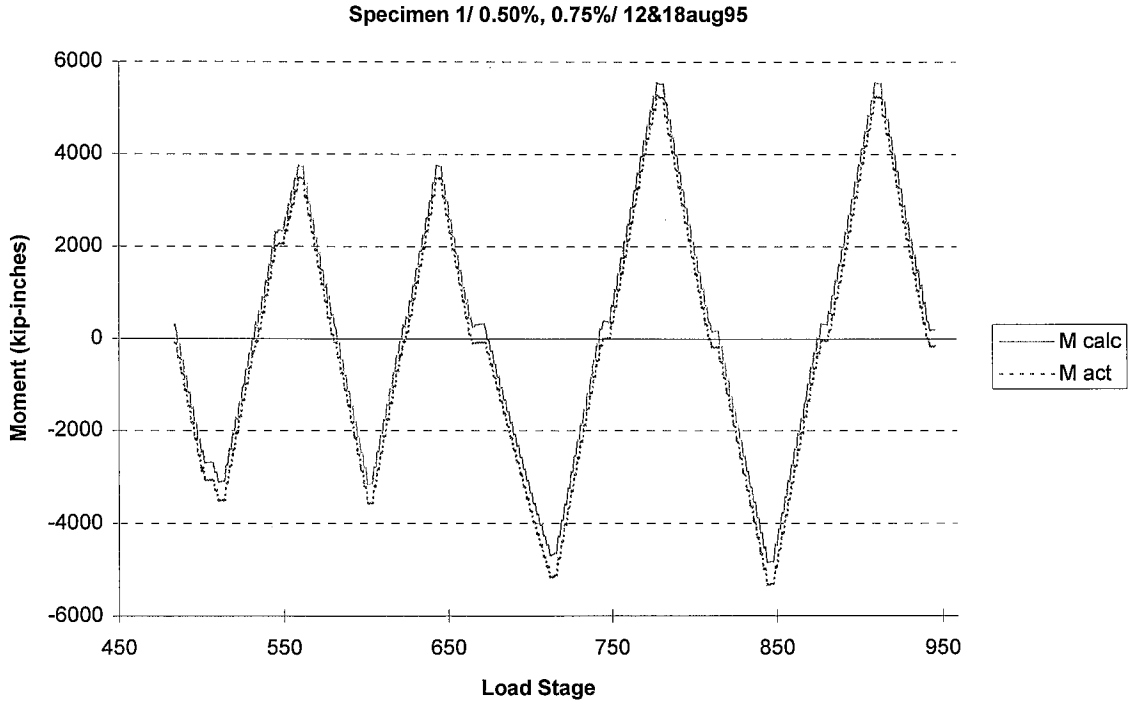

Figure G.7: Actual vs. Calculated Girder Moment (East Girder of Specimen 1)

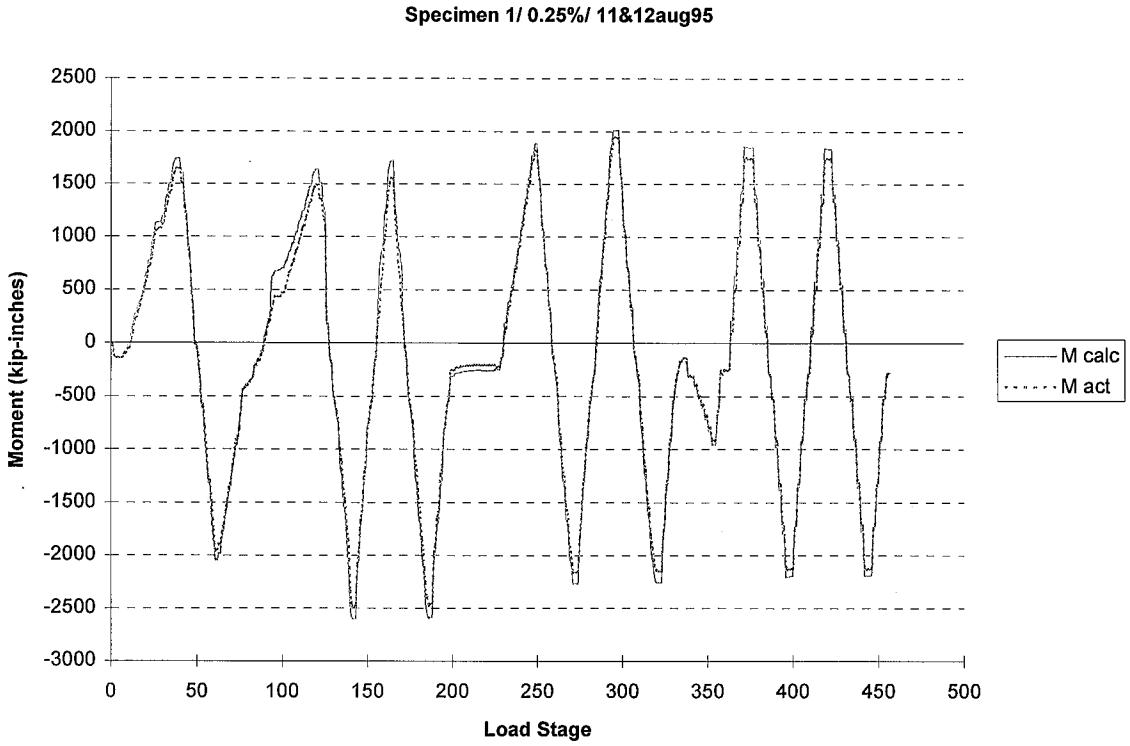

Figure G.8: Actual vs. Calculated Girder Moment (West Girder of Specimen 1)

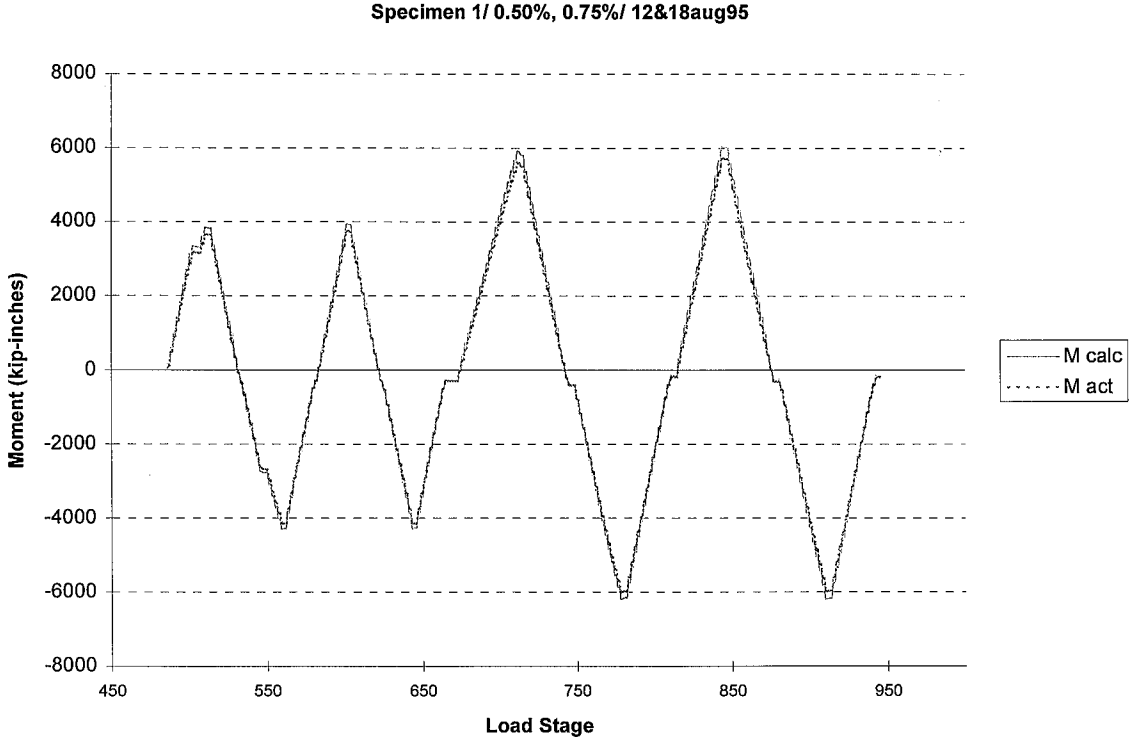

Figure G.9: Actual vs. Calculated Girder Moment (West Girder of Specimen 1)

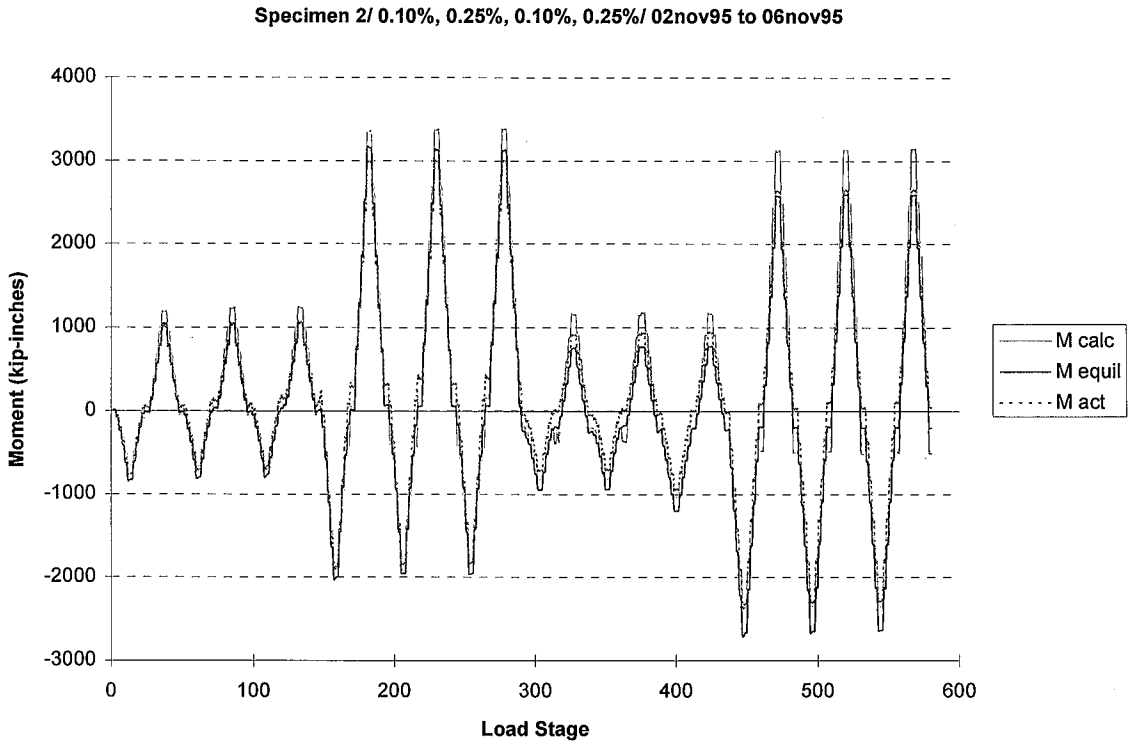

Figure G.10: Actual vs. Calculated Girder Moment (East Girder of Specimen 2)

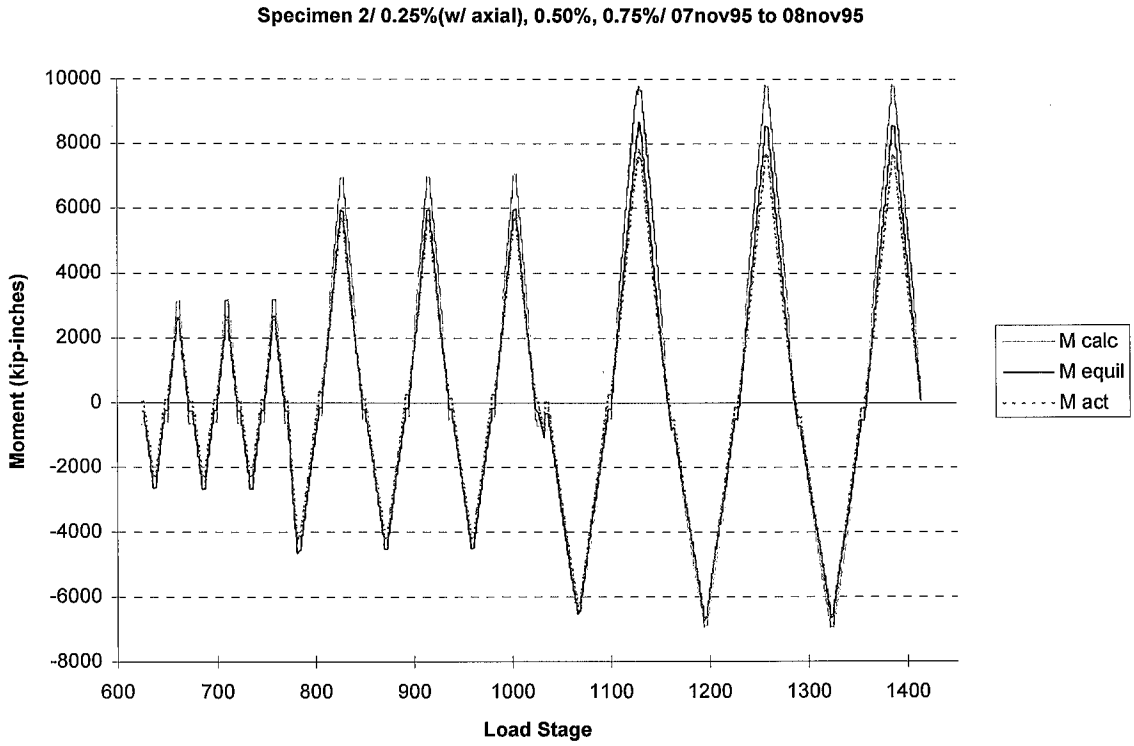

Figure G.11: Actual vs. Calculated Girder Moment (East Girder of Specimen 2)

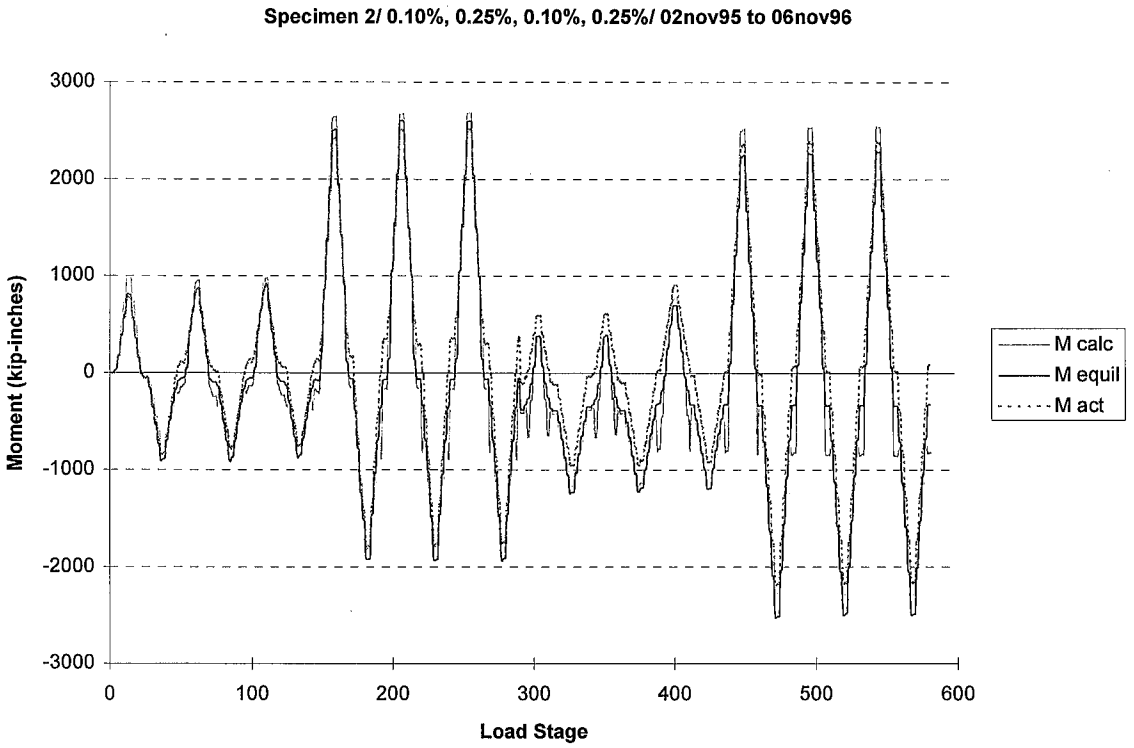

Figure G.12: Actual vs. Calculated Girder Moment (West Girder of Specimen 2)

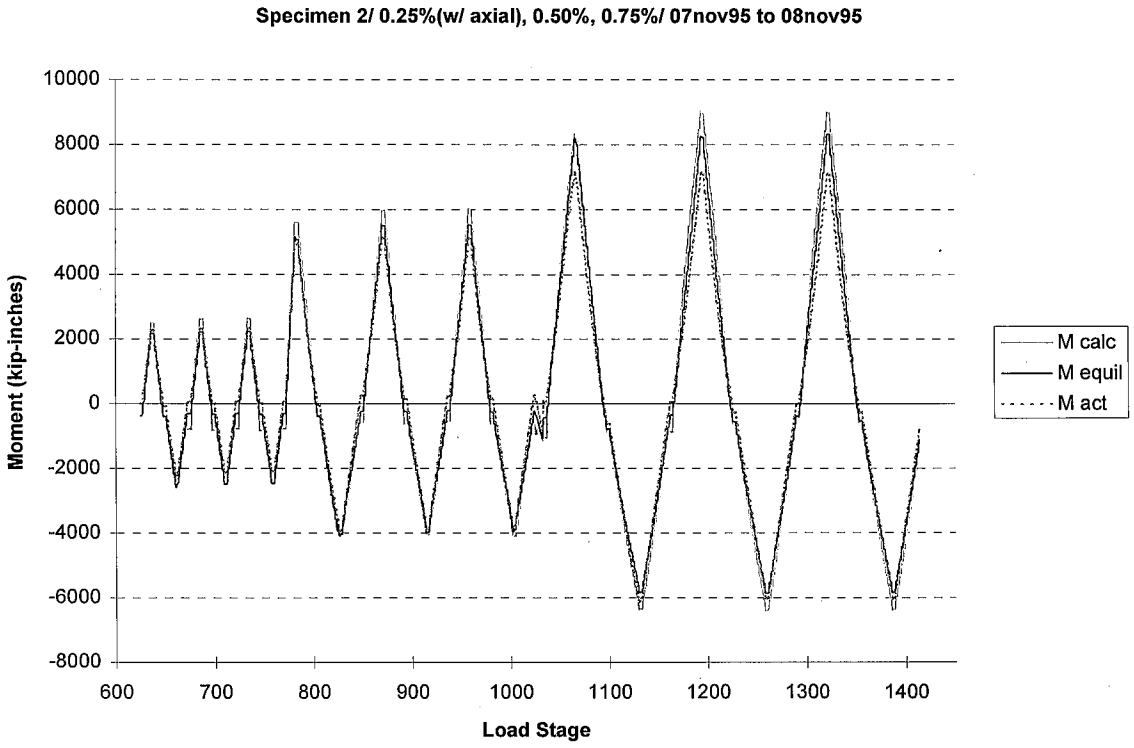

Figure G.13: Actual vs. Calculated Girder Moment (West Girder of Specimen 2)

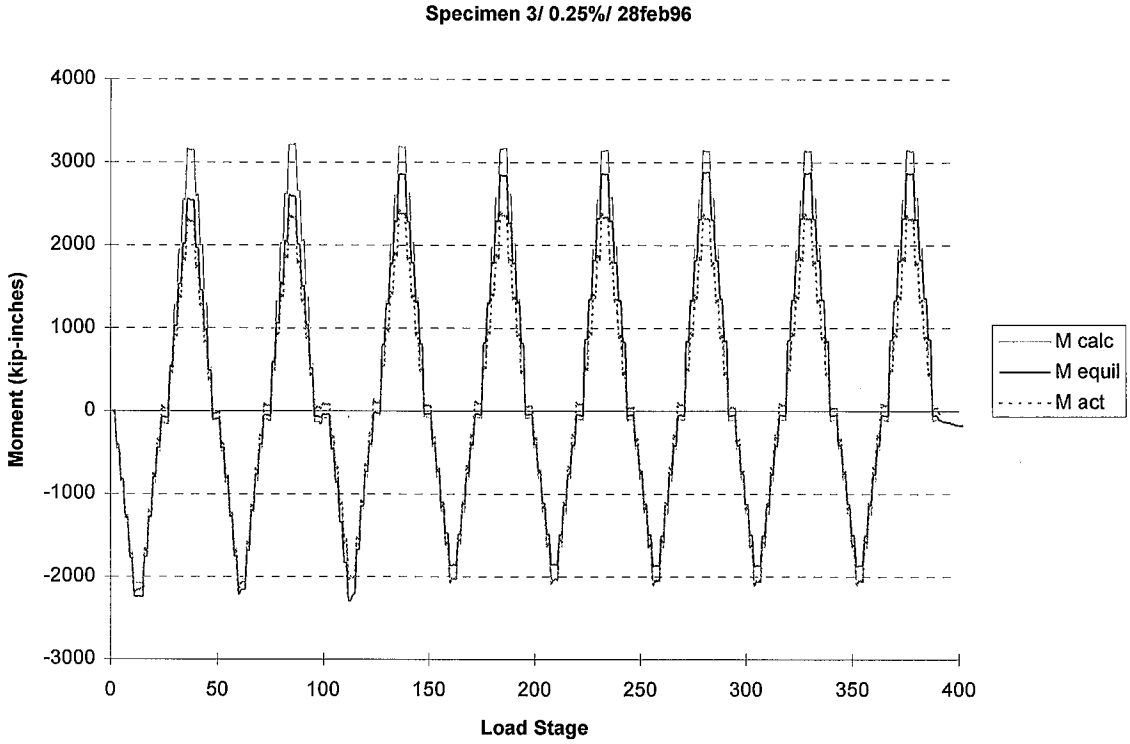

Figure G.14: Actual vs. Calculated Girder Moment (East Girder of Specimen 3)

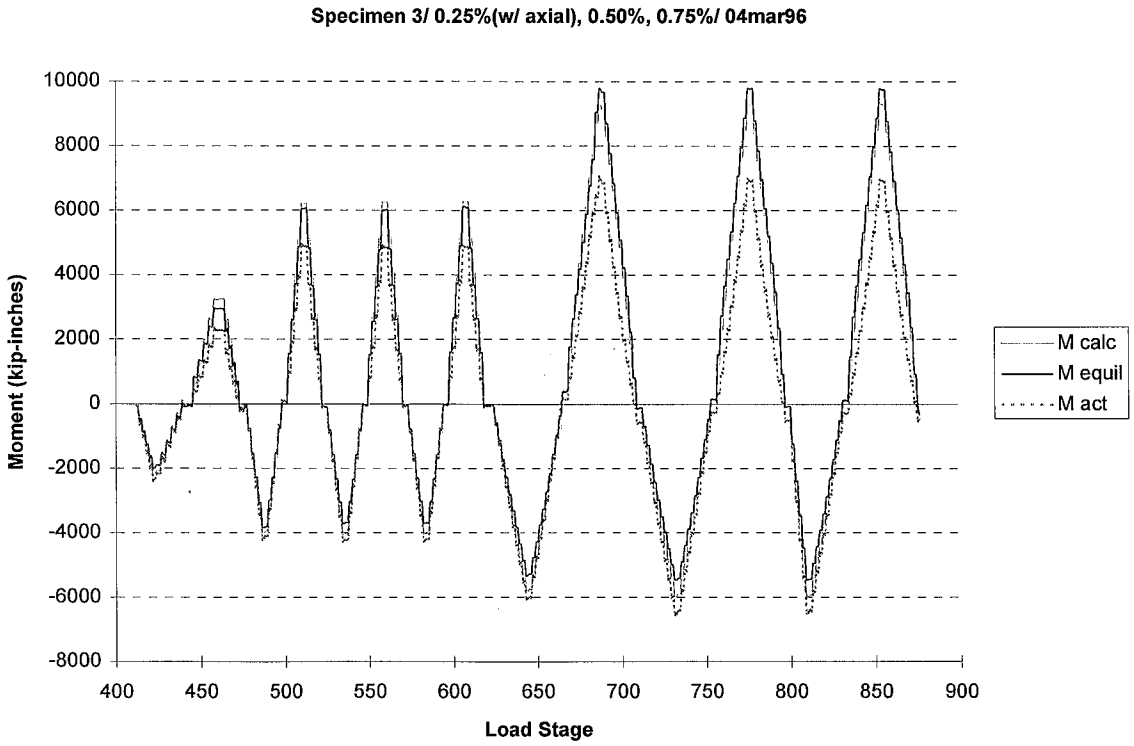

Figure G.15: Actual vs. Calculated Girder Moment (East Girder of Specimen 3)

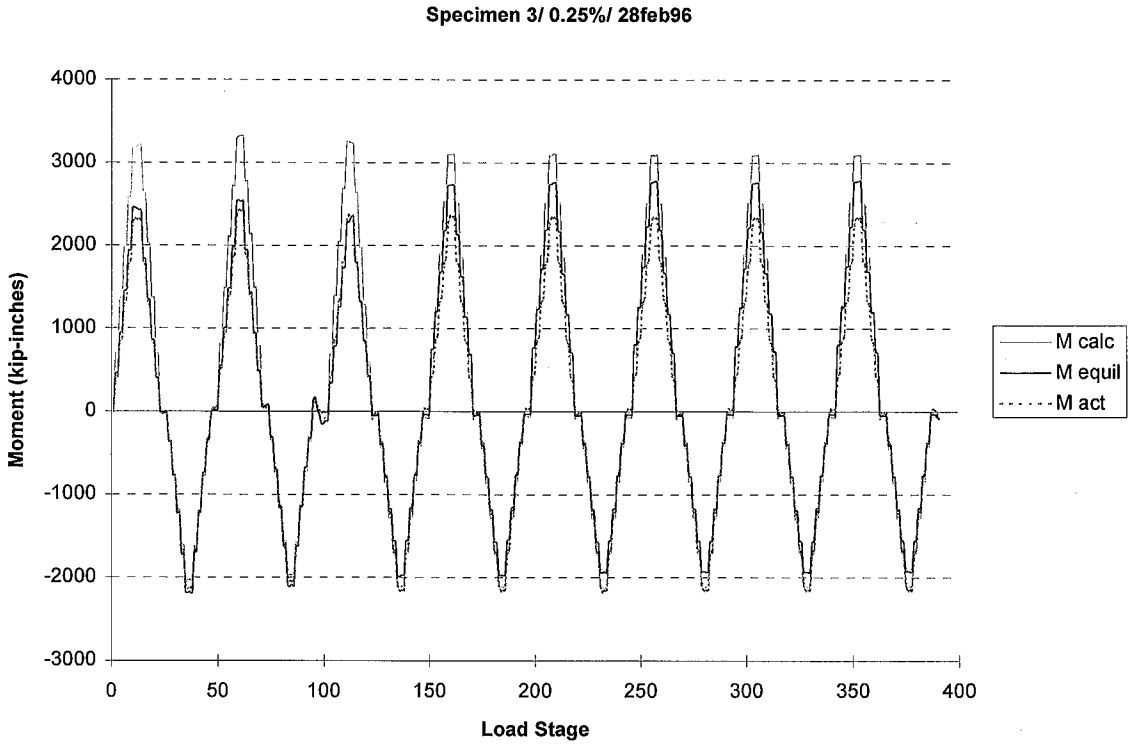

Figure G.16: Actual vs. Calculated Girder Moment (West Girder of Specimen 3)

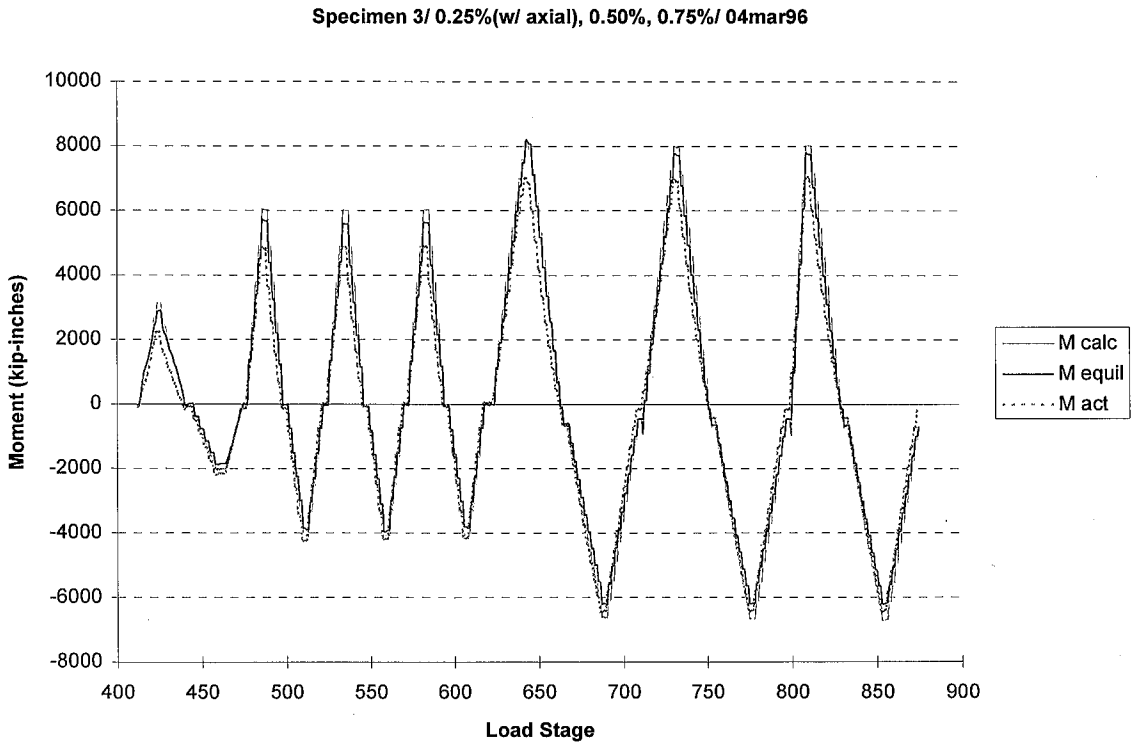

Figure G.17: Actual vs. Calculated Girder Moment (West Girder of Specimen 3)

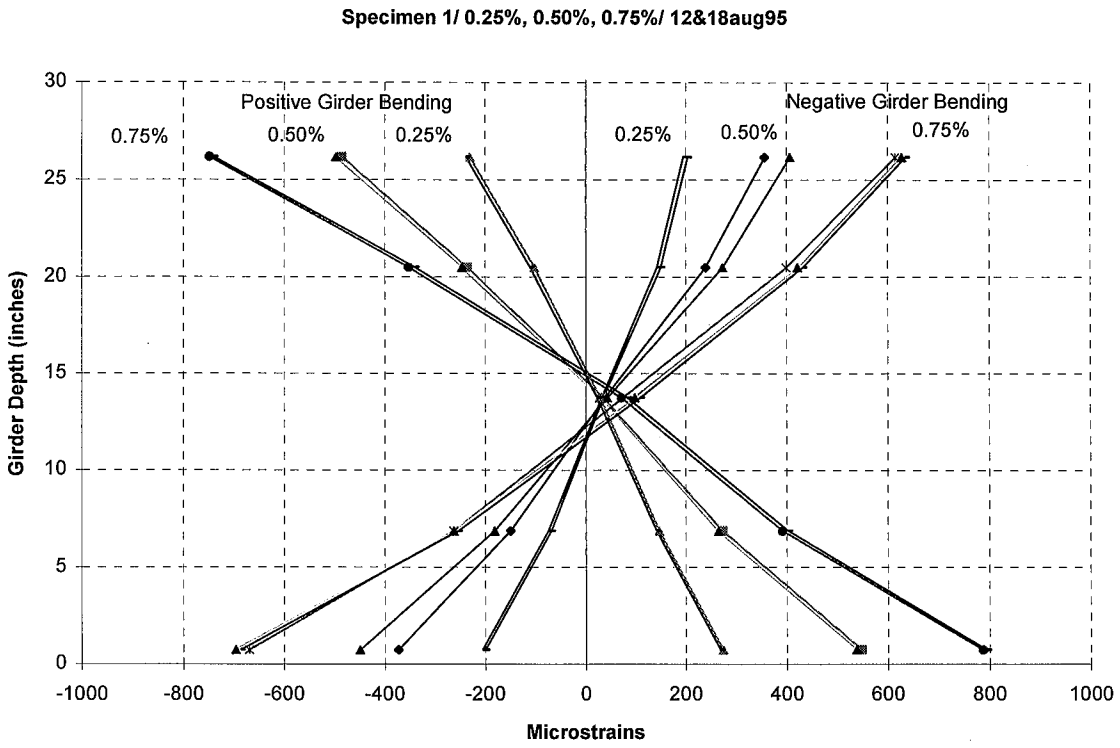

Figure G.18: Steel Girder Strain Distribution (East Girder of Specimen 1)

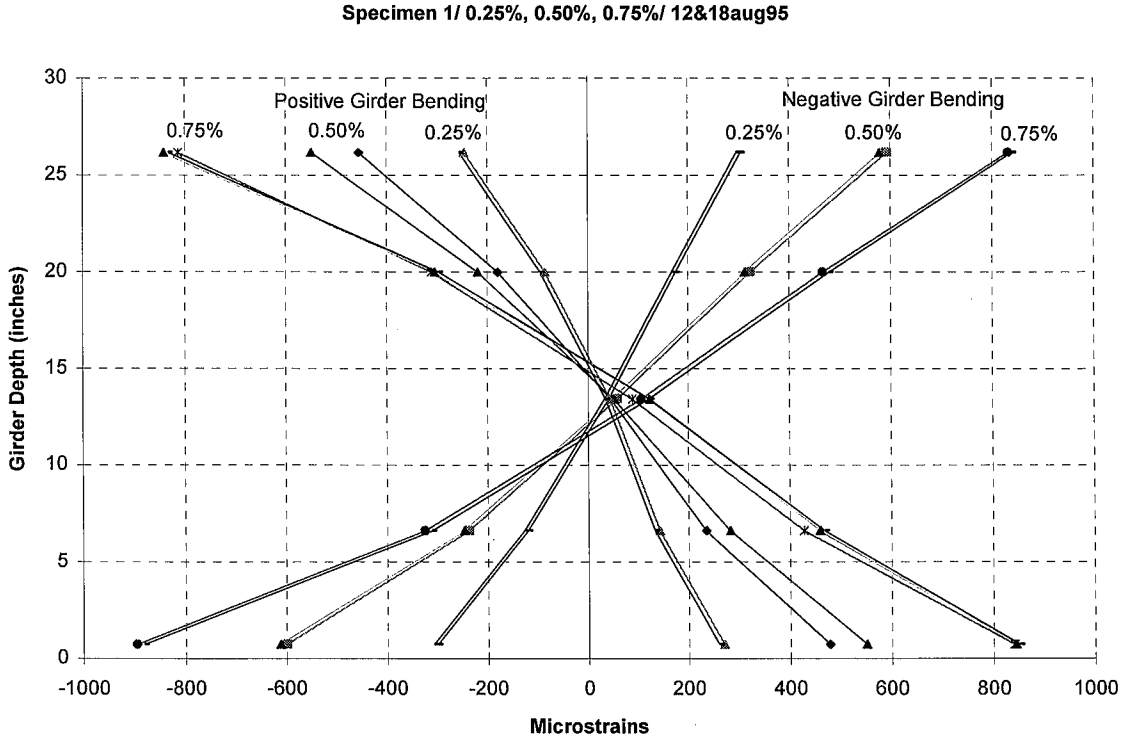

Figure G.19: Steel Girder Strain Distribution (West Girder of Specimen 1)

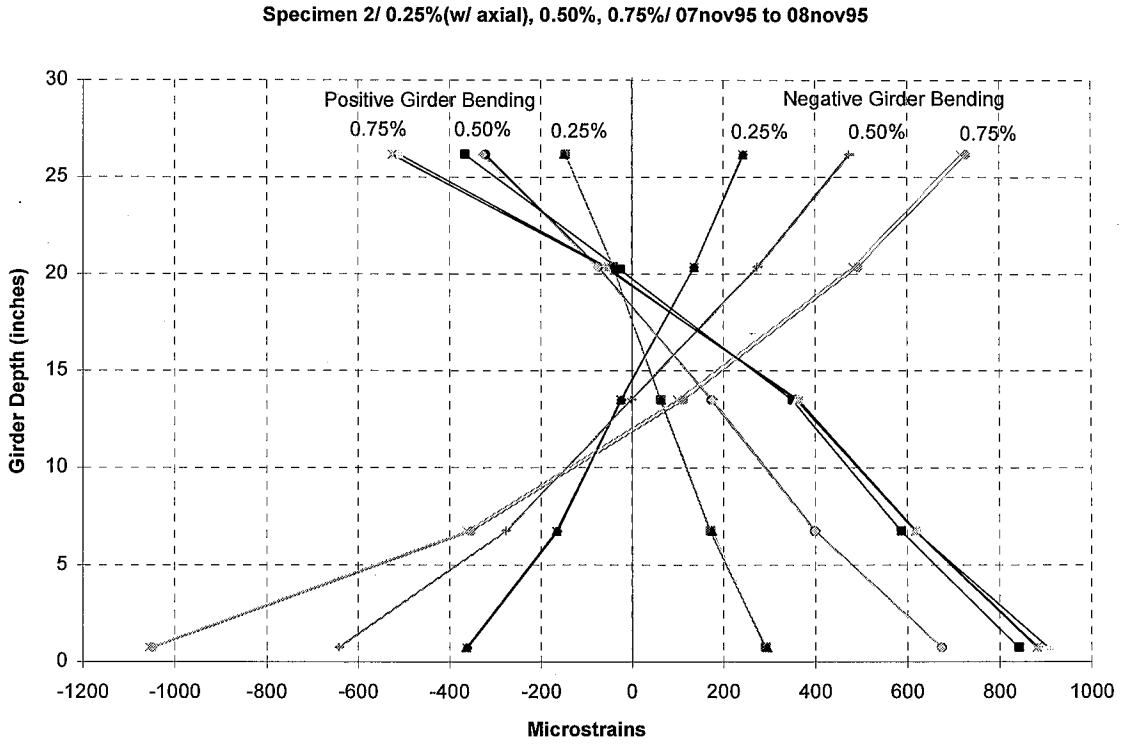

Figure G.20: Steel Girder Strain Distribution (East Girder of Specimen 2)

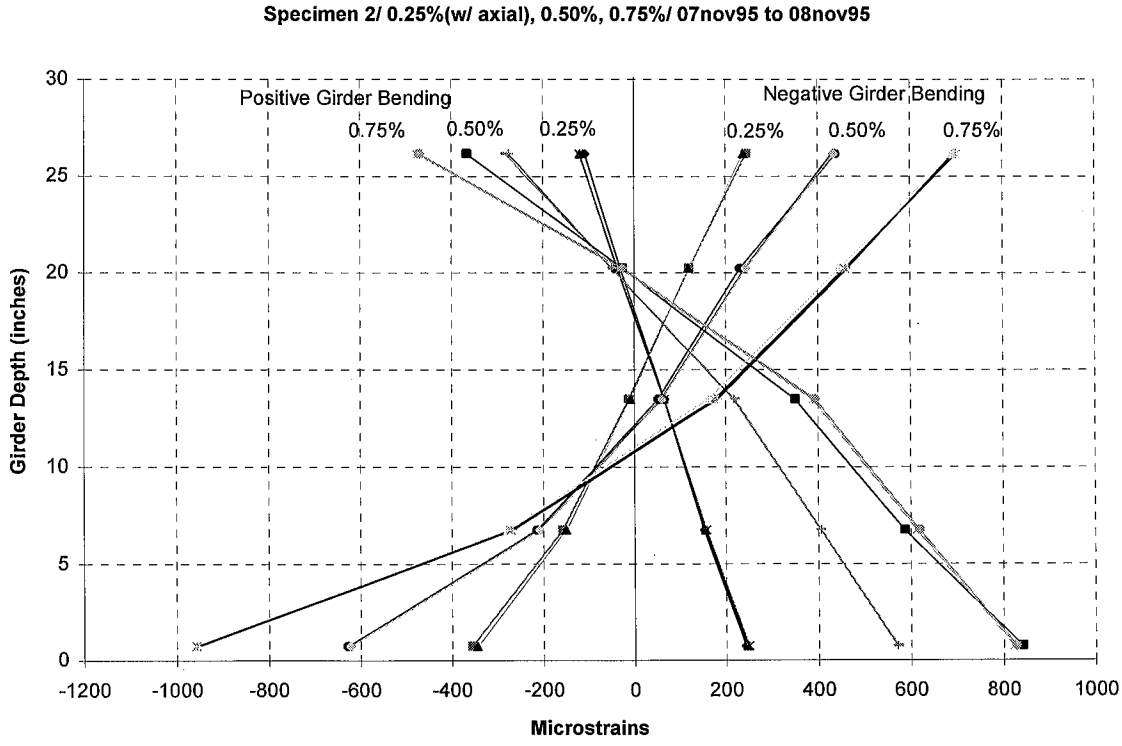

Figure G.21: Steel Girder Strain Distribution (West Girder of Specimen 2)

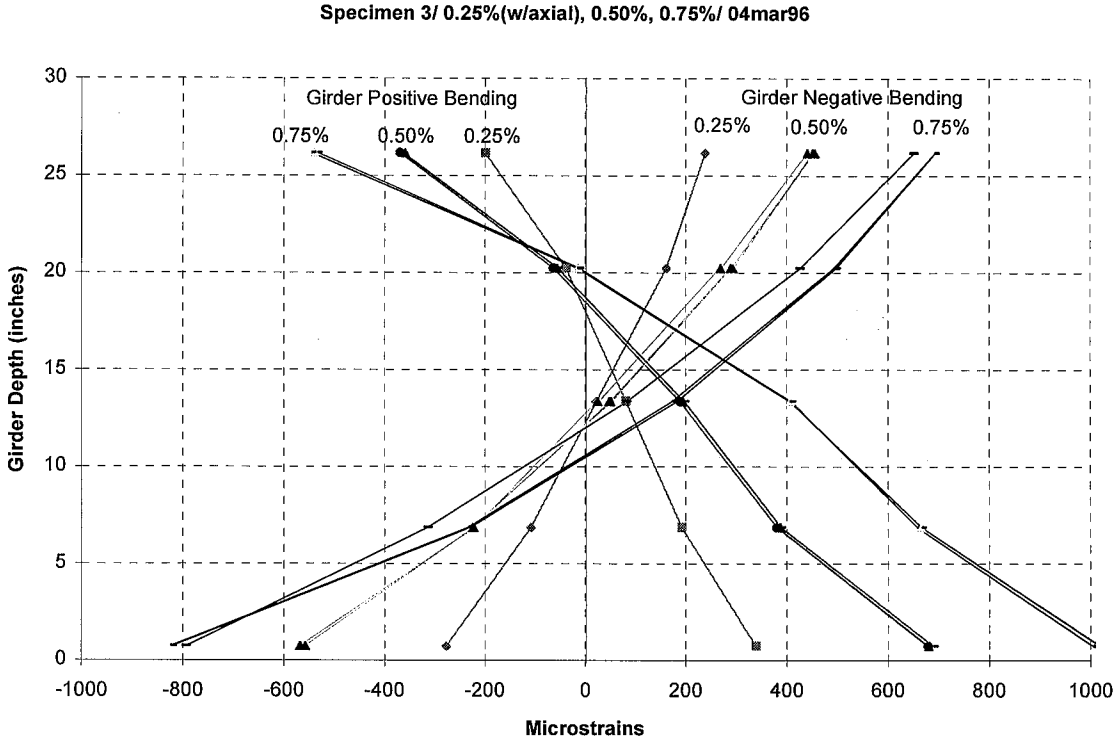

Figure G.22: Steel Girder Strain Distribution (East Girder of Specimen 3)

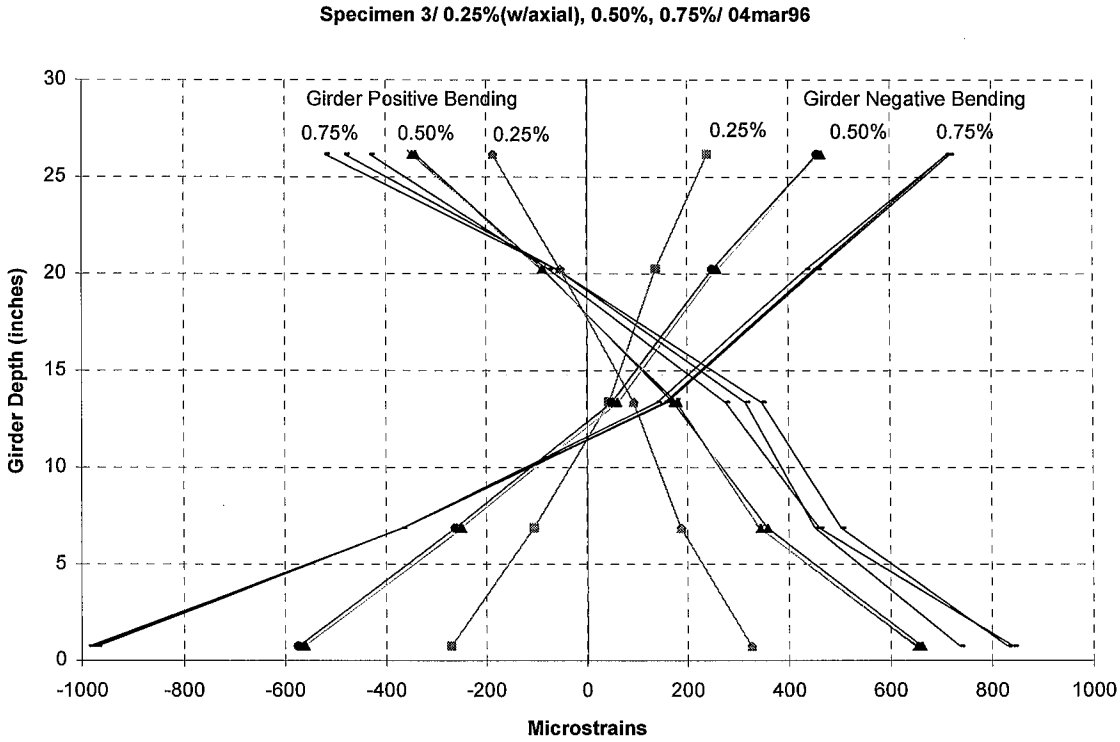

Figure G.23: Steel Girder Strain Distribution (West Girder of Specimen 3)

predominantly to the effects of a nonlinear strain distribution within the steel girder cross-section.

During the drift cycles up through 0.75% for Specimen 2, the equilibrium and actual girder moments demonstrate minimal differences when the East and West girders are subjected to negative bending (Figures G.10 to G.17). This may imply that distortion of the cross section was minimal at 13.5" from the column face during negative girder bending up through the 0.75% drift cycles. However, when directly observing the strain distribution of the East and West girders at 13.5" from the column face, a nonlinear strain distribution is clearly evident even at the 0.25% drift levels in negative bending, but especially in the 0.75% drift levels (Figures G.20 and G.21).

During the drift cycles up through 0.75% for Specimen 3, the equilibrium and actual girder moments show a strong correlation when the East and West girders are subjected to negative bending (Figures G.14 to G.17). However, similarly to girders of Specimen 2, the strain distribution of the East and West girders at 13.5" from the column face exhibit evidence of a nonlinear strain distribution starting mainly at the 0.50% drift cycles (Figures G.2 to G.23). When the East and West girders of Specimen 3 are subjected to positive girder bending, the equilibrium moment is observed to be slightly greater in magnitude than the actual girder moment starting at 0.25% drift cycles. This difference begins to increase at the 0.75% drift cycles, especially for the East girder. Also, the measured strain distributions within the steel cross section are relatively linear up to 0.50% drift cycles when subjected to positive bending, but they become increasingly nonlinear thereafter. Further discussion of the nonlinear strain distribution along the steel cross section of the girders is also reported in Section 5.1.1.

G.2.2 Measured Concrete Strains

Before the effects of composite slip are investigated, it must be determined whether the strains measured by the reinforcing steel or the strains measured in the concrete accurately represent the strains in the concrete slab during positive girder

bending. For the East girder of Specimens 2 and 3, the magnitudes of strain were similar between those in the concrete slab rosette and those in the steel reinforcement of the concrete slab (Figures G.24 to G.31). However, for the West girders of Specimens 2 and 3, the strains measured by the concrete rosette were relatively larger and smaller, respectively, in magnitude than the strains measured by the reinforcing steel.

These differences may be attributed to several conditions. First, the strains in the concrete were measured at a distance of 4" from the column face, whereas the strains in the reinforcing steel were measured at 13.5" from the column face. Also, higher strains may have occurred within the concrete than in the reinforcing steel due to confinement of the concrete near the column. In addition, it is possible that the reinforcing steel and the concrete did not maintain composite action, resulting in slip of the reinforcing steel past the concrete. It is difficult to conclude which type of strain measurement accurately represents the actual strains in the concrete slab. However, since the concrete rosette strains represent actual strains in the concrete slab and not strains of the reinforcing steel, the strains measured by the concrete rosette are assumed to be a good estimate of the strains in the concrete slab, particularly in the lower drift levels.

G.2.3 Effects of Composite Slip

A nonlinear or discontinuous strain distribution between the steel girder and the concrete slab is caused by the break down of composite action between the steel girder and concrete slab. This phenomena is seen predominantly during positive girder bending, when the concrete slab is under compression. Because reverse cyclic loads are being applied to the girders, the friction and adhesion between the composite slab and the shear connectors are reduced at a higher rate than if the girders are loaded monotically. Also, since the shear connectors are designed to fail before the concrete slab crushes or the steel girder yields (i.e., partially composite design), the studs may be stressed into the inelastic range quite early in the load history. The effects of composite slip can be observed by

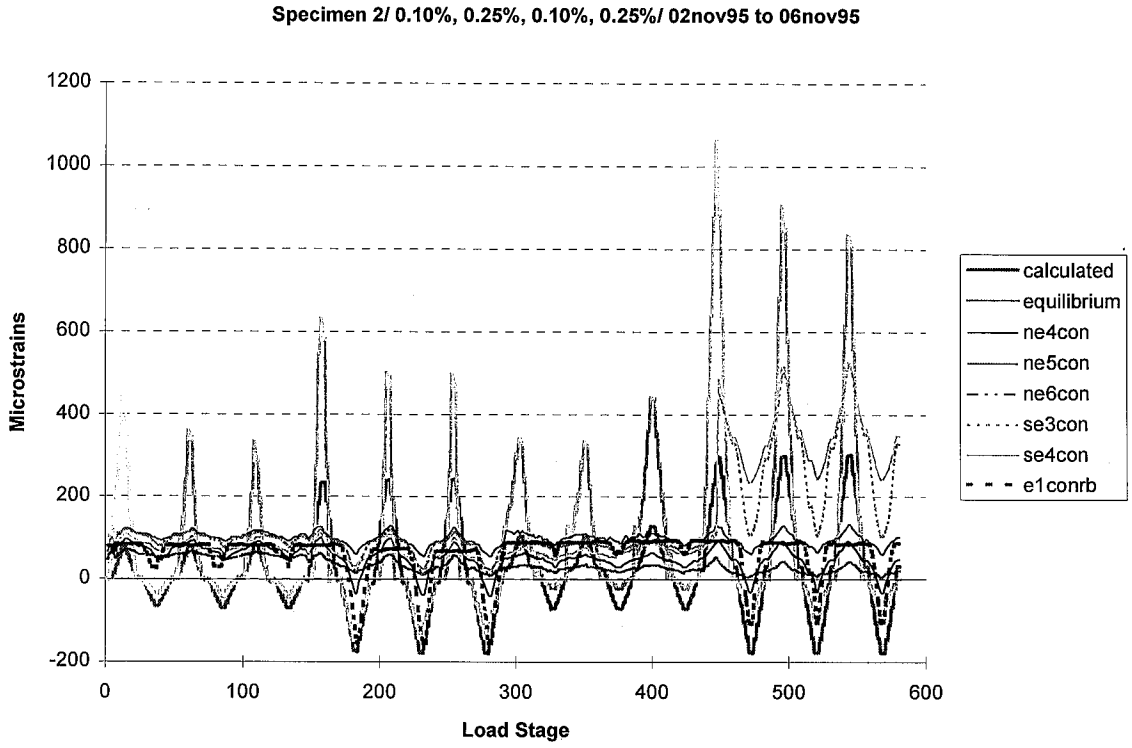

Figure G.24: Actual vs. Computed Concrete Strains (East Girder of Specimen 2)

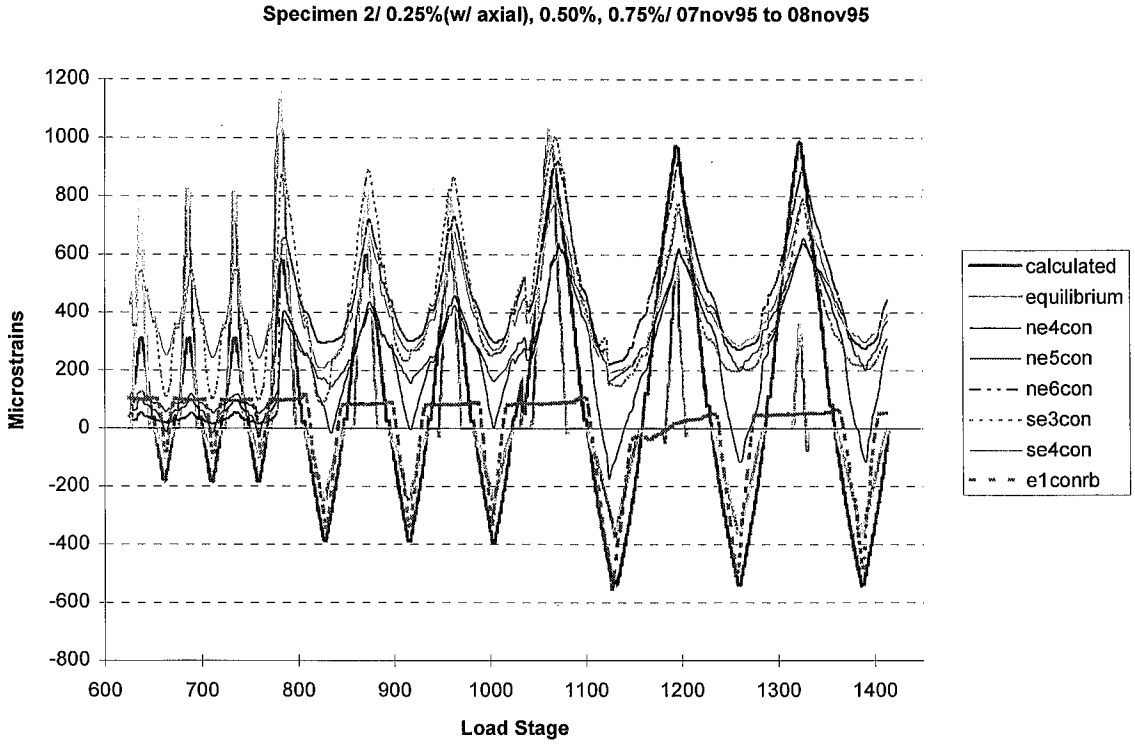

Figure G.25: Actual vs. Computed Concrete Strains (East Girder of Specimen 2)

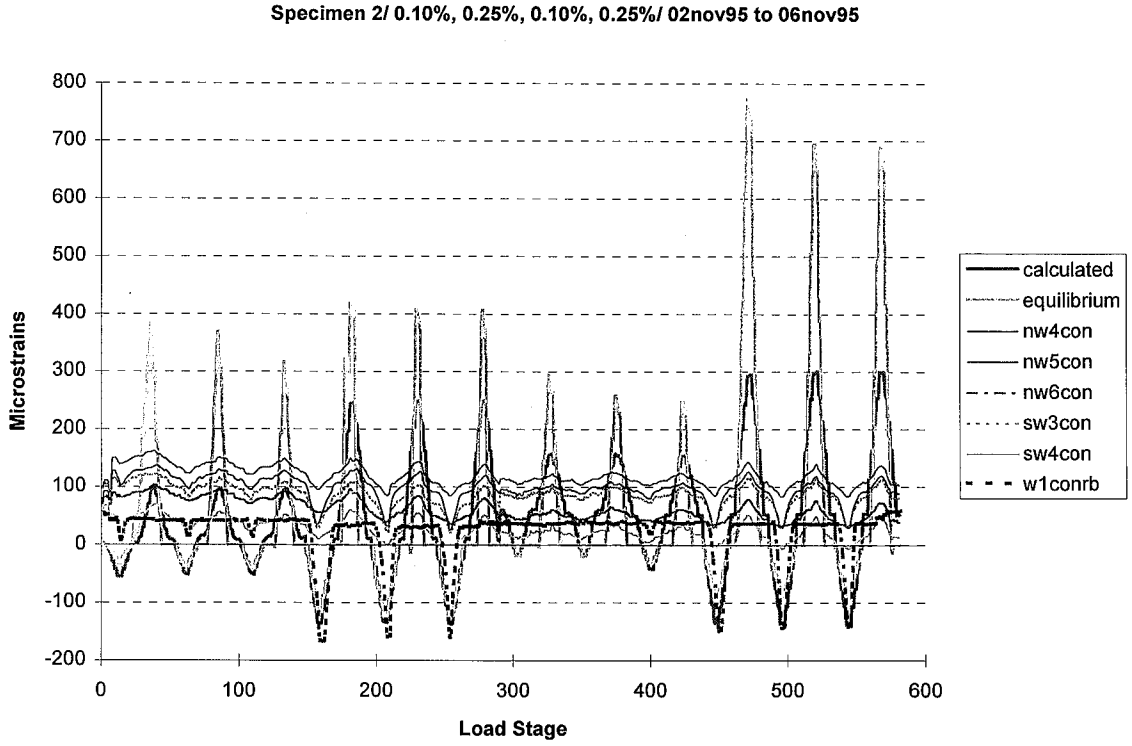

Figure G.26: Actual vs. Computed Concrete Strains (West Girder of Specimen 2)

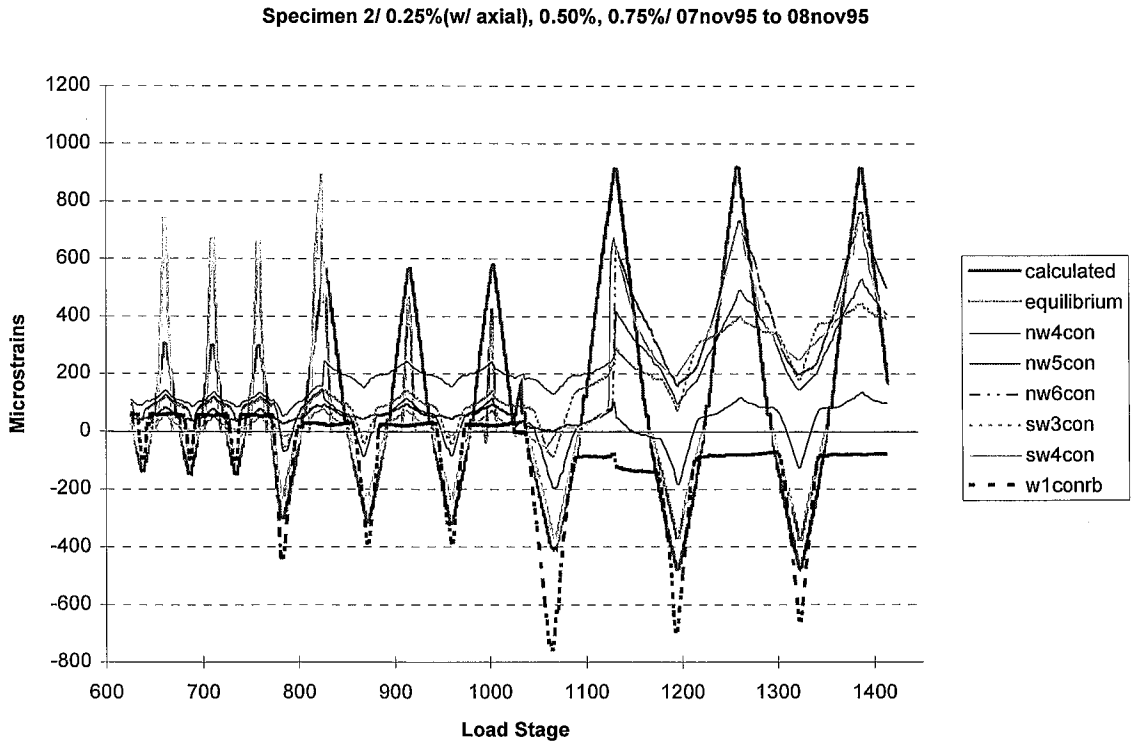

Figure G.27: Actual vs. Computed Concrete Strains (West Girder of Specimen 2)

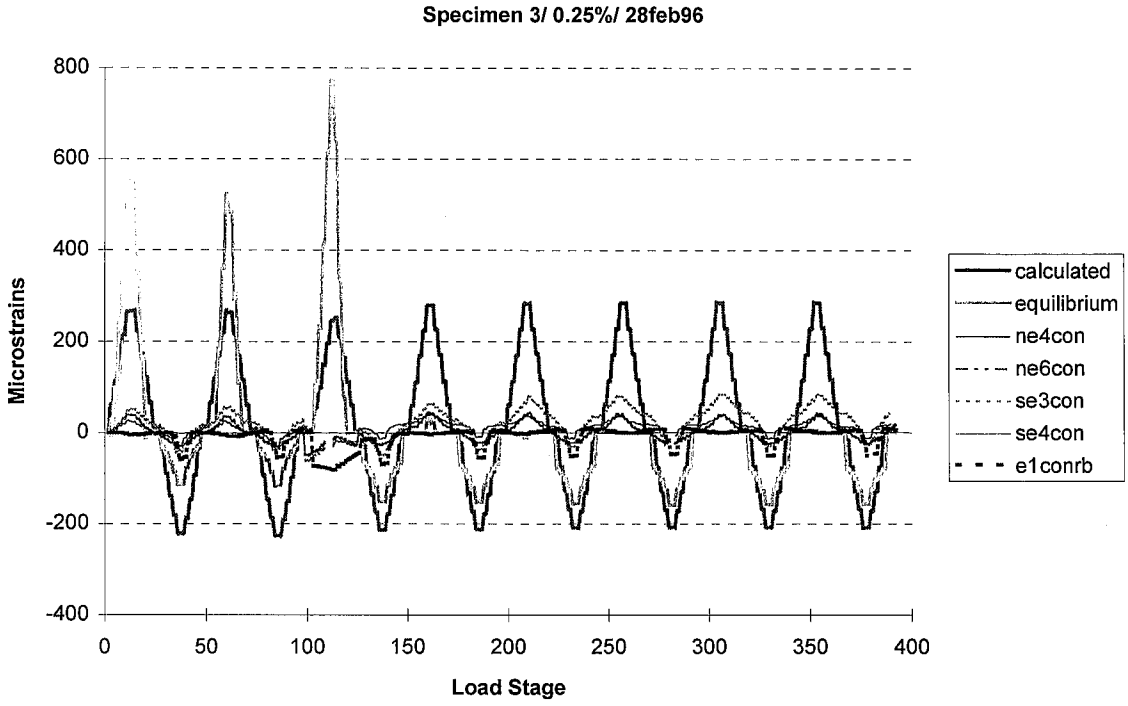

Figure G.28: Actual vs. Computed Concrete Strains (East Girder of Specimen 3)

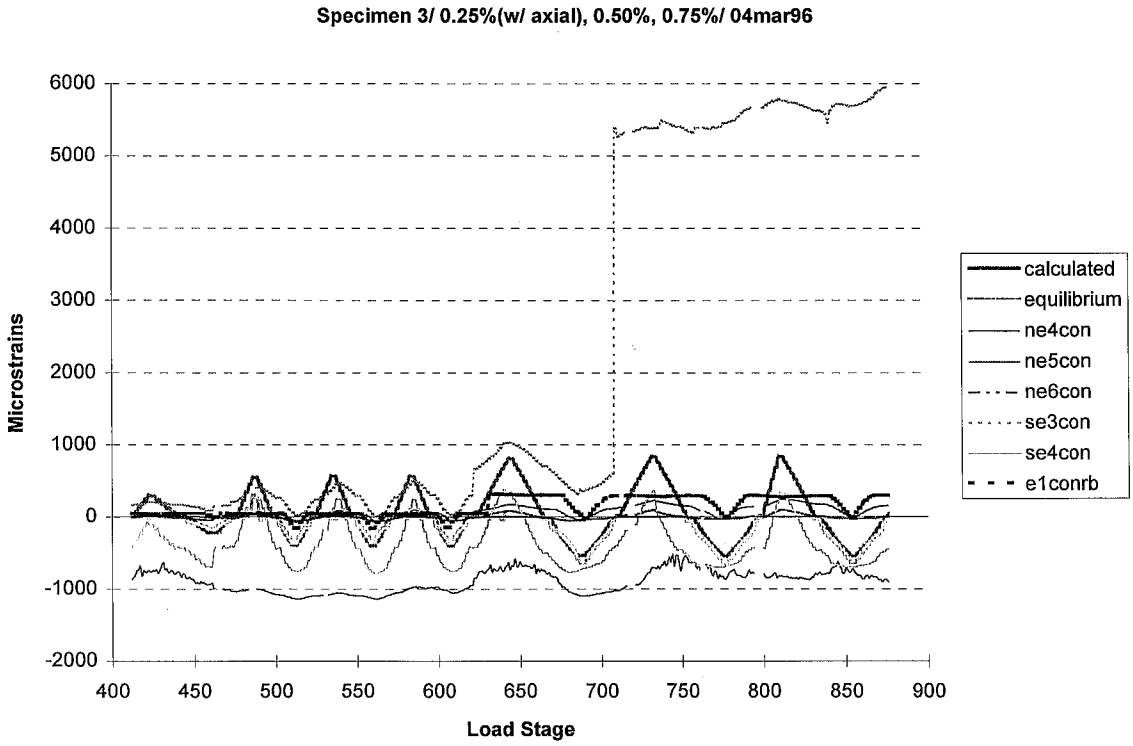

Figure G.29: Actual vs. Computed Concrete Strains (East Girder of Specimen 3)

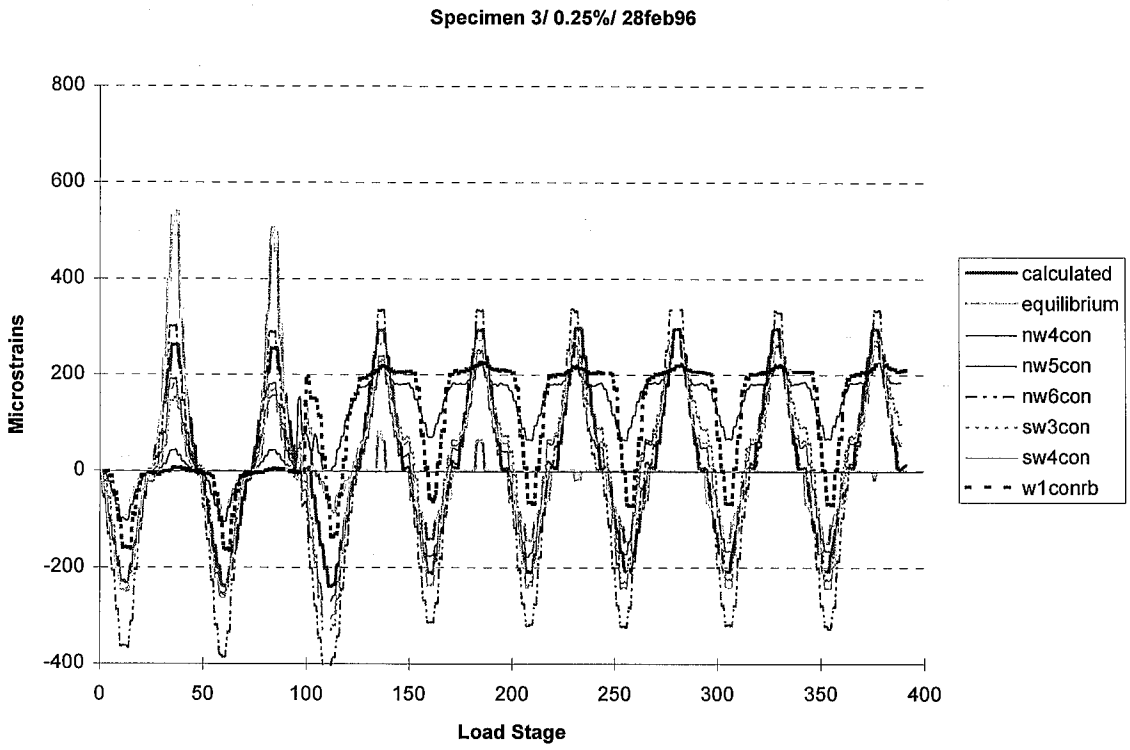

Figure G.30: Actual vs. Computed Concrete Strains (West Girder of Specimen 3)

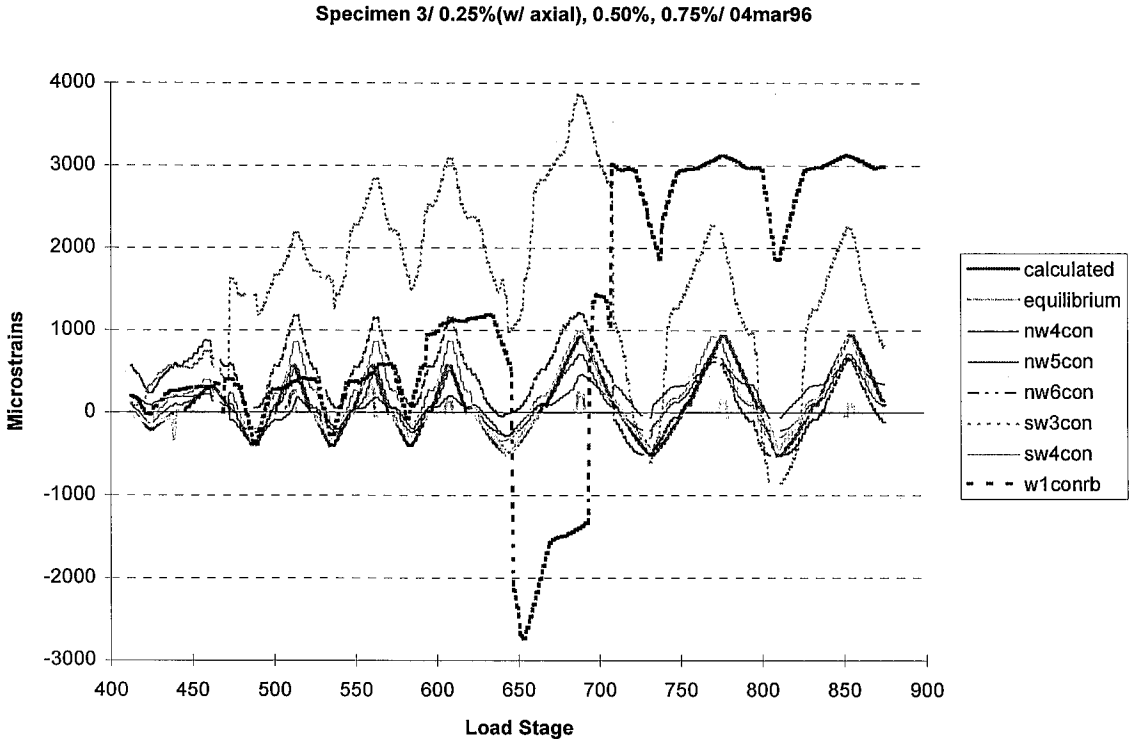

Figure G.31: Actual vs. Computed Concrete Strains (West Girder of Specimen 3)

comparing the actual strains measured in the concrete slab to the calculated strains in the concrete slab during girder positive bending.

The actual concrete strains are measured values; therefore, they are dependent upon the composite slip in the girder and nonlinear strain behavior within the steel section, but are not dependent upon the concrete modulus (see Table G.2). The calculated strains are based upon an assumption of no composite slip, and a linear strain distribution within the steel section, but are also not dependent upon the actual concrete modulus. The effects of a nonlinear strain distribution in the steel girders of Specimens 2 and 3 are observed to be minimal up to the 0.50% drift cycles during girder positive bending and determined to be negligible up to the 0.75% drift cycles during girder negative bending. Therefore, the differences in magnitude between the actual and calculated concrete strains in the early stages of loading (up to 0.50% drift cycles) may be largely attributed to composite slip within the composite girders.

When the East and West girders of Specimen 2 are subjected to positive bending at the 0.10% to 0.75% drift cycles, they show strains measured by the concrete rosette that are smaller than the calculated strains during the initial drift cycles of 0.10% and 0.25% (Figures G.24 to G.27). Differences in error during these small drift cycles may be largely attributed to measurement error. However, during the 0.50% and 0.75% drift cycles, the actual strains measured in the concrete rosette are still less than the calculated strains. This implies that, though not extensive, composite slip occurs in the East and West girders of Specimen 2 during load cycles up to 0.75%. Some of this error may be due to the effects of a nonlinear strain behavior within the steel girders, since larger calculated concrete strains would then be computed. It is interesting to note that the West girder is seen to experience more composite slip than the East girder up to the 0.75% drift cycles, since the error between the actual and calculated strains is slightly larger for the West girder than for the East girder.

The East girder of Specimen 3 demonstrates substantially smaller actual strains in the concrete slab (using both the reinforcing steel strains and the concrete rosette strains) than what is calculated during positive girder bending for drift cycles at 0.25% to 0.75%

(Figures G.28 and G.29). Even when taking into account the effects of a nonlinear strain behavior within the steel girders, substantial composite slip may have occurred in the East girder of Specimen 3 during the load cycles up to 0.75%. The West girder of Specimen 3 shows similar magnitudes between the actual and calculated concrete strains during positive girder bending (Figures G.30 and G.31). It is, therefore, concluded that composite action within the West girder of Specimen 3 is minimal to moderate up to the 0.75% drift cycles, just as was observed in the girders of Specimen 2.

G.2.4 Effects of Concrete Modulus Variability

The third condition that affects the girder moment and strain behavior of Specimens 2 and 3 is the modulus of the concrete (see Table G.2). This value was estimated for Specimens 2 and 3 using a modulus equation provided by ACI Section 8.5.1 (ACI, 1995). This reference states that the actual E_c can vary up to 20% from a typical estimated E_c. Furthermore, E_c is assumed constant throughout the load history and is estimated based on elasticity theory, which is applicable for only uncracked concrete. Since the girder concrete slabs experience microcracking during the lower drift cycles, especially because of reverse loading, the estimation of the stresses in the concrete slabs after these cycles becomes more complex.

The equilibrium concrete strains are dependent upon the calculated concrete modulus (see Eqs. G.33 and G.34) and an assumed linear strain distribution within the steel cross section during positive girder bending. The actual strains in the concrete are not dependent upon the concrete modulus but may be affected by a nonlinear strain distribution along the steel cross section of the girder. As previously mentioned, the effects of a nonlinear strain distribution in the steel girders of Specimens 2 and 3 are observed to be relatively small up to the 0.50% drift cycles during positive girder bending. Therefore, during positive girder bending at these lower drift cycles, the difference between the actual and equilibrium concrete strains may be attributed primarily to an assumed modulus of concrete.

When the girders of Specimen 2 are subjected to positive bending at the 0.10% to 0.50% drift cycles, the East girder shows actual strains measured by the concrete rosette similar to those in the equilibrium strains up through the 0.50% drift cycles (Figures G.24 to G.25). However, the West girder demonstrates concrete strains actually exceeding the equilibrium strains up to the 0.50% drift cycles (Figures G.26 and G.27). For the East girder of Specimen 3, the actual concrete strains measured by the concrete rosette are smaller than the equilibrium concrete strains for drift cycles at 0.25% to 0.50% (Figures G.28 and G.29). The West girder of Specimen 3 exhibits similar magnitudes between the actual and equilibrium concrete strains during positive girder bending (Figures G.30 and G.31).

These results indicate that it may be possible that the calculated E_c used in computing the equilibrium concrete strains in the West girder of Specimen 2 is slightly higher than the actual E_c during the initial loading cycles. For the East girder of Specimen 3, it is possible that the calculated E_c was underestimated. The significance of these observations is that they show that the calculation of E_c and, therefore, the effective moment of inertia, I_{eff}, is only an approximation and that the differences observed in other analysis (such as the girder tip deflection study which exhibited differences up to 15% to 20%, see Appendix E) may be largely due to this parameter.

G.2.5 Effects of Concrete Resistance to Tensile Loading

In the design of composite sections, the participation of concrete under tensile loads is typically ignored, even with the presence of reinforcing steel. It is observed, however, during the early drift cycles of Specimens 2 and 3, that the concrete provides some resistance to tensile forces in the concrete composite girders. This is concluded based on comparisons between the equilibrium and actual concrete strains (Figures G.24 to G.31).

The effects of composite slip are not included in the actual and equilibrium concrete strains during girder negative bending. However, the actual concrete strain is

affected by any nonlinear strain distributions within the steel section, while the equilibrium concrete strains are not. Based on earlier observations, these effects may be ignored for negative girder bending up to the drift cycles of 0.50%. Therefore, it may be assumed that the differences in magnitude between the actual and equilibrium concrete strains during negative girder bending are due primarily to the axial rigidity, E_sA_r, that is estimated when calculating the concrete equilibrium strains. Note that only the area of the reinforcing steel, A_r, and Young's modulus of steel, E_s, are used to calculated the equilibrium concrete strains. If the concrete slab provides some resistance to the tensile stresses, the axial rigidity used in the formulation of the equilibrium concrete strain may be underestimated (Eq. G.28), thereby overestimating the strain in the concrete slab.

During negative bending of the East and West girders of Specimen 2, the equilibrium concrete strain is substantially larger (up to five times as large) than the actual concrete strains up to the first and second drift cycles at 0.50% drift cycles, respectively (see Figures G.24 to G.27). Also, when the East and West girders of Specimen 3 are subjected to negative bending, the equilibrium concrete strains are larger than the actual concrete strains up through the first two cycles at 0.25% drift cycles (see Figures G.28 to G.31).

The strain at which concrete cracks under tension, ε_r, can be estimated using E_c and the modulus of rupture, f_r'. The modulus of rupture is taken as $7.5\sqrt{f_c'}$ in units of psi, and has a variance of +/- 10% to 15% (ACI, 1995). For Specimens 2 and 3, ε_r is estimated at 130 $\mu\varepsilon$. The East and West girder concrete slabs of Specimen 2 are seen to lose their tensile resistance at around 1000 $\mu\varepsilon$ and 600 $\mu\varepsilon$, respectively. For the East and West girders of Specimen 3, the concrete slabs appear to lose their tensile resistance at around 50 $\mu\varepsilon$ and 300 $\mu\varepsilon$, respectively. It is difficult to see any correlation between the estimated ε_r based on the ACI provisions and the observed ultimate tensile strain in the concrete slabs of Specimens 2 and 3. However, when considering the high variability in the estimating f_r' and E_c, the results are reasonable.

It is concluded that the concrete slabs of East and West girders of Specimen 2 appear to have provided moderate resistance to tensile stresses up to the first cycle at 0.50% and the second cycle at 0.50% drift cycles, respectively. Similarly, the East and West girders of Specimen 3 demonstrate concrete slab resistance to tensile stresses during the first two cycles at 0.25% drift cycles. Recall that during the testing of Specimen 3, one the actuators jumped up to 11 kips at the end of the first two cycles at 0.25% drift cycles.

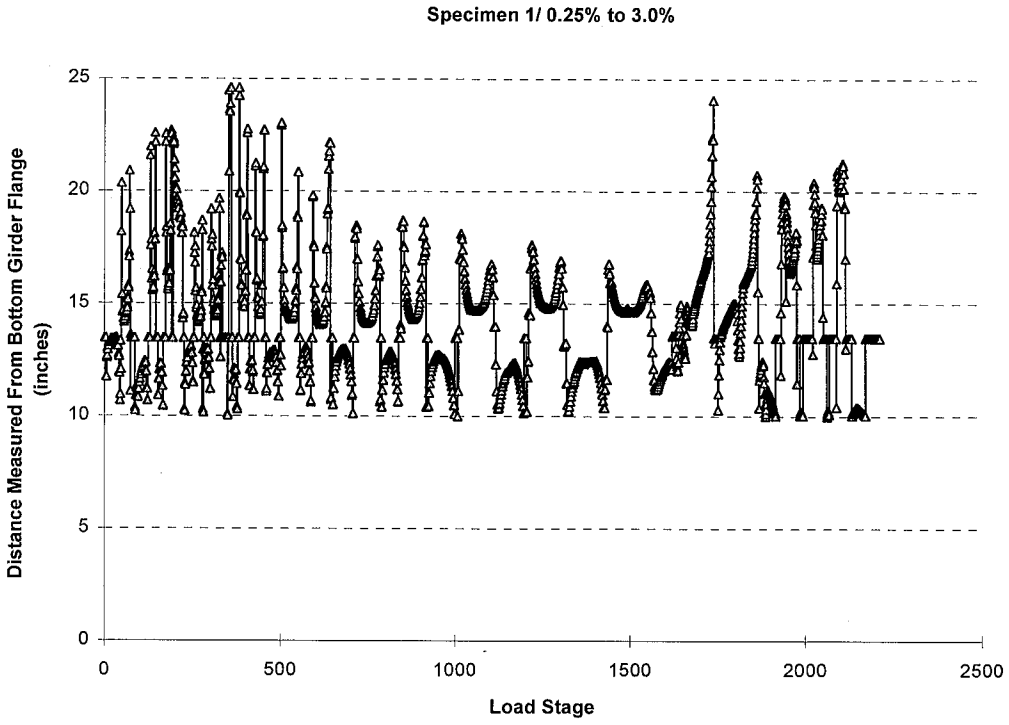

Figure G.32: Neutral Axis Position Along the Girder Cross Section (East Girder of Specimen 1)

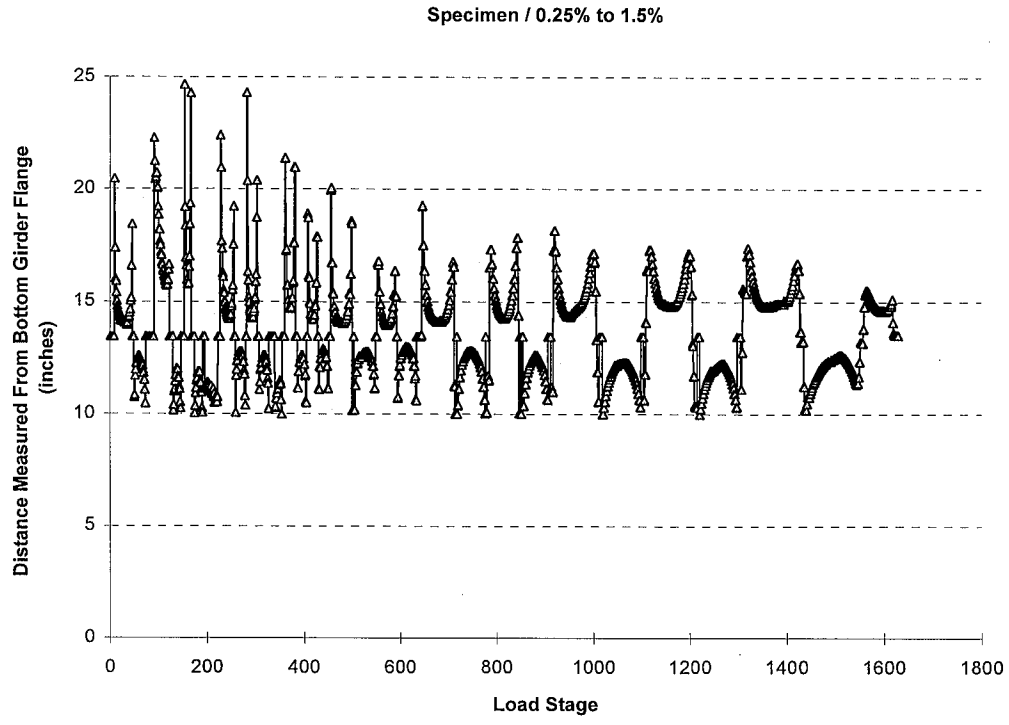

Figure G.33: Neutral Axis Position Along the Girder Cross Section (West Girder of Specimen 1)

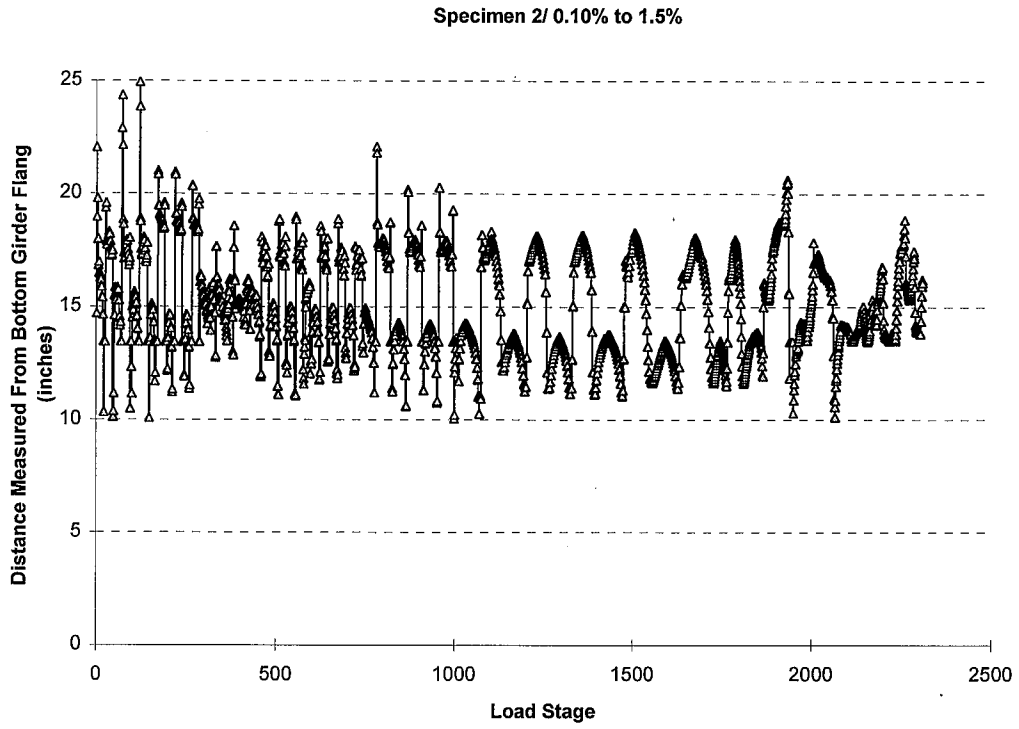

Figure G.34: Neutral Axis Position Along the Girder Cross Section (East Girder of Specimen 2)

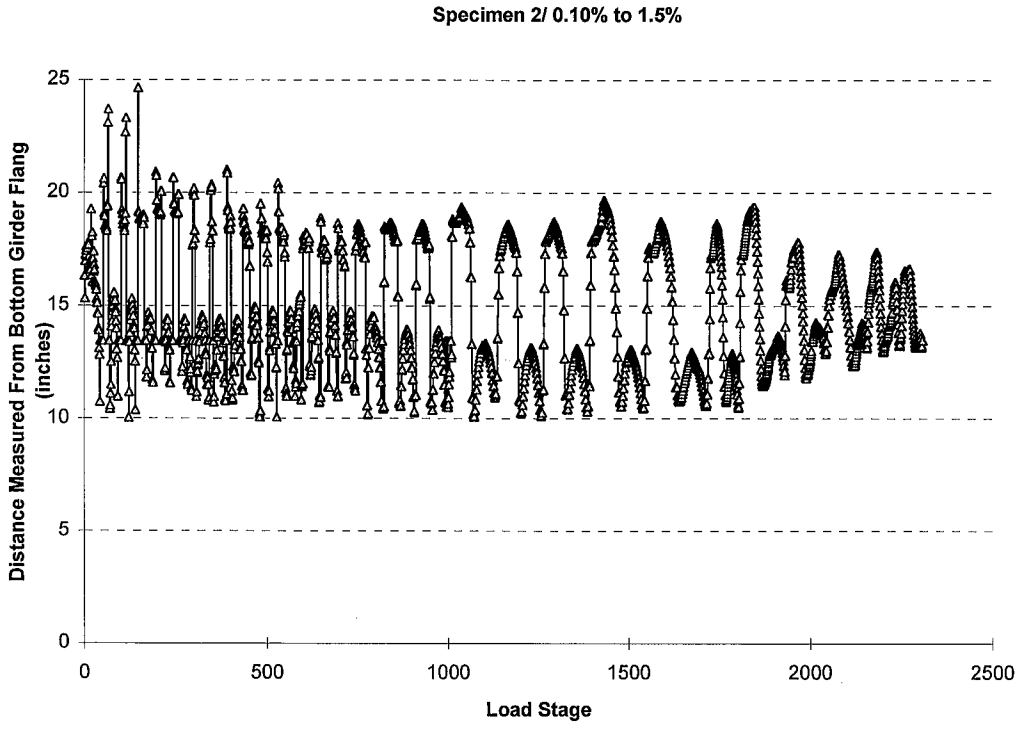

Figure G.35: Neutral Axis Position Along the Girder Cross Section (West Girder of Specimen 2)

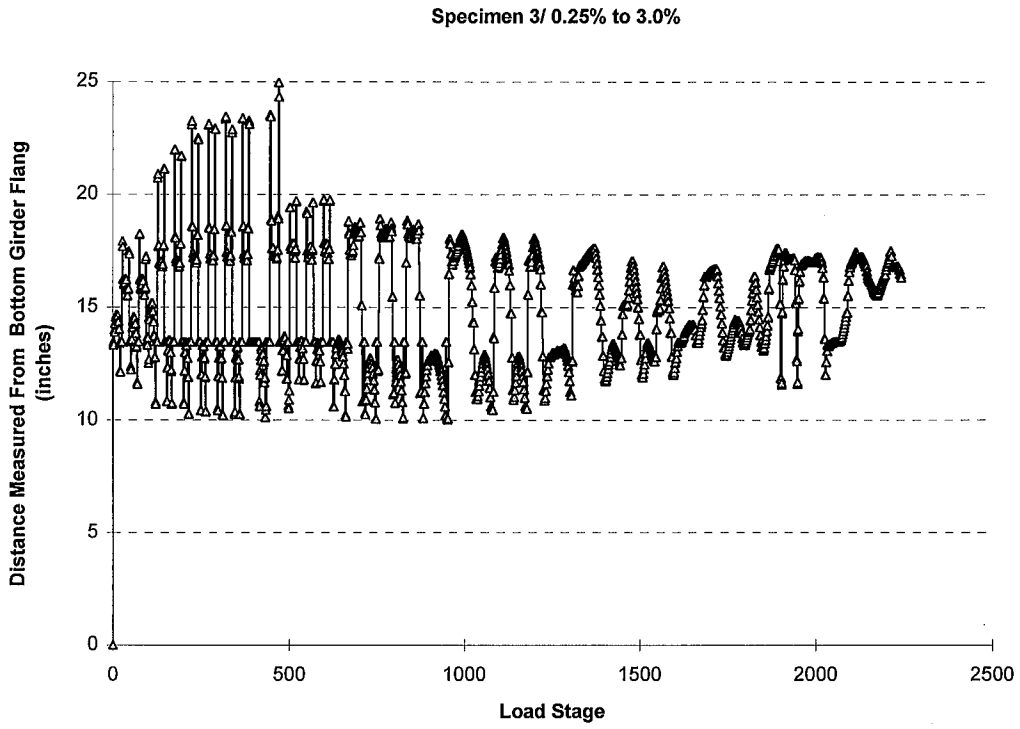

Figure G.36: Neutral Axis Position Along the Girder Cross Section (East Girder of Specimen 3)

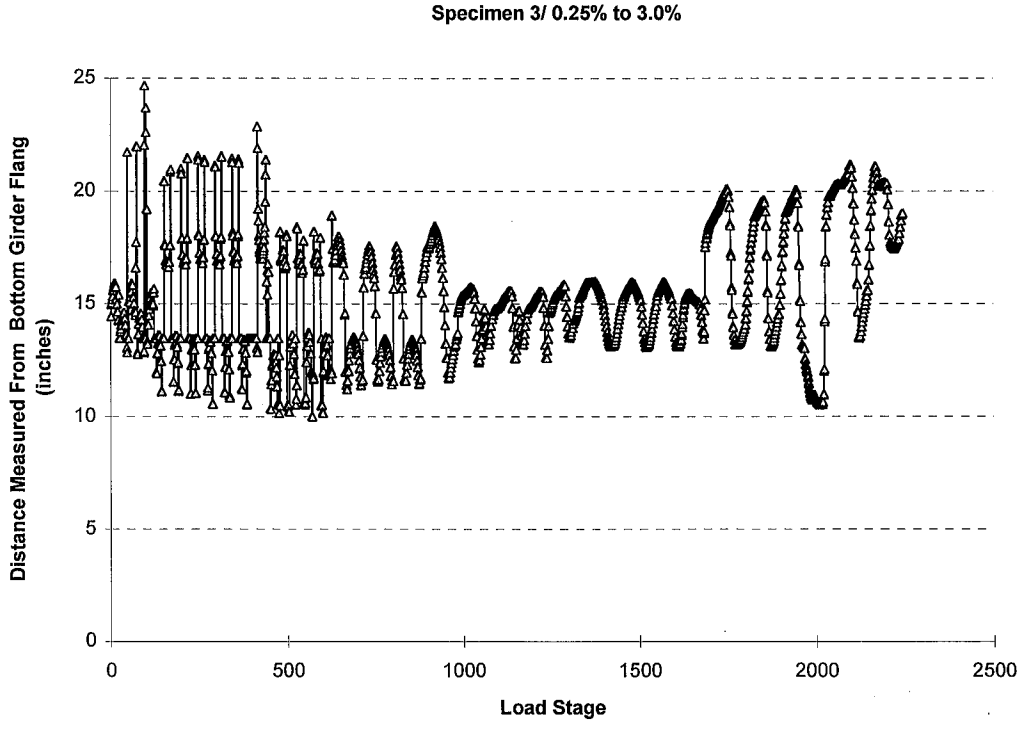

Figure G.37: Neutral Axis Position Along the Girder Cross Section (West Girder of Specimen 3)

Appendix H

Specimen Event Histories: Strain and Acoustic Emission Activity Near the Bottom Connection Regions

This appendix correlates the strain behavior and the acoustic emission (AE) activity that is measured within the connection regions of the specimens in order to describe the event history for each specimen. Comparisons of the strains near the top and bottom access holes highlight the effects of composite floor slabs and the placement of the shear tab on the strain distribution within the connection region. The strain levels and the amount of permanent straining near the location of failure may be correlated to the fracture of the of the six connections at the bottom girder flange region. Also, the quantity, frequency, and location of AE events may be studied to identify the type and location of failure within the bottom connection regions of the specimens.

The strains are measured at six locations on the girder flanges at a distance of approximately 1.5" from the column flange surface using high elongation strain gages (Figure H.1, see also Section 2.4.3). The strain gages are oriented so that strains are measured along the longitudinal axis of the girders. The strain behavior of the East and West connections of Specimens 1, 2, and 3 are shown in Figs. H.2-H.11, H.24-H.31, and H.40-H.51, respectively.

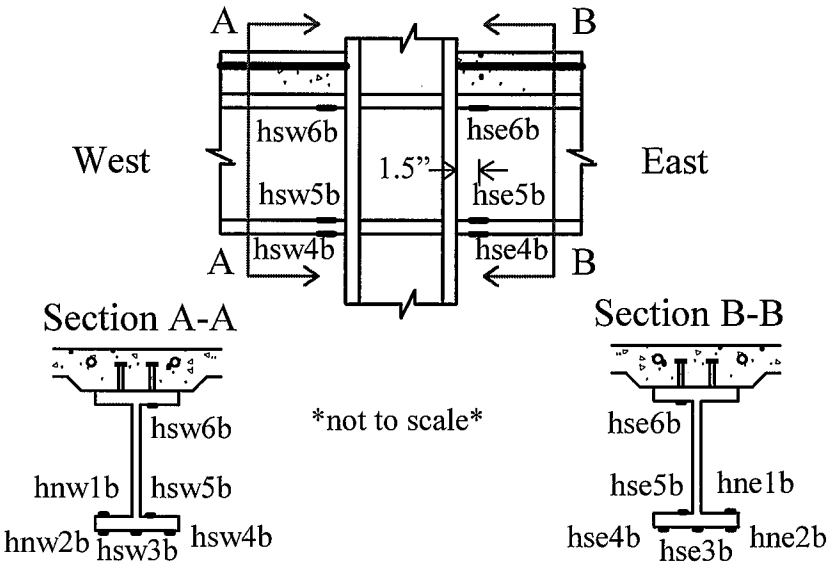

Figure H.1: Locations of High Elongation Strain Gages

The AE data that will be used for correlation consists of AE event rates and one-dimensional source locations of the AE events. The AE data is arranged by loading increments and quarter cycles. Recall that these tests were performed under displacement control. Thus loading ramps were performed with a beginning actuator stroke and an ending actuator stroke. As many as three and as few as one of these ramps composed a quarter cycle during testing. These displacement ramps are defined as Loading Increments for the AE analysis. The AE for Specimens 1, 2, and 3 are illustrated in Figures H.12-H.23, H.32-H.39, and H.52-H.63, respectively.

Note that the AE Event Source Location vs. AE Test Time (or Load and Displacement) plots provide a profile view of the AE activity across the width of the bottom connection region. For the East and West connections of Specimen 1 and the West connection of Specimen 3, the North and South girder flange tips correspond to a 0" and 14" source location, respectively (see Figures H.14, H.15, H.18- H.20, H.22, and H.23). For the East connections of Specimens 2 and 3, the South and North girder flange tips correspond to a 0" and 14" source location, respectively (see Figures H.33, H.36-H.39, H.54, H.55, and H.57-H.63).

Only one AE transducer array was attached to Specimen 2. A four-transducer rectangular array was attached to the East face of the column flange (see Section 2.4.4). This transducer configuration was used in order separate the AE events due to microfracturing near the bottom connection region from the AE events due to cracking of the concrete deck. Also, this configuration precluded the ability to separate events that originated from the East connection from those that originated from the West connection. Larger errors in source location of West events would occur due to the transducer configuration whereas the source locations of events originating from the East connection would be accurate. This implies that correlation of source location data to West connection failure patterns, though discussed, may be erroneous.

H.1 Connection Strain Behavior and AE Activity Prior to Failure (Specimen 1)

The East and West connections of Specimen 1 exhibit strain amplitudes near the bottom access holes (gages hse5b and hsw5b) that are approximately 1 to 1.5 times larger than strains near the top access holes (gages hse6b and hsw6b) up through the first cycle at the 1.5% drift level (see Figures H.3, H.5, H.7, and H.9). Significant amounts of yielding generally initiate in both the top and bottom flanges during the 0.75% to 1.0% drift cycles. The strains in both of the top access holes, especially for the East girder of Specimen 1, show an accumulation of net tensile strain predominantly during the 1.0% and 1.5% drift cycles (see Figures H.7 and H.9). This behavior implies that substantial permanent deformation is occurring near the top access holes of the connections during negative girder bending at these drift levels.

The top access hole region of the East connection (gage hse6b) demonstrates minimal strain after a large increase in strain to nearly 18,000 $\mu\varepsilon$ during the first quarter cycle of the first cycle at 1.5% drift (see Figure H.7). It is possible that a localized strain condition occurred near the top access hole. Peak to peak strain amplitudes shown near the bottom access hole (hse5b) following the first cycle at 1.5% drift are moderately less

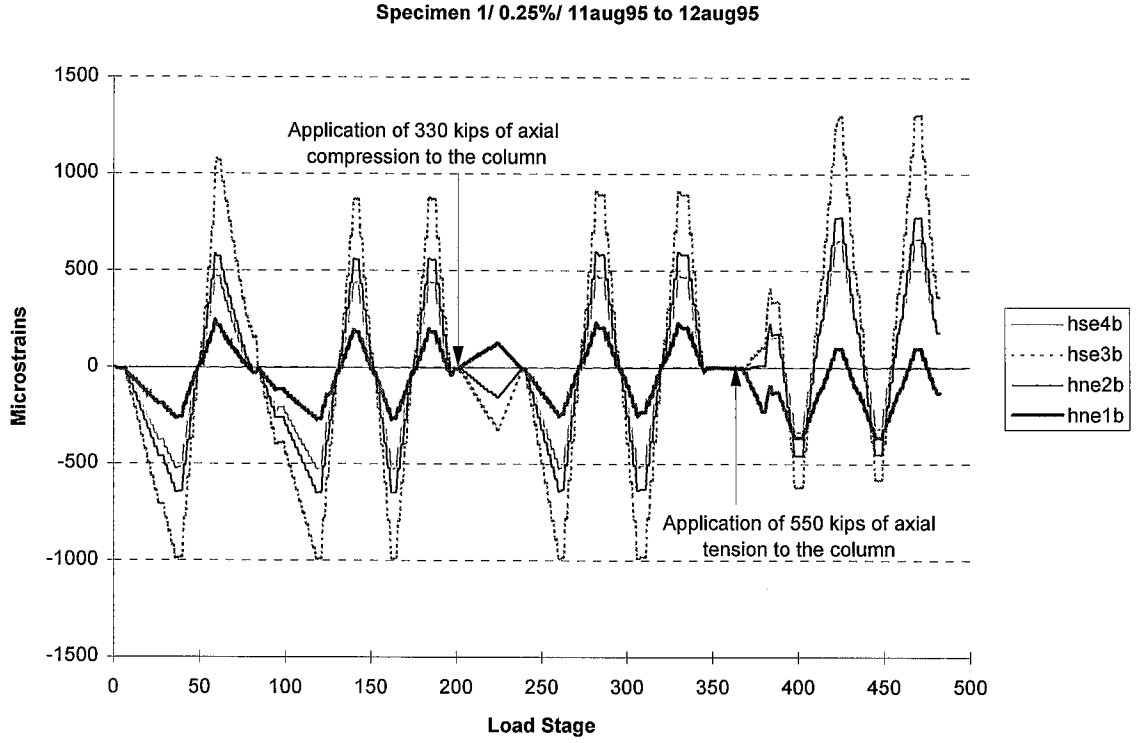

Figure H.2: Girder Bottom Flange Strains (East Girder of Specimen 1)

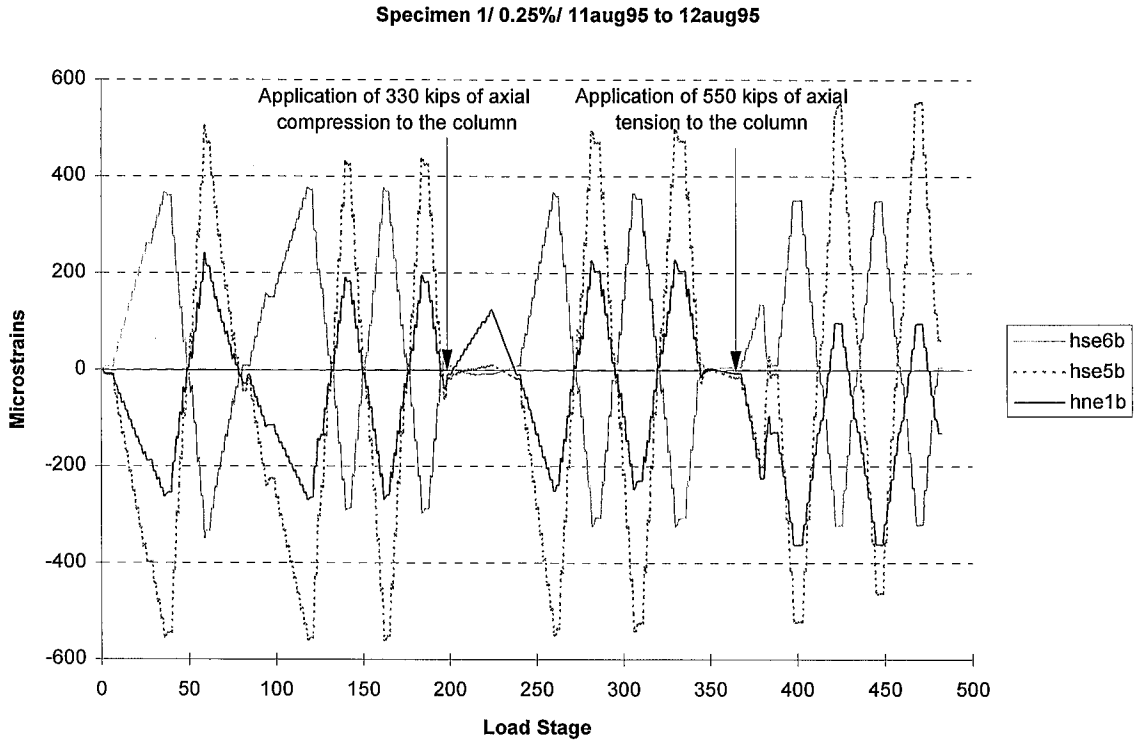

Figure H.3: Top and Bottom Access Hole Strains (East Girder of Specimen 1)

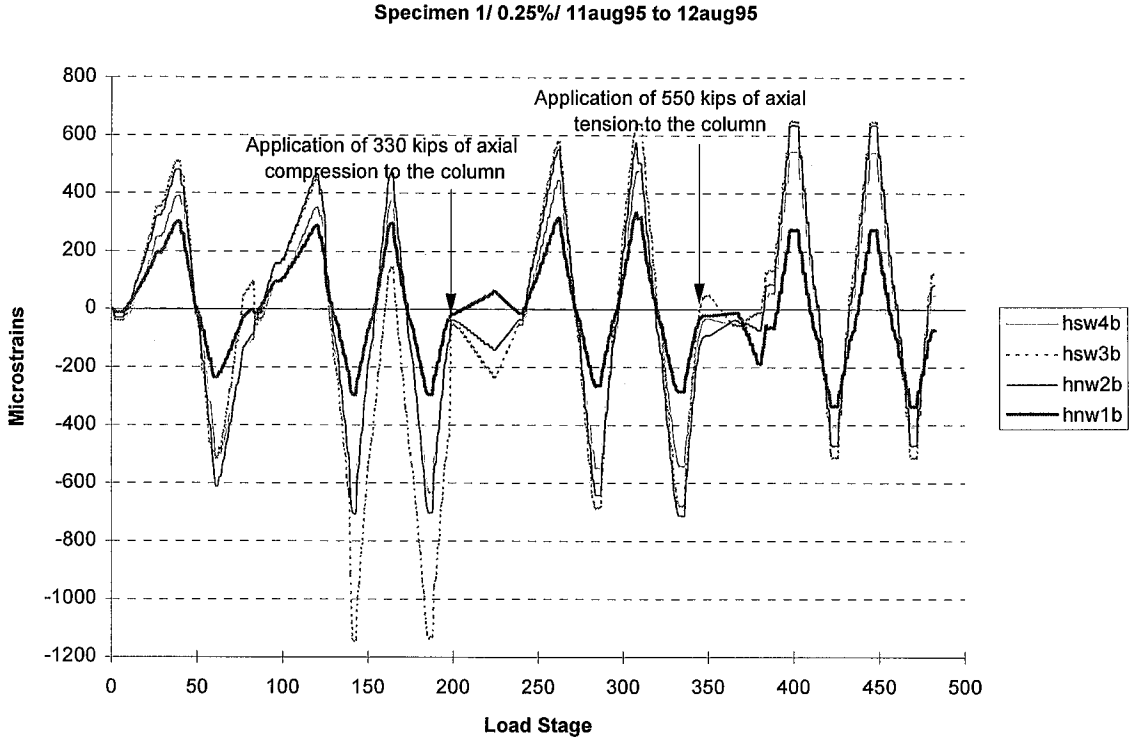

Figure H.4: Girder Bottom Flange Strains (West Girder of Specimen 1)

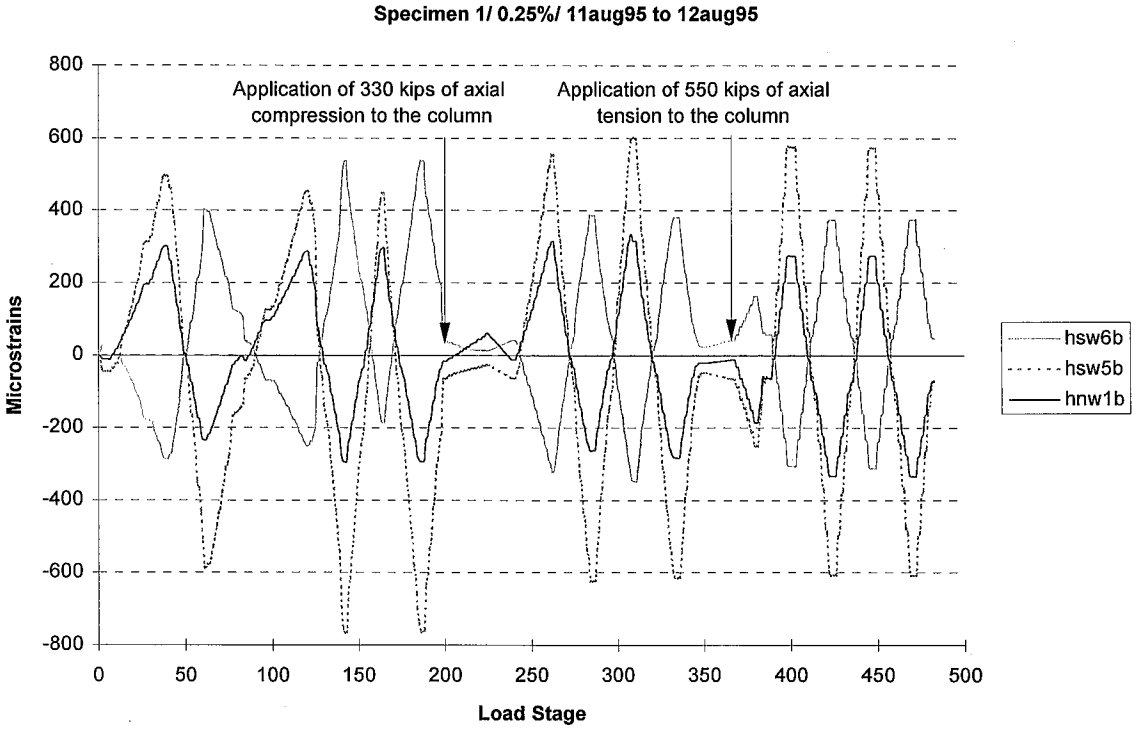

Figure H.5: Top and Bottom Access Hole Strains (West Girder of Specimen 1)

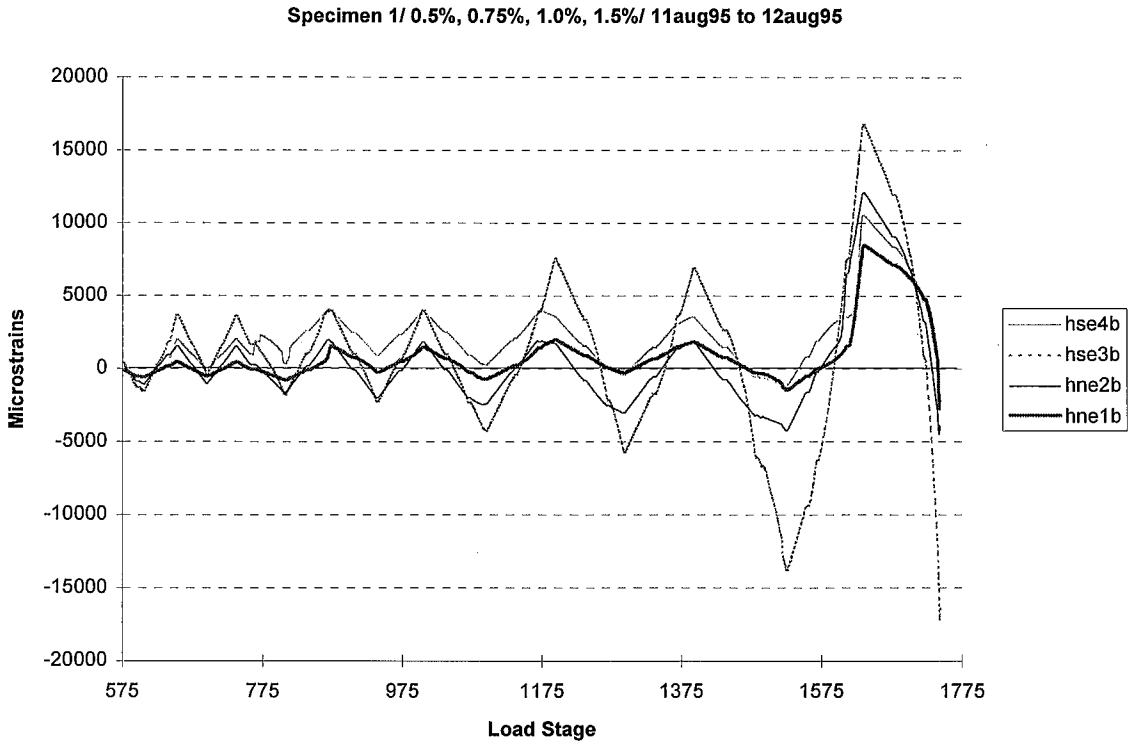

Figure H.6: Girder Bottom Flange Strains (East Girder of Specimen 1)

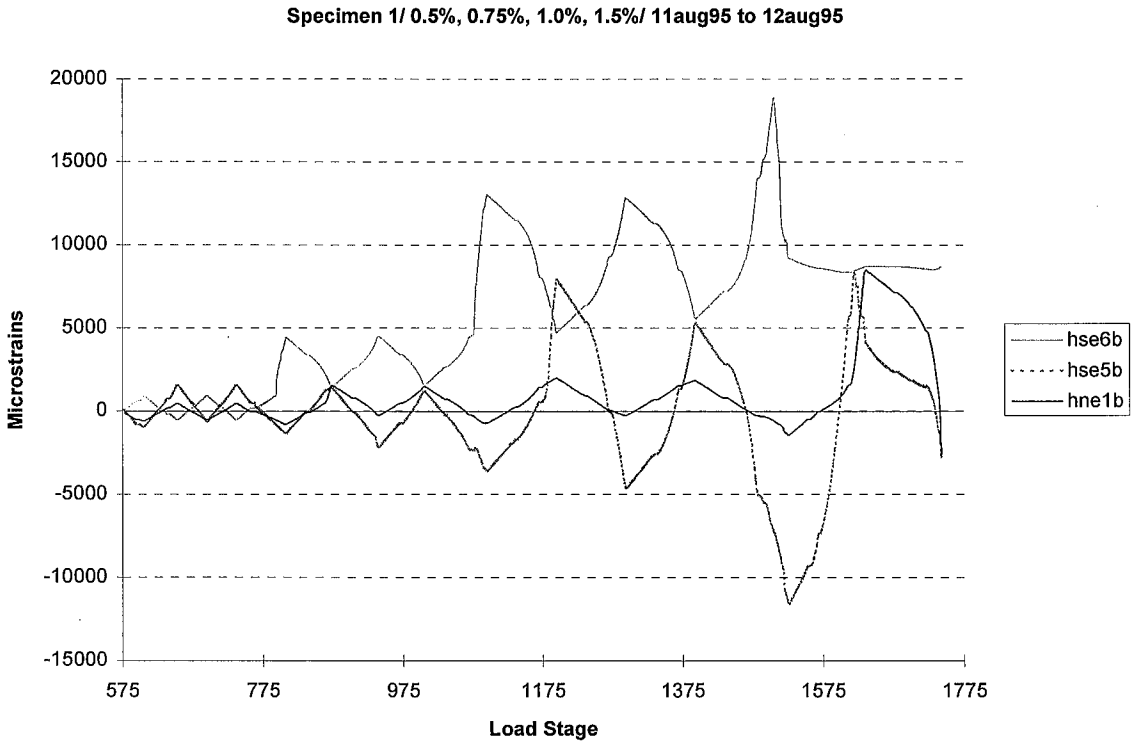

Figure H.7: Top and Bottom Access Hole Strains (East Girder of Specimen 1)

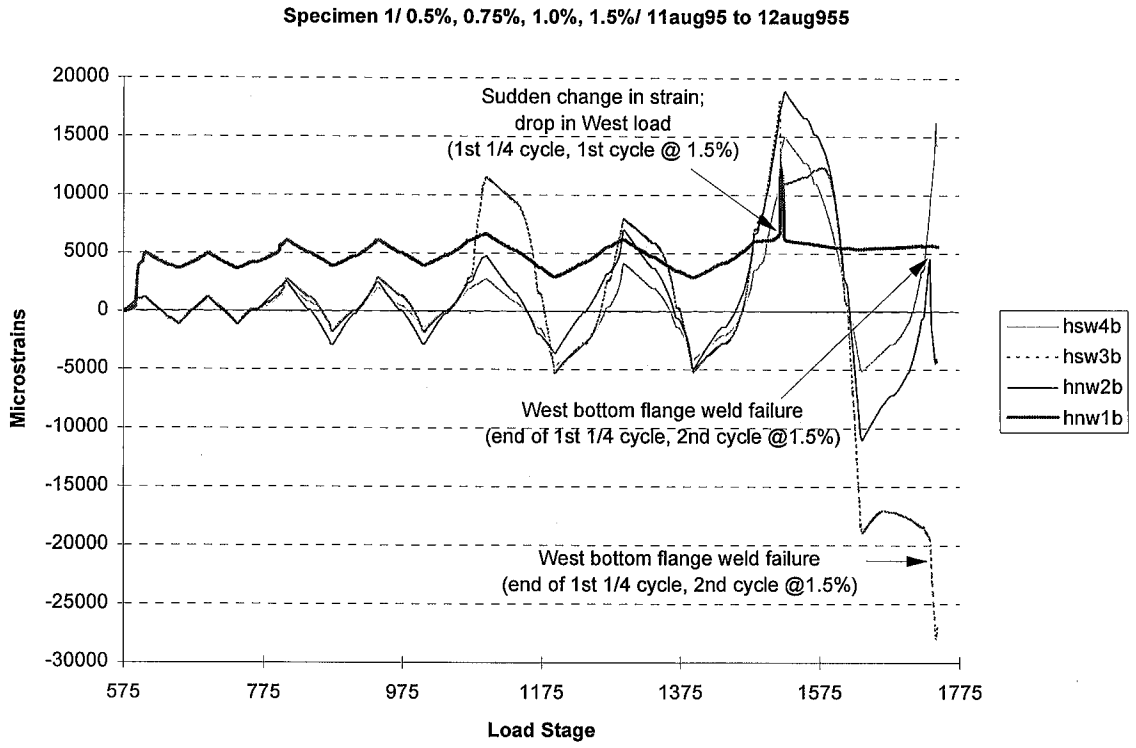

Figure H.8: Girder Bottom Flange Strains (West Girder of Specimen 1)

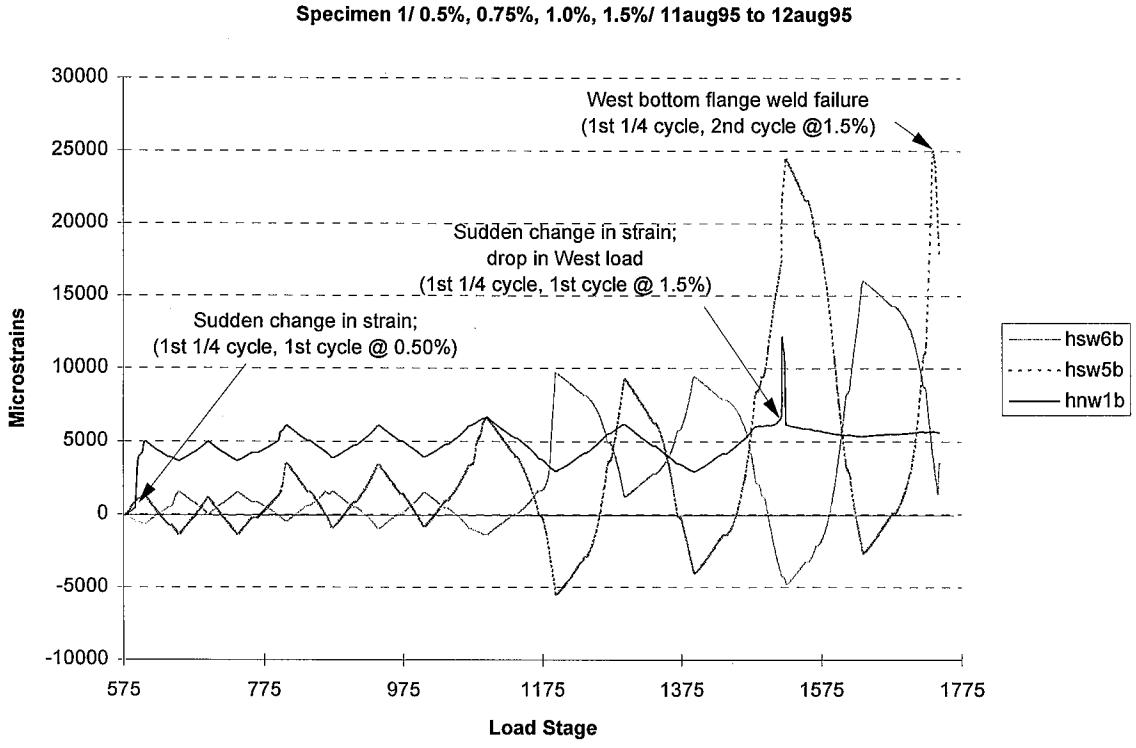

Figure H.9: Top and Bottom Access Hole Strains (West Girder of Specimen 1)

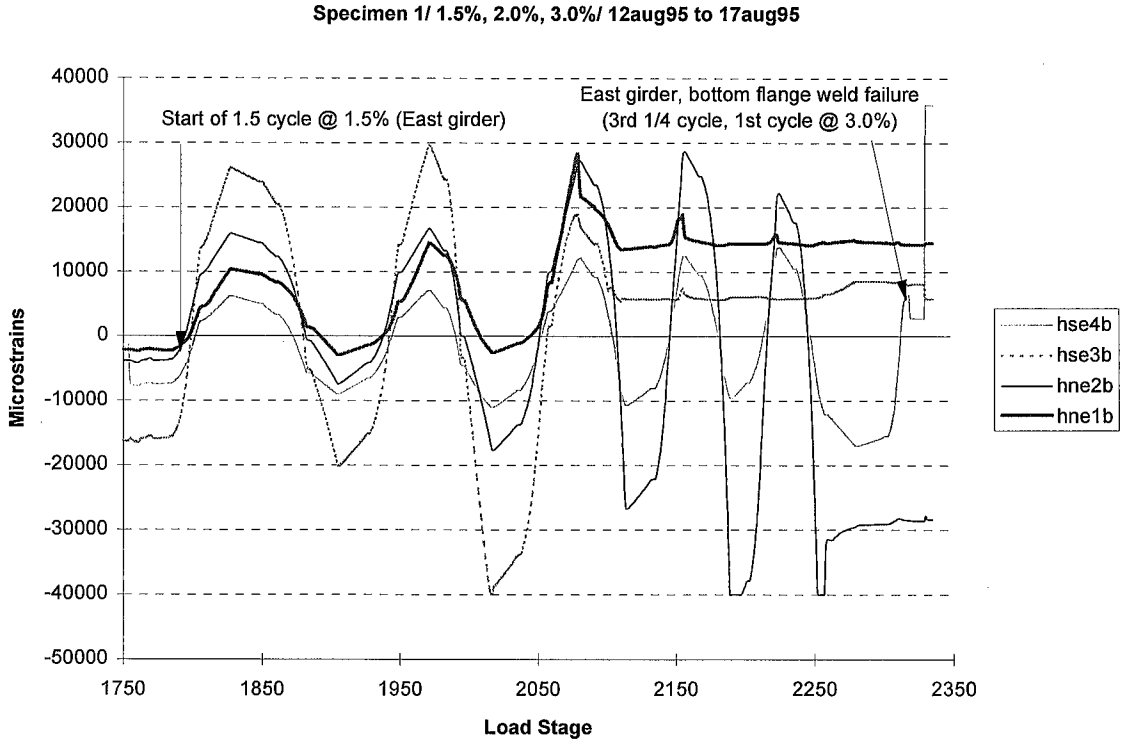

Figure H.10: Girder Bottom Flange Strains (East Girder of Specimen 1)

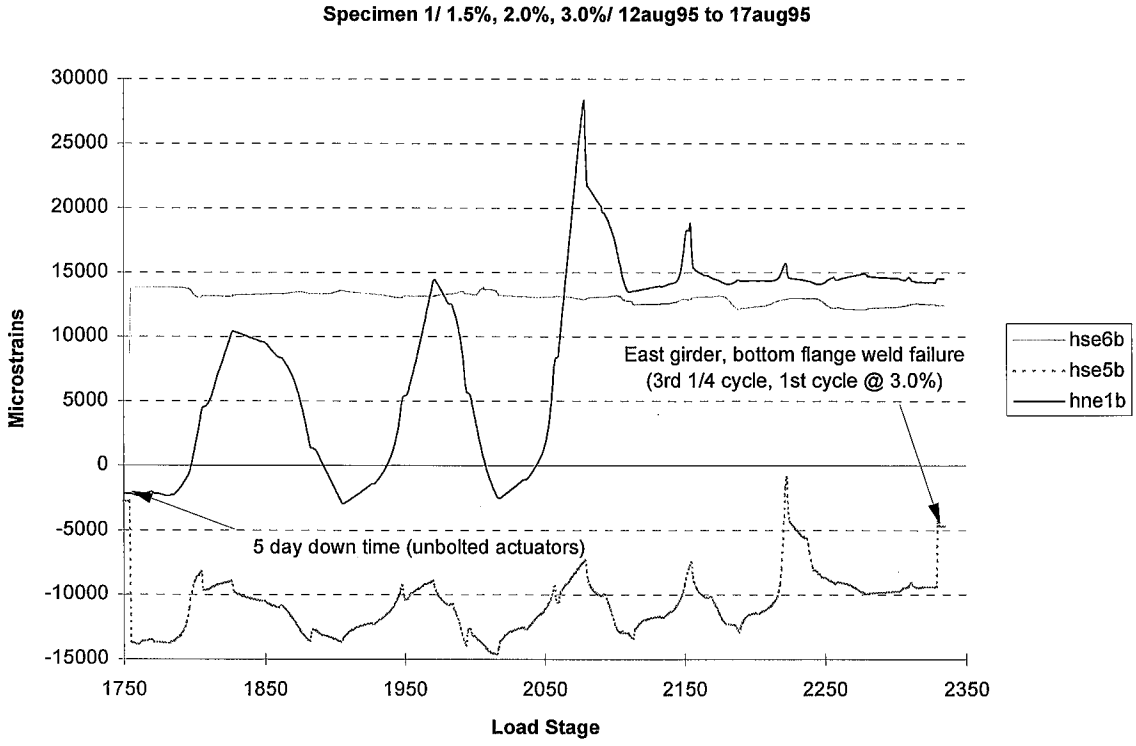

Figure H.11: Top and Bottom Access Hole Strains (East Girder of Specimen 1)

Table H.1: AE Loading Increment Data (Specimen 1)

Increment Number	Begin Stroke (in)	End Stroke (in)	East Events		West Events		Percent Drift	Quarter Cycle
			# of AE Events	Cum. Events	# of AE Events	Cum. Events		
1	0	-0.35	0	0	1	1	0.25	1
2	-0.35	0.35	0	0	0	1	0.25	2, 3
3	0.35	-0.35	0	0	0	1	0.25	4, 5
4	-0.35	0.35	0	0	0	1	0.25	6, 7
5	0.35	0	0	0	0	1	0.25	8
6	0	-0.7	0	0	1	2	0.5	1
7	-0.7	0.7	0	0	0	2	0.5	2, 3
8	0.7	-0.7	0	0	0	2	0.5	4, 5
9	-0.7	0.7	1	1	1	3	0.5	6, 7
10	0.7	0	0	1	0	3	0.5	8
11	0	-1.05	4	5	3	6	0.75	1
12	-1.05	0	0	5	0	6	0.75	2
13	0	1.05	2	7	0	6	0.75	3
14	1.05	0	0	7	0	6	0.75	4
15	0	-1.05	3	10	2	8	0.75	5
16	-1.05	0	0	10	0	8	0.75	6
17	0	1.05	0	10	0	8	0.75	7
18	1.05	0	0	10	0	8	0.75	8
19	0	-1.05	1	11	2	10	1	1
20	-1.05	-1.37	3	14	3	13	1	1
21	-1.37	0	0	14	0	13	1	2
22	0	1.05	0	14	0	13	1	3
23	1.05	1.4	1	15	2	15	1	3
24	1.4	0	1	16	1	16	1	4
25	0	-1.05	0	16	0	16	1	5
26	-1.05	-1.4	5	21	3	19	1	5
27	-1.4	0	0	21	0	19	1	6
28	0	1.05	0	21	0	19	1	7
29	1.05	1.4	0	21	0	19	1	7
30	1.4	0	0	21	0	19	1	8

Table H.1: AE Loading Increment Data (Specimen 1) (Cont.)

Increment Number	Begin Stroke (in)	End Stroke (in)	East Events		West Events		Percent Drift	Quarter Cycle
			# of AE Events	Cum. Events	# of AE Events	Cum. Events		
31	0	-1.4	1	22	0	19	1.5	1
32	-1.4	-2.1	10	32	4	23	1.5	1
33	-2.1	-0.69	0	32	0	23	1.5	2
34	-0.69	0	0	32	0	23	1.5	2
35	0	1.4	2	34	2	25	1.5	3
36	1.4	2.1	3	37	5	30	1.5	3
37	2.1	0.6	0	37	0	30	1.5	4
38	0.6	-1.05	0	37	0	30	1.5	5
39	-1.05	-2.1	63	100	58	88	1.5	5
39	-2.1	-0.8	63	100	58	88	1.5	6
40	-0.8	1.4	1	101	1	89	1.5	7
41	1.4	2.1	5	106	1	90	1.5	7
42	2.1	1.5	0	106	0	90	1.5	8
43	1.5	0.6	0	106	0	90	1.5	8
44	0.6	-1.4	1	107	0	90	1.5	9
45	-1.4	-2.1	7	114	2	92	1.5	9
46	-2.1	-0.8	1	115	1	93	1.5	10
47	-0.8	1.4	0	115	0	93	1.5	11
48	1.4	2.1	0	115	0	93	1.5	11
49	2.1	0.7	0	115	0	93	1.5	12
50	0.7	-1.4	0	115	0	93	2	1
51	-1.4	-2.8	5	120	0	93	2	1
52	-2.8	-1.3	0	120	0	93	2	2
53	-1.3	1.4	0	120	0	93	2	3
54	1.4	2.8	0	120	0	93	2	3
55	2.8	1.3	0	120	0	93	2	4
56	1.3	-2.8	3	123	2	95	2	5
57	-2.8	-1.3	0	123	0	95	2	6
58	-1.3	2.8	2	125	0	95	2	7
59	2.8	1.3	0	125	0	95	2	8
60	1.3	-2.8	4	129	2	97	2	9
61	-2.8	-1.4	0	129	0	97	2	10
62	-1.4	2.8	2	131	2	99	2	11
63	2.8	1.4	0	131	0	99	2	12
64	1.4	-2.8	11	142	4	103	3	1
65	-2.8	-4.2	18	160	4	107	3	1
66	-4.2	-2.7	4	164	2	109	3	2
67	-2.7	1.4 (0)	19	183	7	116	3	3

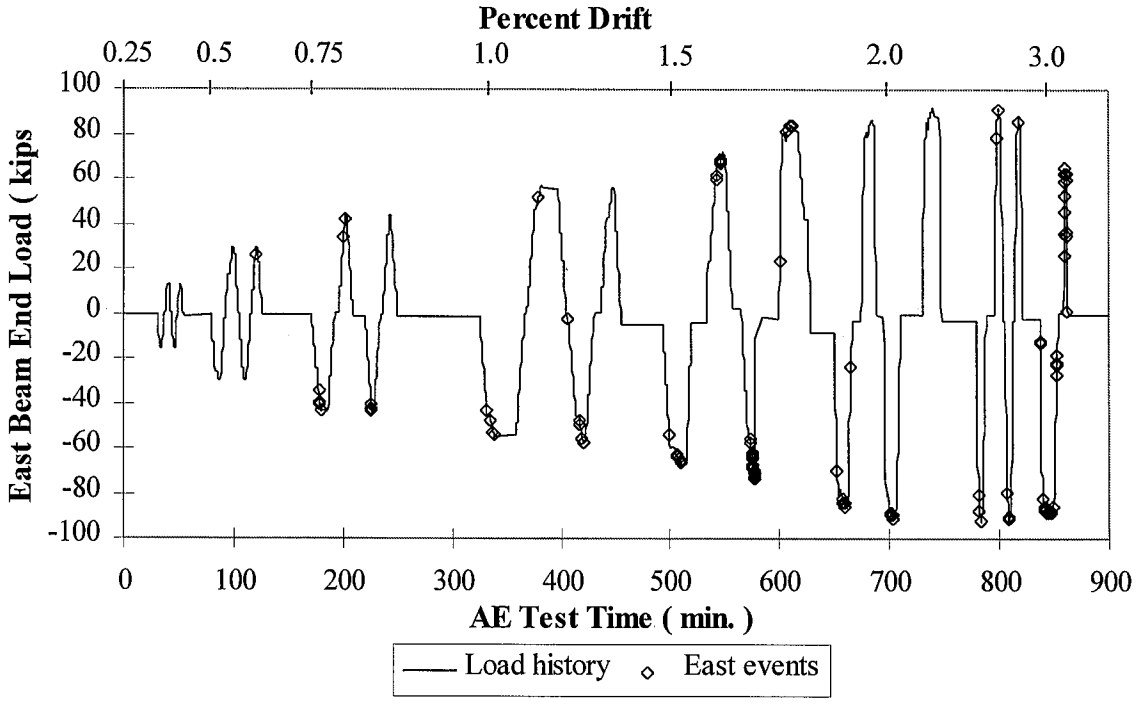

Figure H.12: AE Activity Load History (East Connection of Specimen 1)

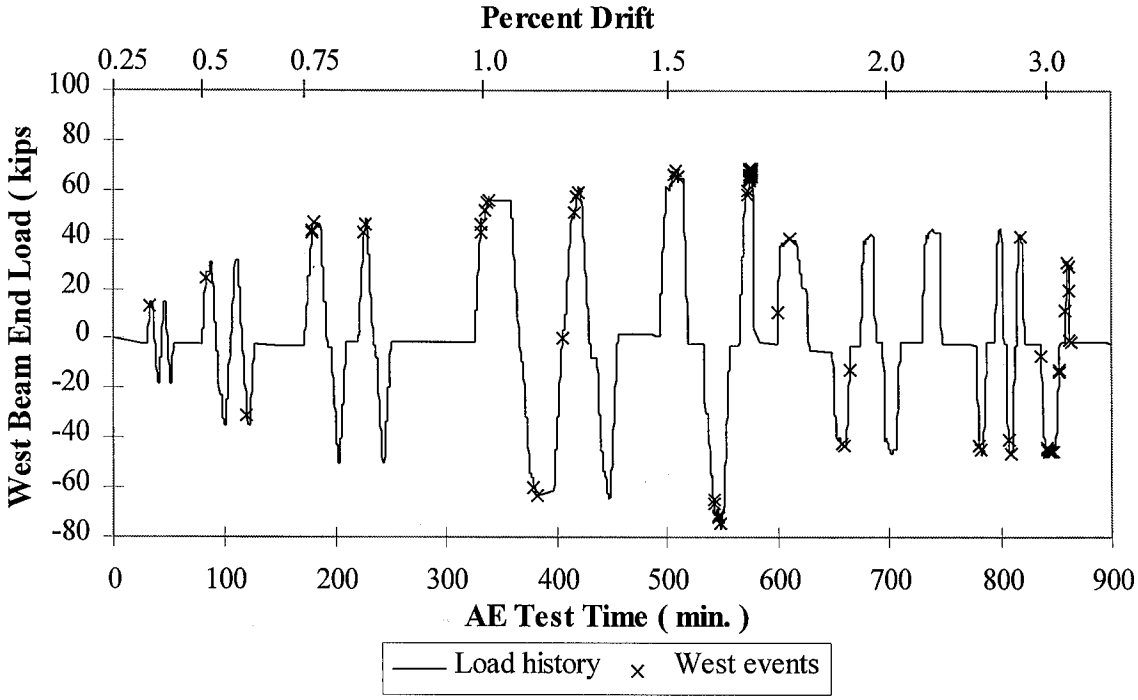

Figure H.13: AE Activity Load History (West Connection of Specimen 1)

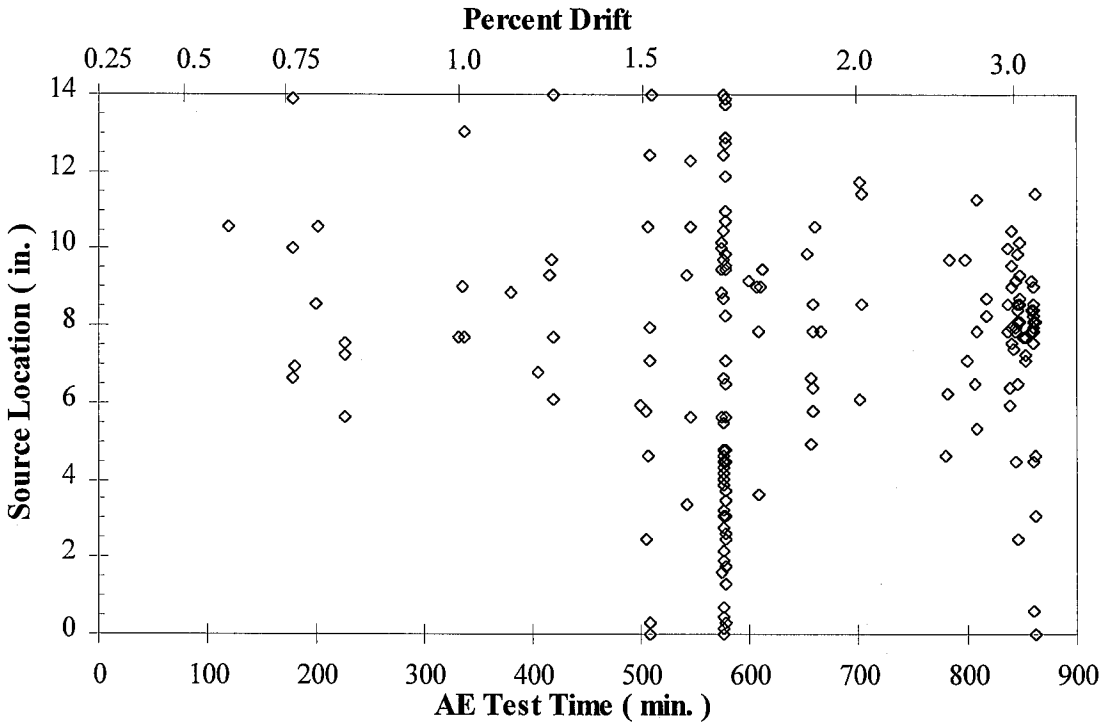

Figure H.14: AE Event Source Location vs. AE Test Time
(East Connection of Specimen 1)

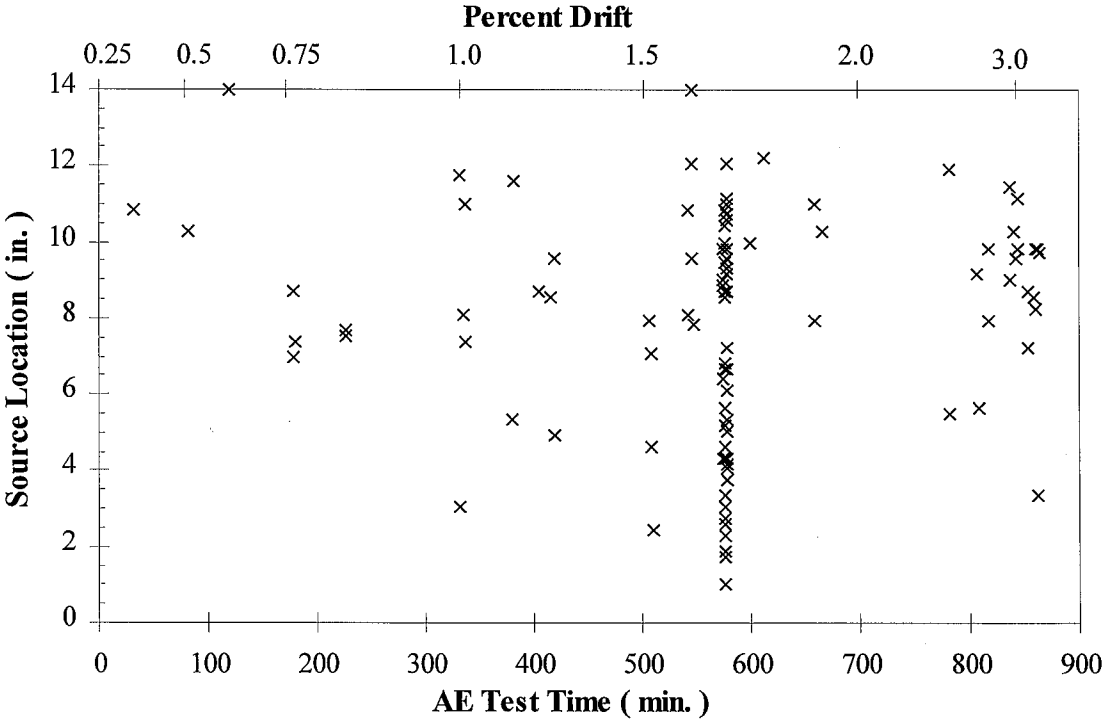

Figure H.15: AE Event Source Location vs. AE Test Time
(West Connection of Specimen 1)

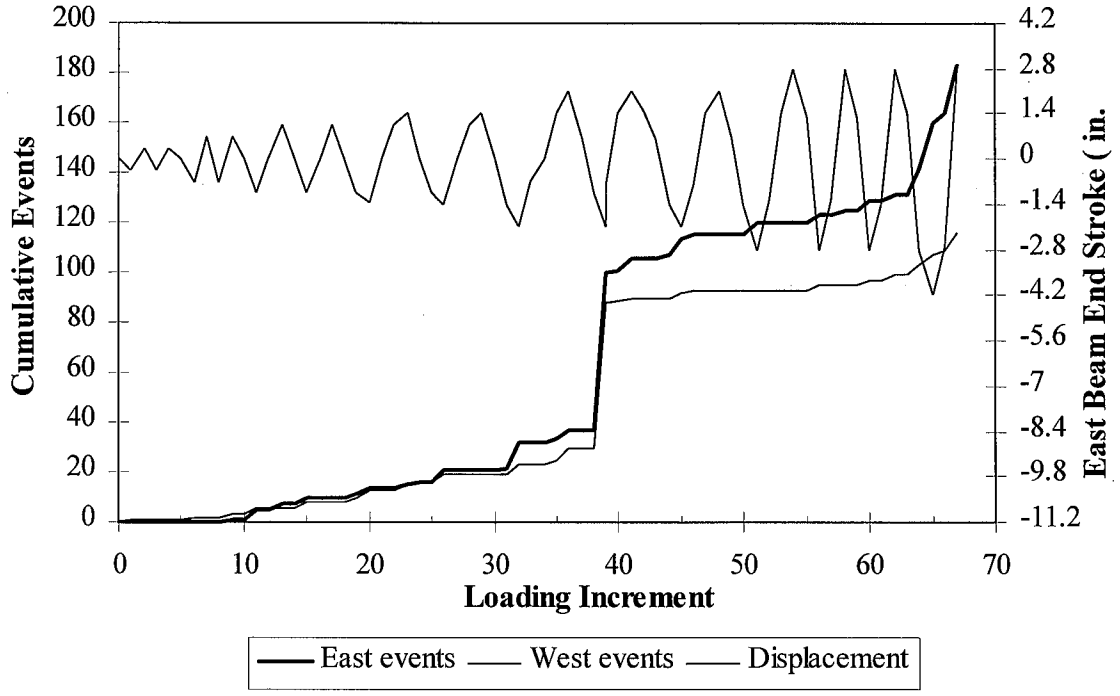

Figure H.16: Cumulative Events vs. Loading Increment (Specimen 1)

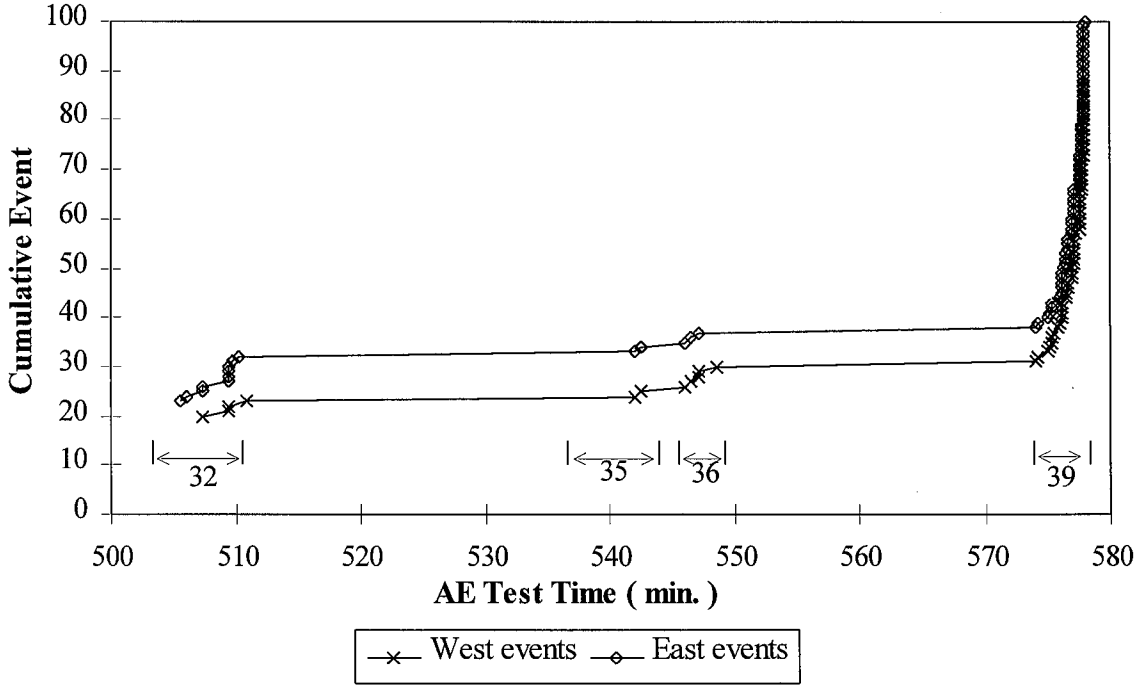

Figure H.17: Cumulative Events vs. AE Test Time
(First to fifth quarter cycles at 1.5% drift)

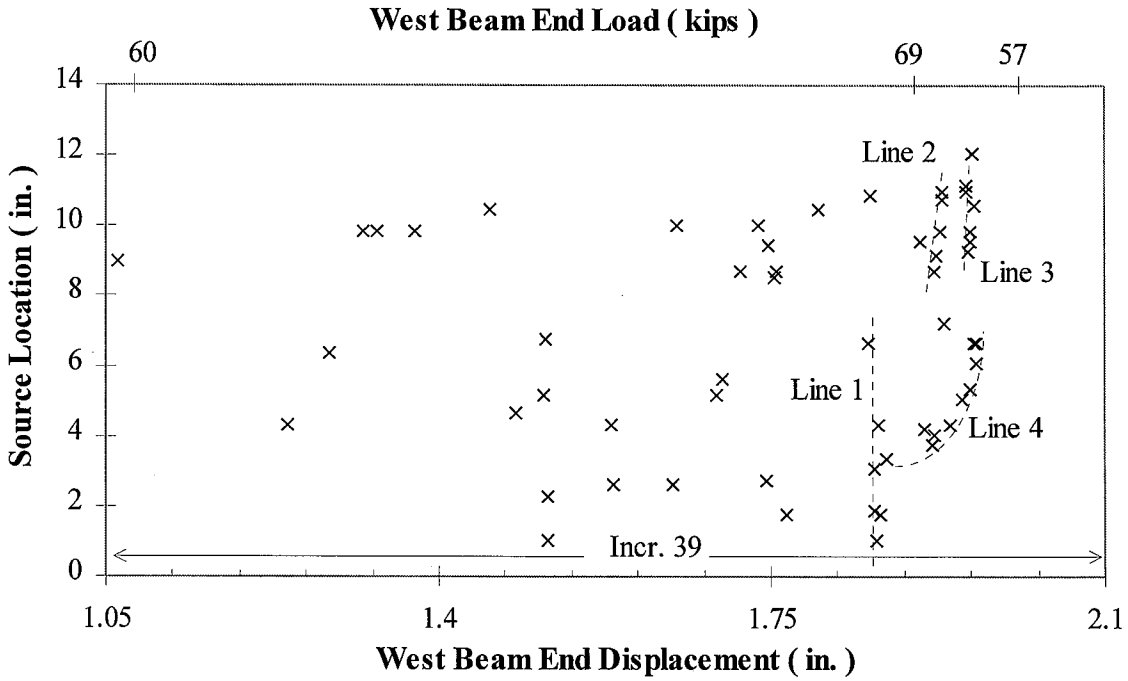

Figure H.18: AE Source Location vs. Load and Displacement
(First quarter cycle of the second cycle at 1.5% drift/ West Connection of Specimen 1)

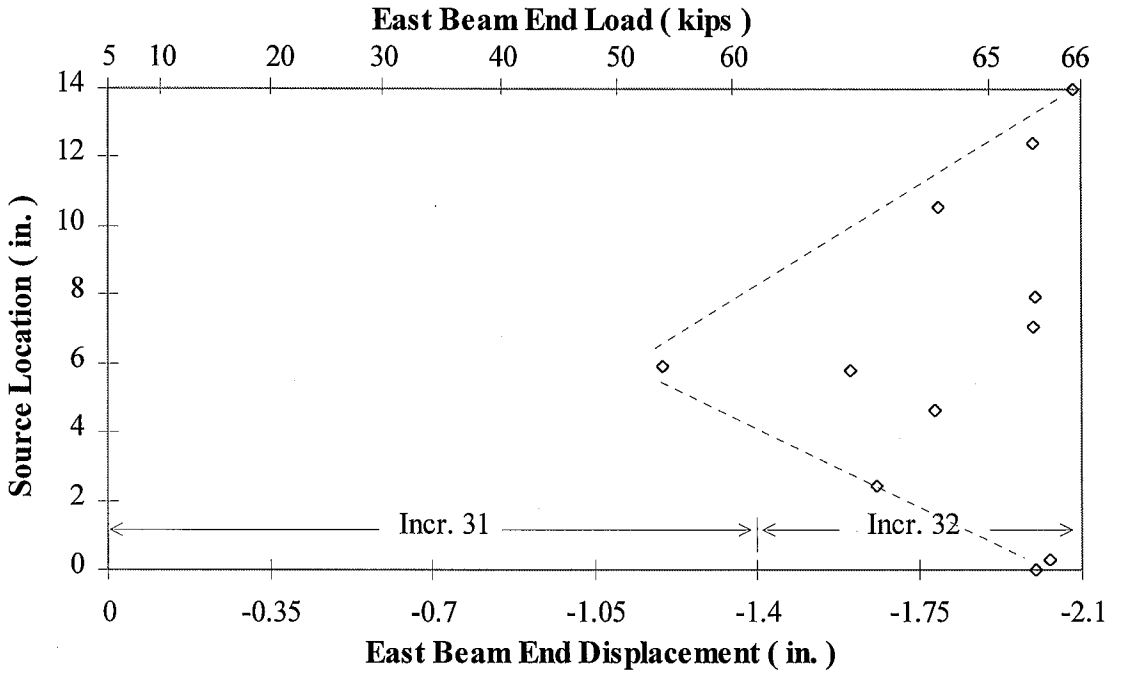

Figure H.19: AE Source Location vs. Load and Displacement
(First quarter cycle of the second cycle at 1.5% drift/ East Connection of Specimen 1)

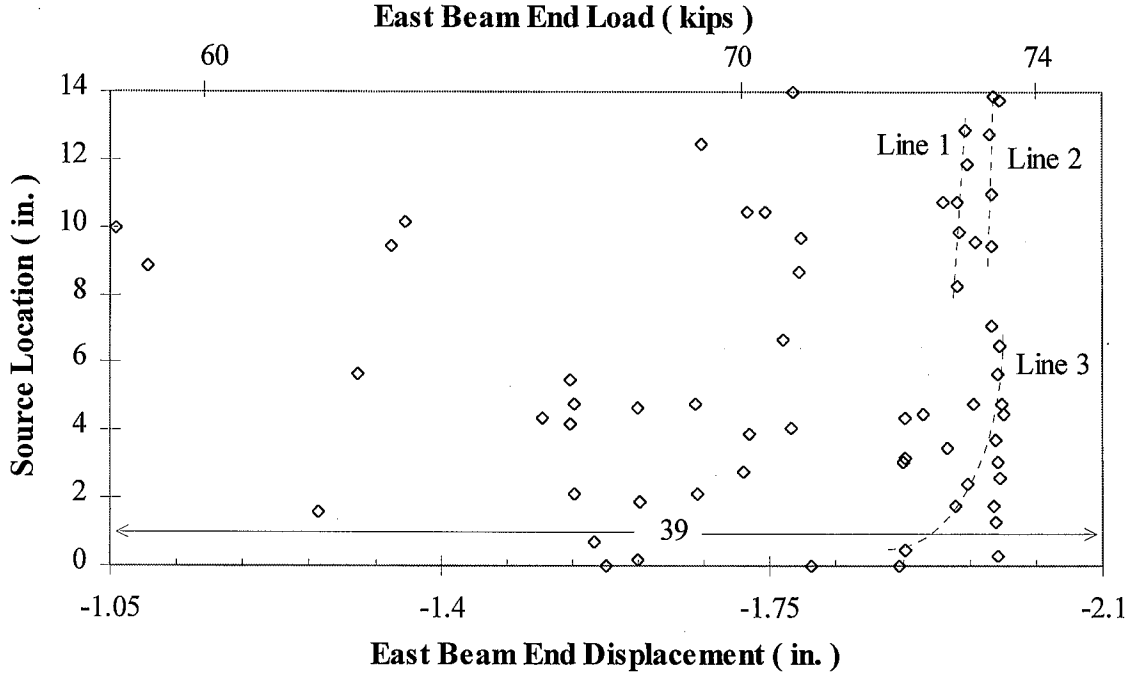

Figure H.20: AE Source Location vs. Load and Displacement
(First quarter cycle of the second cycle at 1.5% drift/ East Connection of Specimen 1)

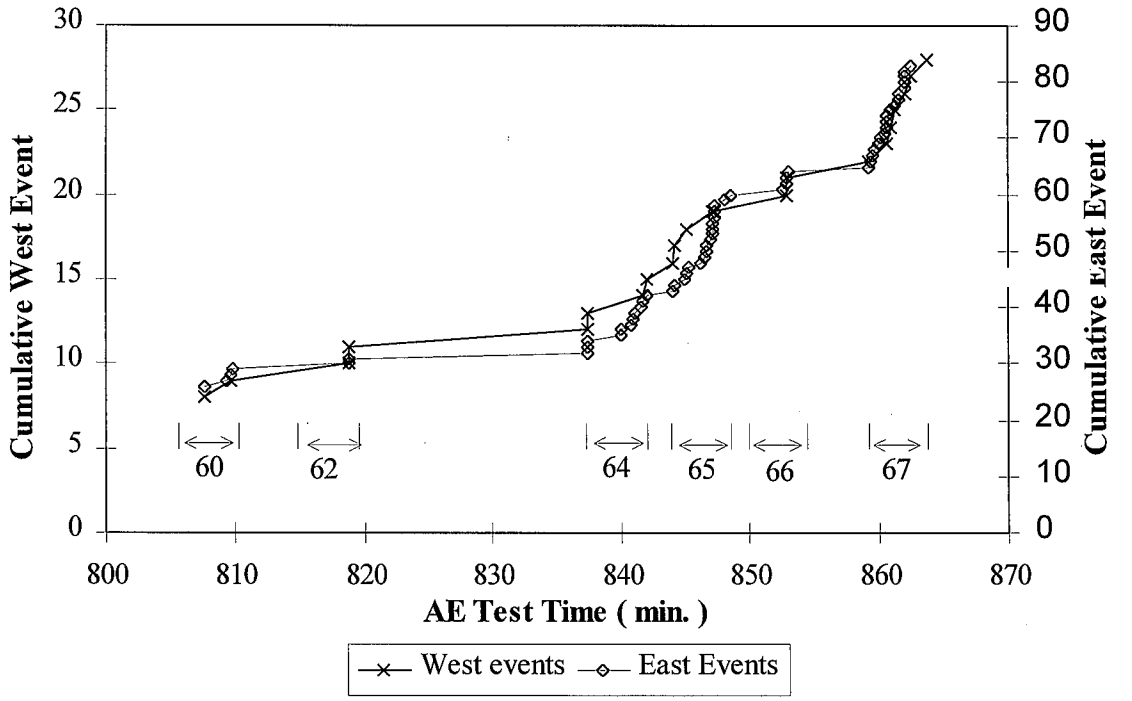

Figure H.21: Cumulative Events vs. AE Test Time
(Third cycle at 2.0% drift and first cycle at 3.0% drift/ Specimen 1)

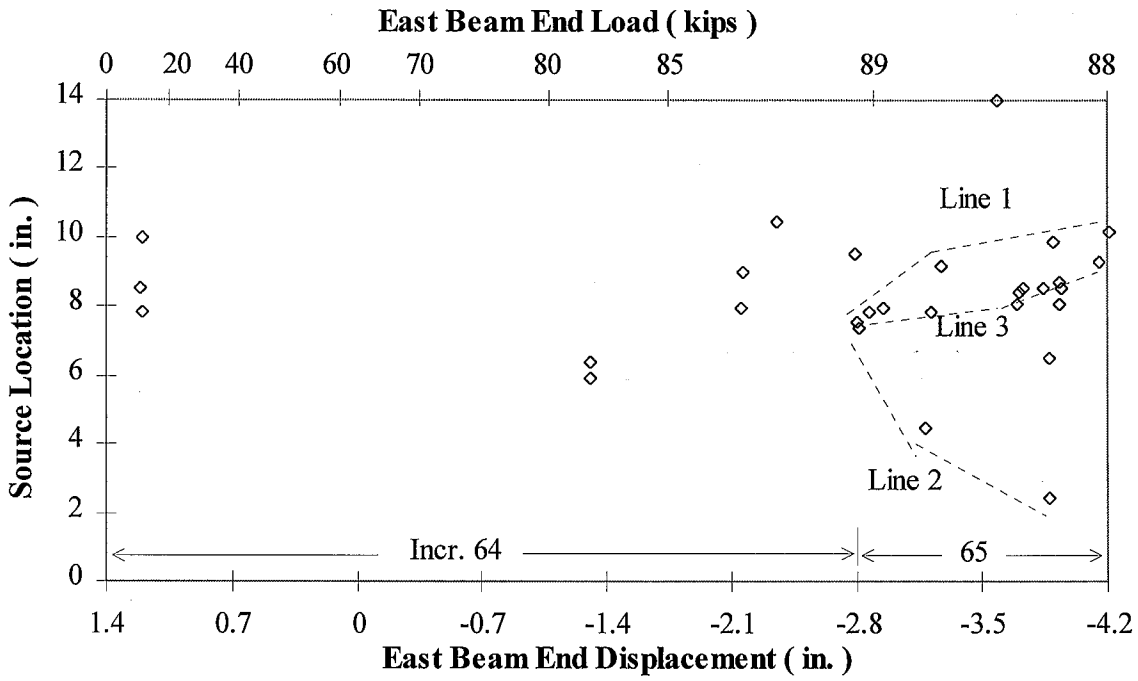

Figure H.22: AE Source Location vs. Load and Displacement
(First quarter cycle of the first cycle at 3.0% drift/ East Connection of Specimen 1)

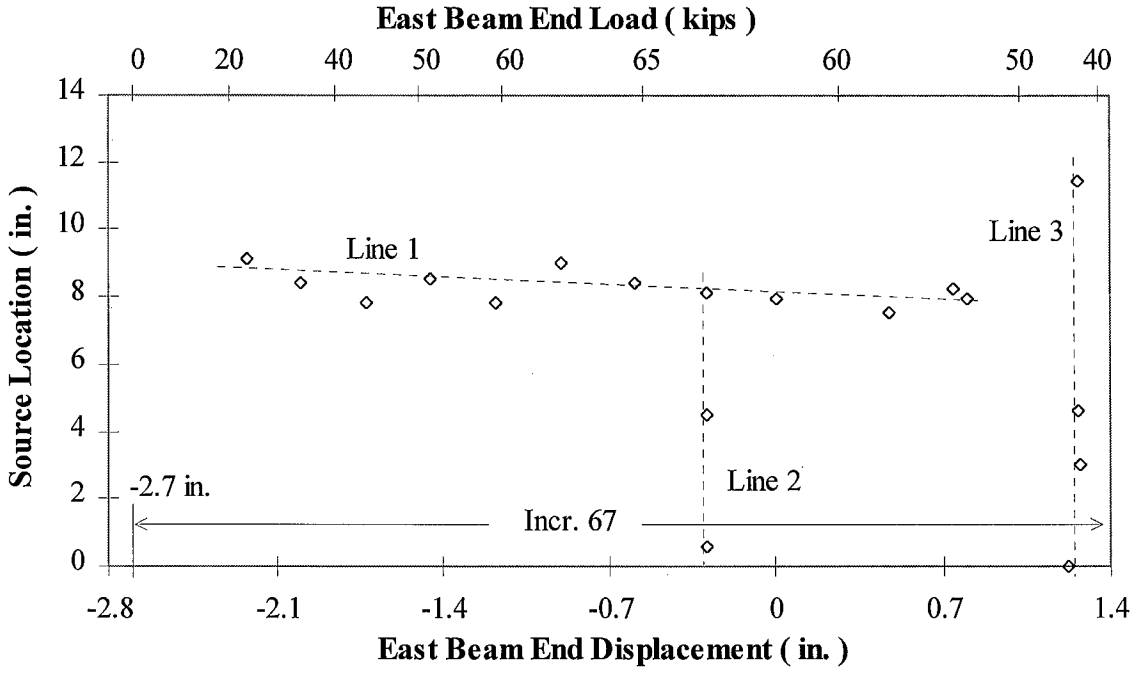

Figure H.23: AE Source Location vs. Load and Displacement
(Third quarter cycle of the first cycle at 3.0% drift/ East Connection of Specimen 1)

than the strains shown at the 0.75% and 1.0% drift cycles and also exhibit sudden small drops in strain magnitudes during the 1.5% and 2.0% drift cycles (see Figures H.7 and H.11). These strain changes correspond to drops in the East girder tip load due to relaxation of the specimen in between loading excursions.

Table H.1 and Figures H.12 to H.16 show both significant East and West AE activity began during the first cycle at 0.75% drift (Increment 11). This observation corresponds to first noticeable net strain shifts for the East and West girders in the strain gages hse6b, hse5b, and hsw5b. It is also shown that the rate of East and West event increase is similar and relatively slow from Increments 11 to 30 (0.75% drift cycles and 1.0% drift cycles). This would imply relatively stable connection behavior during the 0.75% through the 1.0% drift cycles. Only one strain gage (hsw3b) showed any drastic increases or decreases in strain during the 0.75% or 1.0% drift cycles.

Recall that the West bottom flange strains (hsw3b, Fig. H.8) increased significantly during the first quarter cycle at 1.0% drift. Table H.1 shows that 5 of the 11 West connection events at 1.0% drift occurred during the first quarter cycle at 1.0% drift.

H.2 Connection Strain Behavior and AE Activity At Failure (Specimen 1)

The West connection failed by brittle fracture of the metal surrounding the weld in the HAZ between the weld and the column flange during the first quarter cycle of the second cycle at the 1.5% drift cycles (see also Section 3.2). Some evidence of partial fracturing of the bottom region of the bottom welded girder-to-column connection, resulting in a transfer in strain into the upper region of the weld, may have occurred during the first quarter cycle of the first cycle at 1.5% (see Figures H.8 and H.9). The release of strain in the center of the bottom of the bottom flange (hsw3b) and the increase in the strain near the center of the top of the bottom flange (hsw5b) indicate that the bottom portion of the bottom flange released from the column face, which may have caused a redistribution of forces to the upper portion of the bottom flange weld resulting

in the strain increase seen in gage hsw5b. It is important to note that a drop in strain may correspond to failure of a strain gage rather than a release in strain due to weld fracture. Nevertheless, the strain behavior of this connection may be correlated with the AE activity.

This behavior of the bottom West connection region of Specimen 1 is also observed in the acoustic emission data (see Table H.1, Figs. H.13, H.15, H.16, and H.18). Figure H.16 shows a sudden increase in the number of East and West events during Increment 32. Table H.1 shows that Increment 32 corresponds to the last half of the first quarter cycle at 1.5% drift. Table H.1 also shows that 4 west events occurred during the first quarter cycle at 1.5% drift. Figure H.15 summarizes the source locations of the West events vs. AE Test Time for Specimen 1. The first quarter cycle at 1.5% drift began approximately 500 min. (AE Test Time) into the testing of Specimen 1. Figure H.15 shows that the source locations of the 4 events have source locations between 2 in. and 8 in. These source locations correspond to the northern half of the West bottom flange. The first two events had source locations of 7.95 in. and 7.1 in., respectively. The last two events had 4.65 in. and 2.45 in. source locations, respectively. Therefore, the events progressed from the central region of the weld towards the North flange tip. This may be indicative of crack propagation from the central region of the weld toward the North flange tip.

During the first quarter cycle of the second cycle at 1.5% drift, the West bottom flange weld failed completely. Table H.1 shows that 58 West events occurred during Increment 39. Figure H.17 is a Cumulative events vs. AE test time chart for Specimen 1. This figure shows data for the loading period leading up to the brittle fracture of the West weld, where an increase in the number of East events and West events occur during Increment 39 (first quarter cycle of the second cycle at 1.5% drift) (see Figures H.18 and H.20). The increase in the East bottom flange events is anomalous (based on the equipment used for this test, it was not entirely possible to distiguish the source locations of the AE events occurring at the East and West connection regions). No apparent

damage to the East connection was observed and no drastic changes in the East strain behavior is shown during Increment 39.

The source locations of the West events that occurred during the first quarter cycle of the second cycle at 1.5% drift correlate well with the behavior illustrated by the strain readings. All of the bottom flange strain gages show sudden releases of strain during this quarter cycle (see Figures H.8 and H.9). Figure H.8 shows that the North bottom flange strain gage (hnw2b) released its strain moments before the South end strain gage (hsw4b). This behavior, which is supported by the AE data, indicates that the North end of the weld fractured before the South end.

The source location patterns shown in Figure H.18 illustrate that the failure of the West bottom flange weld initiated at the weld's North end and propagated to the South end. Figure H.18 is an AE Source Location vs. Load and Displacement chart for the West events that occurred during the first quarter cycle of the second cycle at 1.5% drift. This figure illustrates several interesting source location patterns labeled Line 1, Line 2, Line 3 and Line 4. Line 1 shows a group of events that occurred in rapid succession with source locations consistent with the North end of the West bottom flange weld. No West events with source locations between 1 in. and 3 in. occurred after Line 1. This indicates that the North weld tip failed at this time. Line 4 shows a group of events that propagate with increasing rapidity towards the center of the flange. Lines 2 and 3 represent two similar source location patterns. Both of them are consistent with crack propagation from the central region of the weld toward the South weld tip.

The East connection failed due to the propagation of a tear located approximately one inch from the column flange within the bottom flange base metal near the bottom access hole (see Section 3.2). This tear ultimately severed the bottom girder flange from the weld region and the column flange. The bottom flange tear initiated in the region of the access hole and propagated out towards the flange tips until the connection exhibited minimal strength during the third quarter cycle of the first cycle at 3.0%, at which time the girder flange was completely severed from the column flange. The failure may be

classified as a low-cycle fatigue failure, as it was a gradual failure that resulted from several stress reversals within the bottom flange.

Evidence of high straining in this region is seen in the strain gage data during the third quarter cycle of the first cycle at 2.0% in the East connection (see Figure H.10). In this region of the center and North flange tip of the bottom girder flange, the strains continue to be large during the 2.0% drift cycles (exhibiting peak-to-peak strain amplitudes as high as 60,000 to 70,000 με in gage hne2b). A decrease in strain amplitude is also observed after the third quarter cycle of the first cycle at 2.0% at the top surface of the North bottom flange tip (gage hne1b) and at the bottom surface of the bottom flange below the access hole (gage hse3b).

However, the East connection AE data does not correlate well with the supposition that the strain behavior mentioned above corresponds to the fracturing of the central underside weld region and the top of the North flange tip weld region during the third quarter cycle of the first cycle at 2.0% drift. In addition, Table H.1 shows that no East events occurred during this quarter cycle (Increments 53 and 54). Therefore, it is concluded that the lack of any AE indicates that the strain gages were merely malfunctioning after achieving large strains at this point in the loading. This seems particularly reasonable because no visual observations indicate structural damage in these areas either during the third quarter cycle or during the quarter cycles shortly after.

The AE data does correlate with the observation that North end of the bottom flange fractured completely and South flange tip remained intact after the failure noted during the third quarter cycle of the first cycle at 3.0% drift (see Figures H.10 and H.14). Figure H.23 also shows that only one event occurred with a source location at the southern end of the East bottom flange. This event had a source location of 11.5 in. and is one of the events highlighted by the dashed line labeled Line 3 in Figure H.23. Line 2 in Figure H.23 highlights the severing of the North flange tip.

The AE data also correlates with the actual failure of the East and West connections of Specimen 1. Figure H.21 is a Cumulative Events vs. AE Test Time chart for the East and West events that occurred during the third cycle at 2.0% drift and the first

cycle at 3.0% drift. Figure H.21 shows a pattern of gradually increasing AE activity within the East connection. Figure H.17 summarizes the events that occurred during the first five quarter cycles at 1.5% drift. Comparing Figure H.17 to Figure H.21 shows the differences between the event rate patterns for a brittle failure (West connection) and a low-cycle fatigue failure. The exponential increase in the event rate during the first quarter cycle of the second cycle at 1.5% drift (Increment 39) is indicative of brittle fracture. The more gradual increase in the event rate is indicative of a gradual release of strain energy that would accompany a low-cycle fatigue failure.

The gradual release of strain energy is more clearly illustrated in Figures H.22 and H.23. Figure H.23 is Source Location vs. AE Test Time chart for the East events that occurred during the third quarter cycle at 3.0% drift. This figure shows a series of events highlighted by a dashed line and labeled Line 1. A complete East beam end displacement increment is taking place during the occurrences of these events. This implies an ordered build up and release of strain energy accompanied the East connection failure.

H.3 Connection Strain Behavior and AE Activity Prior to Failure (Specimen 2)

The strains in the East connection region of Specimen 2 exhibit permanent strain shifts during positive girder bending at the first cycle of 0.50% drift (see Figures H.24 and H.25). This behavior may be attributed to the yielding within these regions of the East connection. The center of the bottom surface of the girder bottom flange continued to strain more than the North end, and especially the South end, up to the first cycle at 1.5% drift (see Figure H.28).

The top surface of the bottom, North girder flange tip of the West girder (gage hnw1b) exhibits a rapid increase in strain of approximately 1000 με during the positive girder bending at the first cycle at 0.25% drift (see Figures H.26 and H.27). Even though

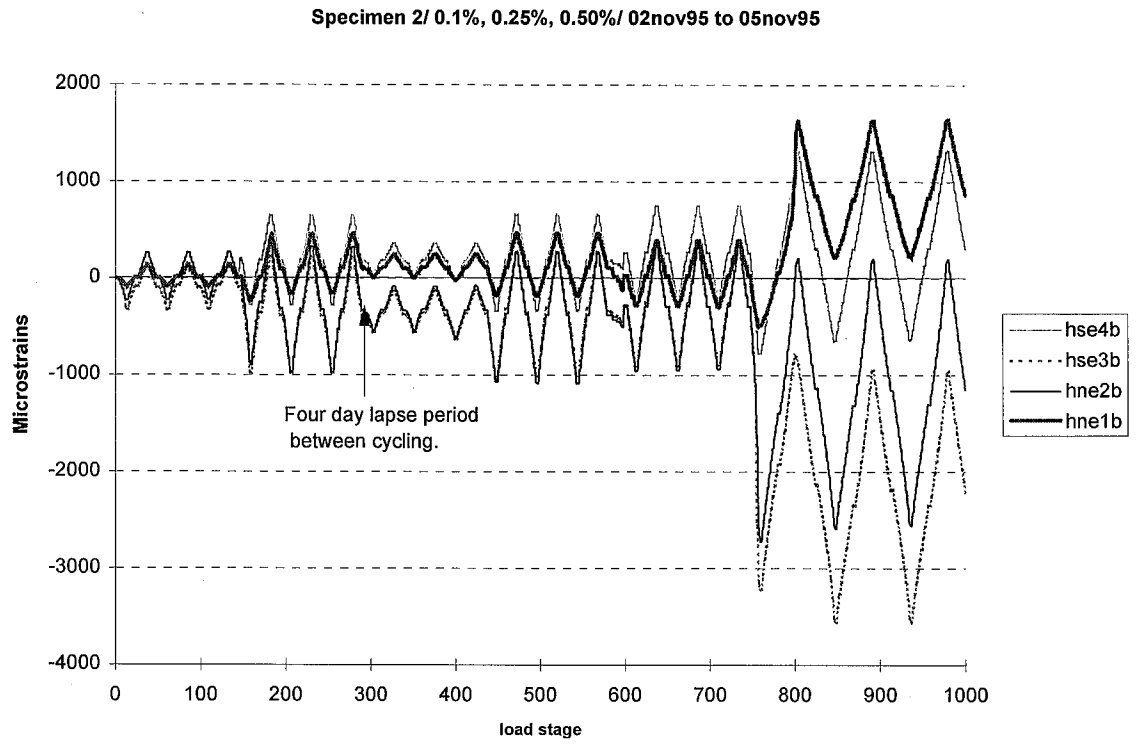

Figure H.24: Girder Bottom Flange Strains (East Girder of Specimen 2)

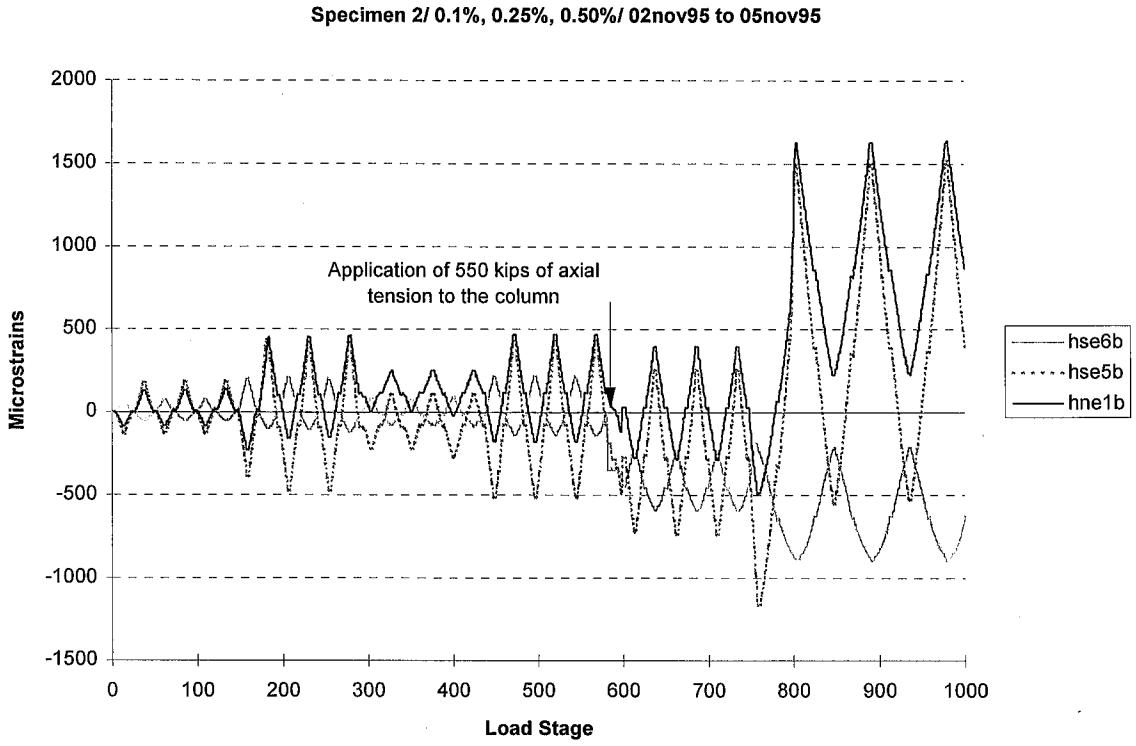

Figure H.25: Top and Bottom Access Hole Strains (East Girder of Specimen 2)

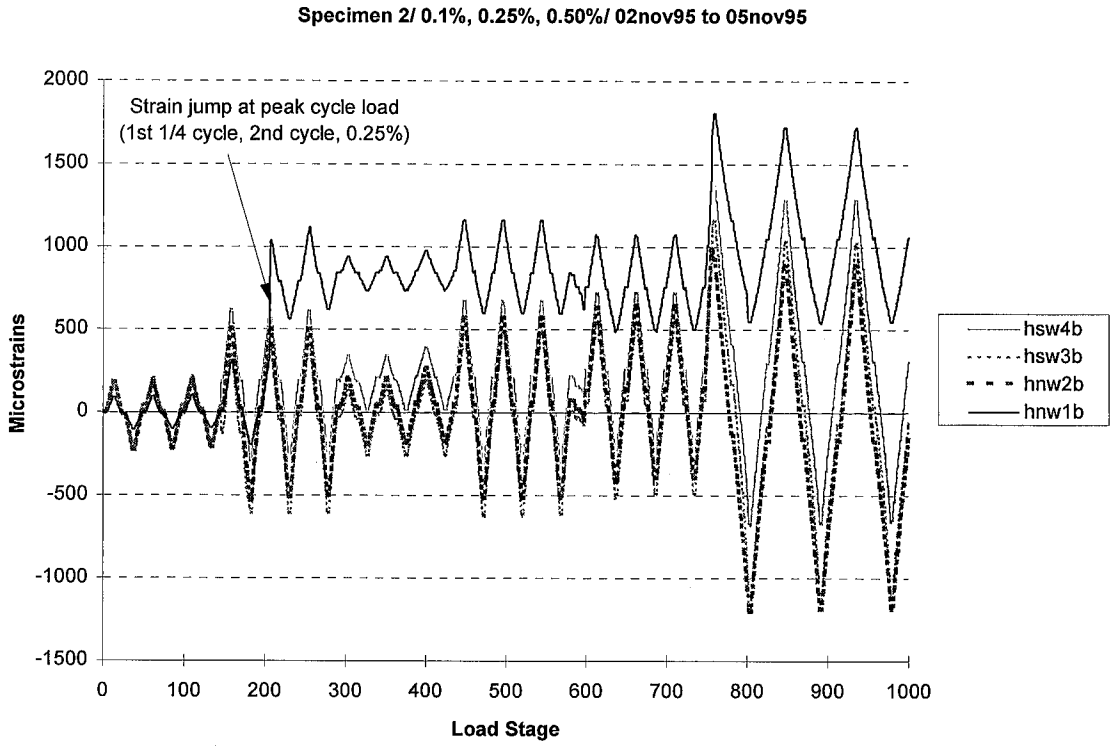

Figure H.26: Girder Bottom Flange Strains (West Girder of Specimen 2)

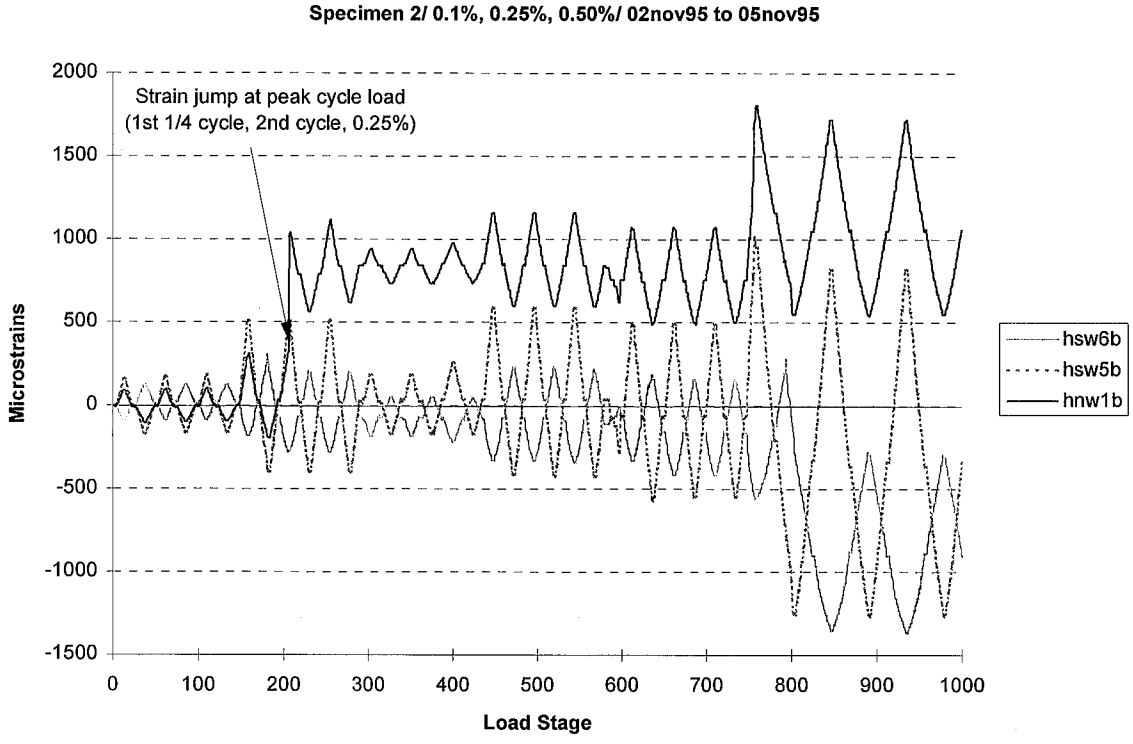

Figure H.27: Top and Bottom Access Hole Strains (West Girder of Specimen 2)

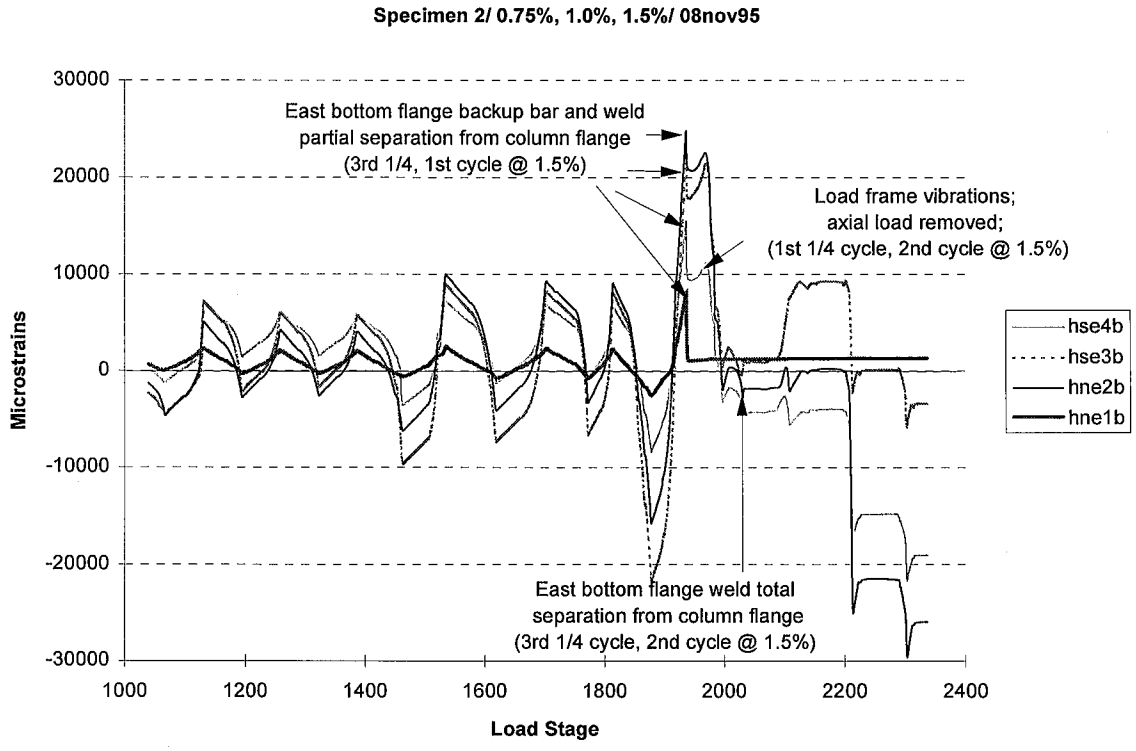

Figure H.28: Girder Bottom Flange Strains (East Girder of Specimen 2)

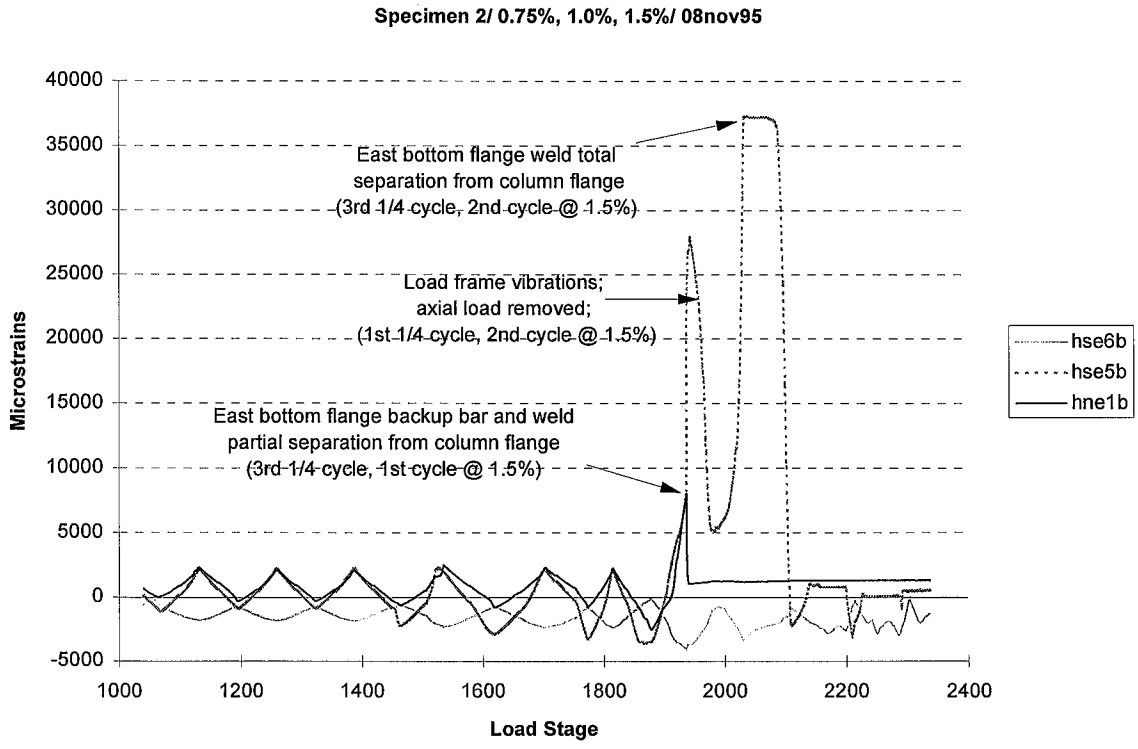

Figure H.29: Top and Bottom Access Hole Strains (East Girder of Specimen 2)

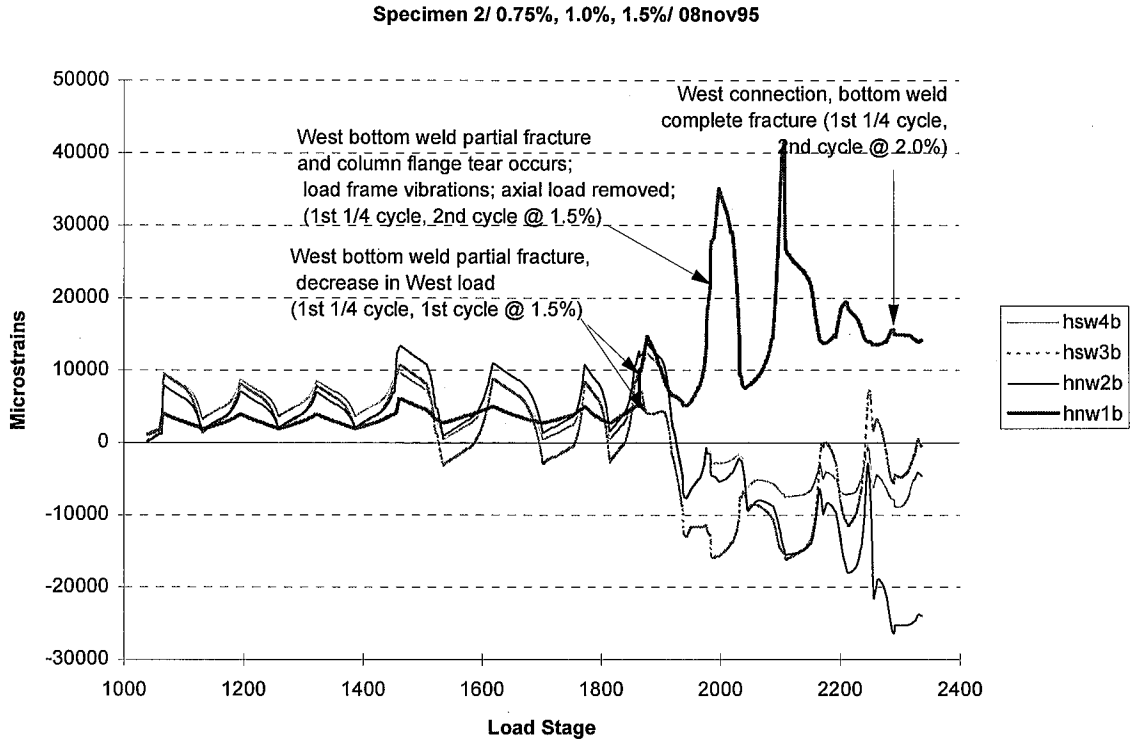

Figure H.30: Girder Bottom Flange Strains (West Girder of Specimen 2)

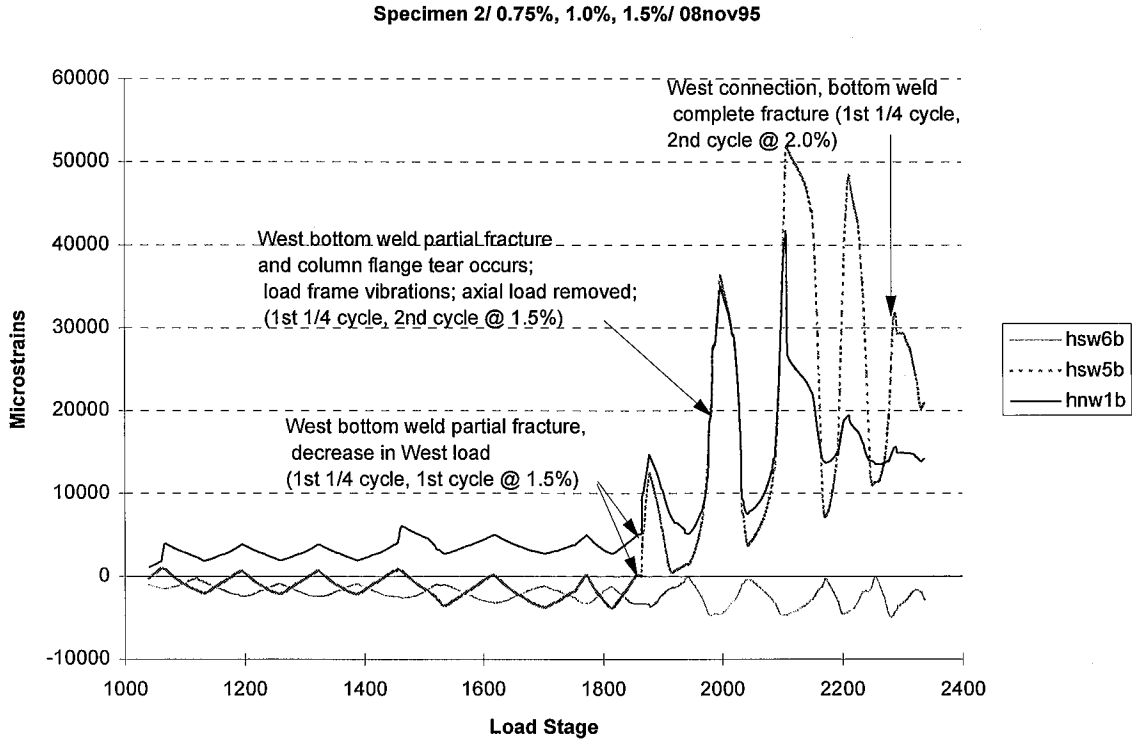

Figure H.31: Top and Bottom Access Hole Strains (West Girder of Specimen 2)

Table H.2: Loading Increment Data (Specimen 2)

Increment Number	Begin Stroke (in)	End Stroke (in)	Initial test time (min)	Final test time (min)	# of AE Events	Cum. Events	Percent drift	Quarter Cycle
1	0	-0.35	24.17	27.50	0	0	0.25	1
2	-0.35	0	29.50	33.00	0	0	0.25	2
3	0	0.35	33.83	38.00	0	0	0.25	3
4	0.35	0	38.67	42.00	0	0	0.25	4
5	0	-0.35	56.83	60.00	0	0	0.25	5
6	-0.35	0	61.50	64.67	0	0	0.25	6
7	0	0.35	65.83	69.17	0	0	0.25	7
8	0.35	0	70.50	74.00	0	0	0.25	8
9	0	-0.35	74.83	78.17	0	0	0.25	9
10	-0.35	0	79.33	82.67	0	0	0.25	10
11	0	0.35	83.83	87.17	0	0	0.25	11
12	0.35	0	88.00	91.33	0	0	0.25	12
13	0	-0.7	116.67	122.83	0	0	0.5	1
14	-0.7	0	142.17	152.17	0	0	0.5	2
15	0	0.7	188.67	195.00	0	0	0.5	3
16	0.7	0	203.50	209.83	0	0	0.5	4
17	0	-0.7	211.33	217.83	0	0	0.5	5
18	-0.7	0	219.00	225.33	0	0	0.5	6
19	0	0.7	227.00	233.50	0	0	0.5	7
20	0.7	0	234.83	241.17	0	0	0.5	8
21	0	-0.7	242.17	248.50	0	0	0.5	9
22	-0.7	0	249.67	256.00	0	0	0.5	10
23	0	0.7	257.33	263.67	0	0	0.5	11
24	0.7	0	265.00	271.13	0	0	0.5	12
25	0	-1.05	281.47	287.80	12	12	0.75	1
26	-1.05	0	323.47	329.80	0	12	0.75	2
27	0	1.05	332.13	338.47	8	20	0.75	3
28	1.05	0	360.05	366.30	0	20	0.75	4
29	0	-1.05	367.97	374.30	0	20	0.75	5
30	-1.05	0	375.30	381.63	0	20	0.75	6
31	0	1.05	383.13	389.30	2	22	0.75	7
32	1.05	0	390.30	396.80	0	22	0.75	8
33	0	-1.05	397.97	404.13	0	22	0.75	9
34	-1.05	0	405.63	411.63	0	22	0.75	10
35	0	1.05	413.63	419.97	0	22	0.75	11
36	1.05	0	421.30	426.63	0	22	0.75	12

Table H.2: Loading Increment Data (Specimen 2) (Cont.)

Increment Number	Begin Stroke (in)	End Stroke (in)	Initial test time (min)	Final test time (min)	# of AE Events	Cum. Events	Percent drift	Quarter Cycle
37	0	-1.05	426.97	433.30	0	22	1	1
38	-1.05	-1.4	434.95	438.97	7	29	1	1
39	-1.4	0	467.30	475.47	0	29	1	2
40	0	1.05	482.63	487.13	7	36	1	3
41	1.05	1.4	493.13	496.63	11	47	1	3
42	1.4	0	514.13	522.30	1	48	1	4
43	0	-1.4	528.30	536.47	4	52	1	5
44	-1.4	0	538.30	546.47	1	53	1	6
45	0	1.4	547.80	555.97	1	54	1	7
46	1.4	0	557.30	566.30	0	54	1	8
47	0	-1.4	635.30	640.80	0	54	1	9
48	-1.4	0	644.13	649.63	0	54	1	10
49	0	1.4	650.47	655.97	0	54	1	11
50	1.4	0	656.80	662.47	0	54	1	12
51	0	-1.4	663.80	669.30	1	55	1.5	1
52	-1.4	-1.9	674.13	677.30	8	63	1.5	1
53	-1.9	-2.1	682.30	685.30	16	79	1.5	1
54	-2.1	0	697.13	702.70	1	80	1.5	2
55	0	1.4	704.17	709.60	7	87	1.5	3
56	1.4	2	712.63	718.13	40	127	1.5	3
57	2	2.1	747.30	748.47	3	130	1.5	3
58	2.1	0	749.47	754.97	9	139	1.5	4
59	0	-1.6	761.30	766.53	16	155	1.5	5
60	-1.6	-1.8	785.47	786.50	14	169	1.5	5
61	-1.8	-2.1	787.50	791.17	165	334	1.5	5
62	-2.1	0	793.00	799.83	0	334	1.5	6
63	0	1.36	846.67	852.50	115	449	1.5	7
64	1.36	2.1	864.83	868.42	53	502	1.5	7
65	2.1	0	869.08	878.67	24	526	1.5	8
66	0	-2.1	885.67	893.00	48	574	1.5	9
67	-2.1	0	896.33	906.17	49	623	1.5	10
68	0	2.1	907.67	913.55	100	723	1.5	11
69	2.1	0	915.02	920.67	38	761	1.5	12
70	0	-2.8	920.67	927.72	119	880	2	1
71	-2.8	0	928.67	933.83	64	944	2	2
72	0	2.8	936.33	943.33	183	1127	2	3
73	2.8	0	944.00	951.17	66	1193	2	4
74	0	-1.9	951.33	956.17	74	1267	2	5
75	-1.9	-2.8	967.50	971.17	14	1281	2	5
76	-2.8	0	971.50	978.50	112	1393	2	6
77	0	0.77	979.83	981.83	107	1500	2	7
78	0.77	0	1001.00	1003.17	10	1510	2	8

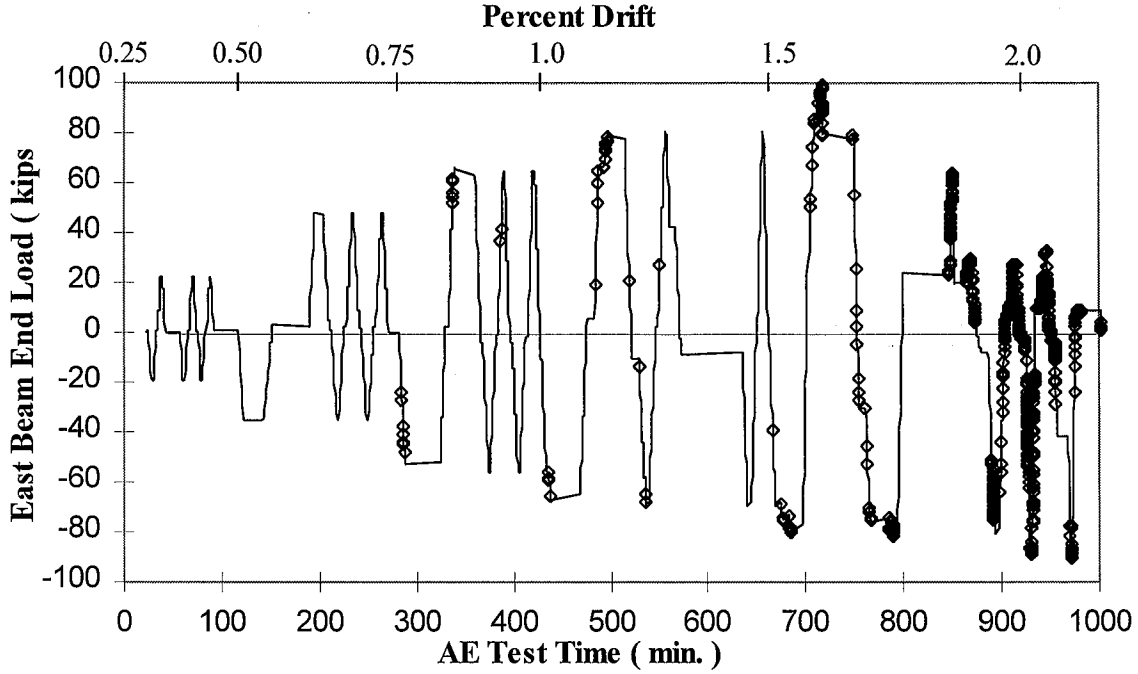

Figure H.32: AE Activity Loading History (East Connection of Specimen 2)

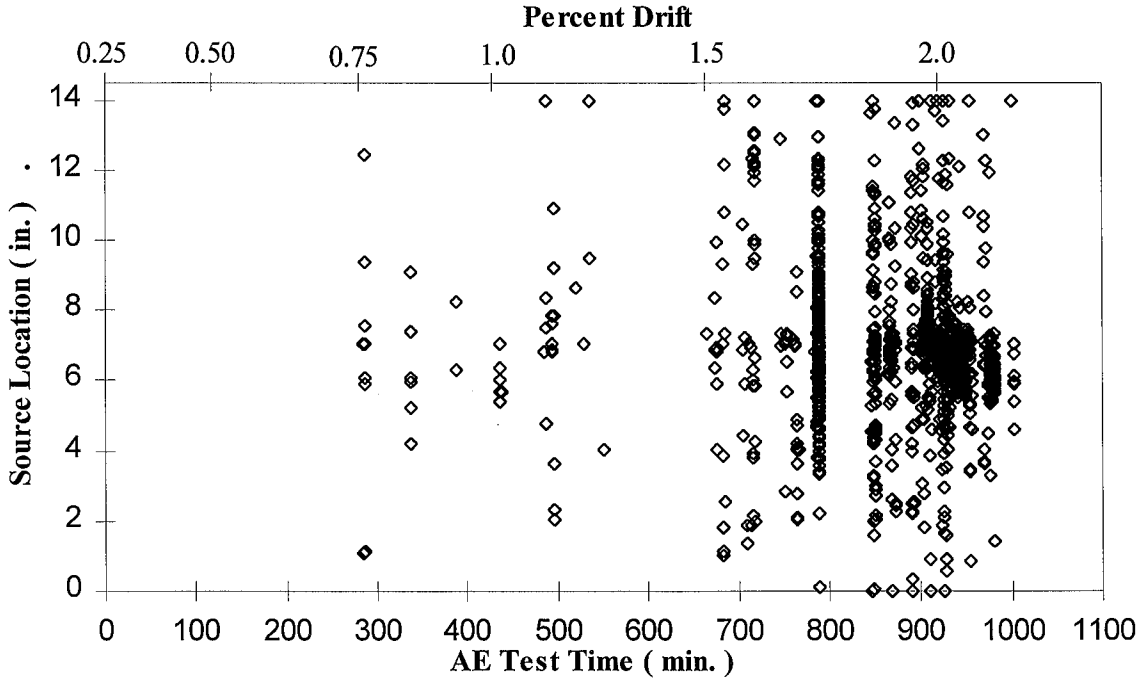

Figure H.33: AE Source Location vs. AE Test Time
(East Connection of Specimen 2)

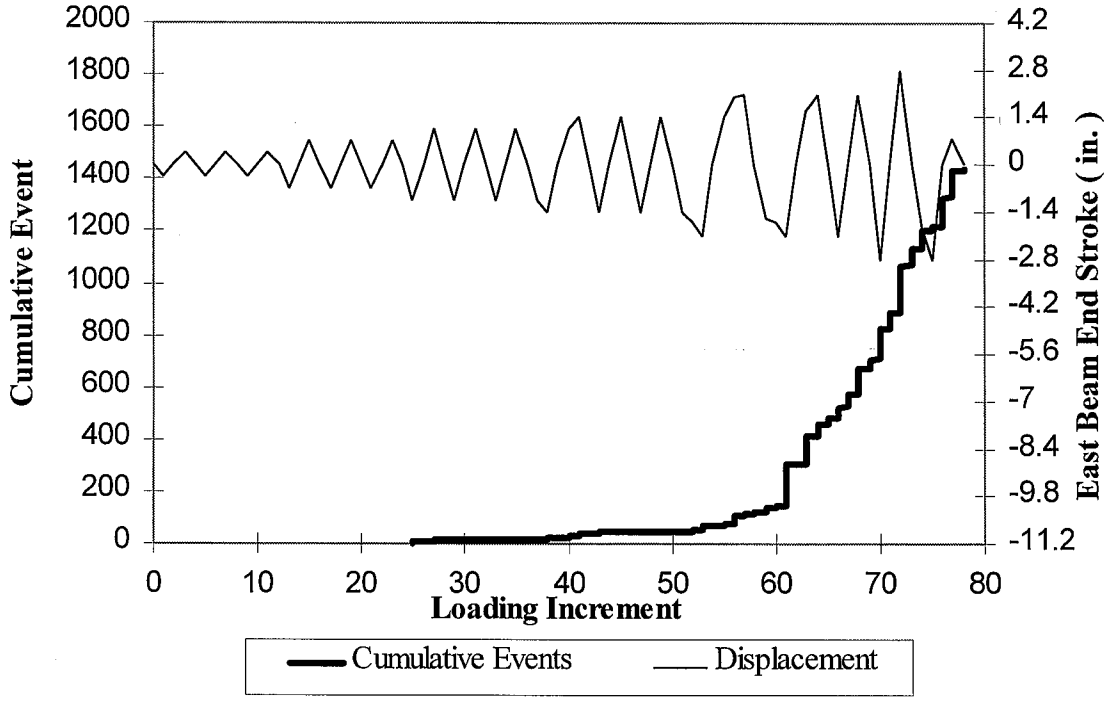

Figure H.34: Cumulative Events vs. Loading Increment (Specimen 2)

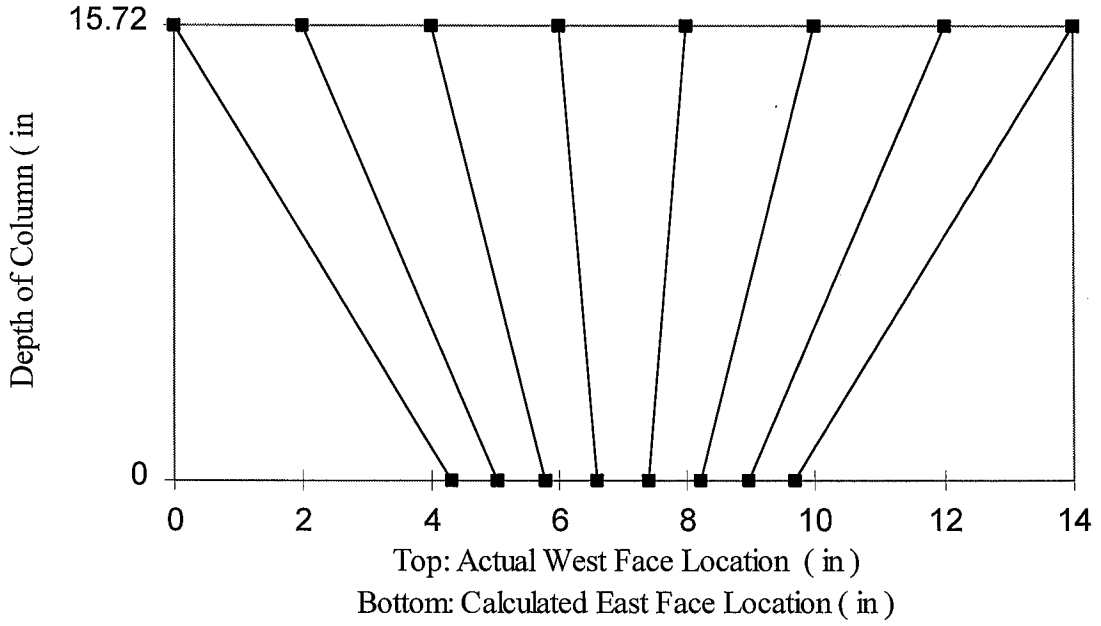

Figure H.35: AE Source Location Error (Specimen 2)

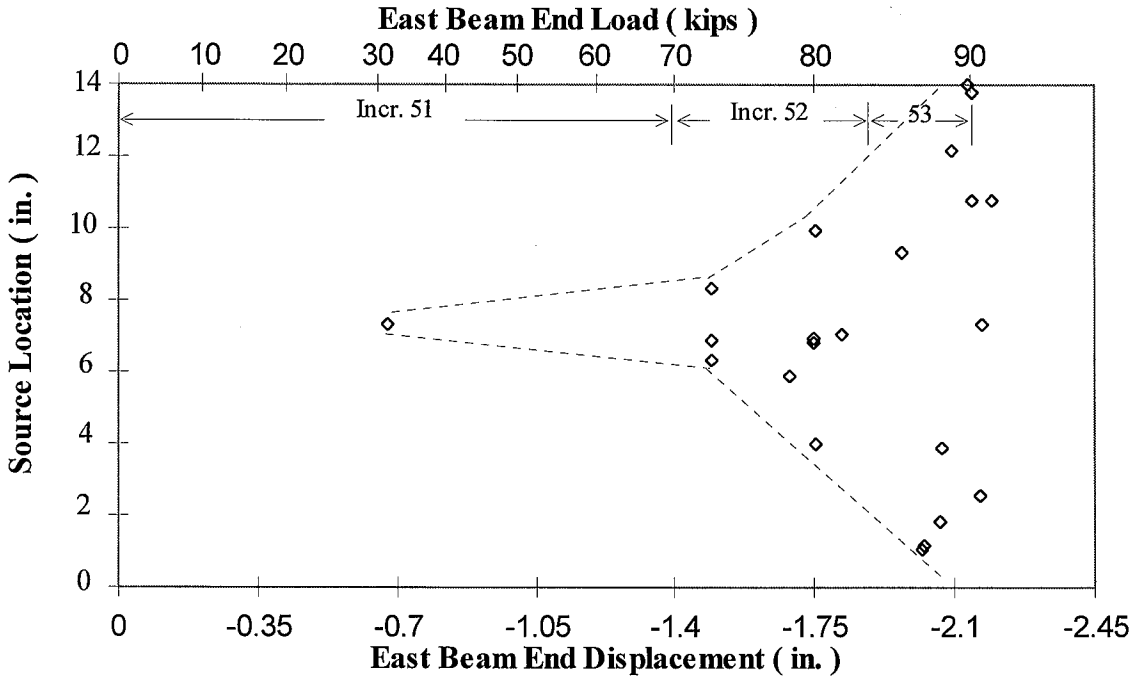

Figure H.36: AE Source Location vs. Load and Displacement
(First quarter cycle of the first cycle at 1.5% drift/ East Connection of Specimen 2)

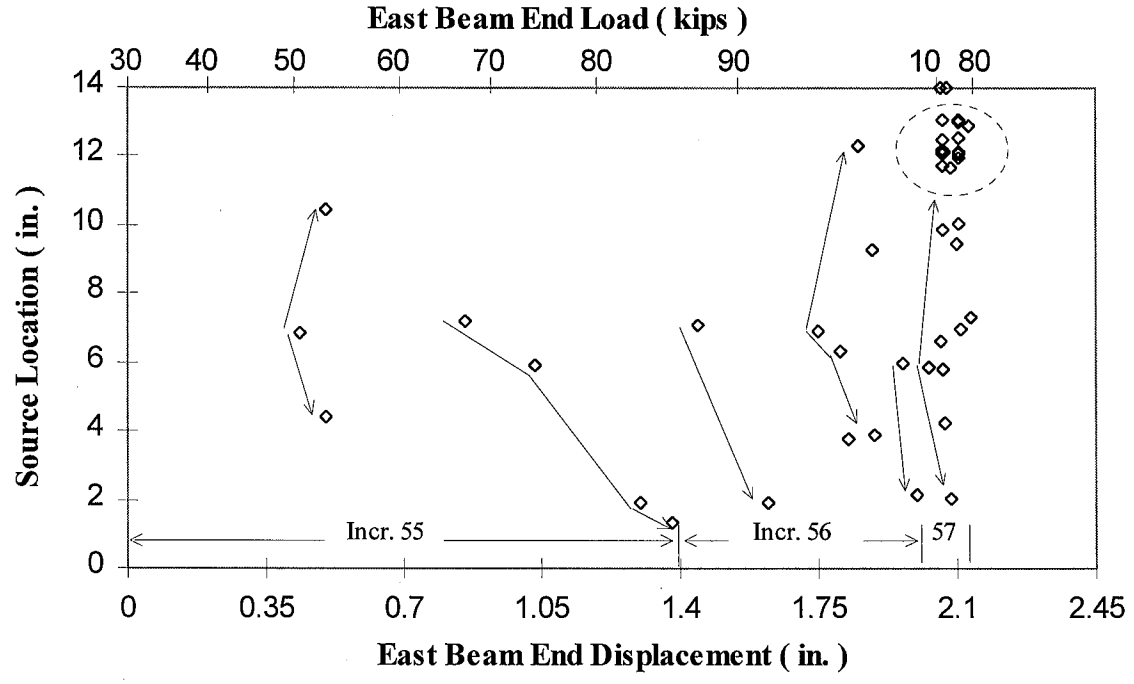

Figure H.37: AE Source Location vs. Load and Displacement
(Third quarter cycle of the first cycle at 1.5% drift/ East Connection of Specimen 2)

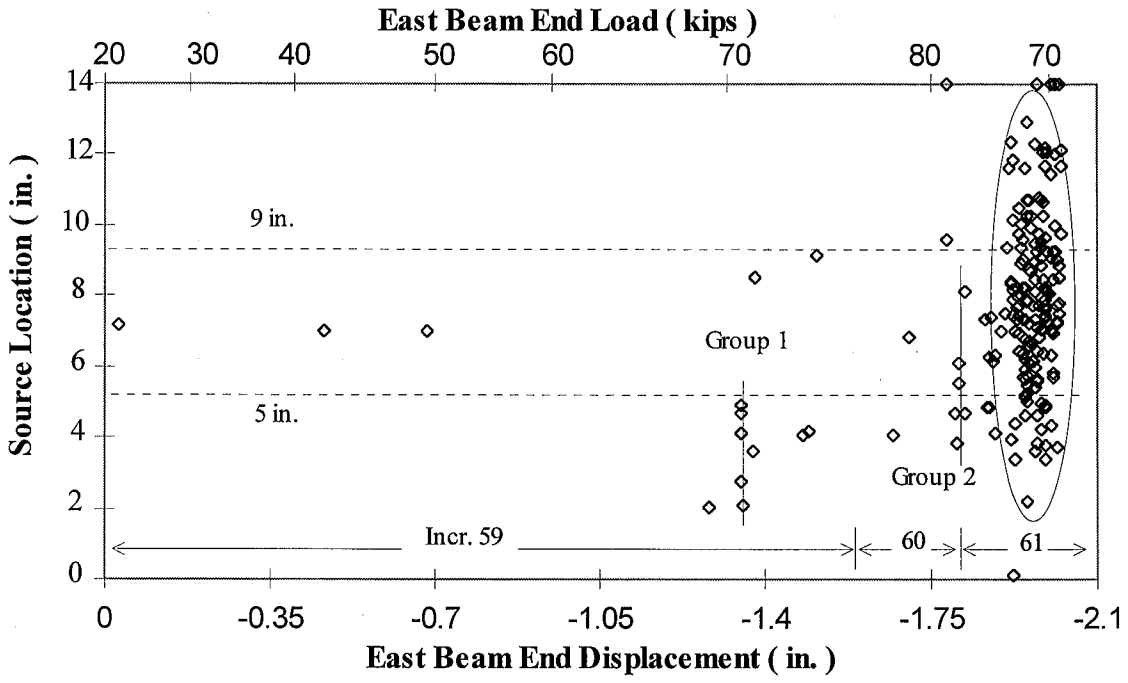

Figure H.38: AE Source Location vs. Load and Displacement
(First quarter cycle of the second cycle at 1.5% drift/ East Connection of Specimen 2)

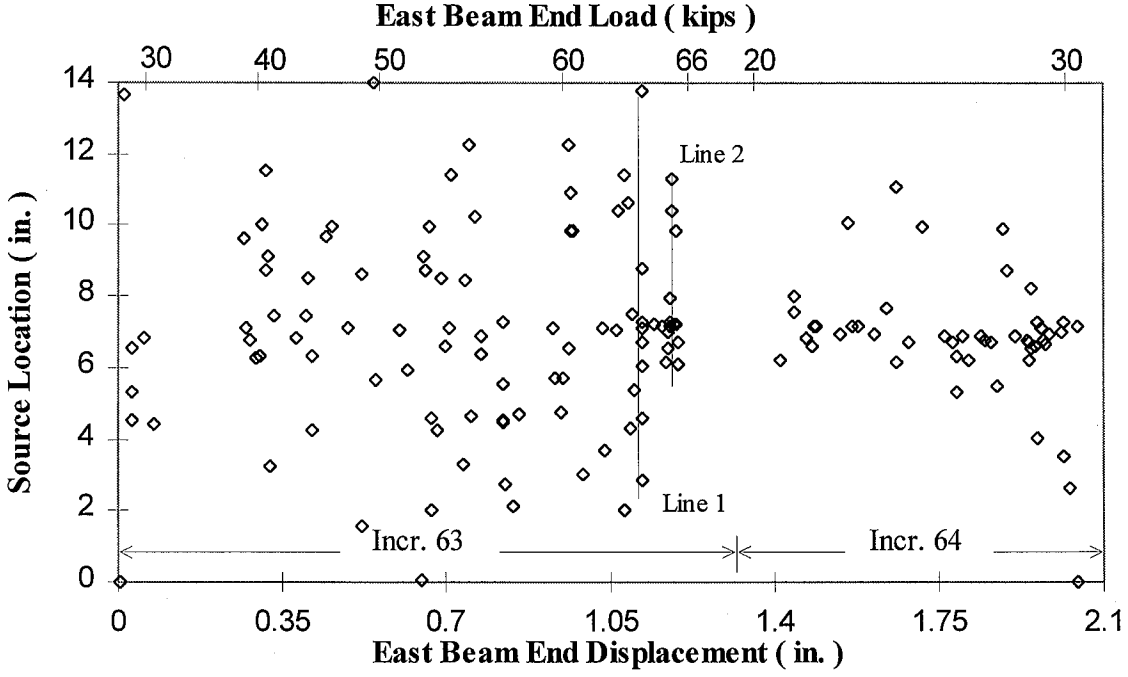

Figure H.39: AE Source Location vs. Load and Displacement
(Third quarter cycle of the second cycle at 1.5% drift/ East Connection of Specimen 2)

this increase is significant, substantial yielding does not reoccur until the 0.5% drift cycles. Permanent strain shifts in the West connection of Specimen 2 are first observed near the top and bottom access holes during positive girder bending at the first cycle of 0.50% drift (see Figure H.27). This is in contrast to Specimen 1, where the strain gages showed little permanent deformation during the 0.5% drift cycle (see Figures H.6-H.8). The strain amplitudes across the width of the bottom flange of the West girder are similar in magnitude during the 0.75% drift cycles (see Fig. H.30). During the 1.0% drift levels, however, the center region of the bottom surface of the West bottom flange demonstrates larger strains than the bottom surface of the flange tips.

No correlation between the AE data the net strain increases that occurred during the 0.25% drift and 0.5% drift cycles is evident. No bottom flange AE activity occurred during any of the cycles at 0.25% and 0.5% drift. This is not surprising since yielding is a ductile phenomena and not necessarily accompanied by micro fracture that is needed to produce AE. During the 0.75% drift and 1.0% drift cycles, the majority of the AE activity occurred during the first cycles. This is expected since the test specimens were exposed to new load levels only during the first cycle (i.e., the largest East and West connection strains during the 0.75% and 1.0% drift cycles occurred during the first cycles; see Figures H.28-31).

H.4 Connection Strain Behavior and AE Activity At Failure (Specimen 2)

The East connection of Specimen 2 failed in a brittle fashion, similar to the failure mode of the West connection of Specimen 1, during the 1.5% drift cycles; the connection failed primarily at two points in the load history. The bottom weld partially fractured from the column flange and the bottom backup bar completely separated from the column flange during the third quarter cycle of the first cycle at 1.5% drift. Prior to this event, the strains at the bottom surface of the East bottom flange near the South region and the

North and center regions were approximately 15,000 με and 25,000 με, respectively (see Figure H.28).

After the first event of fracturing of the East connection, the strain amplitudes at the bottom surface of the bottom flange (hse2b, hse3b, and hse4b) and the top surface of the North flange tip (hne1b) decreased significantly (see Figure H.28). In addition, the strains near the bottom access hole located near the top surface of the bottom flange increased dramatically (see Figure H.29, gage hse5b). This behavior indicates that the bottom region of the bottom weld was partially fracturing from the column flange, and that the upper portion of the bottom weld near the center of the girder flange remained connected to the column flange, resulting in a high strain condition at the top surface of the bottom flange below the bottom access hole. This behavior was confirmed by visual observations that the middle portion of the bottom weld was still intact to the column flange after the first cycle at 1.5% drift. It is important to note that a drop in strain may correspond to failure of a strain gage rather than a release in strain due to weld fracture.

The second event corresponding to fracture of the East connection bottom weld occurred during the third quarter cycle of the second cycle at 1.5% drift, at which time the bottom weld completely fractured from the column flange. Again, it is evident that strains near the bottom access hole at the top surface of the bottom flange (hse5b) achieved strain magnitudes of nearly 37,000 με, while the strain behavior along the entire bottom surface of the bottom flange was minimal (see Figures H.28 and H.29). This behavior may confirm that only the upper portion of the bottom weld near the bottom access hole remained connected to the column flange prior to the complete fracture of the bottom weld. However, it is again important to note that a drop in strain may correspond to failure of a strain gage.

The AE data measured at the East column flange of Specimen 2 correlate well with the fracture behavior exhibited by the strains in the connection (see Table H.2, Figures H.32 to H.34). Figure H.34 shows a jump in the cumulative events during Increment 56. Table H.2 shows that 40 events occurred during Increment 56, which is one of the increments that compose the third quarter cycle of the first cycle at 1.5% drift

(Increments 55 through 57). The forty events constituted over a 40% increase in AE activity. An increase of this magnitude is indicative of significant structural damage.

The East event source locations also correlate with the strain data. It is likely that the central portion of the bottom of the bottom flange failed first because the strains near the center of the bottom of the bottom flange (hse3b, Figure H.28) were very high during the third quarter cycle of the first cycle at 1.5% drift. Figure H.37 is a Source Location vs. Load and Displacement chart for the third quarter cycle of the first cycle at 1.5% drift, and clearly shows several patterns of event source locations. Recall that the 0" and 14" source location for this connection corresponds to the South and North girder flange tips, respectively. All of them are indicative of crack propagation from the central portion of the East bottom flange weld towards the flange tips. In addition, Figure H.37 clearly shows a concentration of AE activity at a source location of 12 in. This correlates with the large strain losses in the North bottom flange strain gages (hne1b and hne2b, Figure H.28). The accuracy of the AE source locations precludes the source location of events across the thickness of the weld. Therefore, the AE can neither confirm nor deny the supposition that the underside of the bottom flange failed and the top surface did not.

Figure H.34 shows a substantial increase in the number of events during Increment 63, which occurs during the third quarter cycle of the second cycle at 1.5% drift. Table H.2 shows that a total of 168 events occurred during this quarter cycle at 1.5% drift (Increments 63 and 64). This behavior corresponds to an increase of nearly 50% in AE activity and is consistent with the existence of significant structural damage to the bottom connection region.

Figure H.39 is a Source Location vs. Load and Displacement chart for the third quarter cycle of the second cycle at 1.5% drift. This figure shows that AE events have source locations that span the entire 14 in. flange width up to an East beam end displacement of 1.2 in. After this point, the East beam end load decreases rapidly and the AE activity ceases until a 1.4 in. East beam end displacement is achieved. At this point, the events have source locations within a relatively narrow band near 7 in. These patterns suggest that complete failure of the East beam occurred at an actuator stroke at 1.2 in.

The events that came after 1.4 in. probably originated from the East beam shear tab. The shear tab was subjected to substantial load after the fracture of the East beam bottom flange.

The West connection also demonstrated a brittle fracture of the bottom weld that occurred in a multi-step fashion starting at the 1.5% drift cycles. However, this fracture also extended into both flanges of the column (see Section 3.2). The first major event of the fracturing of the bottom weld occurred during the first quarter cycle of the first cycle at 1.5% drift (see Figures H.30 and H.31). During this load excursion, the strain magnitudes at the bottom surface, center region of the bottom flange decreased several thousand microstrain, while the top surface of the bottom flange near the access hole as well as the flange tips continued to show increases in strain. As the loading excursion continued, the strains at the bottom surface near the North and South bottom flange tips also decreased in strain. This behavior may due to fracturing that starts near the center and bottom portion of the bottom weld and continues out towards the flange tips. It is also possible that the decreases in strain are not due to micro-fracturing, but rather strain gage failure at this point in the load history.

During the first quarter cycle of the second cycle at the 1.5% drift cycles, a pull-out type column flange fracture occurred (see Section 3.2). The fracture of the North column flange began at the North girder flange tip and extended nearly 6 inches towards the column web region. This fracture is visible on both the outside and inside surfaces of the Northwest column flange. There is also evidence of a horizontal crack that is 2 inches in length located on the outside surface of the column flange, positioned 2 inches above the center of the bottom weld. At the South end of the bottom flange, the fracture line is visible on the column flange tip surface, where it extends up into the column flange surface approximately 0.5." Also, a crack propagated horizontally across the inside of the South column flange surface near the column web and above the bottom continuity plate. Therefore, it may be concluded that a substantial amount of the West column flange was severed due to the fracture of the West welded girder-to-column connection.

During the loading excursion at which the column flange tear occurred, the strain magnitudes were minimal along the bottom surface of the bottom flange, but were approximately 35,000 με at the top surface of the bottom flange near the bottom access hole and the North flange tip (gages hsw5b & hnw1b) (see Figure H.31). This strain behavior implies that the top interface of the bottom weld had not yet fractured from the column flange at this point in the load history. Note that during this loading progression, the partial failure of the West connection region may have caused several jumps in strain magnitude within the West, and possibly the East, connection regions. This event also generated large vibrations throughout the load frame and resulted in the removal of the 550 kips of axial tension applied to the column.

The strains at the top surface of the West connection bottom flange near the bottom access hole (gage hsw5b) continued to increase up through the third cycle at the 1.5% drift levels, where they reach a peak strain of 54,000 με, while strains near the top surface of the North bottom flange tip (gage hnw1b) decrease (see Figure H.31). This strain behavior implies that once the North region top surface of the bottom flange fractured from the column flange, the weld region near the bottom access hole was required to carry a substantial amount of the girder moment, thereby, increasing the strain within this region. Complete failure of the West bottom weld occurred during the first quarter cycle of the second cycle at 2.0% drift, at which time a sudden drop in strain near the bottom access hole is observed. It is again important to note that a drop in strain may correspond to failure of a strain gage rather than a release in strain due to weld fracture.

As previously stated, only the East face of the East column flange of Specimen 2 possessed AE transducers, and so source locations of the West connection region, which are interpreted from the East connection transducer array, may be erroneous (see Figure H.35). However, some interpretation of the fracturing of the West bottom connection of Specimen 2 may be reported based on the AE activity measured with the East connection transducer array.

The partial fracture of the West bottom flange weld of Specimen 2 during the first quarter cycle at 1.5% drift is supported by the AE event rate data. Figure H.36 shows that

a minor increase in the AE activity occurred during the first quarter cycle at 1.5% drift (Increments 51 through 53). The minor appearance of the increase in first quarter cycle AE activity is due to the scale of Figure H.36. Table H.2 shows that 25 events occurred during the first quarter cycle, resulting in a 45% increase in AE activity. The percent increase in AE activity suggests that significant structural damage occurred. As stated before, the source locations of the events are not useful for correlation to West connection failure patterns.

The West connection failure progressed during the first quarter cycle of the second cycle at 1.5% drift. Figure H.38 clearly shows a dramatic increase in the AE activity during the this quarter cycle at 1.5% drift (Increments 59 through 61). Table H.2 and Figure H.38 show that 195 events occurred during this quarter cycle, a 140% increase in AE activity. This is clearly consistent with the failure that occurred at this point; however, the separation was not complete. The top central region of the bottom flange weld remained connected to the column flange, causing a tear into the column flange. Figures H.34 and H.39 illustrate that the AE activity continued to increase rapidly after the first quarter cycle of the second cycle at 1.5% drift (i.e., after Increment 61). This may indicate that some portion of the bottom flange region was still connected to the column, since if complete separation of the bottom flange occurred, the bottom flange AE activity would decrease dramatically after the failures of both the East and West bottom flange welds.

H.5 Connection Strain Behavior and AE Activity Prior to Failure (Specimen 3)

Permanent tensile strain offsets within the bottom flange region of the East and West connections of Specimen 3 are evident during the 0.50% and 0.75% drift cycles (see Figures H.40 to H.43). The regions near the bottom access holes of the East and West connections also exhibited permanent tensile straining during the 1.5% to 2.0% and 2.0% to 3.0% drift levels, respectively (see Figures H.45, H.47, H.49, and H.51; gage hsw5b).

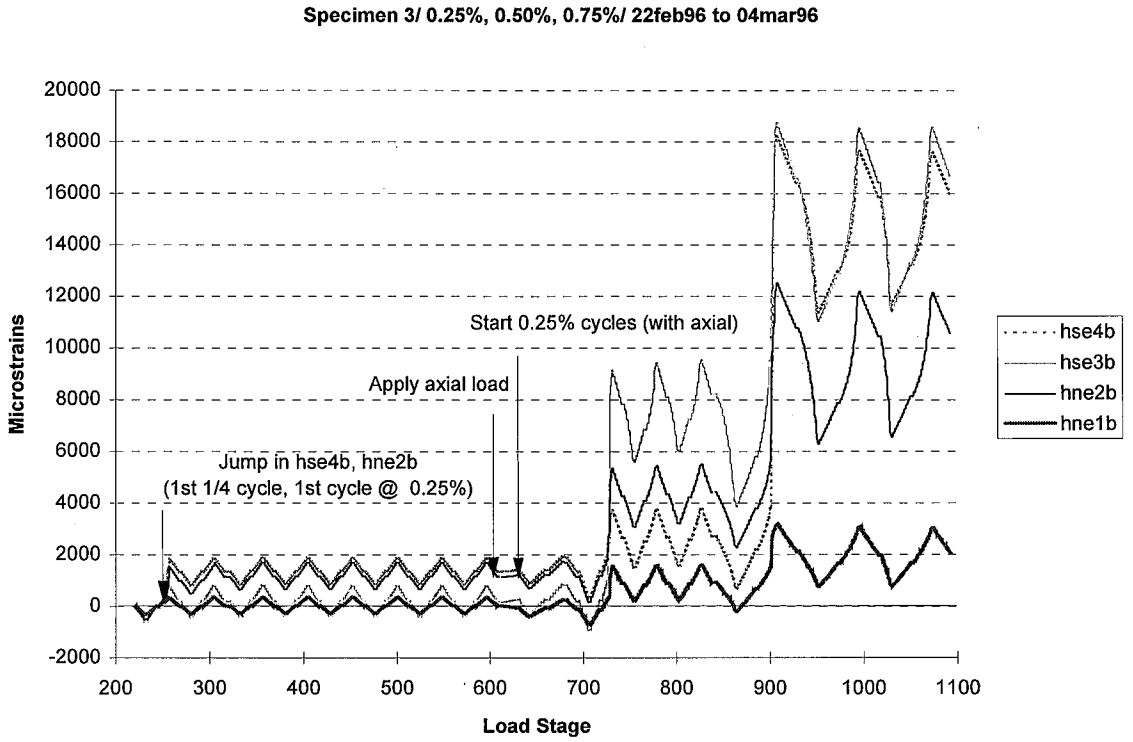

Figure H.40: Girder Bottom Flange Strains (East Girder of Specimen 3)

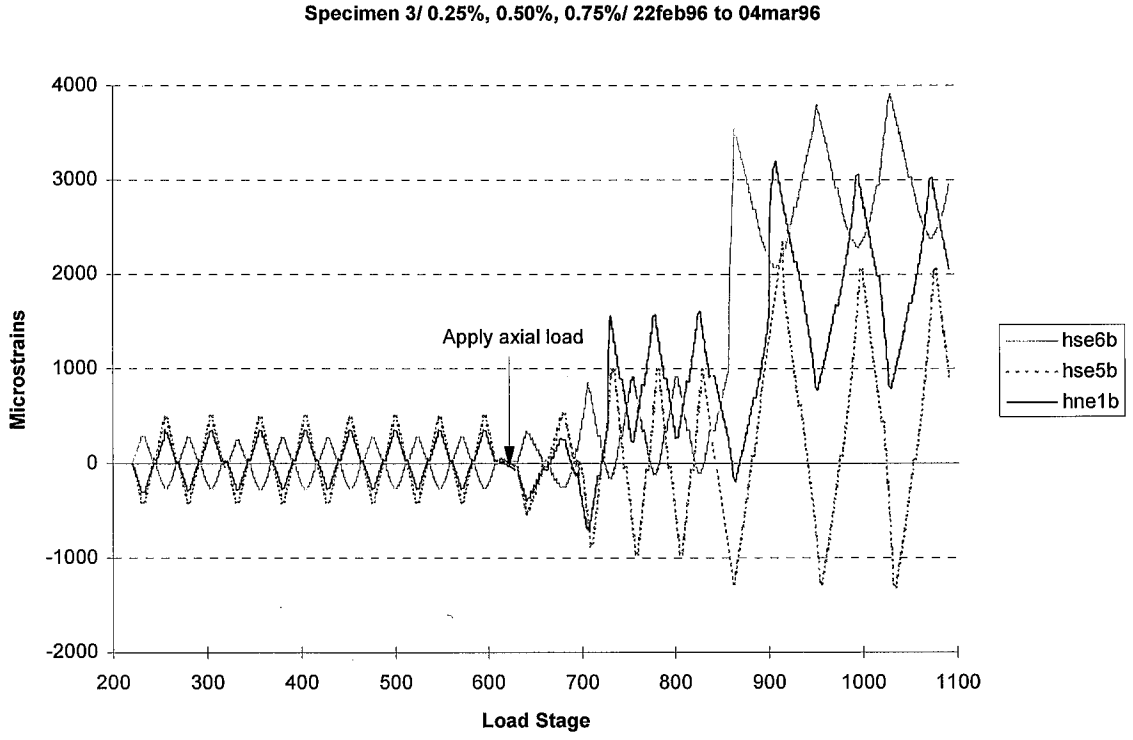

Figure H.41: Top and Bottom Access Hole Strains (East Girder of Specimen 3)

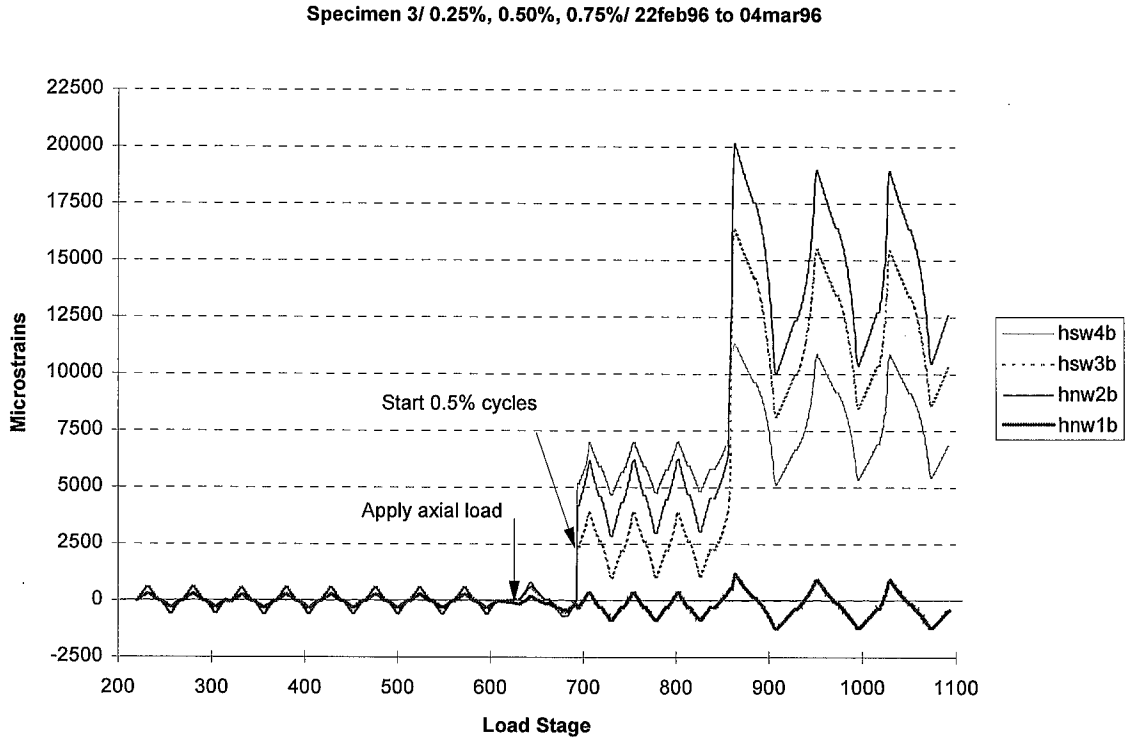

Figure H.42: Girder Bottom Flange Strains (West Girder of Specimen 3)

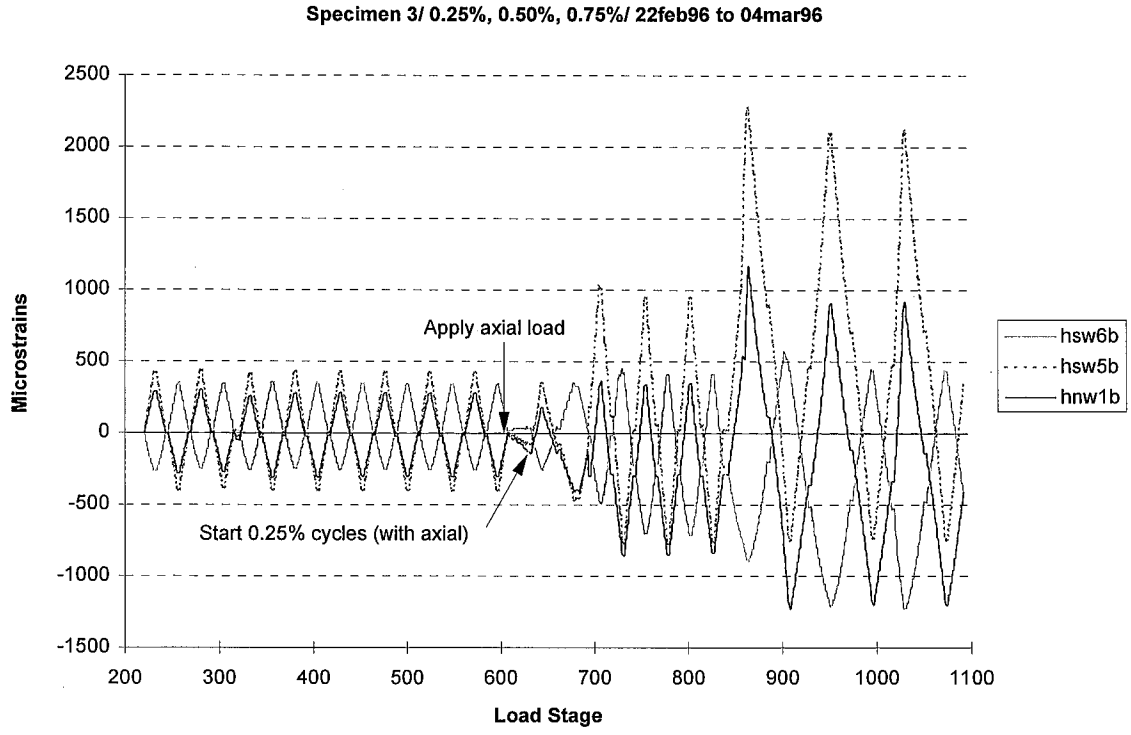

Figure H.43: Top and Bottom Access Hole Strains (West Girder of Specimen 3)

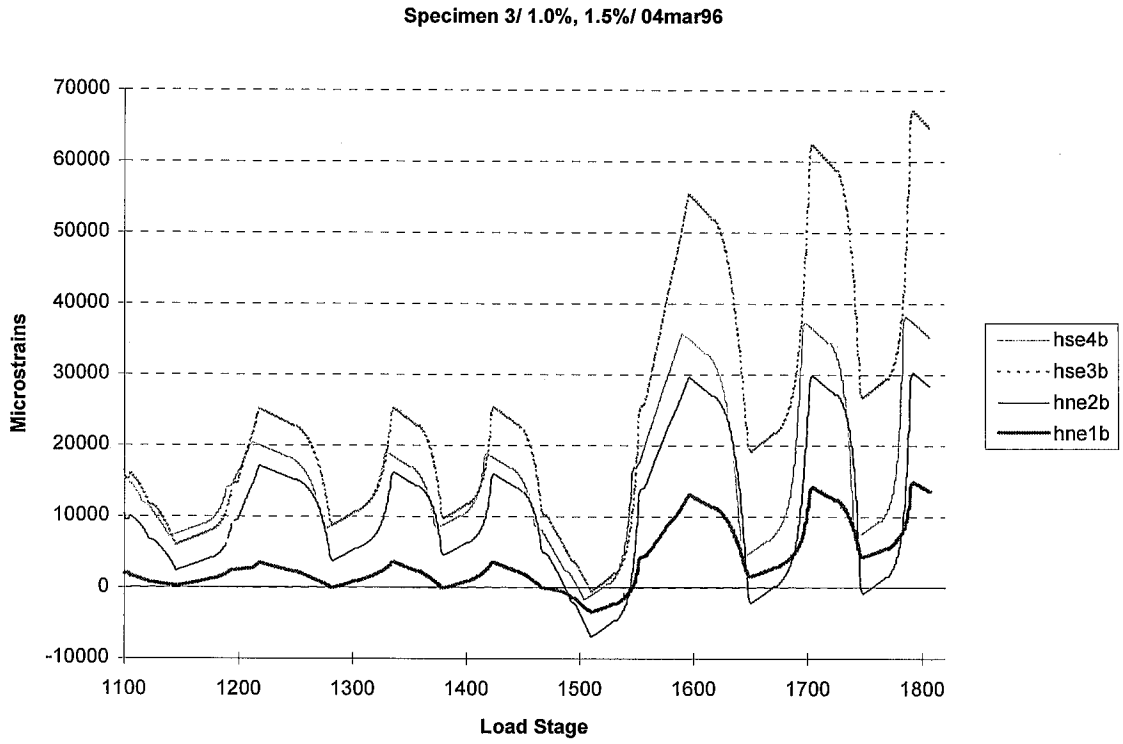

Figure H.44: Girder Bottom Flange Strains (East Girder of Specimen 3)

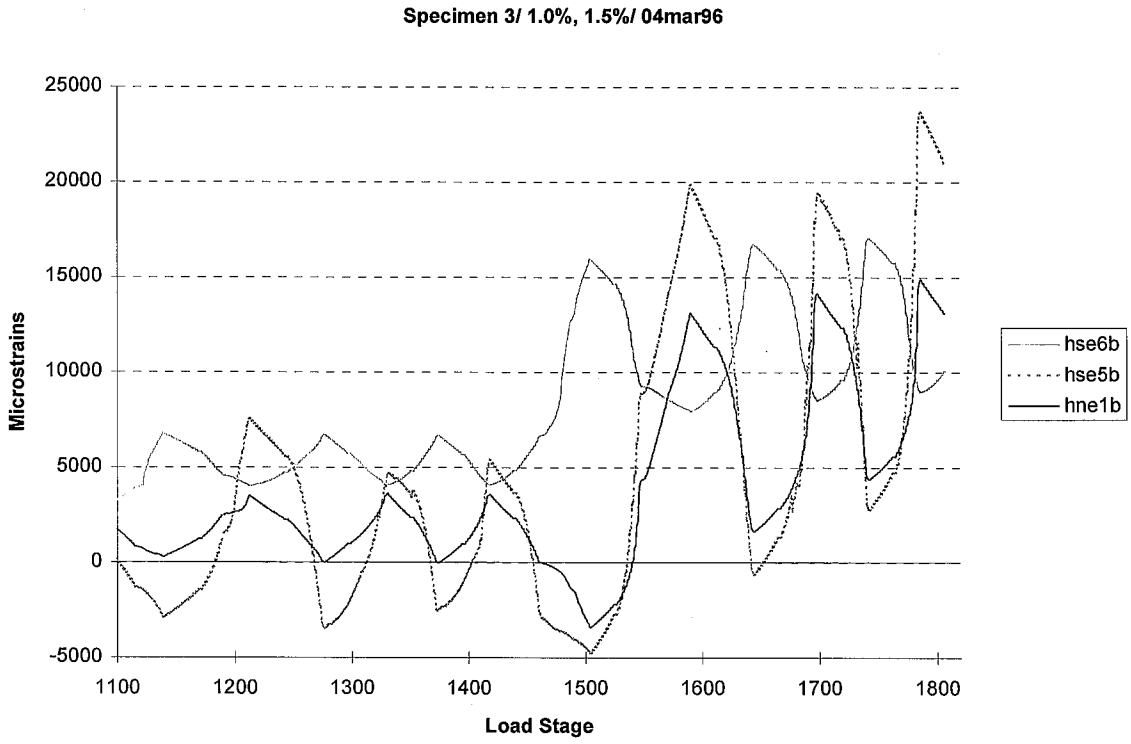

Figure H.45: Top and Bottom Access Hole Strains (East Girder of Specimen 3)

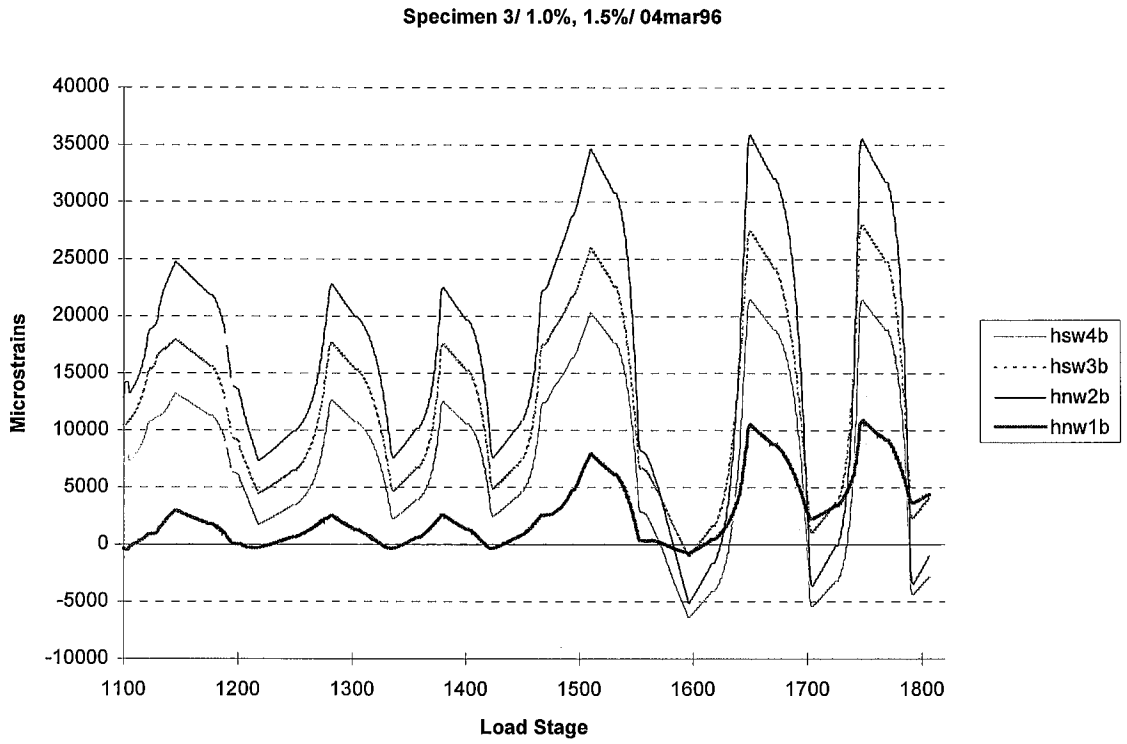

Figure H.46: Girder Bottom Flange Strains (West Girder of Specimen 3)

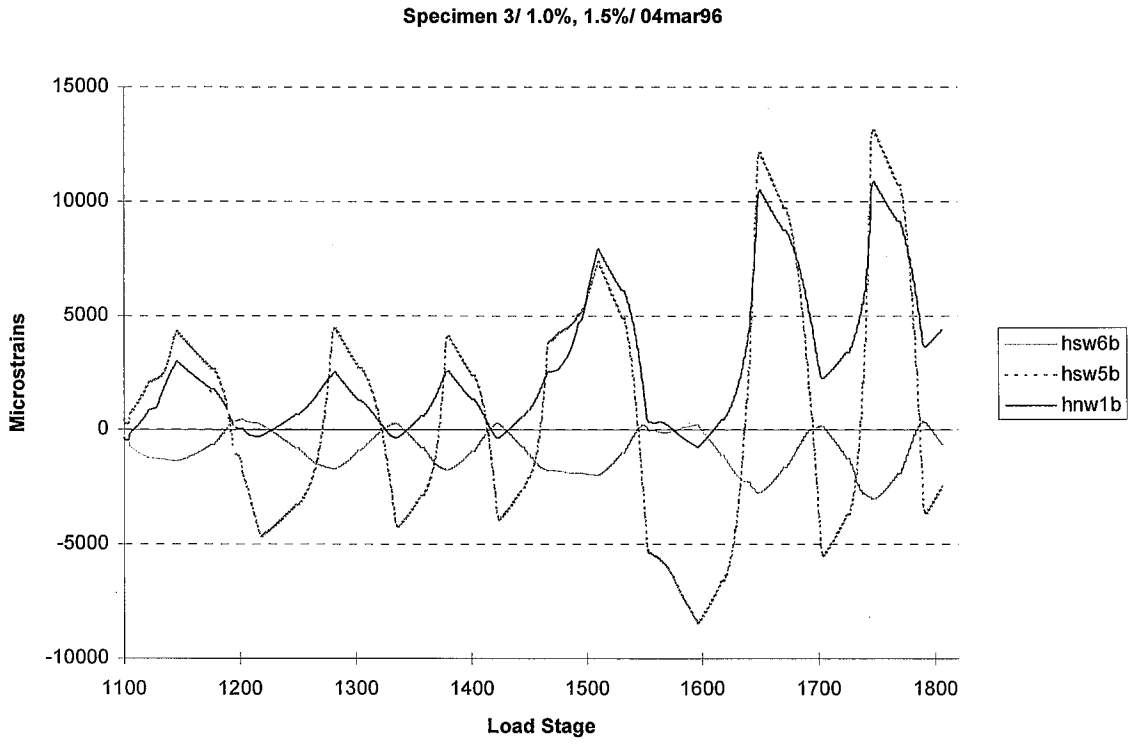

Figure H.47: Top and Bottom Access Hole Strains (West Girder of Specimen 3)

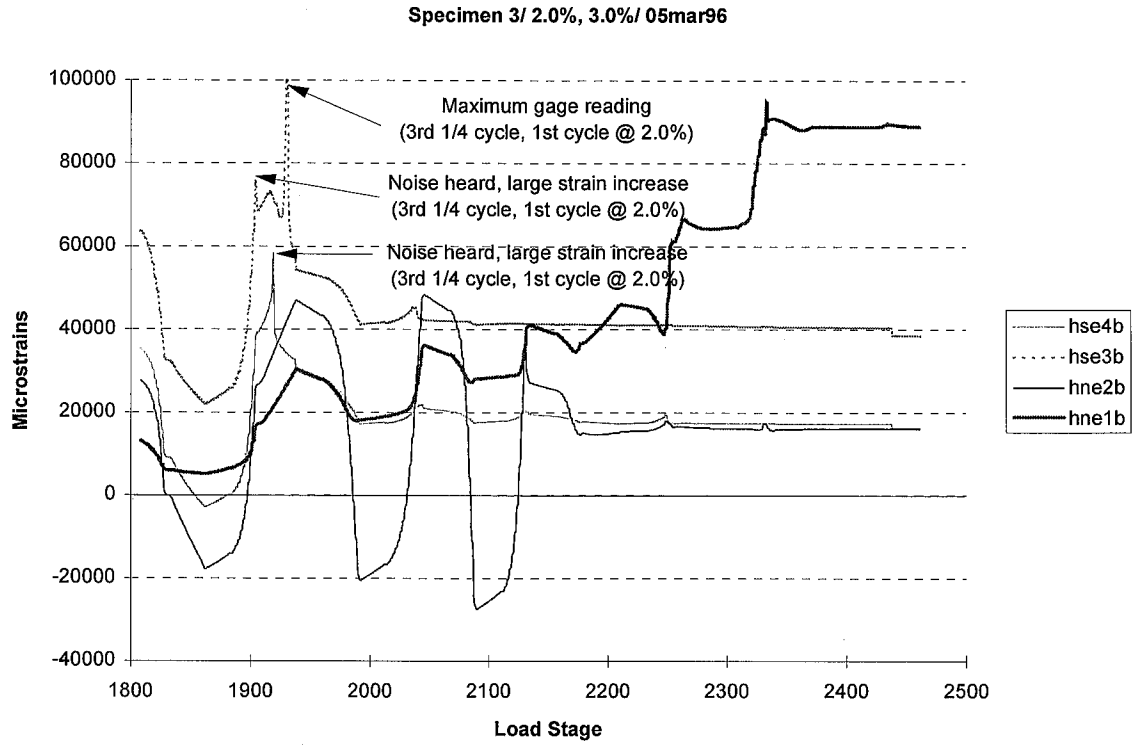

Figure H.48: Girder Bottom Flange Strains (East Girder of Specimen 3)

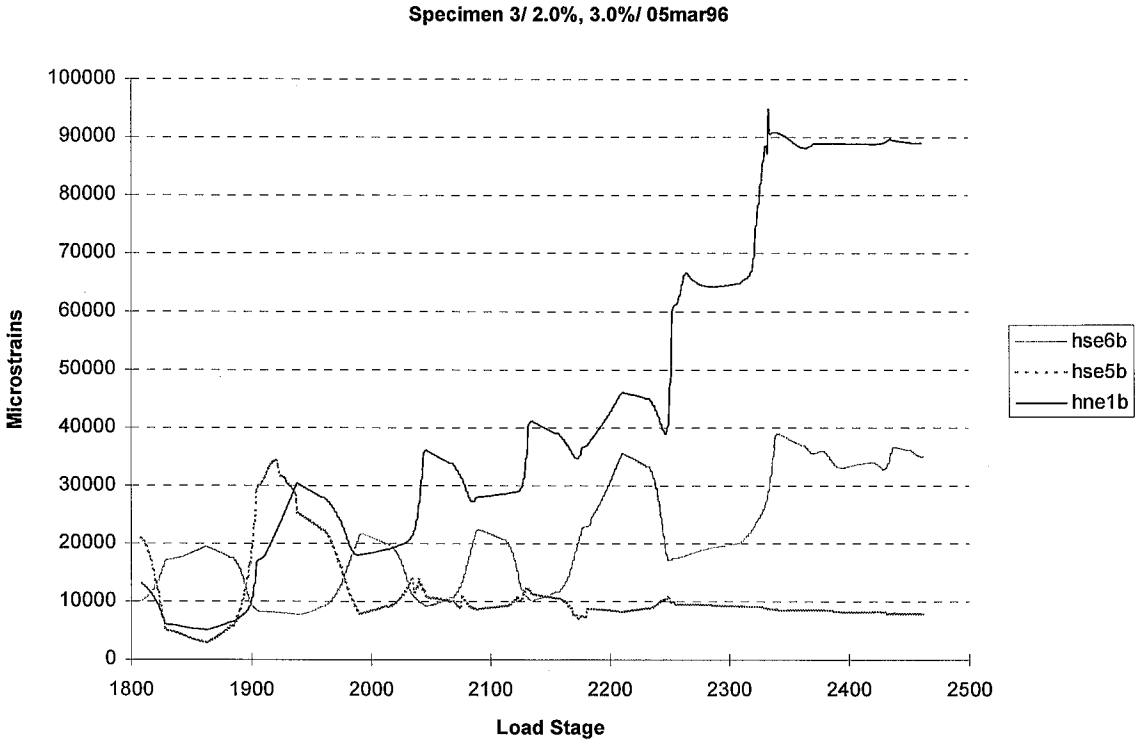

Figure H.49: Top and Bottom Access Hole Strains (East Girder of Specimen 3)

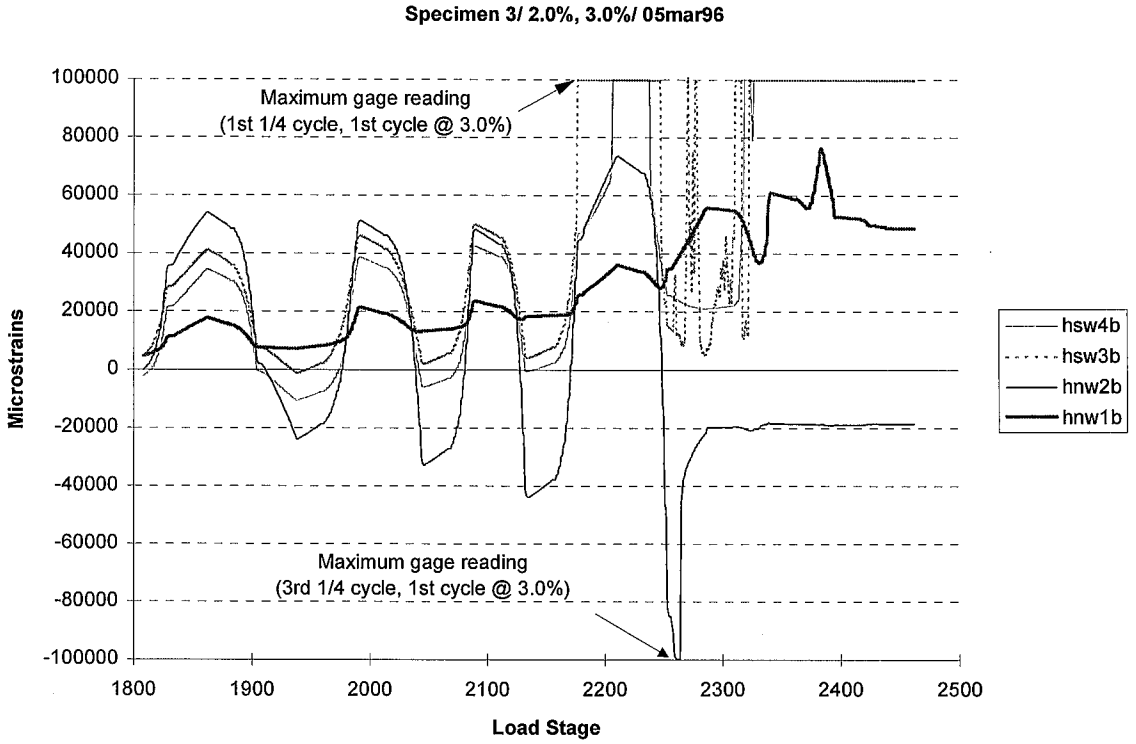

Figure H.50: Girder Bottom Flange Strains (West Girder of Specimen 3)

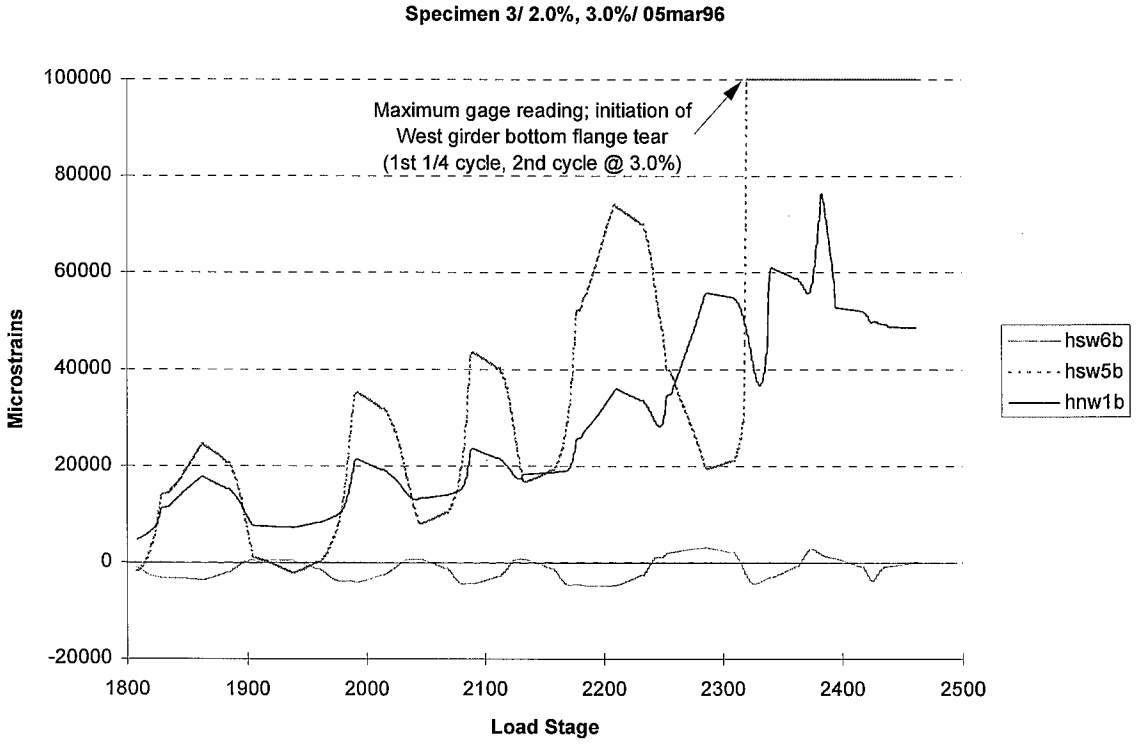

Figure H.51: Top and Bottom Access Hole Strains (West Girder of Specimen 3)

Table H.3: Loading Increment Data (Specimen 3)

Increment Number	Begin Stroke (in)	End Stroke (in)	East Events		West Events		Percent Drift	Quarter Cycle
			# of AE Events	Cum. Events	# of AE Events	Cum. Events		
1	0	-0.35	0	0	0	0	0.25	9
2	-0.35	0	0	0	0	0	0.25	10
3	0	0.35	0	0	0	0	0.25	11
4	0.35	0	0	0	0	0	0.25	12
5	0	-0.7	0	0	0	0	0.5	1
6	-0.7	0	0	0	0	0	0.5	2
7	0	0.7	0	0	0	0	0.5	3
8	0.7	0	0	0	0	0	0.5	4
9	0	-0.7	0	0	0	0	0.5	5
10	-0.7	0	0	0	0	0	0.5	6
11	0	0.7	0	0	0	0	0.5	7
12	0.7	0	0	0	0	0	0.5	8
13	0	-0.7	0	0	0	0	0.5	9
14	-0.7	0	0	0	0	0	0.5	10
15	0	0.7	0	0	0	0	0.5	11
16	0.7	0	0	0	0	0	0.5	12
17	0	-1.05	0	0	0	0	0.75	1
18	-1.05	0	0	0	0	0	0.75	2
19	0	1.05	0	0	1	1	0.75	3
20	1.05	0	0	0	0	1	0.75	4
21	0	-1.05	0	0	0	1	0.75	5
22	-1.05	0	0	0	0	1	0.75	6
23	0	1.05	0	0	0	1	0.75	7
24	1.05	0	0	0	1	2	0.75	8
25	0	-1.05	0	0	0	2	0.75	9
26	-1.05	0	0	0	0	2	0.75	10
27	0	1.05	0	0	1	3	0.75	11
28	1.05	0	0	0	0	3	0.75	12
29	0	-1.05	0	0	0	3	1	1
30	-1.05	-1.4	0	0	0	3	1	1
31	-1.4	-0.25	0	0	0	3	1	2
32	-0.25	1.05	0	0	0	3	1	3
33	1.05	1.4	0	0	0	3	1	3
34	1.4	0.25	0	0	0	3	1	4
35	0.25	-1.4	0	0	0	3	1	5
36	-1.4	-0.25	0	0	0	3	1	6
37	-0.25	1.4	0	0	0	3	1	7
38	1.4	0.25	0	0	0	3	1	8
39	0.25	-1.4	0	0	0	3	1	9
40	-1.4	-0.25	0	0	0	3	1	10
41	-0.25	1.4	0	0	0	3	1	11
42	1.4	0.25	0	0	0	3	1	12

Table H.3: Loading Increment Data (Specimen 3) (Cont.)

Increment Number	Begin Stroke (in)	End Stroke (in)	East Events		West Events		Percent Drift	Quarter Cycle
			# of AE Events	Cum. Events	# of AE Events	Cum. Events		
43	0.25	-1.4	0	0	1	4	1.5	1
44	-1.4	-2.1	3	3	1	5	1.5	1
45	-2.1	-0.6	0	3	0	5	1.5	2
46	-0.6	1.4	0	3	0	5	1.5	3
47	1.4	2.1	1	4	0	5	1.5	3
48	2.1	0.6	0	4	0	5	1.5	4
49	0.6	-2.1	0	4	2	7	1.5	5
50	-2.1	-0.6	0	4	0	7	1.5	6
51	-0.6	2.1	0	4	1	8	1.5	7
52	2.1	0.6	0	4	0	8	1.5	8
53	0.6	-2.1	0	4	0	8	1.5	9
54	-2.1	-0.6	0	4	0	8	1.5	10
55	-0.6	2.1	2	6	0	8	1.5	11
56	2.1	0.6	0	6	0	8	1.5	12
57	0.6	-2.1	2	8	1	9	2	1
58	-2.1	-2.8	2	10	0	9	2	1
59	-2.8	-0.75	0	10	0	9	2	2
60	-0.75	2.1	6	16	2	11	2	3
61	2.1	2.8	3	19	0	11	2	3
62	2.8	0.9	0	19	1	12	2	4
63	0.9	-2.8	12	31	0	12	2	5
64	-2.8	-0.9	0	31	0	12	2	6
65	-0.9	2.8	28	59	1	13	2	7
66	2.8	0.9	0	59	0	13	2	8
67	0.9	-2.8	16	75	0	13	2	9
68	-2.8	-0.9	1	76	1	14	2	10
69	-0.9	2.8	17	93	4	18	2	11
70	2.8	0.9	0	93	0	18	2	12
71	0.9	-2.8	17	110	3	21	3	1
72	-2.8	-4.2	4	114	2	23	3	1
73	-4.2	-2.1	0	114	0	23	3	2
74	-2.1	2.8	19	133	4	27	3	3
75	2.8	4.2	5	138	1	28	3	3
76	4.2	3.2	0	138	0	28	3	4
77	3.2	-4.2	18	156	11	39	3	5
78	-4.2	-2.1	11	167	0	39	3	6
79	-2.1	4.2	28	195	5	44	3	7
80	4.2	2.8	1	196	0	44	3	8
81	2.8	-4.2	44	240	22	66	3	9
82	-4.2	-2.5	2	242	0	66	3	10

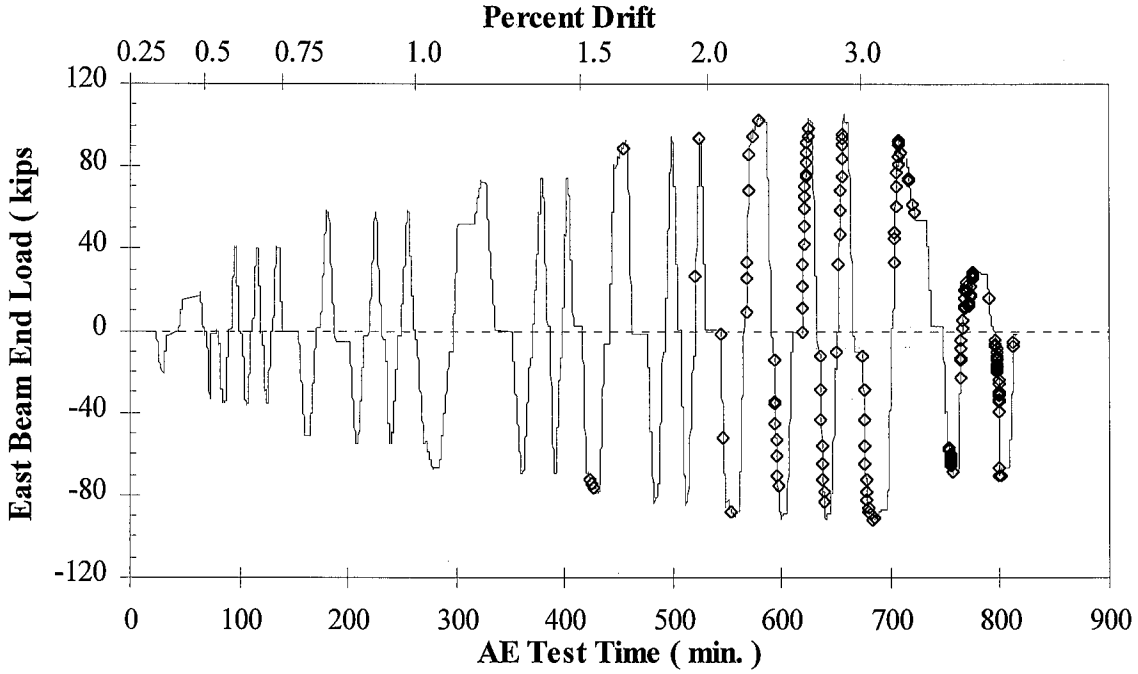

Figure H.52: AE Activity Loading History (East Connection of Specimen 3)

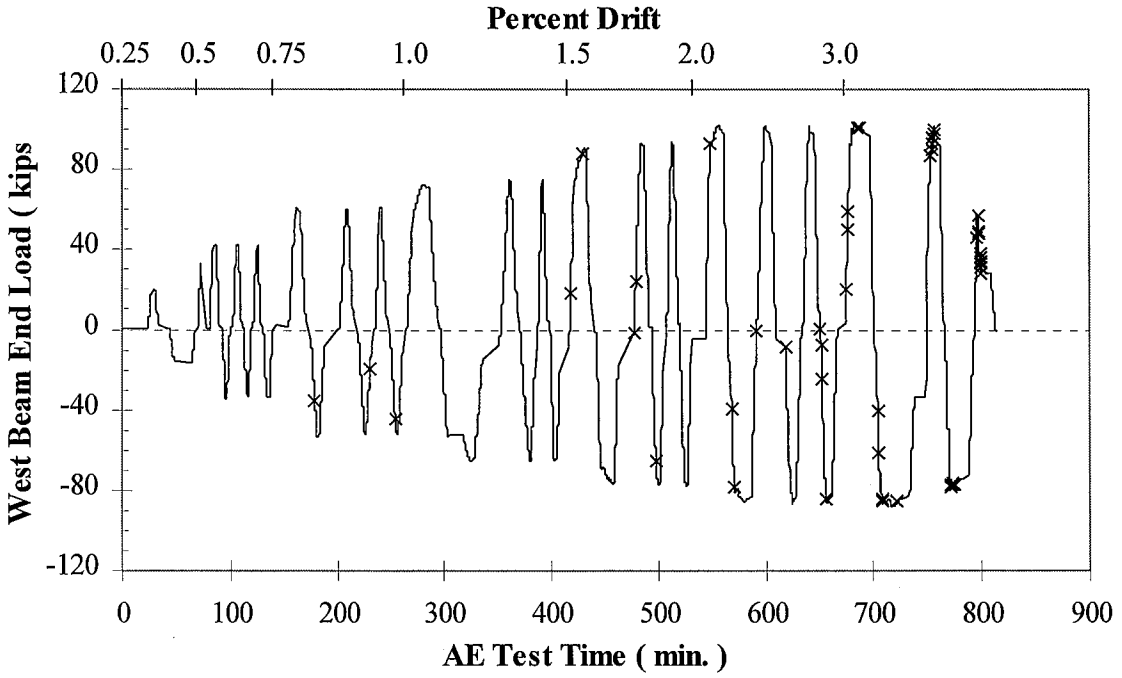

Figure H.53: AE Activity Loading History (West Connection of Specimen 3)

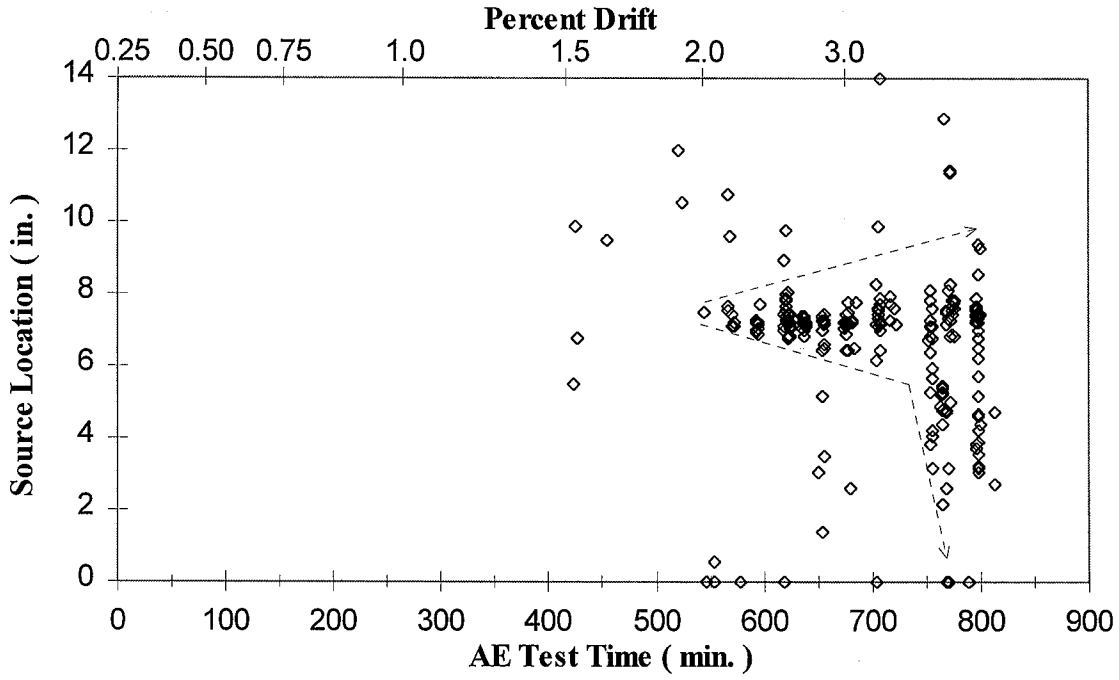

Figure H.54: AE Source Location vs. AE Test Time
(East Connection of Specimen 3)

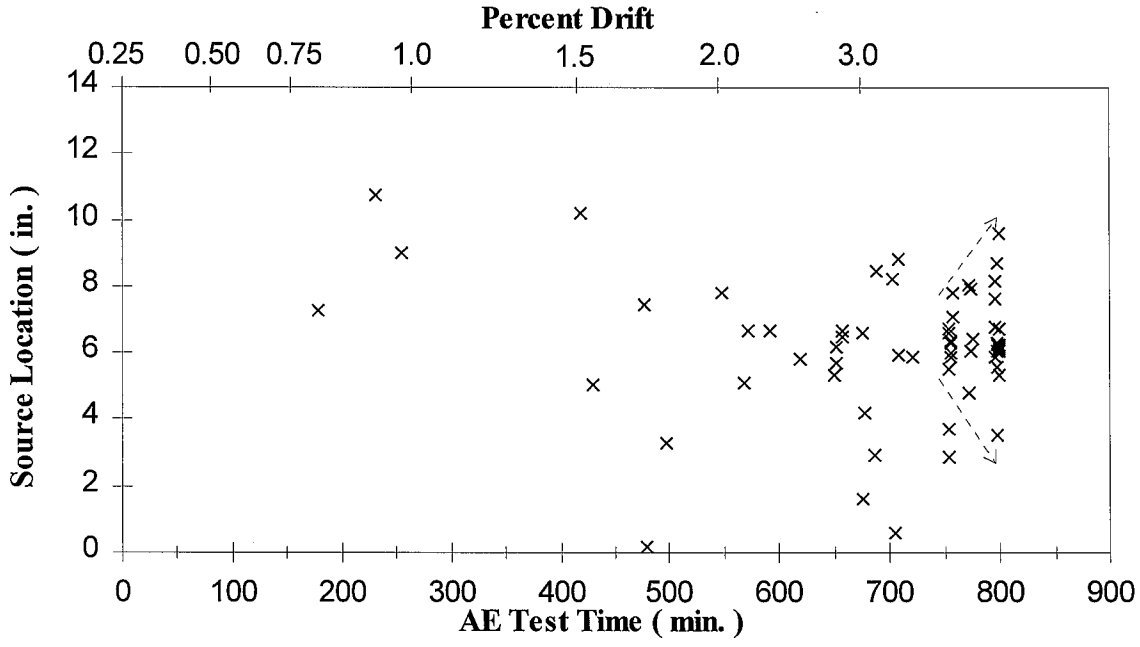

Figure H.55: AE Source Location vs. AE Test Time
(West Connection of Specimen 3)

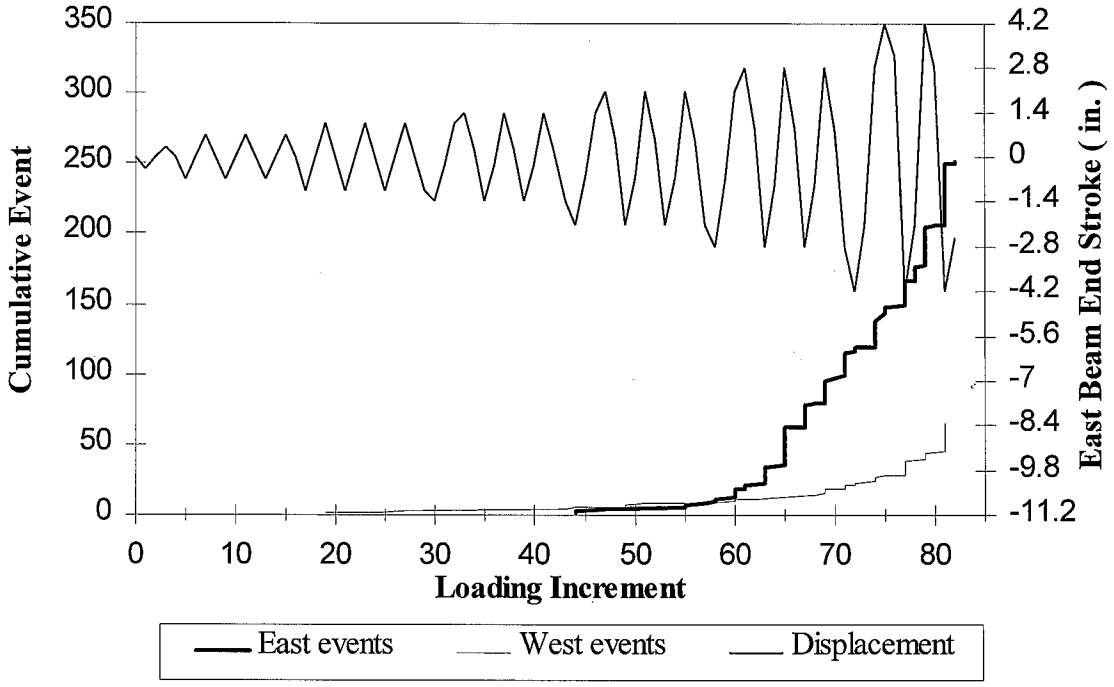

Figure H.56: Cumulative Events vs. Loading Increment (Specimen 3)

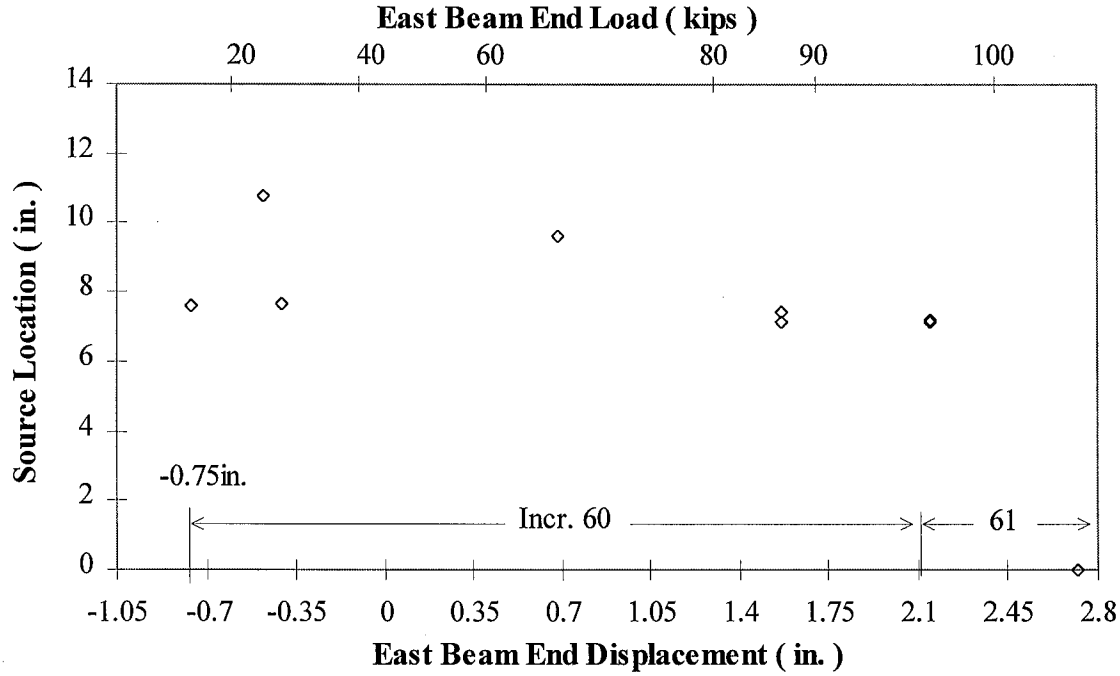

Figure H.57: AE Source Location vs. Load and Displacement
(Third quarter cycle of the first cycle at 2.0% drift/ East Connection of Specimen 3)

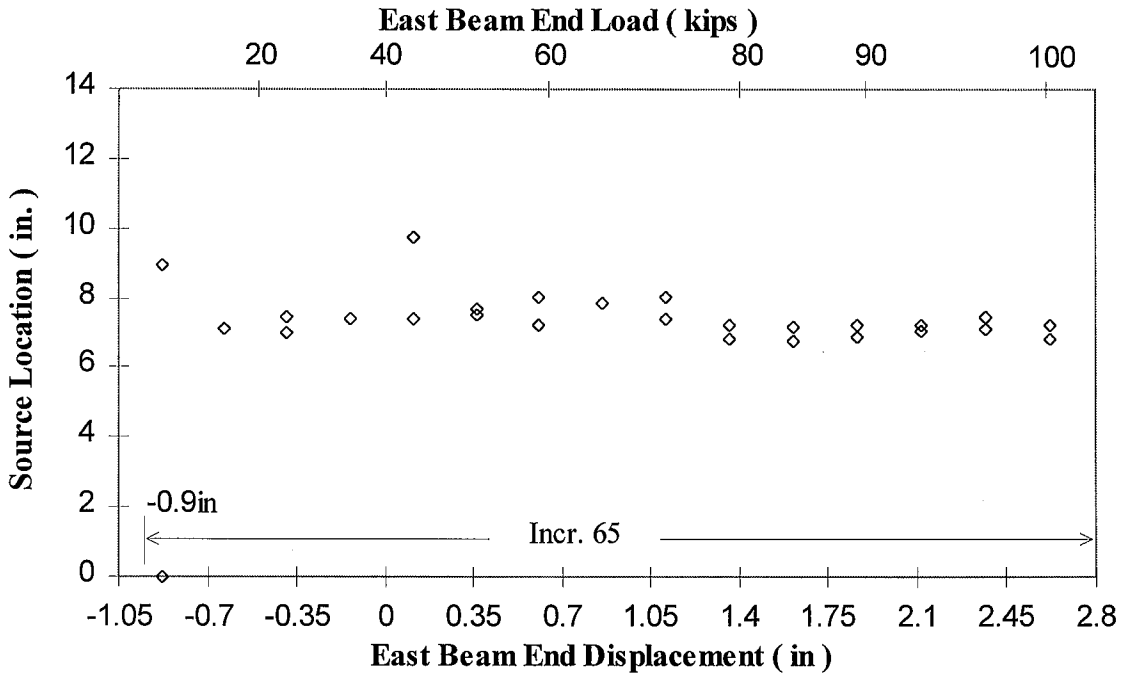

Figure H.58: AE Source Location vs. Load and Displacement
(Third quarter cycle of the second cycle at 2.0% drift/ East Connection of Specimen 3)

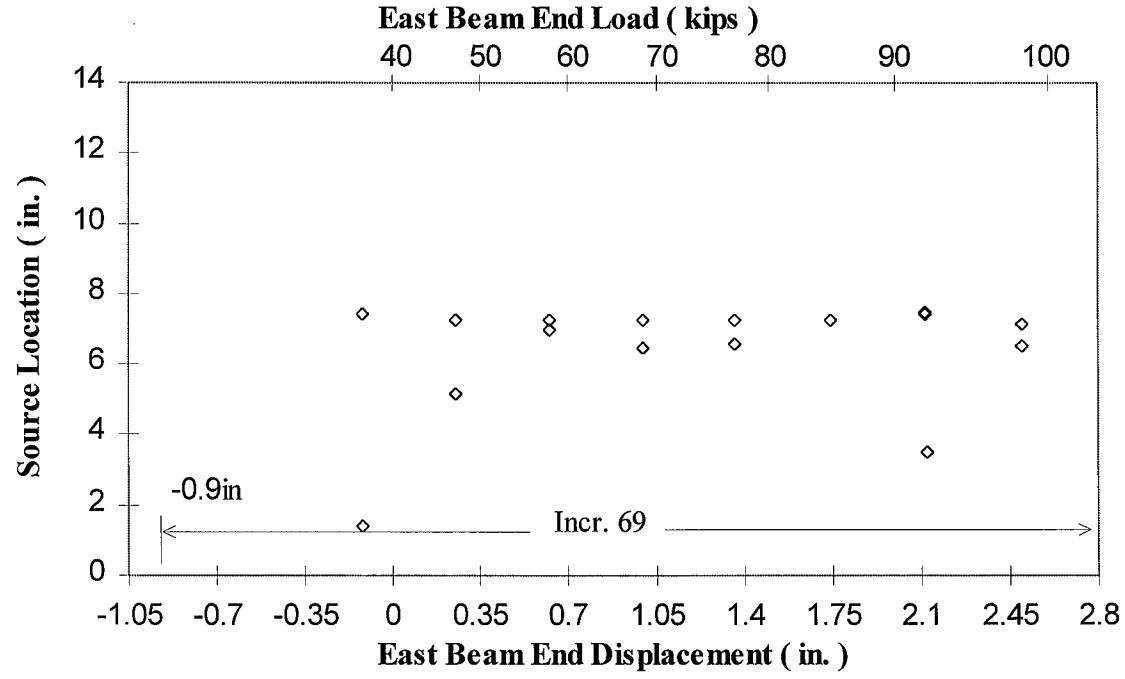

Figure H.59: AE Source Location vs. Load and Displacement
(Third quarter cycle of the third cycle at 2.0% drift/ East Connection of Specimen 3)

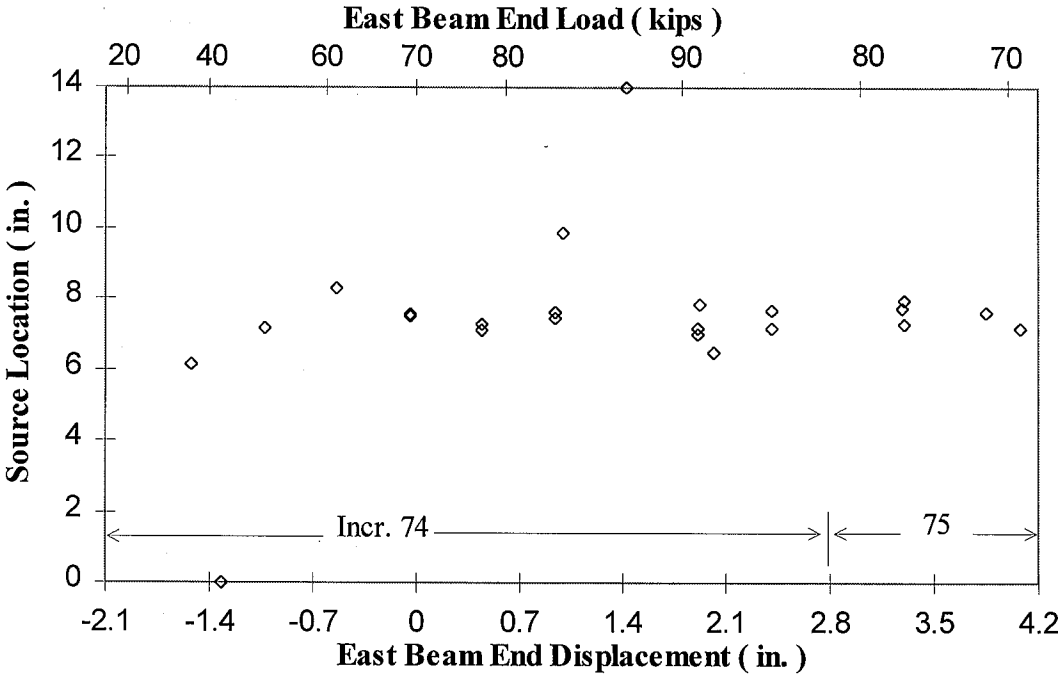

Figure H.60: AE Source Location vs. Load and Displacement
(Third quarter cycle of the first cycle at 3.0% drift/ East Connection of Specimen 3)

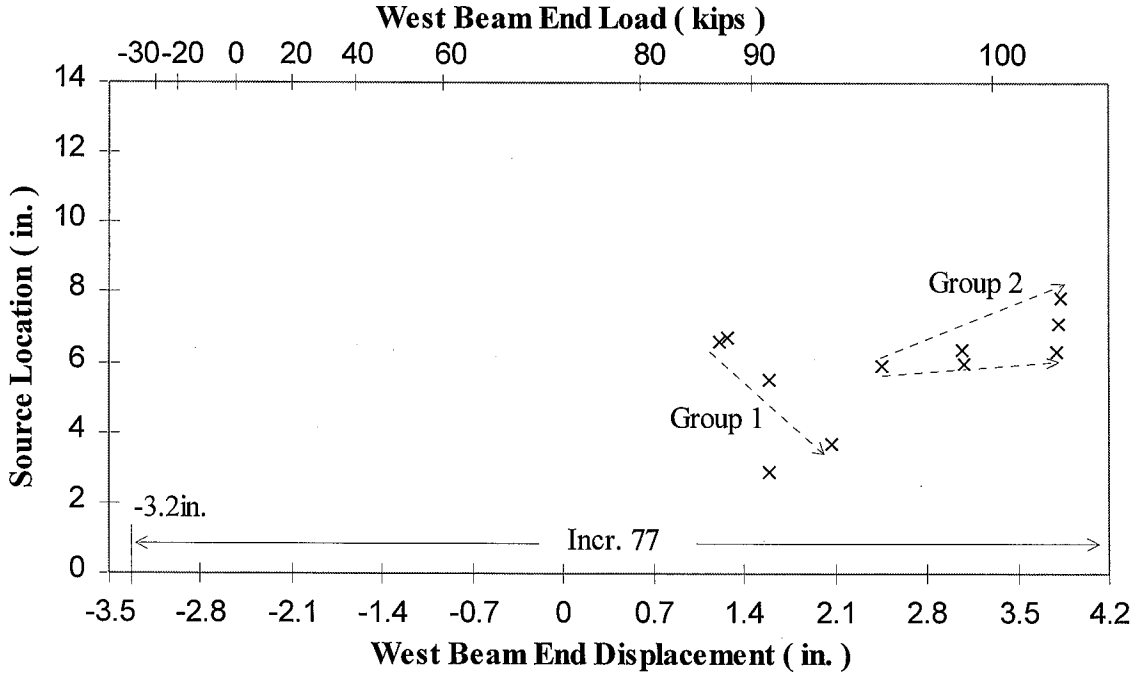

Figure H.61: AE Source Location vs. Load and Displacement
(First quarter cycle of the second cycle at 3.0% drift/ West Connection of Specimen 3)

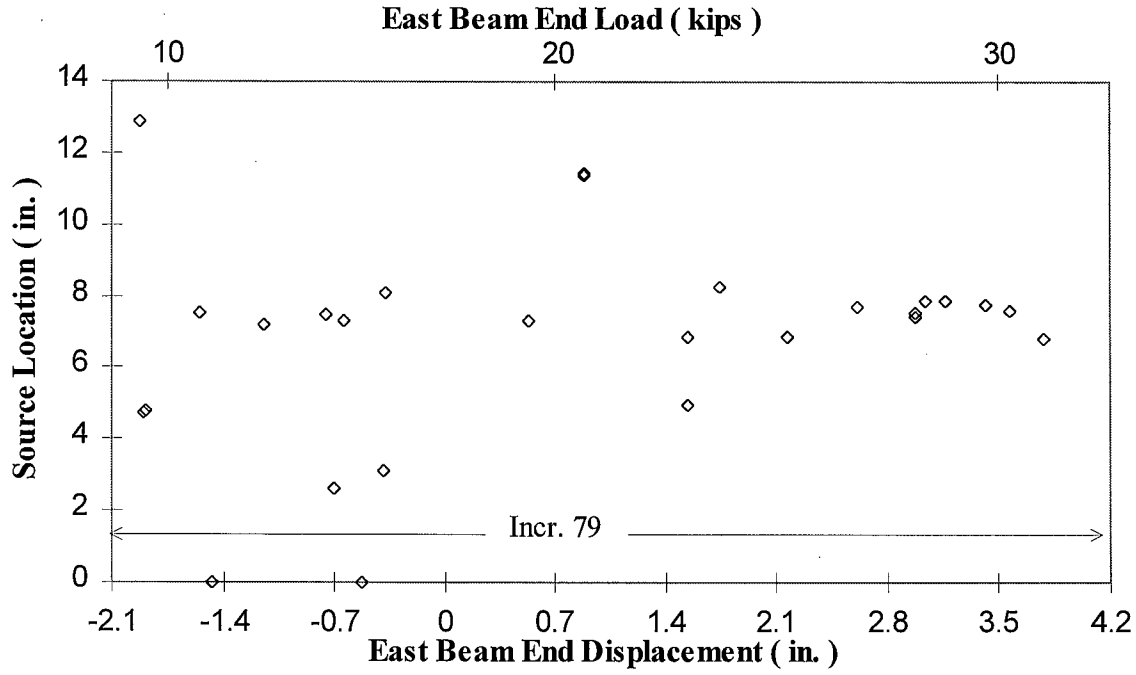

Figure H.62: AE Source Location vs. Load and Displacement
(Third quarter cycle of the second cycle at 3.0% drift/ East Connection of Specimen 3)

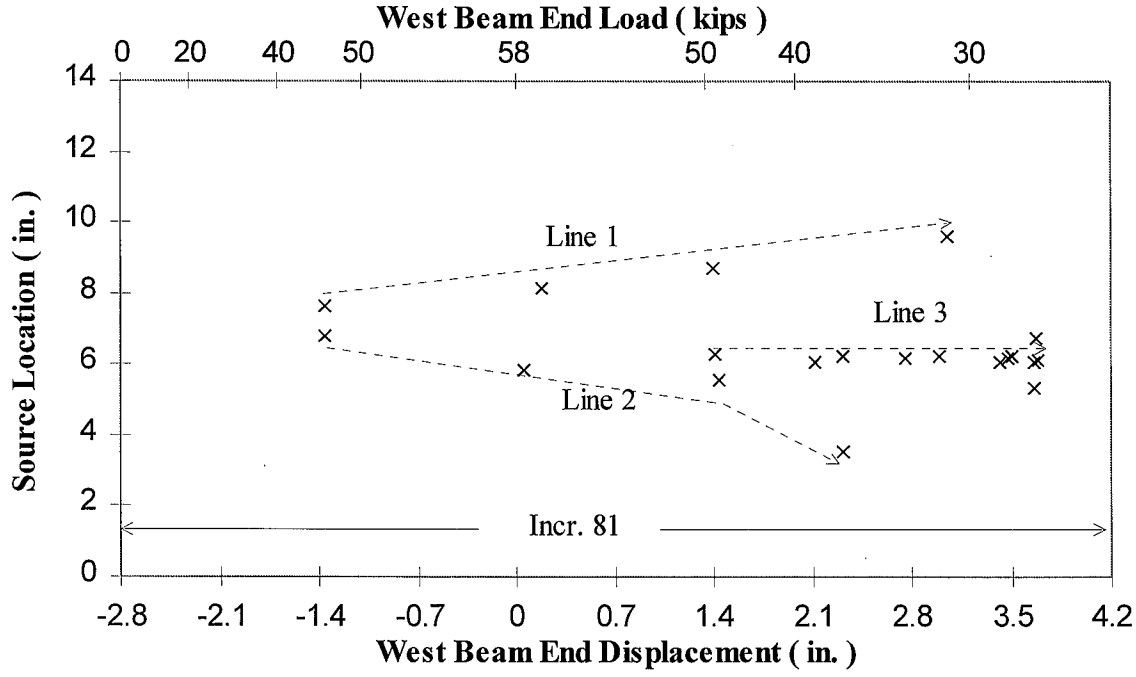

Figure H.63: AE Source Location vs. Load and Displacement
(First quarter cycle of the third cycle at 3.0% drift/ West Connection of Specimen 3)

Furthermore, it is shown that a significant amount of straining occurred near the North bottom flange tip of the East and West connection during the 1.5% to 3.0% cycles (see Figures H.48 and H.50; gages hne2b and hnw2b). In addition, during the 2.0% drift cycles, the bottom surface of the North flange tip of the West girder not only showed the largest strain amplitudes at the bottom flange, but it also demonstrated permanent compressive straining during negative girder bending at the third quarter cycle of the third cycle at 2.0% drift (see Figure H.50; hnw2b). This extensive amount of straining and permanent deformation may be attributed to the effects of local flange buckling of the East and West bottom girder flanges of Specimen 3.

It is important to note that the strains near the top access hole were much higher in the East connection than in the West connection (see Figures H.45, H.47, H.49, and H.51). Furthermore, the strains near the top access hole in the East connection exhibited significantly more permanent tensile straining than in the West connection, inferring that significantly more plastification near the top access hole of the East connection was occurring (see also Section 5.3.1). However, in general, the composite action of the two connections of Specimen 3 was comparable (see Section 5.1).

The Specimen 3 AE activity does not correlate with the large strains that are evident during the 0.5% drift through the 1.5% drift cycles. Very little East or West AE activity is evident until the first cycle at 2.0% drift (see Table H.3 and Figures H.52 to H.63). Figure H.56 is a Cumulative Events vs. Loading Increment chart for the events that occurred during Test 3. This chart clearly shows the lack of significant AE data through the third cycle at 1.5% drift (Increments 0 through 56). Once again, this lack of correlation between the AE and strain behavior is possible, since the yielding of the connection observed in the strain behavior is a ductile phenomena and not necessarily accompanied by micro fracture that is needed to produce AE.

H.6 Connection Strain Behavior and AE Activity At Failure (Specimen 3)

The East and West connections of Specimen 3 failed by the severing of the girder bottom flange base metal at a distance of approximately 1.5" from the column flange surface. The failure of the East connection began from the initiation of a tear in the bottom flange near the bottom access hole during the third quarter cycle of the first cycle at the 3.0% drift levels, and resulted in the ultimate severing of the bottom girder flange during the third quarter cycle of the second cycle at the 3.0% drift levels (see Section 3.2).

For the East connection, the bottom surface of the girder bottom flange demonstrated three sudden increases in strain during the third quarter cycle of the first cycle at 2.0% drift (Figure H.28). These events may have been the precursors to the extensive levels of straining, plastification, and eventual failure of the East connection. For example, during this quarter cycle, the South bottom flange tip (hse4b) showed a substantial increase in strain to 58,000 με followed by a sudden drop in strain to 35,000 με. Also, the North bottom flange tip of the East connection exhibited substantial peak-to-peak strain amplitudes of 60,000 με and permanent tensile strain up through the 2.0% drift cycles (gage hne2b).

It is seen that strains at the bottom and top surface of the bottom flange near the bottom access hole (gage hse3b, hse5b) showed evidence of minimal strain during the third quarter cycle of the first and second cycles at the 2.0% drift cycles, respectively (see Figure H.48 and H.49). This minimal strain behavior was also evident at the bottom surface of the South flange tip (gage hne2b) during the third quarter cycle of the first cycle at 2.0% drift. This inactive strain behavior exhibited by these strain gages during the 2.0% drift levels may be attributed to gage failure. For example, a very shallow tear in the underside of the East bottom flange visibly split the center underside strain gage of

the East bottom flange (hse3b) resulting in the malfunction of the strain gage during the third quarter cycle of the first cycle at 3.0% drift.

The low-cycle fatigue rupture of the East bottom flange is clearly indicated by the AE data (see Figures H.52-H.56). The East bottom flange failure occurred primarily during the third quarter cycle of the first cycle at 3.0% drift. The bottom flange rupture was not complete until after the third quarter cycle of the second cycle at 3.0% drift. Figure H.56 shows that the East AE activity increased rapidly but steadily beginning at the first quarter cycle of the first cycle at 2.0% drift. This steady increase in the AE activity is indicative of an gradual release of strain energy that would accompany a low-cycle fatigue failure.

Figure H.54 is a AE Source Location vs. AE Test Time chart for the East bottom flange events of Specimen 3, identifying the South girder flange tip with a 0" source location. It shows a gradually expanding band of source locations beginning at the first quarter cycle of the first cycle at 2.0% drift. The source locations occur near the center of the connection and then gradually approach the flange tips during the three cycles at 2.0% drift (Increments 57 through 70) and then expand rapidly toward the flange tips after the third quarter cycle of the first cycle at 3.0% drift (Increments 74 through 82). The beginning of this pattern of expanding AE activity correlates with a small but sudden decrease in the strains of the central underside of the East bottom flange (hse3b, Fig. H.48). The acceleration of the AE sources spreading during the 3.0% drift cycles clearly correlates with the East bottom flange rupture that began at the center of the bottom flange weld and propagated towards the flange tips.

The gradual release of strain energy within the central portions of the bottom flange is clearly illustrated by the AE data. Figures H.58-H.60 are AE Source Location vs. Load and Displacement charts for the East events that occurred between the third quarter cycle of the second cycle at 2.0% drift and the third quarter cycle of the first cycle at 3.0% drift. Each of these charts show a nearly constant displacement interval between event occurrences. In addition, the source locations of these events is consistent with the central region of the East bottom flange. These charts clearly display an ordered release

of strain energy within the central portion of the bottom flange well before any visual signs of failure became apparent.

Similarly, the West connection exhibited a tear in the girder flange base metal during the first quarter cycle of the second cycle of the 3.0% drift levels and resulted in the ultimate severing of the bottom girder flange during the first quarter cycle of the third cycle at the 3.0% drift levels. The initiation of a tear in the West connection bottom flange is observed from the strain behavior near the bottom access hole during first quarter cycle of the second cycle at the 3.0% drift levels (see Figure 5.51, hsw5b). Note that during the first cycle at the 3.0% drift cycles, the strain gages located near the center, North, and South regions of the bottom flange bottom surface exceeded their strain measuring capabilities (see Figures H.50 and H.51). Therefore, strains measured after the first quarter cycle at 3.0% drift within these regions are assumed not to be valid.

The primary fracture of the West connection bottom flange near the bottom access hole occurred during the first quarter cycle of the third cycle of 3.0% drift. Based on visual observations and a drop in applied load to the West connection, the bottom flange severed from the column flange near the end of the first quarter cycle of the third cycle of 3.0% drift.

The AE data is consistent with the initiation of a shallow tear during the first quarter cycle of the second cycle at 3.0% drift. Figure H.56 (Cumulative events vs. Loading Increment for Specimen 3) shows a significant increase in the number of West events during this quarter cycle at 3.0% drift (Increment 77). Table H.3 shows that 11 West events occurred during this quarter cycle as well. This results in a 40% increase in the West AE activity, and is indicative of structural damage sustained by the bottom region of the West connection of Specimen 3.

The source locations of the West events of this quarter cycle also indicate that failure initiated at this point in the load history. Figure H.65 is a Source Location vs. Load and Displacement chart for the first quarter cycle of the second cycle at 3.0% drift, and shows two groups of events labeled Group 1 and Group 2. The Group 1 events are indicative of crack propagation from the center of the bottom flange toward the North

flange tip. The Group 2 events are consistent with the initiation and propagation of a small rupture in the underside of the bottom flange.

The AE data also is consistent with the mode of West bottom flange failure noted during the first quarter cycle of the third cycle at 3.0% drift. For example, Figure H.56 shows another substantial increase in West AE activity during this quarter cycle and Table H.3 reports that 22 West events occurred, or a 50% increase in the West AE activity, during this quarter cycle. In addition, Figure H.67 is a Source Location vs. Load and Displacement chart for the West events that occurred during the this quarter cycle. This figure shows dashed lines labeled Line 1 and Line 2 that illustrate AE activity starting near the center of the bottom connection and then spreading towards the flange tips. This expansion of AE activity from the center connection region is consistent with a tear initiating at the center of the bottom flange and propagating toward the flange tips. As the band of source location increases, the load applied to the West girder tip begins to decrease. Then, while the tear continues to propagate, the load is redistributed to the bottom of the shear tab. The source location of the events illustrated by Line 3 are consistent with the location of the West shear tab fracturing.

Appendix I

Effects of a Triaxial State of Tensile Stress

This section discusses the analysis procedure employed to study the presence of a triaxial state of tensile stress at the bottom CJP weld of the connections. Specifically, it outlines the equations and assumptions incorporated into the estimation of the stress states of two Elements A and B (see Figure I.1). Also, results of the analysis are provided.

I.1 Calculation of the Normal Stresses of Elements A and B

To study the possibility of a triaxial stress condition at the bottom weld region of a typical welded girder flange-to-column connection, Elements A and B are studied. The centroid of Element A is located at the intersection of the top surface of the bottom girder flange with the face of the column flange, in the region of the interface between the complete joint penetration groove weld and the column flange. Note that a portion of Element A is embedded in the column flange while another portion is located within the full penetration weld (denoted with dashed lines). Element B is defined later.

The normal strains in Element A are approximated using measured strains within close proximity to the weld region. The validity of this method of estimation is dependent upon St. Venant's principle, in that strains measured within an approximate

distance of t_m, the material thickness, away from Element A provide a good estimation of the strains in Element A (Cook and Young, 1985).

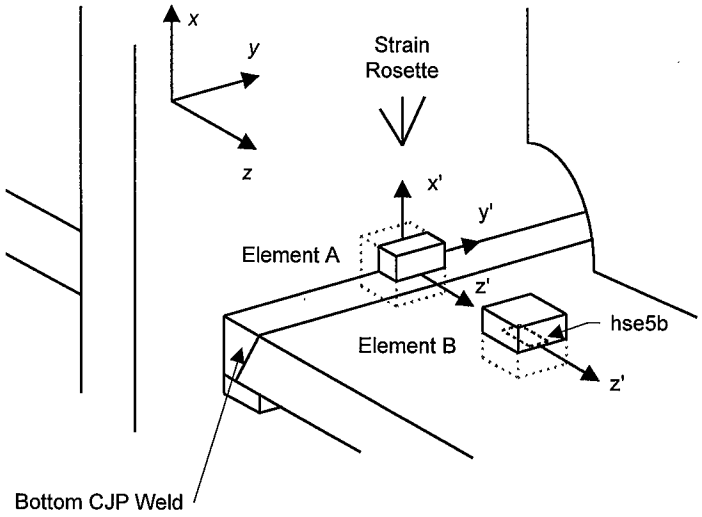

Figure I.1: Elements A and B (Typical View of Bottom CJP Weld Region)

To estimate the two normal strains of Element A oriented within the plane of the column flange, a rosette strain gage located on the surface of the column flange is utilized to measure strains ε_A, ε_B, and ε_C at points A, B, and C, respectively (see Figures I.2 and I.3). A local coordinate system is defined in order to specify the orientations of these strains. The x-axis is oriented orthogonal to the plane of girder web and is defined as positive when directed away from the girder flange tip for the SE connection region. For the SW connection region, the x-axis is oriented orthogonal to the plane of girder web, but it is defined as positive when directed toward the girder flange tip for the SW connection region. The y-axis is oriented vertically, defined as positive upwards. The z-axis is oriented orthogonal to the plane of the column flange. It is parallel to the longitudinal axis of the girder and is defined as positive when directed away from the column flange. The x-y axes define the plane of the column flange surface. To measure strain in the z direction, a strain gage at point D is used (see Figures I.2 and I .3).

The strains ε_A, ε_B, and ε_C are oriented at 45 degree increments, in a counterclockwise direction, with ε_B being parallel to the y-axis (see Figures I.2 and I.3). The dimensions q, r, s, and t represent the positions of the centroid of Element A and the strain gages A, B, C, and D. Table I.1 lists the values of these dimensions for the East and West connection regions for all three specimens, along with the flanges thicknesses of the column and girder.

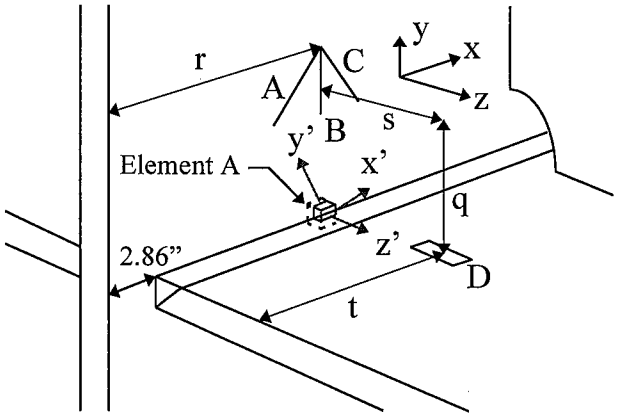

Figure I.2: Element A (Specimens 1 and 2/ SE Girder-to-Column Weld Region)

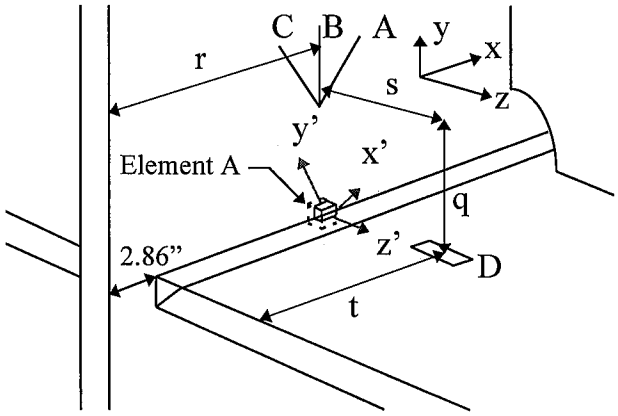

Figure I.3: Element A (Specimen 3/ SE Girder-to-Column Weld Region)

Table I.1: Positions of Strain Gages Relative to Element A (inches)

Parameter	Specimen 1 SE Region	Specimen 1 SW Region	Specimen 2 SE Region	Specimen 2 SW Region	Specimen 3 SE Region	Specimen 3 SW Region
q	2.00	2.00	2.00	2.00	2.19	2.13
r	5.86	5.86	5.86	5.86	6.42	5.86
s	1.50	1.50	1.50	1.50	1.44	1.63
t	3.88	3.88	3.50	4.00	3.56	3.00
girder t_f	0.745	0.745	0.745	0.745	0.745	0.745
column t_f	1.560	1.560	1.560	1.560	1.560	1.560

As previously stated, the three normal strains in Element A are assumed to be valid only if they are estimated with strains that are measured at a distance from Element A approximately equal to or less than the thickness of the loaded material. Based on the values in Table I.1, it is observed that q is approximately 1.3 to 1.4 times larger than the column flange thickness and s is approximately 2.0 times larger than the girder flange thickness. Therefore, it may assumed within reason that St. Venant's principle is upheld and that the strains measured at points A, B, C, and D are a good approximation of the strains in Element A, although it should be recognized that the strain gradient in this region may be large.

Mohr's Circle may be generated based on the two-dimensional state of strain specified by ε_A, ε_B, and ε_C on the plane of the column flange surface (see Figure I.4). The horizontal and vertical axes of this diagram are defined as the normal strain, ε, and the shear stain, γ. The radius of the circle, R, may be expressed in terms of ε_A, ε_B, and ε_C using Pythagorean's theorem:

$$R = \sqrt{\left(\frac{(\varepsilon_A - \varepsilon_C)}{2}\right)^2 \left(\frac{(\varepsilon_A + \varepsilon_C)}{2} - \varepsilon_B\right)^2} \tag{I.1}$$

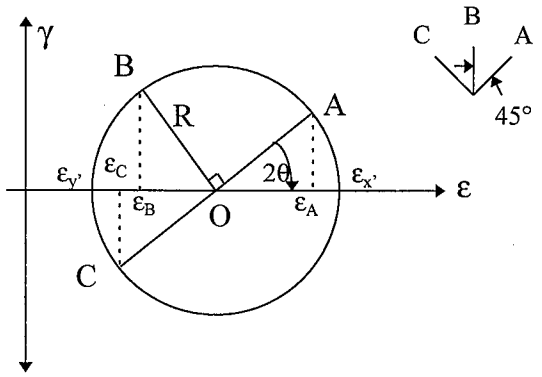

Figure I.4: Mohr's Circle Diagram (Strain Gage Location)

After factoring out a constant of 1/2 from the radical and performing algebraic operations on Eq. I.1, R may be expressed as:

$$R = \frac{1}{\sqrt{2}}\sqrt{(\varepsilon_A - \varepsilon_B)^2 + (\varepsilon_B - \varepsilon_C)^2} \tag{I.2}$$

Using ε_A, ε_B, and ε_C and Eq. I.2, it is possible to determine the normal strains in the plane of the column flange surface, $\varepsilon_{x'}$ and $\varepsilon_{y'}$ (see Figure I.4), for which the shear strains are equal zero. These strains are expressed in terms of the strain at center of the circle (point O) and the radius of the circle, R:

$$\varepsilon_{x'} = O + R = \left(\frac{\varepsilon_A + \varepsilon_C}{2}\right) + \frac{1}{\sqrt{2}}\sqrt{(\varepsilon_A - \varepsilon_B)^2 + (\varepsilon_B - \varepsilon_C)^2} \tag{I.3}$$

$$\varepsilon_{y'} = O - R = \left(\frac{\varepsilon_A + \varepsilon_C}{2}\right) - \frac{1}{\sqrt{2}}\sqrt{(\varepsilon_A - \varepsilon_B)^2 + (\varepsilon_B - \varepsilon_C)^2} \tag{I.4}$$

where ε_A = strain measured by rosette strain gage A

ε_B = strain measured by rosette strain gage B

ε_C = strain measured by rosette strain gage C

In order to observe the orientation of $\varepsilon_{x'}$ and $\varepsilon_{y'}$ relative to the measured strains in the x'-y' plane, Element A may be viewed along the z and z' axes (Figure I.5).

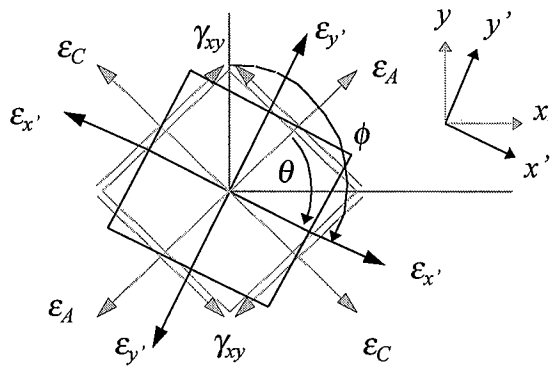

Figure I.5: Element A Strain Transformation (x'-y' plane)

Note that the shear strains in the x-y direction, γ_{xy}, were not measured in this study, but are included in Figure I.5 to accurately represent the strain state of Element A oriented in the x-y direction. The direction of $\varepsilon_{x'}$ is arbitrarily defined as the larger of the two normal strains in the plane of the column flange. Its orientation is measured relative to the orientation of strain gage A as 2θ, when observing Mohr's Circle (see Figure I.4) and as θ when observing Element A (see Figure I.5):

$$2\theta = \cos^{-1}\left(\frac{\frac{\varepsilon_A - \varepsilon_C}{2}}{\sqrt{2}\sqrt{(\varepsilon_A - \varepsilon_B)^2 + (\varepsilon_B - \varepsilon_C)^2}}\right) \tag{I.5}$$

For small strains, substantial error is obtained in determining 2θ, in which the parenthetical term in Eq. I.5 became greater than 1. Therefore, in these cases, 2θ is set equal to zero (in radians) (note that the strain field information is not critical during small

loading cycles). With respect to Element A, $\varepsilon_{x'}$ and $\varepsilon_{y'}$ are oriented orthogonal to one another along the x' and y' axes, respectively (see Figures I.6 and I.7).

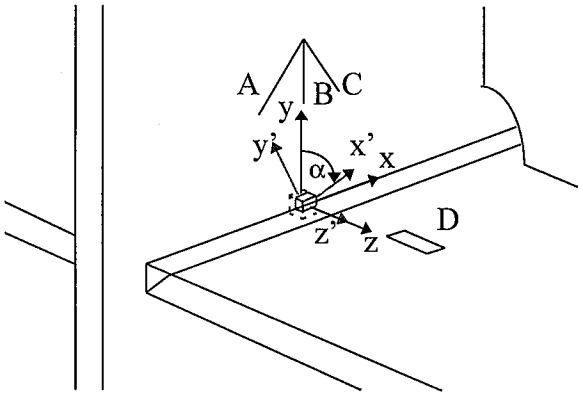

Figure I.6: Element A (Specimens 1 and 2/ SE Girder-to-Column Weld Region)

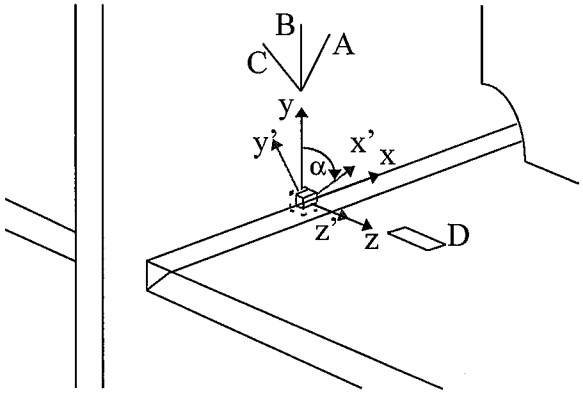

Figure I.7: Element A (Specimen 3/ SE Girder-to-Column Weld Region)

The angle α, located on the face of the column flange (x-y plane), defines the orientation of $\varepsilon_{x'}$ relative to the y-axis for the specimens (see Figures I.5 -I.7). This angle is measured off the vertical since the angle α then represents the deviation of the strains from the uniaxial strain state due to axial force and flexure in the column. The angle α is determined by using θ and the position of ε_B with respect to the strain at the center of the circle, $\frac{\varepsilon_A + \varepsilon_C}{2}$:

$$\alpha = \begin{cases} -45 - \theta & if\ \varepsilon_B \le \left| \dfrac{\varepsilon_A + \varepsilon_C}{2} \right| \\ -45 + \theta & if\ \varepsilon_B \ge \left| \dfrac{\varepsilon_A + \varepsilon_C}{2} \right| \end{cases} \tag{I.6}$$

Note that a change in θ with respect to Element A corresponds to a change in 2θ on the Mohr's Circle diagram.

A third normal strain is needed to specify the three-dimensional strain condition in element A. The strain along the z'-axis, $\varepsilon_{z'}$, is equal to the strain measured parallel to the longitudinal axis of the girder (z-axis) at point D (see Figures I.1-I.3). Note that the z'-axis is oriented orthogonal to the x' and y'-axes.

With three mutually orthogonal normal strains of Element A determined, the corresponding normal stresses, $\sigma_{x'}$, $\sigma_{y'}$, and $\sigma_{z'}$, are calculated in the x', y', and z' directions assuming linear constitutive relations (Eqs. I.7 through I.9).

$$\sigma_{x'} = \frac{E_s}{(1+v)(1-2v)}\left((1-v)\varepsilon_{x'} + v(\varepsilon_{y'} + \varepsilon_{z'})\right) \tag{I.7}$$

$$\sigma_{y'} = \frac{E_s}{(1+v)(1-2v)}\left((1-v)\varepsilon_{y'} + v(\varepsilon_{x'} + \varepsilon_{z'})\right) \tag{I.8}$$

$$\sigma_{z'} = \frac{E_s}{(1+v)(1-2v)}\left((1-v)\varepsilon_{z'} + v(\varepsilon_{x'} + \varepsilon_{y'})\right) \tag{I.9}$$

where E_s = modulus of elasticity of steel

v = Poisson's ratio of steel

The modulus of elasticity of steel is taken as 29,000 ksi (effects of material nonlinearities are not included in this analysis) and Poisson's ratio is assumed as 0.30. Note that while x' and y' are principal directions in two dimensions, they do not necessarily correspond to the three-dimensional principal directions in the region of Element A. That is, while Eqs.

I.7 through I.9 yield valid values for the normal stresses in the x', y', and z' directions, the shear stresses and strains may not be nonzero (and are unknown) for this orientation of Element A.

An unrestrained element, identified as Element B, is next located within close proximity of strain gage D. It is assumed that the element is loaded only in the z'-direction; therefore, the strain condition in Element B is assumed to be estimated by strain gage D (see Figure I.8).

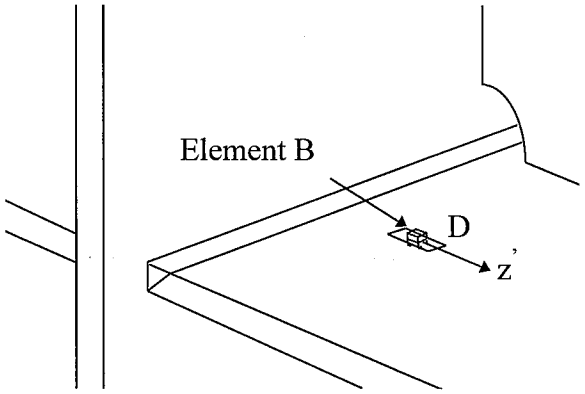

Figure I.8: Typical View of Bottom CJP Weld Region (Element B)

When subjected to this uniaxial loading condition, Element B is assumed to have values of $\sigma_{x'}$ and $\sigma_{y'}$ equal to zero and strains $\varepsilon_{x'}$ and $\varepsilon_{y'}$ equal to $(-\nu\varepsilon_{z'})$. The uniaxial tensile stress of Element B is then expressed as σ_t using equations I.7 through I.9:

$$\sigma_t = E_s \varepsilon_{z'} \tag{I.10}$$

I.2 Approximation of Uniaxial and Triaxial States of Stress of Elements A and B

It is next possible to compare the triaxial and uniaxial stress states of Elements A and B, respectively. When Element B is subjected to uniaxial loading, a ductile failure may occur; that is, its shear yield stress may be breached by the maximum shear stress before its ultimate tensile stress is breached by the maximum normal stress, σ_t.

However, when Element A is subjected to multiaxial strains, a high state of triaxial tension may lead to brittle fracture prior to ductile yielding. This is because the ultimate tensile stress may be reached by the maximum normal stress, $\sigma_{z'}$, before its shear yield stress is reached by the maximum shear stress.

To investigate these two possible modes of failure in Elements A and B, their maximum shear stresses are calculated. Once again a Mohr's Circle diagram is used, but for three-dimensions rather than two-dimensions for Element A (see Figure I.9).

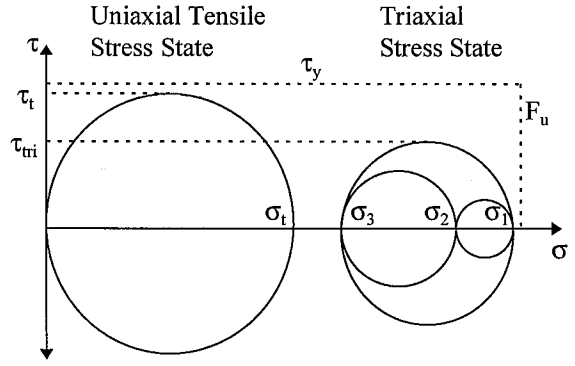

Figure I.9: Uniaxial Tensile and Triaxial 3-D Stress States Using Mohr's Circle [after (Cook and Young, 1985)]

Note that the shear yield stress and the ultimate tensile stress are shown as τ_y and as F_u, respectively.

For Element A, it must now be assumed for this comparison of Elements A and B that the shear stresses along the faces of Element A are equal to zero; therefore, the normal stresses, $\sigma_{x'}$, $\sigma_{y'}$, and $\sigma_{z'}$, are assumed to be equal the principal stresses σ_1, σ_2, and σ_3, where σ_1 is equal to the largest principal stress and σ_3 is equal to the smallest principal stress (see Figure I.9):

$$\sigma_1 = max \begin{Bmatrix} \sigma_{x'} \\ \sigma_{y'} \\ \sigma_{z'} \end{Bmatrix} \tag{I.11}$$

$$\sigma_3 = \min \begin{Bmatrix} \sigma_{x'} \\ \sigma_{y'} \\ \sigma_{z'} \end{Bmatrix} \tag{I.12}$$

For Element A, the maximum shear stress under a triaxial stress state is defined as τ_{tri} and is equal to one half of the difference between the largest and smallest principal stress:

$$\tau_{tri} = \frac{\sigma_1 - \sigma_3}{2} \tag{I.13}$$

The maximum shear stress, τ_t, for Element B is expressed using Eq. I.13 and by noting that the uniaxial tensile stress, σ_t, is equal to the principal stress, σ_1:

$$\tau_t = \frac{\sigma_1}{2} \tag{I.14}$$

I.3 Existence of a Triaxial State of Tensile Stress

Figures I.10 through I.19 relate the three normal stresses along with the uniaxial tensile stress, σ_t. Figures I.20 and I.29 compare the magnitudes of the three normal strains: $\varepsilon_{x'}$, $\varepsilon_{y'}$, and $\varepsilon_{z'}$. Finally, Figures I.30-I.39 compare the absolute values of the maximum shear stresses for the uniaxial and triaxial stress states. Note that the figures study the stress and strain states near the bottom weld regions of the all six connections, except the West weld region for Specimen 2 (invalid strains were measured by the column flange rosette for this connection).

By comparing the three calculated normal stresses of Element A, $\sigma_{x'}$, $\sigma_{y'}$, and $\sigma_{z'}$, to the uniaxial tensile stress in Element B, σ_t, only a small increase in the normal stresses is observed near the bottom CJP weld regions in the three specimens due to the

application of a tension load of 550 kips to the column during the 0.25% drift cycles. In fact, the East and West connections of the specimens all demonstrate an increase in normal stress of approximately 5 ksi (Figures I.10-I.19). It is important to note that the application of 550 kips of tension load to the column may not be large enough to observe any significant change in a triaxial stress state within the connection region (i.e., the column elongates by only 300 microstrains under 550 kips of loading). Nevertheless, it is felt that the effect of axial column tension on the stress state at Element A is minimal.

It is observed in all three tests that a triaxial state of stress is present within the proximity of the SE and SW bottom girder flange-column flange welds prior to connection failure. This is demonstrated by comparing the three calculated normal stresses of Element A, $\sigma_{x'}$, $\sigma_{y'}$, and $\sigma_{z'}$, to the uniaxial tensile stress in Element B, σ_t, that is calculated along the z'-axis. Figures I.10-I.19 show that the magnitude of stress in the z'-direction is significantly greater than the magnitude of the uniaxial tensile stress for all three specimens throughout the entire load history. Also, note that when comparing the strain magnitudes of Element A, $\varepsilon_{x'}$ and $\varepsilon_{y'}$ are at times approximately equal to zero (Figures I.20-I.29). This type of strain behavior is typical of a triaxial stress state, since for a uniaxial stress state to have existed, $\varepsilon_{x'}$ and $\varepsilon_{y'}$ must have values that are the opposite in magnitude to that of $\varepsilon_{z'}$.

I.4 Non-Ductile Connection Failure Due to a Triaxial State of Stress

As previously stated, a brittle fracture may occur if the ultimate tensile stress, F_u of the material, is reached by the maximum normal stress before the shear yield stress is breached by the maximum shear stress (i.e., before yielding initiates) (see Boldgett, 1995). Note that the ultimate tensile strength, F_u, is taken here as an approximation of the fracture strength of the material. Values of these critical stresses have been determined based on uniaxial tensile coupon tests, where the ultimate tensile stress, F_u, and the yielding tensile stress, F_y, are equal to 59.5 ksi and 38 ksi, respectively (see

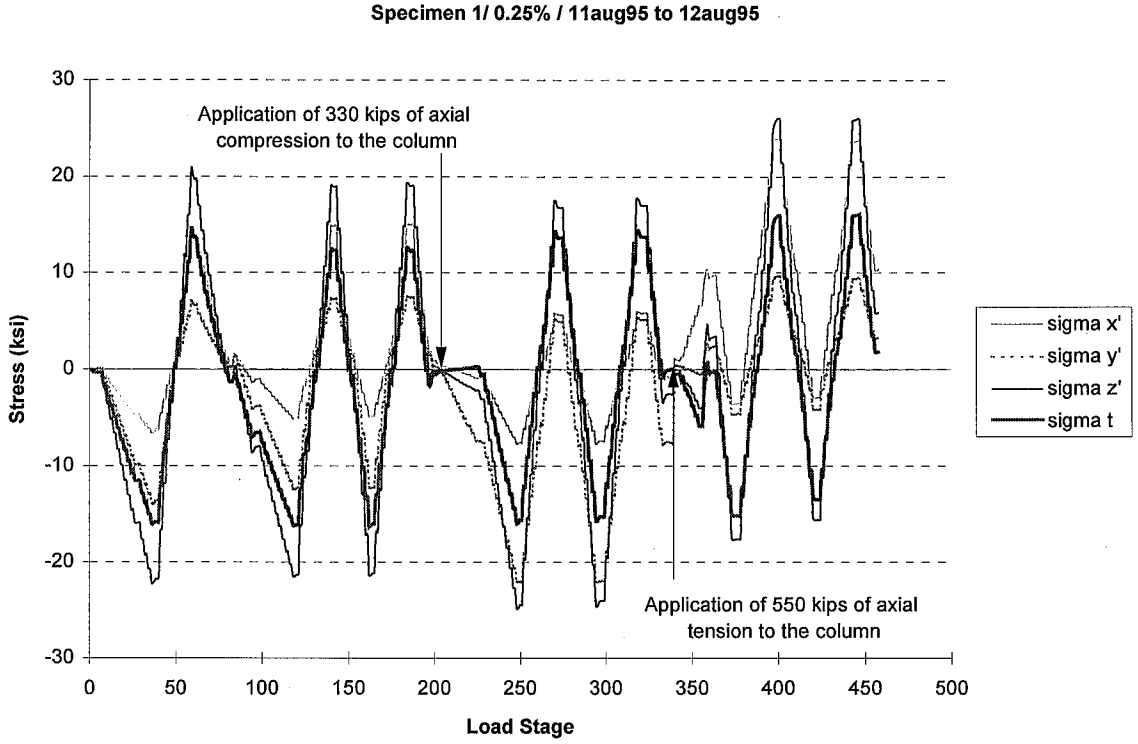

Figure I.10: Normal Stresses at Elements A and B (SE Connection of Specimen 1)

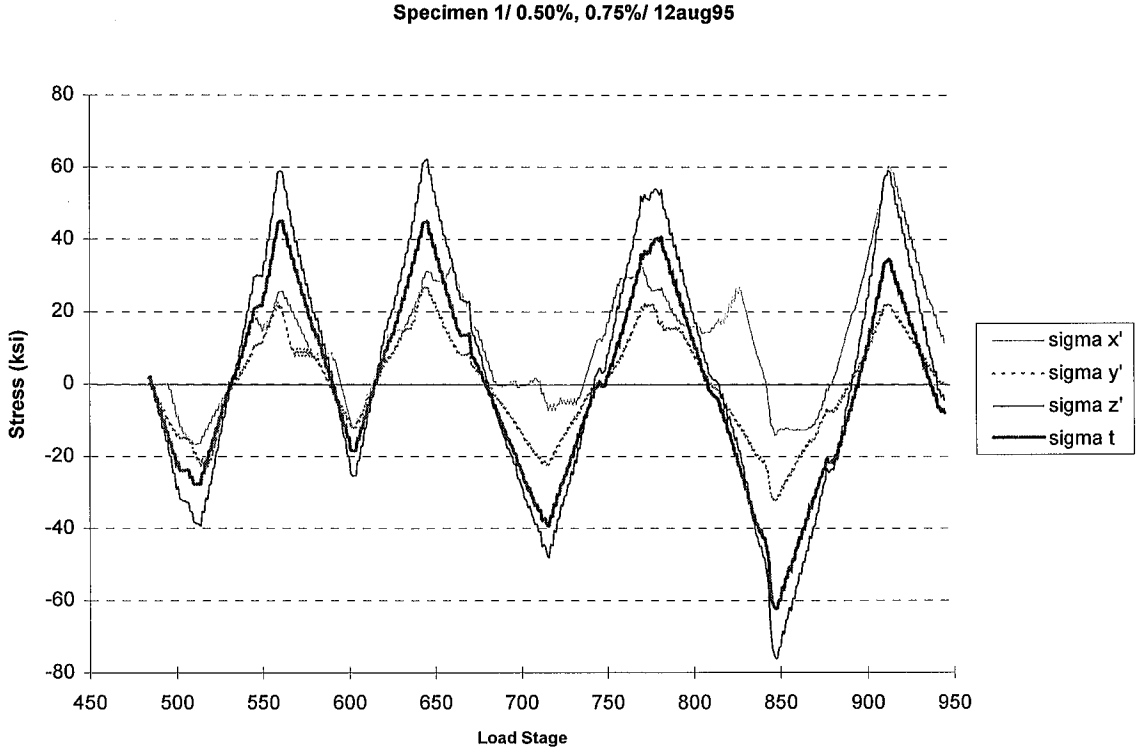

Figure I.11: Normal Stresses at Elements A and B (SE Connection of Specimen 1)

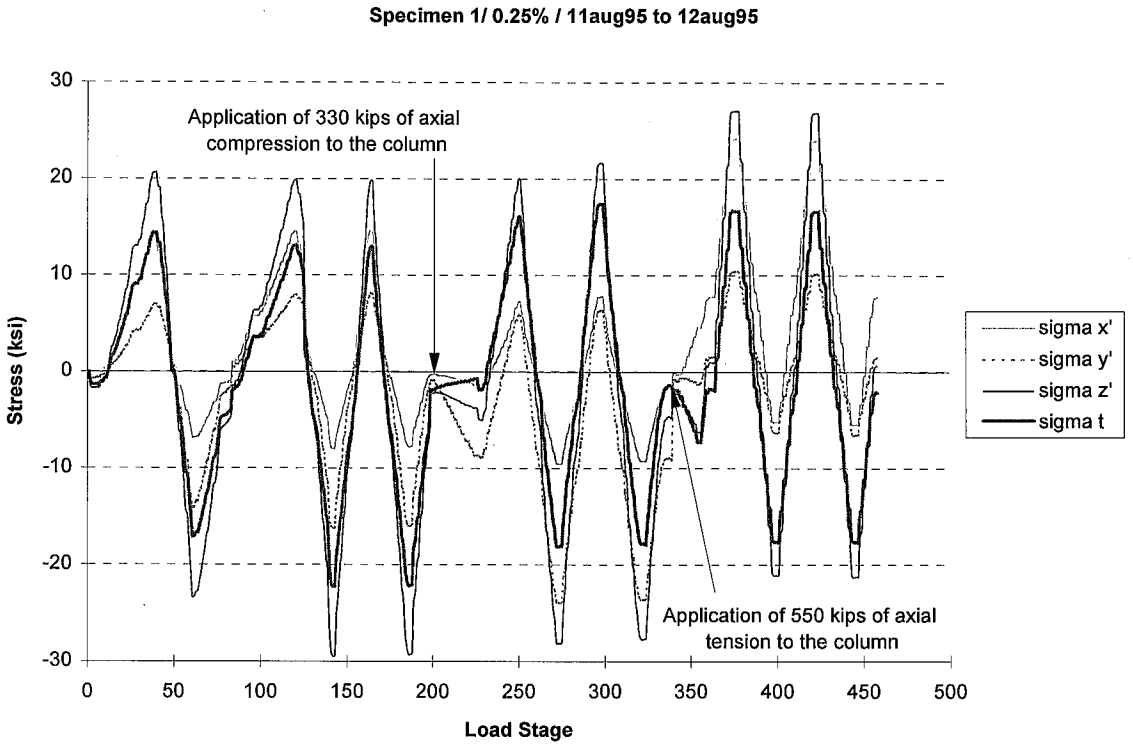

Figure I.12: Normal Stresses at Elements A and B (SW Connection of Specimen 1)

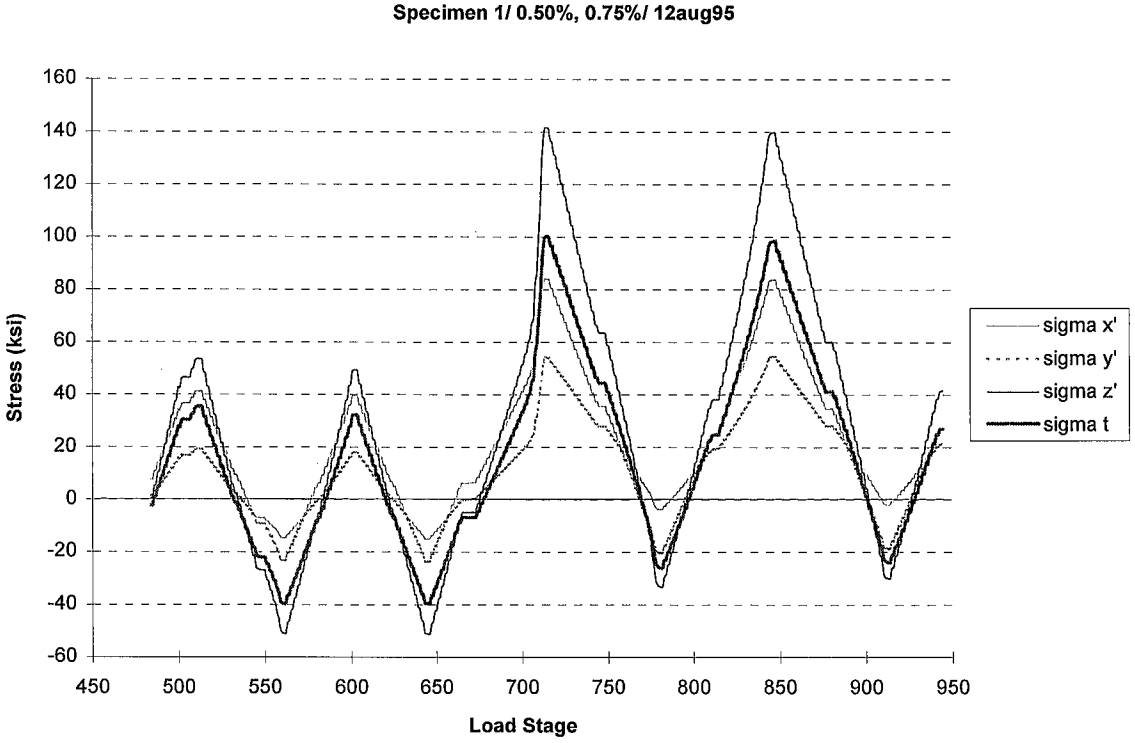

Figure I.13: Normal Stresses at Elements A and B (SW Connection of Specimen 1)

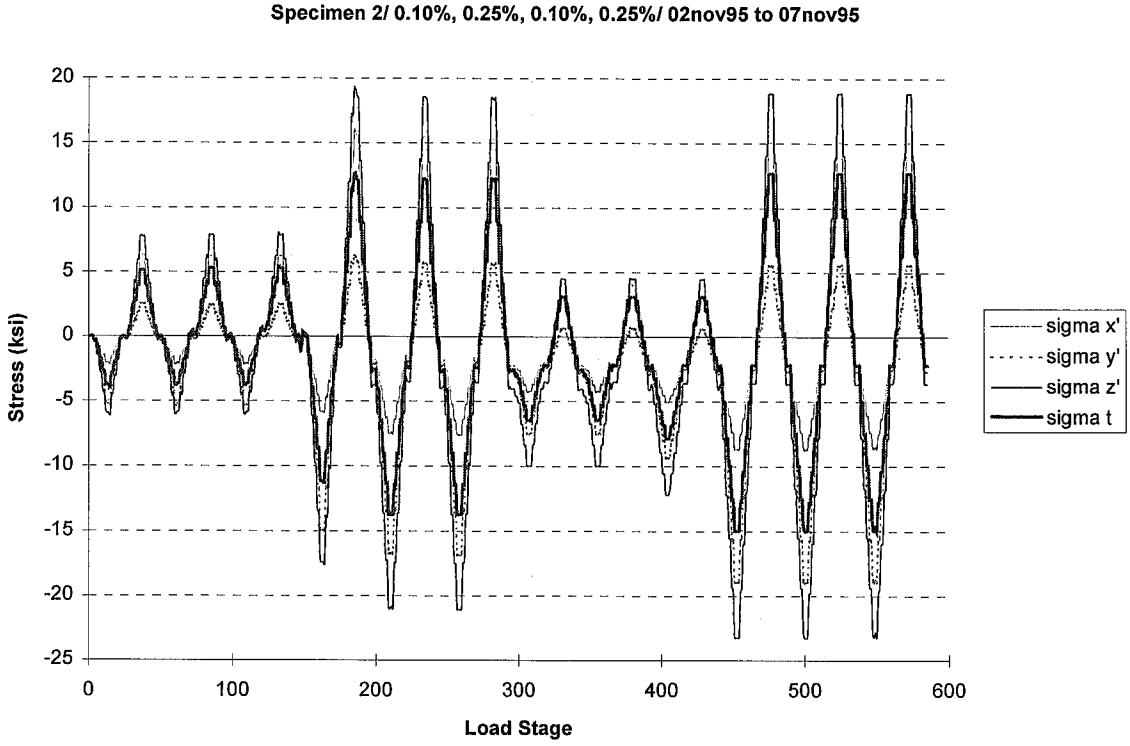

Figure I.14: Normal Stresses at Elements A and B (SE Connection of Specimen 2)

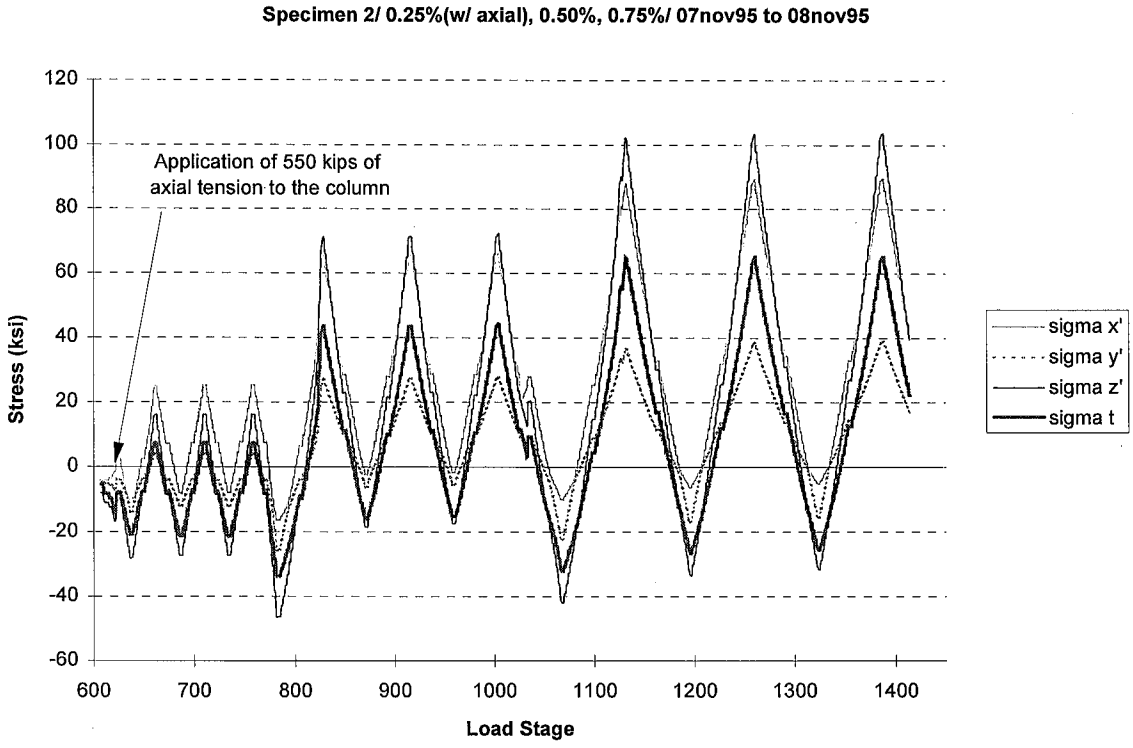

Figure I.15: Normal Stresses at Elements A and B (SE Connection of Specimen 2)

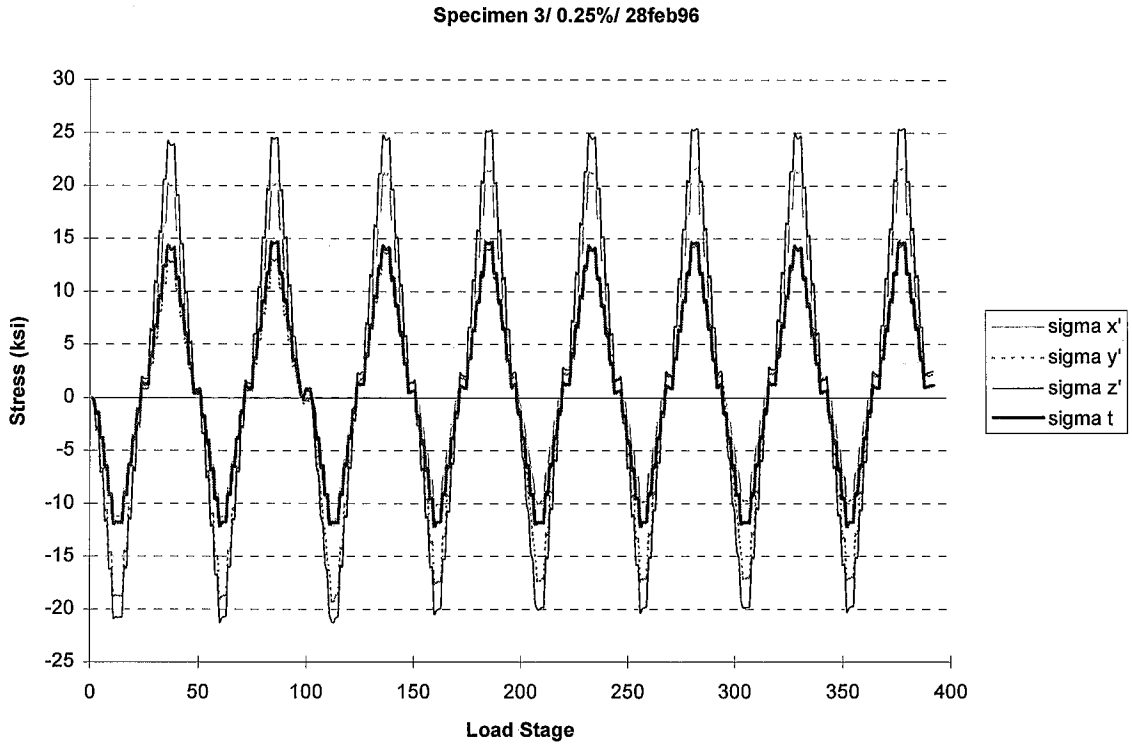

Figure I.16: Normal Stresses at Elements A and B (SE Connection of Specimen 3)

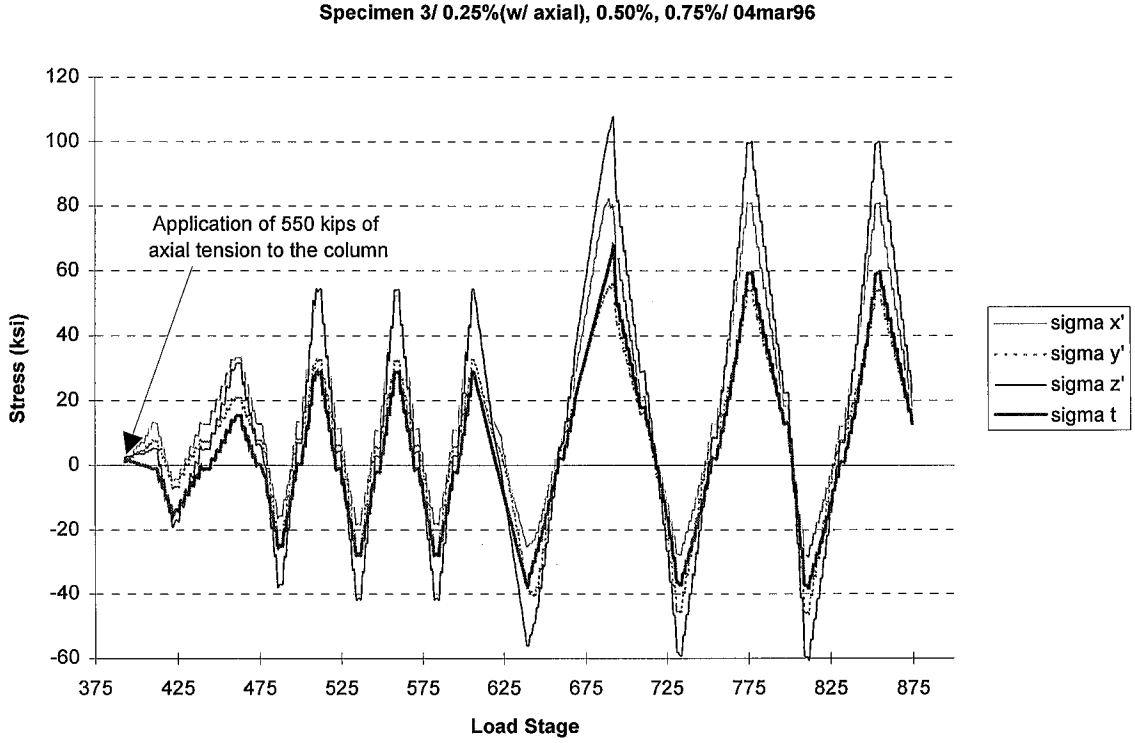

Figure I.17: Normal Stresses at Elements A and B (SE Connection of Specimen 3)

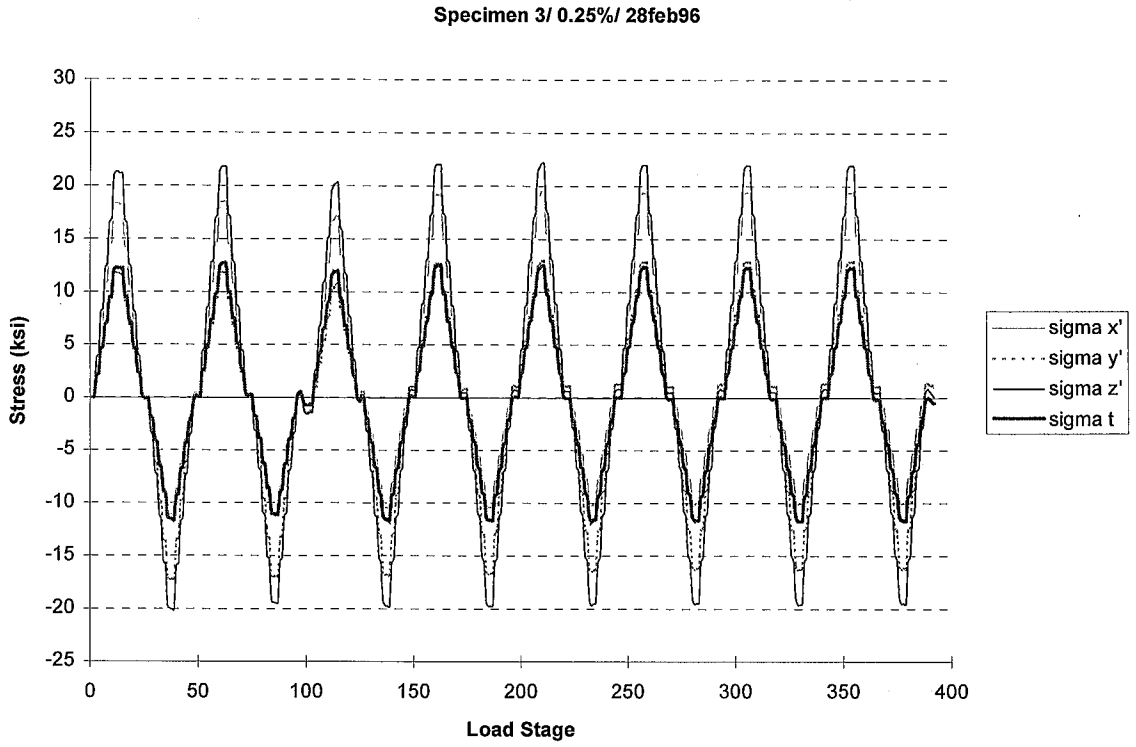

Figure I.18: Normal Stresses at Elements A and B (SW Connection of Specimen 3)

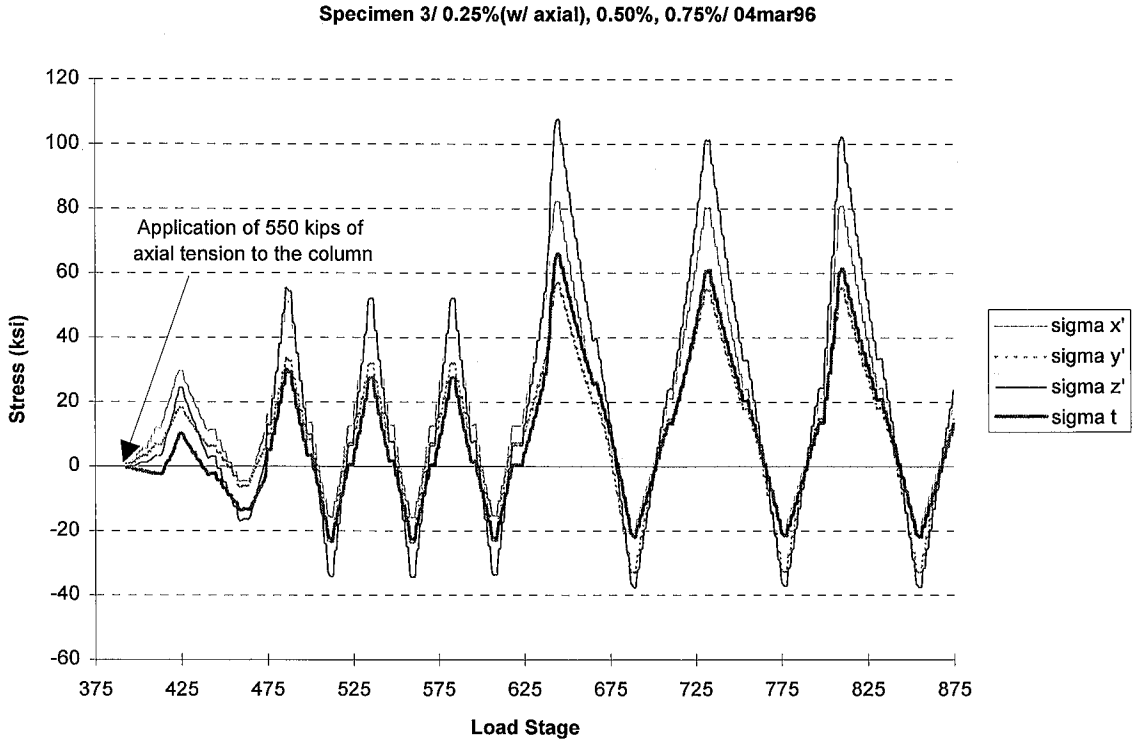

Figure I.19: Normal Stresses at Elements A and B (SW Connection of Specimen 3)

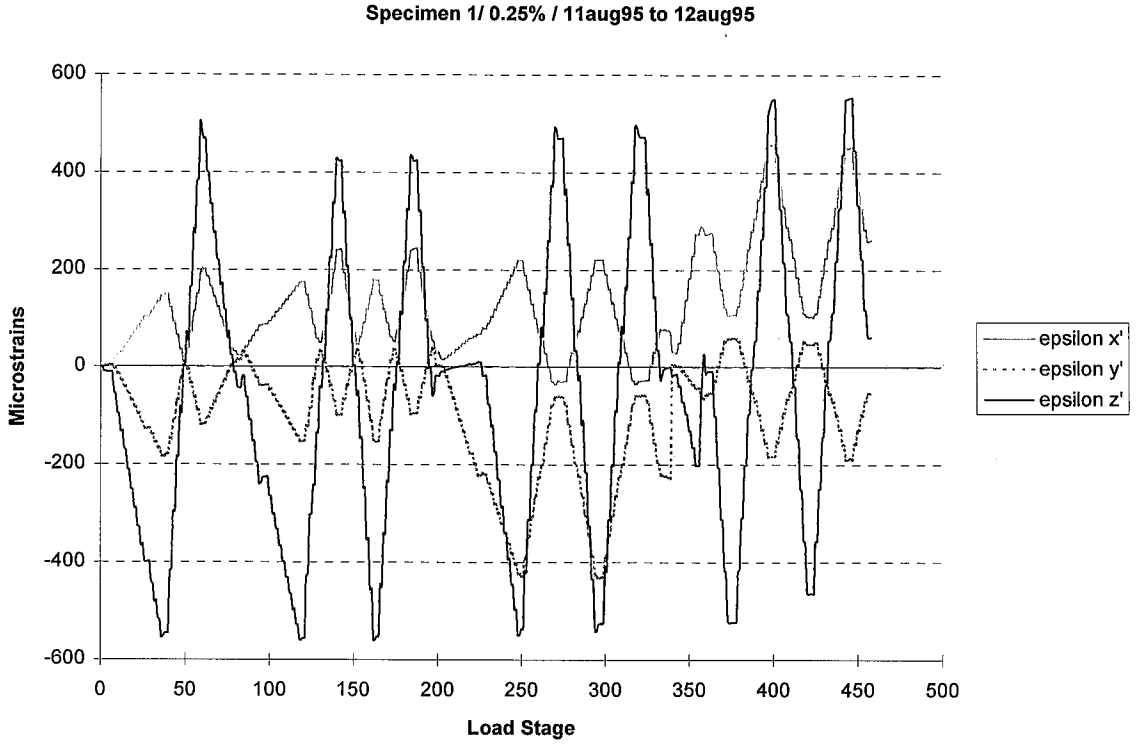

Figure I.20: Normal Strains at Element A (SE Connection of Specimen 1)

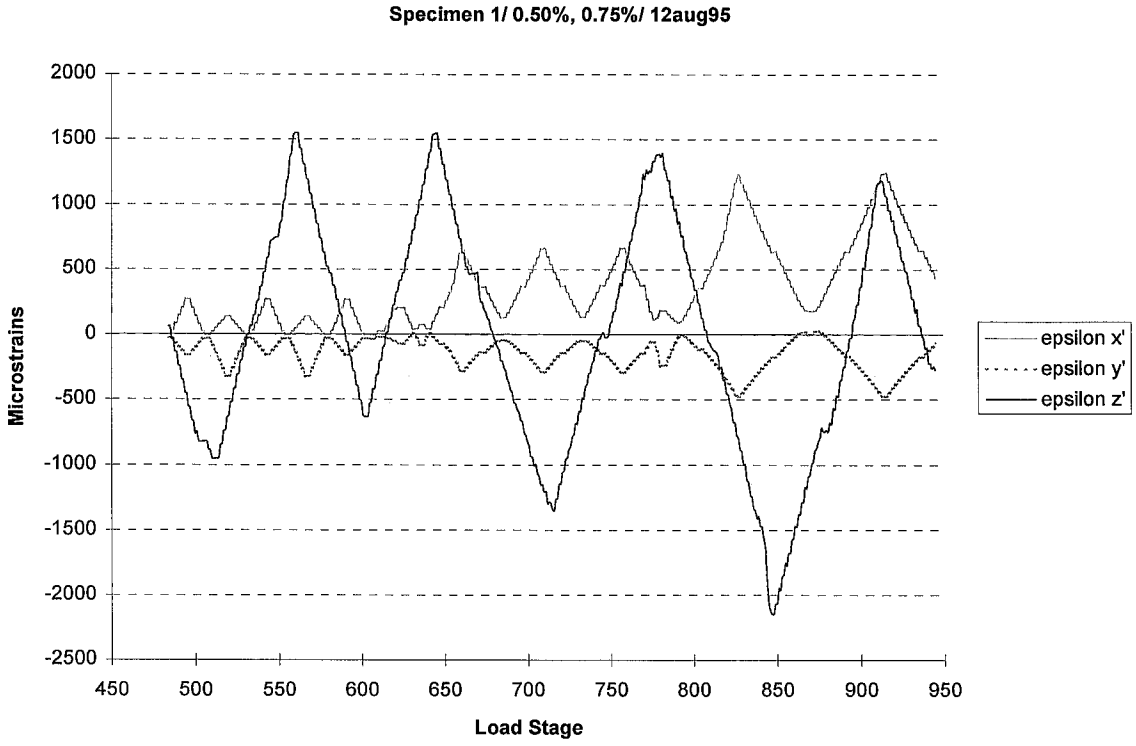

Figure I.21: Normal Strains at Element A (SE Connection of Specimen 1)

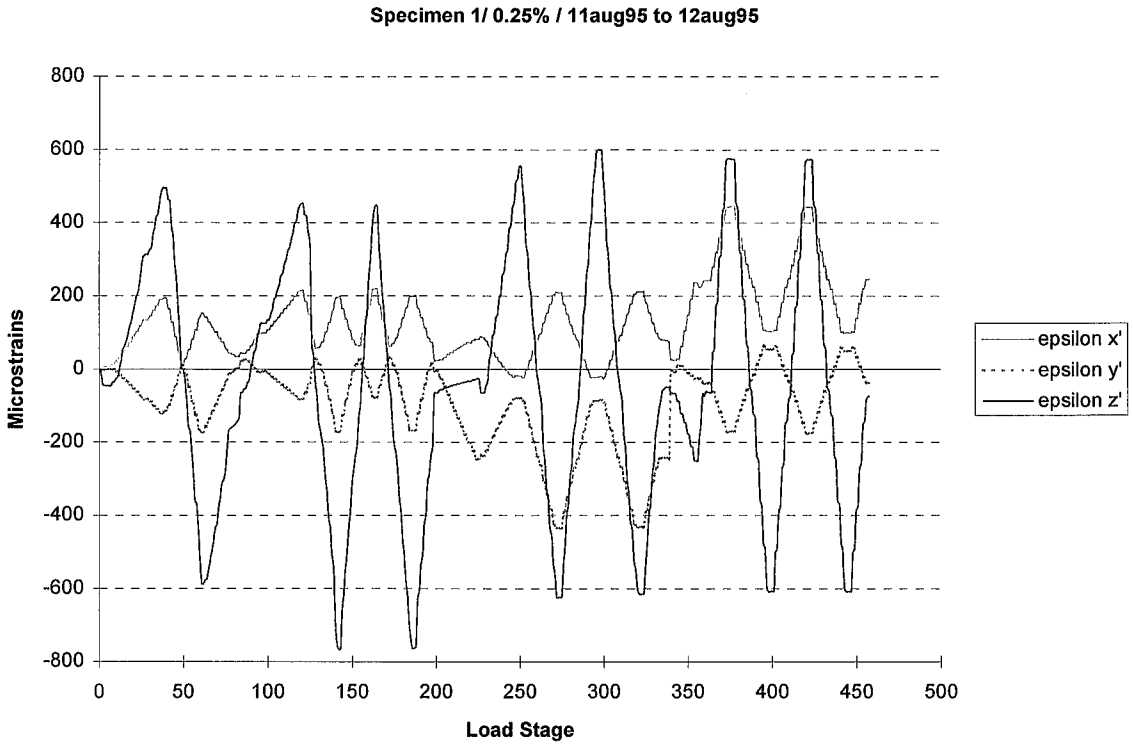

Figure I.22: Normal Strains at Element A (SW Connection of Specimen 1)

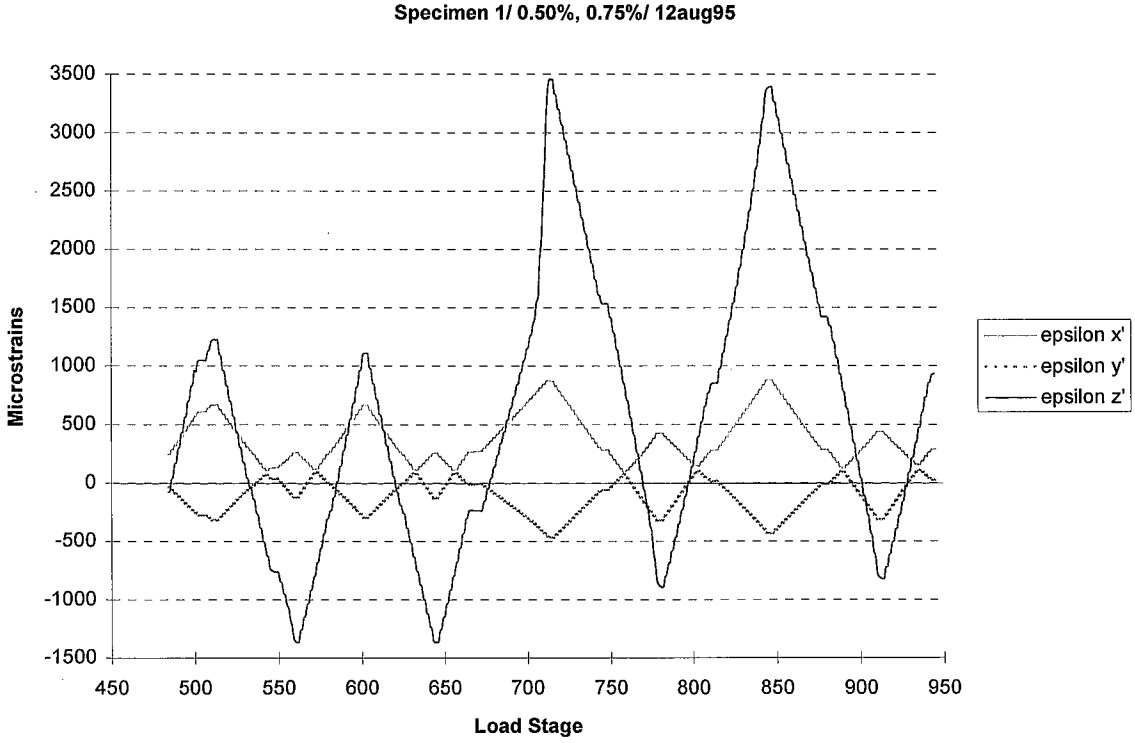

Figure I.23: Normal Strains at Element A (SW Connection of Specimen 1)

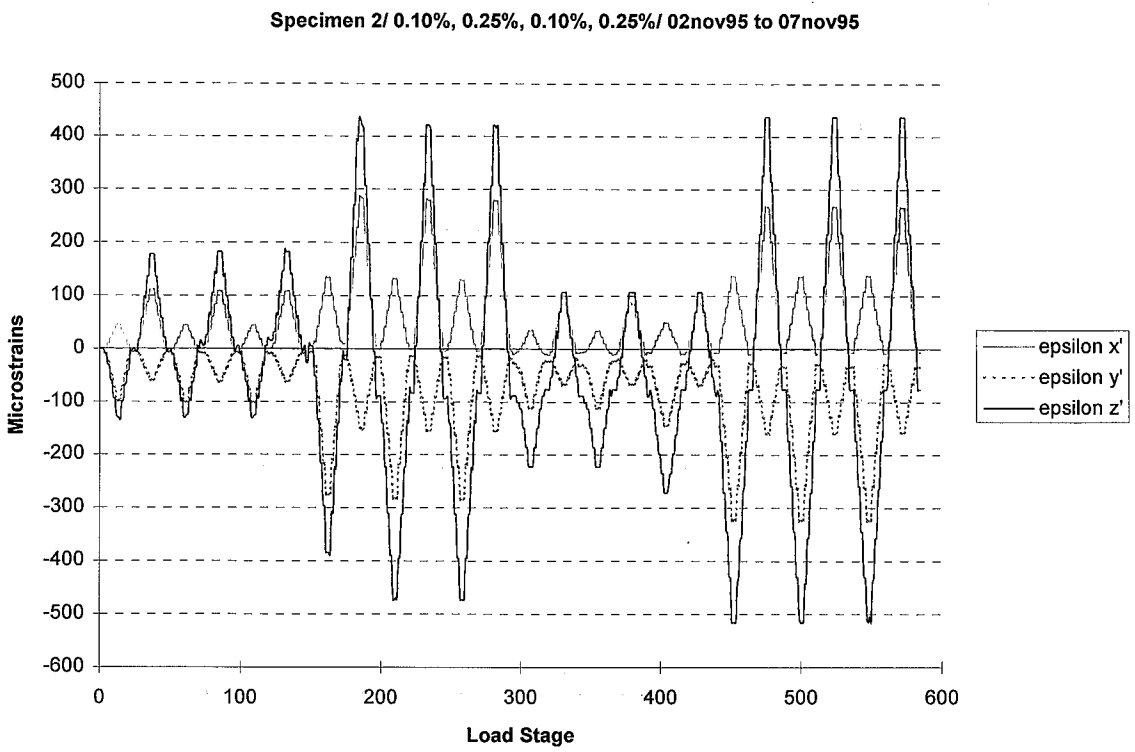

Figure I.24: Normal Strains at Element A (SE Connection of Specimen 2)

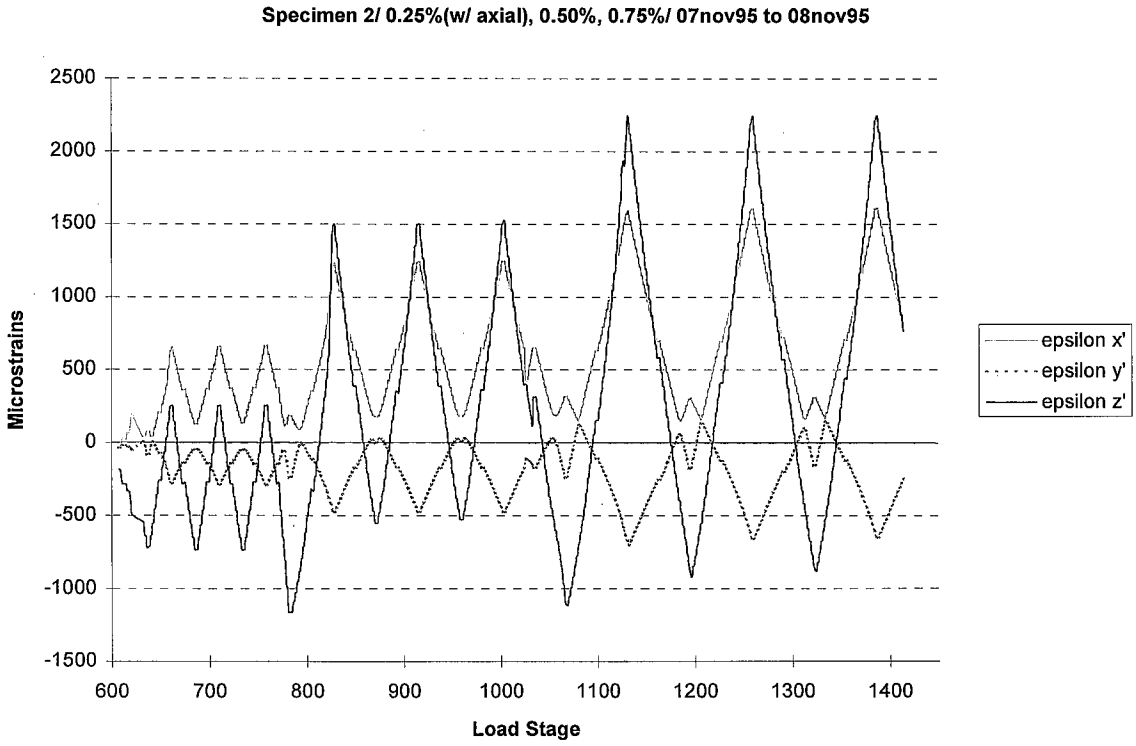

Figure I.25: Normal Strains at Element A (SE Connection of Specimen 2)

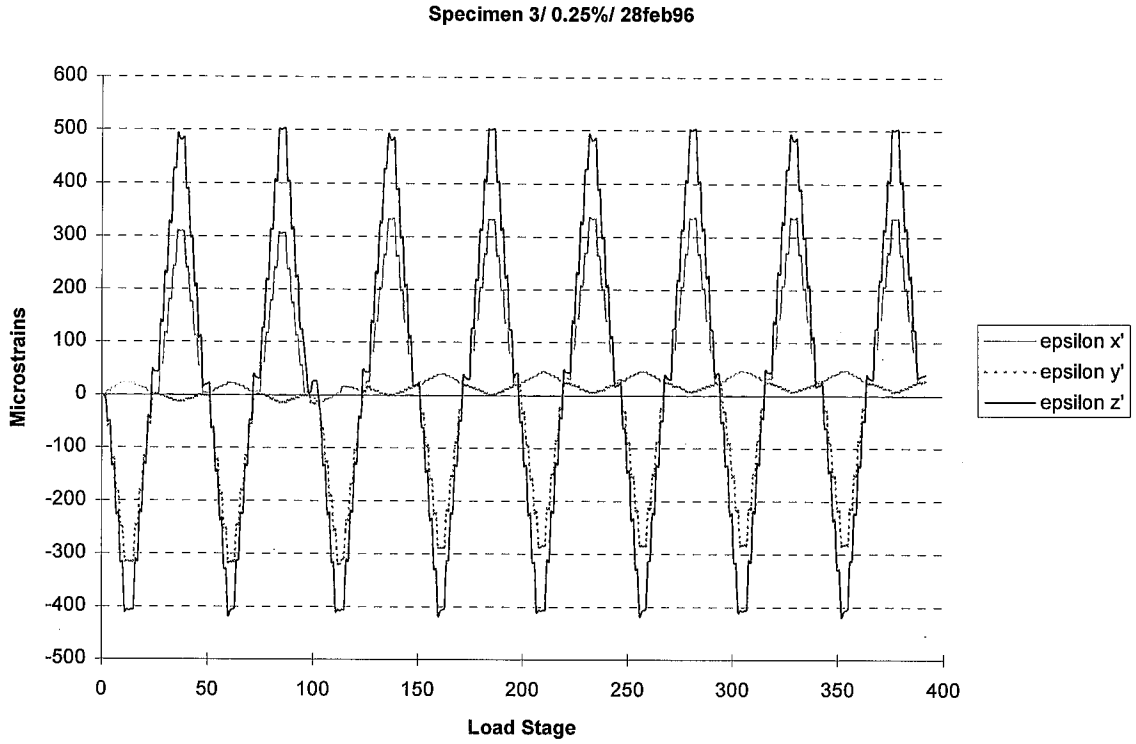

Figure I.26: Normal Strains at Element A (SE Connection of Specimen 3)

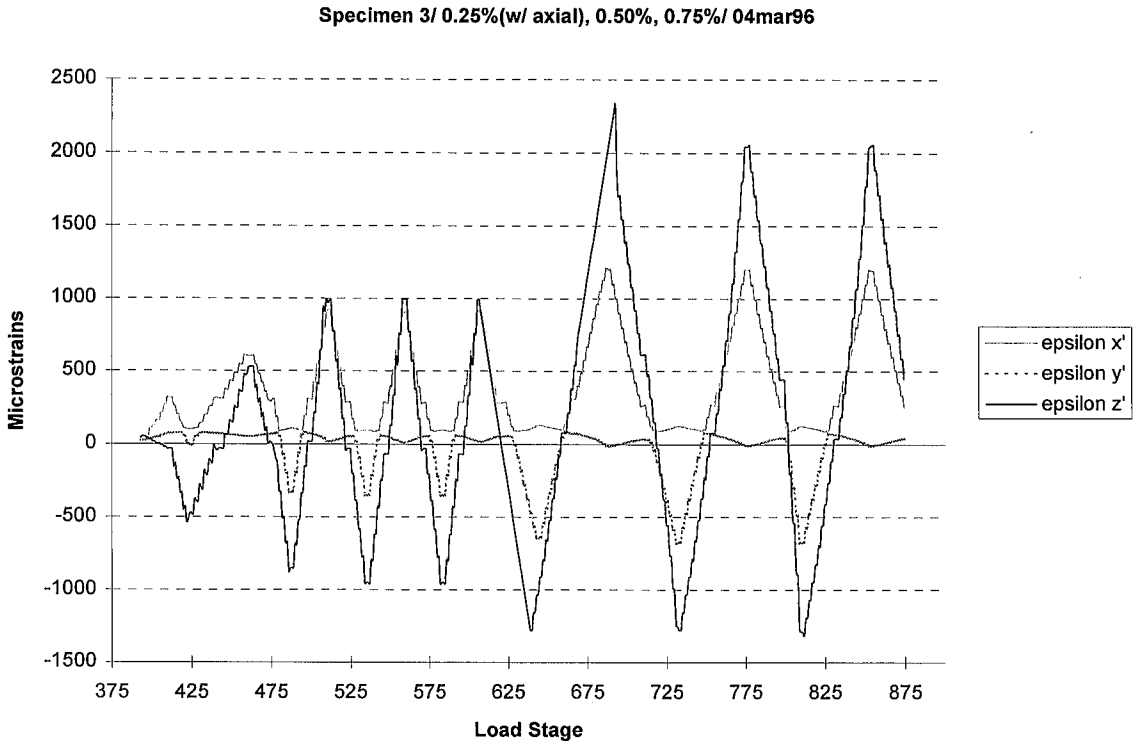

Figure I.27: Normal Strains at Element A (SE Connection of Specimen 3)

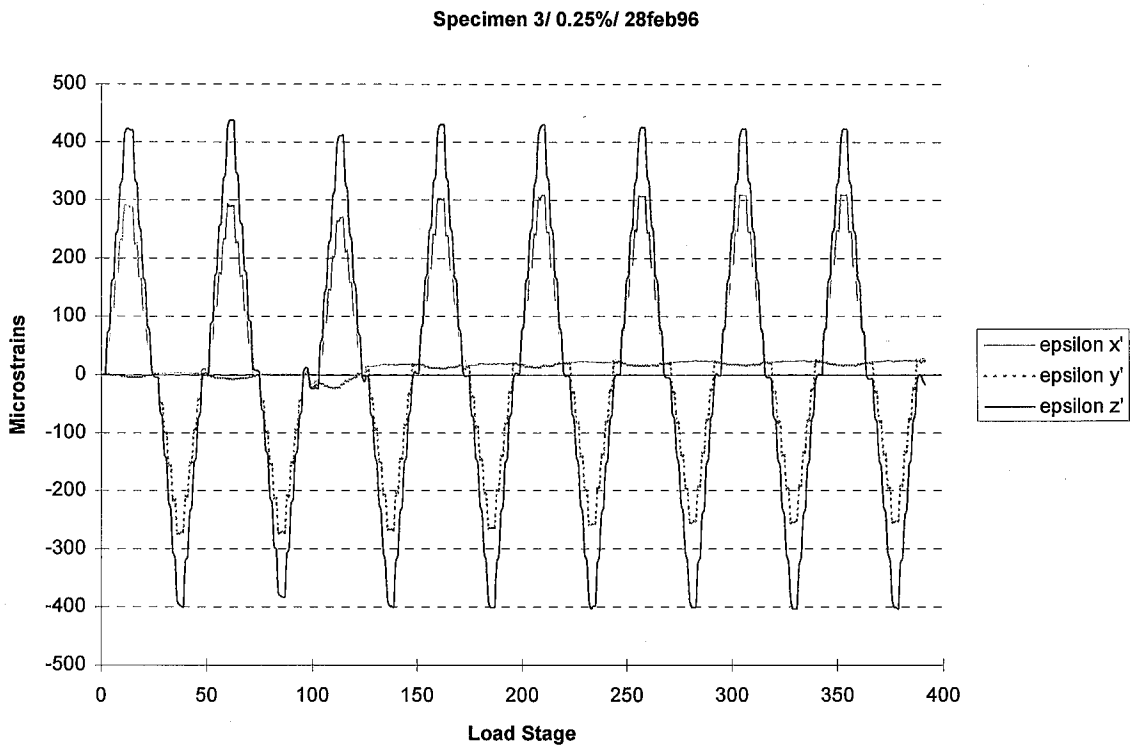

Figure I.28: Normal Strains at Element A (SW Connection of Specimen 3)

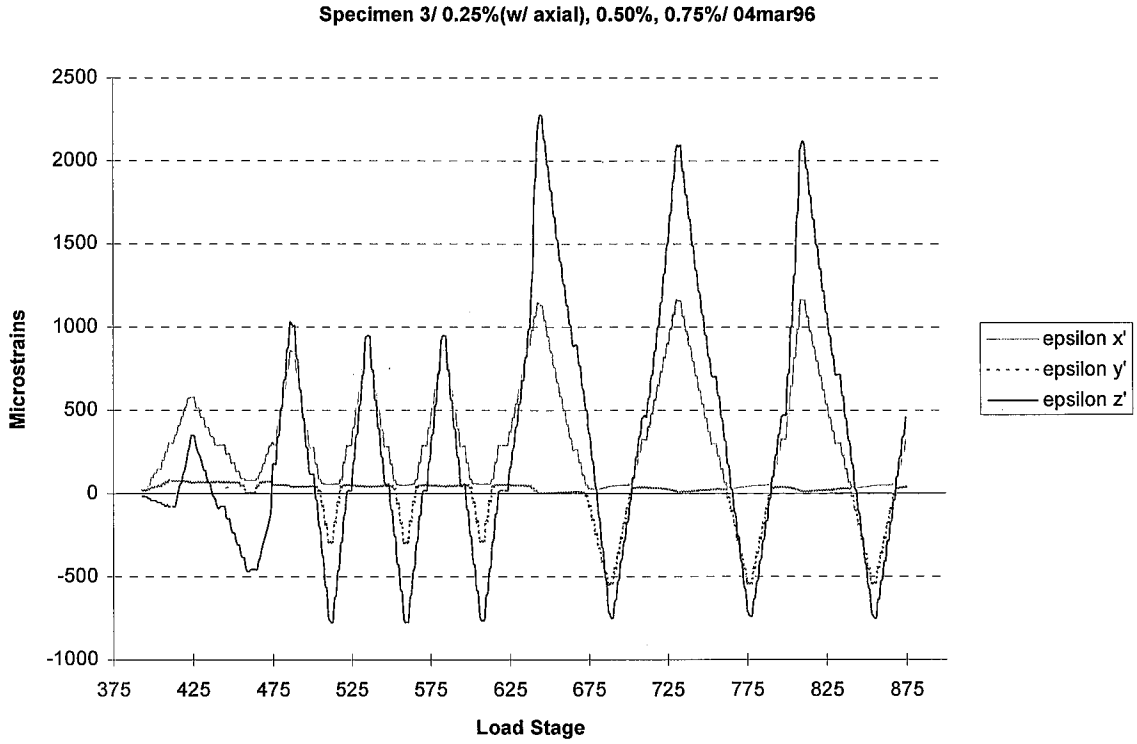

Figure I.29: Normal Strains at Element A (SW Connection of Specimen 3)

Section 2.2.1). The shear yield stress varies among different failure criteria (Cook and Young, 1985), but if using the Von Mises failure criterion, it is estimated as $0.6F_y$ or approximately 23 ksi.

Figures I.30 to I.39 plot the maximum shear stress at Element A (due to a triaxial state of stress; see Equation I.13), τ_{tri}, and the maximum shear stress at Element B (due to a uniaxial state of stress; see Equation I.14), τ_t. No strong correlation is made between the brittle-type fractures of three of the six connections with the stress condition defined above. This is observation is based on comparing the maximum shear stress at Element A (a triaxial state of stress) and at B (a uniaxial state of stress) to the shear yield stress. However, this comparison, which is based on linear elastic behavior, may be inappropriate past the 0.25% drift levels, due to the level of material nonlinearity occurring near the bottom weld region. Nevertheless, from Figures I.10 to I.39, it is concluded that a triaxial state of tensile stress is evident near the bottom girder flange-to-column weld region of all the connections, and that this condition may have resulted in high tensile stresses near the bottom CJP weld region.

Note that when calculating the maximum shear stress in Element A, the normal stresses are assumed to be equal to the principal stresses. This is a conservative assumption, since the normal stresses are only a component of the actual principal stresses and, therefore, the level of a triaxial state of stress in Element A may be greater than estimated.

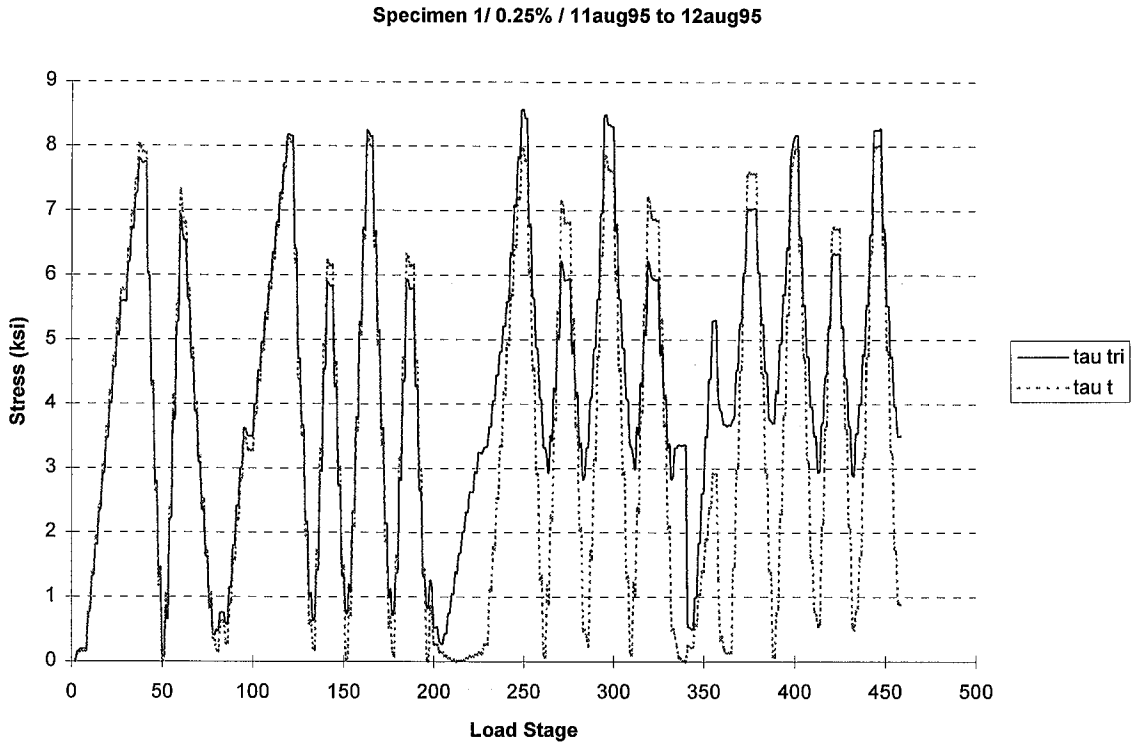

Figure I.30: Shear Stresses at Elements A and B (SE Connection of Specimen 1)

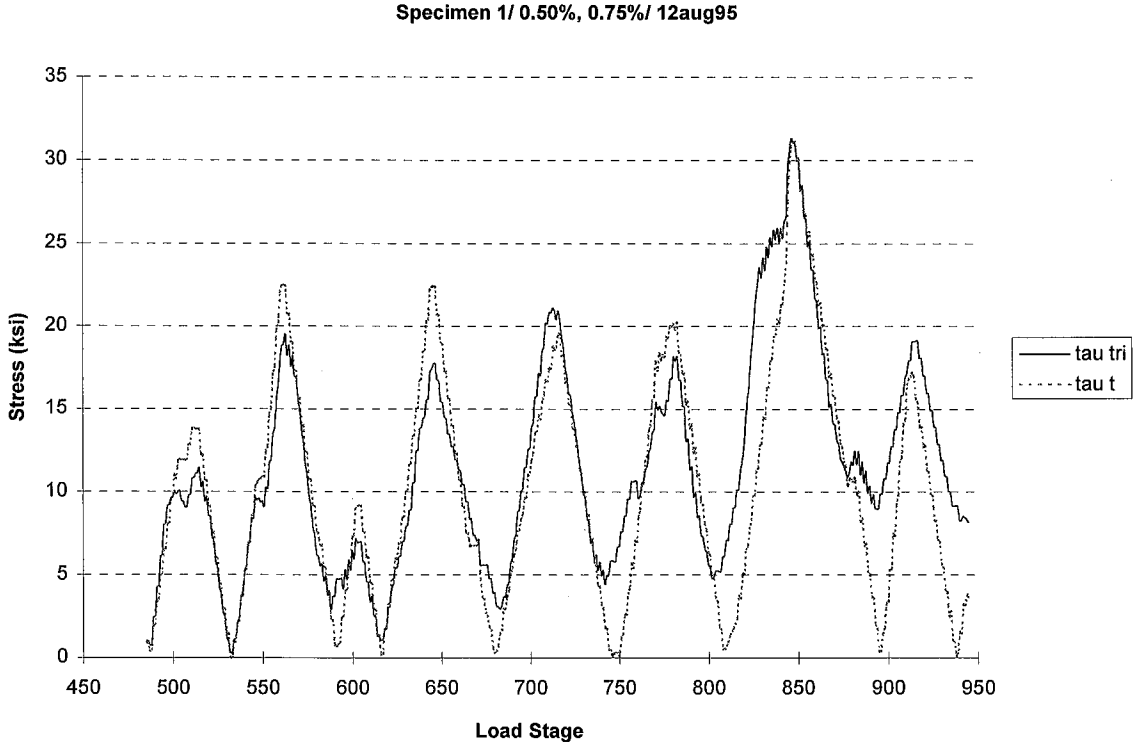

Figure I.31: Shear Stresses at Elements A and B (SE Connection of Specimen 1)

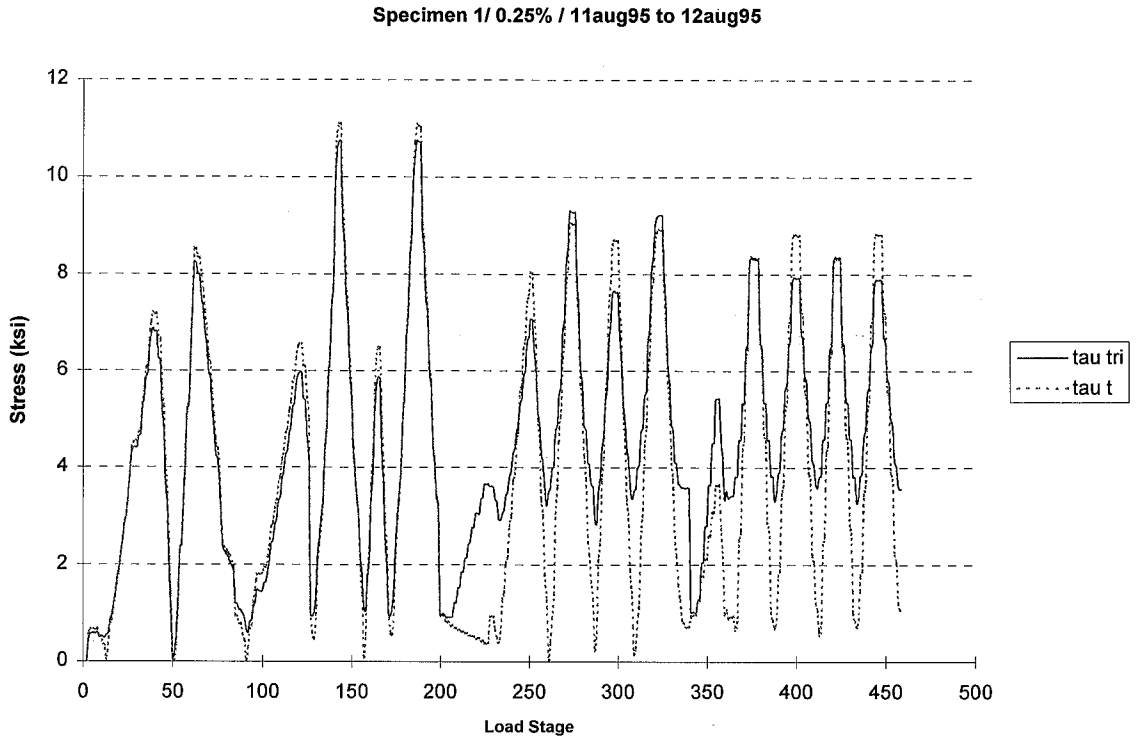

Figure I.32: Shear Stresses at Elements A and B (SW Connection of Specimen 1)

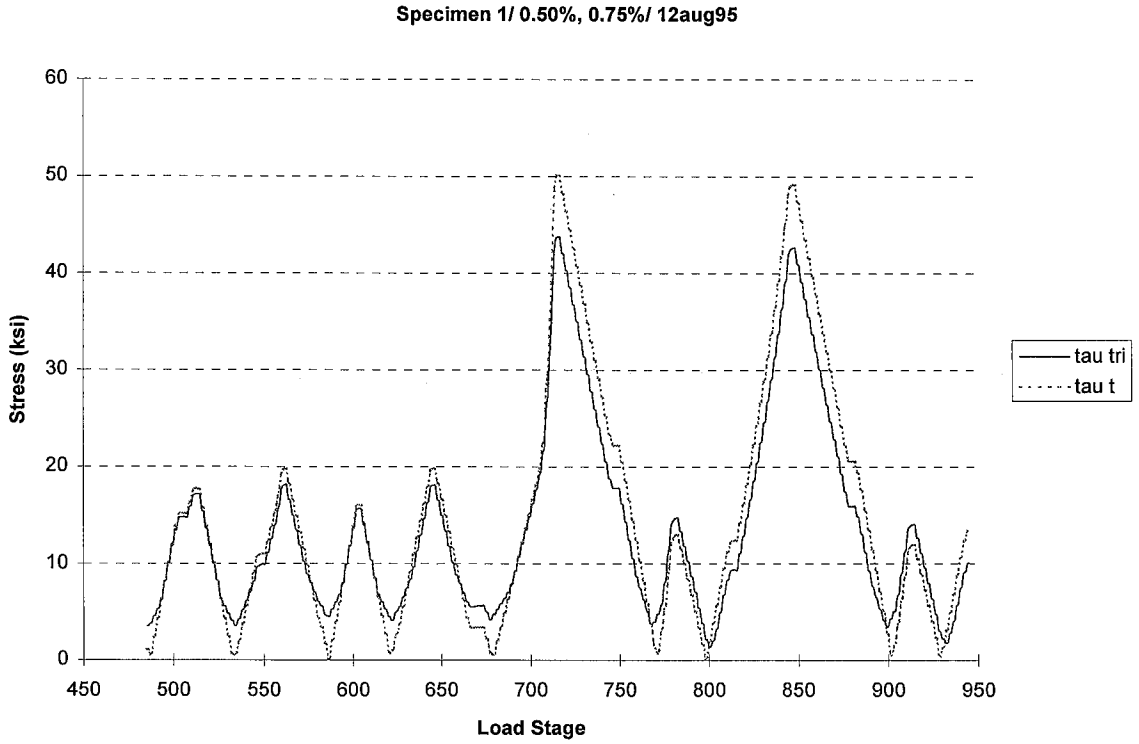

Figure I.33: Shear Stresses at Elements A and B (SW Connection of Specimen 1)

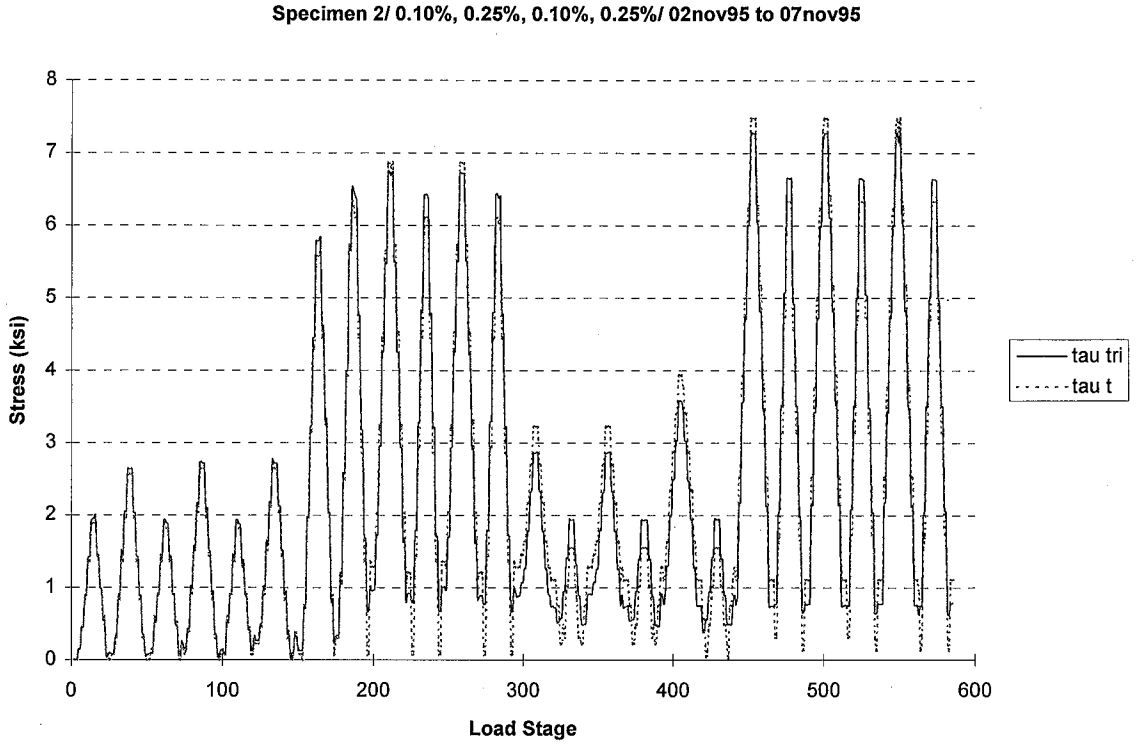

Figure I.34: Shear Stresses at Elements A and B (SE Connection of Specimen 2)

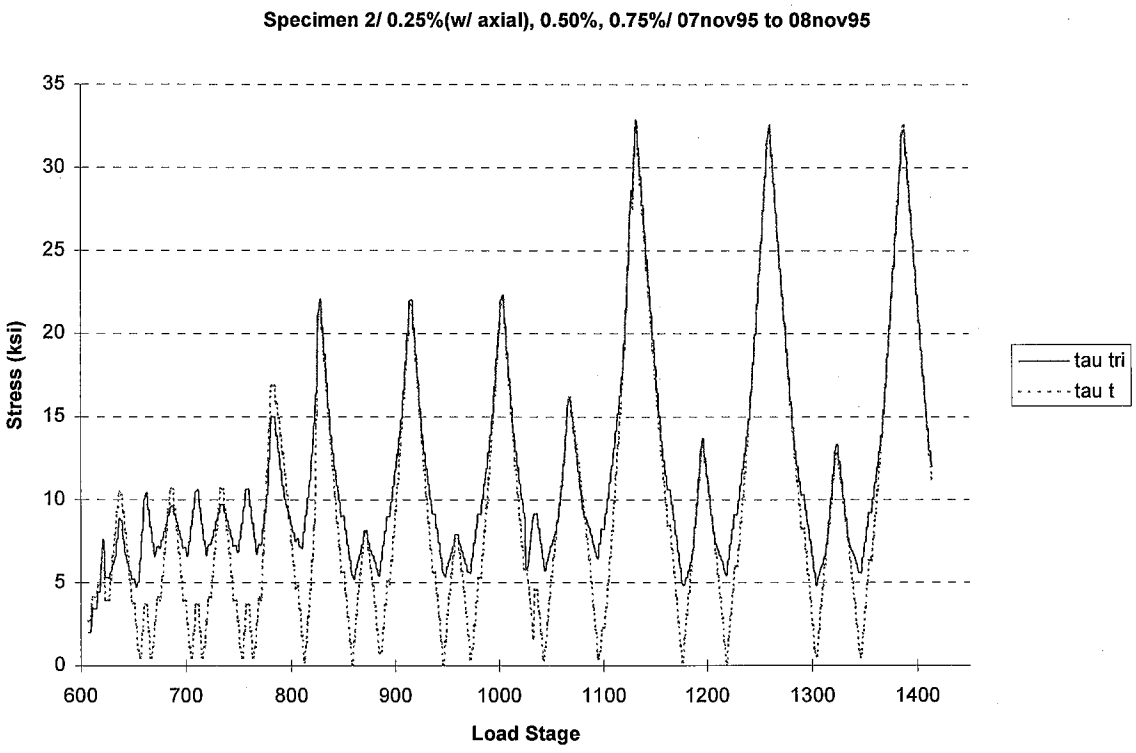

Figure I.35: Shear Stresses at Elements A and B (SE Connection of Specimen 2)

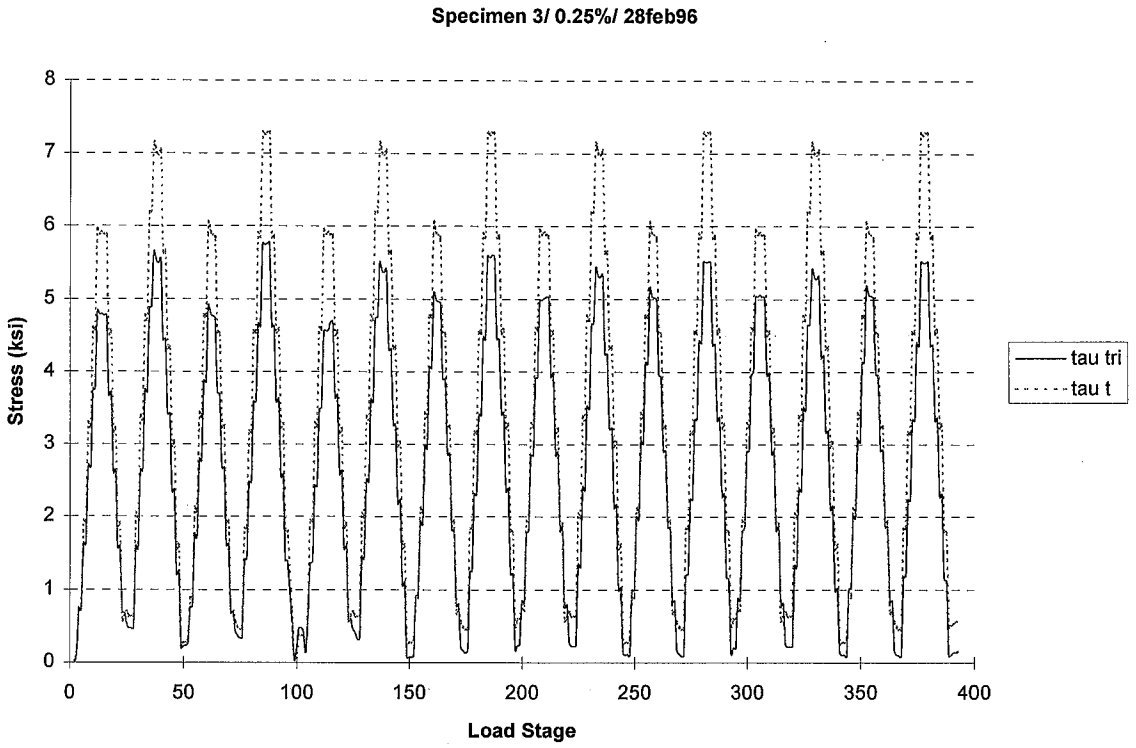

Figure I.36: Shear Stresses at Elements A and B (SE Connection of Specimen 3)

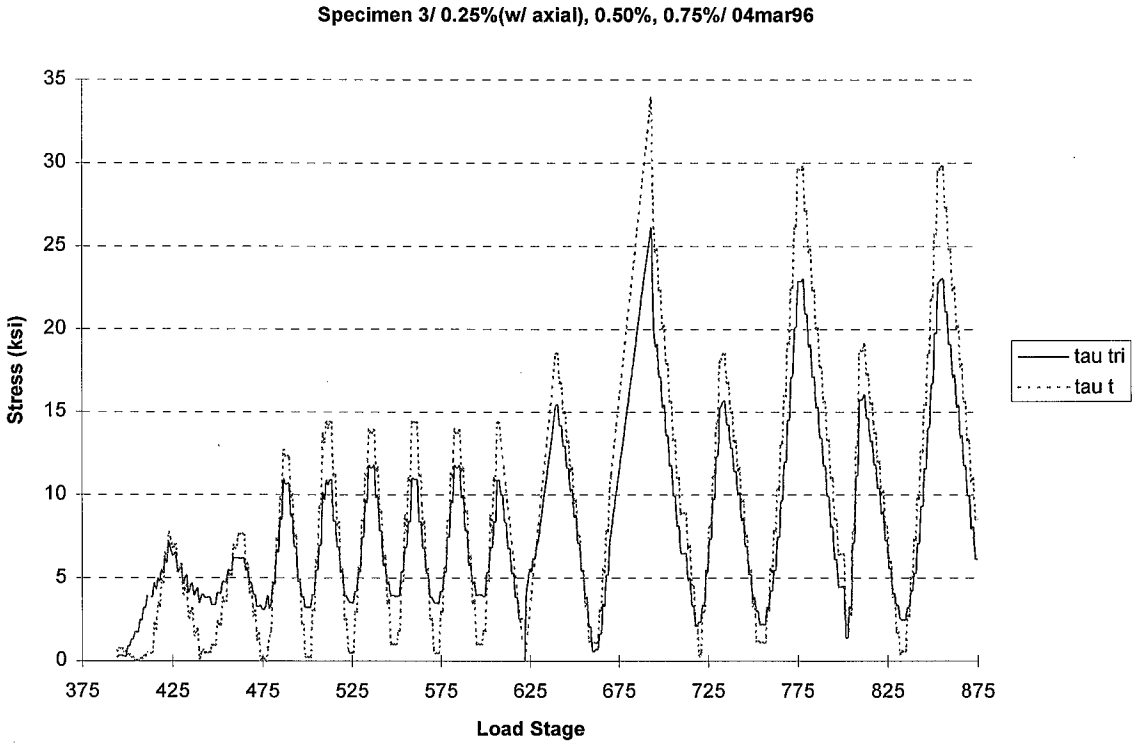

Figure I.37: Shear Stresses at Elements A and B (SE Connection of Specimen 3)

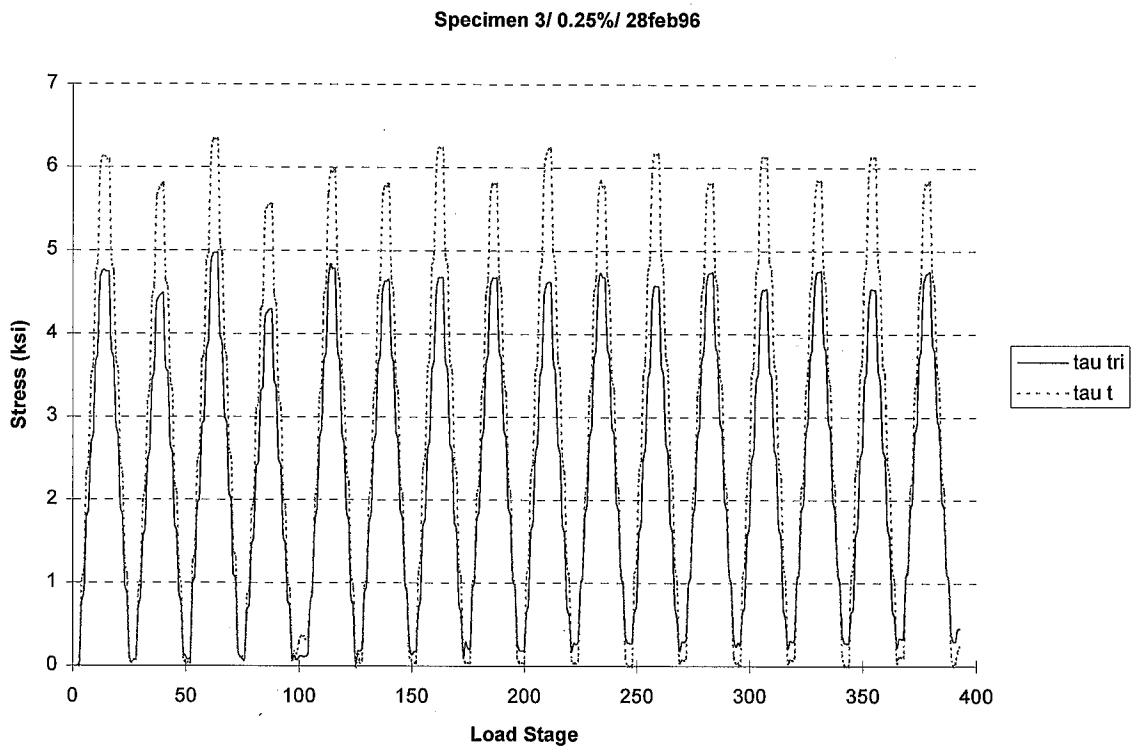

Figure I.38: Shear Stresses at Elements A and B (SW Connection of Specimen 3)

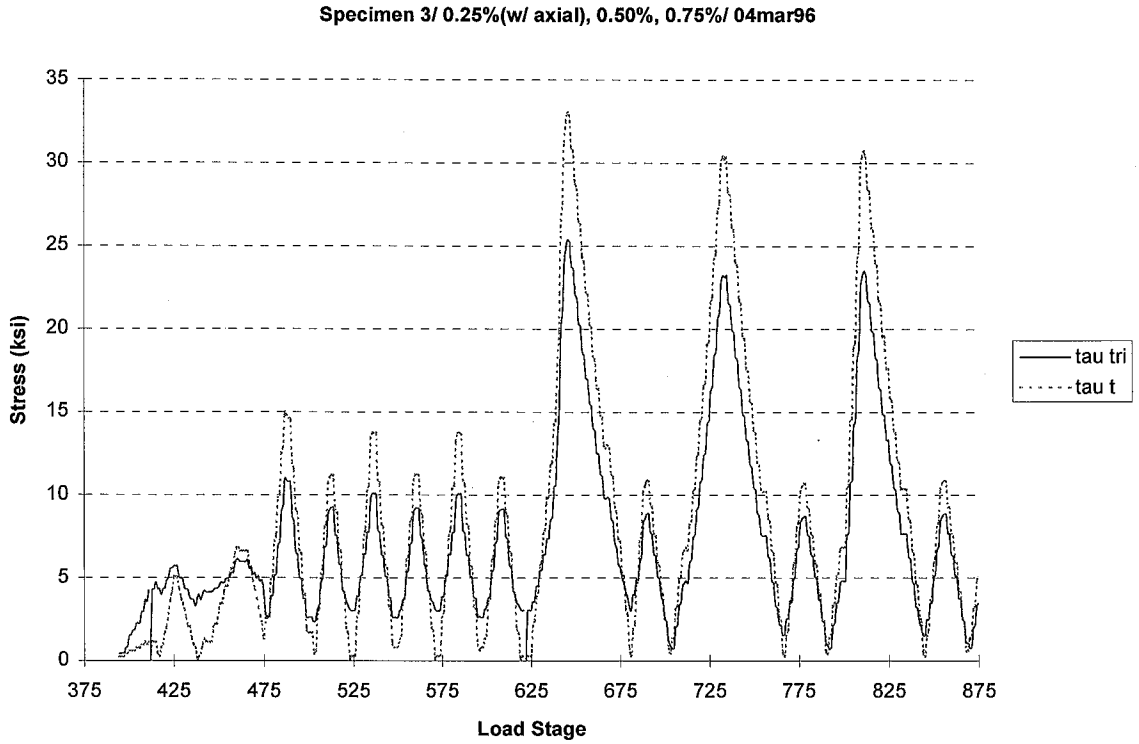

Figure I.39: Shear Stresses at Elements A and B (SW Connection of Specimen 3)

Appendix J

List of Symbols

a' = angular panel zone distortion arc length

c = line-intercept used to compute an average strain distribution based on linear regression

h_{story} = interstory height

k = spring stiffness at column supports representing rotational resistance due to load pin friction

k_{lf} = lateral spring stiffness at top column support representing the test specimen resistance to rotation due to load frame deformation

m = slope of a linear regression line (linear strain diagram) incorporating seven strain gage readings located at 13.5" along the girder cross section

n = number of strain measurements taken along the girder cross section

t_m = thickness of material; approximate distance away from Element A in which strains are valid

t_{tf} = measured thickness of top girder flange

t_{bf} = measured thickness of bottom girder flange

y_{bf} = distance between centroid of the bottom flange region and the neutral axis of the girder cross section

y_c = distance between centroid of the concrete slab and the neutral axis of the girder cross section

y_{lw} = distance between centroid of the lower web region and the neutral axis of the girder cross section

y_{tf} = distance between centroid of the top flange region and the neutral axis of the girder cross section

y_{uw} = distance between centroid of the upper web region and the neutral axis of the girder cross section

y_i = the *i*th strain gage location along the girder cross section measured from the bottom of the bottom girder flange

y_{NA} = location of the calculated neutral axis based on linear regression, measured from the bottom of the bottom girder flange

A_{tf} = cross-sectional area of the steel top flange of the steel girder

A_{uw} = cross-sectional area of the steel upper web of the steel girder

A_{lw} = cross-sectional area of the steel lower web of the steel girder

A_{bf} = cross-sectional area of the steel bottom flange of the steel girder

F_c^+ = force in the concrete slab due to positive girder bending

F_c^- = force in the concrete slab due to negative girder bending

F_{equil} = force in the concrete slab based on equilibrium of forces

F_{tf} = force in the top flange of the steel girder

F_{uw} = force in the upper web of the steel girder

F_{lw} = force in the lower web of the steel girder

F_{bf} = force in the bottom flange of the steel girder

H = horizontal reaction force at the top and bottom load pins

M_{ab} = fixed end moment at top support of column section AB

M_{act} = actual girder moment computed using applied load to the girder tip

M_{ba} = fixed end moment at top edge of panel zone

M_{cd} = fixed end moment at bottom edge of panel zone

M_{dc} = fixed end moment at bottom support of column section DC

M_{equil} = calculated girder moment based on equilibrium of forces

M_{load} = calculated column moment based on static equilibrium

M^{+}_{calc} = calculated girder moment for positive girder bending

M^{-}_{calc} = calculated girder moment for negative girder bending

$M_{p\,calc}$ = computed nominal girder moment strength for steel girder

$M_{p}^{+}{}_{calc}$ = computed nominal girder moment strength for positive girder bending

$0.8M_{p}^{+}{}_{calc}$ = 80% of the computed nominal girder moment strength for positive girder bending

$M_{p}^{+}{}_{max}$ = maximum girder moment achieved during girder positive bending

$M_{p}^{-}{}_{calc}$ = computed nominal girder moment strength for negative girder bending

$M_{p}^{-}{}_{max}$ = maximum girder moment achieved during girder positive bending

M_{load} = internal column moment calculated based on strains measured at the column flange surface

O = center of origin of Mohr's Circle

P = load applied to the girder tip

P_{axial} = axial load applied to the top of the column

P_{east} = load applied to the East girder tip

P_{max} = maximum load applied to the girder tip

P_{west} = load applied to the West girder tip

Q_{bf} = first moment area of bottom flange region

Q_{lw} = first moment area of lower web region

Q_{uw} = first moment area of upper web region

Q_{tf} = first moment area of top flange region

Q_{slab} = first moment area of concrete slab

R = radius of Mohr's Circle

$\overline{Y}$ = mean of the strain gage locations measured from the bottom of the bottom girder flange at a distance of 13.5" from the column face

α = angle representing the deviation of the calculated normal strains from the uniaxial strain state due to axial force and flexure in the column

β = angle relating δ and a' within the panel zone region

ε_{avg_east} = average strain measured at the East top or bottom column flange surface at a distance L_{sb} from the top or bottom load pins

ε_{avg_west} = average strain measured at the West top or bottom column flange surface at a distance L_{sb} from the top or bottom load pins

ε_A, ε_B, and ε_C = strains measured on column flange surface near bottom access hole

ε^{+}_{equil} = strain calculated in concrete slab during positive girder bending based on equilbrium of forces

ε^{-}_{equil} = strain calculated in concrete slab during negative girder bending based on equilbrium of forces

$\bar{\varepsilon}$ = mean of the strain magnitudes measured from the bottom of the bottom girder flange at a distance of 13.5" from the column face

ε_{bf} = strain measured in the top flange region of the steel girder

ε_c = strain calculated at the center of the concrete slab (assuming no slip)

ε_i = the *i*th strain magnitude measured along the girder cross section at a distance of 13.5" from the column face

ε_{lw} = strain measured in the lower web region of the steel girder

ε_r = strain at which concrete cracks under tension

ε_{tf} = strain measured in the top flange region of the steel girder

ε_{uw} = strain measured in the upper web region of the steel girder

$\varepsilon_{x'}$ = normal strain measured in the plane of the column flange (x'-axis)

$\varepsilon_{y'}$ = normal strain measured in the plane of the column flange (y'-axis)

$\varepsilon_{z'}$ = strain measured parallel to the longitudinal axis of the girder (z'-axis)

ε_{NA} = strain magnitude of zero is measured at the neutral axis along the girder cross section at a distance of 13.5" from the column face

δ = average of the top and bottom panel zone LVDT measurements

γ_{xy} = engineering shear strain in the x-y direction

γ_{pz} = angular panel zone distortion

γ_1 = angular panel zone distortion component w.r.t the horizontal direction

γ_2 = angular panel zone distortion component w.r.t the vertical direction

ϕ = curvature measured along the girder cross section at a distance of 13.5" from the column face

ϕ_{col} = curvature measured along the column cross section at a distance L_{sb} from the top or bottom load pins

σ_t = uniaxial tensile stress in Element B (z-axis)

$\sigma_{x'}$ = normal stress in Element A (x'-axis)

$\sigma_{y'}$ = normal stress in Element A (y'-axis)

$\sigma_{z'}$ = normal stress in Element A (z'-axis)

σ_1, σ_2, σ_3 = principal stresses in Element A

τ_t = maximum shear stress under a uniaxial stress state

τ_{tri} = maximum shear stress under a triaxial stress state

θ_a = angle measuring the transformation of the x'-y'axes from the x-y axis

θ_{back_calc} = back calculated girder-to-column plastic rotation

θ_a = column rotation at the top column support

θ_b = joint rotation at top edge of panel zone region

θ_c = joint rotation at bottom edge of panel zone region

θ_d = column rotation at the bottom column support

θ_{joint} = rotation of the joint or connection relative to the test specimen

θ_{lf} = rotation of test specimen due to load frame deformation

θ_p = girder-to-column plastic rotation

$\theta_p^{+}{}_{max}$ = maximum girder-to-column plastic rotation achieved during girder positive bending

$\theta_p^{-}{}_{max}$ = maximum girder-to-column plastic rotation achieved during girder positive bending

Δ = horizontal displacement of top and bottom edges of panel zone

Δ_{act} = actual girder tip deflection; average measured displacement of two actuators at the girder tip

Δ_{back_calc} = back calculated girder tip deflection

Δ_{bot} = measured displacements by the bottom girder relative to column LVDTs

Δ_{calc} = calculated girder tip deflection

Δ_{col} = girder tip deflection component due to column flexural deformation

Δ_{ew_lf} = measured horizontal deflection of the load frame

Δ_{flex} = girder tip deflection component due to girder and column flexural deformation

$\Delta_{gird\,flex}$ = girder tip deflection component due to girder flexural deformation

$\Delta_{gird\,shear}$ = girder tip deflection component due to girder elastic shear deformation

Δ_{joint} = girder tip deflection component due to joint rotation

Δ_{lf} = girder tip deflection component due to load frame deformation

Δ_{lp} = deflection of top load pin due to load frame deformation

Δ_{pz} = girder tip deflection component due to panel zone shear distortion

Δ_{rel} = girder tip deflection component due to girder-to-column rotation

Δ_{story} = interstory lateral displacement

Δ_{tip} = girder tip deflection

Δ_{top} = displacement measured by the top girder relative to column LVDTs

Δ_1 = displacement measured at the bottom panel zone LVDTs

Δ_2 = displacement measured at the top panel zone LVDTs

Appendix K

List of Parameters

a	= effective thickness of concrete slab (in.)	
	(full composite action)	4.0
	(Specimen 2)	2.33
	(Specimen 3)	1.64
b	= effective width of panel zone region (in.)	15.72
b'	= horizontal distance between top and bottom panel zone LVDTs (in.)	
	(Specimen 1)	10.05
	(Specimen 2)	10.05
	(Specimen 3)	9.00
b_e	= effective width of concrete slab width (in.)	60
d	= depth of W27X94 steel section (in.)	26.92
d_{bar}	= diameter of #4 steel reinforcing bar (in.)	0.50
d_c	= depth of W14X211 steel column section (in.)	15.72
d'	= vertical distance between girder relative to column rotation LVDTs (in.)	
	(East girder of Specimen 1)	21.44
	(East girder of Specimen 2)	21.75
	(East girder of Specimen 3)	21.19

(West girder of Specimen 1) 21.17

(West girder of Specimen 2) 22.00

(West girder of Specimen 3) 21.32

d_1 = distance measured from the centroid of the force in the concrete to the top of the steel section (in.)

(Specimen 2/ positive girder bending) 3.84

(Specimen 3/ positive girder bending) 4.18

(Specimen 2 and 3/ negative girder bending) 3.25

d_2 = distance measured from the centroid of the force in the steel section to the top of the steel section (in.)

(Specimen 2/ positive girder bending) 0.302

(Specimen 3/ positive girder bending) 0.635

(Specimen 2 and 3/ negative girder bending) 2.74

d_3 = distance measured from P_y to the top of the steel section (in.) 13.46

f_c' = compressive strength of concrete slab (psi)

(Specimen 2) 4910

(Specimen 3) 4436

f_r' = modulus of rupture of concrete slab (psi)

(Specimen 2) 525

(Specimen 3) 500

f_s = shear form factor for girder cross section

(Specimen 1) 2.08

(Specimen 2/ positive girder bending) 3.73

(Specimen 3/ positive girder bending) 3.49

(Specimens 1, 2, and 3/ negative girder bending) 2.08

h = effective depth of panel zone region (in.)

h' = vertical distance between top and bottom panel zone LVDTs (in.)

(Specimen 1) 24.25

(Specimen 2) 24.25

	(Specimen 3)	22.00
n	= modular ratio = E_s / E_c	
	(Specimen 2)	7.64
	(Specimen 3)	7.26
t_f	= thickness of girder flange (in.)	0.745
q, r, s, and t	= distances measured from edge of column flange and top surface of bottom girder flange to the centroids of the column flange strain gage rosette and bottom girder flange post-yield strain gage located near bottom access hole (see Figures I.2 and I.3; Table I.1)	
t_s	= thickness of slab measured from the top of the concrete slab to the top of the steel girder (in.)	5.0
t_w	= thickness of girder web (in.)	0.49
x	= length measured from center of top load pin to E-W LVDT (in.)	37.86
y_e	= location of the elastic centroidal axis of the girder cross section measured from bottom of the bottom flange (in.)	
	(Specimen 1/ positive and negative girder bending)	13.46
	(Specimen 2/ positive girder bending)	22.57
	(Specimen 2/ negative girder bending)	14.15
	(Specimen 3/ positive girder bending)	21.27
	(Specimen 3/ negative girder bending)	14.15
y_p	= location of the plastic centroidal axis of the girder cross section measured from top of the top flange (in.)	
	(Specimen 1/ positive and negative girder bending)	13.46
	(Specimen 2/ positive girder bending)	0.604
	(Specimen 2/ negative girder bending)	11.56
	(Specimen 3/ positive girder bending)	3.50
	(Specimen 3/ negative girder bending)	11.56

$y_1, y_2, \ldots y_5$	= distances measured from bottom of bottom steel section a respective position along the girder cross section located 13.5" from the column flange surface (in.) (see Table G.1)	
cover	= top concrete cover of steel reinforcing bars (in.)	1.5
A_c	= cross-sectional area of concrete slab (in^2)	240
A_r	= cross-sectional area of reinforcing bars (in^2)	1.18
A_s	= gross area of steel section (in^2)	27.7
A_{sc}	= cross-sectional area of a 3/4" diameter shear connector (in^2)	0.442
A_{tr}	= transformed cross-sectional area of composite girder (in^2)	
	(Specimen 2)	61.93
	(Specimen 3)	58.72
$A_{tr\ slab}$	= transformed cross-sectional area of concrete slab (in^2)	
	(Specimen 2)	34.34
	(Specimen 3)	31.02
C	= compressive force in the concrete slab (kips)	
	(Specimen 2)	583.2
	(Specimen 3)	371.1
E_c	= modulus of concrete (ksi)	
	(Specimen 2)	3994
	(Specimen 3)	3796
E_s	= modulus of elasticity of steel (ksi)	29,000
F_{ry}	= yielding stress of reinforcing bars (ksi)	60
F_y	= yielding stress of steel (ksi)	38
F_u	= ultimate tensile stress of steel (ksi)	59
F_{uc}	= ultimate tensile strength of a shear connector (ksi)	60
G	= shear modulus of steel (ksi)	11,154
I_c	= moment of inertia of W14X211 steel section (in^4)	2660
I_{eff}	= effective moment of inertia of composite girders (in^4)	
	(Specimen 2/ positive girder bending)	6476

	(Specimen 2/ negative girder bending)	3595
	(Specimen 3/ positive girder bending)	5901
	(Specimen 3/ negative girder bending)	3595
I_{tr}	= transformed moment of inertia of composite girders (in^4)	
	(Specimen 2/ positive girder bending)	7471
	(Specimen 3/ positive girder bending)	7378
I_{xx}	= moment of inertia of W27X94 steel section (strong-axis bending)	
	(Specimen 1) (in^4)	7471
L_a	= length measured from the column face to girder relative to column rotation LVDTs (in.)	13.5
L_c	= length measured from center of column support to top edge of panel zone (in.)	72.04
L_g	= length measured from column face to point of applied load (in.)	132.0
L_{sg}	= length measured from center of load pin to column strain gage locations (in.)	58.3
N_{bars}	= number of reinforcing bars along the width of the concrete slab	6
N_{sc}	= number of shear connectors along the length, L_g, of the top girder flange	
	(Specimen 2)	22
	(Specimen 3)	14
P_y	$= A_s F_y$ = tensile strength of girder steel section (kips)	1053
P_{yf}	= tensile strength of girder flanges (kips)	289.5
Q_n	= shear capacity of a shear connector (kips)	26.51
T	= tensile force in the concrete slab (kips)	70.69
Z_x	= plastic modulus of a W27X94 steel section (in^3)	273
τ_y	= shear yield stress (ksi)	23
ν	= Poisson's ratio of steel	0.3

References

American Concrete Institute (1995). "Building Code Requirements for Structural Concrete (ACI 318-95) and Commentary (ACI 318R-95)." ACI Committee 318, Farmington Hills, MI.

American Institute of Steel Construction (1992). "Seismic Provisions for Structural Steel Buildings." American Institute of Steel Construction, Chicago, IL.

American Institute of Steel Construction (1993). "Load and Resistance Factor Design Specification for Structural Steel Buildings." Internal Report, 2nd Ed., American Institute of Steel Construction, Chicago, Illinois.

American Institute of Steel Construction (1995). "Statistical Analysis of CVN For Steel Wide Flange Structural Shapes." Internal Report, American Institute of Steel Construction, Chicago, IL.

Barrett, C., Nix, W., and Tetelman, A. (1973). *The Principles of Engineering Materials*, Prentice-Hall, Inc., Englewood Cliffs, NJ.

Bertero, V. V., Popov, E. P., and Krawinkler, H. (1973). "Further Studies on Seismic Behavior of Steel Beam-Column Subassemblages." *Report No. UCB/EERC-73/27*, Earthquake Engineering Research Center, University of California, Berkeley, CA.

Blackman, B. and Popov, E. P. (1995). "Studies in Steel Moment Resisting Beam-to-Column Connections for Seismic-Resistant Design." *Report No. UCB/EERC-95/11*, Earthquake Engineering Research Center, University of California, Berkeley, CA.

Blodgett, O. (1995). "Details to Increase Ductility in SMRF Connections." *The Welding Innovation Quarterly*, Vol. 12, No. 2, pp. 16-18.

Carlson, P. C. (1997). "The Behavior of Earthquake Resistant, Composite Steel Moment Resisting Frame Connections." M.S. thesis, Department of Civil Engineering, University of Minnesota, Minneapolis, MN.

Chen, W. F. and Yamaguchi, E. (1996). "Spotlight on Steel Moment Frames." *Civil Engineering,* ASCE, March, pp. 44-46.

Cook, R. D. and Young, W. C. (1985). *Advanced Mechanics of Materials*, Macmillan Publishing Company, New York, NY.

Earthquake Engineering Research Institute (1995). *Earthquake Spectra, Northridge Earthquake Reconnaissance Report,* Vol. 1, April.

Earthquake Engineering Research Institute (1996). *Earthquake Spectra, Northridge Earthquake Reconnaissance Report,* Vol. 2, January.

Engelhardt, M.D. and Husain, A. (1993). "Cyclic-Loading Performance of Welded Flange-Bolted Web Connections." *Journal of Structural Engineering,* ASCE, Vol. 119, No. 12, pp. 3537-3550.

Fisher, J., Dexter, R., and Kaufmann, E. (1995). "Fracture Mechanics of Welded Structural Steel Connections." Internal Report, Center for Advanced Technology for Large Structural Systems, Lehigh University, Bethlehem, PA.

Forcier, G. (1994). "Seismic Performance of Older Steel Frames." Ph.D. dissertation, Department of Civil Engineering, University of Minnesota, Minneapolis, MN.

Gere, J. and Timoshenko, S. P. (1990). *Mechanics of Materials*, 3rd Ed., PWS-KENT Publishing Company, Boston, MA.

Goel, S. C., Stojadinovic, B., and Lee, K.-H. (1996). "A New Look at Steel Moment Connections." *Research Report No. UMCEE 96-19*, Department of Civil and Environmental Engineering, College of Engineering, University of Michigan, Ann Arbor, MI.

Gourley, B. C. and Hajjar, J. F. (1994). "Cyclic Nonlinear Analysis of Three-Dimensional Concrete-Filled Steel Tube Beam-Columns and Composite Frames." *Structural Engineering Report No. ST-94-3*, Department of Civil Engineering, University of Minnesota, Minneapolis, MN.

Gross, J. L. (1997). Internal report, National Institute of Standards and Technology, Gaithersburg, MD.

Hajjar, J. F., O'Sullivan, D. P., Leon, R. T., Gourley, B. C. (1995). "Evaluation of the Damage to the Borax Corporate Headquarters Building as a Result of the Northridge Earthquake." *SAC Rep. No. 95-07*, SAC Joint Venture, Sacramento, CA.

Hajjar, J. F. and Gourley, B. C. (1996). "Representation of Concrete-Filled Steel Tube Cross-Section Strength." *Journal of Structural Engineering*, ASCE, Vol. 122, No. 11, November, pp. 1327-1336.

Hajjar, J. F. and Gourley, B. C. (1997). "A Cyclic Nonlinear Model for Concrete-Filled Tubes. I. Formulation." *Journal of Structural Engineering*, ASCE, Vol. 123, No. 6, June, pp. 736-744.

Hajjar, J. F., Gourley, B. C., and Olson, M. C. (1997). "A Cyclic Nonlinear Model for Concrete-Filled Tubes. II. Verification." *Journal of Structural Engineering*, ASCE, Vol. 123, No. 6, June, pp. 745-754.

Igarashi, S., Inoue, K., Kim, S. E., and Tada, M. (1984). "A Study on Elastic-Plastic Response Analysis of Framed Structures Composed of Composite Beams." *Trans.*, Architectural Institute of Japan, 337, pp. 39-52.

Kaufmann, E., Fisher, J., Lu, L., and Xue, M. (1996). "Achieving Ductile Behavior of Moment Connections." *Modern Steel Construction*, AISC, January, pp. 30-39.

Kaufmann, E. J. and Fisher, J. W. (1997). "Dynamic Tension Tests of Simulated Moment Resisting Frame Weld Joints." Proceedings of the Northridge Earthquake Research Conference, Los Angeles, California, August 20-23, 1997, California Universities for Research in Earthquake Engineering, Sacramento, California.

Krawinkler, H., Bertero, V.V., and Popov, E. P. (1971). "Inelastic Behavior of Steel Beam-to-Column Subassemblages." *Report No. UCB/EERC-71/07*, Earthquake Engineering Research Center, University of California, Berkeley, CA.

Larsen, R. J. and Marx, M. L. (1981). "An Introduction to Mathematical Statistics and its Applications." Prentice-Hall, Inc., Englewood Cliffs, NJ, pp. 406.

Lee, L. and Lu, S. (1989). "Cyclic Tests of Full-Scale Composite Joint Subassemblages." *Journal of Structural Engineering*, ASCE, Vol. 115, No. 8, August, pp. 1977-1998.

Leon, R. T. (1983). "The Influence of Floor Members on the Behavior of Reinforced Concrete Beam-Column Joints Subjected to Severe Cyclic Loading." University of Texas at Austin, Austin, TX.

Leon, R. T. and Hajjar, J. F. (1997). "Effect of Floor Slabs on Behavior of Full Moment Steel Connections." *Building to Last*, Proceedings of the American Society of Civil Engineers Structures Congress '97, Kempner, L. and Brown, C. B. (eds.), Portland, Oregon, April 13-16, 1997, ASCE, New York, pp. 772-776.

Leon, R. T., Hajjar, J. F., and Shield, C. K. (1997a). "The Effect of Composite Floor Slabs on the Behavior of Steel Moment-Resisting Connections in the Northridge Earthquake." *Composite Construction III,* Buckner, D. C. and Shahrooz, B. M. (eds.), Engineering Foundation, American Society of Civil Engineers, New York, NY, pp. 739-751.

Leon, R. T., Hajjar, J. F., Shield, C. K., and Gustafson, M. A. (1997b). "The Effect of Composite Floor Behavior on the Failure of Steel Moment-Resisting Connections." Proceedings of the Northridge Earthquake Research Conference, Los Angeles, California,

August 20-23, 1997, California Universities for Earthquake Engineering Research, Sacramento, CA.

Lincoln Electric Company (1997). "Electrode Specification Report." Lincoln Electric Engineering Report, Lincoln Electric, Cleveland, OH.

Mukudai, Y. and Matsuo, A. (1983). "A Study of the Analysis and the Behavior of Multi-Storied Frames With Concrete Slab During a Severe Earthquake." *Journal of Structural Engineering*, Japan, 29, pp. 211-220.

Olson, S. (1980). "Strength and Fatigue Evaluation of 20 Year-Old AASHTO Type III Girders." M.S. thesis, Department of Civil Engineering, University of Minnesota, Minneapolis, MN.

Popov, E. P. (1983). "Seismic Moment Connections for Moment-Resisting Steel Frames." *Report No. UCB/EERC-83/02*, Earthquake Engineering Research Center, University of California, Berkeley, CA.

Popov, E. P. and Stephen, R. M. (1970). "Cyclic Loading of Full-Scale Steel Connections." *Report No. UCB/EERC-70/03*, Earthquake Engineering Research Center, University of California, Berkeley, CA.

Roeder, C. W. and Foutch, D. A. (1996). "Experimental Results for Seismic Resistant Steel Moment Frames." *Journal of Structural Engineering*, ASCE, Vol. 122, No. 6, pp. 581-588

Rogec, J. E., Huang, J. S. and Chen, W. F. (1973). "Test of Fully-Welded Beam-to-Column Connections." *Publication No. 188*, Welding Research Council.

SAC Joint Venture (1995). "Interim Guidelines: Evaluation, Repair, Modification and Design of Welded Steel Moment Frame Structures." *Report No. SAC-95-02*, SAC Joint Venture, Sacramento, CA.

SAC Joint Venture (1996a). "SAC Steel Project; The FEMA Program to Reduce the Earthquake Hazards of Steel Moment Frame Structures." SAC Joint Venture, Sacramento, CA.

SAC Joint Venture (1996b). "Interim Guidelines Advisory No. 1. Supplement to FEMA 267." *Report No. SAC-96-03*, SAC Joint Venture, Sacramento, CA.

Steel Committee of Kinki Branch of the Architectural Institute of Japan (1995). "Reconnaissance Report on Damage to Steel Building Structures Observed from the 1995 Hyogoken-Nanbu (Hanshin/Awaji) Earthquake." Architectural Institute of Japan, May.

Structural Stability Research Council (1986). "SSRC Technical Memorandum No. 7: Tension Testing." Structural Stability Research Council, Bethlehem, PA.

Structural Stability Research Council (1987). "SSRC Technical Memorandum No. 8: Standard Methods and Definitions for Tests For Static Yield Stress." Structural Stability Research Council, Bethlehem, PA.

Tagawa, Y., Kato, B., and Aoki, H. (1989). "Behavior of Composite Beams in Steel Frame Under Hysteretic Loading." *Journal of Structural Engineering*, ASCE, Vol. 115, No. 8, pp. 2029-2045.

Tide, R. H. R. (1996). "Stability of Weld Metal Subjected To Cyclic Static And Seismic Loading." *Innovations In Stability Concepts And Methods For Seismic Design In Structural Steel*, U.S./Japan Seminar, Honolulu, Hawaii, July 15-18, 1996.

Tide, R. H. R. (1997). "Experimental Verification of "k"-Area Steel Properties After Cracking Observed." *Innovations in Structural Design: Strength, Stability, Reliability*, Hajjar, J. F. and Leon, R. T. (eds.), Structural Stability Research Council, Bethlehem, PA, pp. 61-71.

Tremblay, R., Tchebotarev, N., and Filiatrault, A. (1997). "Influence of the Loading Rate and the Floor Slab on the Seismic Performance of RBS Connections for Steel Moment Resisting Frames." Proceedings of the Northridge Earthquake Research Conference, Los Angeles, California, August 20-23, 1997, California Universities for Earthquake Engineering Research, Sacramento, CA.

Tsai, K. C. (1988). "Steel Beam-Column Joints in Seismic Moment Resisting Frames." Ph.D. Dissertation, Department of Civil Engineering, University of California, Berkeley, CA.

Tsai, K. C., and Popov, E. P. (1988). "Steel Beam-Column Joints in Seismic Moment Resisting Frames." *Report No. UCB/EERC-88/19*, Earthquake Engineering Research Center, University of California, Berkeley, CA.

Tsai, K. C., Wu, S., and Popov, E. P. (1995). "Cyclic Performance of Steel Beam-Column Moment Joints." *Engineering Structures,* Vol. 17, No. 8.

Uang, C. M. and Bertero, V. V. (1986). "Earthquake Simulation Tests of a 0.3 Scale Model of a Six Story Concentrically Braced Steel Structure." *Report UCB/EERC-86/10*, Earthquake Engineering Research Center, University of California, Berkeley, CA.

Udagawa, K. and Mimura, H. (1991). "Behavior of Composite Beam Frame By Pseudodynamic Testing." *Journal of Structural Engineering*, ASCE, Vol. 117, pp. 1317-1325.

United States Steel (1971). *The Making, Shaping, and Treating of Steel*, 9th Ed., United States Steel Corporation, p. 1240.

Visual Analysis (1994). "User's Manual." Version 2.5, Integrated Engineering Software.

Yang, T. S. and Popov, E. P. (1995). "Behavior of Pre-Northridge Moment Resisting Steel Connections." *Report No. UCB/EERC-95/08,* Earthquake Engineering Research Center, University of California, Berkeley, CA.

Youssef, N. F. G., Bonowitz, D., and Gross, J. L. (1995). "A Survey of Steel Moment-Resisting Frame Buildings Affected by the 1994 Northridge Earthquake." *Rep. No. NISTIR 5625*, NIST, Gaithersburg, MD.